TECHNICAL REPORT SL-86-46

US Army Corps
of Engineers

AD-A181 388

LOADING RATE EFFECTS ON THE ONE-DIMENSIONAL COMPRESSIBILITY OF FOUR PARTIALLY SATURATED SOILS

by

John V. Farr

Structures Laboratory

DEPARTMENT OF THE ARMY
Waterways Experiment Station, Corps of Engineers
PO Box 631, Vicksburg, Mississippi 39180-0631

DTIC
S ELECTE D
JUN 1 5 1987

December 1986
Final Report

Approved For Public Release. Distribution Unlimited

87 5 12 039

STRUCTURES
LABORATORY

Destroy this report when no longer needed. Do not return
it to the originator.

The findings in this report are not to be construed as an official
Department of the Army position unless so designated
by other authorized documents.

The contents of this report are not to be used for
advertising, publication, or promotional purposes.
Citation of trade names does not constitute an
official endorsement or approval of the use of
such commercial products.

REPORT DOCUMENTATION PAGE

1a. REPORT SECURITY CLASSIFICATION	1b. RESTRICTIVE MARKINGS
Unclassified	

2a. SECURITY CLASSIFICATION AUTHORITY	3 DISTRIBUTION / AVAILABILITY OF REPORT
	Approved for public release; distribution
2b. DECLASSIFICATION / DOWNGRADING SCHEDULE	unlimited

4. PERFORMING ORGANIZATION REPORT NUMBER(S)	5. MONITORING ORGANIZATION REPORT NUMBER(S)
Technical Report SL-86-46	

6a. NAME OF PERFORMING ORGANIZATION	6b. OFFICE SYMBOL (If applicable)	7a. NAME OF MONITORING ORGANIZATION
USAEWES Structures Laboratory	WESSD	

6c. ADDRESS (City, State, and ZIP Code)	7b. ADDRESS (City, State, and ZIP Code)
PO Box 631 Vicksburg, MS 39180-0631	

8a. NAME OF FUNDING / SPONSORING ORGANIZATION	8b. OFFICE SYMBOL (If applicable)	9. PROCUREMENT INSTRUMENT IDENTIFICATION NUMBER
See reverse		

8c. ADDRESS (City, State, and ZIP Code)	10. SOURCE OF FUNDING NUMBERS See reverse			
	PROGRAM ELEMENT NO.	PROJECT NO.	TASK NO.	WORK UNIT ACCESSION NO

11 TITLE (Include Security Classification)
Loading Rate Effects on the One-Dimensional Compressibility of Four Partially Saturated Soils

12. PERSONAL AUTHOR(S)
Farr, John V.

13a. TYPE OF REPORT	13b. TIME COVERED	14. DATE OF REPORT (Year, Month, Day)	15. PAGE COUNT
Final report	FROM Mar 85 TO Nov 86	December 1986	373

16 SUPPLEMENTARY NOTATION
Available from National Technical Information Service, 5285 Port Royal Road, Springfield, VA 22161.

17	COSATI CODES		18. SUBJECT TERMS (Continue on reverse if necessary and identify by block number)
FIELD	GROUP	SUB-GROUP	Dynamic soil properties One-dimensional compressibility
			High pressure soil tests Rate-dependent soil behavior
			Loading rate effects Uniaxial strain

19 ABSTRACT (Continue on reverse if necessary and identify by block number)

The one-dimensional or uniaxial strain response of most soils subjected to high-intensity transient loads differs from the response measured under static conditions. As the time to peak pressure decreases, most soils exhibit a stiffening of the stress-strain response. That stiffening is usually referred to as a loading rate effect. Some researchers have suggested that, as the time to peak pressure approaches the submillisecond range, an increase up to fivefold in the modulus occurs. Other researchers have shown no loading rate effects for a soil under uniaxial strain conditions.

In the past, large-scale field tests have been performed to determine uniaxial strain characteristics because existing laboratory devices could only produce and measure the response for supermillisecond rise times. An explosive-loaded uniaxial strain test device was modified and used in this study to obtain submillisecond loading times in the laboratory. The results obtained in this device were supplemented with those from an existing

(Continued)

20 DISTRIBUTION / AVAILABILITY OF ABSTRACT	21. ABSTRACT SECURITY CLASSIFICATION
☒ UNCLASSIFIED/UNLIMITED ☐ SAME AS RPT ☐ DTIC USERS	Unclassified
22a. NAME OF RESPONSIBLE INDIVIDUAL	22b. TELEPHONE (Include Area Code) 22c. OFFICE SYMBOL

DD FORM 1473, 84 MAR   83 APR edition may be used until exhausted.   SECURITY CLASSIFICATION OF THIS PAGE
All other editions are obsolete.

8a. & c. NAME OF FUNDING/SPONSORING ORGANIZATION/ADDRESS (Continued).

DEPARTMENT OF THE ARMY, US Army Corps of Engineers, Washington, DC 20314-1000, and
Defense Nuclear Agency, Washington, DC 20305-1000.

10. SOURCE OF FUNDING NUMBERS (Continued).

Department of the Army Project No. 4A161102AT22, Task BO, Work Unit 005, and DNA Task RSRB,
Work Unit 00058.

19. ABSTRACT (Continued).

state-of-the-art uniaxial strain device to obtain measurements of loading rate effects for
rise times to peak pressure ranging from submilliseconds to minutes.

Test results at pressures typically on the order of 10,000 psi (69 MPa) at strain
rates up to 100 percent/msec were obtained for four soils--two clean sands, a clayey sand,
and a silty clay. These test results showed that a drastic stiffening did not occur in
the submillisecond range. Instead, a gradual stiffening occurred. The maximum ratio of
the measured dynamic-to-static modulus was approximately 2. Based upon these test results,
a strain-rate and strain-level dependent modulus stiffening model was developed. This
model was implemented into a one-dimensional plane wave propagation computer code to pre-
dict the results of field tests that were performed on two of the soils tested in this
study. A comparison between the laboratory-based model predicted behavior and the response
obtained from the field events agreed favorably. This comparison provided verification of
the laboratory results and interpretation techniques.

PREFACE

The work reported herein was sponsored by the Office, Chief of Engineers, US Army, under Project No. 4A161102AT22, Task BO, Work Unit 005, "Constitutive Properties for Natural Earth and Man-Made Materials," and the Defense Nuclear Agency, under DNA Task RSRB, Work Unit 00058, "Test Equipment and Techniques."

This report was prepared by Mr. John V. Farr of the Geomechanics Division (GD), Structures Laboratory (SL), US Army Engineer Waterways Experiment Station (WES). It is essentially his thesis submitted to the University of Michigan in partial fulfillment of the requirements for the degree of Doctor of Philosophy in Civil Engineering. Responsibility for coordinating this program was assigned to Dr. J. G. Jackson, Jr., Chief, GD. The test results presented herein were obtained with the assistance of GD personnel and the Instrumentation Services Division. Classification and index tests were conducted by personnel of the Soils Testing Facility, Soil Mechanics Division, Geotechnical Laboratory. The petrographic analysis was performed by personnel of the Petrographic Unit of the Materials and Concrete Analysis Group, SL.

COL Allen F. Grum, USA, was the previous Director of WES. COL Dwayne G. Lee, CE, is the present Commander and Director. Dr. Robert W. Whalin is Technical Director. Mr. Bryant Mather is Chief, SL.

1

A-1

TABLE OF CONTENTS

LIST OF FIGURES

v

LIST OF TABLES

CONVERSION FACTORS, NON-SI TO SI (METRIC)
UNITS OF MEASUREMENTS

Non-SI units of measurement used in this report can be converted to SI (metric) units as follows:

Multiply	By	To Obtain
degrees (angle)	0.01745329	radians
feet	0.3048	meters
gallons (US liquid)	3.785412	cubic decimeters (litres)
inches	25.4	millimeters
kips (force)	4.448222	kilonewtons
kips (force) per square inch	6.894757	megapascals
megatons (nuclear equivalent of TNT)	4.184	petajoules
pounds (force) per square inch	6.894757	kilopascals
pounds (mass)	0.4535924	kilograms
pounds (mass) per cubic foot	16.01846	kilograms per cubic meter

LOADING RATE EFFECTS ON THE ONE-DIMENSIONAL COMPRESSIBILITY
OF FOUR PARTIALLY SATURATED SOILS

CHAPTER I

INTRODUCTION

1.1 Background

Soil mechanics involves the study of soil behavior, including the
interpretation of stress-strain and strength data for soils, and its
application to the solution of real-world problems comprising a variety
of loading and boundary configurations. Soil dynamics is a branch of
soil mechanics that deals with the effects of short duration loadings
on the stress-strain and strength characteristics. The field of soil
dynamics addresses problems such as earthquakes, machine vibrations,
pile driving, explosions, etc. One of the prime areas of research
within this field deals with the stress-strain characteristics of soils
subjected to explosively induced loads. Before World War II, research
in this area was basically directed toward predicting ground motions
induced by mining and blasting. World War II brought the use of large
conventional explosives and the advent of nuclear weapons, and
considerable research effort has been directed toward explosively
induced ground motions ever since. Predicting ground motions is
important because the physical devastation created by a nuclear
explosion necessitates that protective structures (silos, shelters,
etc.) be located underground to protect personnel, equipment, and
supplies.

Brode (1964) lists nine interrelated phenomena associated with a nuclear explosion:

1) fireball growth

2) thermal radiation

3) nuclear radiation

4) electromagnetic radiation

5) cratering and ground shocks from cratering

6) airblast

7) ground shock (airblast-induced)

8) cloud rise, fallout, and debris

9) fires

This report will be restricted to ground shock phenomena. Some excellent references that present in detail the effects associated with a nuclear detonation are in a United States Atomic Energy Commission (USAEC) publication entitled, "The Effects of Nuclear Weapons," a Defense Atomic Support Agency publication entitled, "Nuclear Geoplosics, A Sourcebook of Underground Phenomena and Effects of Nuclear Explosions," and an Air Force Weapons Laboratory publication entitled, "The Air Force Manual for Design and Analysis of Hardened Structures."

For detonations near the ground surface or in the ground, a substantial portion of the energy released is transferred directly to the soil. Ground motions induced by this process are termed directly induced ground motions. Energy also appears in the form of an air shock, which induces ground motions by imposing normal pressures and horizontal shear forces on the ground surface. Ground motions induced

by this process are termed <u>airblast-induced</u> <u>ground</u> <u>motions</u>. These general features are shown in Fig. 1.1.1. The directly induced ground motions are critical for design of buried structures only in the region near the explosion. At some distance from the explosion, the major input to the ground motions will be airblast-induced. Airblast-induced ground motions are especially critical for the design of structures which must be buried at shallow depths for economical or operational reasons.

As an airblast sweeps out over the soil surface, large areas are effectively loaded instantaneously. This concept is illustrated in Figs. 1.1.2 and 1.1.3. The laboratory test that most accurately approximates these conditions is referred to as the one-dimensional compression or uniaxial strain test. The applicability of the one-dimensional compression test in simulating the loading and boundary conditions of an airblast-induced loading has been studied in detail by many researchers (see Whitman, 1963, 1970, and Crawford, et al., 1974).

The motions and stresses experienced by a shallow buried structure due to airblast-induced loadings are a function of the deformability of the structure and the surrounding soil. How the induced stress waves deform the soil and the interaction of these waves with the structure are obviously complex problems in soil dynamics and soil-structure interaction. Numerous techniques ranging from simplified static procedures (see Wilson and Sibley, 1962, and Merritt and Newmark, 1964) to complex finite element methods (FEM) and finite difference techniques are used to analyze the stresses and motions. All of these methods require the one-dimensional compression
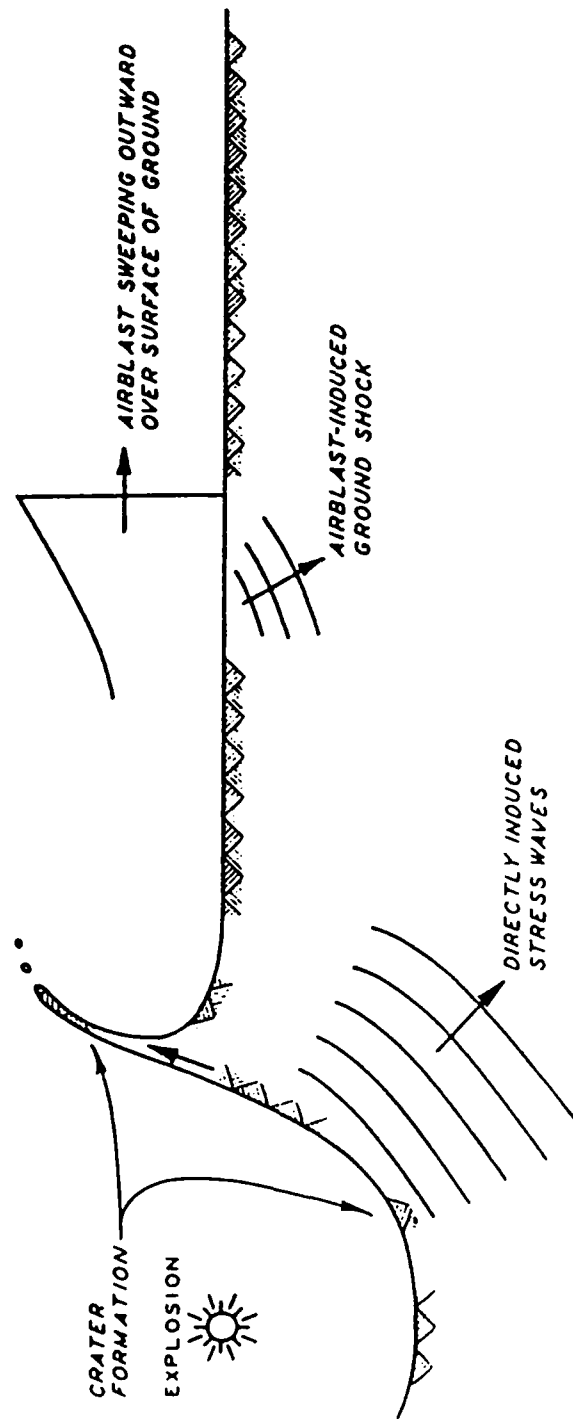
Figure 1.1.1 General features associated with a near-surface nuclear explosion (from Whitman, 1970).
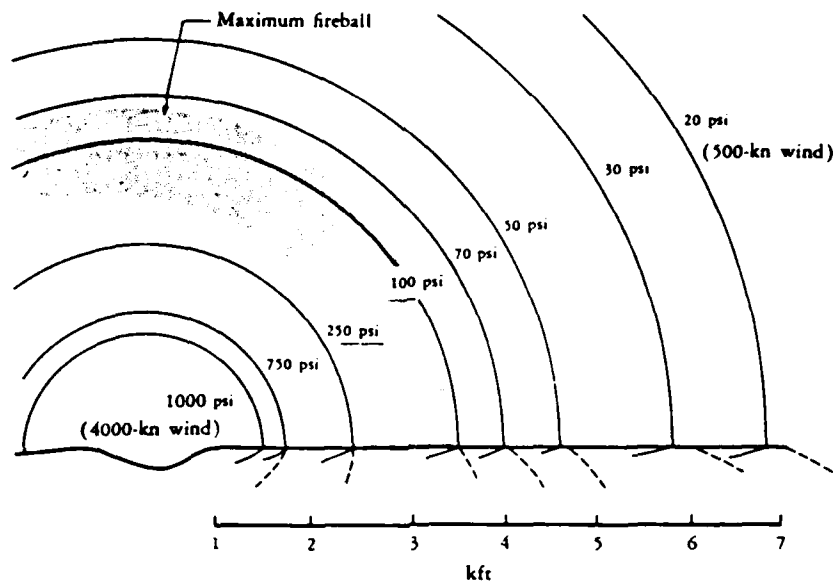
Figure 1.1.2   Distance to various peak overpressures for a
1-MT surface explosion (from Brode, 1964).
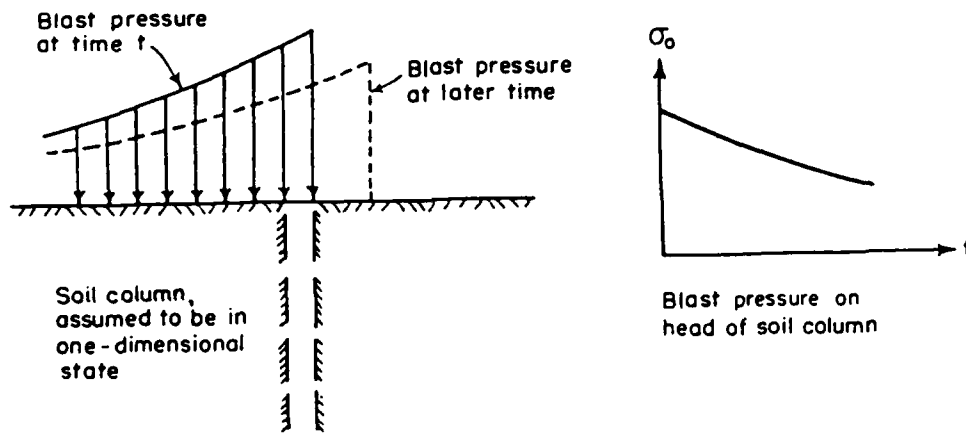
Figure 1.1.3   Moving airblast demonstrating one-dimensionality
(from Whitman, 1963).

characteristics of the surrounding soil as major input into their respective analysis schemes.

In the past, scaled field tests using conventional explosives have been used to model nuclear blasts. Aboveground nuclear tests cannot be performed under the provisions of the Nuclear Test Ban Treaty. From these conventional field events, representative one-dimensional compression characteristics are determined. Unfortunately, there are three major problems associated with using field events to determine one-dimensional compression characteristics:

1) Scaled field tests are expensive, so soil can not be subjected to true one-dimensional plane wave conditions except at shallow depths and for short durations.

2) The one-dimensional compression characteristics measured are only valid for the loading rate generated by the field event.

3) The use of soil stress and strain gauges are themselves complex soil-structure interaction problems.

The cost of performing a field test at each potential site of an underground defense-related structure makes this type of testing cost prohibitive. Laboratory techniques have been developed to simulate the boundary conditions (tens-of-thousands of psi pressure) associated with nuclear and/or large conventional explosions; however, the state-of-the-art has prohibited reproducing the associated rise times (less than a millisecond to peak pressure) and accurately measuring and interpretating the results. In the past, the response has been extrapolated into the submillisecond range based upon slower test results.

As the rise time to peak pressure decreases, the one-dimensional response is apparently affected. This is known as a loading rate

effect or time rate effect. Some researchers have speculated and/or published results that this loading rate effect can produce a drastic stiffening (an initial dynamic-to-static modulus of 10 or greater) if the time to peak pressure is less than a millisecond (see Whitman, 1970, and Jackson, et al., 1979). Some researchers have also published results showing that loading rate effects can generally be ignored for some sands (Felice, et al., 1985). Thus, loading rate effects aren't clearly understood either quantitatively or qualitatively.

If accurate mathematical models are to be developed to predict the one-dimensional compression characteristics over a wide range of loading rates, then the magnitude of this effect must be measured under controlled laboratory loading conditions. Mathematical models can then be developed and implemented into a variety of analysis schemes to accurately predict the soil and soil-structure interaction problems associated with the design of underground protective structures from the effects of near-surface nuclear or large conventional explosions.

1.2 Purpose and Scope

There exists a need to develop techniques for testing, modeling, predicting, and verifying the predictions of the one-dimensional compression characteristics of soils subjected to airblast-induced loadings. Loading rate effects are an important part of developing an accurate model. This report addresses loading rate effects for four soil types; including two clean sands, a clayey sand, and a silty clay. All four soils tested were essentially dry (i.e., the degree of saturation of the test specimens was relatively low), so compressibility

was governed by the soil skeleton and not by pore water. Laboratory measurements of the one-dimensional compression characteristics (stress-strain curves) of these four soils were made at a wide variety of loading rates, including rise times to the peak pressure of less than a millisecond. From these laboratory measurements, a loading rate dependent model was developed. Also, the effects of water content and density upon the magnitude of the loading rate effects for the silty clay will be addressed.

Three of the four soils tested were chosen because of their use as backfill materials during field events and their behavior has been well documented. For two of the four soils, a clean sand and the silty clay, recent field events have been conducted in which the one-dimensional compression characteristics were determined. These one-dimensional compression results are compared to those predicted by the laboratory-based rate dependent model to access the accuracy of the laboratory measurements, the procedures for interpreting the data, and the adequacy of the rate dependent model.

To determine loading rate effects associated with these four soils, a device having the capability to produce large transient pressures (thousands-of-psi) with fast rise times to peak stress (less than a millisecond) had to be developed. Also, computer techniques to interpret the submillisecond test results and a representative mathematical model had to be developed. This model was implemented into a computer code to reproduce the field events for comparison against the actual field results.

Chapter II provides background information relevant to one-dimensional compression and loading rate effects. A detailed explanation of one-dimensional compression along with the configuration and history of the device used to determine one-dimensional compression characteristics is presented. In addition, the physical mechanisms that would explain the existence of loading rate effects are presented.

Chapter III describes the details of the device that was developed to obtain one-dimensional compression characteristics of soil subjected to large transient loadings similar to those produced during a nuclear or large conventional explosion. Details concerning the load application systems, measuring systems, testing procedures, and the problems encountered during development of the device are presented.

Chapter IV summarizes the results of 93 one-dimensional compression or uniaxial strain tests performed on four soils at a variety of loading rates. Detailed material properties and grain crushing characteristics are presented for the four soils tested.

Test results obtained for stress pulses with rise times to peak pressure of less than about 1 msec can be affected by nonuniformities in stress and strain over the height of the sample due to wave propagation. Interpreting the true stress-strain behavior from these tests requires the use of a wave propagation analysis technique. Chapter V describes the factors that can affect uniaxial strain test measurements, including nonuniform stress and strain, and a wave propagation analysis scheme used to deduce the true material response.

Chapter VI presents the loading rate dependent model. A strain-level and strain-rate dependent constrained modulus model is presented with coefficients determined from the test results presented in Chapter IV. Also, the applicability of a stress-rate dependent constrained modulus model and the potential for extending the results to a three-dimensional state will be addressed.

In Chapter VII, results obtained using the rate dependent model are compared with actual measurements obtained from high-explosive field events involving two of the four soils tested.

Chapter VIII shows the use of computer programs, the rate dependent model, and other data interpretation techniques described in Chapters V and VI to reanalyze some existing work that has been published relative to laboratory measurements of loading rate effects. The discrepancies between the results contained herein and those published results are addressed.

Lastly, Chapter IX presents the summary, conclusions, and recommendations for further research. Appendices presenting some of the techniques and computer programs used in interpretating the test results are presented. Also, the individual laboratory test results summarized in Chapter IV along with the one-dimensional wave propagation simulations of the submillisecond results discussed in Chapter V are presented as Appendices.

CHAPTER II

UNIAXIAL STRAIN TESTING FOR GROUND SHOCK PROBLEMS

2.1 Introduction

In one-dimensional compression, all motion takes place in one direction. From a continuum mechanics viewpoint, the term uniaxial strain is a more accurate descriptor of the loading conditions and boundary configuration. Henceforth, the term uniaxial strain will be used to describe one-dimensional compression. Figure 2.1.1 shows the measurements, loading conditions, boundary configuration, and data interpretation associated with the uniaxial strain test.

As illustrated in Fig. 2.1.1, the sample is assumed to be loaded uniformally and deflect a uniform amount. As the pressure is applied as a function of time, $P(t)$, the surface deflection, $\triangle H(t)$, is recorded. Oil is used to transmit pressure from the load application system to the sample surface. Depending upon the loading rate, the axial stress, σ , within the soil sample may be uniform and equal to the pressure in the oil. Also, depending upon the loading rate, the axial strain, ϵ_z , may be uniform throughout the sample and equal to $\triangle H/H$. Depending upon the time to peak pressure and the wave propagation velocity of the soil, stress and strain may not be uniform over the thickness of the sample. Nonuniform stress and strain

11
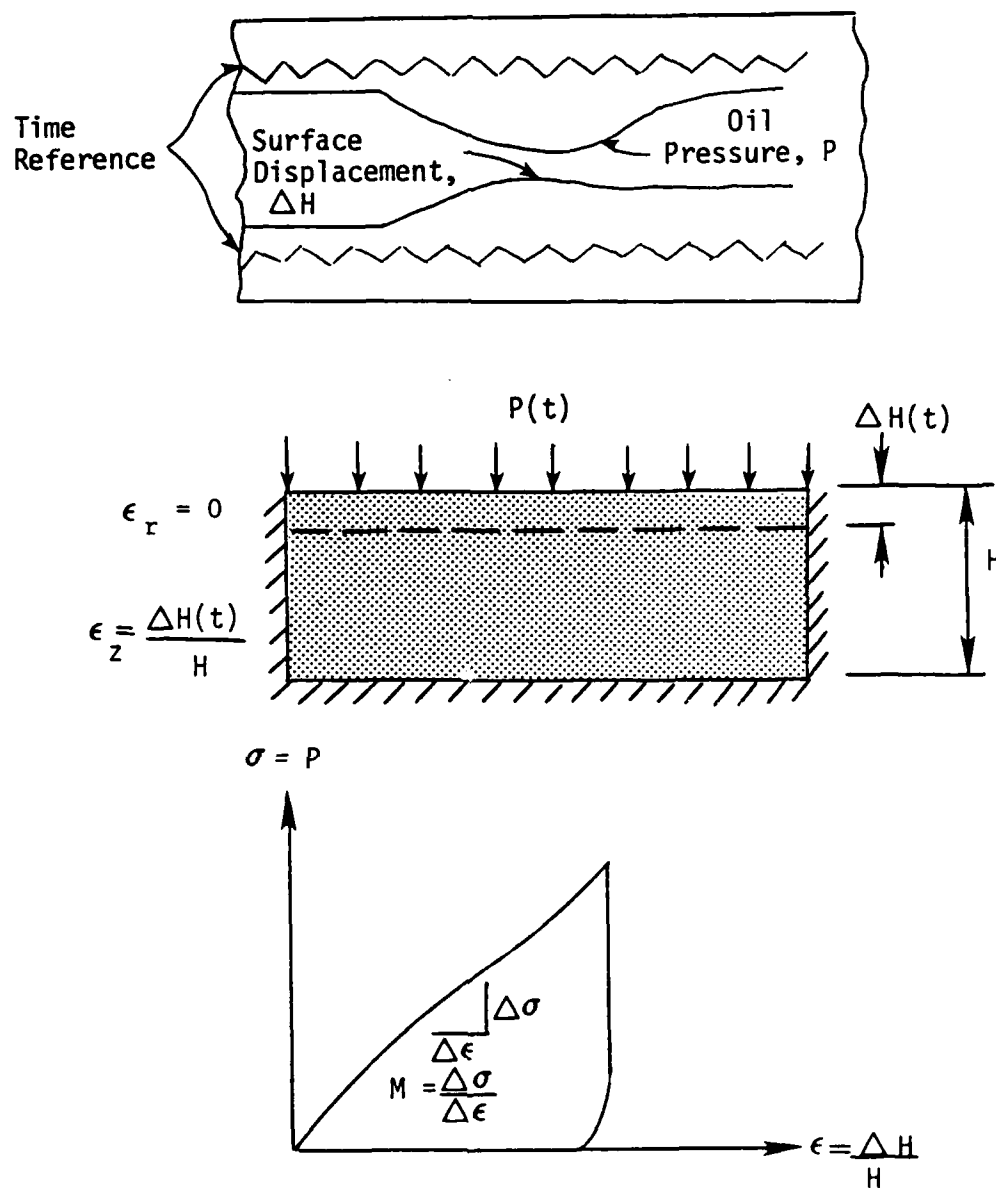
Figure 2.1.1 Measurements, boundary conditions, and data
interpretation for uniaxial strain tests
(after Jackson, et al., 1979).

conditions within a sample due to wave propagation effects are referred to as inertia effects.

Methods other than the uniaxial strain test can be used to indirectly measure the response when inertia enters the problem, and these methods are described in Section 2.2. Interpretation of uniaxial strain test results when inertia effects produce nonuniformities in stress and strain are also addressed in Section 2.2.

The uniaxial strain device was first adapted to weapons effects testing by Whitman (MIT, 1959). Subsequent improvements have been made to the original design by a number of groups. Massachusetts Institute of Technology (Moore, 1963, and Whitman, 1963), Stanford Research Institute (Seaman, 1966), Eric H. Wang Civil Engineering Research Facility of the University of New Mexico (Calhoun and Kraft, 1966), Waterways Experiment Station (Schindler, 1968, and Akers, et al., 1986), and Applied Research Associates, Inc., (Blouin, et al., 1984) are some of the many organizations that have uniaxial strain devices. All of these devices have the same two basic components; a soil container and a pressurized fluid loading container. These two components are bolted together to form a uniaxial strain device. Figure 2.1.2 shows the first device developed by Whitman (MIT, 1959) and these two basic components. Few changes have been made to this configuration. Most advances have been made in the areas of data acquisition, measurement systems, load application devices, and higher pressure capabilities.
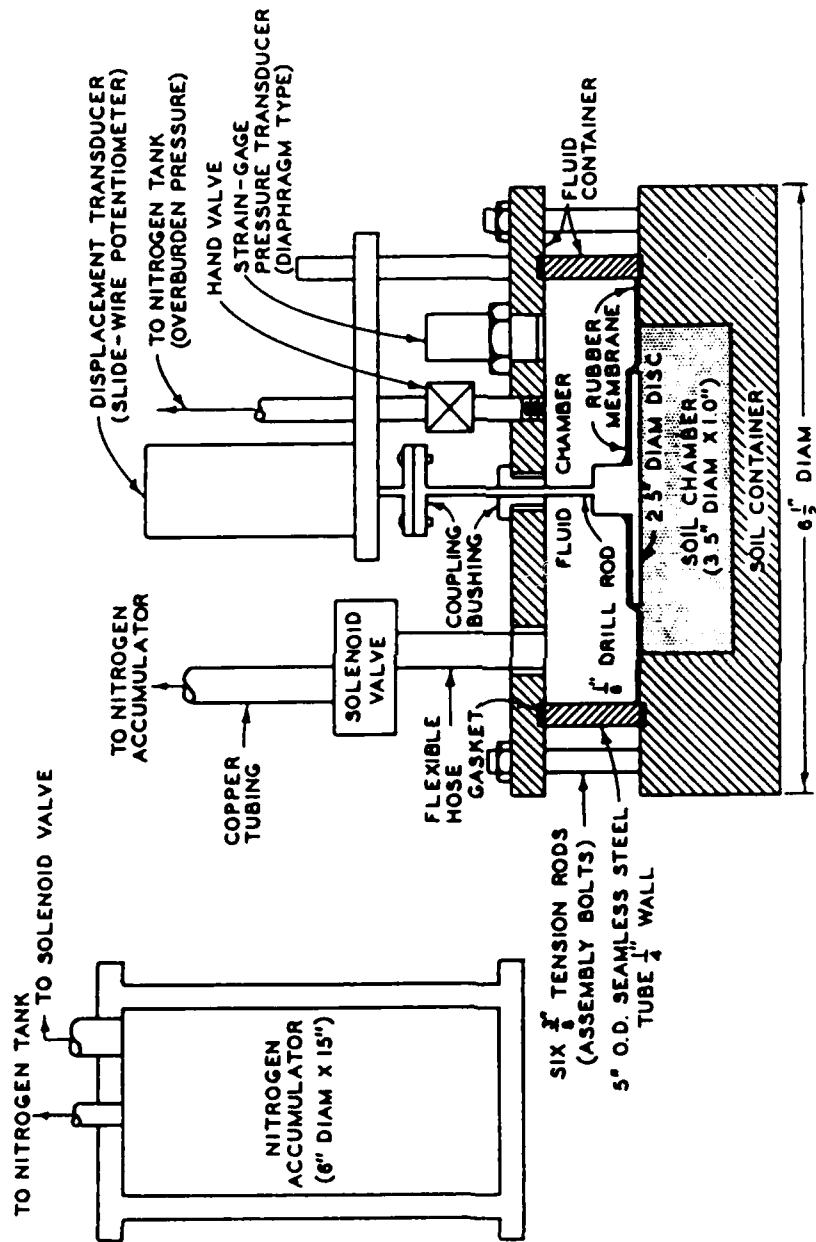
Figure 2.1.2 First uniaxial strain device for weapons effects testing (from MIT, 1959).

Dynamic tests will be defined throughout this text as tests having a rise time to peak pressure of less than 1 sec. The first extensive study of dynamic one-dimensional compressibility was reported by Whitman in 1963. The dynamic uniaxial strain test device used in this study is shown in Figure 2.1.3. This device used an internal displacement transducer and was capable of producing test results with rise times to peak pressure from 15 to 40 msec. At these rise times, inertia problems did not affect the test results.

The physical behavior of soil under uniaxial strain conditions is important to understanding the mechanisms contributing to loading rate effects. Section 2.3 discusses the compositional factors that affect the deformation characteristics of soil. Also, the potential mechanisms that could contribute to a loading rate effect are addressed.

Section 2.4 will address the state-of-the-art in uniaxial testing. Items such as existing devices, load application systems, measurement and data acquisition systems, and devices under development will be described. This section serves a two-fold purpose. First, the existing state-of-the-art is presented to show the capabilities and limitations of existing devices and load application systems. Secondly, most of the equipment described in this section was used to generate portions of the data in this report.
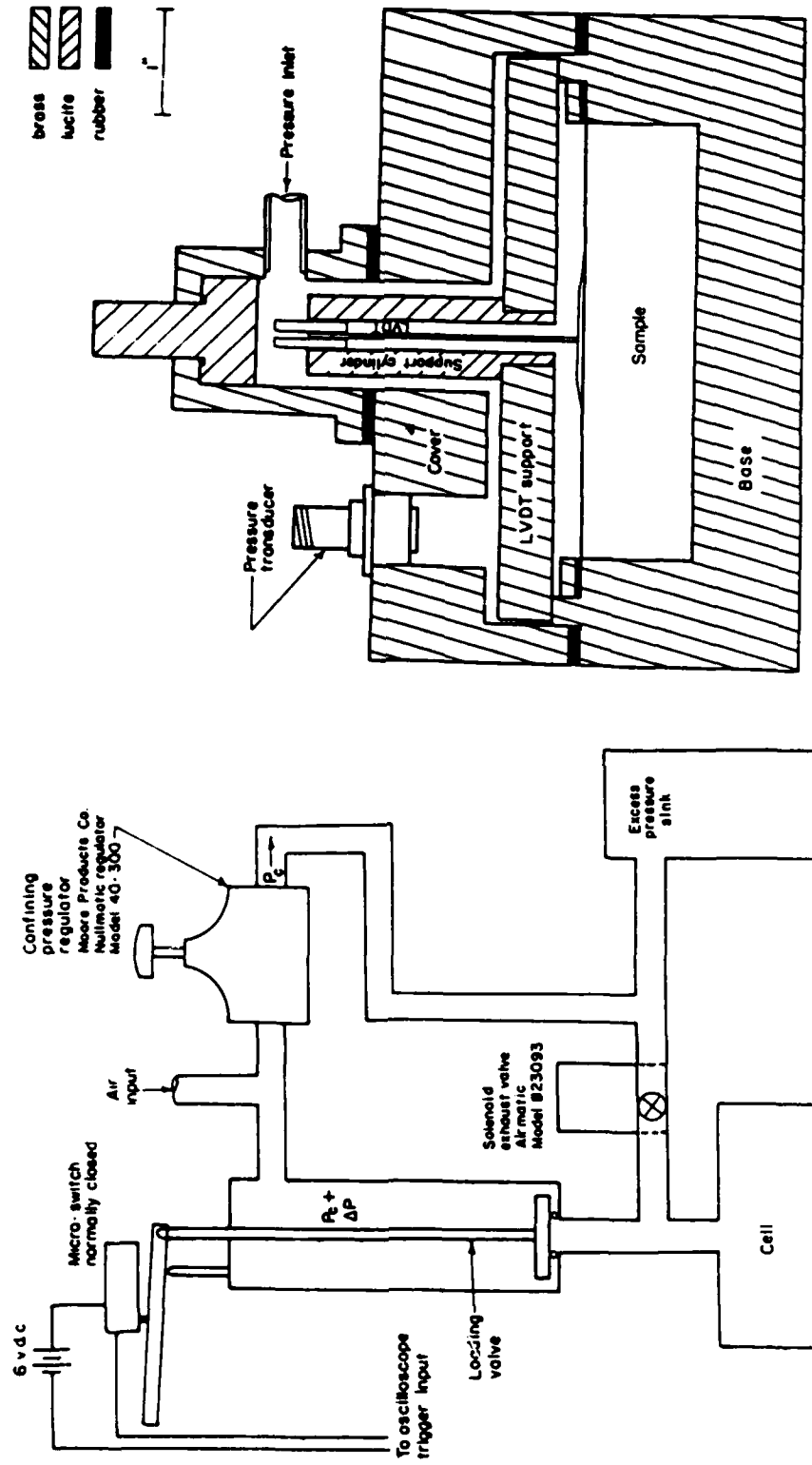
Figure 2.1.3 Dynamic uniaxial strain device (from Whitman, 1963).

2.2 Testing Techniques

If inertia stresses are not a factor (i.e., slow loading rates),
uniaxial strain test devices similar in design to those by Whitman can
be used to determine the one-dimensional compression characteristics of
soil. However, if the loading pulse is applied fast enough such that
inertia stresses enter the problem, several indirect techniques must
be used to determine the true uniaxial strain response. Many of these
techniques are used by various research organizations, with each having
its own merits and disadvantages. This section is presented because
some of these devices have produced results contradicting those
reported herein.

The testing technique that seems the most appropriate involves
using some type of wave propagation experiment. Numerous researchers
have employed this method. Long slender samples of soil are loaded and
radial strain prohibited. Stress and/or strain gauges are embedded in
the sample as shown in Figure 2.2.1. Using the wave propagation
results, stress-strain properties can be determined. There are three
main problems associated with this type of test. First, a long slender
specimen must be used. This restricts testing to remolded samples.
Ideally, the specimen should be long enough for the entire applied
pulse to propagate past an instrumented section before the reflected
pulse returns to that section. These devices typically require samples
that are on the order of tens-of-feet in length. Secondly, sidewall
friction is a major concern in these devices. Teflon tracks (Baker,
1967), greased membranes (Hadala, 1967), membrane-contained fluid
chambers (Zaccor, et al., 1964), segmented rings
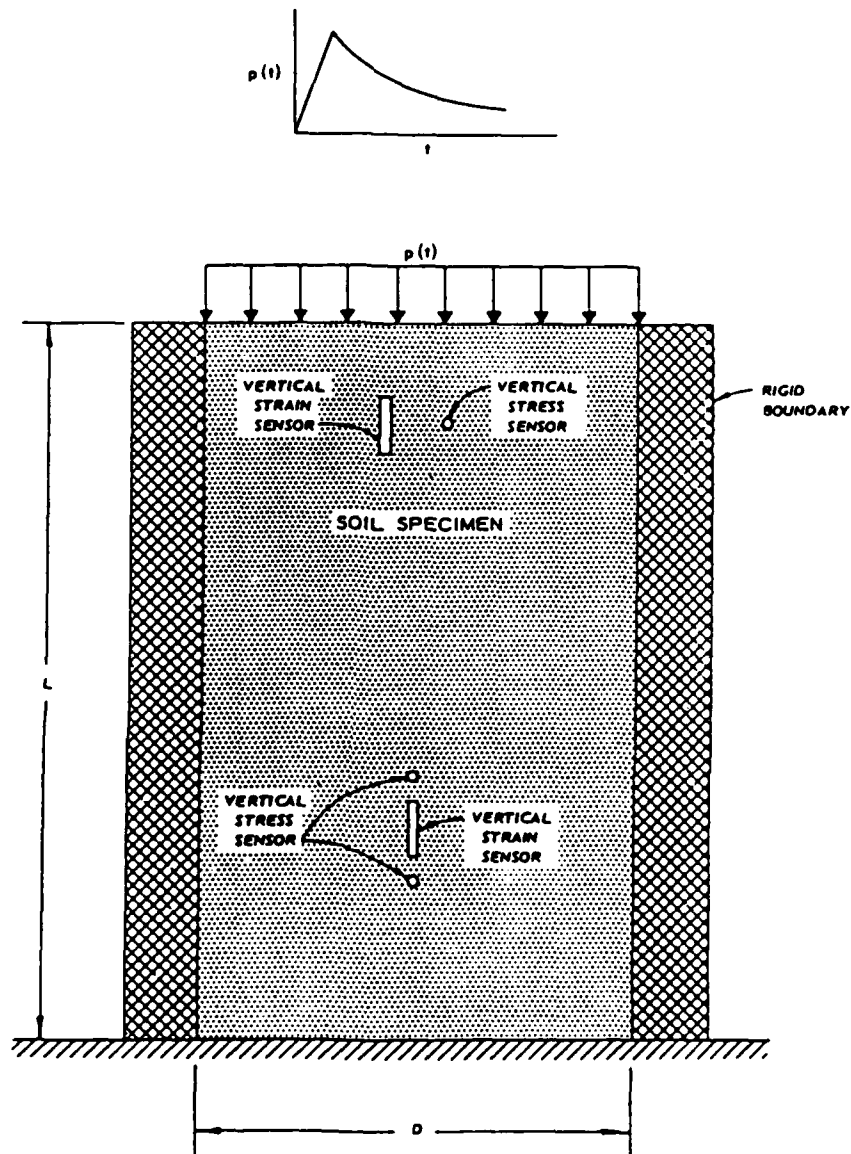
Figure 2.2.1 Sketch depicting characteristics of wave propagation testing technique (from Schindler, 1969).

(Seaman, et al., 1963), etc., are just some of the techniques that have been used to reduce sidewall friction. Most of these techniques allow some lateral strain to occur. Lastly, embedding some type of measuring gauge in the soil sample creates numerous problems. Placement of the gauge creates significant sample disturbance. Problems are also created with arching and acoustic impedance mismatch at the gauges.

Another technique that has recently been adopted to soils involves the use of a split-Hopkinson bar or Kolsky apparatus (Felice, et al., 1985). The device was orginally developed to measure wave propagation properties in solids and is shown in Fig. 2.2.2. In the split-Hopkinson bar, a striker bar is accelerated by using energy stored in a spring or gas gun. When the striker bar impacts the incident bar, constant amplitude compression pulses are generated in the striker bar and incident bar. When the pulse reaches the specimen, part of the pulse is reflected and a portion transmitted to the sample. By tracking the stress pulse, stress-strain characteristics can be determined (see Smith and Glover, 1985, and Zukas, et al., 1982). This device can be used to achieve a _nearly_ uniaxial state of strain by placing the soil sample in a rigid confining ring. Numerous problems are encountered with this type of system. Gaffney, et al., (1985) addresses some of these problems. The major obstacle concerns placing the sample in the device. Testing a cohesionless soil creates problems since a binder isn't present that will allow the sample to hold a vertical face. Also, as the striker bar impacts the sample, material is lost from the end of the containing ring. In addition, the low wave speed and high stress attenuation associated with soil requires that
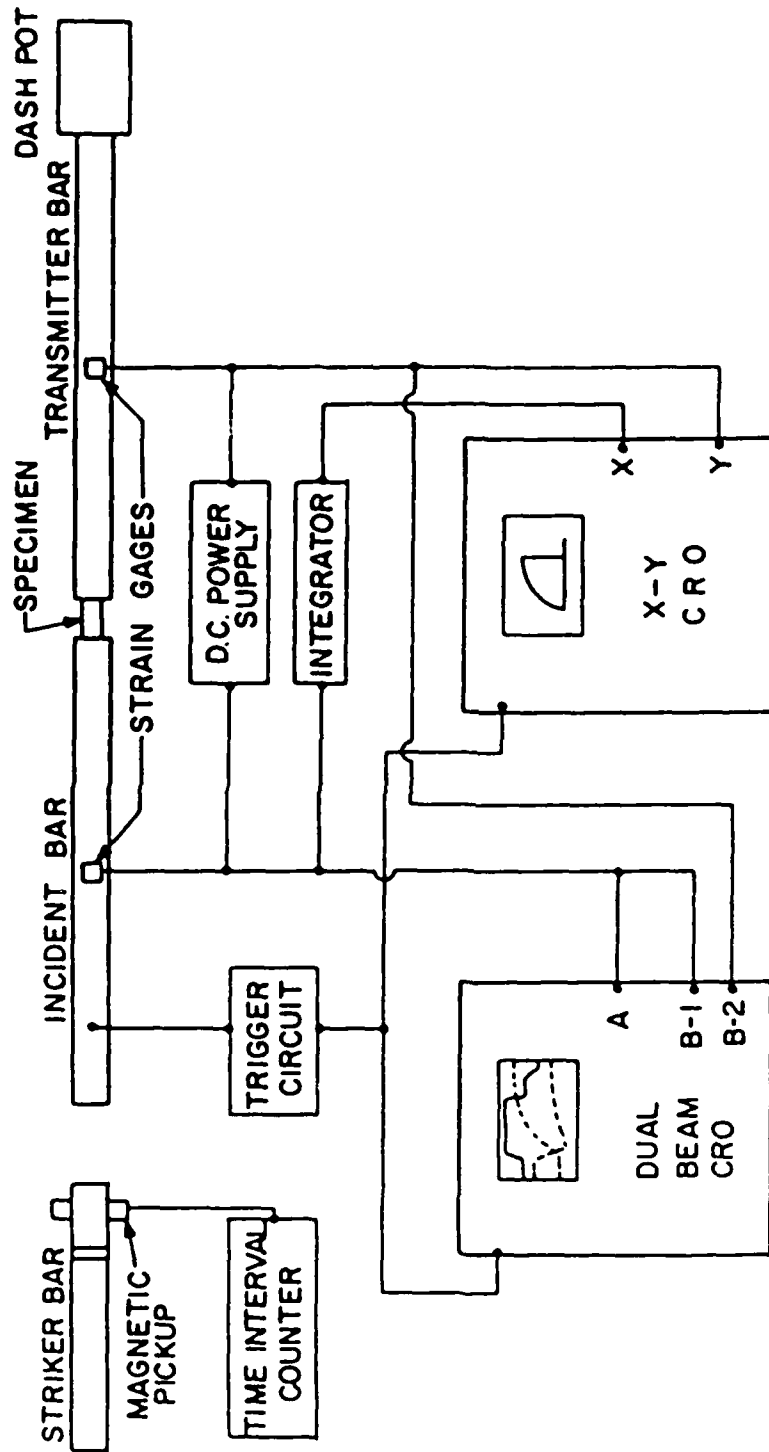
Figure 2.2.2 Schematic of apparatus and instrumentation for compression split-Hopkinson bar (from Zukas, et al., 1982).

thin samples be used. Another problem associated with the device is created by an impedance mismatch between the soil and incident bar. Large stress waves must be imparted by the striker bar to produce significant strain since most of the stress pulse is reflected by the impedance mismatch. Felice, et al., (1985) reported a series of tests on a compacted sand at a variety of loading rates without recording any significant loading rate effects using the split-Hopkinson bar.

The technique that has enjoyed the most popularity involves the use of very thin samples in a uniaxial strain device. When a stress pulse propagates through the soil specimen, the wave is reflected by the rigid steel base of the soil container, returning as a compression wave. When this compression wave strikes the upper soil surface, the stress wave is reduced to the pressure in the oil and sends a rarefaction wave back into the soil (Seaman, 1983). If the pressure is applied slowly, say several milliseconds, the compression and rarefaction waves carry small increments of stress. Thus, the soil is essentially in a uniform state of stress equal to the pressure in the hydraulic fluid and the strains are uniform over the depth of the sample. However, if pressure is applied very rapidly, say 0.1 milliseconds, uniform states of stress and strain do not exist in the sample and the measured pressures and deflections at the sample surface are not representative of the true material response. The implications of nonuniform stress and strain are illustrated in Fig. 2.2.3. The measured strain appears to lag behind the measured stress at the start of the test. This can create the appearance of a significant rate effect for the initial portion of the material response. This
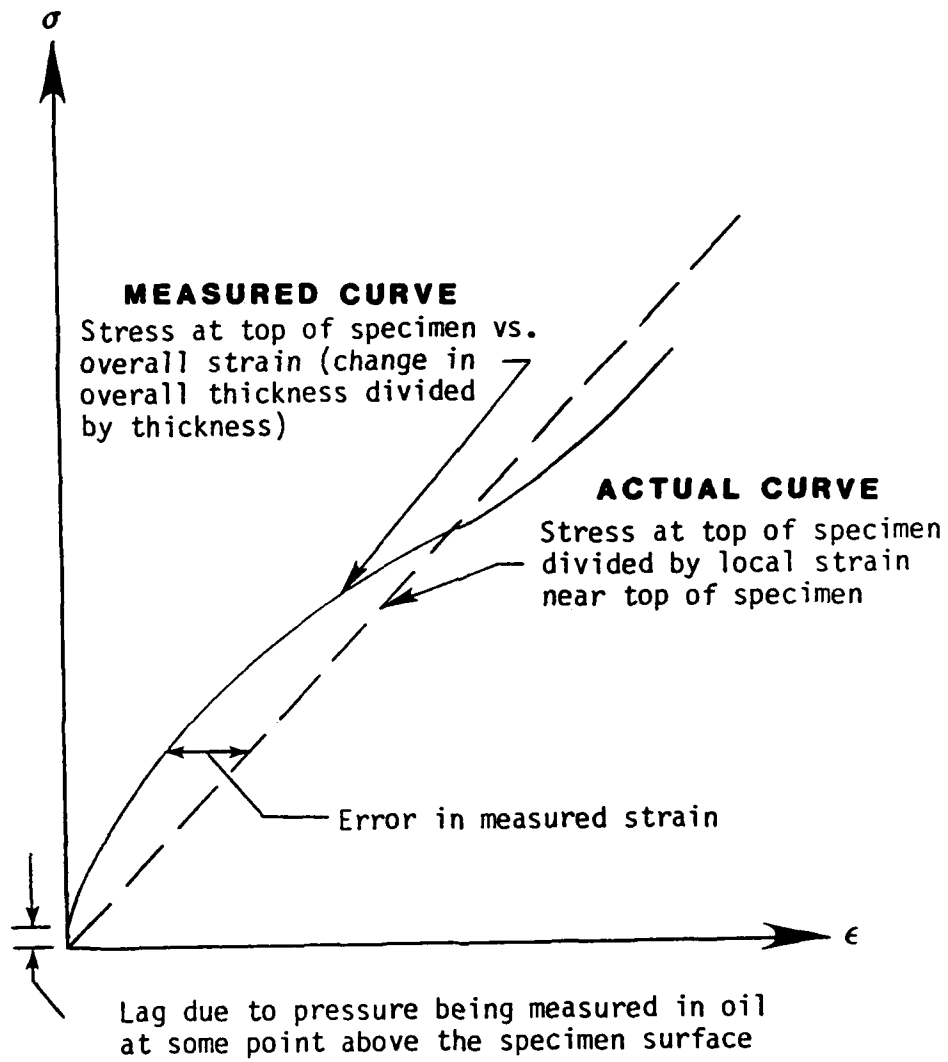
Figure 2.2.3 Actual and apparent stress-strain curve using the multiple reflection technique (after Whitman, 1963).

situation arises because the test system measures stress at some point
above the sample in the hydraulic fluid, but strain is averaged over
the depth of the sample.

Whitman (1963) popularized a technique referred to as the
multiple reflection technique that takes into account inertia effects
during uniaxial testing. This technique involves using thin samples to
minimize the travel time of the wave. Thus, each stress wave carries a
small increment of stress, and stress and strain are essentially
uniform over the height of the sample. However, at some point, the
error induced by inertia effects and the constraints on sample size
produce unacceptable errors.

Other techniques exist to measure one-dimensional compression
characteristics, but are not as popular as those presented. Schindler
(1969) presents a discussion of some of these techniques along with the
advantages and limitations of each.

2.3 Soil Behavior Under Uniaxial Strain Conditions

Soil is a three-phase system consisting of solid, liquid, and
gas. The solids are usually inorganic; the liquid, water; and the gas,
air. Under uniaxial strain loading, soils exhibit hysteresis,
viscosity, and nonlinearity. A stress-strain curve for a dry or
partially saturated soil during unloading will not follow the same path
during reloading. Thus, the soil exhibits hysteresis. Soil also
exhibits viscosity under uniaxial strain loading conditions in the form
of creep and loading rate effects. Lastly, soils are nonlinear at
almost any stress level. The amount of hysteresis, viscosity, and

nonlinearity depends on the characteristics of the applied load, the boundary conditions, and the physical characteristics of the soil mass. Given that a soil mass is a combination of discrete particles, nonhomogenous, and anisotropic, it takes little imagination to realize the complexity of trying to accurately predict the behavior of a soil mass under uniaxial strain conditions with a simple mathematical model.

One can say with a great deal of certainty that soils will exhibit nonlinearity and hysteresis during loading and unloading. However, the problem of viscosity isn't clearly understood. The problem of creep of cohesive soils has been extensively studied. Numerous rheological representations exist to model creep behavior. However, viscosity in the form of a loading rate effect was addressed by Whitman (1963), but hasn't been extensively studied due to the specialized nature of the application of the results.

In a uniaxial strain device the boundary conditions are known, as are the characteristics of the applied load. Therefore, the physical characteristics of the soil should control the response. Mitchell (1976) describes nine environmental and compositional factors (physical characteristics) of a soil that control their compression characteristics:

1) Physical interactions; including bending, sliding, rolling and crushing of soil particles.

2) Physical-chemical interactions in the form of particle surface forces.

3) Chemical and organic environment that can create cementing agents or affect surface forces and water absorption properties.

4) Mineralogical details of the soil solids.

5) Fabric and/or structure, whether the structure is flocculated or dispersed.

6) Stress history, the amount of overconsolidation.

7) Temperature of the sample.

8) Pore water chemistry can affect the interparticle forces.

9) Stress during loading and unloading.

The potential mechanisms for loading rate effects are numerous. Whitman (1959) suspected that a loading rate effect existed in his pioneering work in the field of ground shock studies but didn't offer a general explanation describing the mechanisms. Schindler (1968), in his work at WES in developing their first uniaxial strain device, presented arguments trying to justify the existence of a rate effect phenomenon. Schindler theorized that, "grains can be arranged differently during densification; pore fluids under pressure can flow and transfer additional load to the structural skeleton; interaction amongst the three phases which comprise the soil mass can take several forms; the amount of pore air fluid can be dissolved in the pore is time sensitive; etc." Of these potential mechanisms, particle rearrangement seems to be the major contributor to a loading rate effect, especially for dry or minimally saturated granular materials. As shown in Figure 2.3.1, the initial response of the soil is dictated by elastic deformations at the contact points. The particles then rearrange due to slippage at the contact points at higher stress levels. If the soils cannot rearrange into a denser configuration because the load is being applied too rapidly, the load will be absorbed by deformation of the soil particles instead of the soil
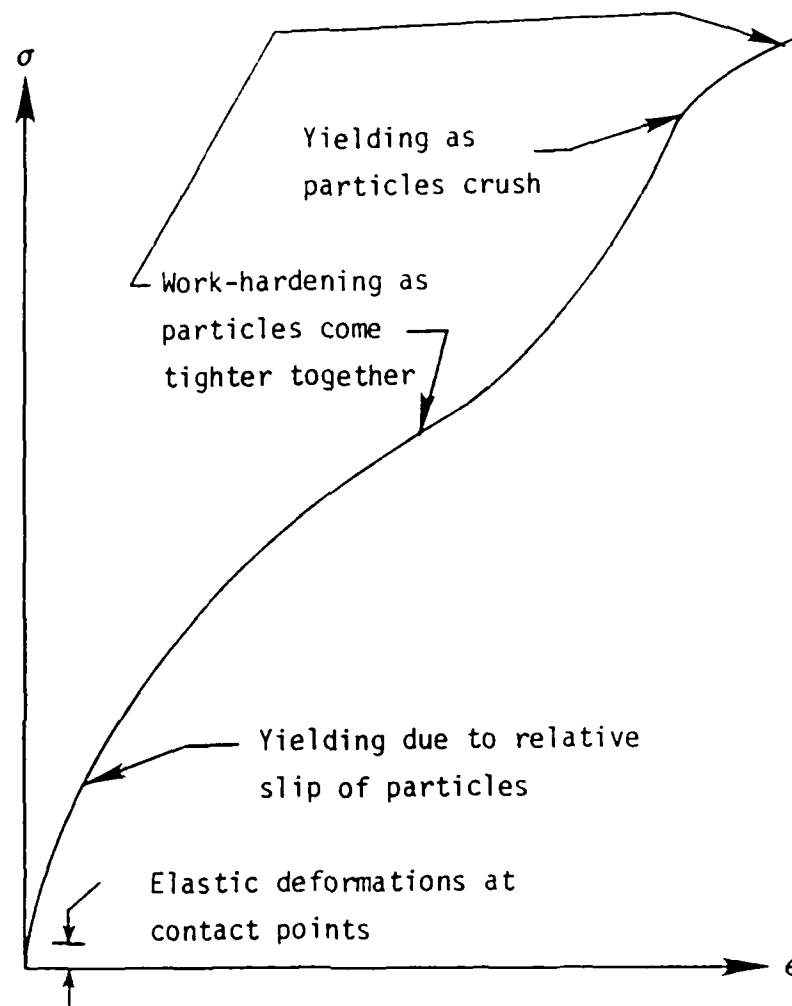
Figure 2.3.1 Uniaxial strain compressibility for a particulate
mass (after Whitman, 1964).

matrix. This would result in an apparent stiffening of the soil. This is the same basic concept used to describe creep. The longer the load is held constant the more particle slippage and rearrangement occurs, resulting in strain at a constant stress level.

2.4 State-of-the-Art in Uniaxial Strain Testing

As previously discussed, the basic configuration of the uniaxial strain device has remained unchanged. Advances have been made in the areas of load application systems, higher pressure devices, miniaturization of electronics, and data measurement and acquisition systems.

Two uniaxial strain devices were used in this study to define loading rate effects for a wide variety of load application rates. A device referred to as the WES 0.1-msec device was used to obtain data with rise times to peak pressure of less than about 1 msec. Modifications to this device also allowed for static testing. Since development of this device was a major part of this dissertation and hasn't been documented, an entire chapter, Chapter III, has been devoted to describing the details of the device, the load application system needed to obtain submillisecond rise times, and the data measurement and acquisition systems. For rise times to peak pressure from about 3 msec to several hundred seconds, a state-of-the-art production uniaxial strain device was used. The device is shown in Figure 2.4.1 and is referred to as the PPUX device for its pore pressure measuring capabilities. This device is described in detail by Akers, et al., (1986). Briefly, the device has a specimen cavity 0.90-
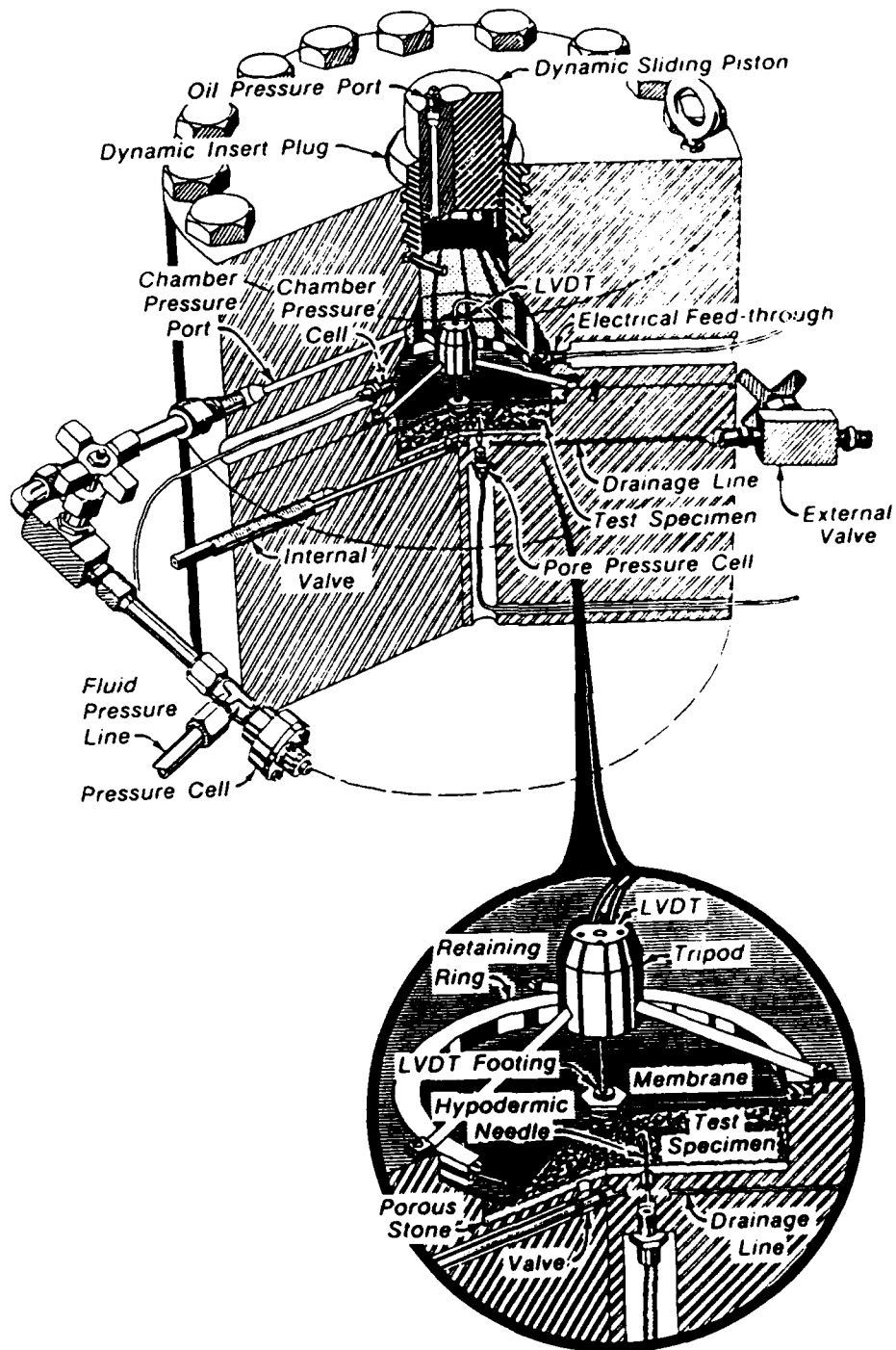
Figure 2.4.1 Production uniaxial strain test device
(from Akers, et al., 1986).

in (2.29-cm) high and 3.8 in (9.65 cm) in diameter. Like most uniaxial devices, this device has an upper and lower assembly. The upper assembly contains the loading piston, fluid chamber, pressure cell, electrical feed-through, and a chamber pressure port. The lower assembly contains the specimen cavity, back pressure saturation and pore pressure measuring capabilities, vertical displacement measuring device, and an external drainage valve. These items are labeled on Fig. 2.4.1. The PPUX device uses a linear variable differential transformer (LVDT) to measure vertical displacements as shown in Fig. 2.4.1. A miniature flush-mounted pressure cell is used to measure fluid pressure in the hydraulic oil. Pore pressure measurements and back pressure saturation capabilities were not utilized. When assembled, the device stands 13-in (33-cm) high, is 14.5 in (36.8 cm) in diameter, and weighs 489 lbs (222 kg). The large mass of the device minimizes deflections and increases its pressure capabilities. The maximum working pressure for this device is approximately 14,500 psi (100 MPa).

For the test results contained in Chapter IV, some modifications were made to the PPUX device. A 0.4-in (1.02-cm) plug was inserted into the base so that the specimen was 0.5-in (1.27-cm) high for all tests except the coral sand. This was done because the WES 0.1-msec device has a 0.5-in- (1.27-cm-) high specimen cavity. Laboratory experiments have shown that sample height will affect the measured stress-strain response at very high pressures due to sidewall friction (Farr, 1986). Also, during testing, all external drainage valves on the PPUX device were closed to assure an undrained state existed. Though

probably insignificant, these modifications were made to ensure the PPUX and WES 0.1-msec devices were as identical as possible.

A load application system must be used to apply a force to the loading piston to produce a pressure in the hydraulic oil to load the sample surface. For static testing, a pneumatic load application system similar to the one used by Whitman in 1959 was used. A schematic of this system is shown in Fig. 2.4.2. This system provides a maximum pressure of 8,000 psi (55 MPa) and is capable of producing rise times to peak pressure from about 3 seconds to in excess of several minutes.

A more advanced loading system was needed to produce dynamic loading rates for a variety of rise, dwell, and decay times. A gas-driven, ram-operated loader was developed to apply a variable peak force and to control the rise, dwell, and decay times (Cunny and Sloan, 1961). This device was capable of applying a controlled dynamic axial force up to 50,000 lbs (225 kN); with rise times to peak load of approximately 3 to 150 msec, load hold times of 0 to 1,000 msec, and decay times from 20 msec to 10 sec. Two additional ram-type loaders were subsequently developed, a 100,000-lb (450-kN) loader described by Ehrgott and Sloan (1971) and a 500,000-lb (2250-kN) loader. These gas-driven loading systems were used in this study to apply dynamic loadings with rise times to peak pressure in the supermillisecond range for the results contained in Chapter IV. These stress-controlled, ram-type loaders can also be used for static testing. Photographs of the three loaders are shown in Figs. 2.4.3 thru 2.4.5.
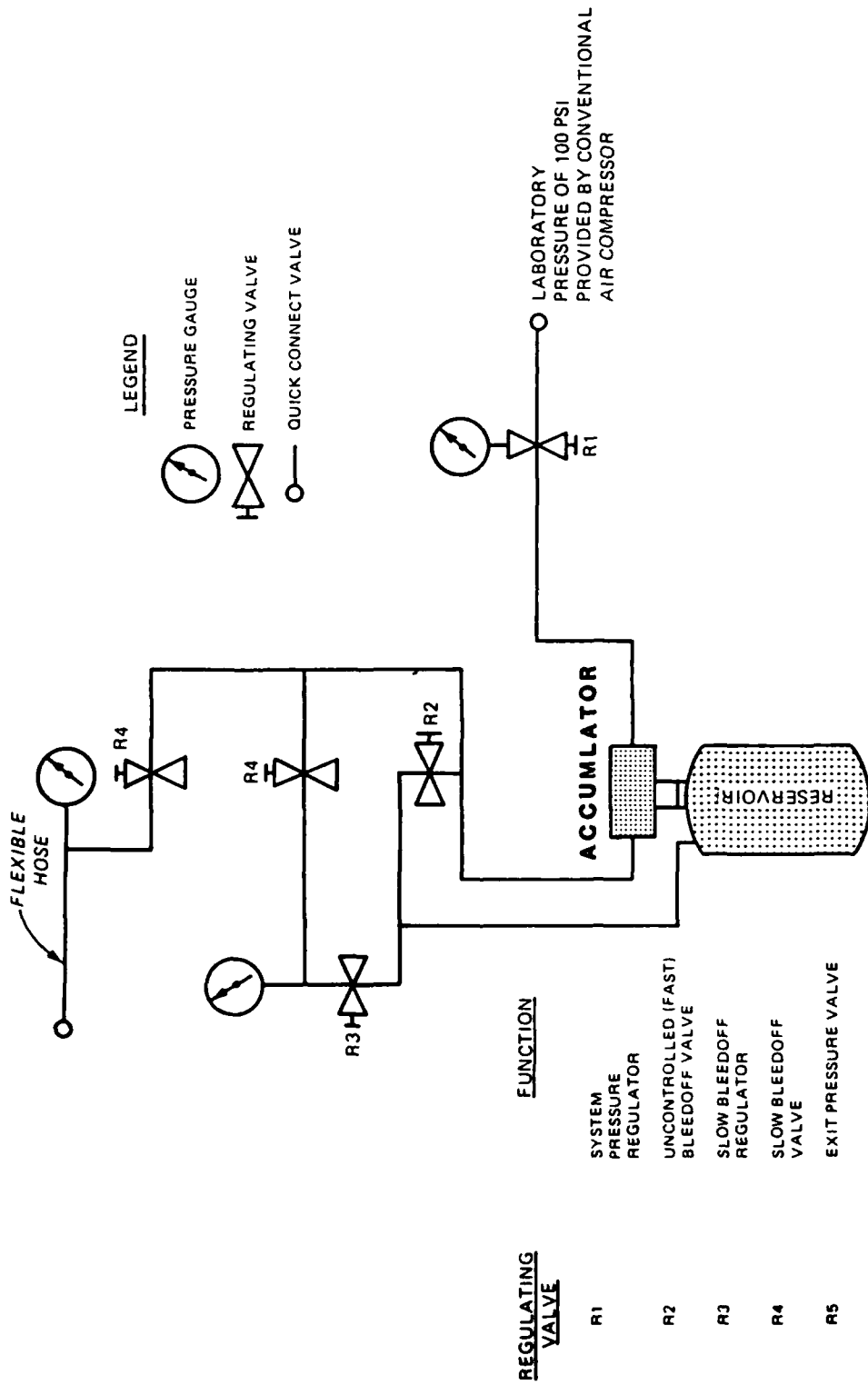
Figure 2.4.2 Pneumatic load application system used to provide pressure for static testing.
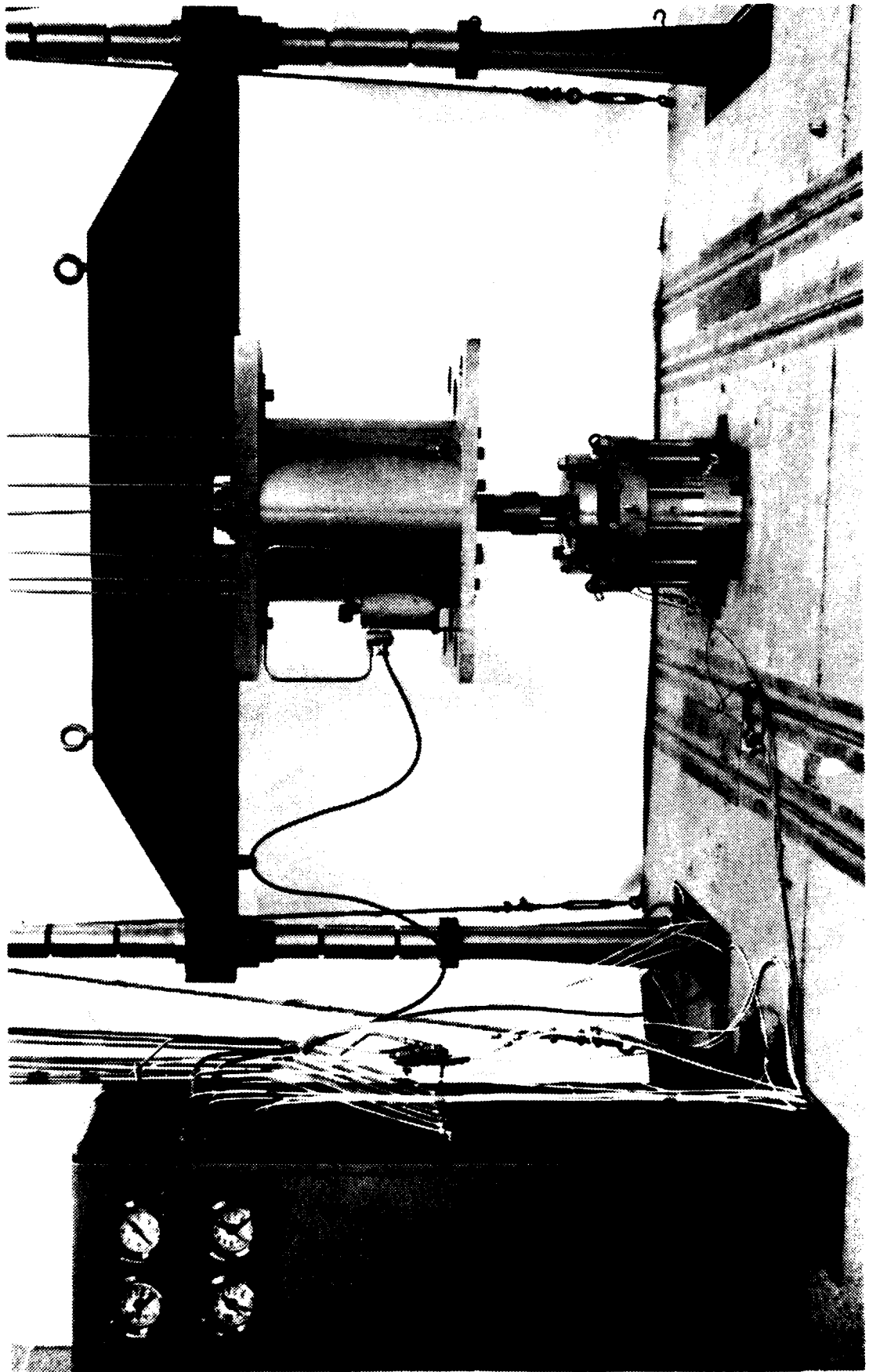
Figure 2.4.3 Photograph of the 50,000-lb (225-kN) ram-type loader.
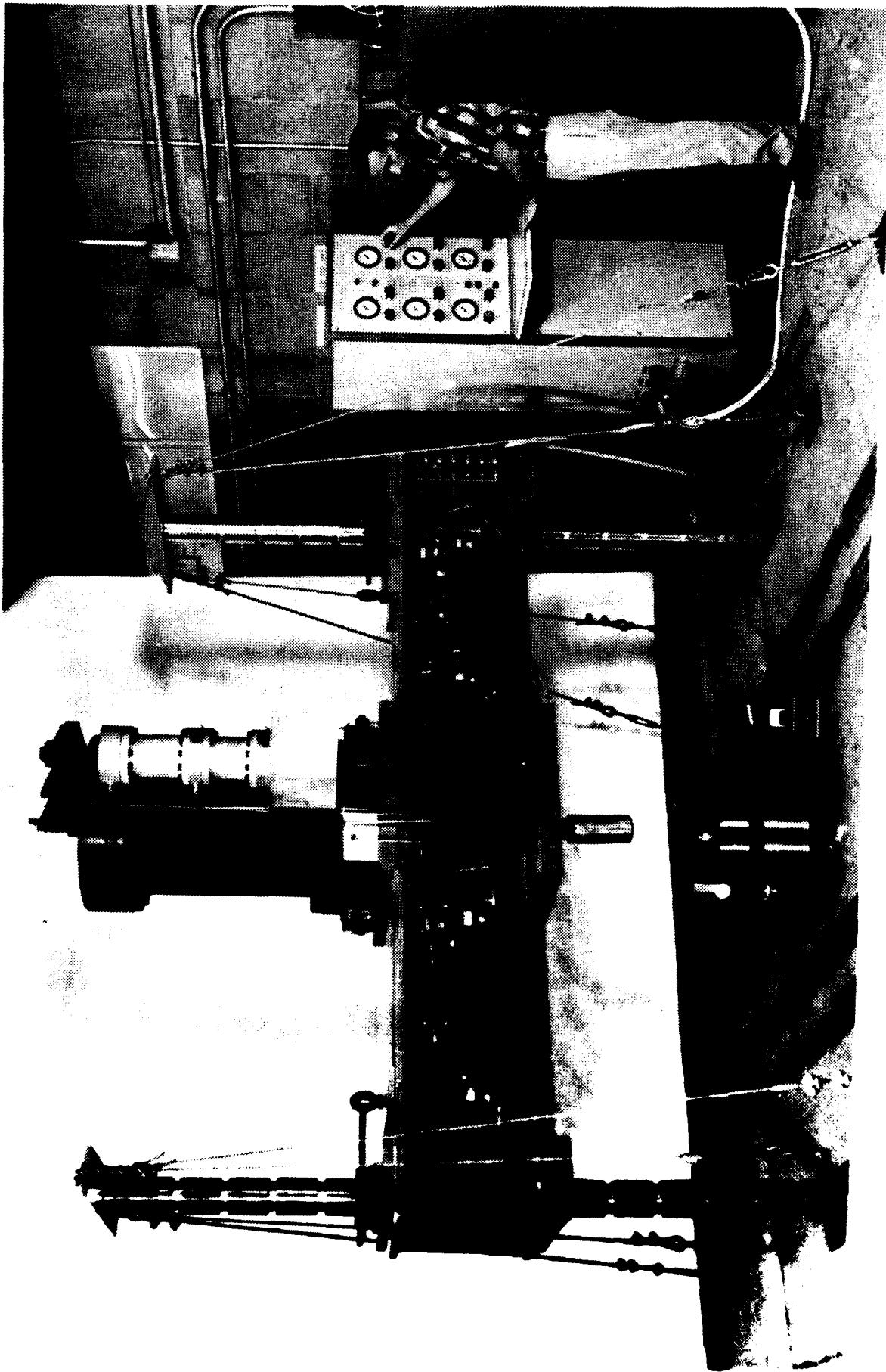
Figure 2.4.4 Photograph of the 100,000-1b (450-kN) ram-type loader.
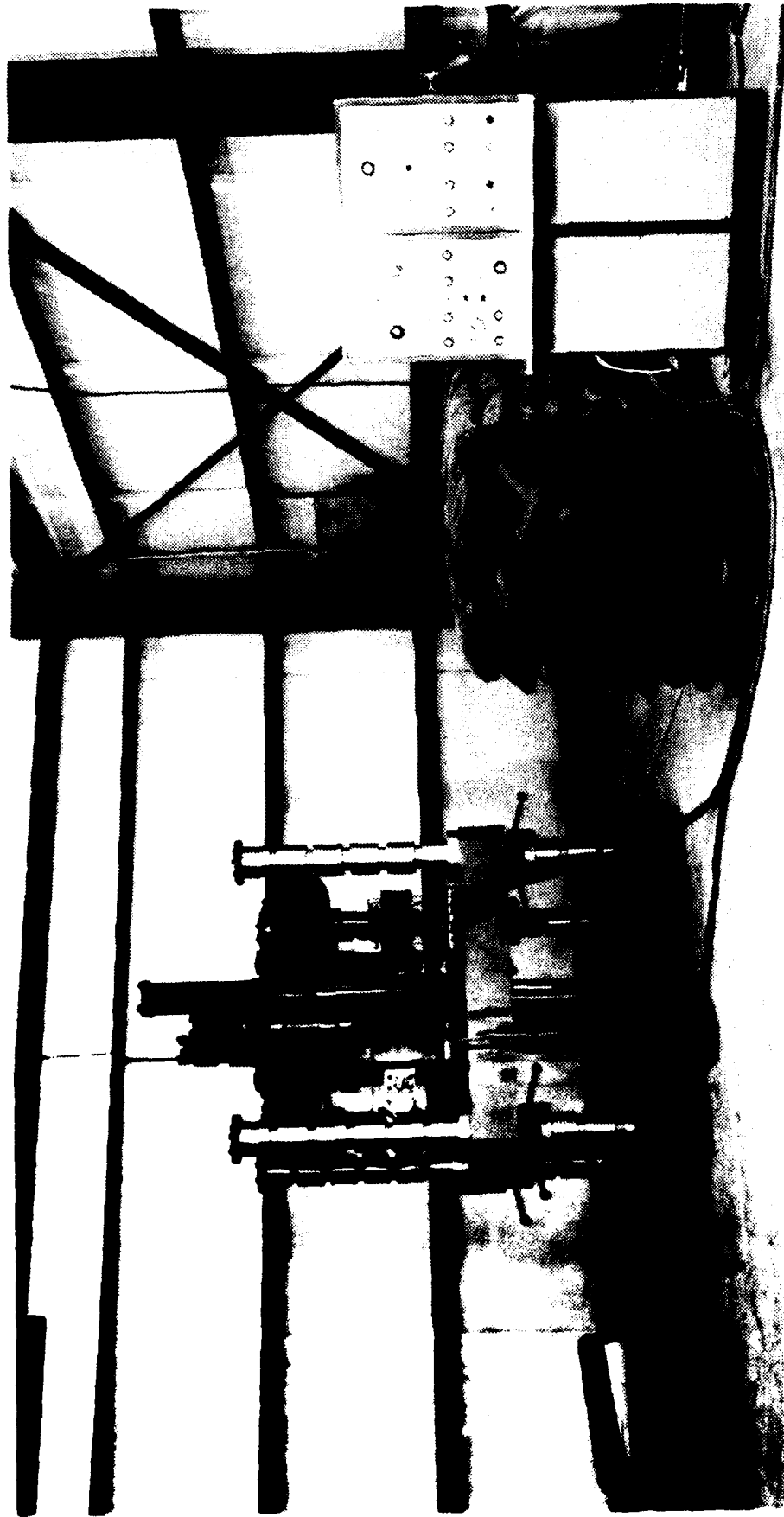
Figure 2.4.5 Photograph of the 500,000-lb (2,250-kN) ram-type loader.

Several different data acquisition systems are available at WES. Two systems were used for the tests performed in the PPUX system. Three analog signals, vertical stress and deformation and a time reference, were recorded using an analog to digital (A/D) convertor with a digital computer. Also, the millivolt readings were recorded on magnetic tape for backup. A computer program was used to process and plot the test data. This system allows the engineer to view the test results within a few minutes of completion of the test in report ready format. The PPUX device used as part of this test program and the associated load application systems and data measurement and acquisition systems are the state-of-the-art in uniaxial strain testing.

CHAPTER III

DESCRIPTION OF THE WES 0.1-MSEC UNIAXIAL STRAIN DEVICE

AND SUPPORT SYSTEMS

3.1 Introduction

This chapter is devoted to describing the apparatus and data
measurement and acquisition systems used in obtaining uniaxial strain
data with a rise time to peak pressure of less than 1 millisecond.
This device is referred to throughout this text as the WES 0.1-msec
device.

Numerous uniaxial strain devices have been developed at WES and
other organizations, but until J. Q. Ehrgott developed an explosive-
loaded device in 1977 none of these devices could produce rise times to
peak pressure into the submillisecond range and measure the response.
Ehrgott used the explosive-loaded device in 1978 to produce the first
set of submillisecond uniaxial strain test results at WES. Testing in
the submillisecond range is important to verify whether, in that range,
the stress-strain characteristics of soil are drastically affected as
speculated by some researchers (see Whitman, 1970 and Jackson, et al.,
1979).

The WES 0.1-msec device described herein is the second generation of Ehrgott's orginal submillisecond device. The major difference in the two devices is the method used to measure axial deformations. The first device used a linear variable differential transformer (LVDT) to measure axial deformation. This device is shown in Figure 3.1.1. The second generation device uses a variable impedance transducer or proximeter to measure axial deformations.

The first generation device had four main problems:

1) The support tripod shown in Figure 3.1.1 could have prevented a planar compression wave from loading the sample surface uniformly.

2) The LVDT footing mass could have prevented the footing from tracking the displacement.

3) The large pressures produced by the explosive sources often destroyed the LVDT.

4) The signal conditioning equipment for the LVDT was at the state-of-the-art, and its response and measuring capabilities could not be verified.

The second generation device was designed by Ehrgott to eliminate these problems by using a proximeter to measure axial deformations. The proximeter was mounted in the base of the sample mold beneath the soil sample. A thin aluminum disk having a diameter of 1.5 in (3.81 cm) and with a mass of 6 grams is placed on the sample surface to serve as a target for the proximeter. Reducing the mass of the measuring system helps to eliminate the problem of tracking the surface displacement during dynamic testing. The proximeter also eliminated the need for the support tripod, allowing a planar compression wave to uniformly load the sample surface. The proximeter can also withstand larger dynamic pressures than an LVDT and is not subject to damage at
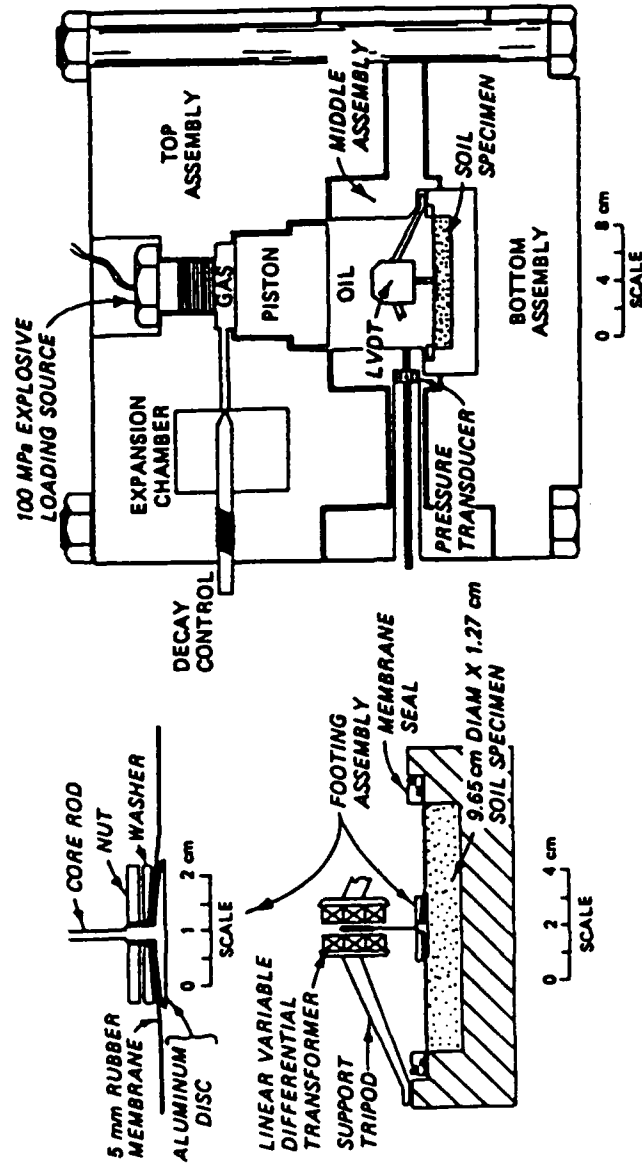
Figure 3.1.1 First generation explosively-loaded uniaxial strain device (from Jackson, et al., 1979).

the stress levels generated within this device. Lastly, the proximeter samples at a higher frequency than the LVDT and is therefore more suited to dynamic measurements.

In addition to describing the details of the WES 0.1-msec device, the data measurement, signal conditioning, and data acquisition systems will be presented. Also, factors such as irregular surface pressure, sidewall friction between the soil sample and the walls of the specimen cavity, radial expansion of the device, and waves propagating through the device instead of through the loading piston can affect the assumption of one-dimensionality. Each of these factors is a function of the design of the device. A discussion of how each of these factors affects the condition of one-dimensionality within the WES 0.1-msec device will be presented. Lastly, the capabilities and limitations of the device will be discussed.

3.2   Device Configuration

The WES 0.1-msec device was designed, machined, and developed at WES. Figure 3.2.1 shows a schematic of the assembled device. A photograph of the assembled device is shown in Fig. 3.2.2. The device has two main components, the upper and lower assemblies. These components are shown in Figures 3.2.1 thru 3.2.6. Figures 3.2.7 thru 3.2.10 present the details of the miscellaneous components associated with the upper and lower assemblies. Both the upper and lower assemblies and their components, with the exception of the loading piston, were machined from 300 Series stainless steel. The loading piston was machined from conventional steel.
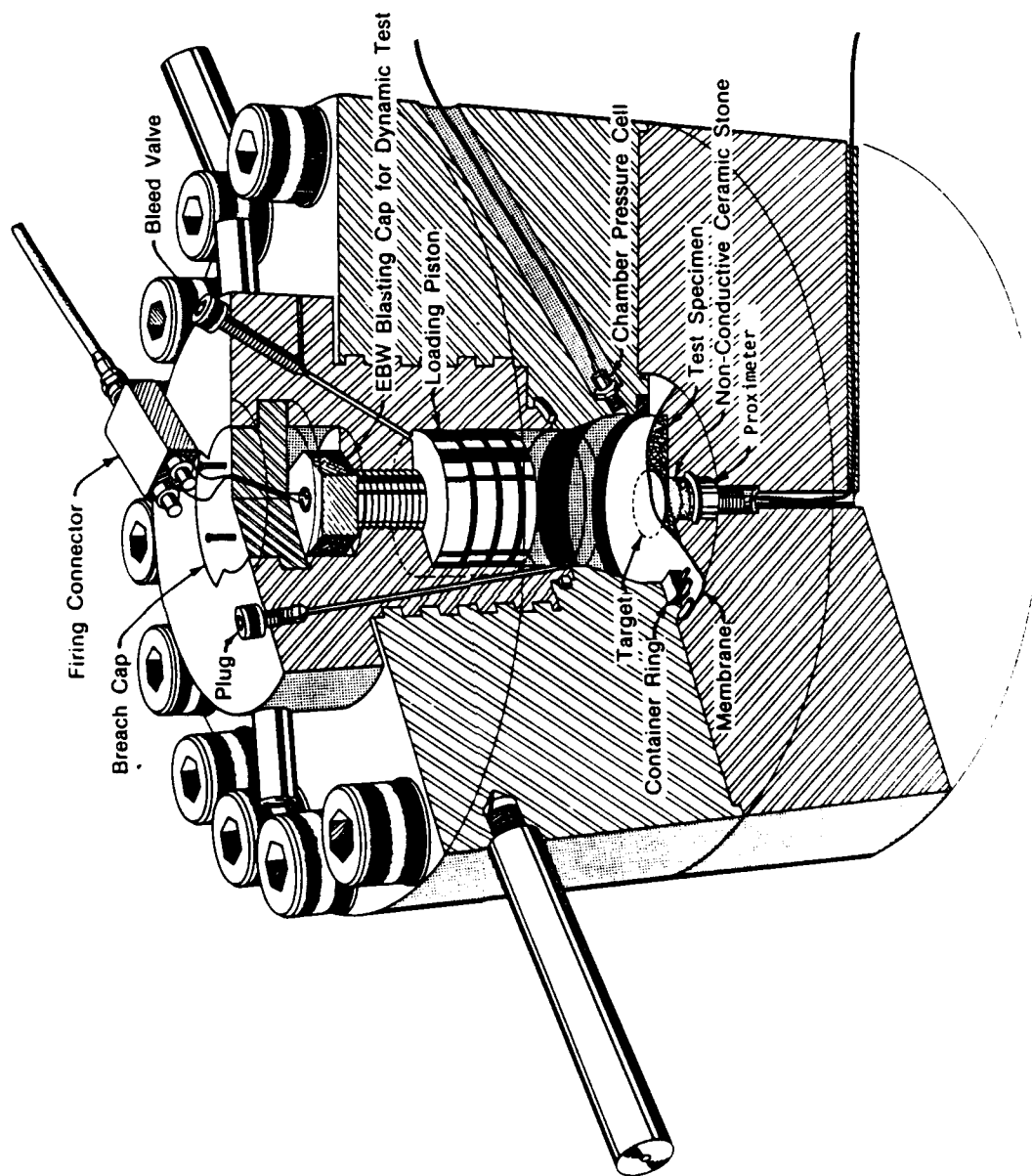
Figure 3.2.1 Schematic of the WES 0.1-msec device configured for dynamic testing.
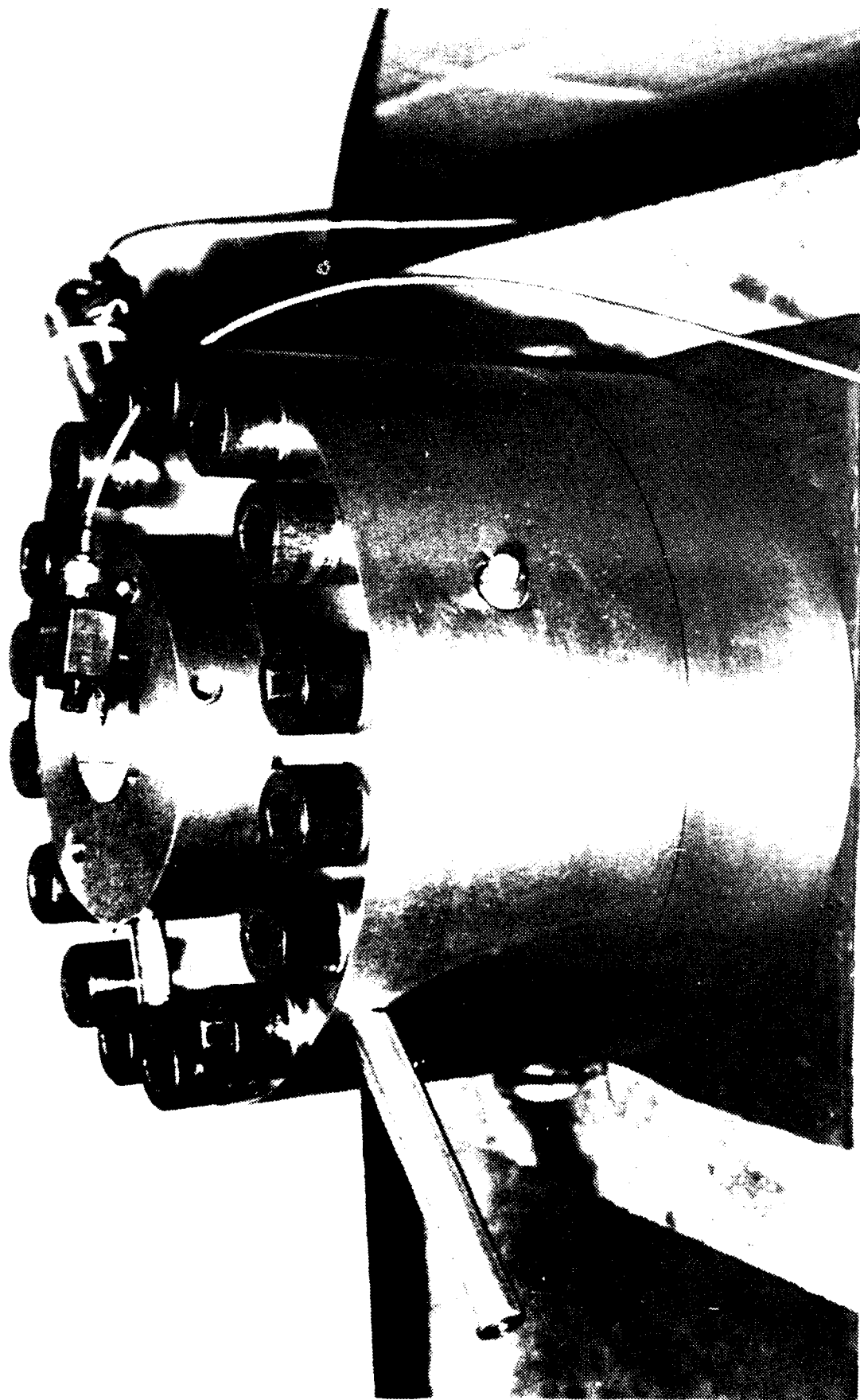
Figure 3.2.2 Photograph of the assembled WES 0.1 msec device configured for dynamic testing.

Figure 3.3.3 Photograph of the lower assembly of the WES 0.1-msec device.

PLAN VIEW

SECTION VIEW
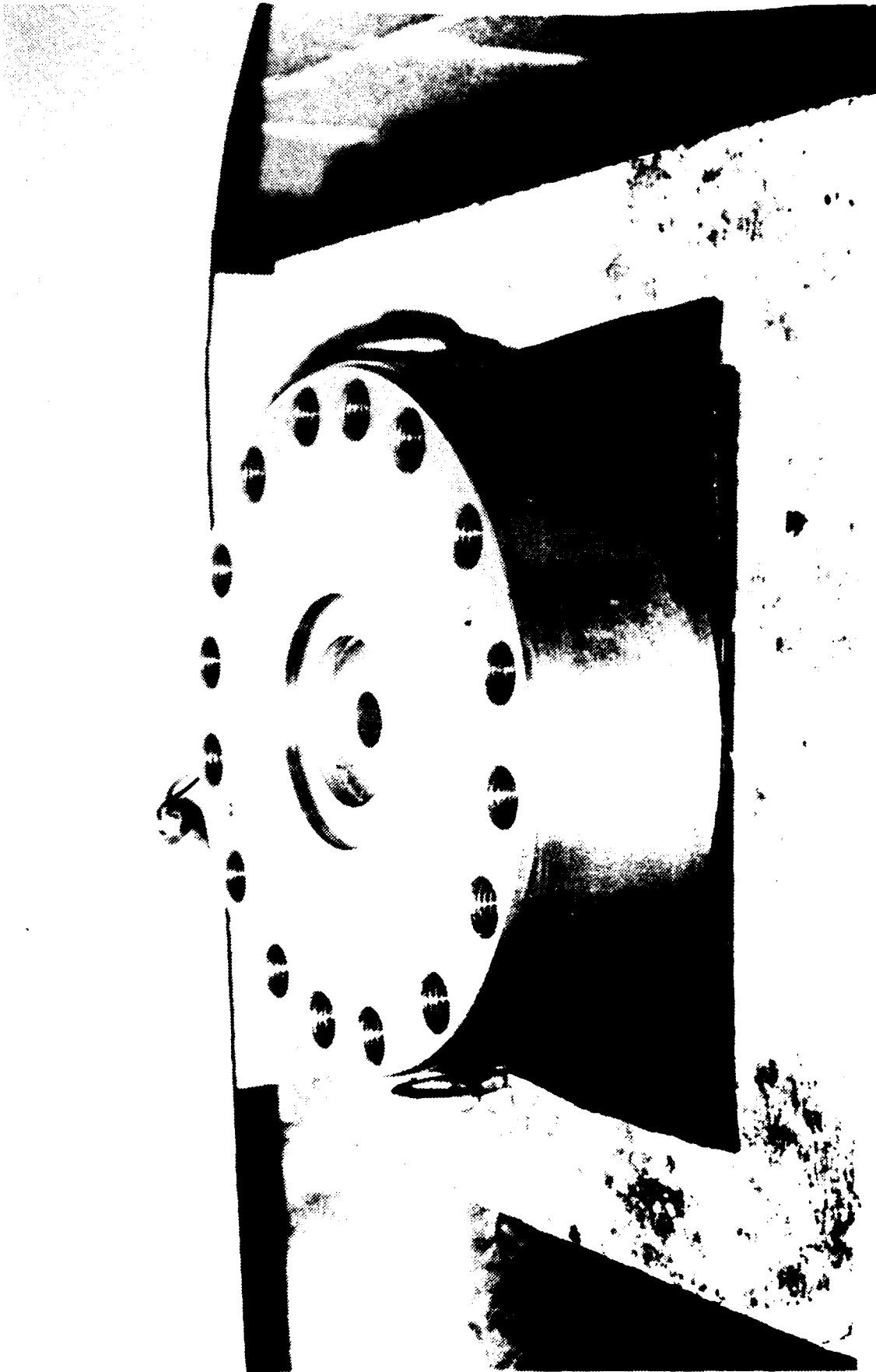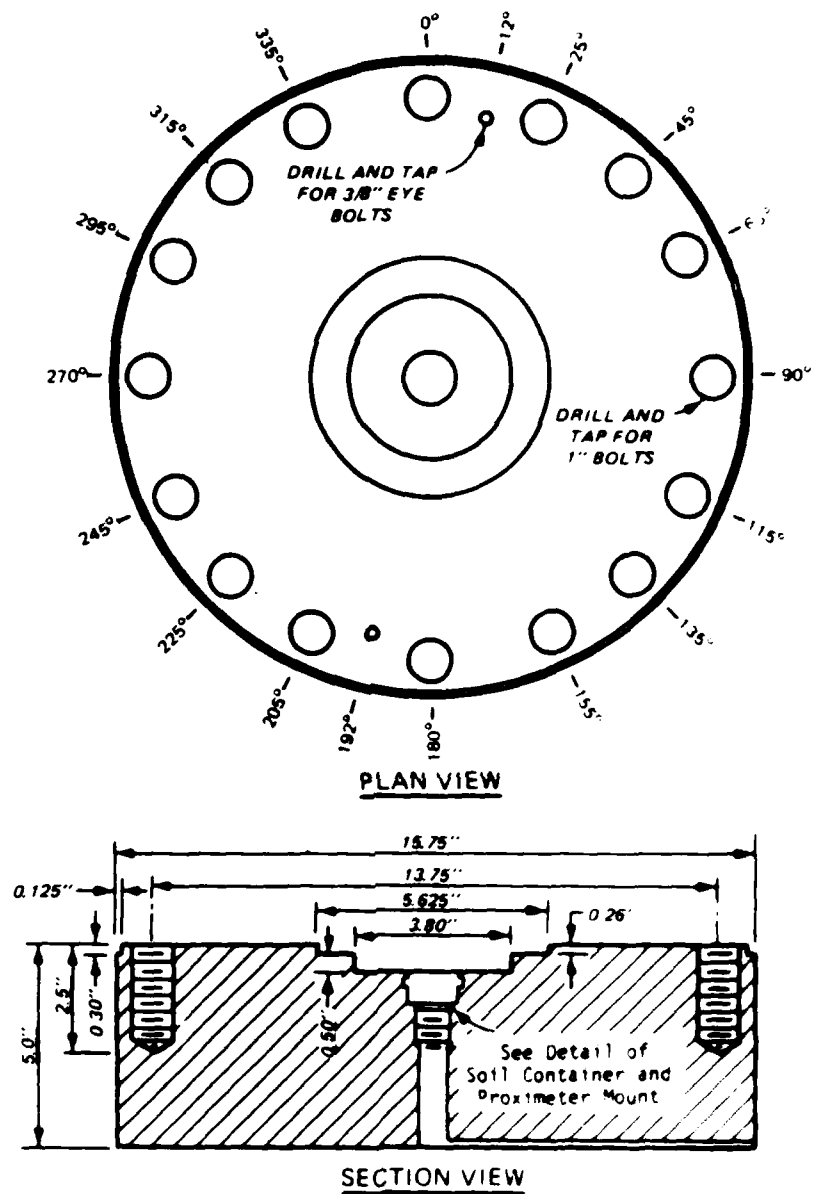
Figure 3.2.4 Drawing of the lower assembly of the WES 0.1-msec
device.

Figure 3.13. Photograph of the upper assembly of the WFS 0.1-msec device.

COUNTER SINK 0.25"
DRILL AND TAP FOR
0.75" NC AND
PROVIDE 12.0"

0

335°

315°

295°

283°

270°

257°

245°

225°

205°

193°

180°

12°

25°

45°

65°

90°

102°

115°

135°

155°

13.0" C/C
DRILL AND TAP
FOR .375"
EYE BOLTS

PLAN VIEW

15.75"

13.75"

6.00"

THREAD
4/1 MOD
ACME

4.00"

3.00"

4.0"

4.5"

5.75"

6.60"

1.0"

30°

4.015"

SEE DETAIL B

68° 12'

SEE DETAIL C

0.75" φ

3.80"

4.501"

5.622"

0.32"

0.12"

SEE DETAIL A

0.28"

SECTION VIEW
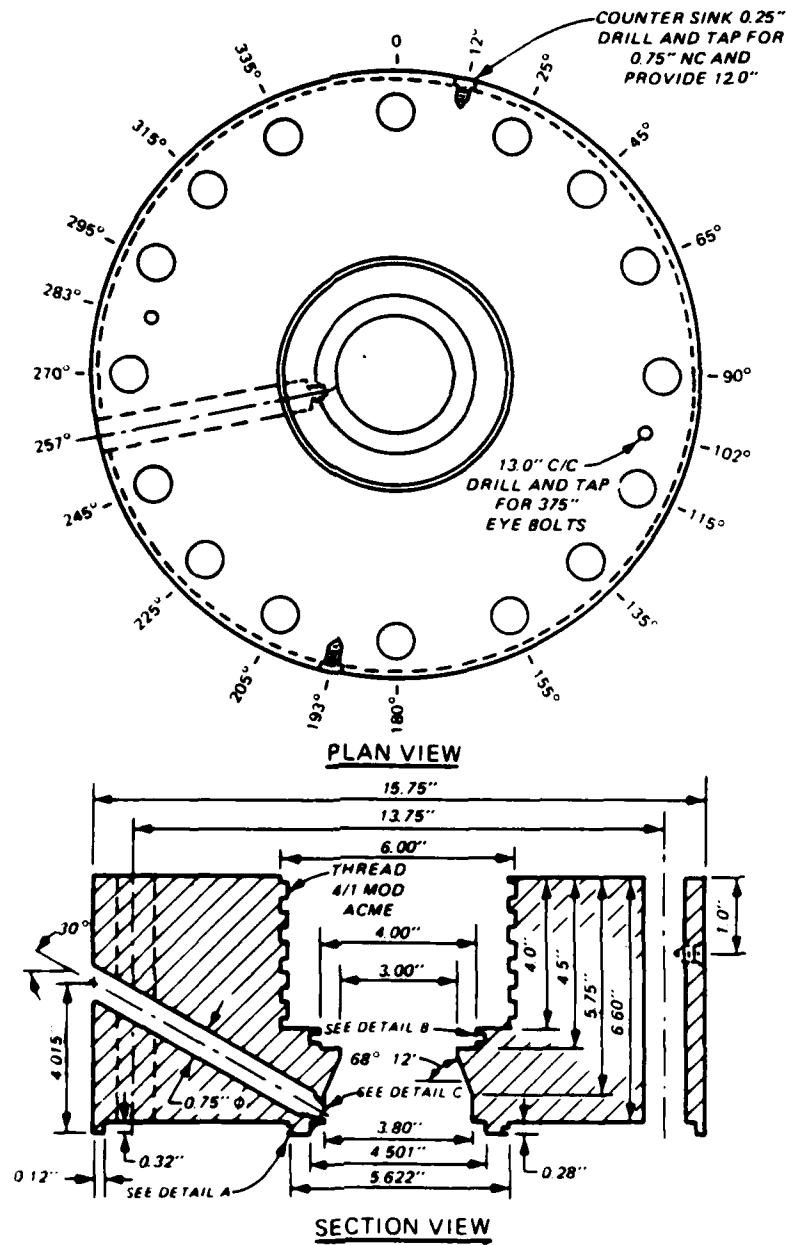
Figure 3.2.6   Drawing of the upper assembly of the WES 0.1-msec
device.

Figure 3.2.? Photograph of the inner-fluid chamber, breech cap, loading piston, and containment ring for the WES 0.1-msec device.

DRILL AND TAP
FOR 1/4"
THREAD FOR
HANDLES

HEX HEAD
WITH 1 4 NC
THREAD
ADJUSTMENT SCREW
DETAIL

HEX HEAD
WITH 1 4 NC
THREAD

PLAN VIEW

PLUG DETAIL

MATE TO ADJUSTMENT
SCREW, SEE DETAIL

3.00"

0 5"

60°

1.0"

MATE TO PLUG
SEE DETAIL

FOR
BREACH
CAP

0.5"

2.00"

0.5"

0.5"

1/16" φ

0.5"

6" DIA
4/1 MOD
ACME
THREADS

1.5"

MATE
TO
EBW
CAP

4 0625"

1/8 φ

1 8" φ

3 00"

4.00"

0 50"

SECTIONAL VIEW
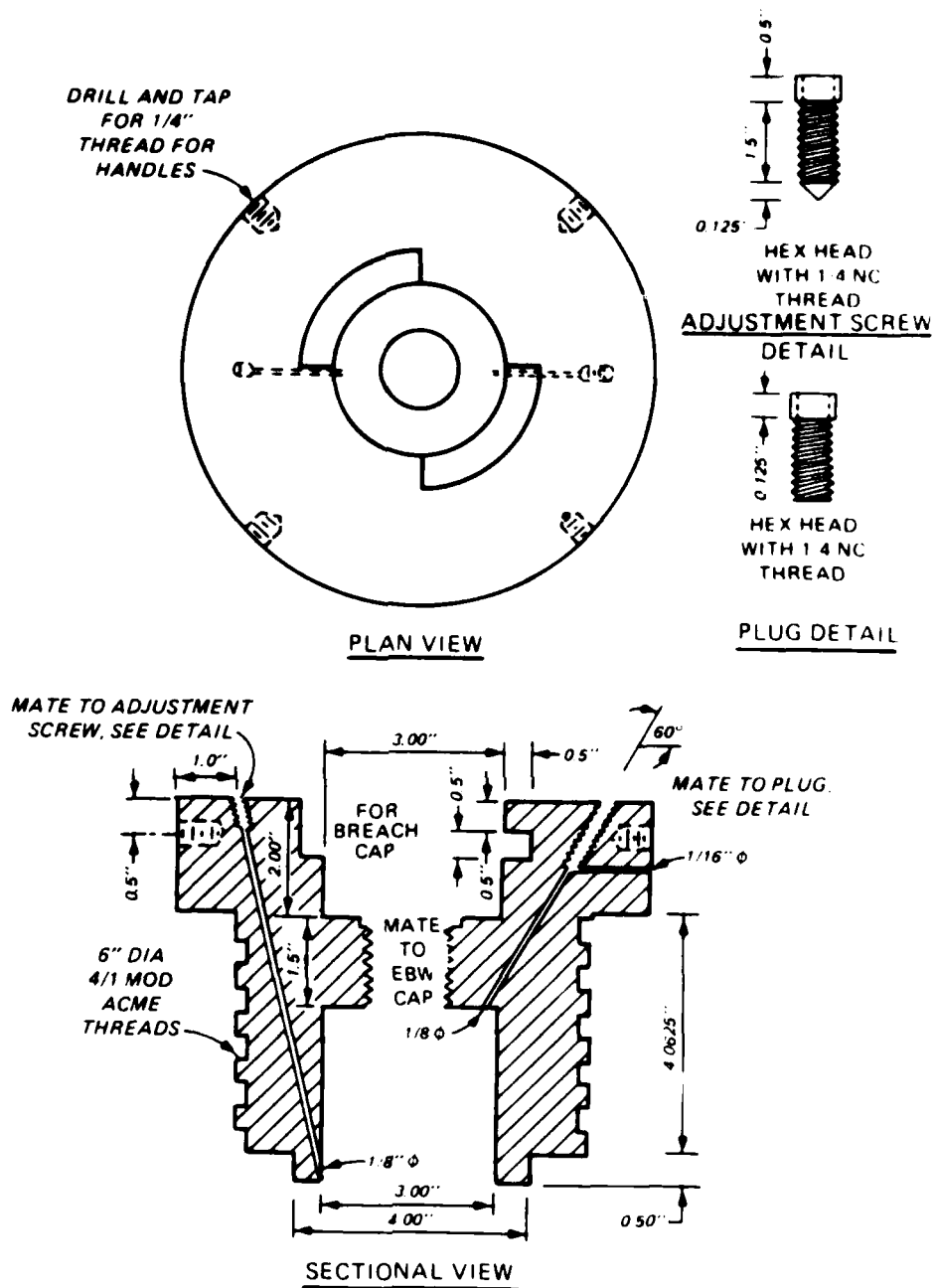
Figure 3.2.8   Drawing of the inner-fluid chamber for the WES
0.1-msec device.

48

Figure 3.2.9 Drawing of the breech cap, loading piston, and miscellaneous details for the WES 0.1-msec device.
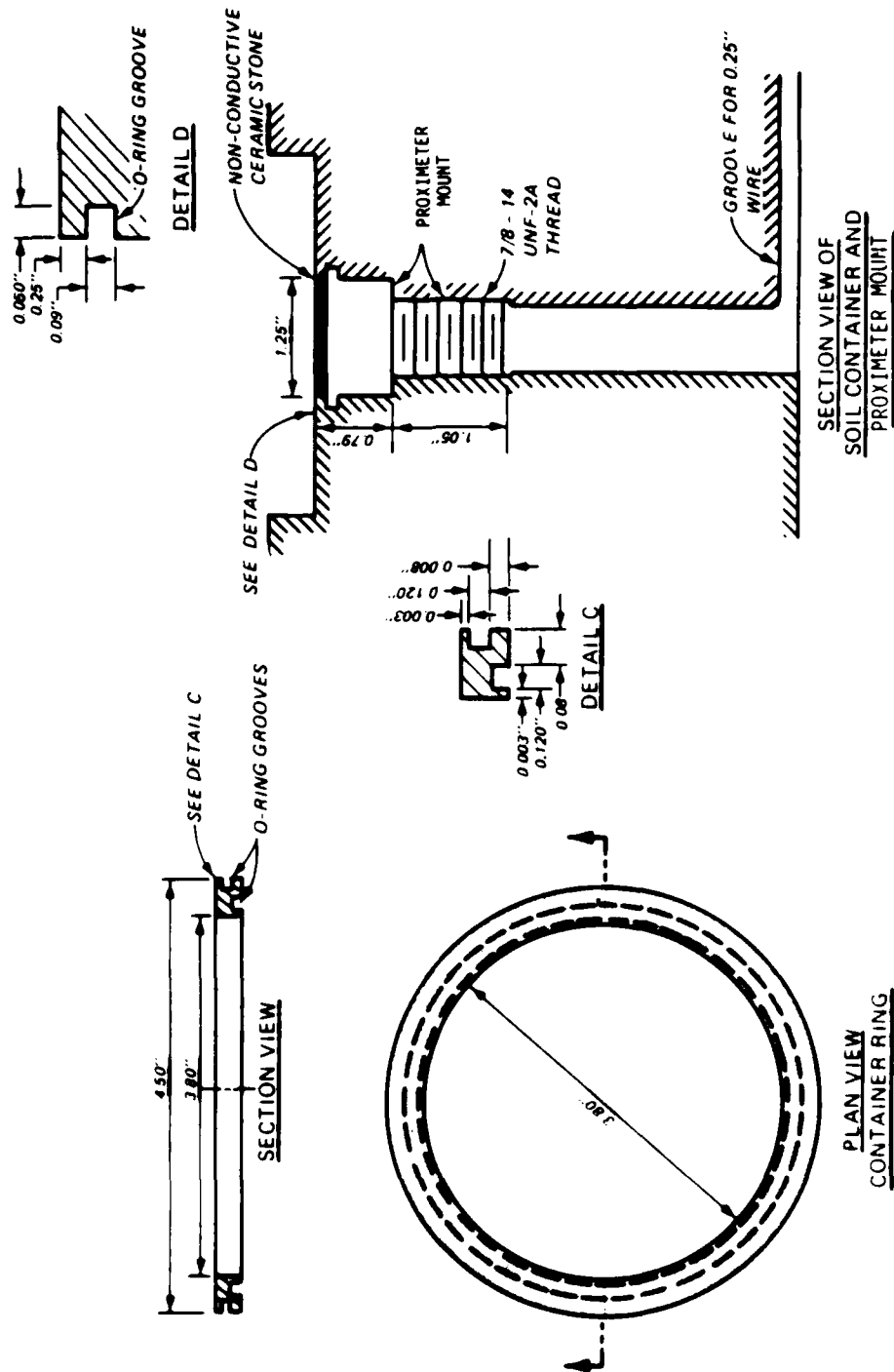
Figure 3.2.10 Drawing of the container ring, soil container, and proximeter mount for the WES 0.1-msec device.

Dynamic testing in the WES 0.1-msec device is relatively simple compared to most uniaxial strain devices. A sample is built in the soil container and an aluminum disk is placed over the soil sample to serve as a target for the proximeter. A rubber membrane is placed over the assembled specimen and the aluminum target to provide a barrier between the hydraulic fluid and the soil. Figure 3.2.11 shows a specimen in the lower assembly ready for testing. The upper assembly is placed over the lower assembly and eighteen 1-in (2.54-cm) bolts are used to seal the two assemblies together. Hydraulic oil (Texaco Aircraft Hydraulic Oil 15) is poured into the upper assembly to a point about 4 in (10.16 cm) from the top. The loading piston is then placed inside the inner fluid chamber (Fig. 3.2.3) flush with the bottom face. An exploding bridgewire (EBW) detonator is screwed into the inner fluid chamber and locked into place with the breech cap. The test is then performed and the results recorded.

Static tests can be performed in the device with some minor modifications. An LVDT attached to a proximeter target is mounted to the lower assembly by means of a mounting ring placed inside the soil container. This arrangement is shown in Figs. 3.2.12 and 3.2.13. This mounting ring has an inside diameter of 3.0 in (7.62 cm). Wiring for the LVDT is connected to a fusite (high pressure fitting that prevents leakage of air pressure or hydraulic oil and allows for electrical connections) placed in the plug hole (see Fig. 3.2.8). This configuration allows for measurement of vertical displacement using two deformation measuring systems. The importance of this type of measuring system is discussed in Section 3.4. A rubber membrane is
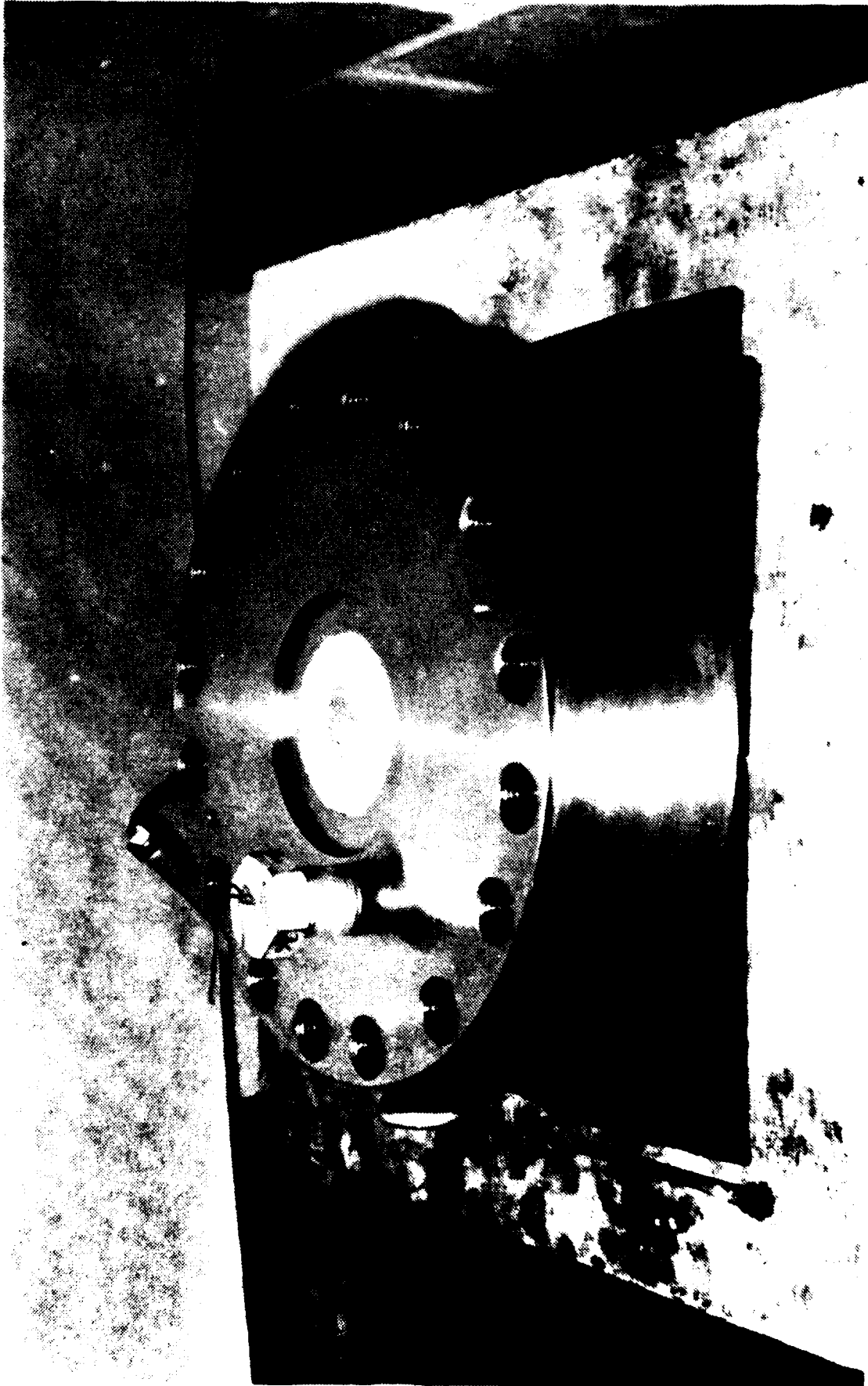
Figure 3.2.11 Photograph of the lower assembly of the WES 0.1-msec device configured for dynamic testing.
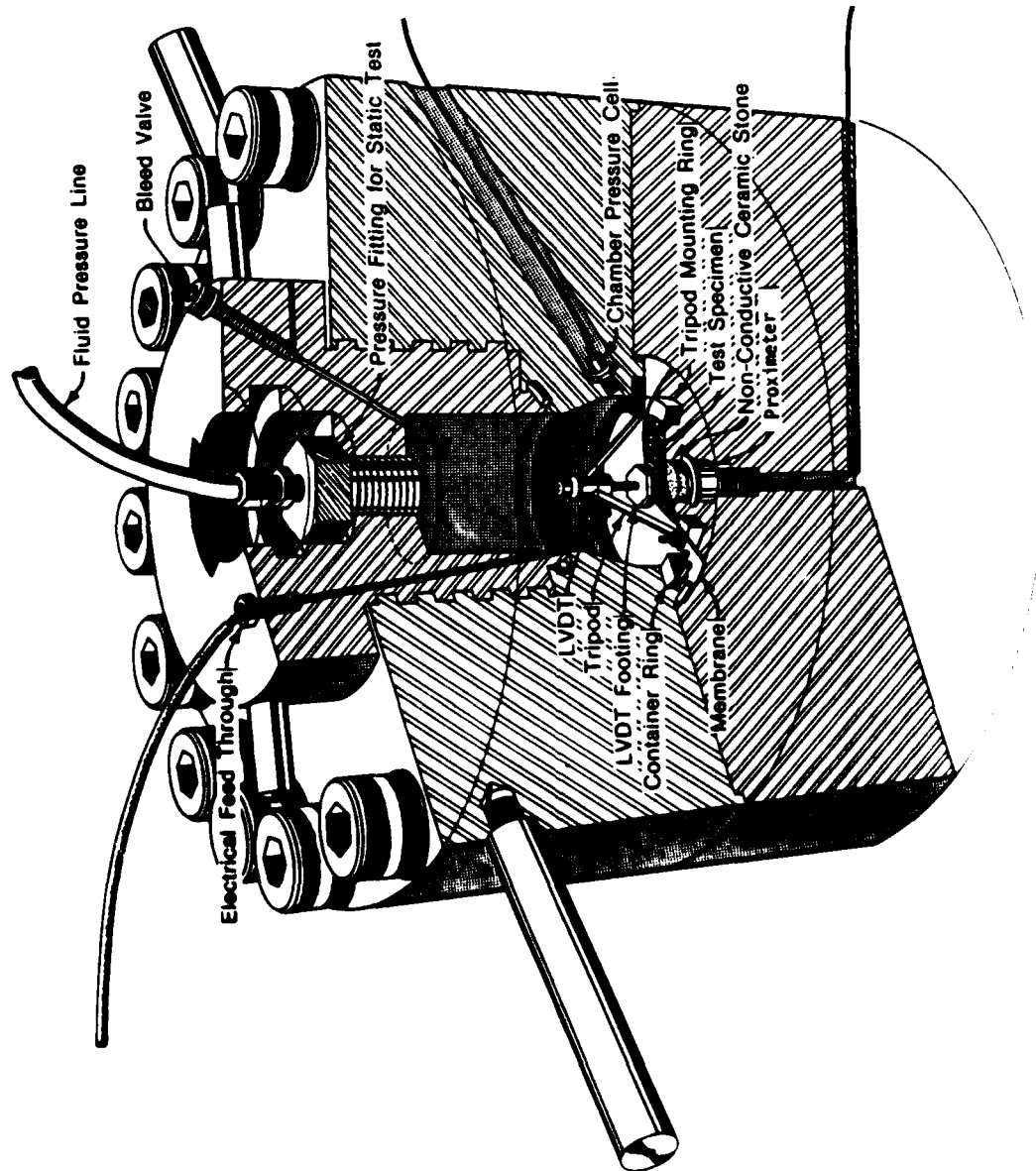
Figure 3.2.12 Schematic of the WES 0.1-msec device configured for static testing.
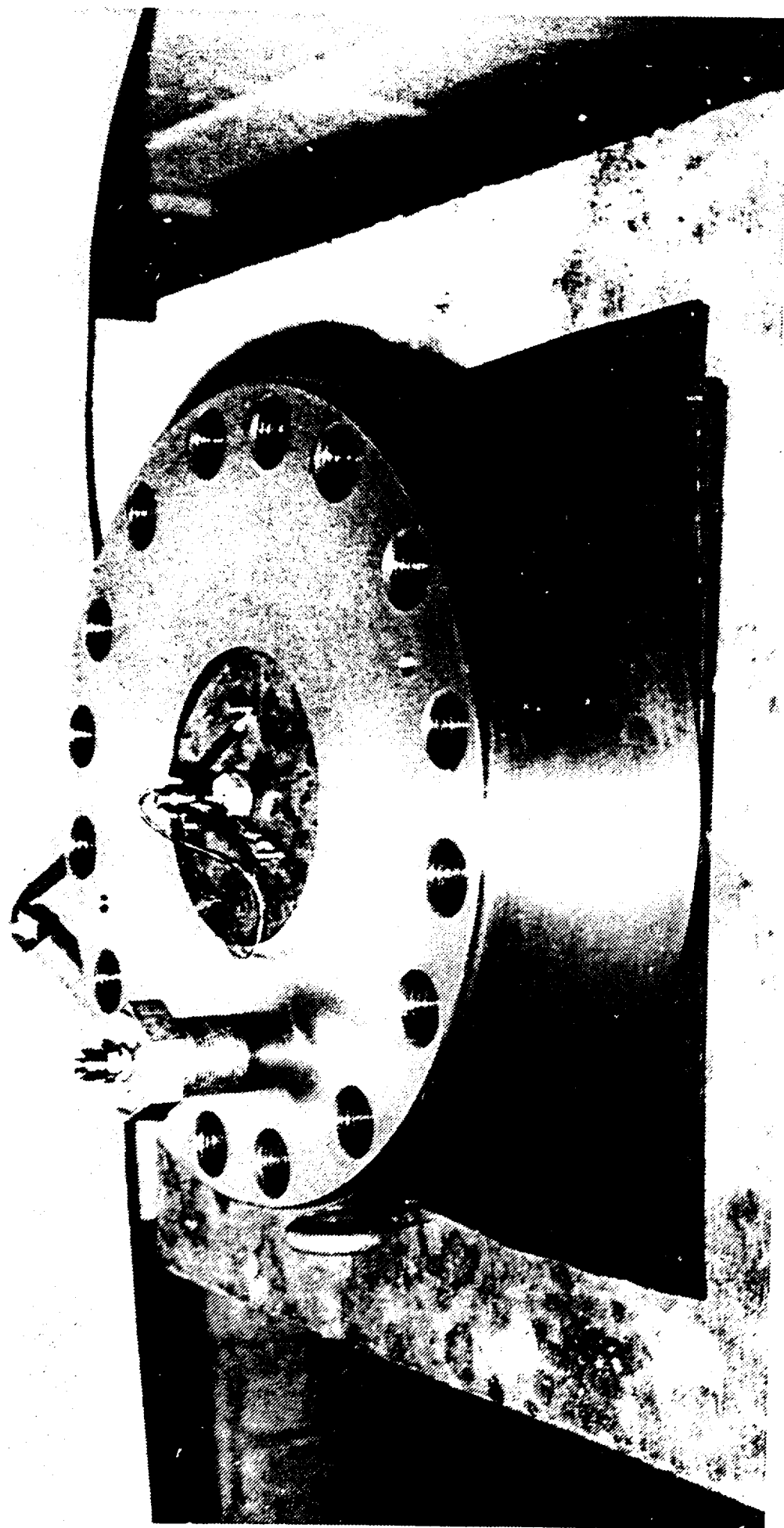
Figure 3.2.13 Photograph of the lower assembly of the WES 0.1-msec device configured for static testing.

used to separate the hydraulic fluid from the sample (See Fig. 3.1.1).
The loading piston is removed from the inner fluid chamber before the
upper and lower assemblies are bolted together. A fitting made from an
EBW cap (Figs. 3.2.12 and 3.2.13) is used as a pressure fitting for the
pneumatic load application system described in Section 2.4.

3.3 Load Application Systems

Different load application systems are used for static and
dynamic testing for the WES 0.1-msec device. The pneumatic load
application system described in Section 2.4 is used for static testing;
whereas, during dynamic testing, loading is applied by means of an EBW
detonator (sometimes referred to as an EBW blasting cap).

To produce rise times to peak pressure in the submillisecond
range, an alternative to the conventional ram-type loaders (see Section
2.4) had to be developed. Existing ram-type loaders cannot produce
loading pulses with rise times to peak force of less than about 3
milliseconds. The EBW detonators used were found to be capable of
producing submillisecond rise times and pressures to 20,000 psi (138
MPa). The components of the EBW load application system, the firing
console and an EBW cap are shown in Fig. 3.3.1.

The basic components of an EBW detonator are shown in Fig. 3.3.2.
These detonators were rated at pressures of 5, 10, and 20 ksi (34.5,
69, 138 MPa). The higher the rated pressure, the larger the explosive
source in the EBW cap. The larger the explosive, the faster the rise
time to a given pressure. A typical rise time for a 10 ksi (69 MPa)
cap was about 0.3 msec to 5 ksi (34.5 MPa) pressure. Whereas, a 20 ksi
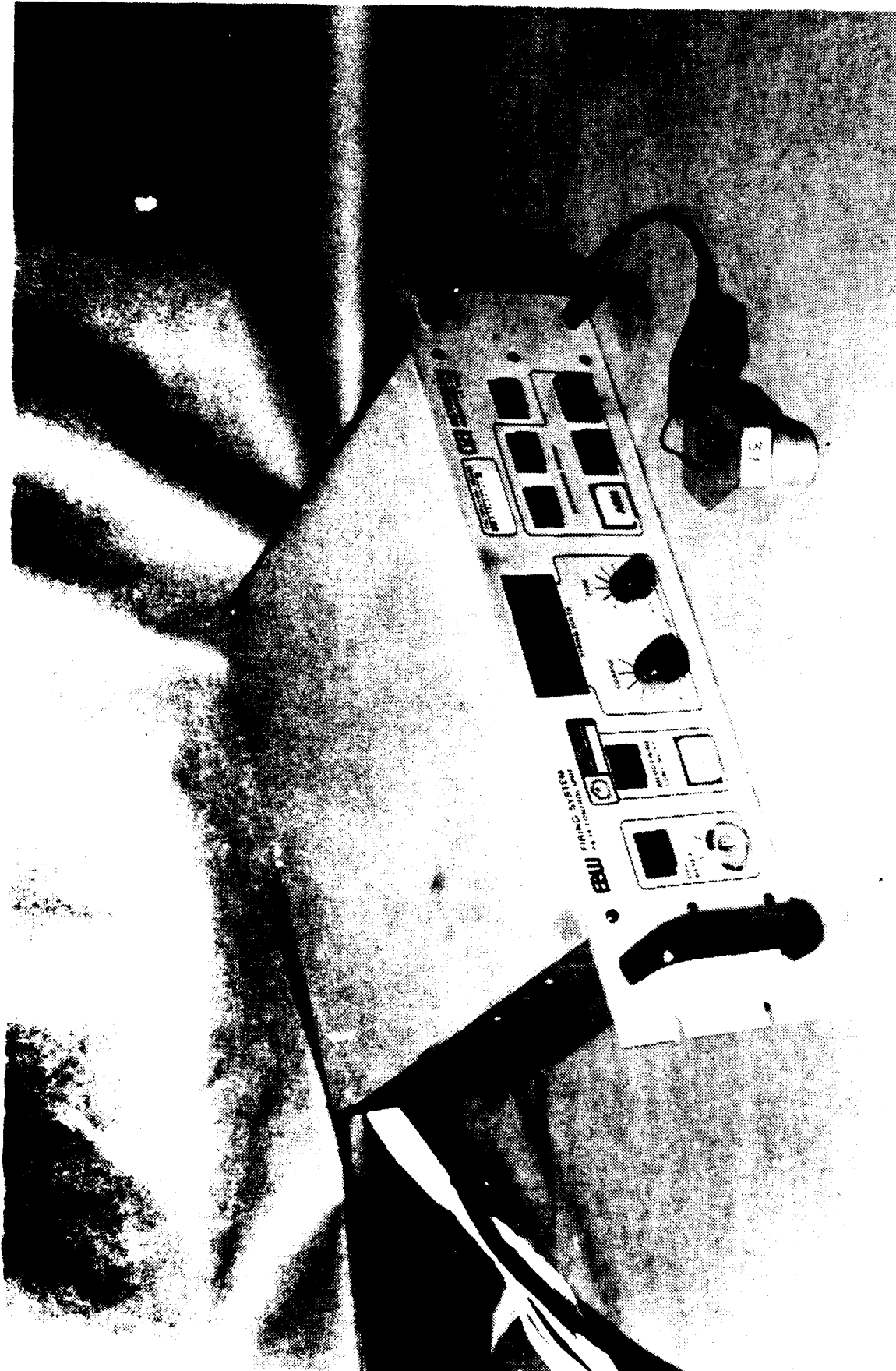
Figure 3.3.1 Photograph of the EBW firing system and EBW cap.

POWER
SUPPLY
~1000 V

CAPACITOR, ~1 MICROFARAD

TRIGGERED
SPARK GAP

BRIDGEWIRE

TRANSMISSION LINE
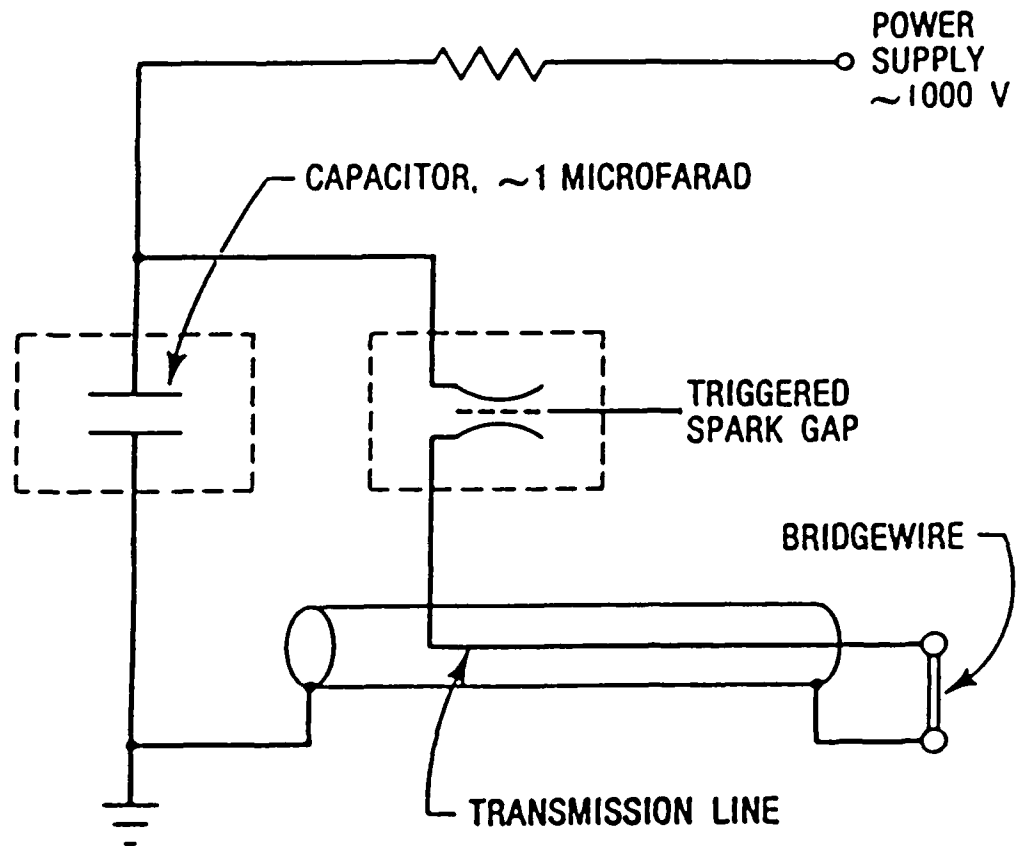
...mponents of an exploding bridgewire detonator

:rom Reynolds Industries, 1978).

(138 MPa) cap typically took 0.15 msec to 5 ksi (34.5 MPa) pressure. These detonators produced erratic results. A cap rated at 10 ksi (69 MPa) often produced pressures of only 5 to 6 ksi (34.5 to 69 MPa) or less. However, the system is simple to operate and does provide usable results.

3.4 Measurement Systems and Data Reduction Techniques

In a conventional uniaxial strain test only two basic measurements are obtained; displacement at the sample surface and pressure in the medium used to transfer load to the sample surface. As described in Section 3.2, two types of measuring devices were used to determine the surface displacement of the soil sample; an LVDT and a proximeter. A miniature, flush-mounted pressure transducer was used to measure pressure in the hydraulic oil. Figures 3.4.1 and 3.4.2 present schematic diagrams of the measurement systems, signal conditioning equipment, and data acquisition systems used for the WES 0.1-msec device under static and dynamic loadings.

The LVDT used in the device was specifically designed for applications where space and/or weight are critical considerations. As shown in Fig. 3.4.3, the LVDT was highly linear over its working range of 0.2 in (0.51 cm). The size of the LVDT was an important consideration for this device because of the size of the fluid chamber (Fig. 3.2.6). A 3 kHz carrier amplifier and signal conditioning module was used to provide AC excitation, signal conditioning for the input-output voltage, and the DC output required by the data acquisition systems. An aluminum footing attached to the core rod of the LVDT as
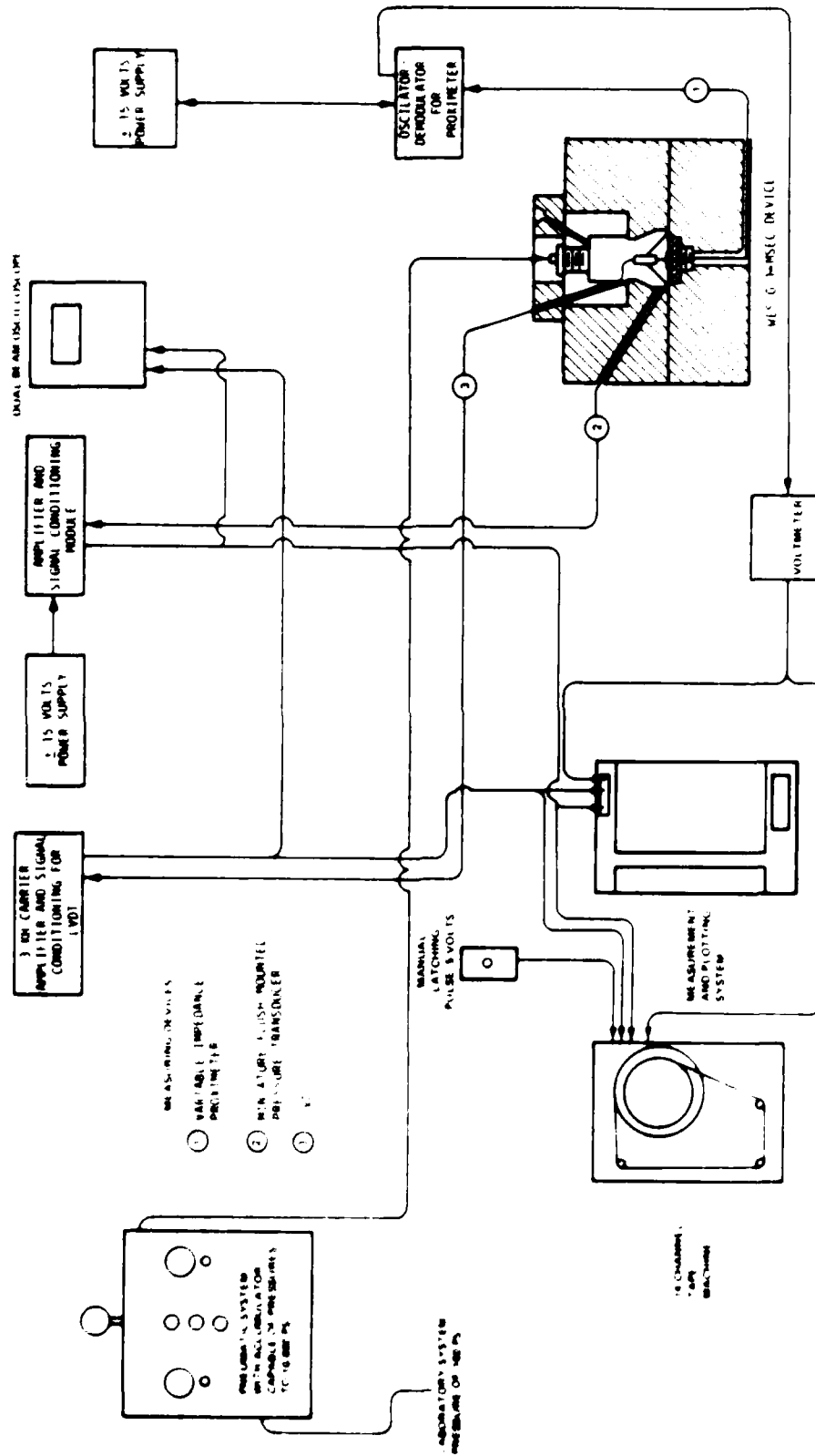
Figure A-14. Schematic diagram of the signal conditioning equipment and data acquisition system for static testing in the WES 0.1-msec device.
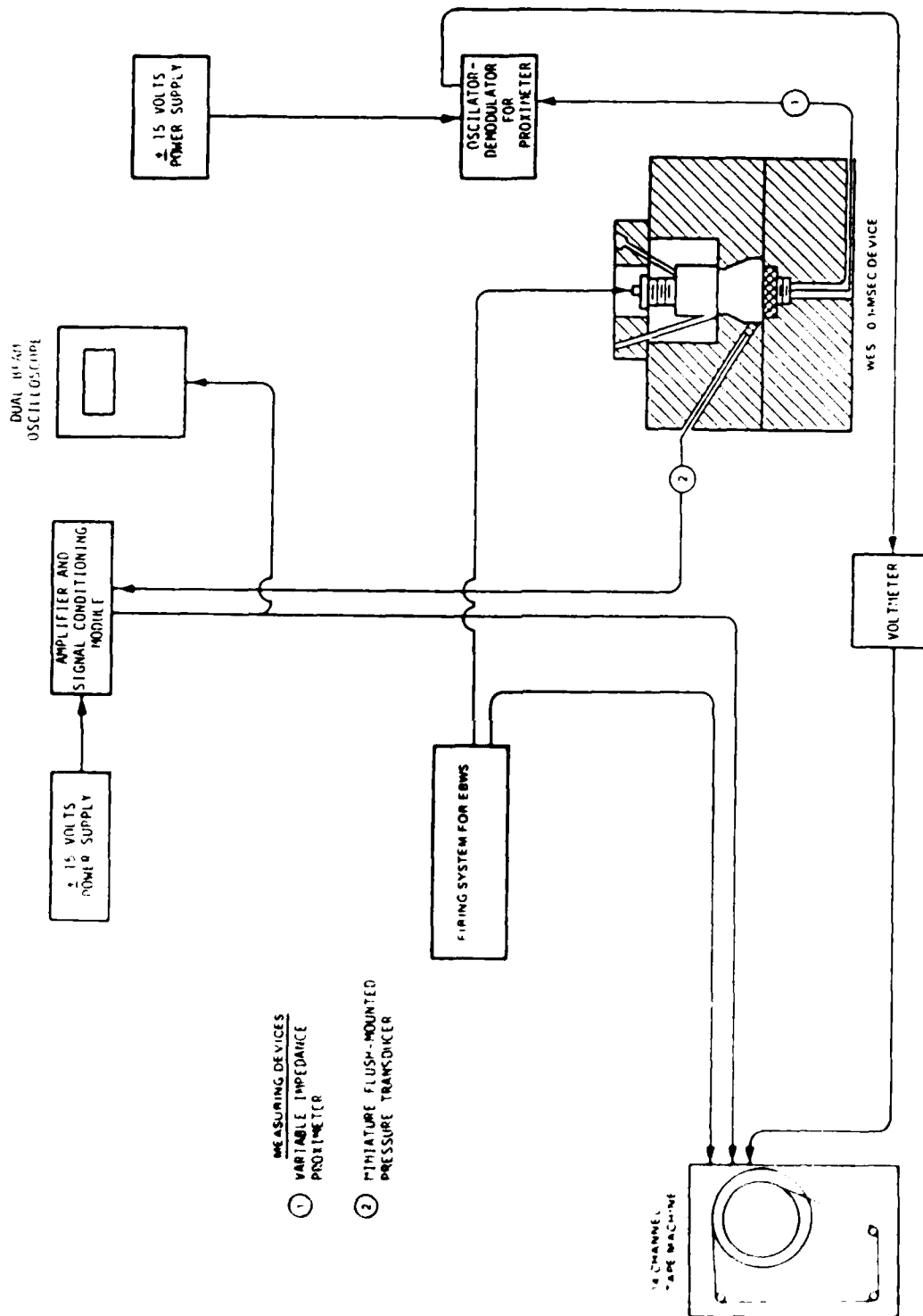
Figure 3.4.2 Schematic diagram of the signal conditioning equipment and data acquisition system for dynamic testing in the WES 0.1-msec device.

DATA INPUT: Y,X

MILS	VOLTS
0	0.0000
20	.8020
40	1.6320
60	2.4400
80	3.2300
100	4.0100
120	4.8000
140	5.5500
160	6.3600
180	7.2000
200	8.0000

DC CALSTEPS
A= 1.3240
B= 2.6320
C= 3.9420
D= 5.2720
E= 6.6120
F= 8.0020

RMS CALSTEPS
A= .0720
B= .1450
C= .2180
D= .2920
E= .3680
F= .4450

TYPE DEVICE: LVDT +/-100 MILS
SERIAL NO: 1404
DATE CALIBRATED: 5/29/85
REMARKS: .1 MIL SEC

AMPLIFIER TYPE: 3kHz CARRIER
100 MILS OFFSET = .224 VOLTS RMS
CALIBRATED BY : KOESTLER/LOFTIN

R^2
-.9999

M 35.122   B .542

A= 32.719
B= 65.579
C= 90.488
D= 131.900
E= 165.563
F= 200.482

Figure 3-3 Typical calibration for the LVDT used in the WES 0.1-msec device.

shown in Fig. 3.4.4 was used to ensure uniform measurements of displacement and to prevent the core rod from penetrating the soil. Calibrations similar to Fig. 3.4.3 were made using standard gauge blocks for relating known displacements to output voltages.

The proximeter used was a variable impedance type transducer which consisted of a variable impedance bridge with an active and reference coil. Variation in impedance results from eddy currents induced in the object used as a target. The coupling between the coil in the sensor and the target is dependent upon the gap between the sensor and the target. A flat aluminum disk is attached to the LVDT footing for static testing to serve as a target (Figs. 3.2.12 and 3.2.13). During dynamic testing, only the aluminum disk is used (Figs. 3.2.1 and 3.2.11). Figure 3.4.4 shows the aluminum disk attached to the LVDT footing for static testing and the aluminum disk used for dynamic testing. Manufacturers suggested properties for a target allowed for the disk to be either magnetic or nonmagnetic and greater than 1.25 in (3.18 cm) in diameter.

As shown in Figures 3.4.1 and 3.4.2, the proximeter requires a power supply and an oscillator-demodulator for signal conditioning. The oscillator-demodulator consists of an oscillator, linearization network, amplifiers, and a demodulator to provide a DC voltage proportional to the distance between the proximeter and the target for the data acquisition systems.

Calibration of the proximeter proved to be a major obstacle in obtaining usable dynamic test results. This proximeter was designed to

Figure ... photograph of the INEL ... tested and testing, and proximeter target.

measure through a non-conductive medium, usually air, to the target. By placing the proximeter in the base of the soil container and the target on top of the sample, the device must measure through the soil sample. Soil contains minerals and usually water and is therefore conductive. Although the proximeter wasn't designed to perform under these conditions, with some adjustments, the system did provide accurate measurements.

Several approaches were used to calibrate the proximeter. Initially, samples were built in the soil container and the offset voltages were recorded at various water contents and densities to determine the effect on the output voltage. This gave some insight into the problem, but did not offer a satisfactory solution. The proximeter was also affected by mineralogical properties and testing pressures. These problems, combined with those created by water and density, introduced too many variables to take into account by using calibration curves.

The final solution involved running uniaxial strain calibration tests using the proximeter and the LVDT as a dual measurement system. As shown in Figs. 3.2.12 and 3.4.4, a target for the proximeter was attached to the LVDT footing to provide two measurements of displacement. This "piggyback" arrangement was used only during static testing. An insert was built to mount the LVDT tripod inside the soil container. This insert reduced the specimen size to 3.0 in (7.62 cm) in diameter. When a sample is placed in the soil container, the conductive properties of the medium creates a positive voltage offset. This value is rezeroed using the zero adjustment of the

oscillator-demodulator. The linearity adjustment is not changed. A static uniaxial strain test is then performed, and plots similar to Fig. 3.4.5 are obtained for a soil specimen at a given water content and density. The combined effects of water, density, pressure, soil mineralogy, etc., on the output voltage of the proximeter can then be evaluated based on these calibration curves and the appropriate corrections applied to the proximeter measured strain for dynamic test results. Fortunately, these calibration tests showed that a plot of proximeter versus LVDT strain were approximately equal for the loading portion. Thus, the change in voltage due to the location of the target relative to the proximeter wasn't affected by the voltage offset. The offset could therefore be zeroed, and the calibration curve obtained in air was valid during the test.

As shown in Fig. 3.4.5, at the transition point from loading to unloading there exists some slack in the measuring systems. This can probably be attributed to the LVDT rather than the proximeter. At the stress reversal, the direction of movement of the LVDT core rod is reversed. Any slack in the LVDT would produce the hook as shown in Fig. 3.4.5.

The device illustrated in Fig. 3.4.6 was used to produce a calibration curve for the proximeter in air. The height of the aluminum target was set using standard gauge blocks. Values of displacement versus output voltage were then measured using the dial gauge to locate the target relative to the proximeter.
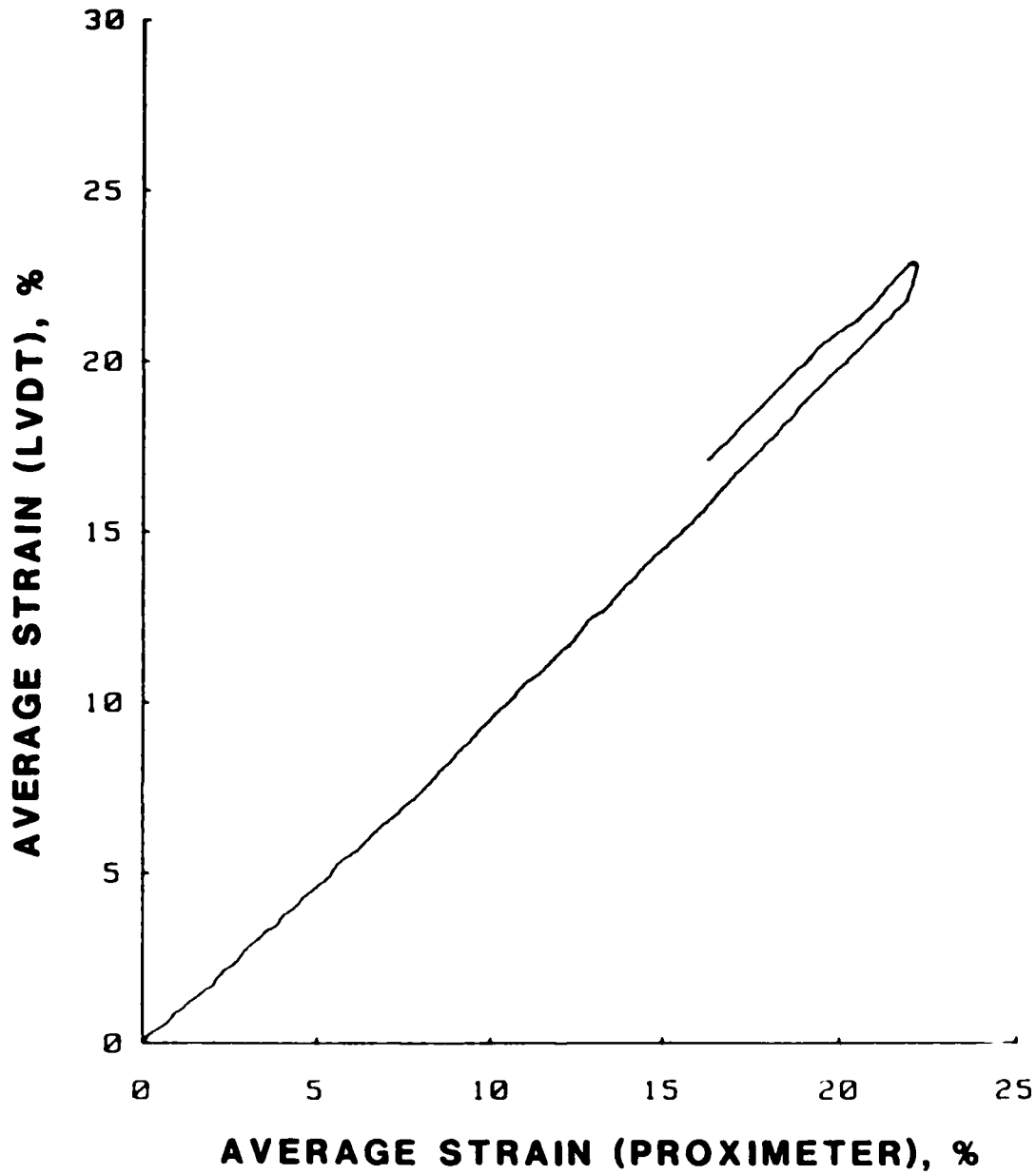
Figure 3.4.5   Plot of proximeter strain versus LVDT strain from a
static uniaxial strain calibration test.
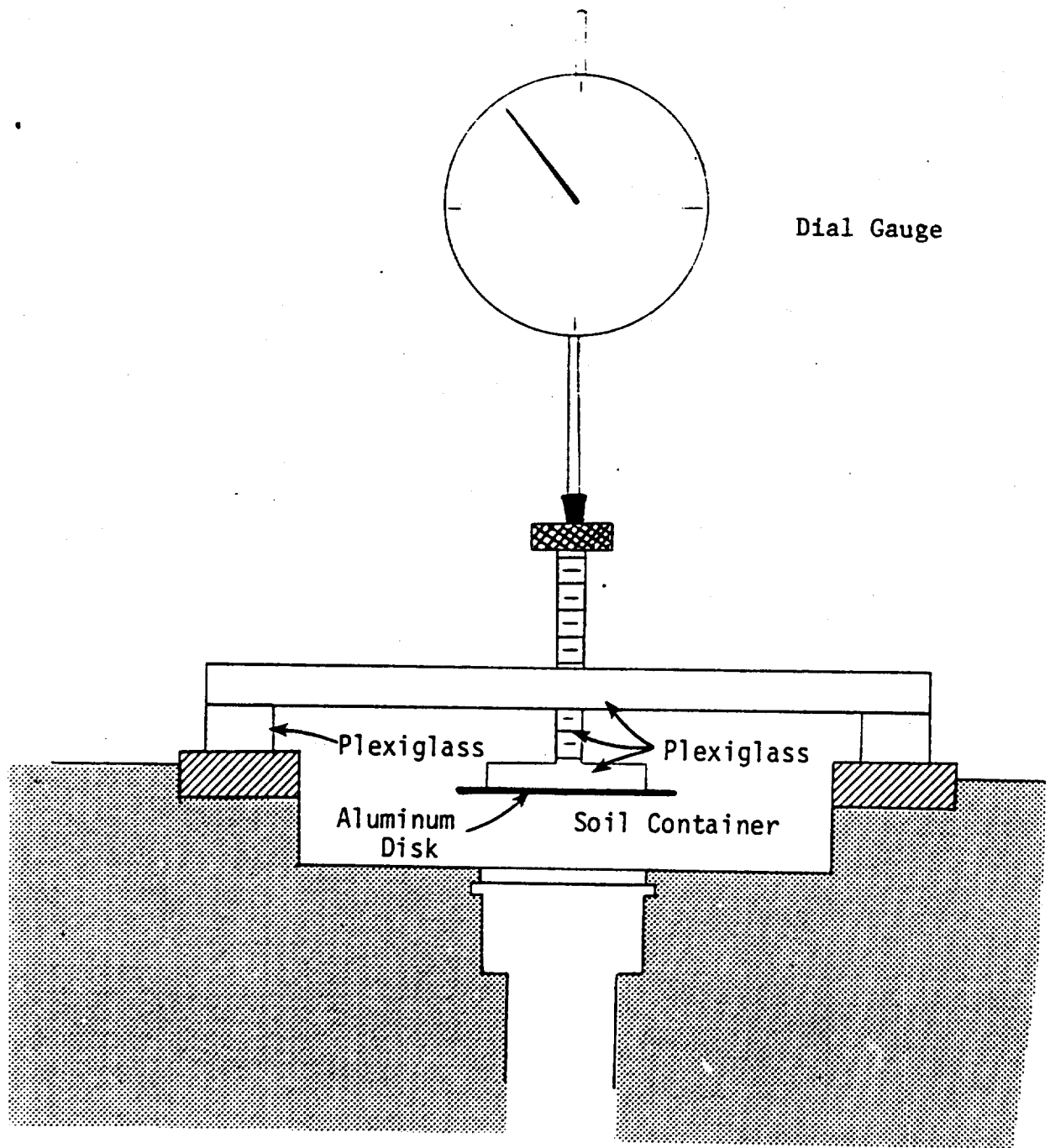
Figure 3.4.6   Dial-gauge arrangement used to calibrate the proximeter.

A miniature pressure transducer was used to measure pressure in the hydraulic fluid in the device. The pressure cell was highly linear as shown by Fig. 3.4.7 and worked extremely well during both static and dynamic testing. This type of pressure transducer utilizes an integrated sensor consisting of a silicon member on which a Wheatstone bridge has been attached. The miniaturization of the device creates a marked increase in natural frequency over conventional pressure transducers, making it ideal for shock type measurements. This device has a minimum natural frequency of 395 kHz. As shown in Figs. 3.4.1 and 3.4.2, the pressure cell requires a DC source, amplifier, and signal conditioning module to produce a DC output proportional to the pressure in the hydraulic oil for the data acquisition system.

As shown in Figs. 3.4.1 and 3.4.2, a 14-channel tape recorder was the primary data acquisition device. For static testing, a measurement and plotting system was also used. The measurement and plotting system allowed for viewing plots of output voltage from any of the measuring devices and time during testing or immediately upon completion of the test. This measurement and plotting system is a digital device and does not have a sampling frequency fast enough to record a submillisecond test. The tape machine provided the only means of data acquisition for dynamic testing.

Programs written on a personal computer were used with a multiprogrammer to reduce and plot the tests from the analog form stored on the magnetic tapes. The multiprogrammer serves as a buffered A/D convertor. The multiprogrammer has a sampling rate of 30 microseconds. A faster sampling rate was needed to reduce the

DATA INPUT: Y,X

LBS / IN²	VOLTS
0	0.0000
2000	.4370
4000	.8650
6000	1.2840
8000	1.6940
10000	2.1220
12000	2.5370
14000	2.9650
16000	3.3630
18000	3.8180
20000	4.2230

DC CALSTEPS
A= .6430
B= 1.2960
C= 2.5910
D= 5.1110

$Y = MX + B$

M	B	R^2
4747.490	-59.499	1.0000

A= 2993.137
B= 6093.247
C= 12241.247
D= 24204.921

TYPE DEVICE: 20 kpsi
SERIAL NO: 2022-5-126
DATE CALIBRATED: 6-19-85
REMARKS: NONE

AMPLIFIER TYPE,D.C.
CALIBRATED BY: GILLIAM

LBS / IN 2

VOLTS

Figure 3.4.7 Typical calibration for the pressure cell used in the WES 0.1-msec device.

submillisecond test results. To improve the sampling rate, the tests were recorded on magnetic tape using a tape recording speed of 60 inches per second (ips). When the tape was replayed through the multiprogrammer, the tape speed was set at 1.875 ips. This produced an equivalent sampling rate of less than a microsecond.

A computer program was developed to take the voltages from the magnetic tape and store them on floppy disks via the multiprogrammer. Another computer program compares these measured voltages with known voltages that correspond to a calibrated displacement or pressure. By using these two programs, report ready plots of any combination of time, stress, and strain could be obtained within 15 minutes of completion of a test.

3.5   Factors Affecting Uniaxial Strain Measurements within the Device

The problems of variations in pressures and deflections across the sample surface, sidewall friction that develops as the soil compresses and moves down the walls of the soil container, radial expansion of the soil container, and waves propagating through the device can affect the assumption of one-dimensionality. These factors are a function of the configuration and geometry of the test device.

During explosively loaded uniaxial strain testing, a planar compression pulse is created by the loading piston as it strikes the top of the hydraulic fluid. As the pulse propagates through the column of hydraulic fluid, any obstructions in the column of hydraulic fluid can interrupt this wave causing irregular pressure at the specimen

surface. As shown in Figs. 3.2.6 and 3.2.8, the fluid chamber is essentially smooth. Since the LVDT and support tripod are not used for dynamic testing, the loading pulse should be planar and uniform at the sample surface.

In an "ideal" uniaxial strain test, there are no shear stresses between the soil and the rigid container as the soil compresses. However, in actuality, this isn't the case. Such shear stresses exist and appear to be significant. These shear stresses are referred to as side or sidewall friction; the effects of which are shown in Fig. 3.5.1. Sidewall friction acts to stiffen the soil near the container wall and is a major concern when trying to interpret uniaxial strain tests; especially when coupled with inertial effects during dynamic testing.

To overcome the measurement errors created by sidewall friction, a large specimen diameter-to-height ratio was used, vertical displacements were measured at the center of the sample, and loading was applied through a flexible membrane. Whitman (1970) recommended that the diameter of the specimen be several times the height, with a value of 4 to 1 being typical. For the results reported herein, this ratio varied from 4.2 to 7.6. No attempt was made to use some type of lubricant between the soil and container wall because of the practical difficulties involved. Based upon laboratory measurements of sidewall friction in a uniaxial strain device by Farr (1986), test results with diameter-to-height ratios of greater than about 4 will not be significantly affected by sidewall friction.
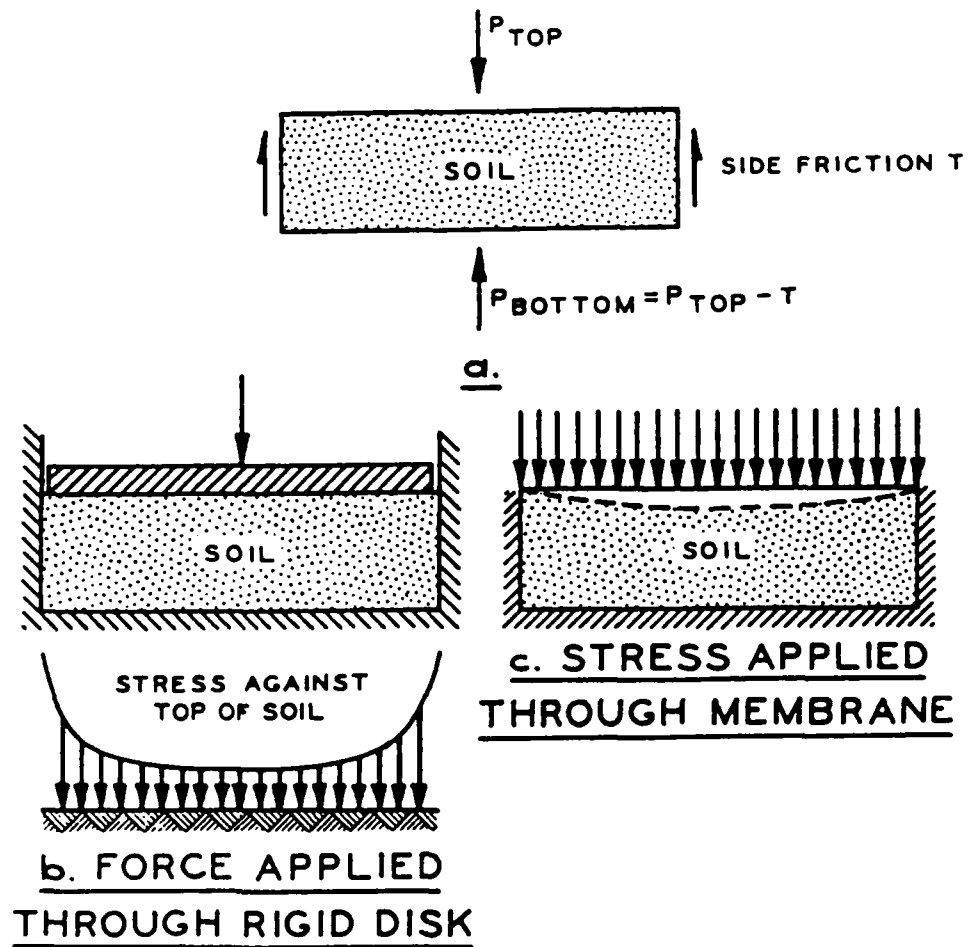
Figure 3.5.1 Effects of sidewall friction (from Whitman, 1970)

In the WES 0.1-msec device, stress is applied through a flexible membrane. As shown in Fig. 3.2.1c, use of a flexible membrane contributes to nonuniform surface displacements. However, the strain was measured over the central portion of the sample. This configuration should minimize the effects of sidewall friction and the sample should deflect uniformly over the central portion.

Both the LVDT and proximeter require some type of rigid disk (LVDT footing assembly and proximeter target) to measure surface displacements. Whitman (1970) also studied the effects of using a rigid disk for measuring surface displacements. He concluded that introducing a rigid disk into the central section will not affect the stress and strain. For the test results contained herein, a 1.5-in (3.81-cm) diameter disk was used. This size disk was slightly smaller than the optimum value (one-half of the specimen diameter) recommended by Whitman (1970).

Under true uniaxial strain conditions, there is no lateral expansion. Uniaxial strain devices for weapons effects testing are specifically designed to be massive and rigid to preclude expansion during high pressure testing. Schindler (1969) and Seaman (1983) addressed the problem of radial expansion of a uniaxial strain device.

If the soil container is assumed to be a infinite thick-walled cylinder, the radial strain can be estimated using elastic theory by:

$$\epsilon_r = \frac{\sigma_r}{G_{st}}$$ (3-1)

where: σ_r = radial stress

G_{st} = shear modulus of steel

This equation is probably an upper bound to the amount of radial deflection because the bottom face of the device is solid. The reduction in axial stress due to the radial expansion of the container can be determined using an elastic solution:

$$\triangle\sigma_a = (2K - 4G)\epsilon_r \qquad (3-2)$$

where: $\triangle\sigma_a$ = change in axial stress

   K = bulk modulus of the soil

   G = shear modulus of the soil

Since the change in axial stress increases proportional to the radial strain, this value should also be an upper bound. Seaman (1983) equated equations 3-1 and 3-2 and expressed the ratio of decrease in axial stress to radial stress, which he called the fractional error and expressed as:

$$\frac{\triangle\sigma_a}{\sigma_r} = \frac{(2K - \frac{4}{3}G)}{2G_{st}} = \frac{(M - 2G)}{G_{st}} \qquad (3-3)$$

where: M = constrained modulus of the soil

For values of M - 2G of less than 1,000,000 psi (6,897 MPa), the fractional error is less than 10 %. For an axial stress of 20,000 psi (138 MPa), the decrease in applied stress is on the order of 50 psi (0.3 MPa) or less for most soils.

Without performing some type of axisymmetric finite element analysis, the effects of wave propagation within a uniaxial strain device during explosively loaded testing cannot be fully evaluated. As

the explosive is detonated, a wave travels down the sides of the device, is reflected at the base of the device and propagates back up through the sample. The WES 0.1-msec was placed on a rubber mat to serve as a isolation system. The test results presented in Chapter IV did not produce any unusual wave forms or irregularities that can be attributed to a reflected wave coming back up through the sample.

3.6 Device Capabilities and Limitations

The WES 0.1-msec uniaxial strain device was designed to test at pressures up to 20,000 psi (138 MPa). The pressure cell, proximeter, and LVDT were all rated to withstand these pressures. The LVDT was not used in dynamic testing; however, previous experience at WES has shown that the commerically available LVDTs will not withstand dynamic application of 20,000 psi (138 MPa) of pressure. The pressure cell and proximeter worked well under these conditions. Also, the pressure cell and proximeter have high natural frequencies, and testing into the submillisecond range did not produce any measuring difficulties.

At present, the state-of-the-art does not offer a better measurement system than the variable impedance proximeter used in the device. However, some improvements are needed. The proximeter provides a workable system, but there are several problems in using it. First, the calibration steps must be applied manually for every test because the oscillator-demodulator has been rezeroed during the previous test. Secondly, a calibration test must be performed for every soil over the range of expected values of water content and density to verify that the proximeter measured displacement is a true

displacement. Lastly, at pressures in excess of 15,000 psi (103 MPa) with rise times to peak of around 0.3 msec or less, the proximeter target will track the surface deflection of the initial compression wave. However, when the compression wave is reflected at the rigid bottom boundary of the soil container and propagates up through to the sample surface, the target tends to separate from the sample surface causing errors in the measured displacements. This problem will addressed in greater detail in Chapter V.

The device was orginally designed to test soils for rise times in the submillisecond range only. The device was modified to perform static tests because of the problems associated with trying to calibrate the proximeter. The next generation device should allow for testing at a wide variety of loading rates to preclude the use of different test devices.

CHAPTER IV

UNIAXIAL STRAIN TEST RESULTS FOR FOUR PARTIALLY SATURATED SOILS

4.1 Introduction

This chapter summarizes the results of 93 uniaxial strain
compression tests that were performed to investigate loading rate
effects on the one-dimensional compression characteristics of four
soils; two clean sands, a clayey sand, and a silty clay. The soils
tested were chosen because of their importance to defense related
projects and the availability of field measurements to verify the
laboratory results. The grain-crushing characteristics, material
properties, and mineralogical composition of each of these four soils
are presented. All tests were performed under undrained, partially
saturated, and remolded conditions.

Two distinct types of sand were tested; carbonate and quartz
sands which are referred to as Enewetak beach and flume sands,
respectively. Of the four soils tested, the most comprehensive
laboratory program was performed using Enewetak beach sand, which was
taken from the beach at the north end of Enewetak Island. A concurrent
test program (documented by Akers, 1986) was performed at WES to define
the uniaxial strain response of this material. Thus, funding and
resources were available to obtain a large number of highly repeatable
test results at a wide variety of loading rates. The flume sand is a

by-product of a concrete aggregate processing facility near Fort Polk, Louisiana.

The clayey sand tested was taken from the Luke Bombing and Gunnery Range, Yuma, Arizona, and is referred to as Yuma clayey sand. This material is also referred to as CARES-Dry sand (Cargile, 1986) in the literature.

The clay tested was a loess deposit from Vicksburg, Mississippi, and is referred to as Vicksburg loess. Like the other three soils, this material was tested at a constant dry density and water content, varying the loading rate. An additional set of tests was performed varying the water content, dry density, and loading rate to determine their effects upon the uniaxial strain response.

The uniaxial strain results presented herein have been smoothed using a technique described in Appendix A. This smoothing does not affect the shape of the measured stress-strain response, but eliminates electrical noise that can mask the measurements obtained during testing. Appendix B contains the individual test results as plots of applied pressure versus average strain and applied pressure and average strain time histories.

For test results with supermillisecond rise times, the applied pressure and the average strain over the depth of the sample are equal to the vertical stress and strain, provided a true one-dimensional state exists (see Section 3.5). When wave propagation within the sample creates nonuniform stress and strain over the depth of the sample, vertical stress and strain are not equal to the applied pressure and

average strain measurements recorded during the test. When these conditions exist, the true stress-strain response must be interpreted from the laboratory measurements of applied pressure and average strain over the depth of the sample. Since this chapter is devoted to presenting laboratory measurements, the test results contained herein will be presented as plots of applied pressure versus average strain.

The PPUX test device was used to obtained supermillisecond test results only; whereas, the WES 0.1-msec device was used to test in the submillisecond range and statically. When compared, static results obtained using these two devices for the four soils tested were nearly identical. The production PPUX device has been used for numerous testing programs, and a high degree of confidence exists in its measuring and data acquisition systems. Since this was the first testing program for the WES 0.1-msec device, these comparisons provided confidence in the measurement and data acquisition systems.

4.2 Enewetak Beach Sand

Twenty-five uniaxial strain tests were performed on remolded samples of Enewetak beach sand at constant initial conditions for various loading rates. In addition, grain-size analyses (pretest and posttest), bulk specific gravity, specific gravity of solids, and maximum and minimum dry density tests were performed. This light-brown sand classified as SP based upon the Unified Soil Classification System (USCS) (Howard, 1977). Four pretest grain-size distribution analyses were performed with nearly identical results. The pretest grain-size distribution curve is shown in Fig. 4.2.1.
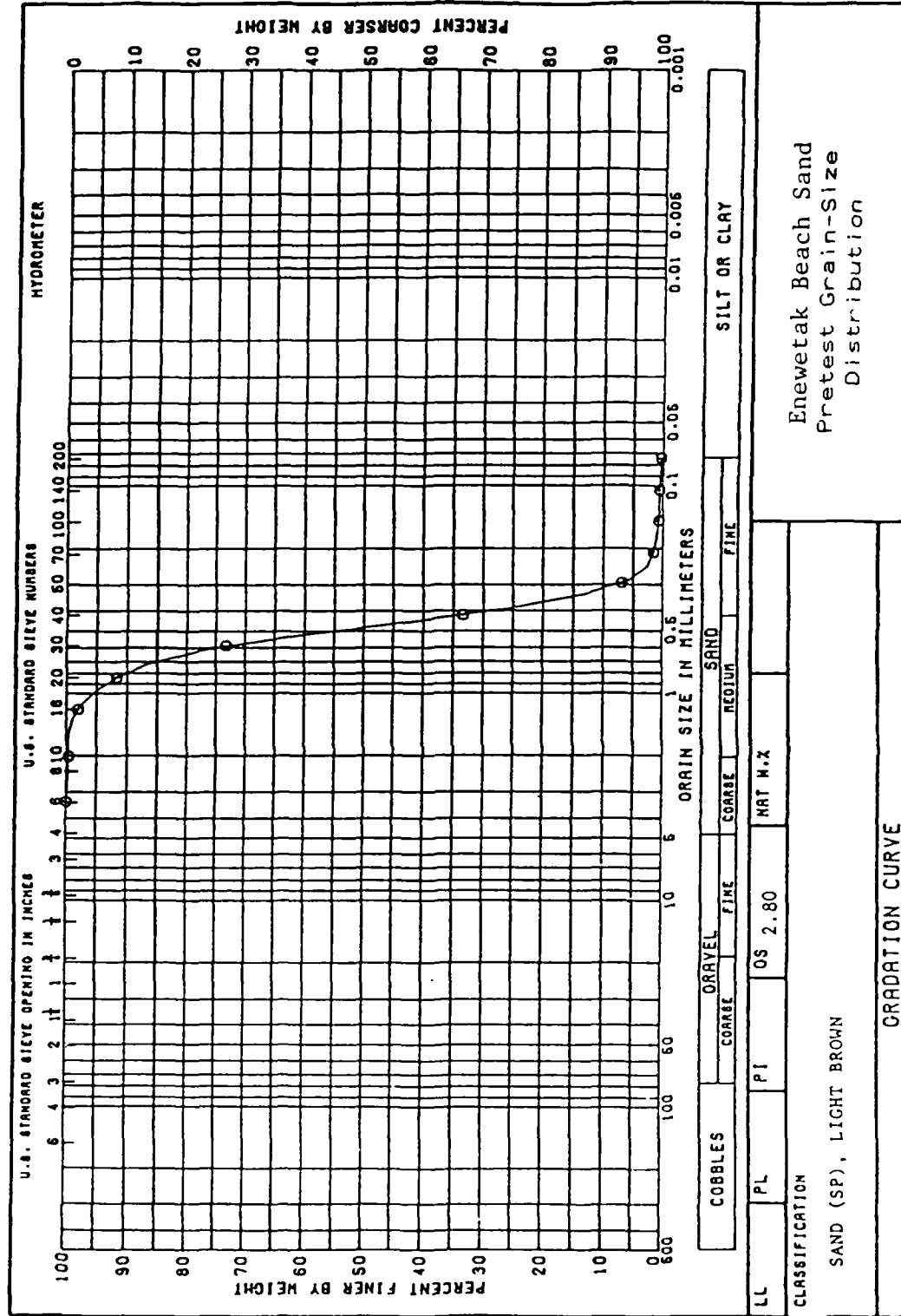
Figure 4.2.1 Pretest grain-size distribution for Enewetak beach sand.

The specific gravity of solids was determined to be 2.78. Based upon this value, the amount of the solid constituents, aragonite and calcite, were estimated to be 26 and 74 %, respectively. Two sets of minimum and maximum dry density values were determined. Average values of minimum dry density of 95.9 pcf (1.54 g/cc) and maximum dry density of 108.7 pcf (1.74 g/cc) were determined.

Tables 4.2.1 and 4.2.2 summarize the conditions and designations used for the Enewetak beach sand testing program. Values of 5 % for the water content and 101.0 pcf (1.62 g/cc) for the dry density (i.e., a relative density of 42.9 %) were target values for the testing program. Since the soil was taken from a salt-water environment, salt water was used to adjust the water content. The water content values shown in Tables 4.2.1 and 4.2.2 were adjusted to account for the salt left on the solids during oven drying. Figure 4.2.2 shows how the dry density, degree of saturation, and volume of air change during uniaxial strain compression based upon these initial conditions.

Sample preparation proved to be very important in obtaining reproducible test results for this material. Samples tested in the PPUX device, designated CS1, were 0.9-in (2.29-cm) high; whereas samples tested in the WES 0.1-msec device, designated CS2, were 0.5-in (1.27-cm) high. All samples were placed in two approximately equal lifts and compacted using a 1-in- (2.54-cm-) diameter tamping rod. The slightest variation from this procedure was found to significantly affect the measured response.

TEST NUMBER	WATER CONTENT (%)		WET UNIT WEIGHT (pcf) (g/cc)		DRY UNIT WEIGHT (pcf) (g/cc)		DESIGNATION
	PRE	POST					
CS1-01	-	-	106.0	1.70	-	-	STATIC
CS1-02	-	-	106.0	1.70	-	-	STATIC
CS1-03	-	5.0	106.0	1.70	101.0	1.62	STATIC
CS1-04	-	4.8	106.0	1.70	101.1	1.62	STATIC
CS1-05	-	5.0	106.0	1.70	101.0	1.62	FAST STATIC
CS1-06	-	4.8	106.0	1.70	101.2	1.62	FAST STATIC
CS1-07	-	4.8	106.0	1.70	101.1	1.62	SLOW DYNAMIC
CS1-08	-	4.9	106.0	1.70	101.1	1.62	SLOW DYNAMIC
CS1-09	-	4.9	106.0	1.70	101.1	1.62	DYNAMIC
CS1-10	-	5.0	106.0	1.70	101.0	1.62	DYNAMIC
CS1-11	-	4.8	106.0	1.70	101.1	1.62	DYNAMIC
CS1-12	-	4.9	106.0	1.70	101.1	1.62	DYNAMIC
CSCREEP-01	-	-	106.0	1.70	-	-	DYNAMIC CREEP
CSCREEP-02	-	4.8	106.0	1.70	101.1	1.62	DYNAMIC CREEP

TABLE 4.2.1 Summary of tests performed on Enewetak beach sand in the PPUX device.

TEST NUMBER	WATER CONTENT (%)		WET UNIT WEIGHT		DRY UNIT WEIGHT		DESIGNATION
	PRE	POST	(pcf)	(g/cc)	(pcf)	(g/cc)	
CS2-01	4.9	-	106.1	1.70	101.1	1.62	STATIC
CS2-02	4.8	-	106.1	1.70	101.1	1.62	STATIC
CS2-03	4.9	-	106.1	1.70	101.1	1.62	STATIC
CS2-04	-	4.8	106.1	1.70	101.3	1.62	DYNAMIC
CS2-05	-	4.9	106.1	1.70	101.1	1.62	DYNAMIC
CS2-06	-	-	106.1	1.70	-	-	DYNAMIC
CS2-07	-	-	106.1	1.70	-	-	DYNAMIC
CS2-08	-	5.8	106.1	1.70	100.3	1.61	DYNAMIC
CS2-09	5.2	4.9	106.1	1.70	101.0	1.62	SLOW STATIC
CS2-10	5.2	-	106.1	1.70	100.9	1.62	SLOW STATIC
CS2-11	-	5.2	106.1	1.70	100.8	1.62	SLOW STATIC

Table 4.2.2   Summary of tests performed on Enewetak beach sand in the WES 0.1-msec device.
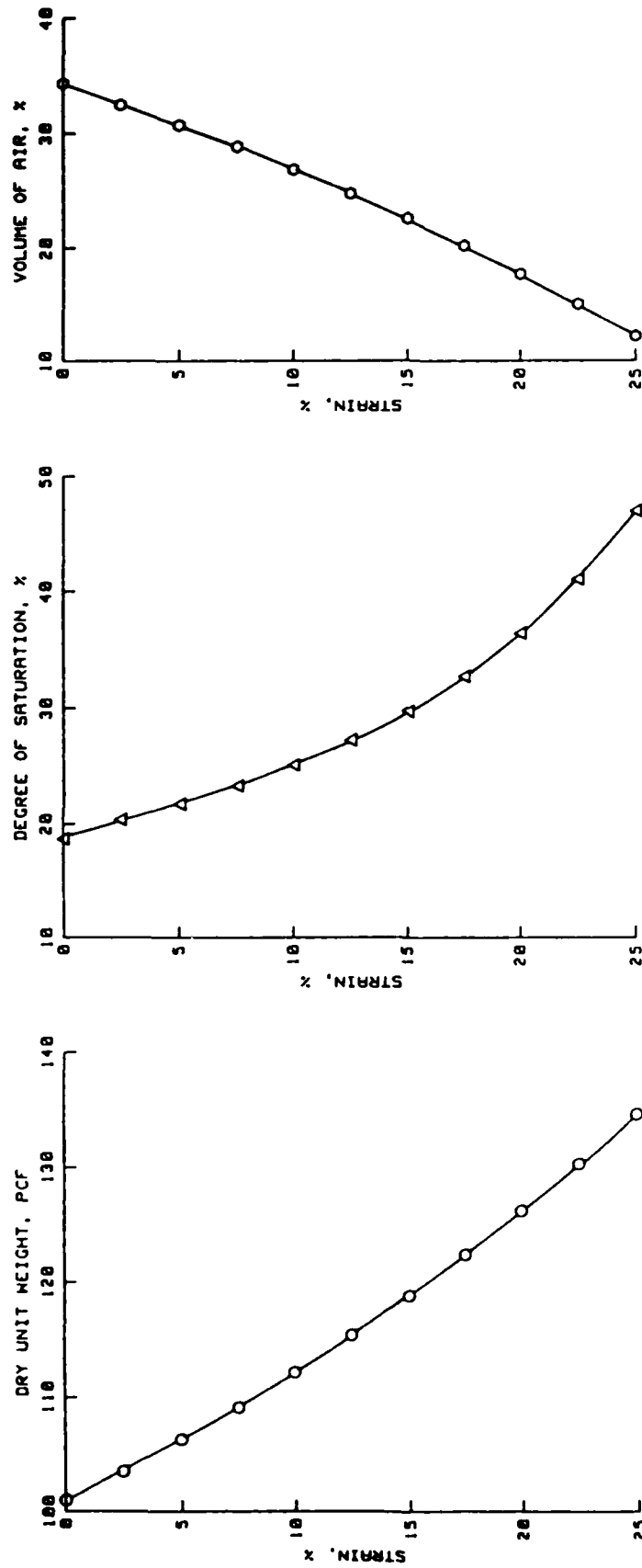
Figure 4.2.2 Dry density, degree of saturation, and volume of air as a function of uniaxial strain for Enewetak beach sand tests.

The term "static" was arbitrarily chosen as being a test with a rise time to peak pressure of about 30-100 seconds. The problems associated with leakage during high-pressure testing prevents long-term loading of most soils. Values with rise times to peak in tens-of-seconds appear to be the norm for static uniaxial strain testing. Figure 4.2.3 presents the results of three series of static tests. The results designated as slow static had rise times to peak pressure ranging from 140 to 210 seconds. The series designated as static had rise times to peak from 30 to 80 seconds. Those tests designated as fast static had rise times to peak of approximately 18 seconds. Depending upon the laboratory, technician, or engineer, any of these tests could be reported as static results. This figure demonstrates the importance of defining a standard rise time or applied stress rate for static testing so that test results between two laboratories or even devices can be objectively compared.

Figure 4.2.4 summarizes the effects of loading rate upon the uniaxial strain response of Enewetak beach sand. These tests are representative of the average uniaxial strain response for various loading rates. Tests CS2-10, CS1-03, and CS1-06 are representative of the average response for tests with loading rates designated as slow static, static, and fast static, respectively. Test CS1-08 is representative of the response that has been termed as slow dynamic. This test is representative of the slower dynamic loading rates that can be achieved using the ram-type loaders described in Section 2.4. These tests had rise times to peak pressure of approximately 150 msec. At these slower dynamic loading rates, the gas-driven, ram-type loaders

Uniaxial Strain Results
Soil Type: Enewetak Beach Sand
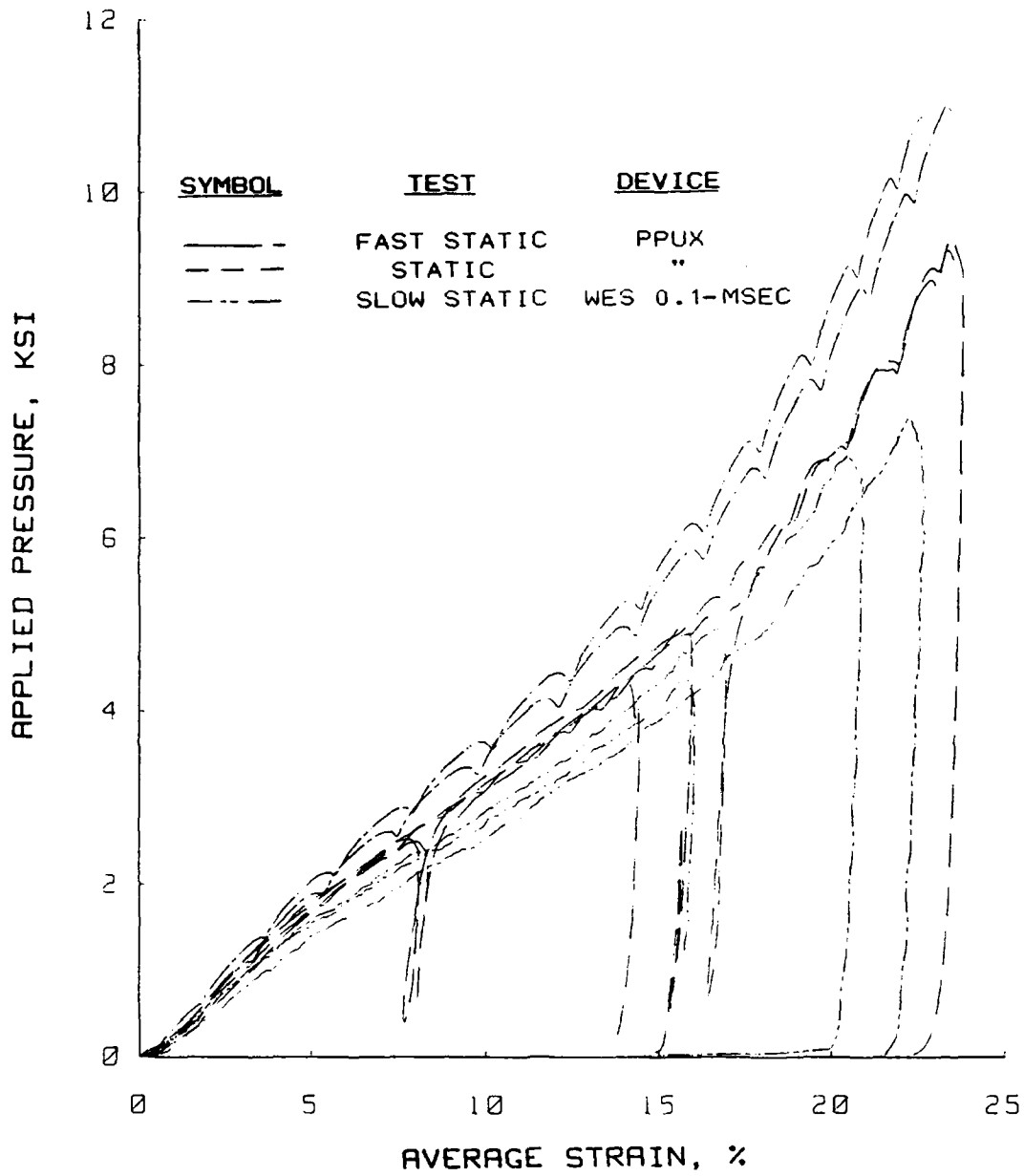
Figure 4.2.5   Three series of static uniaxial strain results for Enewetak beach sand.

Uniaxial Strain Results
Soil Type: Enewetak Beach Sand

SYMBOL	TEST	TIME TO 5 KSI (SEC)
———	CS2-10	155
— — —	CS1-03	12
—·—	CS1-06	5
—··—	CS1-08	0.062
—:·—	CS1-10	0.003
—··—	CS2-05	0.0004
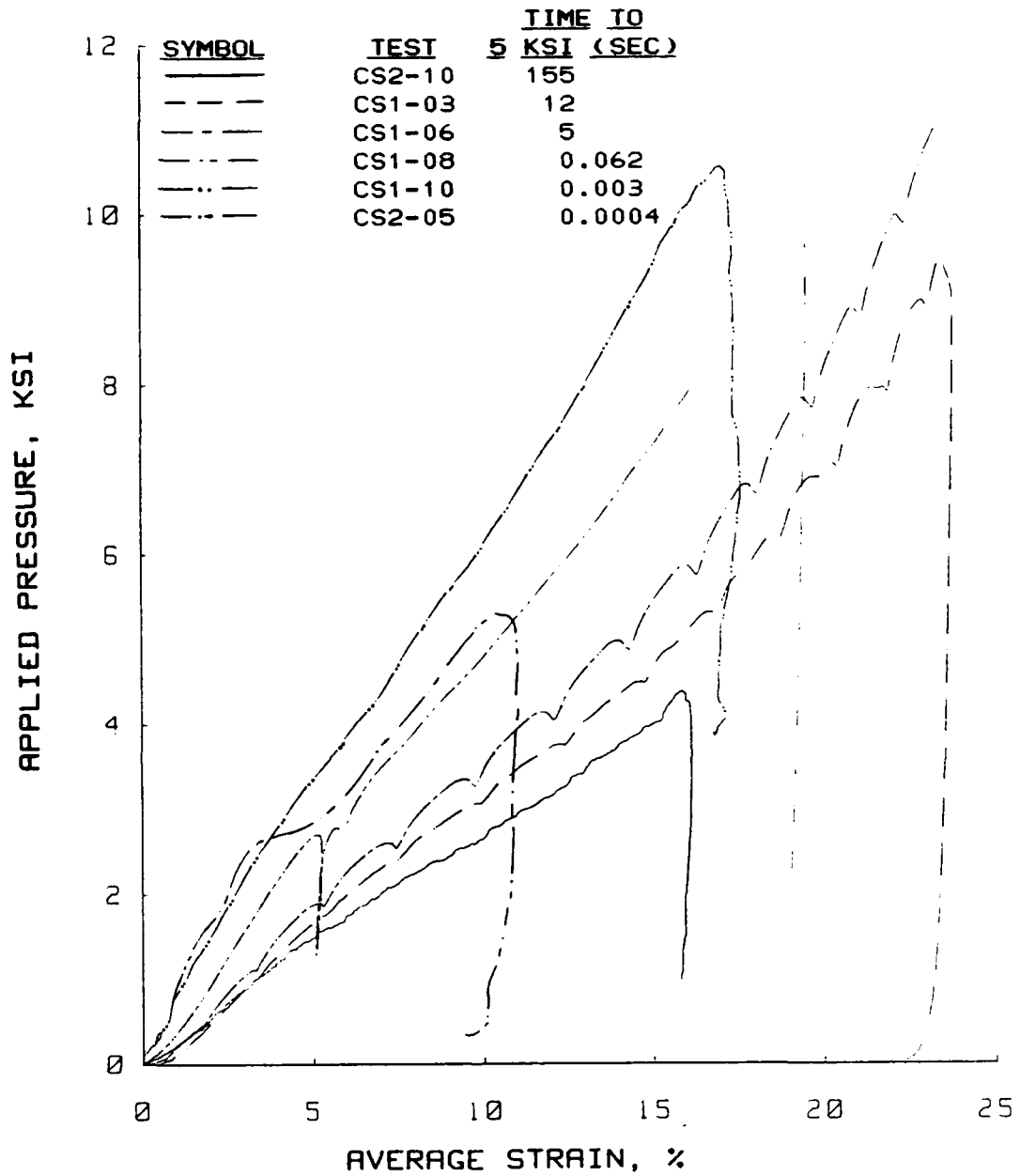
Figure 4.2.4   Loading rate effects for Enewetak beach sand.

created irregular loading pulses producing test results that are difficult to interpret. Test CS1-10 is representative of the loading rate that has been defined as dynamic. These tests typically have rise times to peak pressure of about 6 msec. Test CS2-05 is a typical submillisecond test having a rise time to peak pressure of about 0.5 msec. This test was performed using a 10-ksi (69-MPa) EBW cap. As shown in Fig. 4.2.4, a significant rate effect exists for this material. It is important to note that, in the submillisecond range, a drastic stiffening of the measured response does not occur, but instead a progressive stiffening occurs as the rise time to peak pressure decreases.

Two tests were performed to investigate what has been termed as the dynamic creep behavior of Enewetak beach sand. These tests had rise times of 50 msec and hold times of about 0.5 and 1.0 sec and are presented in Fig. 4.2.5. Also plotted on Fig. 4.2.5, is the stress-strain response for test CS1-06. Test CSC1-02 had a hold time of 1.0 sec at a peak pressure of approximately 9.0 ksi (62.1 MPa). Test CS1-06 reached a stress value of 9.0 ksi (62.1 MPa) in about 10 sec. As shown in Fig. 4.2.5, the average strain values are approximately equal at the peak stress for the creep tests and test CS1-06.

Grain-size distributions were performed on most of the posttest samples under this testing program. These results are summarized in Fig. 4.2.6. As expected, the faster the loading rate, the less strain occurs at a given stress level and the less grain crushing occurs. The mineral constituents of this material, aragonite and calcite, are

Uniaxial Strain Results
Soil Type: Enewetak Beach Sand
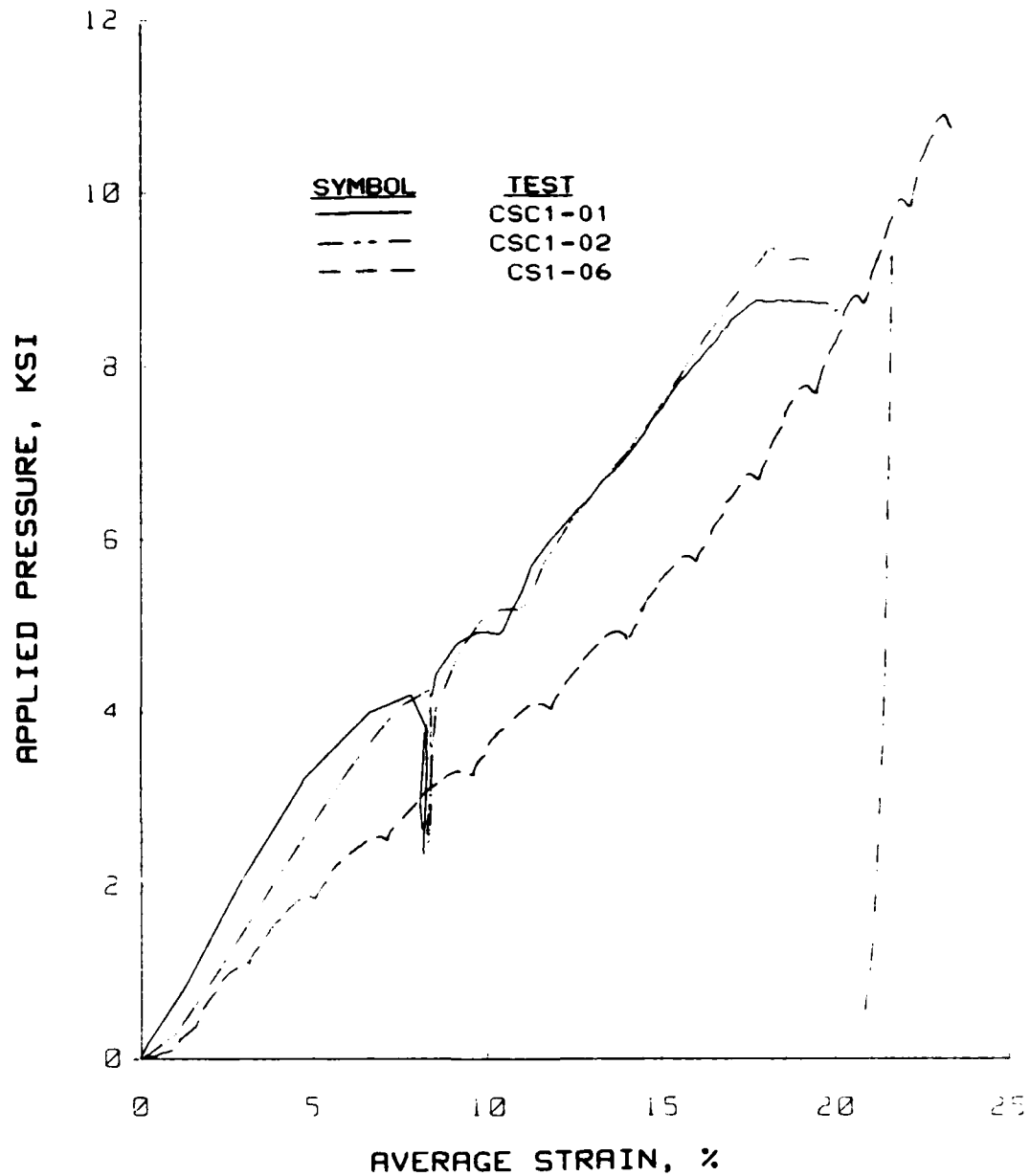
Figure 4.2.5 Dynamic creep tests for Enewetak beach sand.
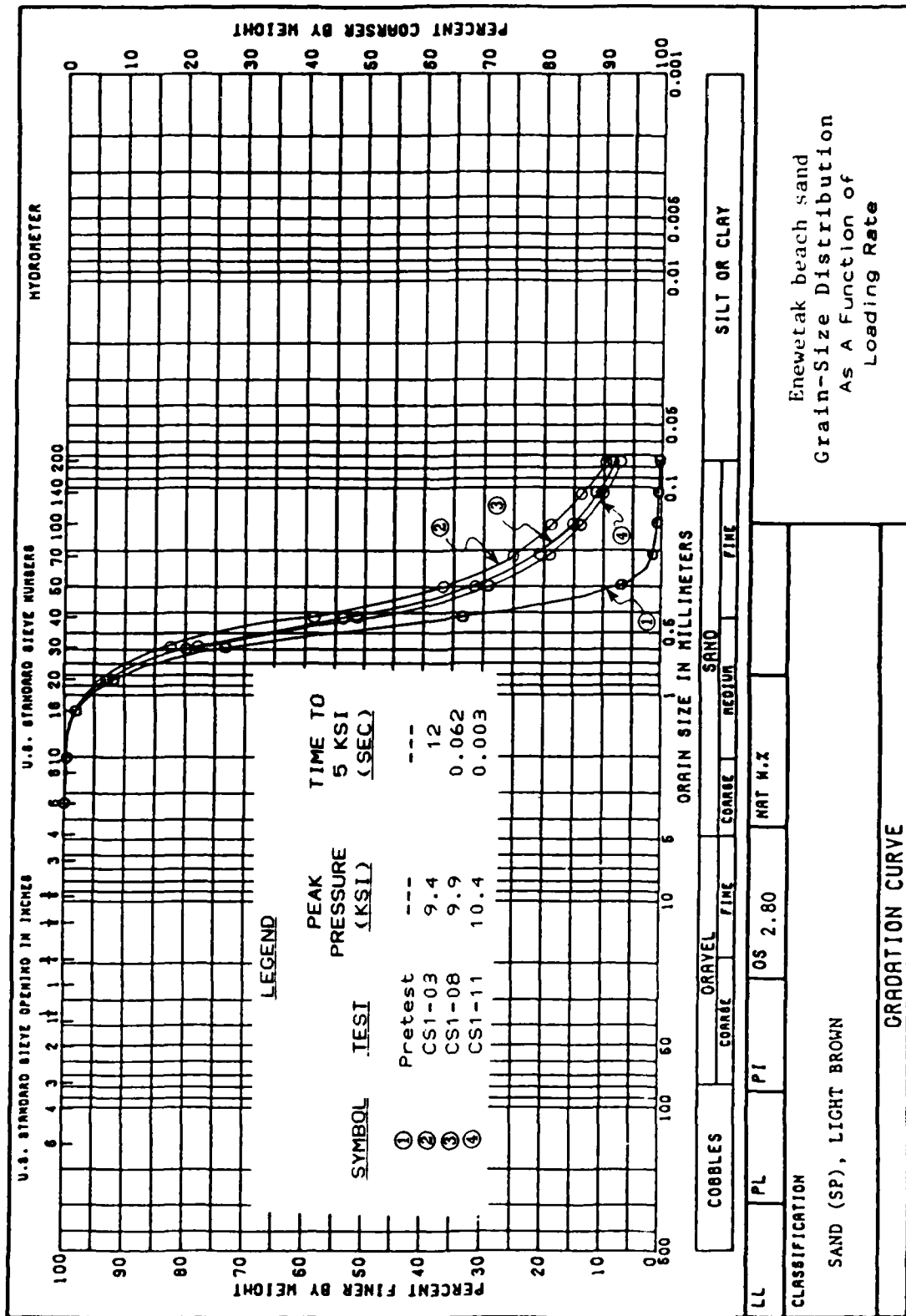
Figure 4.2.6 Grain crushing as a function of loading rate for Enewetak beach sand.

relatively soft minerals and susceptible to grain crushing. Figure 4.2.7 presents pretest and posttest photographs of the individual sand grains.

4.3 Flume Sand

Eighteen uniaxial strain tests were performed on remolded samples of flume sand to investigate loading rate effects. In addition, grain-size analysis (pretest and posttest), specific gravity of solids, and maximum and minimum dry densities are presented. This light-brown sand classified as SP based upon the USCS system.

The material properties of flume sand have been determined and documented (Green, 1986a). The samples used in this testing program were from the same source as those reported by Green (1986a). A comparison of grain-size distributions showed the two samples to be nearly identical. A pretest grain-size distribution is shown in Fig. 4.3.1.

Green (1986a) reported that flume sand had a specific gravity of 2.64, a maximum dry density of 112.3 pcf (1.80 g/cc), and a minimum dry density of 93.6 pcf (1.50 g/cc). The mineral constituents of flume sand as determined by x-ray diffraction are listed in Table 4.3.1.

Table 4.3.2 summarizes the conditions and designations used for the flume sand testing program. Values of 5.5 % and 100.5 pcf (1.62 g/cc) for water content and dry density were target values for this testing program, respectively. Figure 4.3.2 shows how the dry
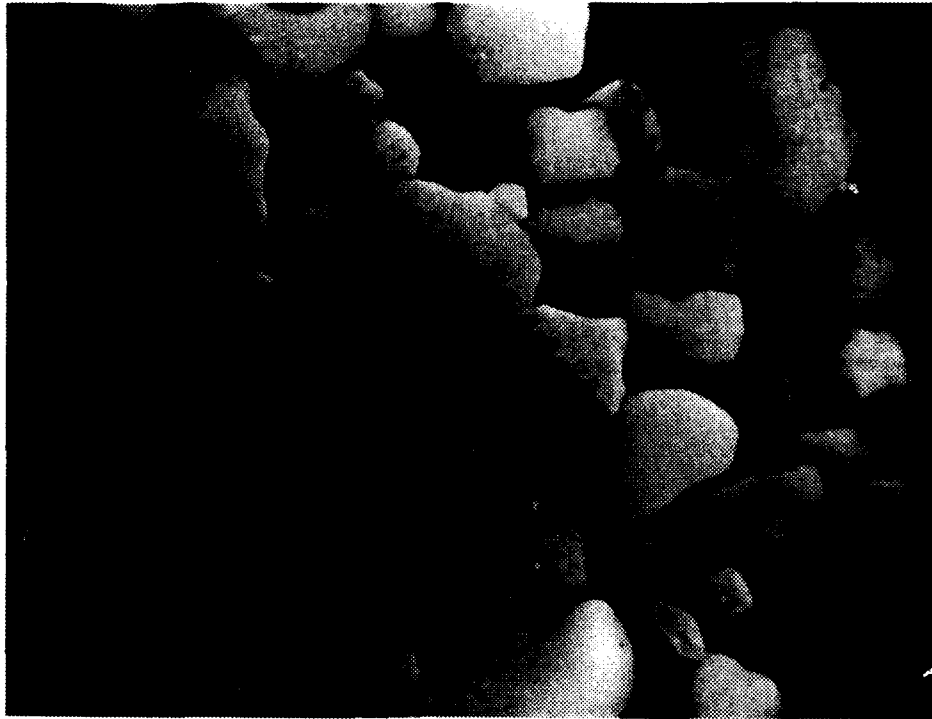
Pretest
(Bulk Sample, 28 X)
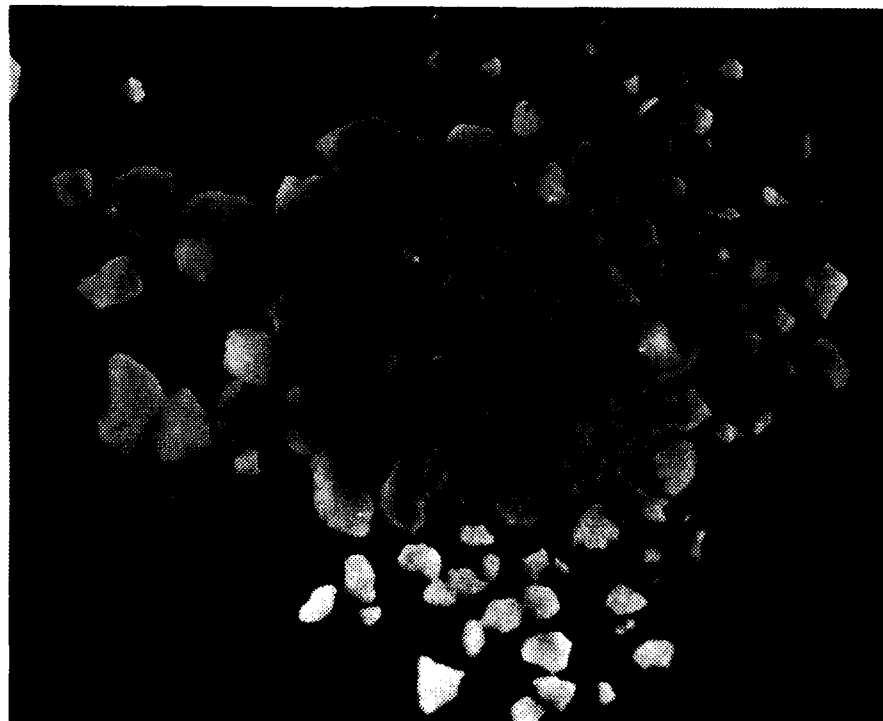
Posttest
(Bulk Sample, Static Test, 28 X)

Figure 4.2.7   Photographs of pretest and posttest grains of Enewetak
beach sand.
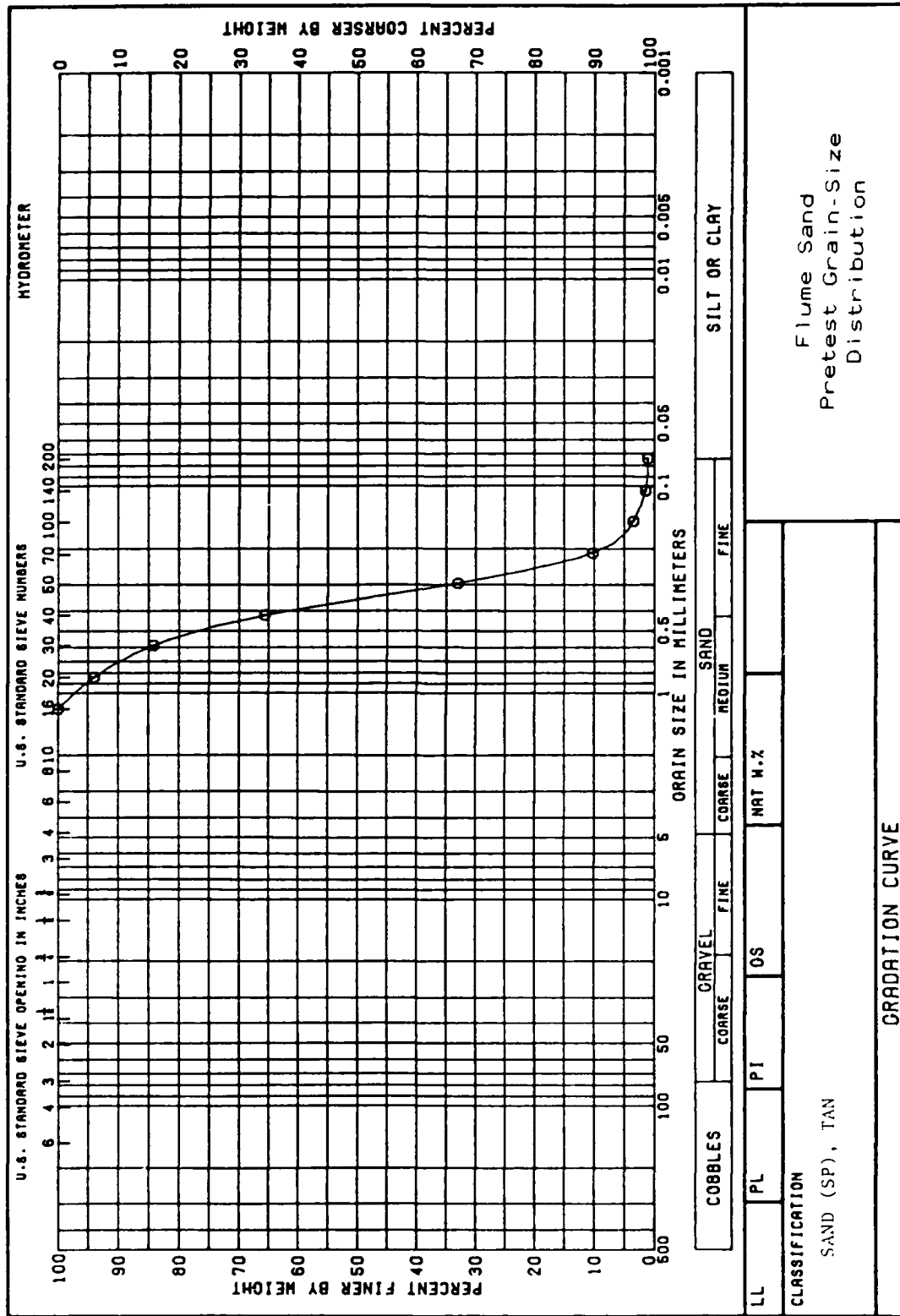
Figure 4.3.1 Pretest grain-size distribution for flume sand.

Mineral Constituents	Amount
Clays	
Smectite	X
Clay-mica	X
Kaolinite	X
Non-Clays	
Quartz	A
Potassium Feldspars	X
Sillimanite	X
Mica	X

Legend

Abundant (A) > 50 %
Intermediate (I) = 25 to 50 %
Common (C) = 10 to 25 %
Minor (M) = 5 to 10 %
Traces (X) = small quantities present

Table 4.3.1 Mineralogical composition of flume sand.

TEST NUMBER	WATER CONTENT (%)		WET UNIT WEIGHT		DRY UNIT WEIGHT		DESGINATION
	PRE	POST	(pcf)	(g/cc)	(pcf)	(g/cc)	
FS1-01	–	5.5	106.0	1.70	100.5	1.61	STATIC
FS1-02	–	5.2	106.0	1.70	100.8	1.62	STATIC
FS1-03	–	5.3	106.0	1.70	100.8	1.62	STATIC
FS2-01	–	5.7	106.0	1.70	100.3	1.61	STATIC
FS2-02	–	5.3	106.0	1.70	100.7	1.61	STATIC
FS2-03	–	5.5	106.0	1.70	100.5	1.61	STATIC
FS2-04	–	5.4	106.0	1.70	100.6	1.61	STATIC
FS1-04	–	5.4	106.0	1.70	100.6	1.61	SLOW DYNAMIC
FS1-05	–	5.4	106.0	1.70	100.6	1.61	SLOW DYNAMIC
FS1-06	–	5.4	106.0	1.70	100.7	1.61	SLOW DYNAMIC
FS1-07	–	5.2	106.0	1.70	100.8	1.62	DYNAMIC
FS1-08	–	5.2	106.0	1.70	100.8	1.62	DYNAMIC
FS1-09	–	5.2	106.0	1.70	100.8	1.62	DYNAMIC
FS2-05	–	5.5	106.0	1.70	100.4	1.61	DYNAMIC
FS2-06	–	5.4	106.0	1.70	100.6	1.61	DYNAMIC
FS2-07	–	5.2	106.0	1.70	100.8	1.62	DYNAMIC
FS2-08	–	5.3	106.0	1.70	100.6	1.61	DYNAMIC
FS2-09	–	5.7	106.0	1.70	100.3	1.61	DYNAMIC

TABLE 4.3.2 Summary of tests performed on flume sand.

Figure 4.3.2 Dry density, degree of saturation, and volume of air as a function of uniaxial strain for flume sand tests.

Initial Conditions

γ_d = 100.5 pcf
w = 5.5 %
γ_w = 62.4 pcf
G_s = 2.64
D_r = 41.2%

density, degree of saturation, and volume of air change during uniaxial strain compression for these initial conditions.

Samples were prepared for this testing program using the same techniques as described for beach sand. However, for these results, a 0.4-in- (1.02-cm-) high plug was placed in the PPUX device making the height of the specimen cavity 0.5 in (1.27 cm). This corresponds to the height of the WES 0.1-msec device specimen cavity. The remainder of the tests performed in the PPUX device (Yuma clayey sand and Vicksburg loess) were conducted with this plug in the specimen cavity. By testing samples with the same height, the error created by different specimen heights due to sidewall friction between the two devices was eliminated.

The results of the flume sand testing program are summarized in Figure 4.3.3. Tests performed in the PPUX and WES 0.1-msec device are designated as FS1 and FS2, respectively. As shown in this figure, a small rate effect exists; however, it does not approach the magnitude of that measured for beach sand. Test FS1-02 is representative of the static behavior. Static tests were performed with rise times to peak ranging from 3 to 160 sec. Unlike the beach sand, a difference in the response could not be detected for various supersecond loadings. Test FS1-05 had a rise time to peak pressure of 225 msec with a hold time of 150 msec at peak. As shown in Fig. 4.3.3, this material did not creep like the beach sand. Test FS1-07 is representative of the dynamic loading rate as produced by the ram-type loaders. This test had a rise time to peak of about 12 msec. As shown in Fig. 4.3.3, the behaviors of tests FS1-05 and FS1-07 are essentially the same. Test FS2-05 is

Uniaxial Strain Results
Soil Type: Flume Sand

SYMBOL	TEST	TIME TO 5 KSI (SEC)
——————	FS1-02	65.0
— — —	FS1-05	0.08
—·—·—	FS1-07	0.006
—··—··—	FS2-05	0.0005

TARGET
SEPARATES

APPLIED PRESSURE, KSI

AVERAGE STRAIN, %
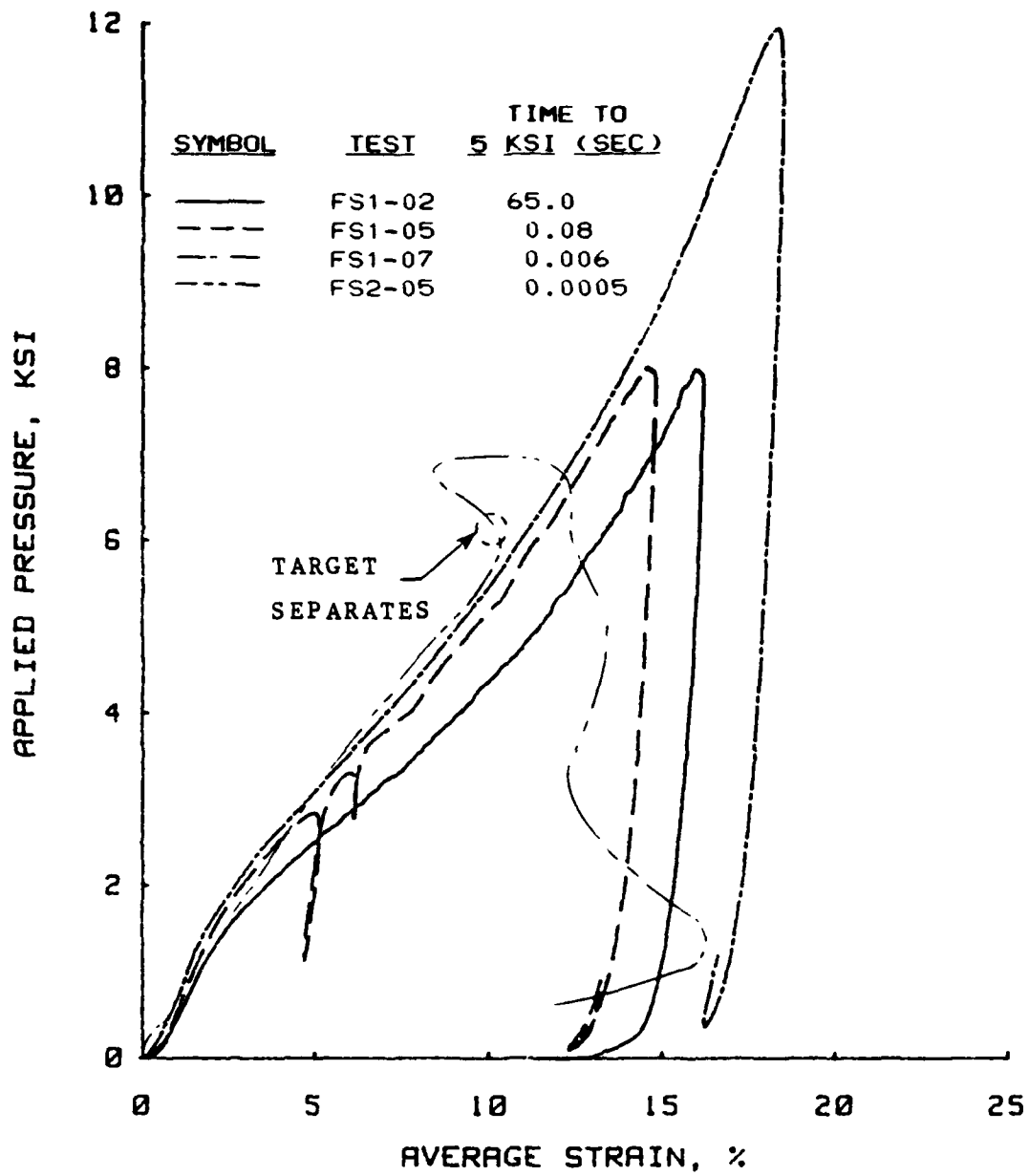
Figure 4.3.3 Loading rate effects for flume sand.

representative of a submillisecond test. Test FS2-05 was performed using a 10-ksi (69-MPa) EBW cap. As with the beach sand, the submillisecond loadings did not produce a drastic stiffening of the material response.

Table 4.3.1 lists the major mineral constituent of flume sand as being quartz. Quartz has a Moh's hardness value of 7, whereas calcite, the major constituent of Enewetak beach sand, has a value of 3 (Dietrich and Skinner, 1979). Posttest grain-size analyses were performed to investigate grain crushing and are presented in Fig. 4.3.4. The amount of grain crushing for the beach and flume sands was about the same for similar peak pressures. This was unexpected based on the relative hardness of the mineral constituents. Figure 4.3.5 shows pretest and posttest photographs of the individual flume sand grains. The posttest photograph was from a static test with a peak pressure of about 8 ksi (55.2 MPa).

The test results for flume sand contained the most scatter of any of the materials tested, especially for submillisecond testing. Also, during dynamic testing, the proximeter target tended to separate from the sample much more easily than with the other three materials. Care was taken to prepare each sample using the same procedure. The scatter can possibly be attributed to the loose pretest condition of the specimens. All tests were performed at an initial relative density of 41.2 %. The submillisecond results did prove conclusively that a drastic stiffening of the material response did not occur in the submillisecond loading range.

66

Figure 4.3.4 Grain crushing as a function of loading rate for flume sand.

Pretest
(Bulk Sample, 45 X)
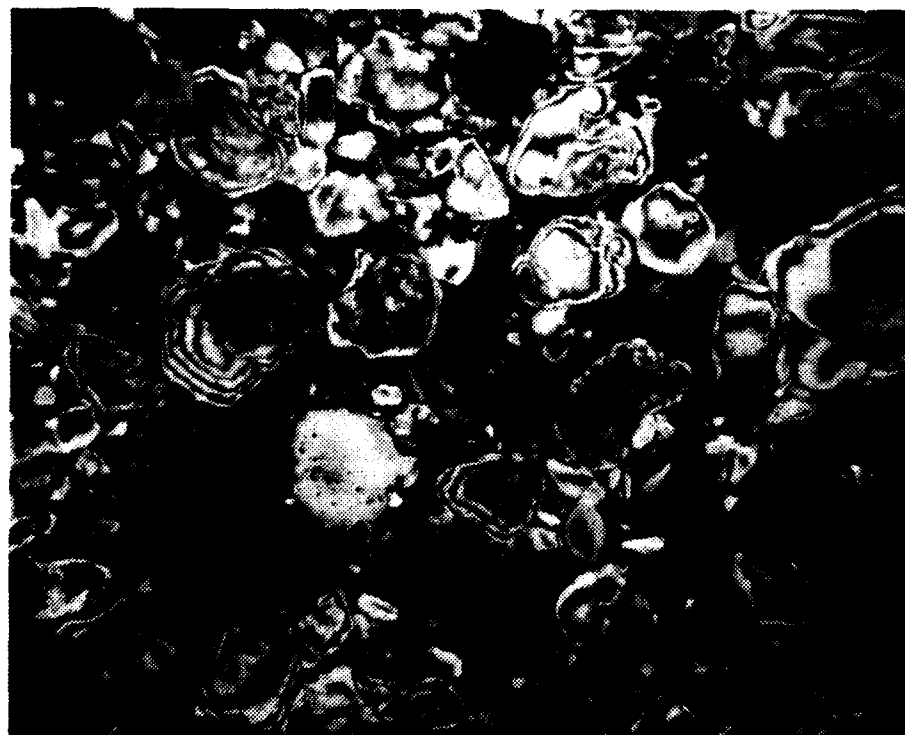
Posttest
(Bulk Sample, Static Test, 45 X)

Figure 4.3.5 Photographs of pretest and posttest grains of flume sand.

4.4   Yuma Clayey Sand

Sixteen uniaxial strain tests were performed on remolded samples of Yuma clayey sand to investigate loading rate effects. In addition, grain-size analysis (pretest and posttest), specific gravity of solids, and compaction test data are presented. This reddish-brown material classified as a SM-SC based upon the USCS system.

The material properties of this soil have been determined and presented by Cargile (1986). The samples tested were from the same source and had approximately the same gradation as those tested by Cargile (1986). A pretest grain-size distribution is shown in Fig. 4.4.1. A liquid limit (LL) of 48 and a plastic limit (PL) of 17 were determined for the sample used for the pretest grain-size distribution. The mineral constituents of this material as determined by x-ray diffraction are listed in Table 4.4.1.

Cargile (1986) reported that Yuma clayey sand had a specific gravity of 2.68. Standard proctor compaction values of maximum dry density of 121.7 pcf (1.95 g/cc) at an optimum water content of 11.6 % and modified proctor test values of maximum dry density of 131.7 pcf (2.11 g/cc) with an optimum water content of 7.9 % were also reported.

Table 4.4.2 summarizes the conditions and designations used for the Yuma clayey sand study. Values of 3.5 % and 115.0 pcf (1.84 g/cc) for water content and dry density were target values for the testing program. Figure 4.4.2 shows how the dry density, degree of saturation,
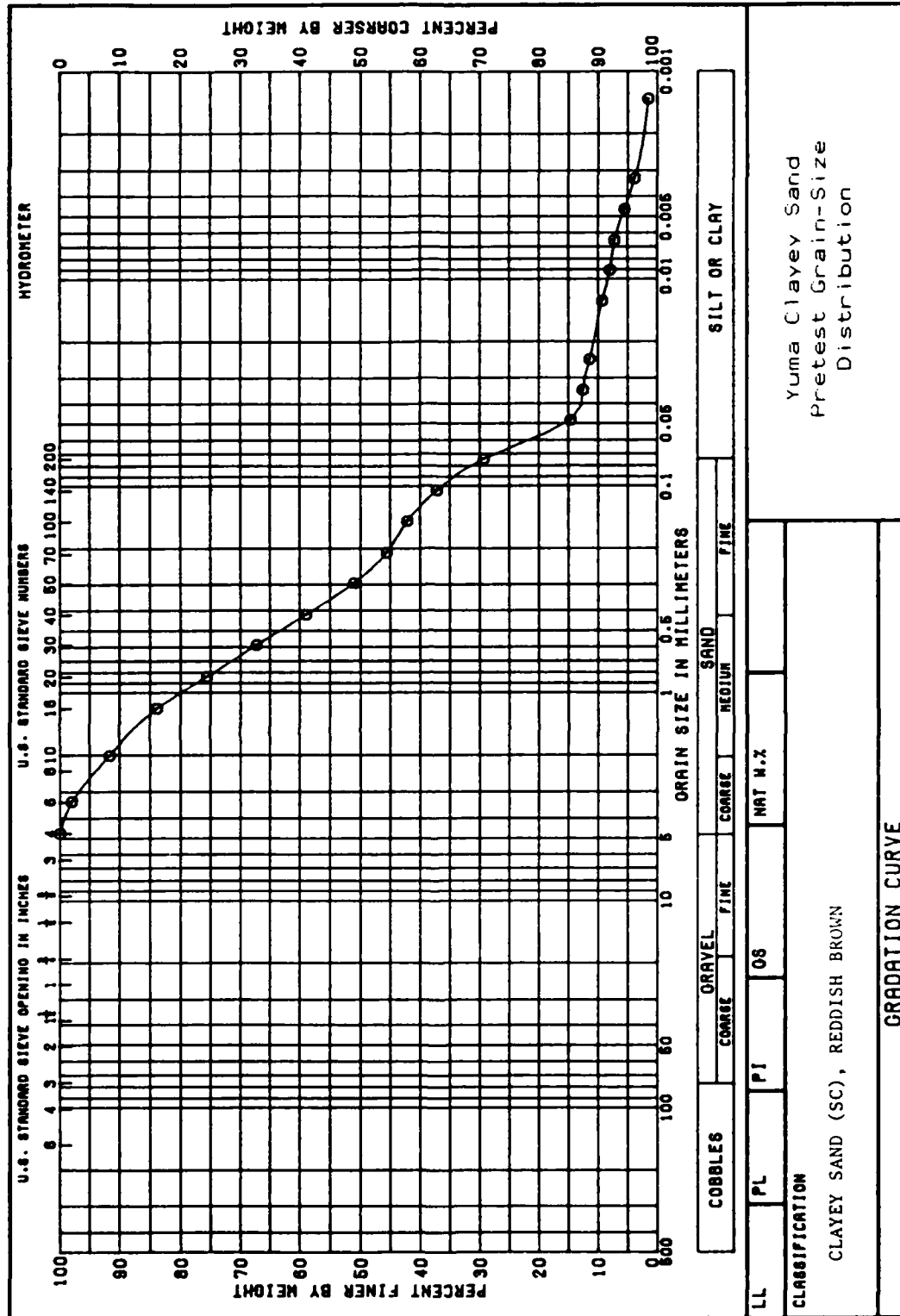
Figure 4.4.1 Pretest grain-size distribution for Yuma clayey sand.

Mineral Constituents	Amount
Clays	
Smectite	X
Chlorite	X
Vermiculite	X
Clay-mica	X
Kaolinite	X
Palygorskite	C
Non-Clays	
Quartz	I
Plagioclase Feldspars	C
Potassium Feldspars	C
Amphibole	X
Gypsum	X
Calcite	M
Dolomite	M
Mica	X
Magnetite	X

Legend

Abundant (A) > 50 %
Intermediate (I) = 25 to 50 %
Common (C) = 10 to 25 %
Minor (M) = 5 to 10 %
Trace (X) = small quanities present

Table 4.4.1 Mineralogical composition of Yuma clayey sand.

TEST NUMBER	WATER CONTENT (%)		WET UNIT WEIGHT		DRY UNIT WEIGHT		DESIGNATION
	PRE	POST	(pcf)	(g/cc)	(pcf)	(g/cc)	
YS1-01	-	-	118.9	1.91	-	-	STATIC
YS1-02	3.8	-	118.9	1.91	114.6	1.84	STATIC
YS1-03	-	3.7	118.9	1.91	114.7	1.84	STATIC
YS2-01	-	-	119.0	1.91	-	-	STATIC
YS2-02	-	-	119.0	1.91	-	-	STATIC
YS2-03	-	-	119.0	1.91	-	-	STATIC
YS1-04	-	3.5	118.9	1.91	114.9	1.84	SLOW DYNAMIC
YS1-05	-	3.9	118.9	1.91	114.5	1.83	SLOW DYNAMIC
YS1-06	-	3.4	118.9	1.91	115.1	1.84	DYNAMIC
YS1-07	-	-	118.9	1.91	-	-	DYNAMIC
YS1-08	-	3.5	118.9	1.91	115.0	1.84	DYNAMIC
YS1-09	-	3.3	118.9	1.91	114.7	1.84	DYNAMIC
YS2-04	-	3.7	119.0	1.91	114.7	1.84	DYNAMIC
YS2-05	-	-	119.0	1.91	-	-	DYNAMIC
YS2-06	-	-	119.0	1.91	-	-	DYNAMIC
YS2-07	-	-	119.0	1.91	-	-	DYNAMIC

TABLE 4.4.2 Summary of tests performed on Yuma clayey sand.
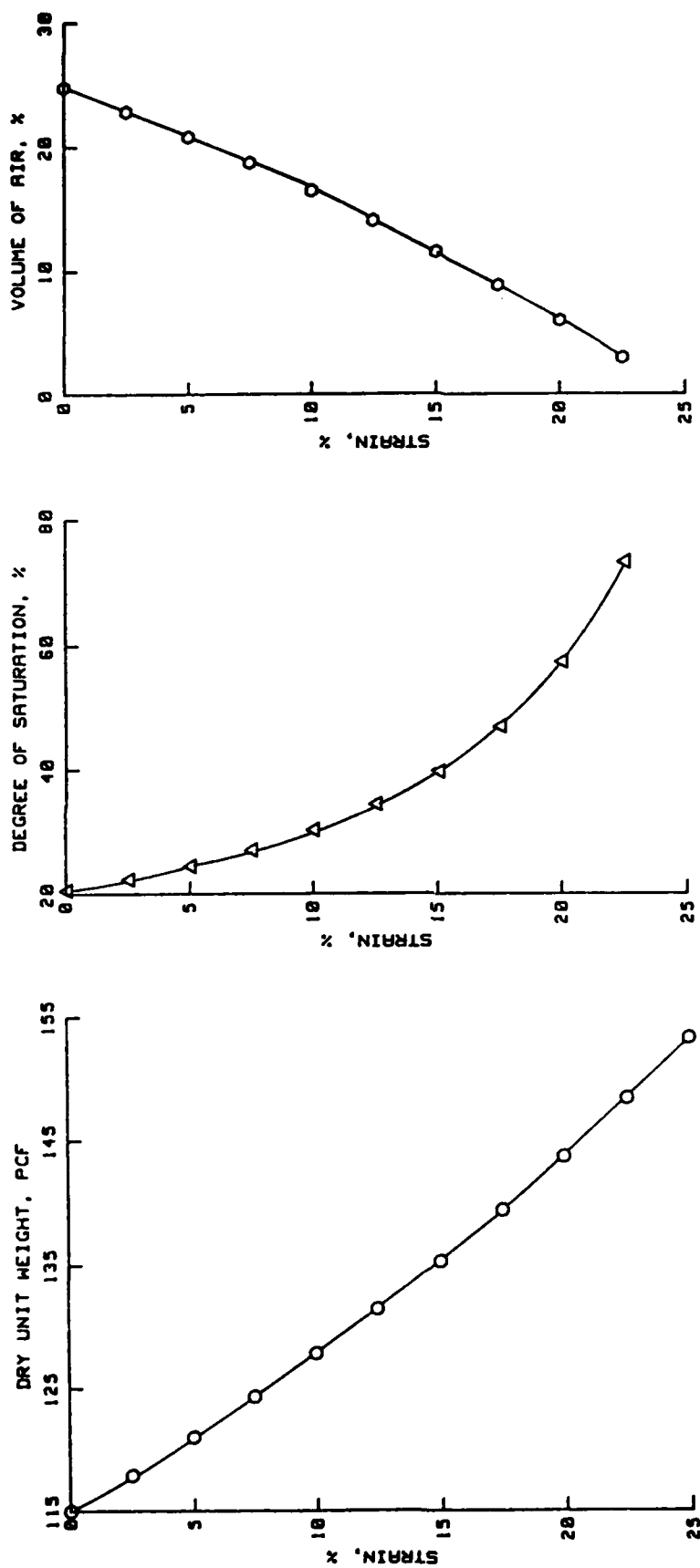
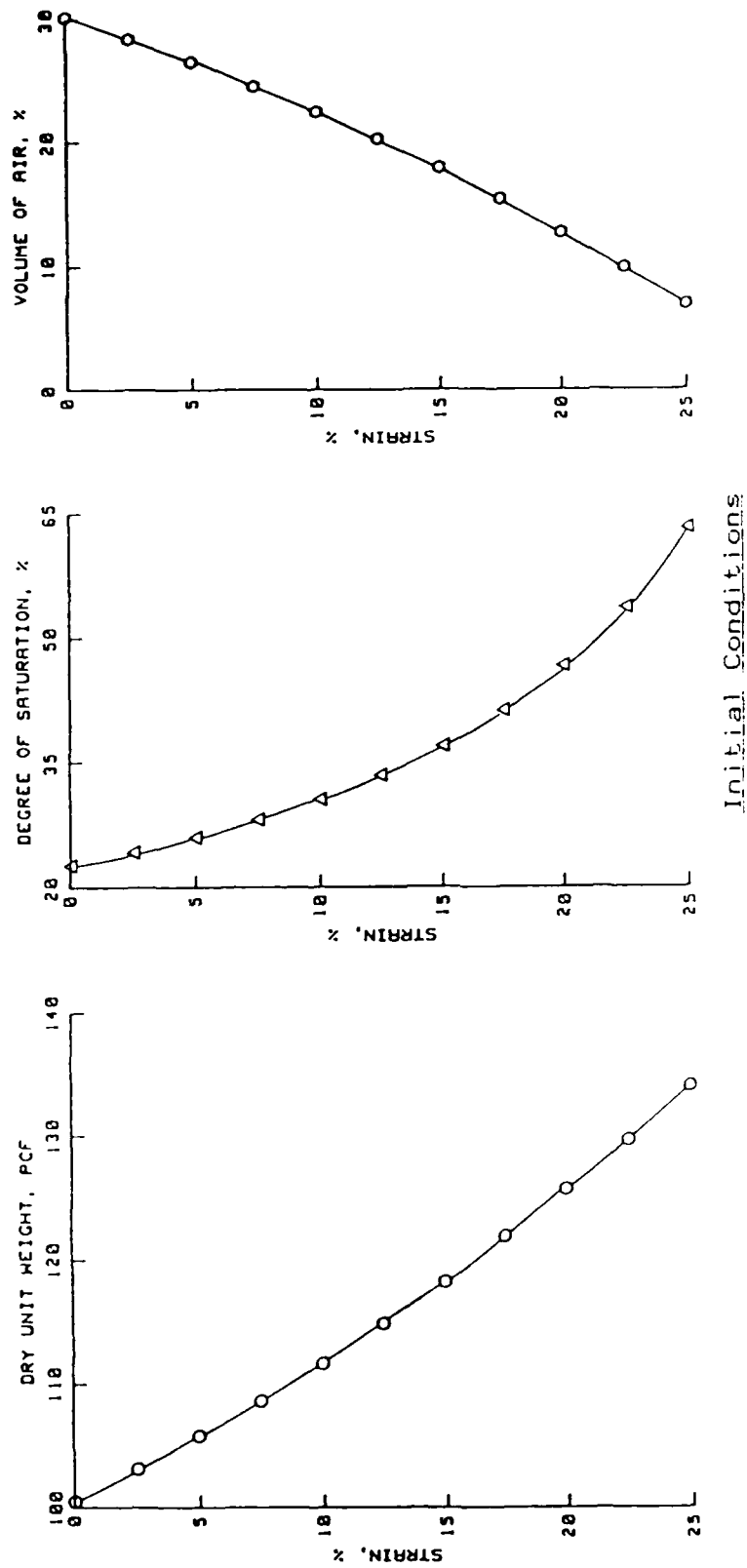Figure 4.4.2 Dry density, degree of saturation, and volume of air as a function of uniaxial strain for Yuma clayey sand tests.

and volume of air change during uniaxial strain compression based upon these initial conditions.

For a water content of 3.5 %, a standard proctor value of 111.5 pcf (1.77 g/cc) and a modified proctor value of 122.5 pcf (1.96 g/cc) were determined. To obtain a dry density value of 115.0 pcf (1.84 g/cc), a significant amount of compaction effort was required. The sample preparation techniques used for beach and flume sand could not produce the desired density. The sample preparation procedure was altered to include placing the sample in three lifts and using a 3.8-in- (9.65-cm-) diameter plate and a rubber mallet to compact the sample in addition to the tamping rod. Unfortunately, the compaction procedure used to produce the desired density created an artificial prestress in the laboratory test specimens that is not present in undisturbed field specimens (Cargile, 1986). Thus, the results presented are probably not representative of in situ behavior at the Luke Bombing and Gunnery Range field test site.

As shown in Fig. 4.4.1, this material contains about 10 % coarse-size sand particles. These particles were very angular and punctured the membrane between the soil and the hydraulic fluid. Numerous tests were required to achieve the desired pressures. A target value of 8.0 ksi (55.2 MPa) was set for this program as a minimum peak pressure. Some of the results presented for Yuma clayey sand did not achieve this pressure because of the leakage problems. The problems encountered with leakage precluded obtaining numerous, highly repeatable tests. Numerous techniques were tried to build the samples so that the leakage problems could be alleviated. One of these techniques involved placing

the coarser-sized particles in the bottom of the sample and placing the fines at the top next to the membrane. However, this technique affected the initial shape of the stress-strain response.

The results of the rate effects study on Yuma clayey sand are summarized in Fig. 4.4.3. As shown in this figure, a rate effect does exist; however, it doesn't approach the magnitude of effect measured for beach sand, but is more than the effect measured for flume sand. Test YS1-02 is representative of a static test. Supersecond loading rates were varied from 35 to 65 sec to 5 ksi (34.5 MPa) without any distinguishable difference in the response. Tests YS1-05 and YS1-07 represent the slow dynamic and dynamic results obtainable with the ram-type loaders. Test YS1-05 had a rise time to a peak pressure of 8 ksi (55.2 MPa) of 170 msec with a load hold time of 280 msec without any creep. Test YS2-05 is representative of a submillisecond test. As with the previous results, the submillisecond loadings did not produce a drastic stiffening of the material response.

Some grain-crushing occurred during testing; however, the amount was less than the beach and flume sands. This can probably be attributed to the amount of fines present. Posttest grain-size analyses were performed on most of the tests and are summarized in Fig. 4.4.4. Pretest and posttest photographs of the individual grains of this material are shown in Fig. 4.4.5. This photograph shows more grain crushing than the posttest grain-size analysis. The posttest photograph was from a static test with 8.0 ksi (55.2 MPa) peak pressure.

Uniaxial Strain Results
Soil Type: Yuma Clayey Sand

SYMBOL	TEST	TIME TO 5 KSI (SEC)
———	YS1-02	65.0
— — —	YS1-05	0.08
—·—	YS1-07	0.008
—··—	YS2-05	0.0004
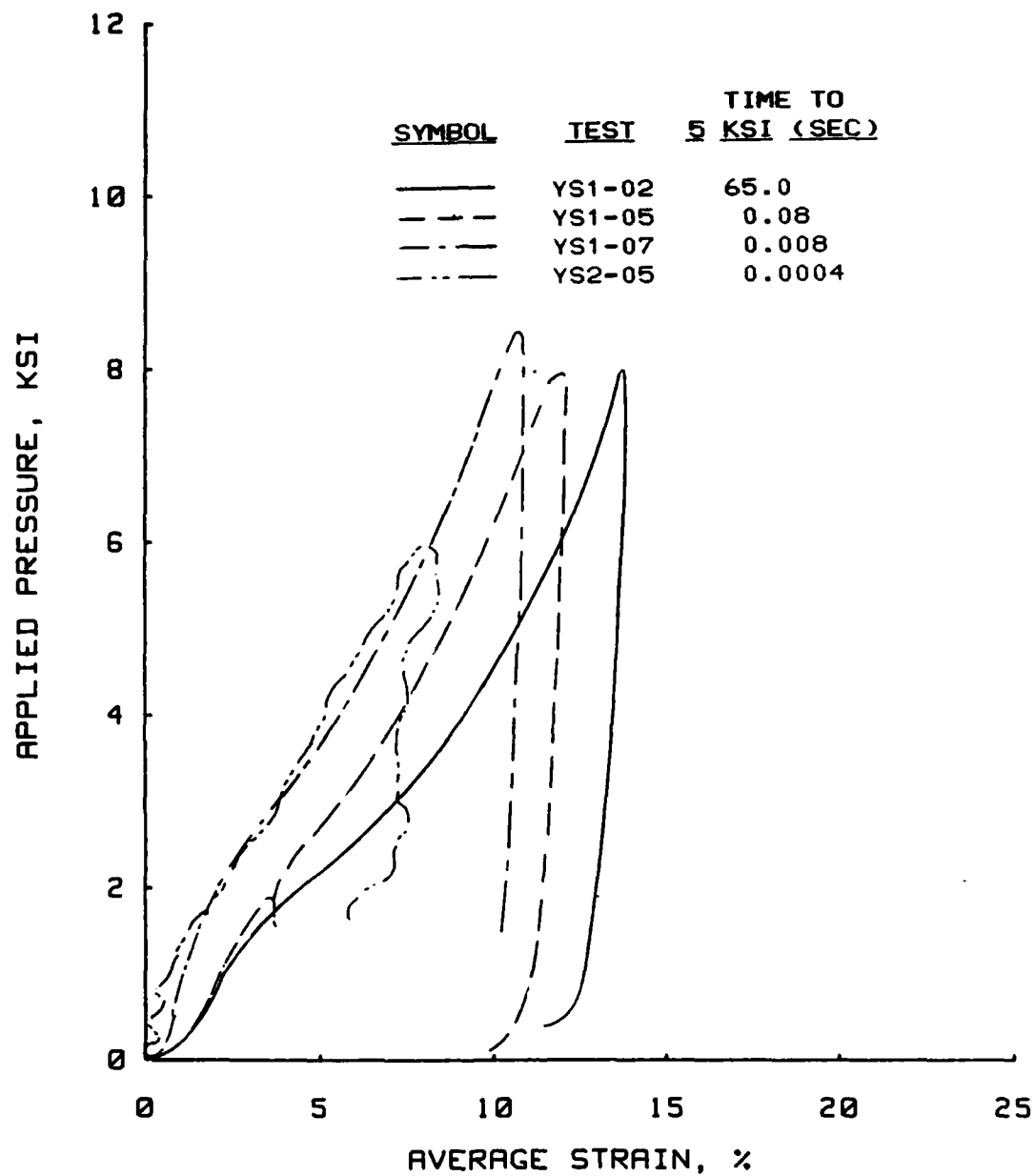
Figure 4.4.3 Loading rate effects for Yuma clayey sand.
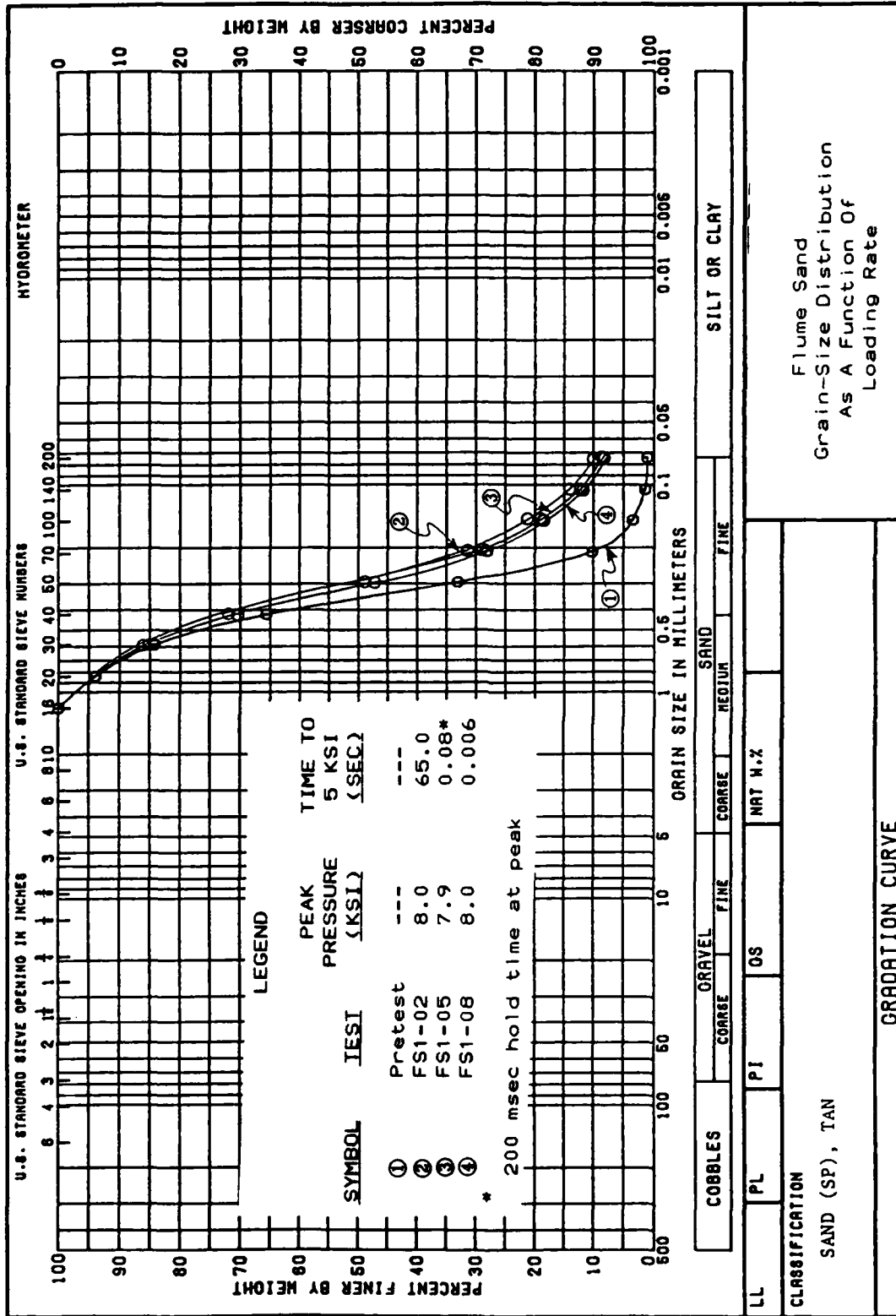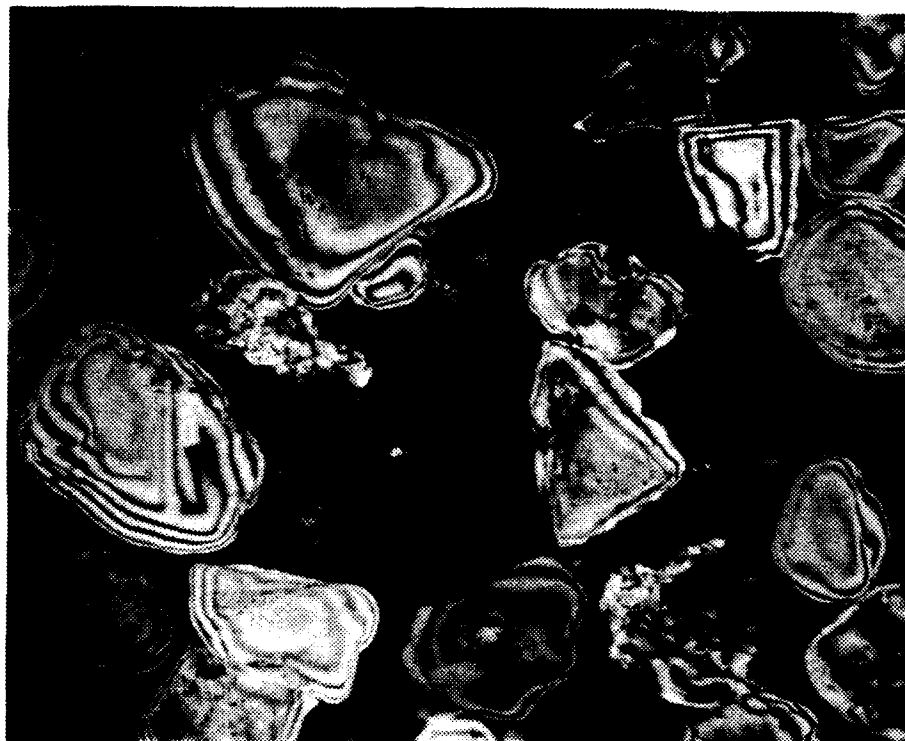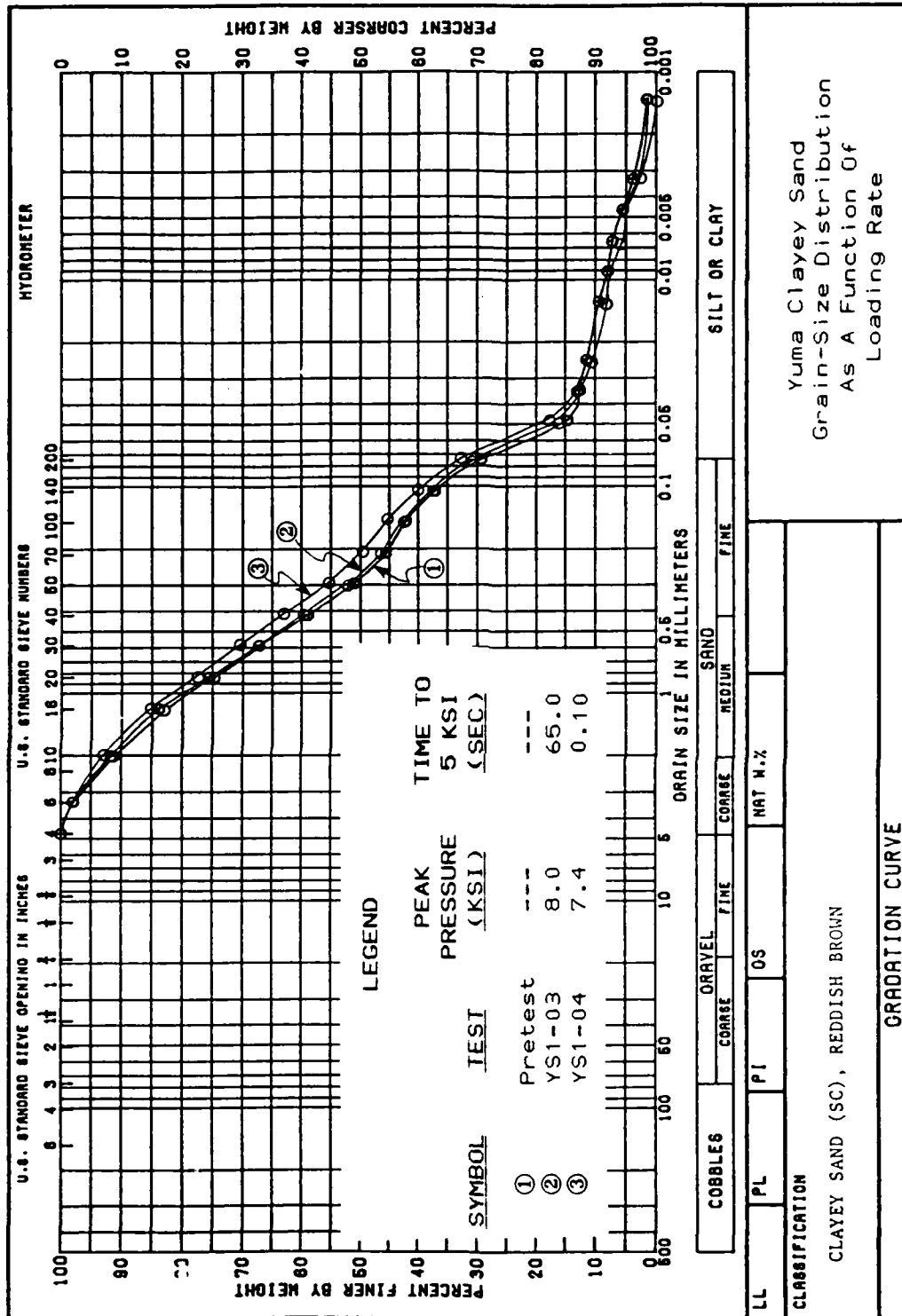
Figure 4.4.4 Grain crushing as a function of loading rate for Yuma clayey sand.
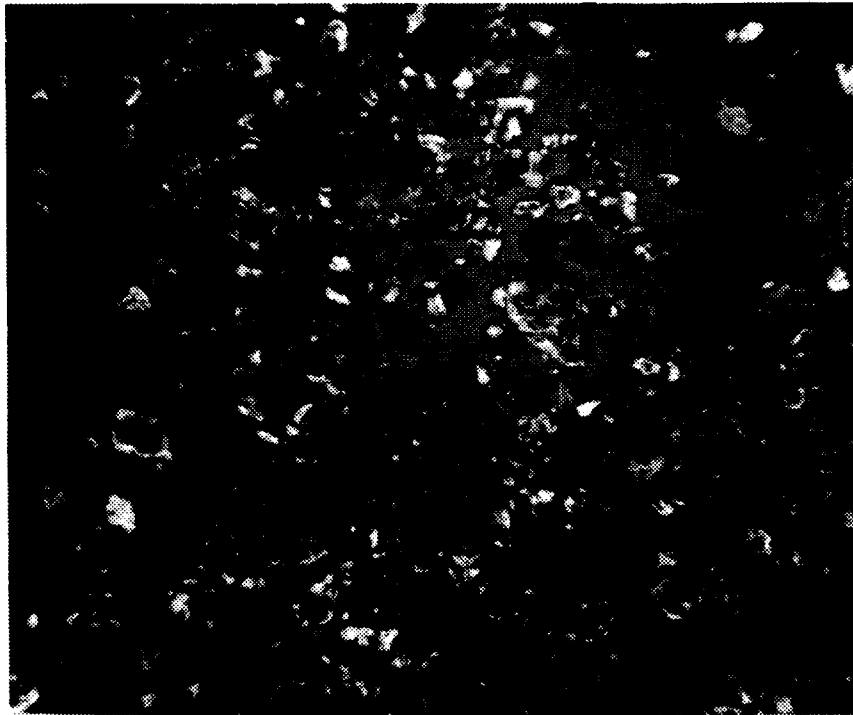
Pretest
(Bulk Sample, 45 X)
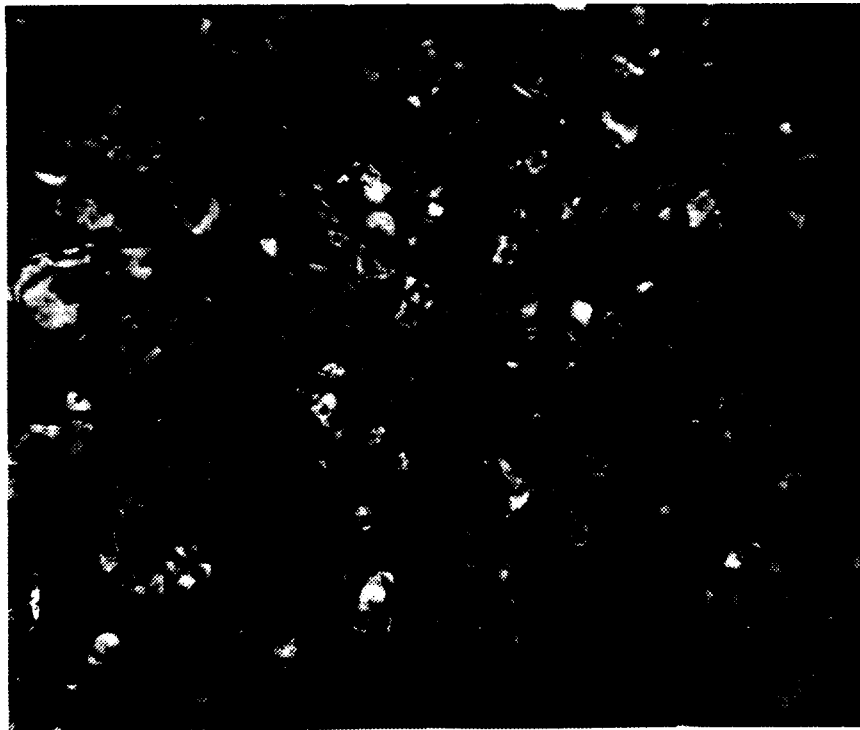
Posttest
(Bulk Sample, Static Test, 45 X)

Figure 4.4.5 Photographs of pretest and posttest grains of Yuma clayey sand.

4.5 Vicksburg Loess

Two testing programs were performed using Vicksburg loess and are designated as either D- or V-series. The D-series testing program was similar to those performed for Enewetak beach, flume, and Yuma clayey sands. A fixed water content and dry density were maintained and the loading rate varied. A series of tests was also performed to study how water content, dry density, and loading rate effects are interdependent and is designated as the V-series of tests.

Initially, this project was conceived to vary the water content, dry density, and loading rates for a given material and evaluate their effects upon uniaxial strain response using only the WES 0.1-msec device. This allowed for testing at basically two loading rates, submillisecond and static. However, as the project progressed, it was decided that loading rate effects for a wide variety of rise times should be addressed to evaluate various constitutive models. Using the results from a representative model fit, the laboratory results could then be compared against field results.

The V-series test program was the initial testing program performed in the WES 0.1-msec device as part of this study. Thus, this testing program served as a "shakedown" testing program for the data measurement and acquisition systems and sample preparation technqiues.

The V-series specimens were placed in two lifts, similar to procedures previously presented. However, a 3-in- (7.62-cm-) diameter compaction hammer, similar to those used for proctor tests, was used to

compact the samples. This compaction technique tended to produce a stiffer material response than using a 1-in- (2.54-cm-) diameter tamping rod. Therefore, the results between the D- and V-series cannot be compared, but they do provide some insight into how water content and dry density affect the magnitude of the loading rate effects.

Seventeen uniaxial strain tests were performed on remolded samples of Vicksburg loess under the D-series test program at a wide variety of loading rates. In addition, grain-size analysis (pretest and posttest), specific gravity of solids, and compaction test data are presented. This brown material classified as a silty clay CL based upon the USCS system.

The material properties of this soil have been documented by Green (1986b). The samples tested were from the same site and had approximately the same gradation and Atterburg limits as those tested by Green (1986b). A pretest grain-size distribution is shown in Fig. 4.5.1. Typical LL values of 32 and PL values of 20 were measured. The mineral constituents of this material as determined by x-ray diffraction are listed in Table 4.5.1.

Green (1986b) reported that Vicksburg loess had a specific gravity of 2.71. Standard proctor compaction results with a maximum dry density of 107.1 pcf (1.72 g/cc) at an optimum water content of 16.2 % and modified proctor test values of maximum dry density of 114.7 pcf (1.84 g/cc) with an optimum water content of 13.7 % were determined.
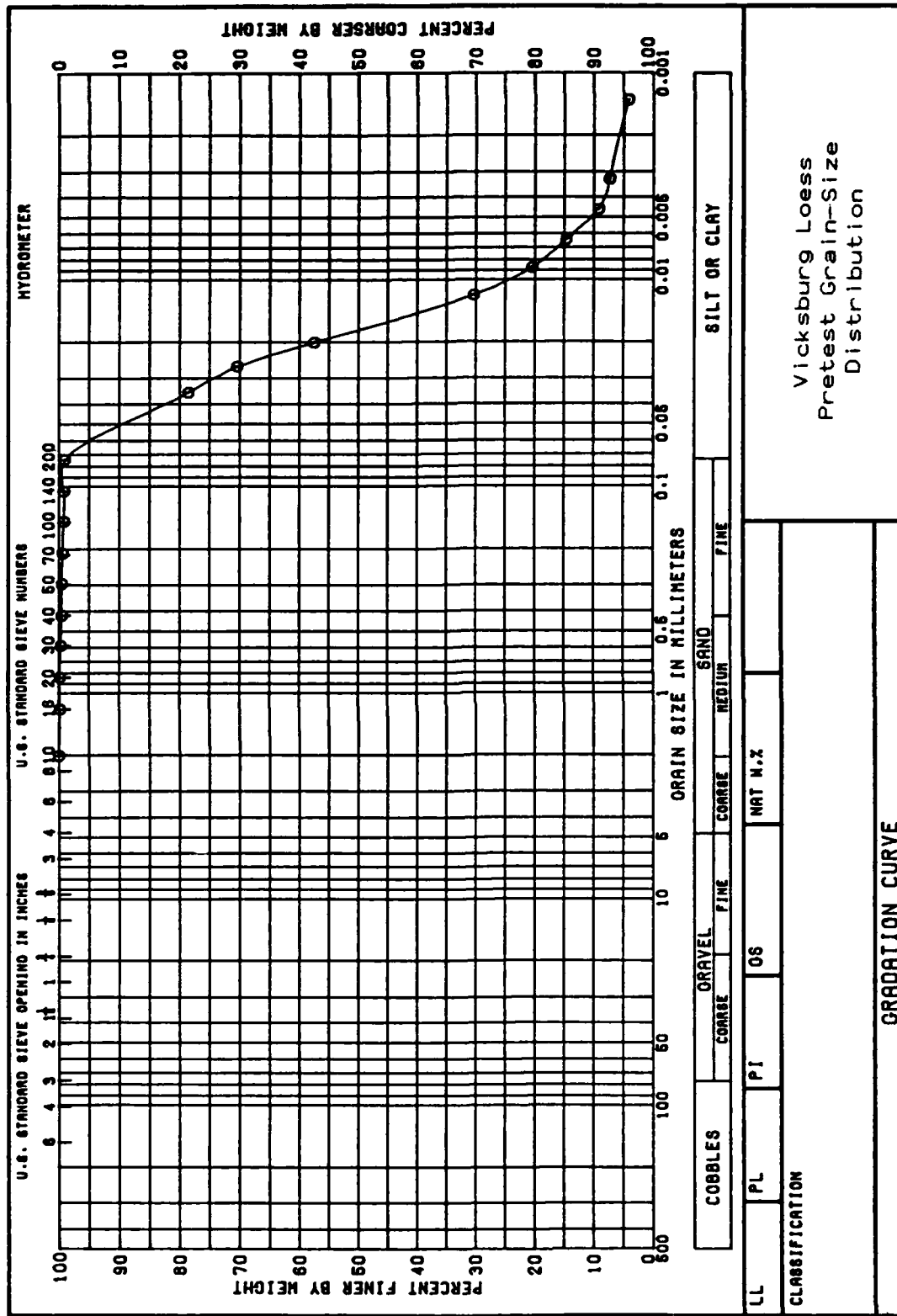
Figure 4.5.1 Pretest grain-size distribution for Vicksburg loess.

Mineral Constituents	Amount
Clays	
Smectite	M
Chlorite	M
Vermiculite	M
Clay-mica	M
Kaolinite	M
Palygorskite	M
Non-Clays	
Quartz	I
Plagioclase Feldspars	M
Potassium Feldspars	M
Amphibole	X
Calcite	X
Dolomite	M
Mica	X
Magnetite	X
Zircon	X
Pyrophyllite	X

Legend

Abundant (A) > 50 %
Intermediate (I) = 25 to 50 %
Common (C) = 10 to 25 %
Minor (M) = 5 to 10 %
Trace (X) = small quanities present

Table 4.5.1 Mineralogical composition of Vicksburg loess.

Table 4.5.2 summarizes the conditions and designations used for the D-series of tests. Values of 11.5 % and 101.5 pcf (1.63 g/cc) for water content and dry density were target values for the testing program. Figure 4.5.2 shows how the dry density, degree of saturation, and volume of air change during uniaxial strain compression based upon these initial conditions.

For a water content of 11.5 %, standard and modified proctor values of 104.5 pcf (1.67 g/cc) and 113.5 pcf (1.82 g/cc) were determined. The target value of 101.5 pcf (1.63 g/cc) corresponds to 97 % of standard and 89 % of modified proctor values. Using the sample preparation techniques described in Section 4.2, the target value of dry density was easily obtained with little compaction effort.

Figure 4.5.3 summarizes the effects of various loading rates upon the uniaxial response of Vicksburg loess. These tests are representative of the average for various loading rates. Test DS1-02 is representative of the static behavior. Loading rates were varied for supersecond tests from 23 to 115 sec to 5 ksi (34.5 MPa) without any distinguishable difference in the uniaxial strain response. Tests DS1-05 and DS1-06 are representative of the slow and fast loading rates generated by the ram-type loaders. Test DS2-07 is representative of the submillisecond behavior. The rate effects for this material are significant compared to the flume and Yuma materials. Like the other three materials, a drastic stiffening of the uniaxial response did not occur in the submillisecond range.

TEST NUMBER	WATER CONTENT (%)		WET UNIT WEIGHT (pcf) (g/cc)		DRY UNIT WEIGHT (pcf) (g/cc)		DESIGNATION
	PRE	POST					
DS1-01	-	-	113.2	1.81	-	-	STATIC
DS1-02	-	-	113.2	1.81	-	-	STATIC
DS1-03	-	-	113.2	1.81	-	-	STATIC
DS2-01	-	11.5	113.1	1.81	101.5	1.63	STATIC
DS2-02	-	11.6	113.1	1.81	101.4	1.63	STATIC
DS2-03	-	11.6	113.1	1.81	101.4	1.63	SLOW STATIC
DS1-04	-	-	113.2	1.81	-	-	SLOW DYNAMIC
DS1-05	-	11.2	113.2	1.81	101.7	1.63	SLOW DYNAMIC
DS1-06	-	-	113.2	1.81	-	-	DYNAMIC
DS1-07	-	-	113.2	1.81	-	-	DYNAMIC
DS2-04	-	11.2	113.0	1.81	101.6	1.63	DYNAMIC
DS2-05	-	11.2	113.0	1.81	101.6	1.63	DYNAMIC
DS2-06	-	11.2	113.0	1.81	101.6	1.63	DYNAMIC
DS2-07	-	11.0	113.0	1.81	101.8	1.63	DYNAMIC
DS2-08	-	11.1	113.0	1.81	101.8	1.63	DYNAMIC
DS2-09	-	11.3	113.0	1.81	101.5	1.63	DYNAMIC
DS2-10	-	11.2	113.0	1.81	101.6	1.63	DYNAMIC

TABLE 4.5.2 Summary of D-series of tests performed on Vicksburg loess.
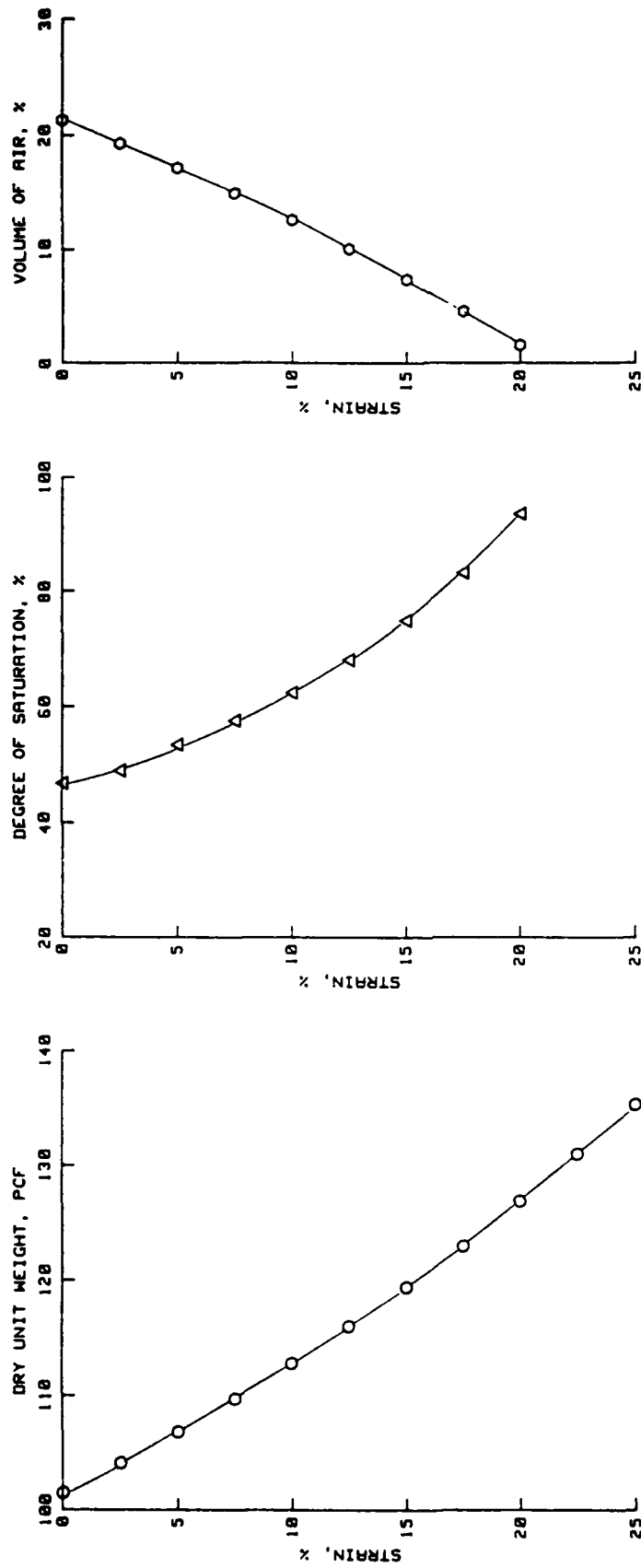
<u>Initial Conditions</u>

γ_d = 101.5 pcf
W = 11.5 %
γ_w = 62.4 pcf
G_s = 2.71

Figure 4.5.2 Dry density, degree of saturation, and volume of air as a function of uniaxial strain for Vicksburg loess, D-series tests.

Uniaxial Strain Results
Soil Type: Vicksburg Loess
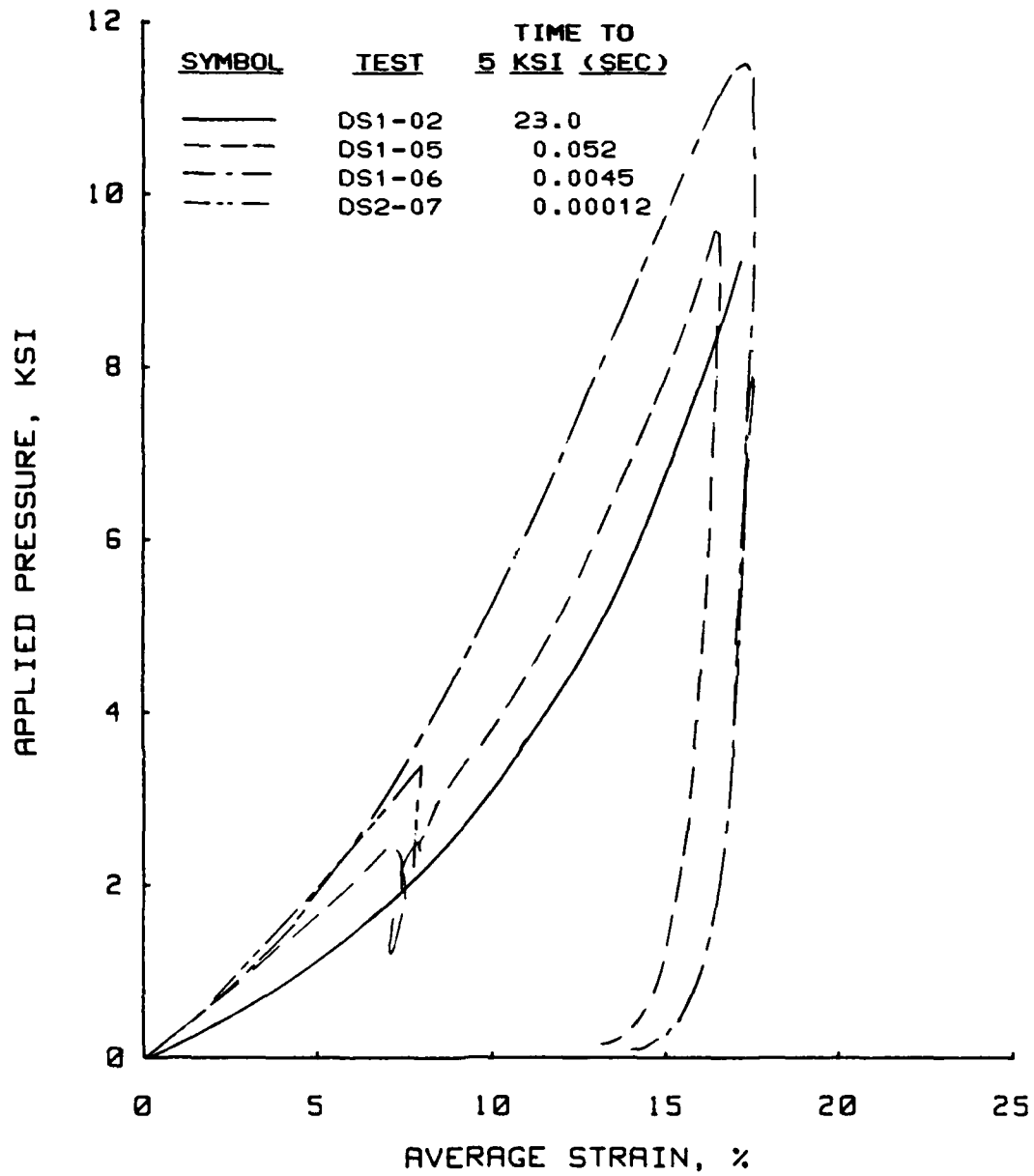
Figure 4.5.3 Loading rate effects for Vicksburg loess, D-series.

Three tests were performed to investigate the creep behavior of this material and are presented in Fig. 4.5.4. These tests had rise times of about 60 msec with load hold times of about 0.90 sec. Like the Enewetak beach sand, these tests creeped towards the static material response (test DS1-02).

The posttest grain-size distributions had a significant amount of scatter, relative to the other three materials. The amount of grain crushing could not be ascertained based on these results. Pretest and posttest samples of the material were viewed under a microscope and did not show any grain crushing.

Table 4.5.3 summarizes the results of the V-series test program. Under this program, nine static and eight dynamic tests were performed solely in the WES 0.1-msec device. All of the dynamic tests reported were obtained with EBW caps rated at 10 ksi (69 MPa) pressure. The dynamic tests typically had a rise time to peak of about 0.5 to 0.6 msec, whereas, the average rise time to peak for the static tests was about 60 sec.

Figure 4.5.5 summarizes the results of five static tests at approximately the same dry density, but with the water content varied. A definite trend exists. As the water content increases, the response becomes softer. This should be expected, because the water tends to lubricate the grains, reducing the amount of friction between the individual particles. Figure 4.5.6 summarizes the results of five static tests at a constant water content, but with the dry density varied. As expected, density significantly affects the uniaxial

Uniaxial Strain Results
Soil Type: Vicksburg Loess
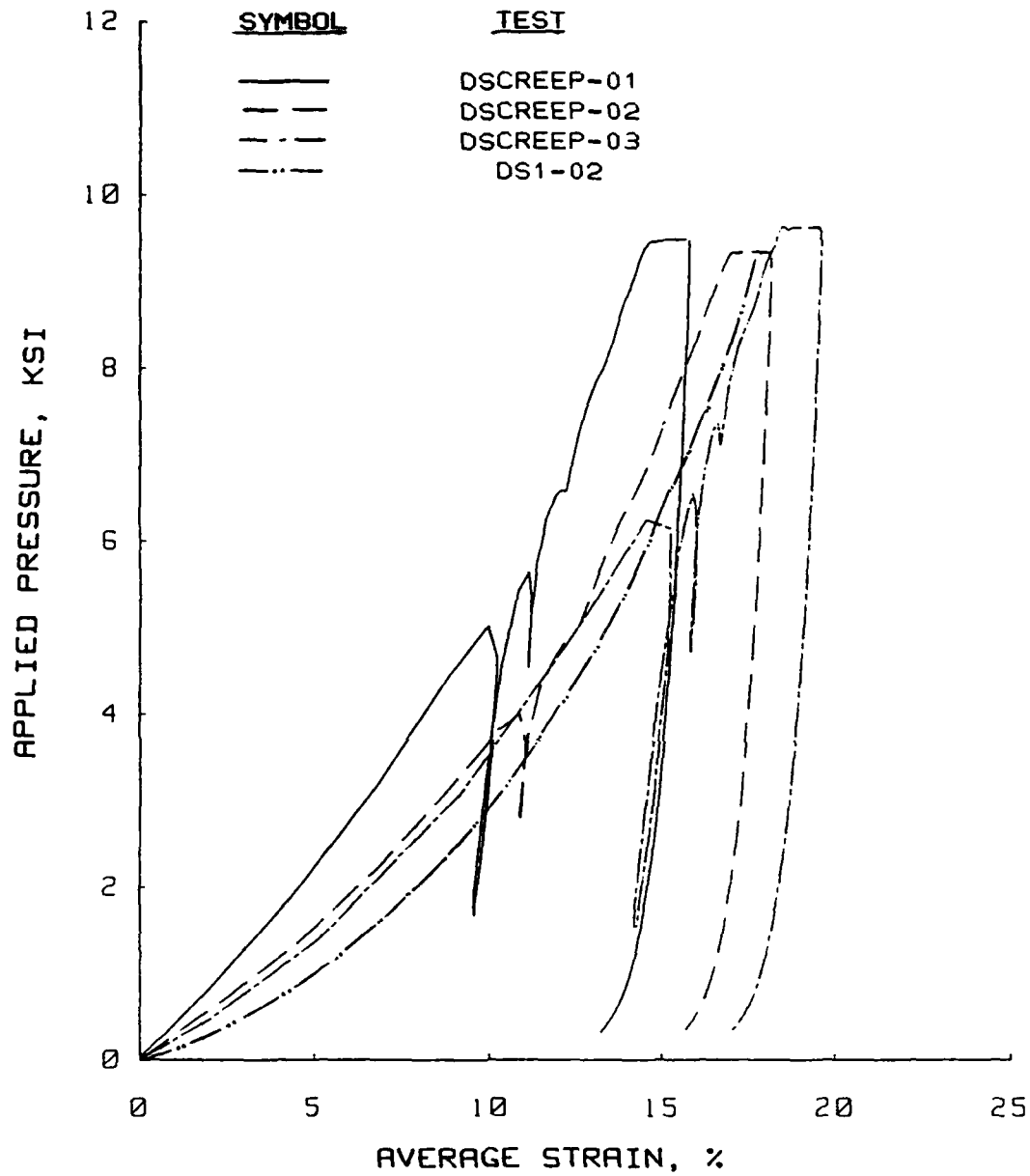
Figure 4.5.4 Dynamic creep tests for Vicksburg loess, D-series.

TEST NUMBER	WATER CONTENT (%)		WET UNIT WEIGHT		DRY UNIT WEIGHT		DESIGNATION
	PRE	POST	(pcf)	(g/cc)	(pcf)	(g/cc)	
VSS-11	15.0	14.7	106.7	1.71	92.9	1.49	STATIC
VSS-12	14.5	14.5	106.7	1.71	93.2	1.49	STATIC
VSS-21	10.2	9.7	111.0	1.78	101.0	1.62	STATIC
VSS-22	10.2	-	111.0	1.78	101.0	1.62	STATIC
VSS-23	12.6	11.9	113.1	1.81	100.8	1.62	STATIC
VSS-24	13.0	12.8	113.1	1.81	100.2	1.61	STATIC
VSS-25	14.8	14.5	113.1	1.81	98.6	1.58	STATIC
VSS-31	14.7	12.6	124.7	2.00	109.7	1.76	STATIC
VSS-32	14.6	14.2	124.7	2.00	109.0	1.75	STATIC
VSD-11	14.5	14.3	106.8	1.71	93.4	1.50	DYNAMIC
VSD-12	14.6	14.5	106.8	1.71	93.2	1.49	DYNAMIC
VSD-21	9.6	9.3	111.0	1.78	101.4	1.63	DYNAMIC
VSD-22	9.6	8.8	111.0	1.78	101.6	1.63	DYNAMIC
VSD-23	12.1	11.7	113.2	1.81	101.2	1.62	DYNAMIC
VSD-24	12.0	11.8	113.2	1.81	101.2	1.62	DYNAMIC
VSD-25	14.4	14.1	115.5	1.85	101.0	1.62	DYNAMIC
VSD-31	14.3	14.0	124.9	2.00	109.4	1.75	DYNAMIC

TABLE 4.5.3 Summary of V-series of tests performed on Vicksburg loess.

Uniaxial Strain Results
Soil Type: Vicksburg Loess

SYMBOL	TEST	W (%)	γ_d (PCF)
——	VSS-21	10.0	101.0
— — —	VSS-22	10.2	101.0
—·—	VSS-23	12.3	100.8
—··—	VSS-24	12.9	100.2
—·—	VSS-25	14.7	98.6
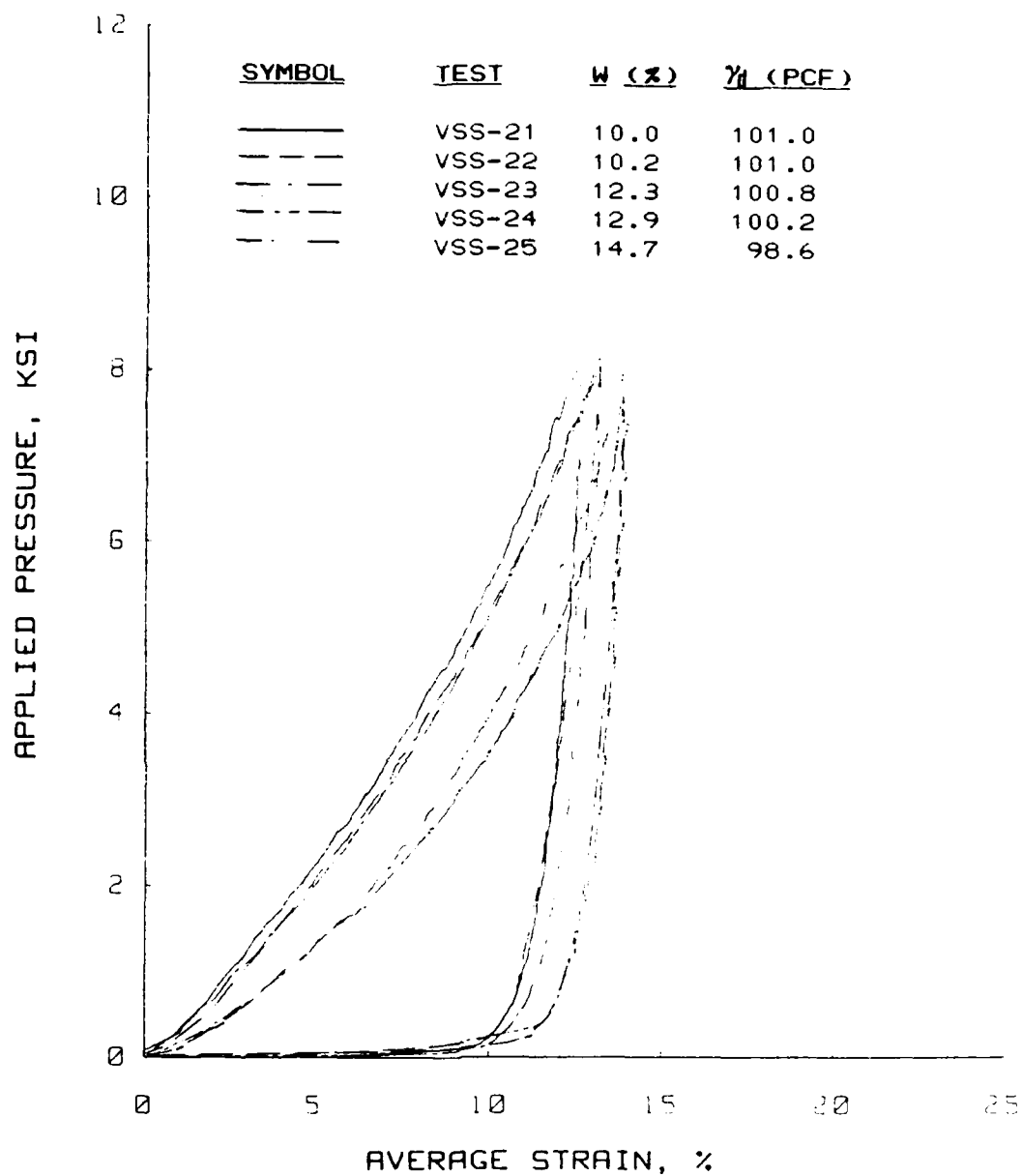
Figure 4.5.5 Static uniaxial strain response as a function of water content for Vicksburg loess, V-series.

Uniaxial Strain Results
Soil Type: Vicksburg Loess

SYMBOL	TEST	W (%)	γ_d (PCF)
———	VSS-11	14.9	92.9
— — —	VSS-12	14.5	93.2
— · —	VSS-25	14.7	98.6
— ·· —	VSS-31	13.7	109.7
— · —	VSS-32	14.4	109.0

AVERAGE STRAIN, %

APPLIED PRESSURE, KSI
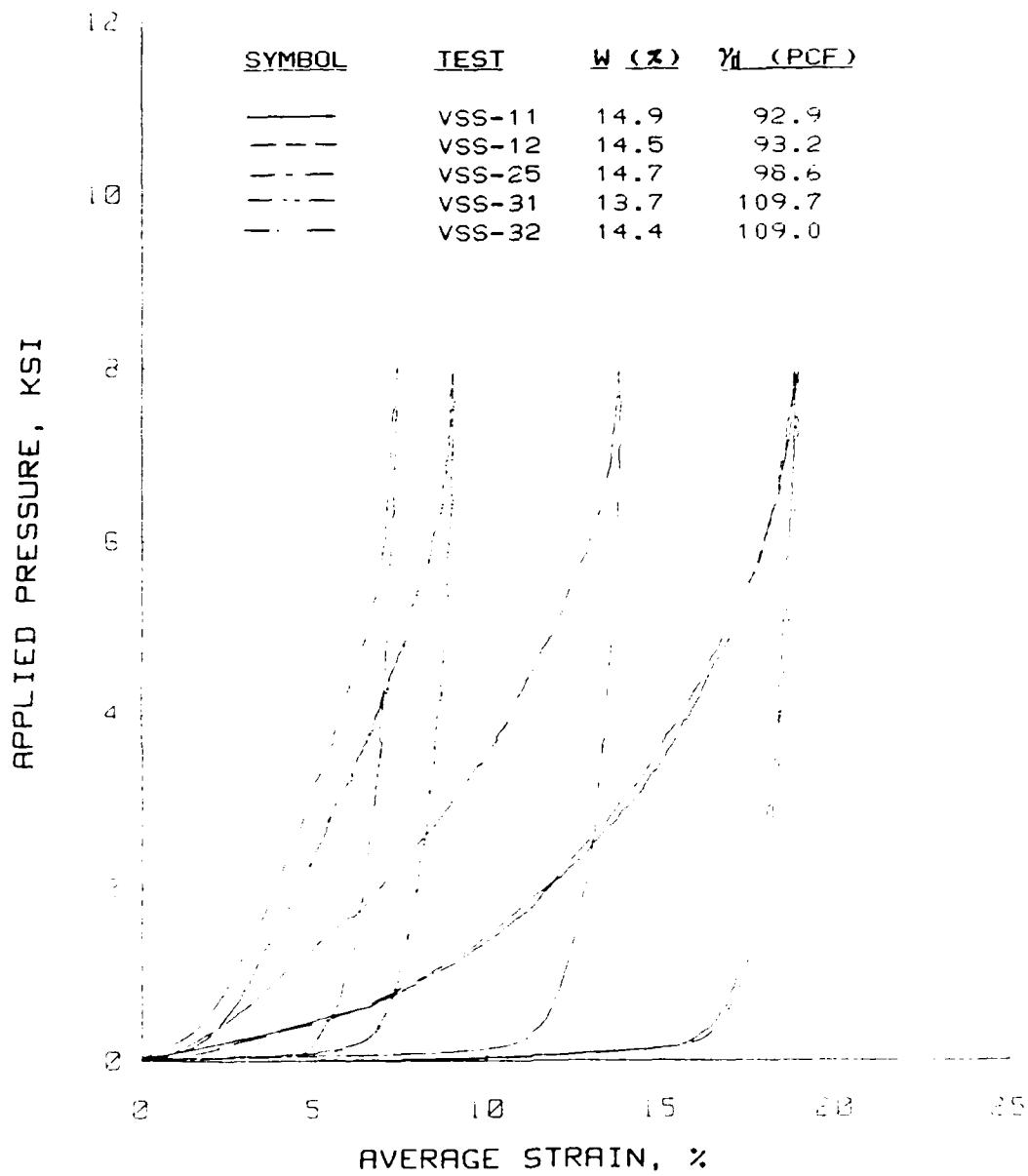
Figure 4.5.6 Static uniaxial strain response as a function of dry
density for Vicksburg loess, V-series.

strain response. The greater the dry density, the stiffer the material response.

Figure 4.5.7 summarizes the results of five dynamic tests at approximately the same dry density, but with the water content varied. The scatter of the data prevents drawing a definitive conclusion about how the water content affects the dynamic response. One would expect an increase in water content to correspond to a softer response. Figure 4.5.8 summarizes the results of four dynamic tests at a constant water content, but with the density varied. A slight, but not significant, stiffer response occurs as the density increases. Based upon the static test results, a more drastic increase in loading rate effects was expected for the submillisecond tests when the dry density was increased.

Figures 4.5.9 thru 4.5.11 presents the results of comparisons between static and dynamic uniaxial strain tests for a constant water content, with density varied. As shown in Fig. 4.5.9, a significant rate effect exists at this relatively loose state. Whereas, as shown in Figs. 4.5.10 and 4.5.11, as the density increases, the rate effect becomes less significant.

Figures 4.5.10, 4.5.12, and 4.5.13 are comparison plots of dynamic and static tests for constant density with the water content varied. Based on these results, no significant change between the loading rate effects can be determined. A slight increase in ratio of the dynamic-to-static modulus appears to occur for the higher water contents at a constant density.
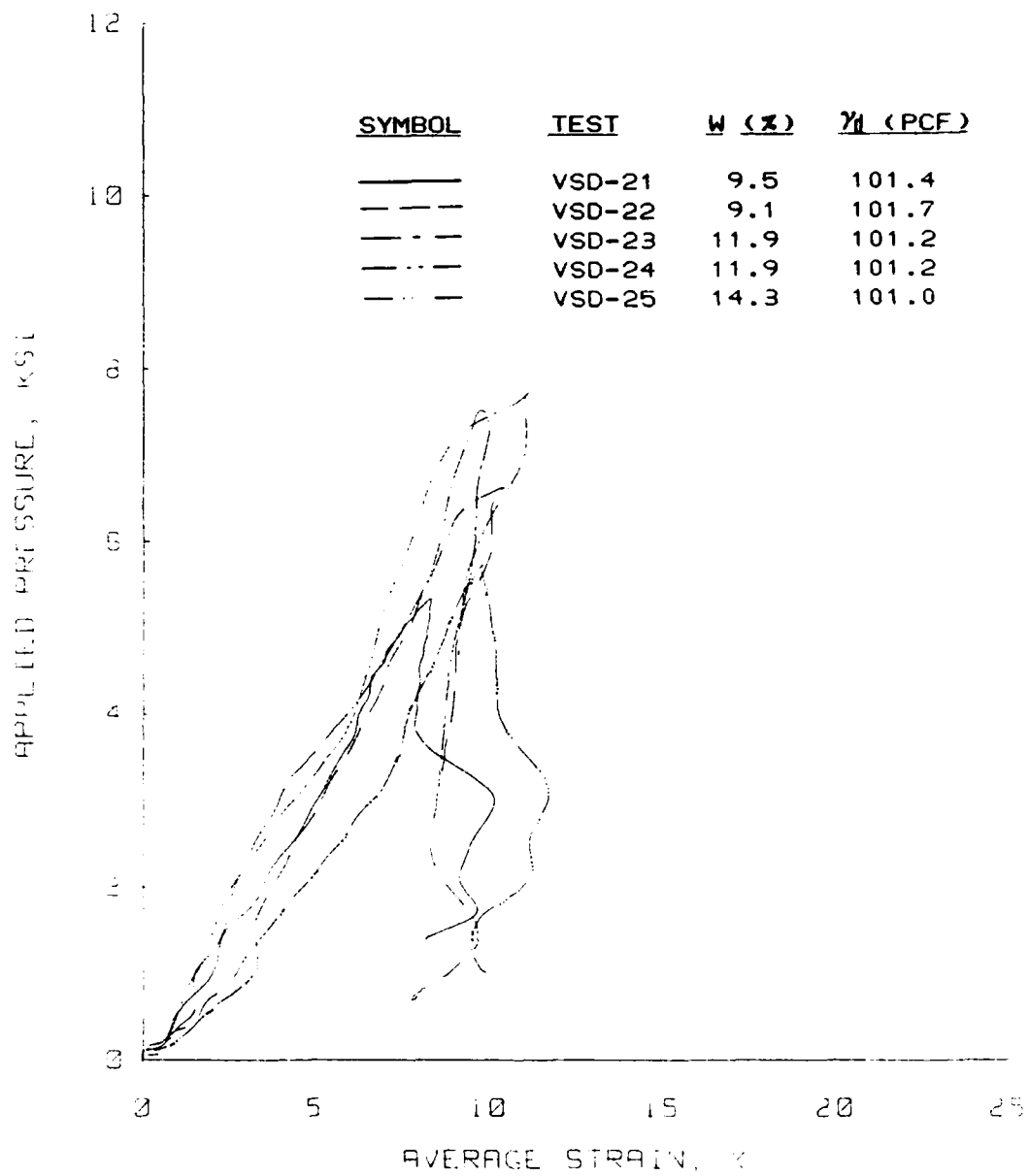
Figure 4.5.7   Dynamic uniaxial strain response as a function of water
content for Vicksburg loess, V-series.

Uniaxial Strain Results
Soil Type: Vicksburg Loess

SYMBOL	TEST	W (%)	γ_d (PCF)
——————	VSD-11	14.4	93.4
— — —	VSD-12	14.6	93.2
— · —	VSD-25	14.3	101.0
— ·· —	VSD-31	14.2	109.4
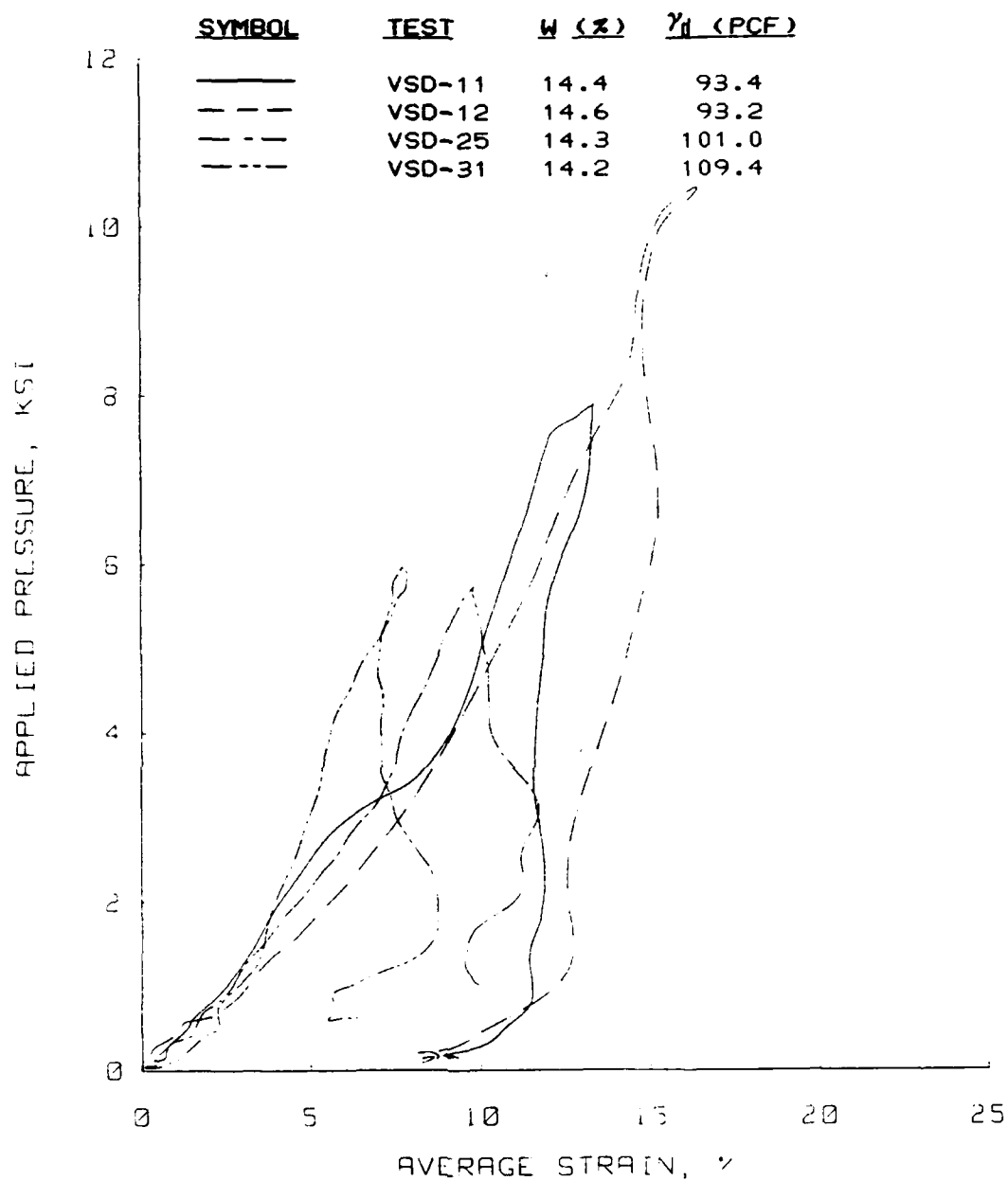
Figure 4.5.8 Dynamic uniaxial strain response as a function of dry density for Vicksburg loess, V-series.

Uniaxial Strain Results
Soil Type: Vicksburg Loess

SYMBOL	TEST	W (%)	γ_d (PCF)
— · —	VSS-11	14.9	92.9
— · · —	VSS-12	14.5	93.2
——	VSD-11	14.4	93.4
— — —	VSD-12	14.6	93.2
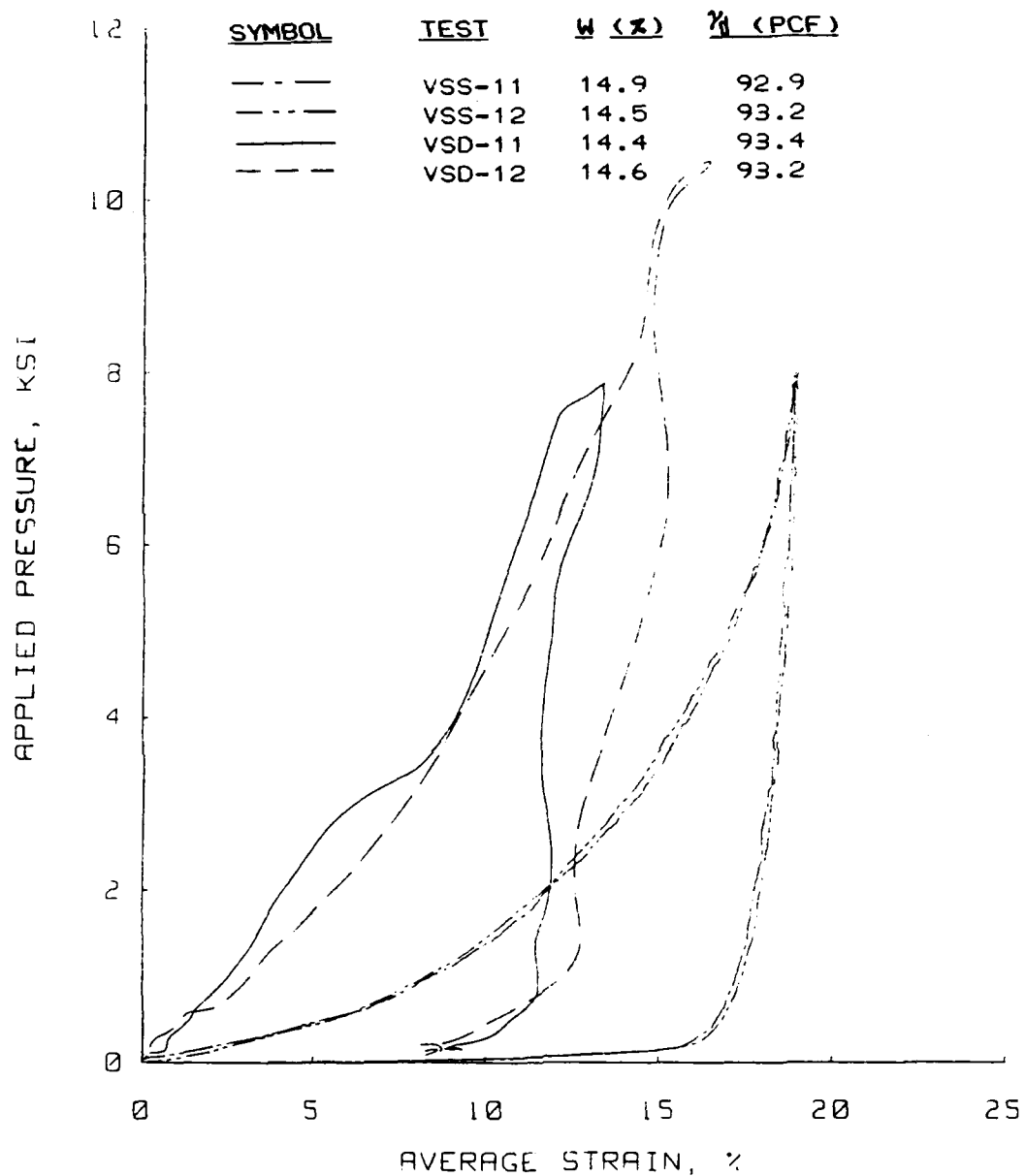
Figure 4.5.9 Loading rate effects for low density/high water content Vicksburg loess, V-series.

Uniaxial Strain Results
Soil Type: Vicksburg Loess

SYMBOL	TEST	W (%)	γ_d (PCF)
———	VSD-25	14.3	101.0
– – –	VSS-25	14.7	98.6
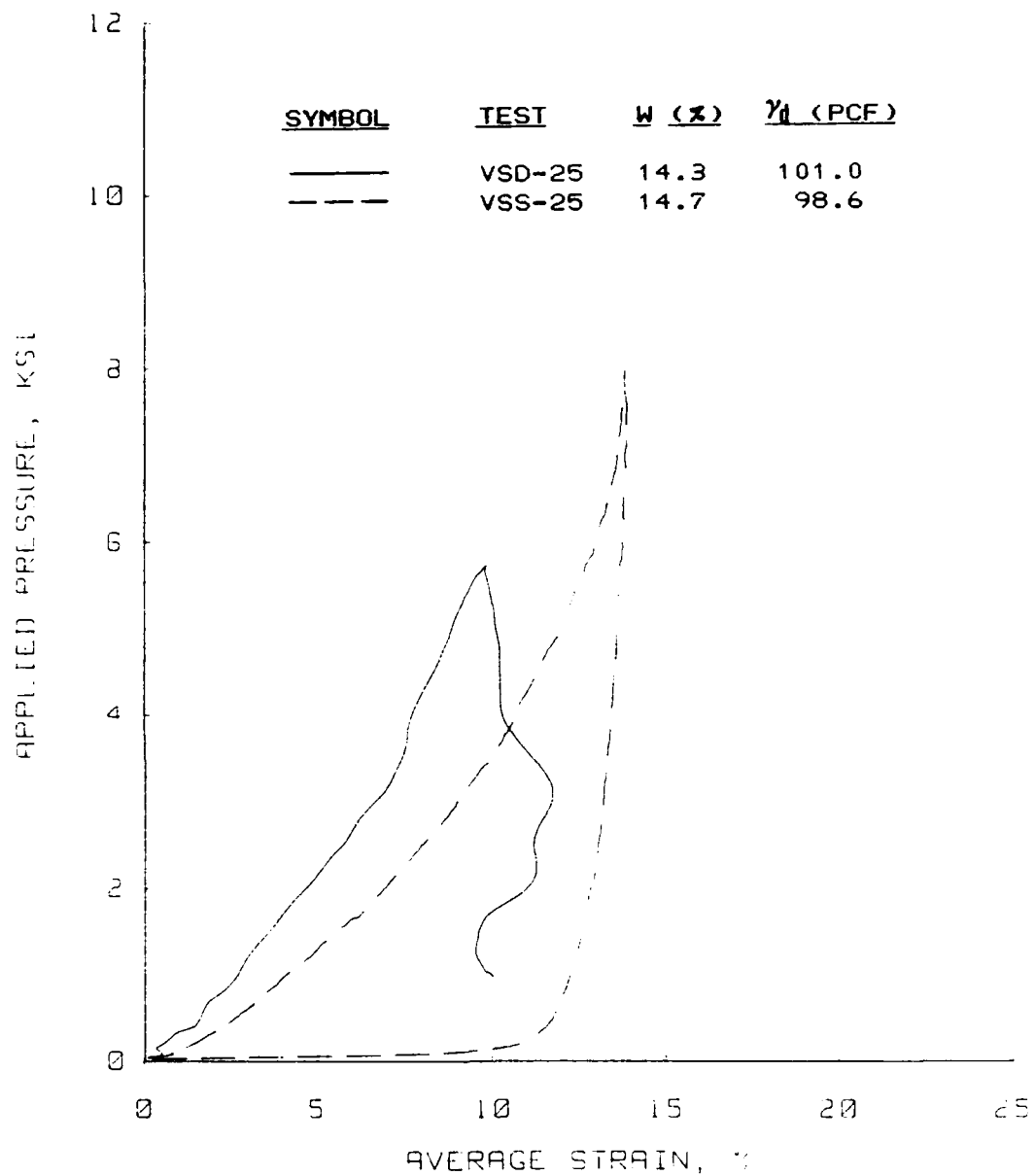
Figure 4.5.10   Loading rate effects for nominal density/high water content Vicksburg loess, V-series.

Uniaxial Strain Results
Soil Type: Vicksburg Loess

SYMBOL	TEST	W (%)	γ_d (PCF)
————	VSD-31	14.2	109.4
— — —	VSS-31	13.7	109.7
— · —	VSS-32	14.4	109.0
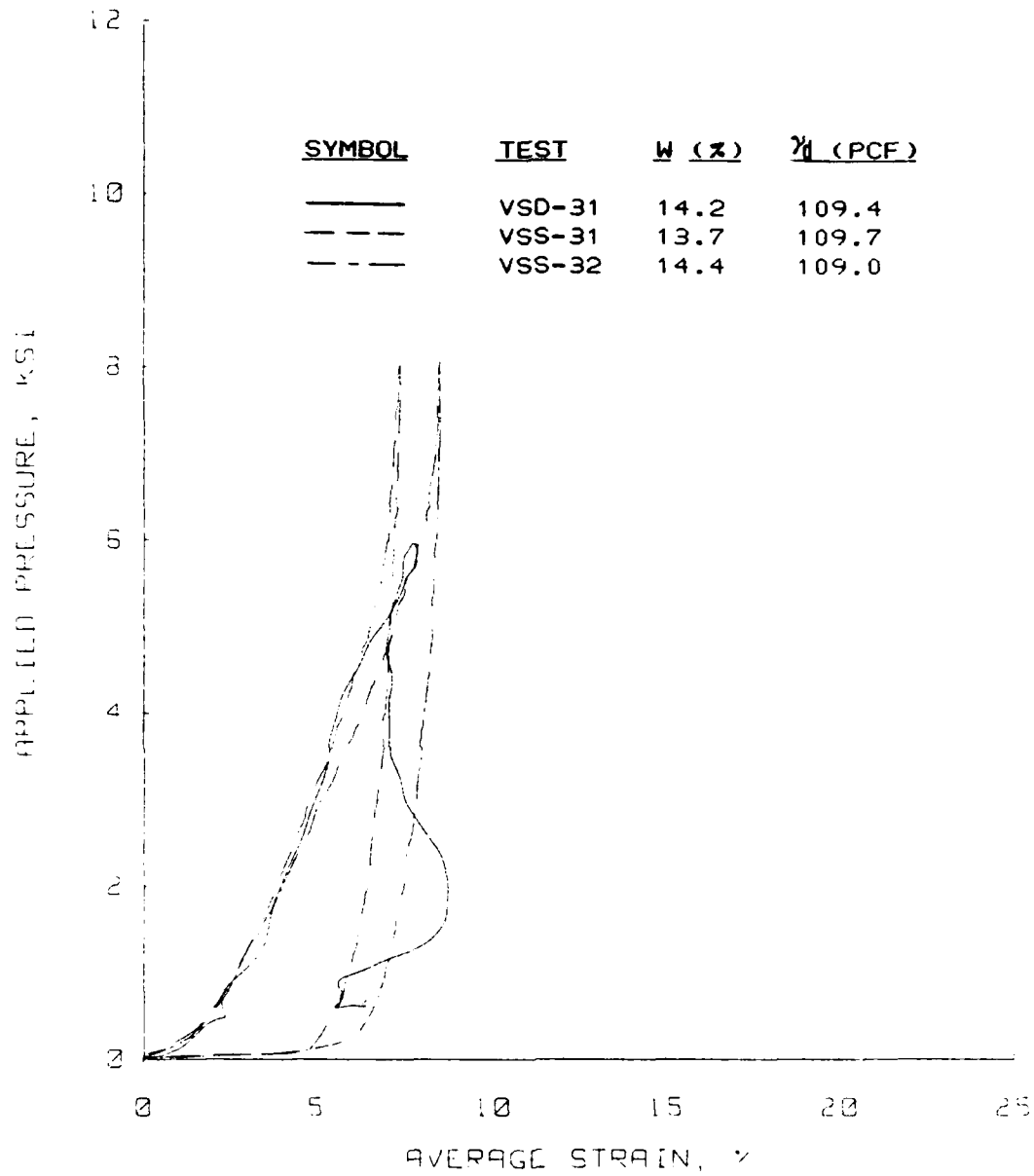
Figure 4.5.11   Loading rate effects for high density/high water
content Vicksburg Loess, V-series.

Uniaxial Strain Results
Soil Type: Vicksburg Loess

SYMBOL	TEST	W (%)	γ_d (PCF)
———	VSD-21	9.5	101.4
— — —	VSD-22	9.2	101.6
—·—	VSS-21	10.0	101.0
—··—	VSS-22	10.2	100.8
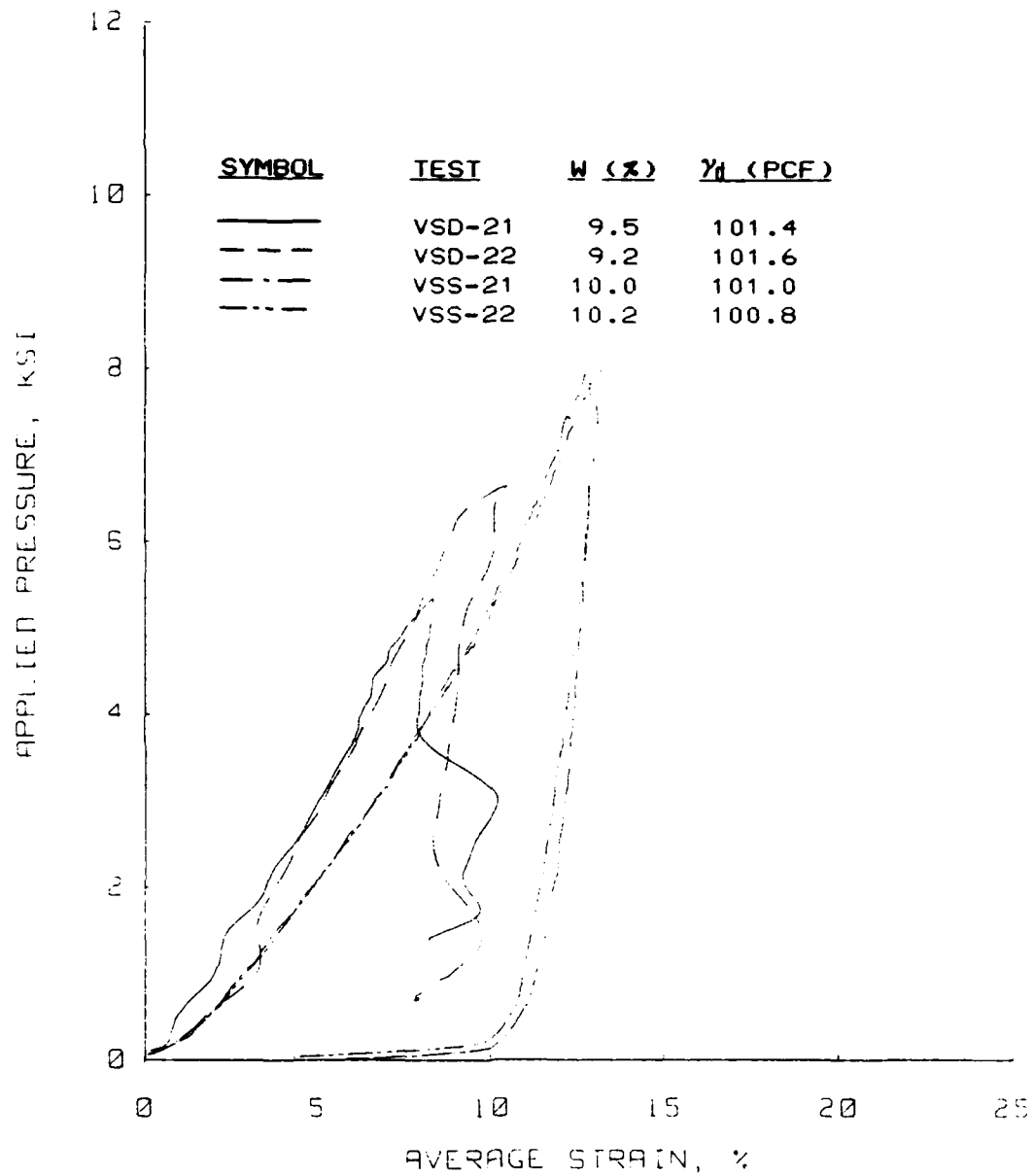
Figure 4.5.12 Loading rate effects for nominal density/low water content Vicksburg loess, V-series.

Uniaxial Strain Results
Soil Type: Vicksburg Loess

SYMBOL	TEST	W (%)	γ_d (PCF)
———	VSD-23	11.9	101.2
— — —	VSD-24	11.9	101.2
—·—	VSS-23	12.3	100.8
—··—	VSS-24	12.9	100.2
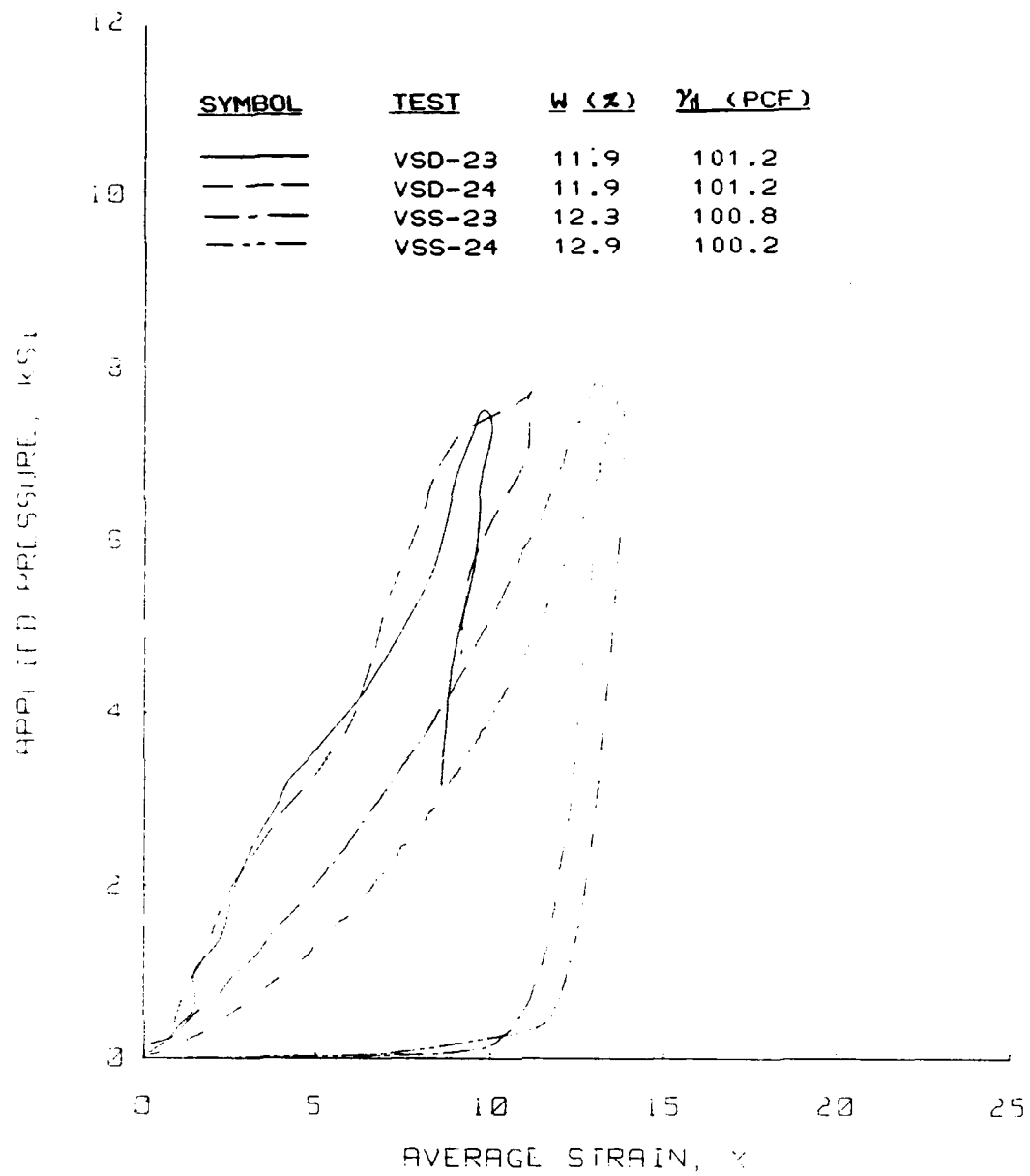
Figure 4.5.13 Loading rate effects for nominal density/nominal water content Vicksburg loess, V-series.

132

Some interesting conclusions can be drawn from these test
results. The static response is slightly affected by an increase in
water content. However, the effects of increasing water content for
dynamic tests are very small, if any. Any increase in density
significantly affects the static uniaxial strain response. A definite
increase in modulus occurs for dynamic tests as the density increases,
however the amount of stiffening isn't that significant.

CHAPTER V

INTERPRETATION OF SUBMILLISECOND TEST RESULTS

5.1   Introduction

The reasons for and the implications of nonuniformities in stress
and strain over the depth of the sample during submillisecond uniaxial
strain tests have been addressed in Section 2.2. It is essential in
submillisecond testing to account for or minimize these nonuniformities
by either reducing the sample height so that the multiple reflection
technique is valid (see Section 2.2), limiting the rise time of the
pressure pulse, and/or interpreting the results as a wave propagation
experiment.

Since the submillisecond range was of particular interest for
this program, the rise time of the stress pulse was fixed. A specimen
cavity 0.5-in (1.27-cm) high was incorporated into the design of the
WES 0.1-msec device so that the multiple reflection technique would be
valid when testing into the submillisecond range. The multiple
reflection technique produced satisfactory results for the stiffer
materials when the 10-ksi (69-MPa) EBW caps were used to provide
loading. However, this technique wasn't valid and did not provide a
satisfactory means for interpreting the true material response (1) for

133

materials with relatively low moduli and hence slow wave

speeds (2) when the 20-ksi (137.9-MPa) EBW caps were used.

A submillisecond uniaxial strain test can be analyzed as a one-
dimensional plane wave propagation experiment. A one-dimensional plane

wave propagation computer program or code written at WES was used to

interpret true material stress-strain response from measurements of

applied pressure and average strain for the explosively loaded uniaxial

strain tests. This program, written by R. W. Meier (1984) and titled

ADLUD (Analysis of Dynamic Loading in a Uniaxial Strain Device), is

based upon a lumped parameter difference approximation; a detailed

description of this program is contained in Appendix C.

5.2 Wave Propagation Analysis of Submillisecond Data

The submillisecond results are presented in Appendix B as plots

of applied pressure at a transducer located at some point above the

sample surface versus time and average strain over the total sample

depth versus time. The original ADLUD code was written to use the

digitized pressure-time history and an assumed rate-independent

material response model to numerically compute time variations of

stress and strain within the simulated test specimen. The assumed

material response model could then be adjusted until the calculated

"measurements" matched those obtained in the laboratory as closely as

possible. Thus, rate dependency could only be inferred from the fact

that different "best fit" rate-independent stress-strain curves were

obtained for tests on the same material but with different applied

loadings. The ADLUD code was modified for this work to account for

rate dependent material behavior directly by incorporating a strain-rate and strain-level dependent incremental constrained modulus model. This model stiffens an inputted static response. Appendix C describes how this model was incorporated into the computer code.

Semilog plots of the ratio of dynamic-to-static modulus as a function of strain rate for different strain levels were made for all tests where the loading rate was applied slow enough so that uniform stress and strain conditions existed. This included all tests except those performed in the WES 0.1-msec device using an explosive source. These results are shown in Figs. 5.2.1 thru 5.2.4. The following logarithmic relationship was fit to these data as a first approximation for the rate dependent term:

$$\frac{M_D}{M_S} = 1 + C1 \left(\log \frac{de}{dt} + C2 \right) \tag{5-1}$$

where: M_D = dynamic constrained modulus

M_S = static constrained modulus

C1, C2 = material constants

This relationship was placed in ADLUD.

For each test to be simulated, a static incremental stress-strain curve was input and the actual loading pulse recorded during the test was used to drive the code. Strain-rate dependency was accounted for using Equation 5-1; strain-level dependency was accounted for by using a simple linear function and a series of IF statements in the code. Plots were then made of applied pressure versus average strain and compared to those measured during the test. The C1 and C2 constants

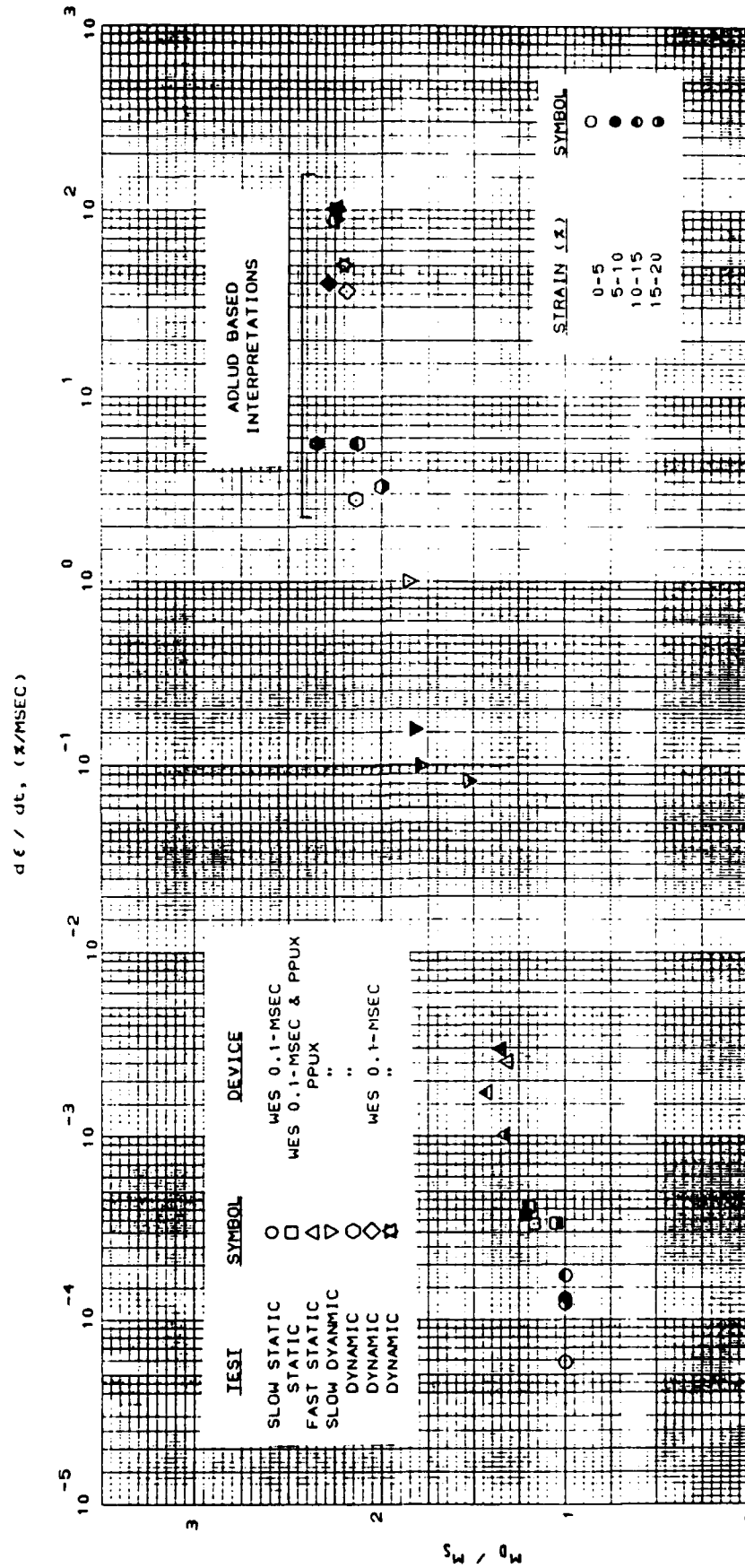Figure 5.2.1 Plot of dynamic-to-static modulus as a function of loading rate for Enewetak beach sand.
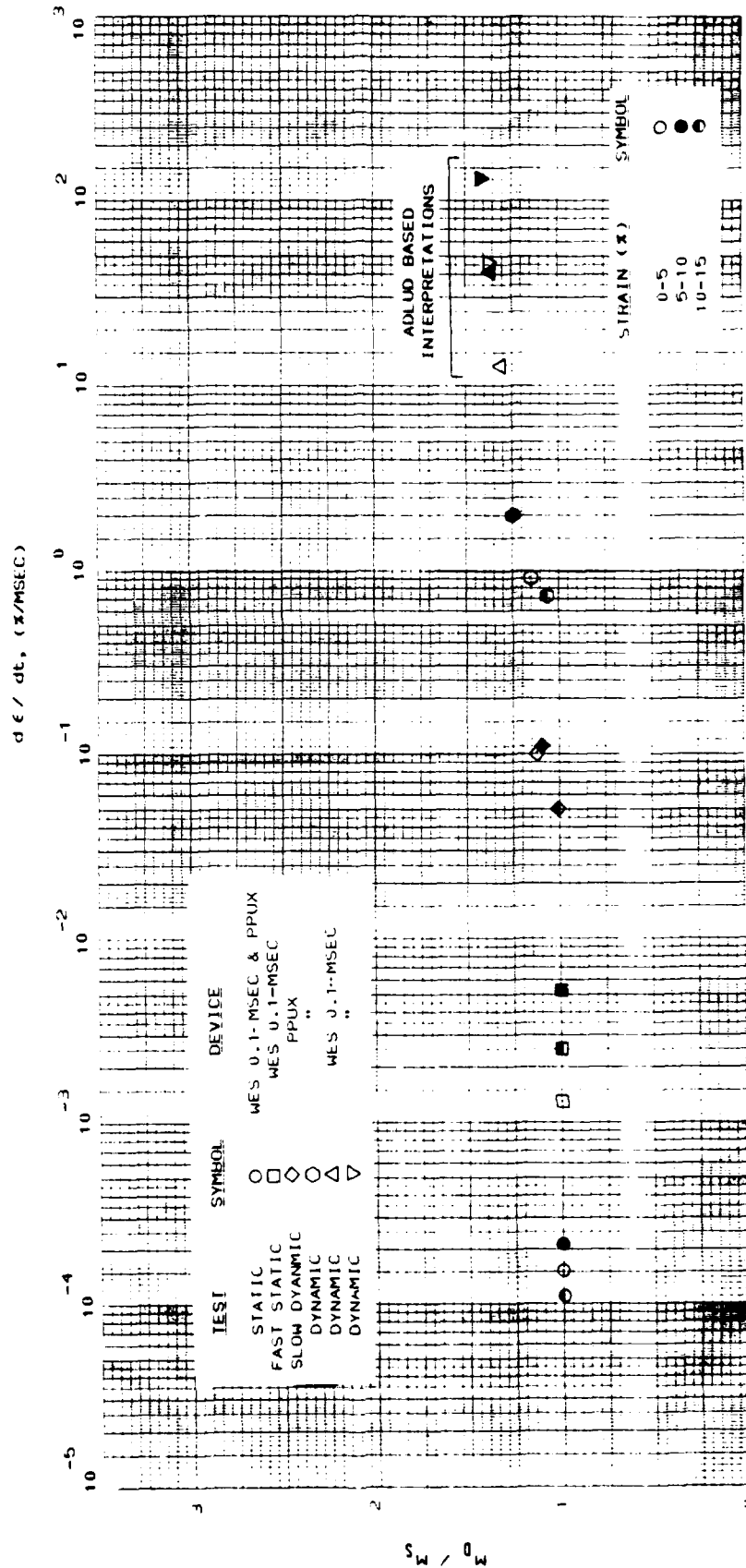
Figure 5.2.2 Plot of dynamic-to-static modulus as a function of loading rate for flume sand.
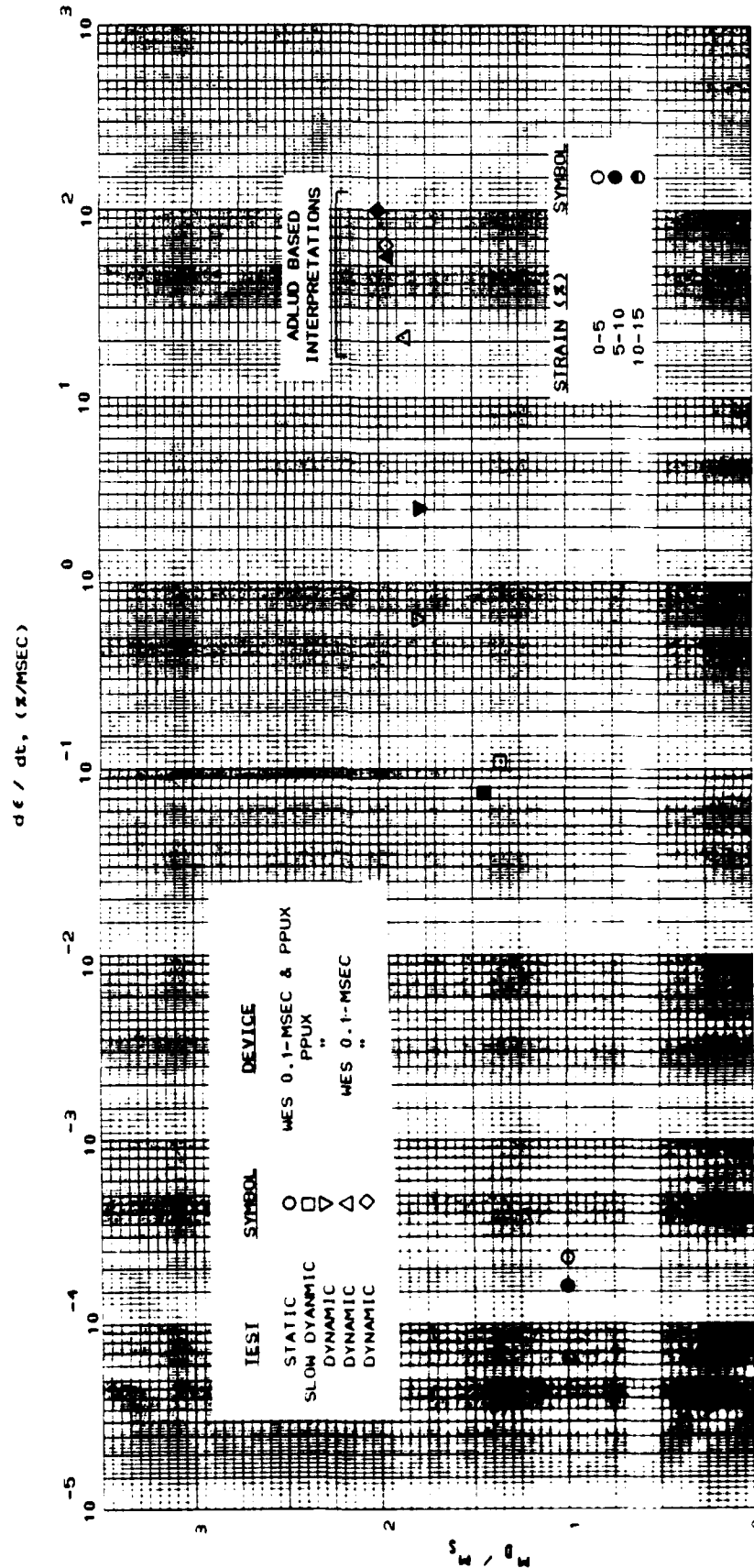
Figure 5.3.2 Plot of dynamic-to-static modulus as a function of loading rate for Yuma clayey sand.
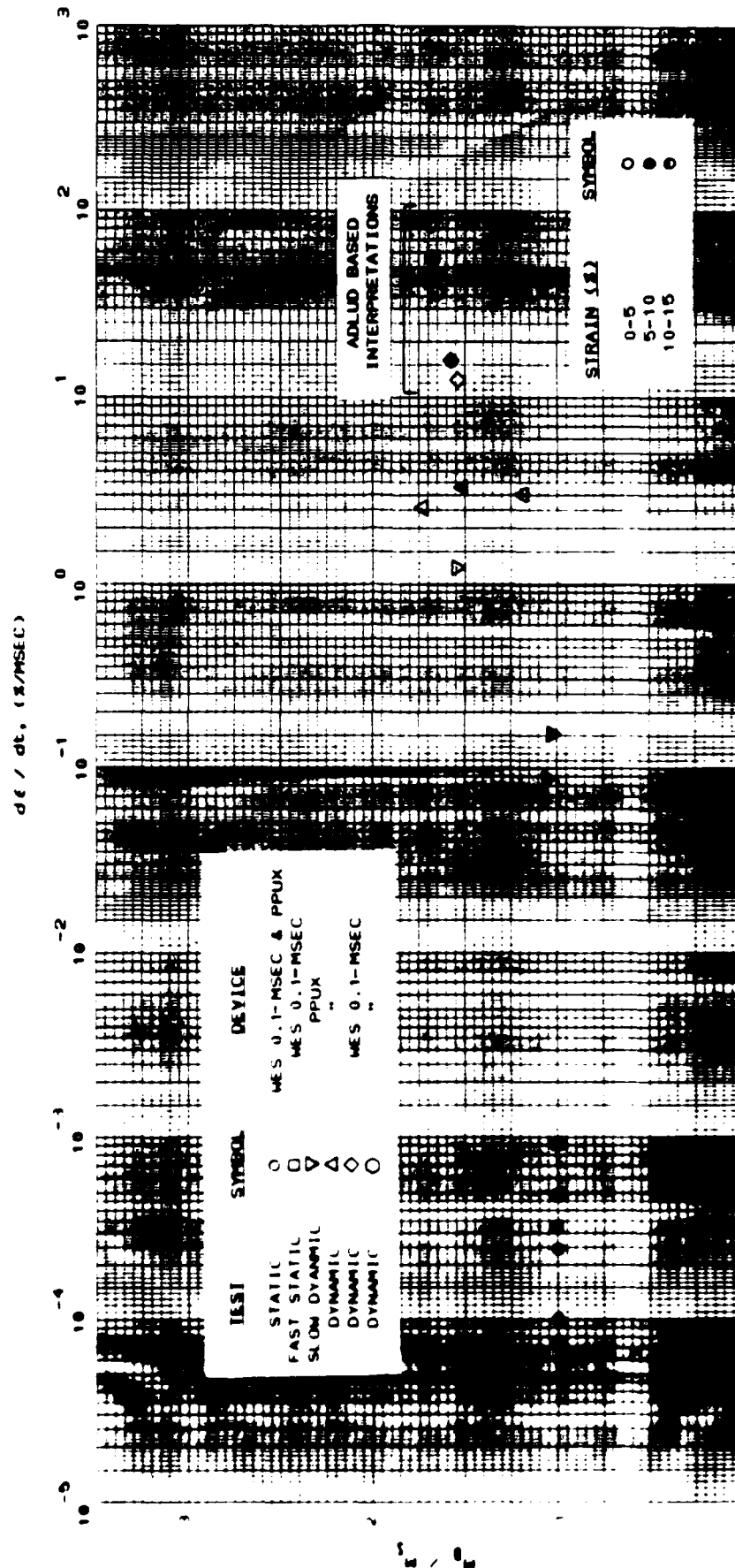
Figure ... Plot of dynamic-to-static modulus as a function of loading rate for Vicksburg loess, D-series.

were adjusted along with the IF statements in the program until the lab results were reproduced. This process was used for the Enewetak beach, flume, and Yuma clayey sands and the Vicksburg loess D-series tests. The ADLUD-based interpretations of the true dynamic-to-static modulus for these WES 0.1-msec tests are shown in Figs. 5.2.1 thru 5.2.4.

Since only two loading rates were used for the Vicksburg loess V-series, IF statements were used to model the strain-rate as well as the strain-level dependency. The Vicksburg loess V-series results are presented on arithmetic plots of the dynamic-to-static modulus as a function of water content and dry density in Figs. 5.2.5 and 5.2.6.

Typical laboratory measured and ADLUD-predicted plots of applied pressure versus average strain are presented in Figs. 5.2.7 and 5.2.8. The results presented in Fig. 5.2.7 are typical of those for a 10-ksi (69-MPa) EBW cap; whereas, those presented in Fig. 5.2.8 are typical for a 20-ksi (137-MPa) EBW cap. The ADLUD simulation for each of the 29 submillisecond tests conducted with the WES 0.1-msec device is presented in Appendix D.

As previously discussed, the proximeter target separated from the sample when the 20-ksi (138-MPa) EBW caps were used for loading. This probably occured when the initial compression wave propagated back up through the sample after being reflected at the rigid base and impinged upon the bottom of the surface proximeter target. The ADLUD simulations predict this behavior. The code predicts a stress increase at a constant or decreasing value of strain at the point where the
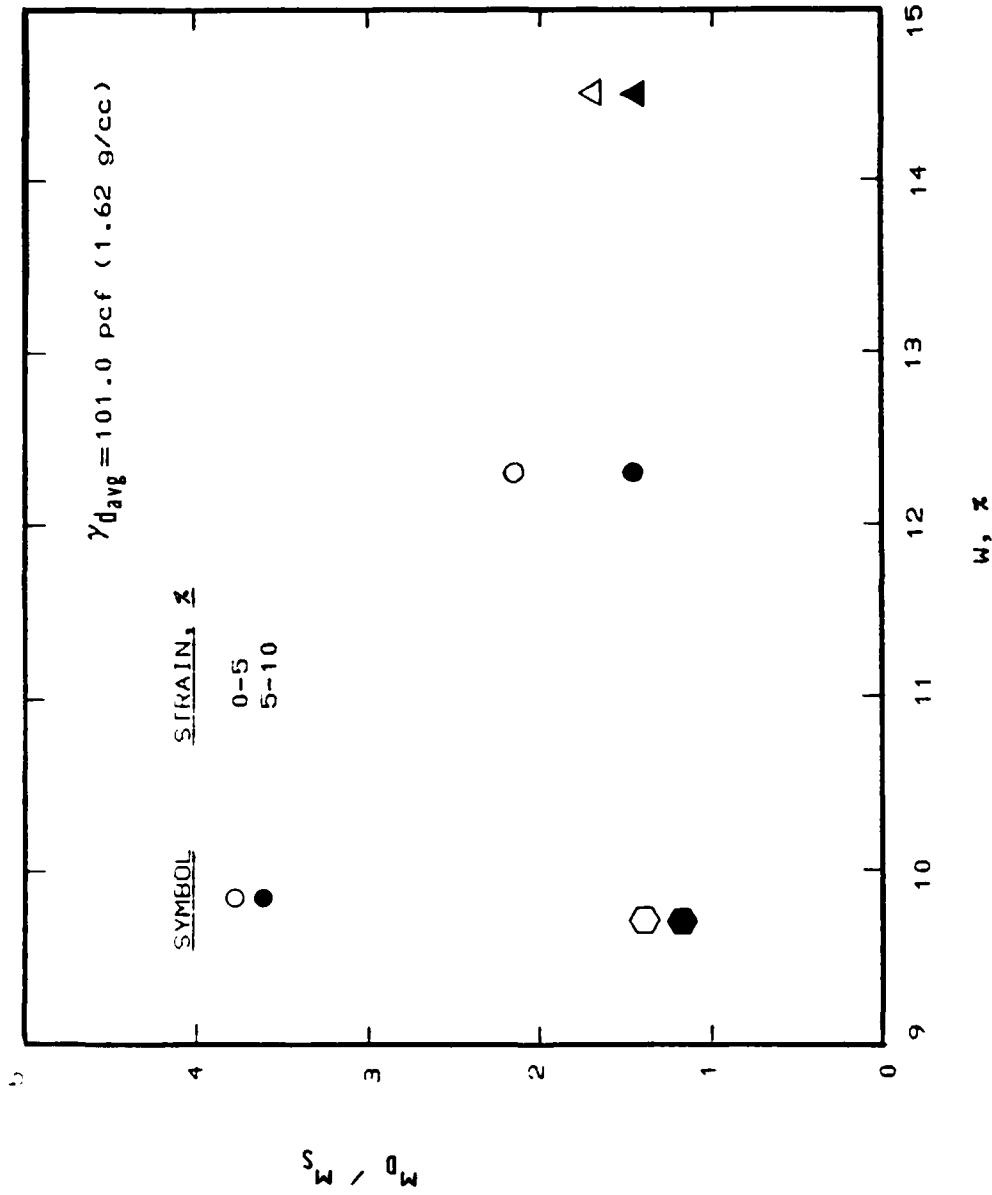
Figure 5.2.5 Plot of dynamic-to-static modulus as a function of water content for Vicksburg loess, V-series.
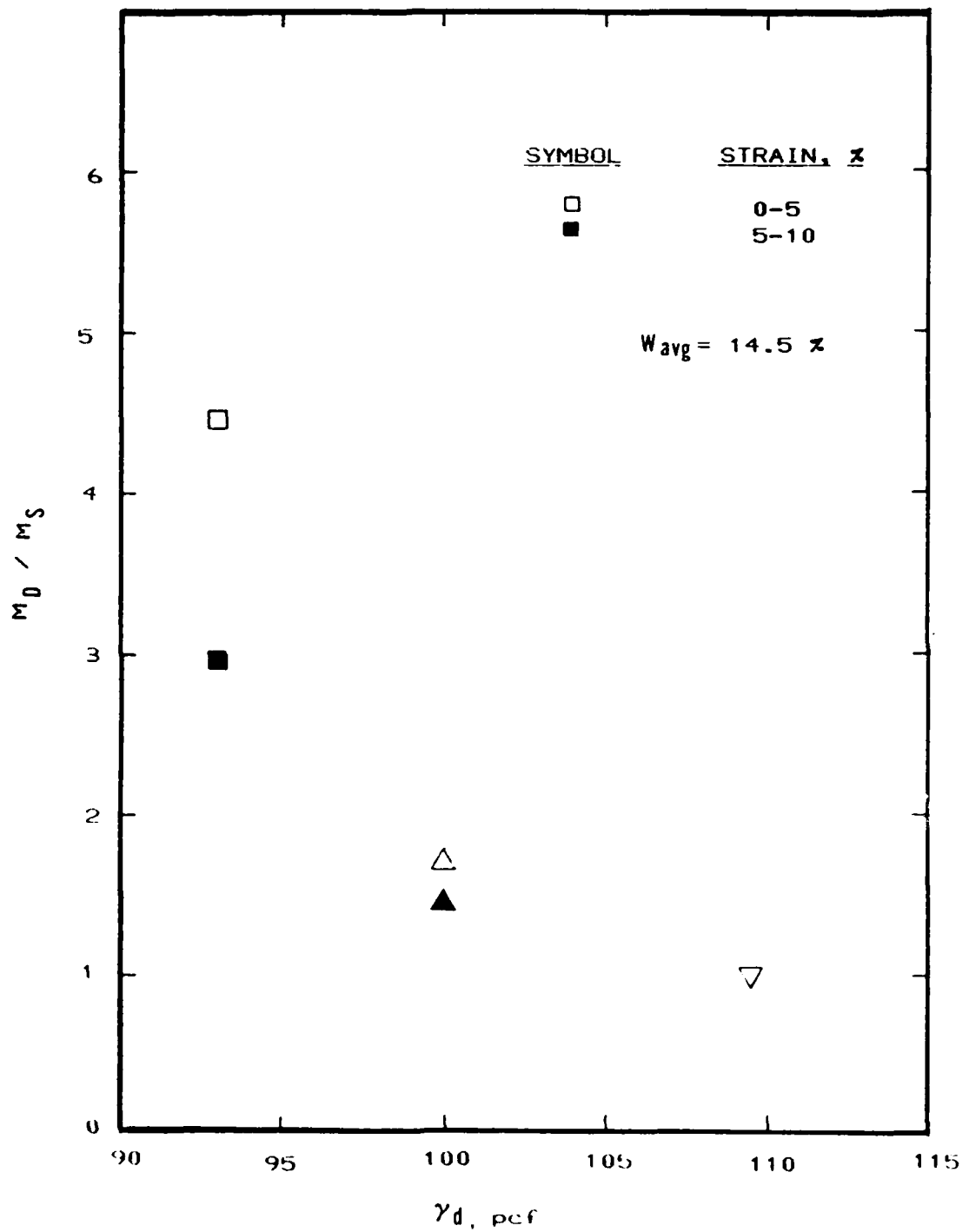
Figure 5.2.6   Plot of dynamic-to-static modulus as a function of dry density
              for Vicksburg loess, V-series.

Uniaxial Strain Results
Soil Type: Enewetak Beach Sand
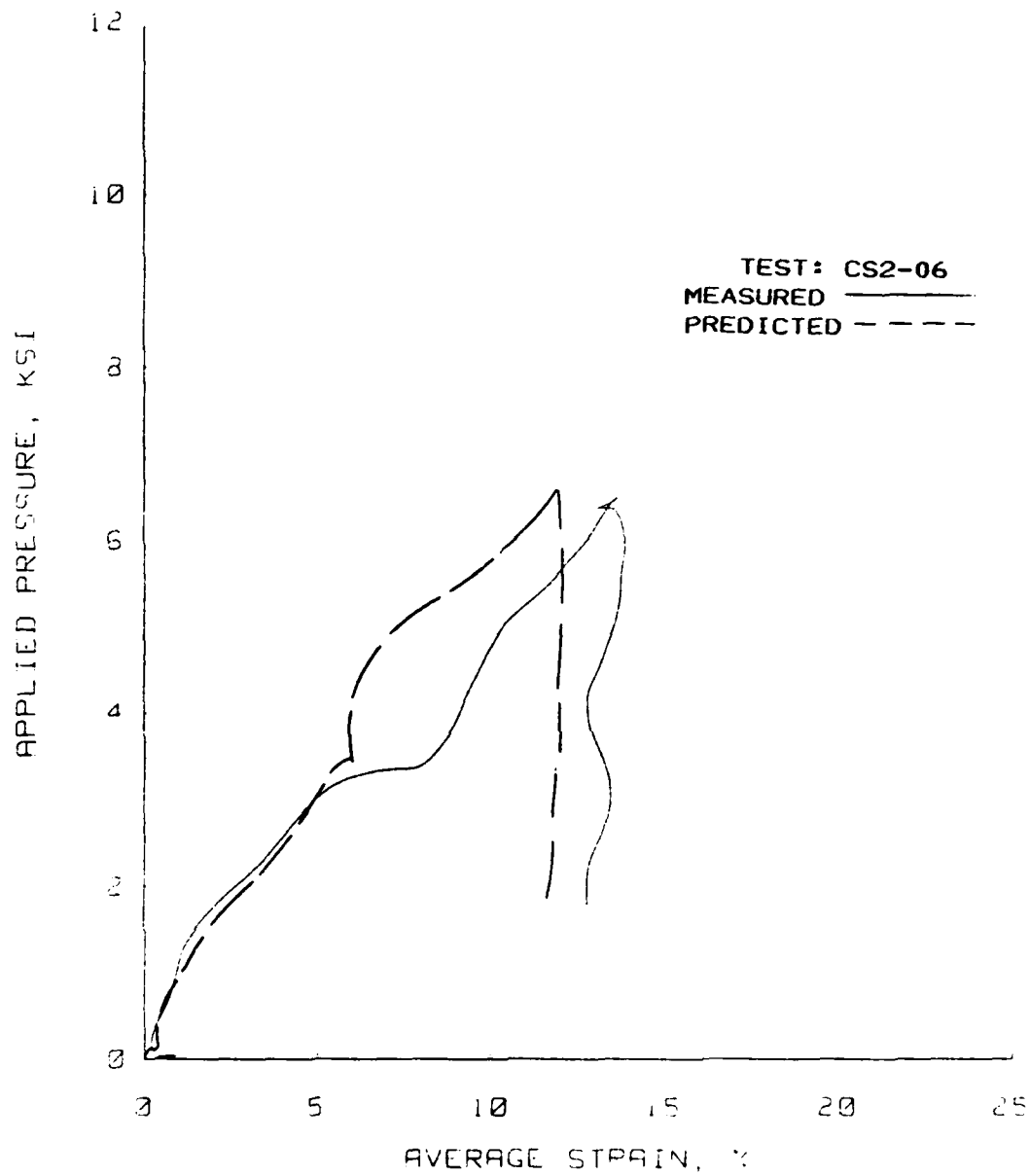
Figure 5.2.7 Typical plots of ADLUD-predicted and laboratory-measured
values of applied pressure versus average strain for a test
using a 10-ksi (69-MPa) EBW cap.

Uniaxial Strain Results
Soil Type: Enewetak Beach Sand
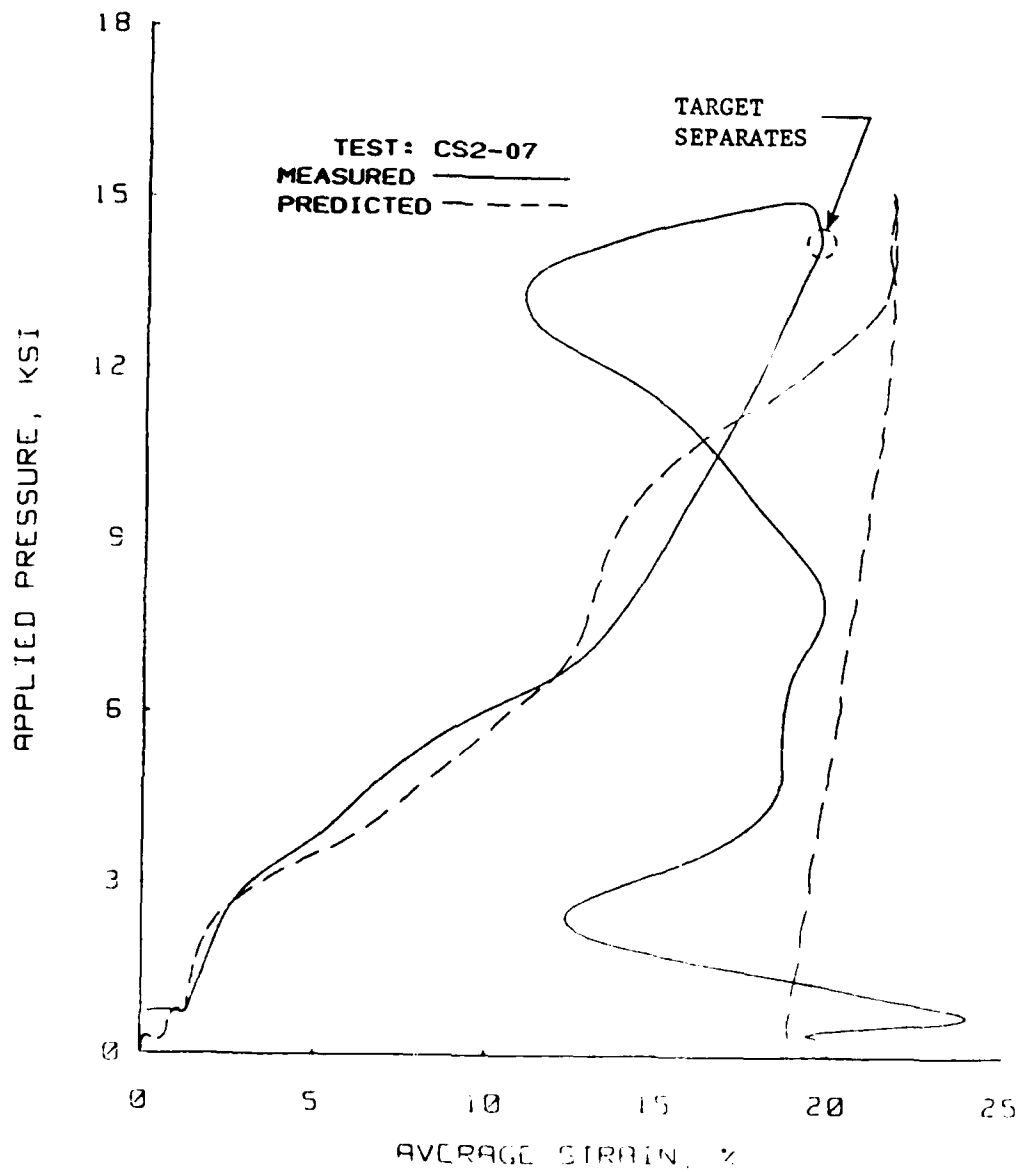
Figure 5.2.8 Typical plots of ADLUD-predicted and laboratory-measured values of applied pressure versus average strain for a test using a 20-ksi (138-MPa) EBW cap.

target separates from the sample (see points noted in Fig. 5.2.8 and applicable figures in Appendix D).

The ADLUD-predicted applied pressure versus average strain plots were found to be very sensitive to the loading pulse used to drive the simulation. When the actual loading pulses were used to drive the program, the code did an excellent job of predicting the nuances of each individual test. As shown by the results in Appendices B and D, this type of approach must be used to correctly interpret the true material response from measurements of applied pressure and average strain for most of the submillisecond test results contained herein.

CHAPTER VI

CONSTITUTIVE MODELS FOR PREDICTING

LOADING RATE EFFECTS

6.1   Introduction

In order to address the complex soil-structure interaction
problems associated with response of underground structures due to high
intensity transient loadings, mathematical representations of the
behavior of the surrounding earthen material must be developed for
computer simulations. These representations are referred to as
constitutive models. Numerous constitutive models incorporating
loading rate effects have been developed (Baladi and Rohani, 1982,
Katona, 1984, and Schreyer and Bean, 1985). Unfortunately, only
limited test data can be found in the literature for the wide variety
of loading rates needed to assess the accuracy of the various modeling
schemes.

Existing rate dependent models were found to be unsatisfactory in
modeling the material response obtained for the series of laboratory
tests reported herein because they do not accurately reproduce the
shape of the measured response (e.g., concave to the applied pressure
axis). Instead, their damping terms tend to produce concavity toward
the average strain axis. Therefore, a simple rate dependent,

146

incremental constitutive model was developed to produce the desired response. This constitutive equation stiffens the static uniaxial strain response as a function of strain magnitude or level and the strain rate created by the loading pulse. The details of this model are presented in Section 6.2. A stress-level and stress-rate dependent incremental model could be formulated using a similar modulus stiffening scheme, as discussed in Section 6.3. Also as discussed in Section 6.3, the one-dimensional strain-level and strain-rate dependent modulus model presented in Section 6.2 can readily be extended to three-dimensions.

6.2 One-Dimensional Strain and Strain-Rate Dependent Incremental Model

A one-dimensional, strain-level and strain-rate dependent incremental modulus model was developed to stiffen the statically determined stress-strain curves as a function of the strain rate. A strain softening term was also incorporated into the model to account for the reduced amount of stiffening that occurs at the higher strain levels. This model is simply a mathematical relationship fitted to the semilog plots of the ratio of the dynamic-to-static modulus as a function of strain level and strain rate shown in Figs. 5.2.1 through 5.2.4. This relationship has the following form:

$$M_D / M_S = A - B \, e^{-CX} + D \, X^n e^{-EX^n} \qquad (6-1)$$

where: M_D = dynamic modulus for a given increment
M_S = static modulus " " " "
$X = d\epsilon / dt$ = strain rate (% / msec)
A, B, C, D, E, n = material constants

This equation can be expressed in terms of the dynamic modulus as:

$$M_D = \left[A - Be^{-CX} + DX^n e^{-EX^n} \right] M_S \tag{6-2}$$

or

$$M_D = S(\dot{\epsilon}) M_S \tag{6-3}$$

where: $S(\dot{\epsilon})$ = strain-rate dependent stiffening function

The increase in modulus (M_I) can be expressed as:

$$M_I = M_D - M_S = S(\dot{\epsilon}) M_S - M_S \tag{6-4}$$

or

$$M_I = M_S (S(\dot{\epsilon}) - 1) \tag{6-5}$$

At the higher strain levels, a strain softening function $(S(\epsilon))$ is needed to decrease the amount of stiffening. This equation can be expressed as a function of strain level:

$$S(\epsilon) = \frac{1}{2} \left[\frac{G + 3}{G + 1} - \frac{1 - G e^{-H\epsilon}}{1 + G e^{-H\epsilon}} \right] \tag{6-6}$$

where: G, H = material constants

The $S(\epsilon)$ equation is a simple step function. At lower strain levels, the equation is approximately equal to one. As the strain level increases, the equation approaches a value of zero. By adjusting the equation constants, the location of the step and its slope can be adjusted.

Equations 6.4 and 6.6 can be combined to reflect the strain rate stiffening and the strain softening at the higher strain values:

$$M_p = \left[M_I{}^* \, S(\epsilon) \right] + M_S \qquad (6\text{-}7)$$

where: M_p = predicted dynamic modulus

The eight material constants needed to fit Equation 6-7 for the four soils tested, exclusive of the Vicksburg loess, V-series, are presented in Table 6.2.1. Plots of the model predicted dynamic-to-static modulus versus the laboratory-measured values are shown in Figs. 6.2.1 through 6.2.4. For some of the materials tested, a strain softening type of behavior was not detected for the strain levels achieved during this testing program. For these materials, $S(\epsilon)$ was assumed to be one and is denoted in Table 6.1 by an asterisk for the strain softening constants G and H.

The mathematical relationships presented can easily be implemented into a one-dimensional wave propagation code. A static material response can be inputted into the code, along with the strain and strain rate dependent equations. Based upon laboratory measurements, the appropriate material constants are developed for a given soil type. Ideally, any type of loading pulse could then be used to drive the program, and the material response would reflect the loading rate effects. This methodology produces a more rational approach than inputting one stress-strain curve and assuming that response was representative of the dynamic behavior for all loading rates.

	Enewetak Beach Sand	Flume Sand	Yuma Clayey Sand	Vicksburg Loess
Dry Unit Weight (pcf)	101.0	100.5	115.0	101.5
Water Content (%)	5.0	5.5	3.5	11.5
A	2.25	1.45	2.00	1.70
B	1.25	0.45	1.00	0.70
C	0.50	0.11	0.19	0.15
D	3.33	0.41	2.10	1.09
E	2.04	1.00	1.50	1.00
n	0.31	0.90	0.60	0.70
G	*	100,000	*	100,000
H	*	1.2	*	1.0

* Denotes a value of 1.0 for the strain-softening term, $S(\epsilon)$

Table 6.2.1 Summary of material constants for the one-dimensional strain and strain-rate modulus stiffening model.
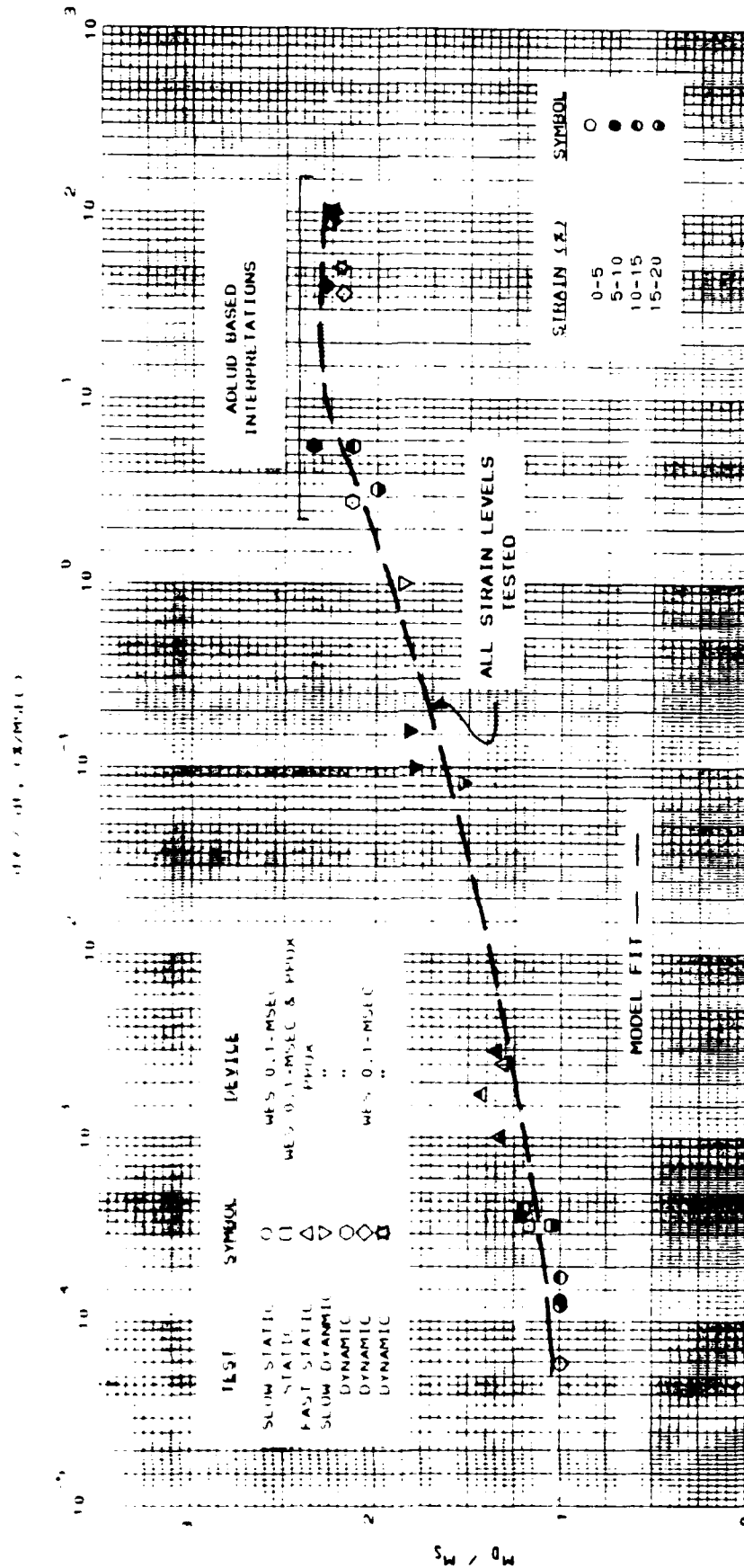
Figure 6.2.1 Plot of strain and strain-rate dependent modulus model fit for the Enewetak beach sand test results.
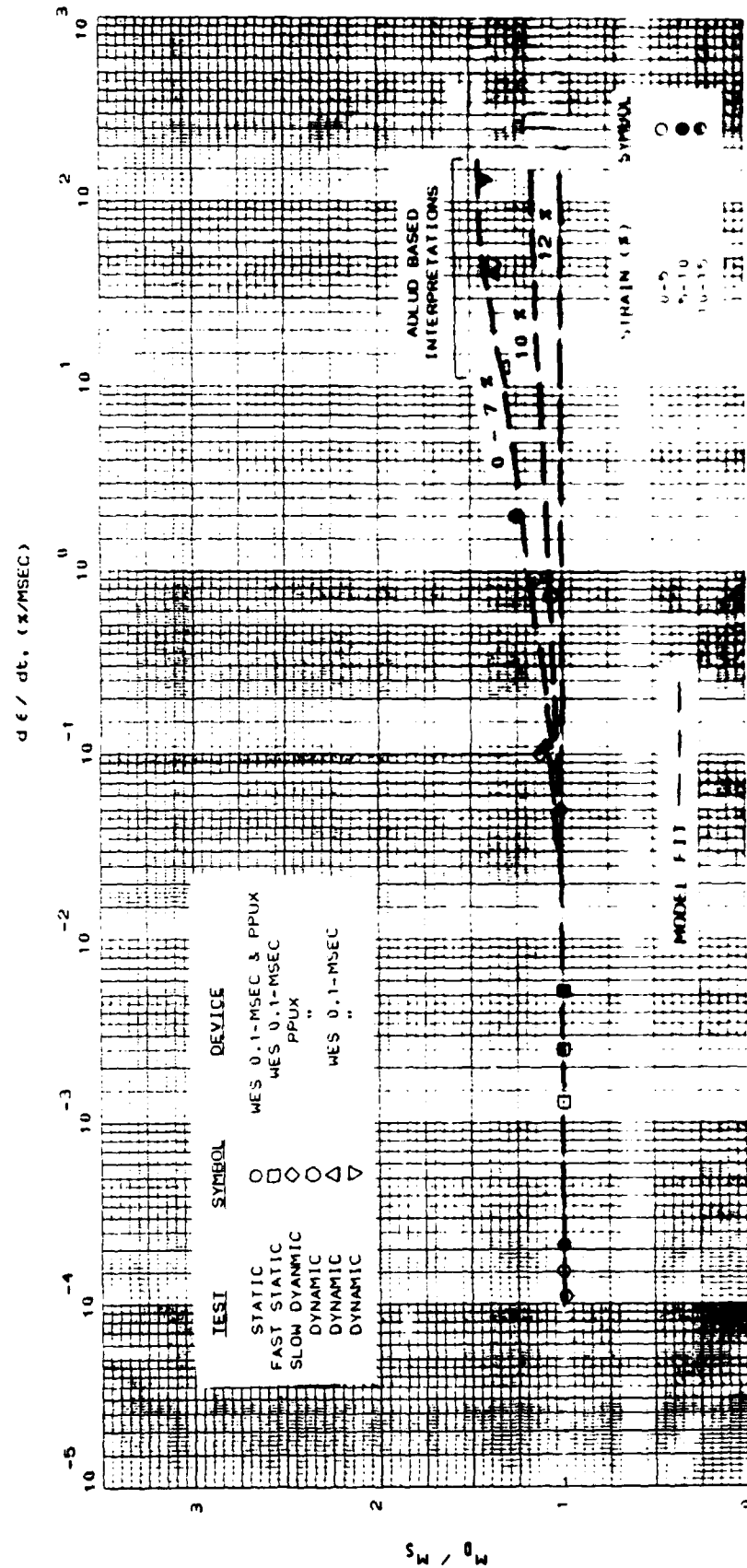
Figure 6.2.2 Plot of strain and strain-rate dependent modulus model fit for the Eluna Sand test results.
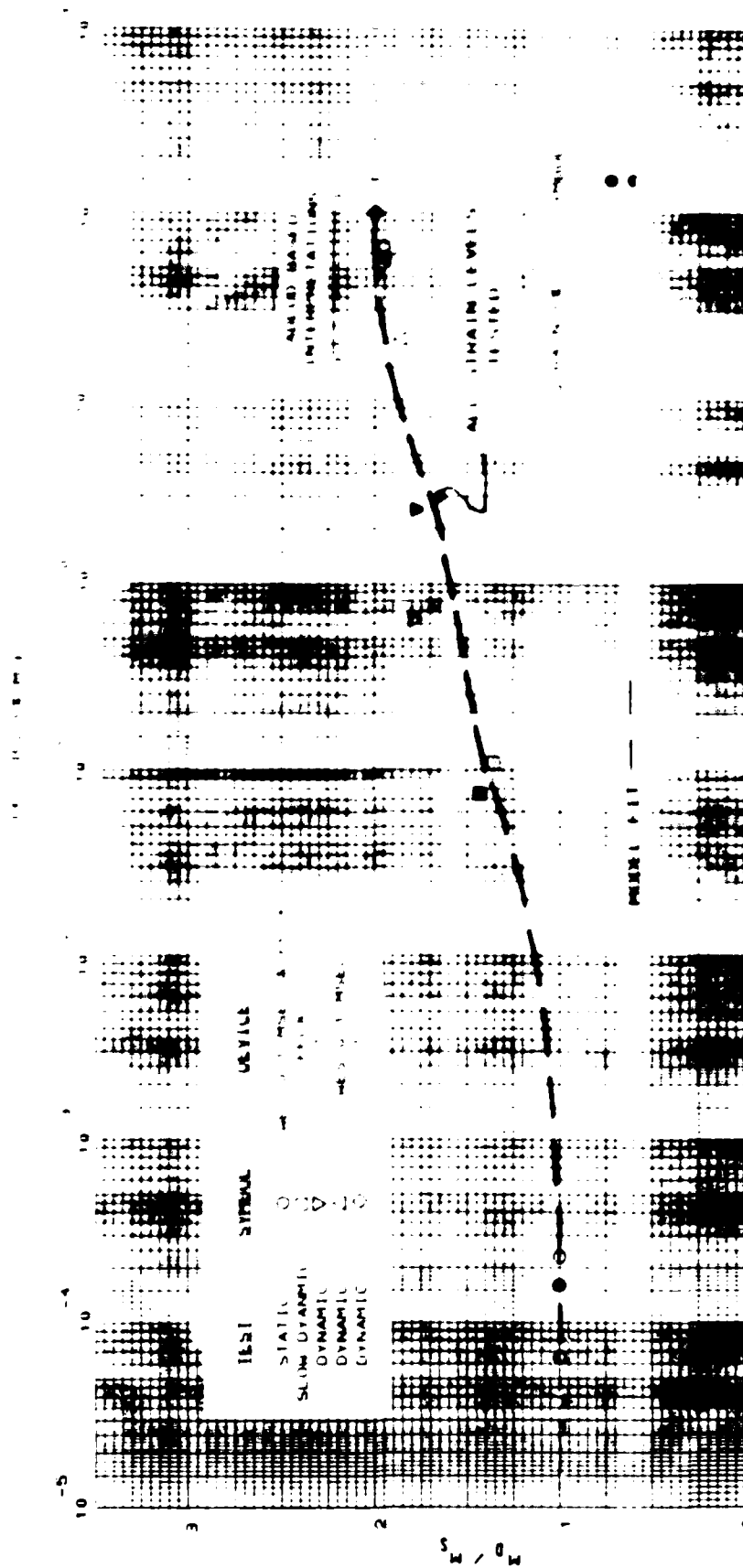
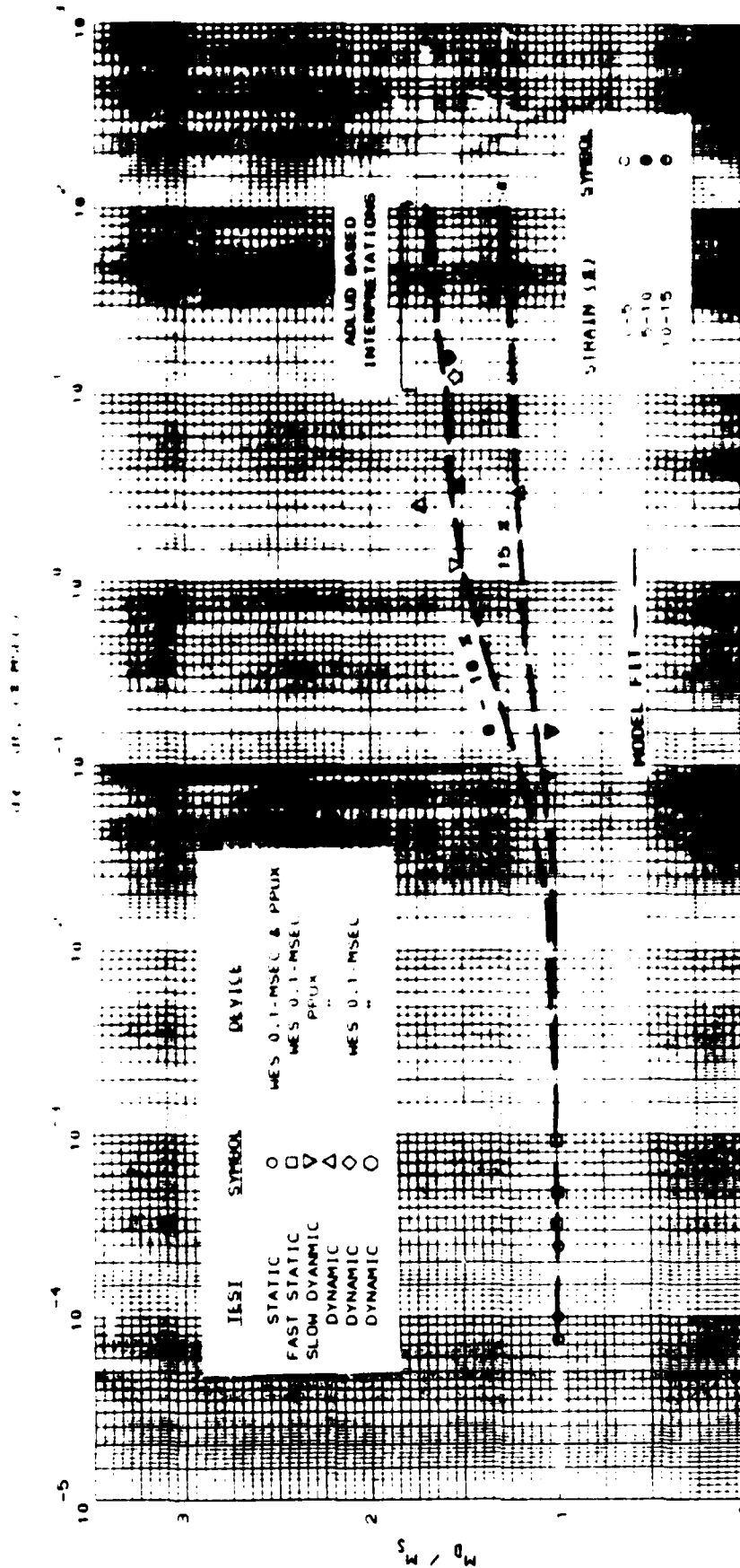Figure 6.2.3 Plot of strain and strain-rate dependent modulus for the beam
results.

154

Figure 6.2.4 Plot of strain and strain-rate dependent modulus model fit for the Vicksburg loess, D-series test results.

6.3 Potential for Development of Other Rate-Dependent Models

The equations presented for the strain-level and strain-rate dependent model can easily be reformulated to produce a stress and stress-rate dependent model. The basic form of Equations 6-1 through 6-7 would be maintained, however, the strain-level and strain-rate terms would be replaced with stress-level and stress-rate terms, respectively. Equations incorporating stress and stress-rate were not developed herein because the equations of motion used in the one-dimensional plane wave propagation scheme dictated that the rate-dependent model be a function of strain or displacement.

The ultimate use of the results and models presented are to contribute to the development of a three-dimensional rate-dependent model. Numerous models have been developed as previously described. However, none of the models operate on the modulus. Most three-dimensional models operate on the strain, causing the basic shape of the stress-strain curve (concave to the stress axis) not to be preserved. If the loading rate effects on the shear strength and shear modulus of a material can be assessed, an accurate three-dimensional rate-dependent modulus model could easily be developed.

CHAPTER VII

COMPARISON OF FIELD TEST RESULTS WITH LABORATORY-BASED

MODEL PREDICTIONS

7.1 Introduction

Field tests are important to the design of underground protective structures. Scaled models of these structures are instrumented and placed in a controlled backfill, and conventional high explosives are detonated near the structure. The results from these field events are used to determine the response of various structural systems and components to explosive-induced airblast and ground shock. If the backfill is properly instrumented with stress and motion gauges, then calculational analysis can be performed to deduce in situ material properties from the gauge measurements. In many of these tests, a large portion of the test bed is subjected to a state of vertical one-dimensional compression for several milliseconds. Thus the backfill property which governs gauge response during this period is uniaxial strain compressibility. And just as with laboratory uniaxial strain tests, these field experiments can be simulated with a one-dimensional plane wave propagation code. Using the airblast pressure time history measured during the field event as a driver for the simulation, a uniaxial strain stress-strain response function is input and then

156

adjusted until the calculated stress time histories mirror the measurements obtained during the field event. Unfortunately, this trial-and-error uniaxial strain response is different for each different loading rate or rates generated throughout the test bed by the specific loading pulse applied on the surface.

Data from two recent high-explosive field tests, one using flume sand and the other using Vicksburg loess as backfill materials, were available for constitutive model validation. The one-dimensional, finite-difference computer program 1D-LAYER (Meier, 1985) was modified to incorporate the strain-level and strain-rate dependent modulus stiffening model described in Chapter VI for the specific purpose of modeling these two field events. Suitable field results were not available for the other two backfill materials. 1D-LAYER uses the same type of computational scheme presented in Appendix C for ADLUP. However, the program can be used to model numerous soil layers with a variety of boundary conditions.

7.2 Flume Sand Field Test Results

A field event was conducted using flume sand as the backfill material (Windham, 1985). As shown in Fig. 7.2.1, the target values for the laboratory testing program of 100.5 pcf (1.61 g/cc) for dry density and 5.5 % for water content are approximately equal to the as-placed backfill conditions, especially for depths greater than 6 ft (1.83 m). Figure 7.2.2 shows the actual stress-time histories measured during the field event. Figure 7.2.3 presents the results of 1D-LAYER simulations using the modulus stiffening model and the laboratory-based
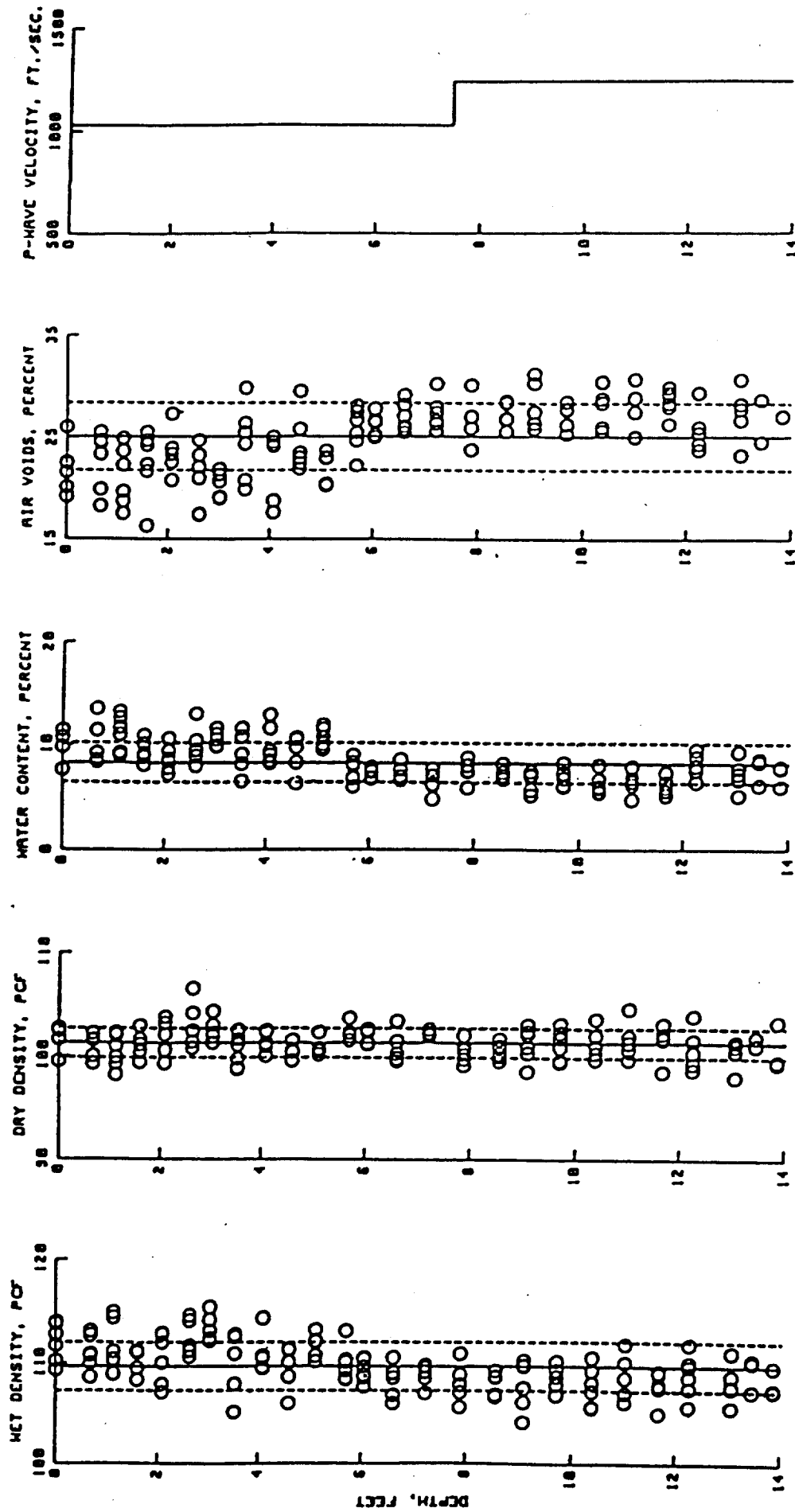
Figure 7.2.1 Measured placement water contents and densities, calculated air voids, and P-wave velocities from downhole geophysical surveys in the flume sand backfill (from Windham, 1985).
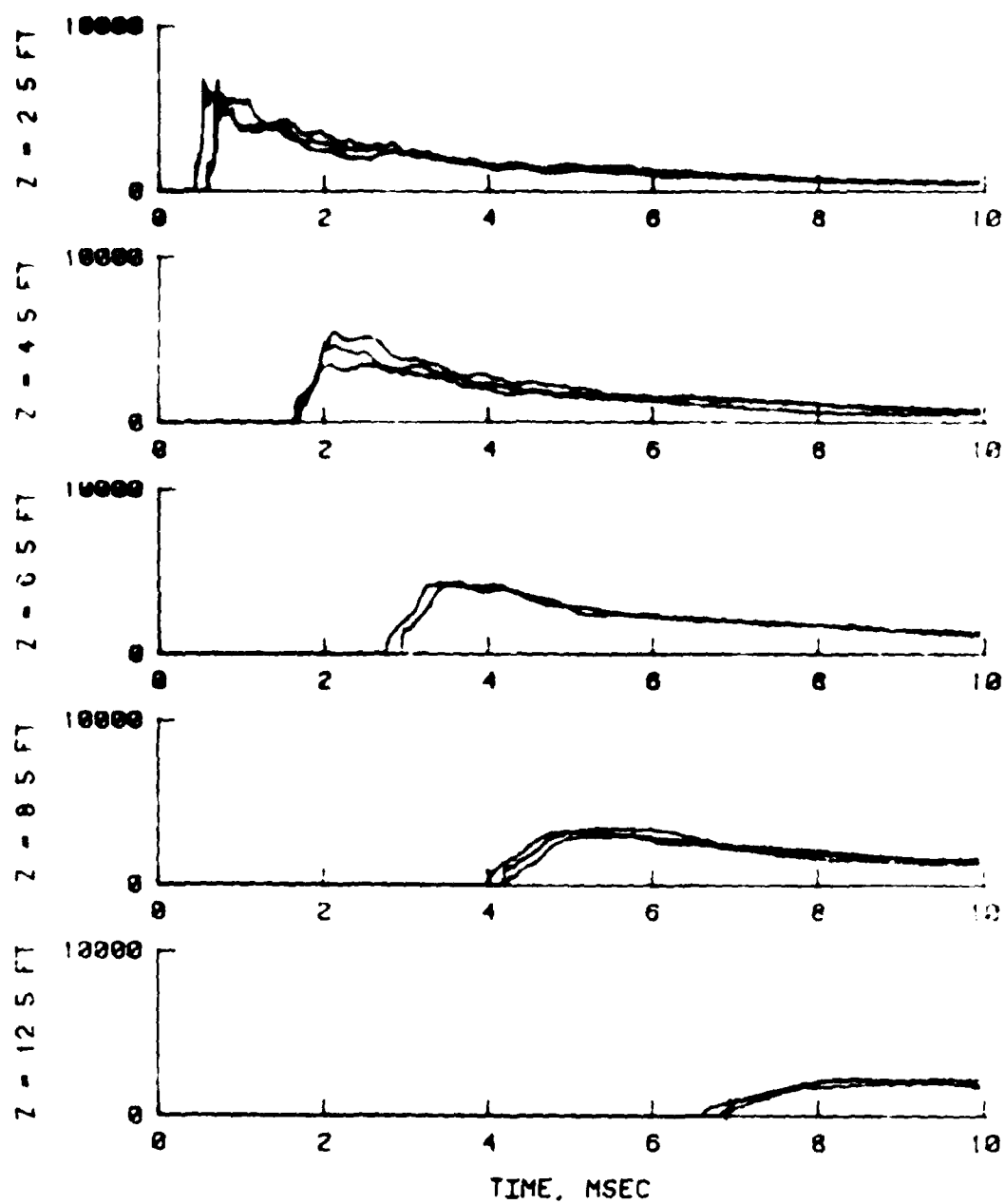
Figure 7.2.2 Measured stress-time histories in the flume sand
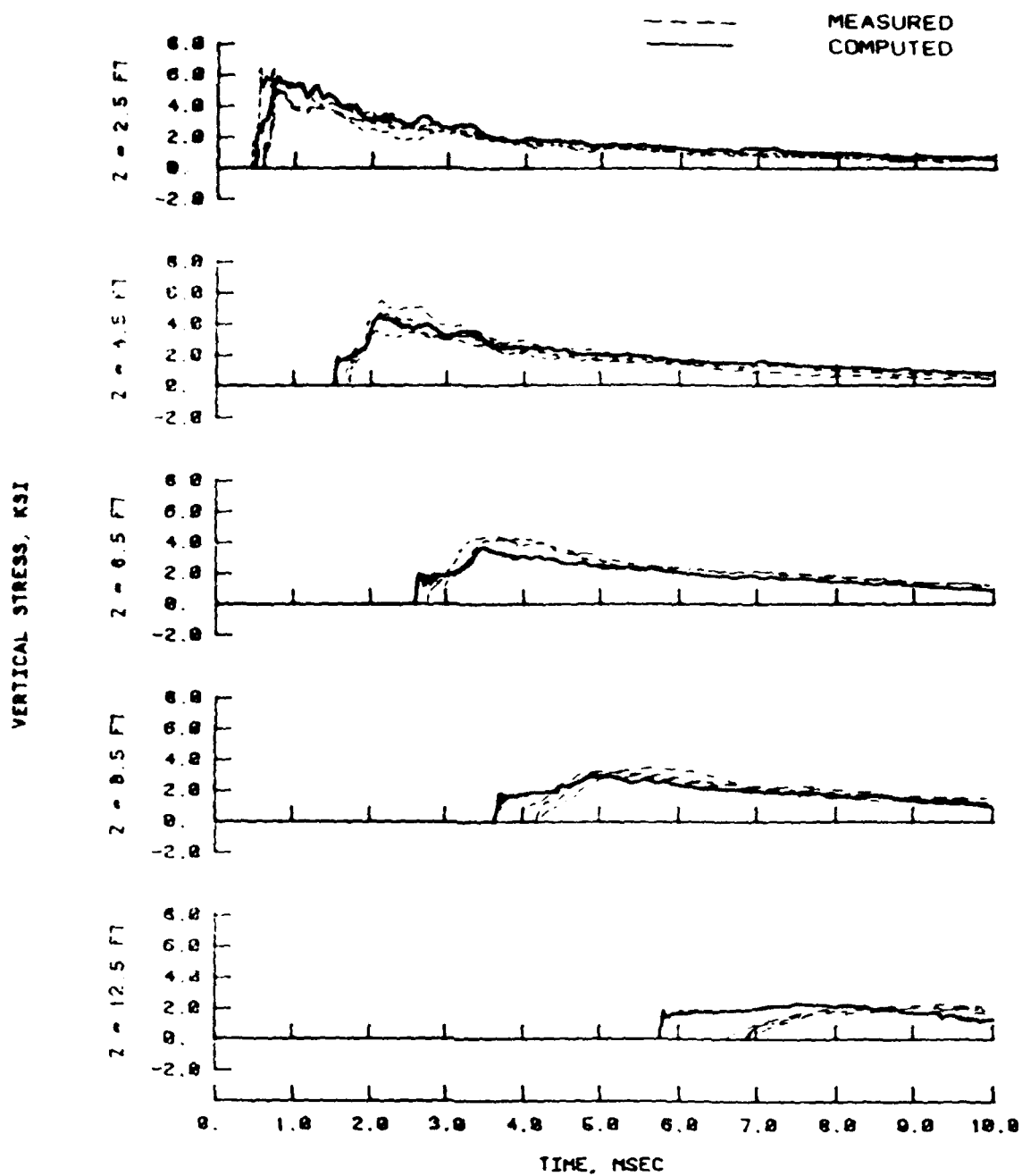backfill (from Windham, 1985).

Figure 7.2.3 Predicted stress-time histories from 1D-LAYER r in
using the modulus stiffening model for the flume
sand backfill.

constants (Table 6.2.1) presented in Chapter VI. During this field
event, the surface gauges were destroyed; thus, the simulations
presented were performed using the average stress-time history recorded
at a depth of 1.5 ft (0.46 m) as a driver. Figure 7.2.4 presents the
postshot predictions using the trial-and-error technique of adjusting
the uniaxial strain response until the 1D-LAYER simulations mirror the
field measurements. Figure 7.2.5 presents a 1D-LAYER simulation using
the static material response as input. This figure is included to show
that the static response is too soft, which causes the slower arrival
time for the wave front when compared to the actual field results.
Figure 7.2.6 presents plots of the model-predicted uniaxial strain
response for the loading rate produced during the field event, the
trial-and-error best fit, and the static material response. Comparison
of the trial-and-error best fit with the laboratory-determined uniaxial
strain response shows that the laboratory-based model predictions are
too stiff initially. This stiffer response causes the waves to
propagate faster than those measured during the field event. As shown
in Fig. 7.2.6, the model increases the modulus by about 45 % initially
(0 to 5 % range). The trial-and-error best fit only increases the
modulus by about 20 % over that same range.

7.3 Vicksburg Loess Field Test Results

A field event was conducted using Vicksburg loess as the backfill
material (Green, 1986c). The properties of the backfill are shown in
Fig. 7.3.1. The laboratory investigation for the Vicksburg loess,
D-series of tests was conducted with target values for dry density of
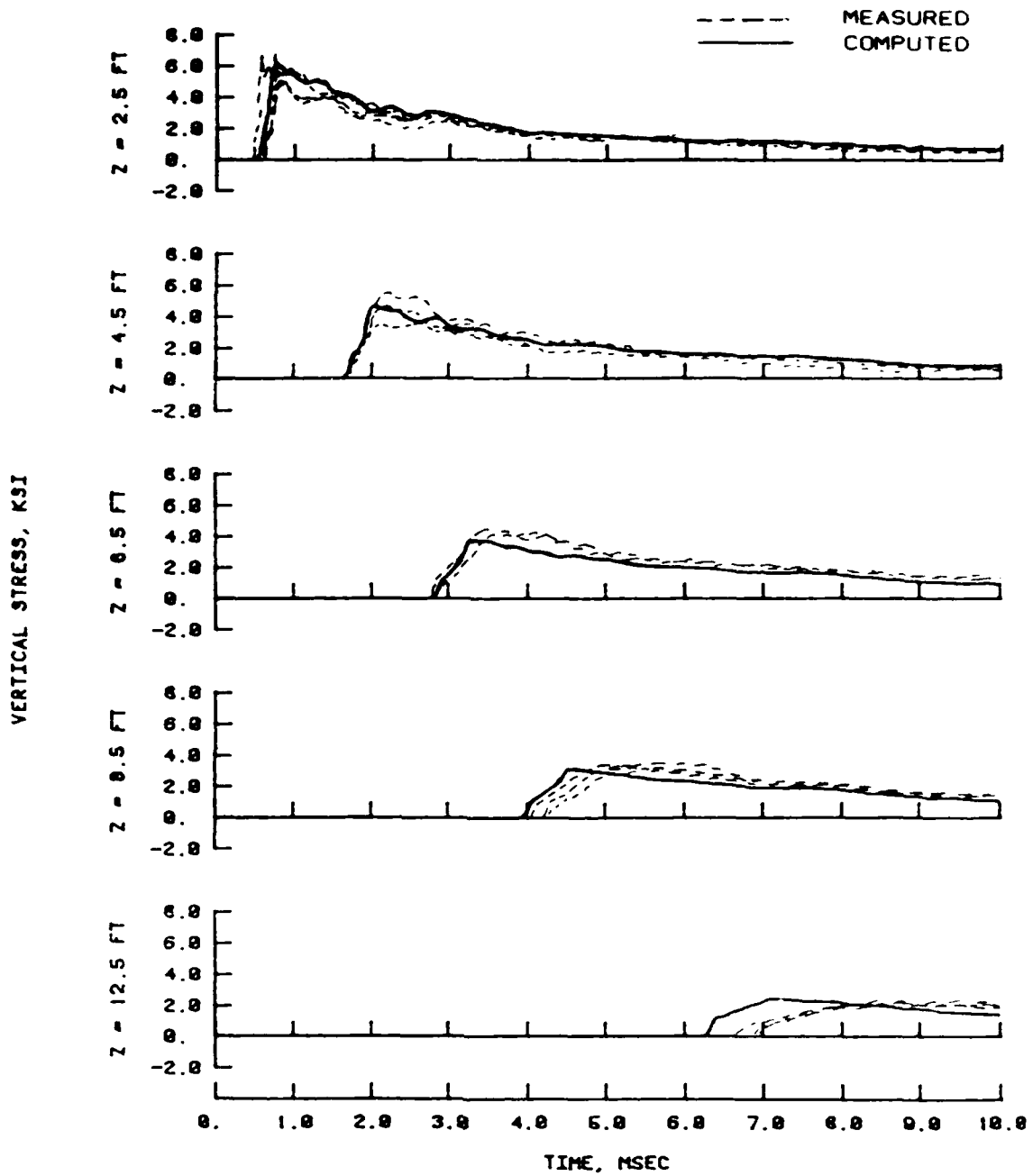
Figure 7.2.4   Predicted stress-time histories from 1D-LAYER run
using a trial-and-error process for the flume
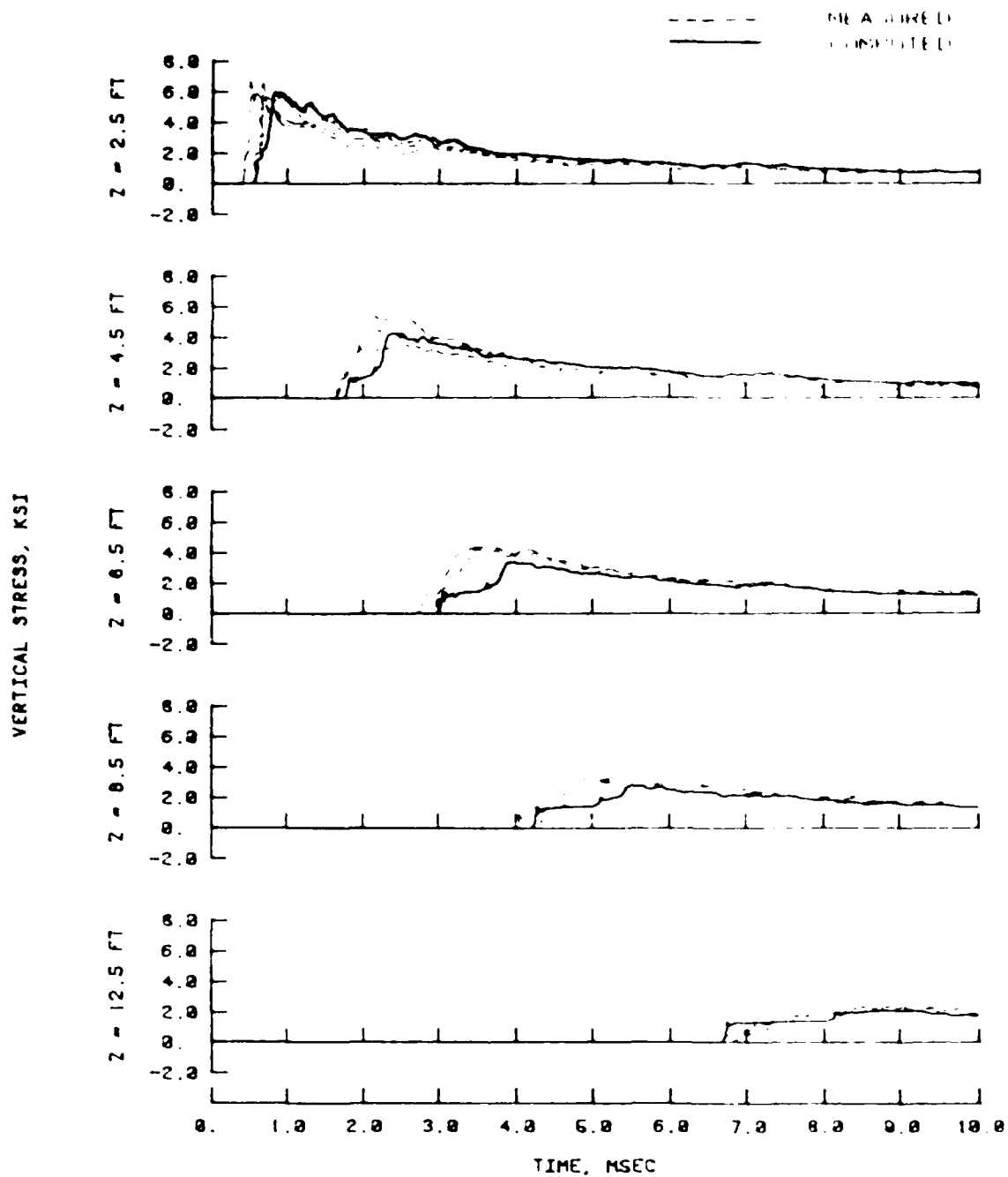sand backfill (from Windham, 1985).

Figure 7.2.5 Predicted stress-time histories from 1D-LAYER run using
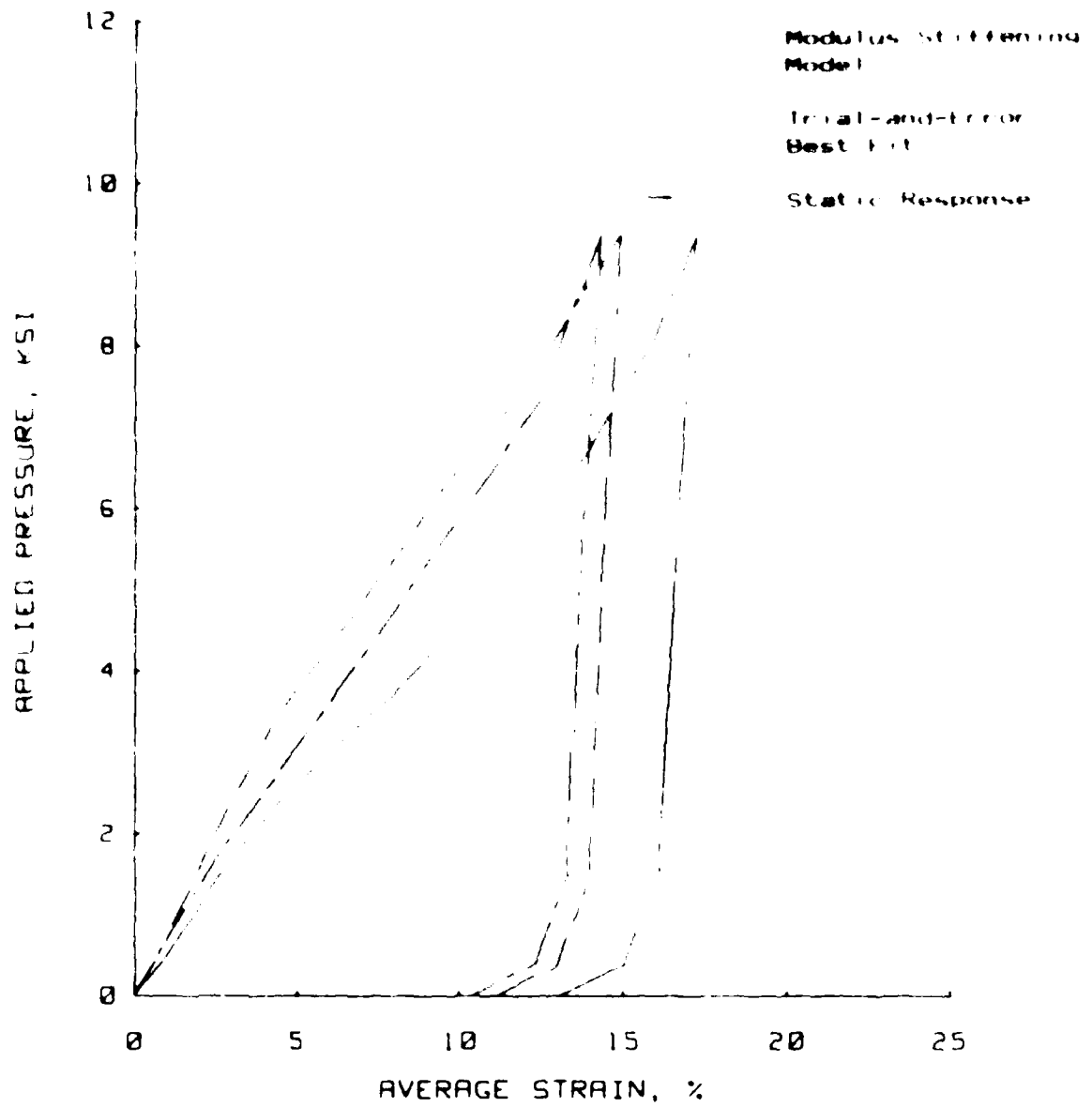the static uniaxial strain response for the flume sand
backfill.

Figure 7.2.6 Comparison of stress-strain curves obtained from the
modulus stiffened model, the trial-and-error best fit,
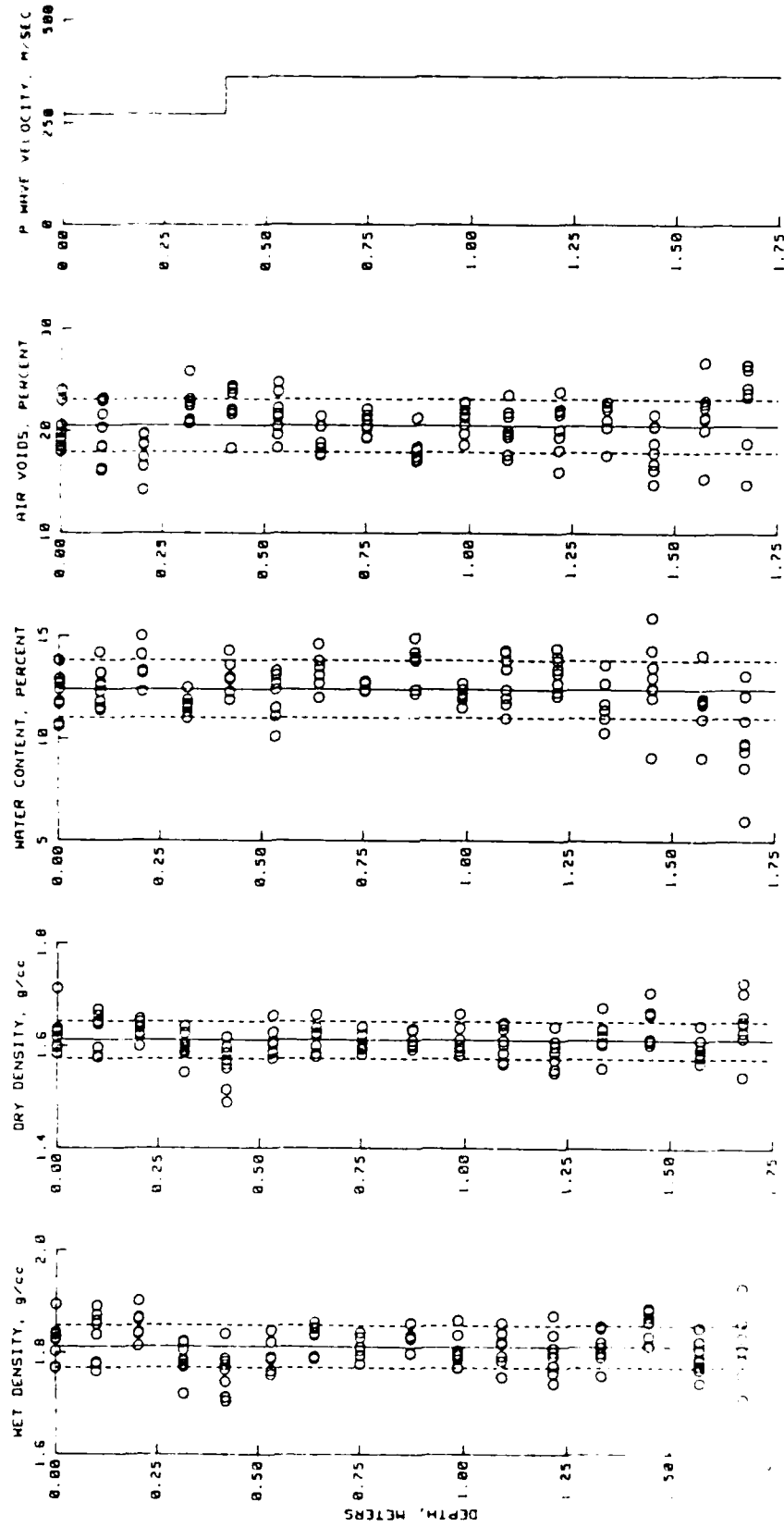and the static uniaxial strain response for flume sand.

Measured placement water contents and densities, calculated air voids, and P wave velocities from downhole geophysical surveys in the Vicksburg loess (from Green, 1986c).

101.5 pcf (1.63 g/cc) at a water content of 11.5 %, which are reasonably representative of the average as-placed conditions for the backfill.

Figure 7.3.2 shows the actual stress-time histories measured during the event. Figure 7.3.3 presents the results of a 1D-LAYER simulation using the modulus stiffening model and laboratory-based constants (Table 6.2.1) presented in Chapter VI. Figure 7.3.4 presents the postshot predictions using the trial-and-error technique of adjusting the uniaxial strain response until the computer simulations reproduce the field measurements. Figure 7.3.5 presents a 1D-LAYER simulation using the static material response. An average of the stress-time histories measured at a depth of 0.5 ft. was used to drive the simulations presented in Figs. 7.3.3 thru 7.3.5. Figure 7.3.6 presents plots of the model-predicted uniaxial strain response for the loading rate generated by the event, the trial-and-error best fit, and the static uniaxial strain response.

Figure 7.3.3 shows that the computer simulation based upon the modulus stiffening model closely mirrors the measured results. The rate-dependent model increases the modulus about 70 % for the loading rates generated by the field event. If the static material response was used without incorporating some type of rate effect model, the results presented in Fig. 7.3.5 would be predicted. Like the flume sand, the static response is too soft. For the Vicksburg loess field event, the rate-dependent modulus model accurately predicts the true material response.
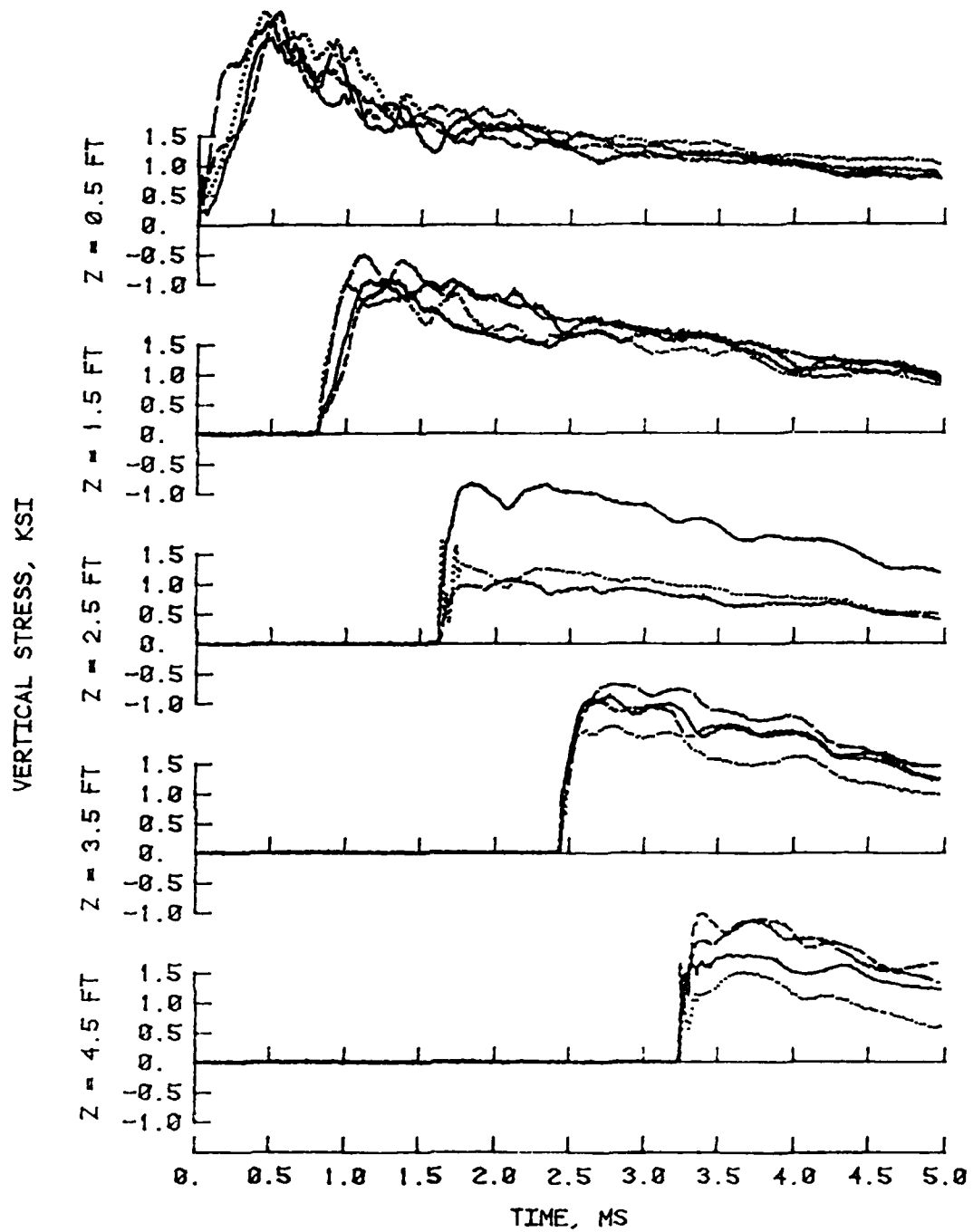
Figure 7.3.2 Measured stress-time histories in the Vicksburg loess backfill (from Green, 1986c).
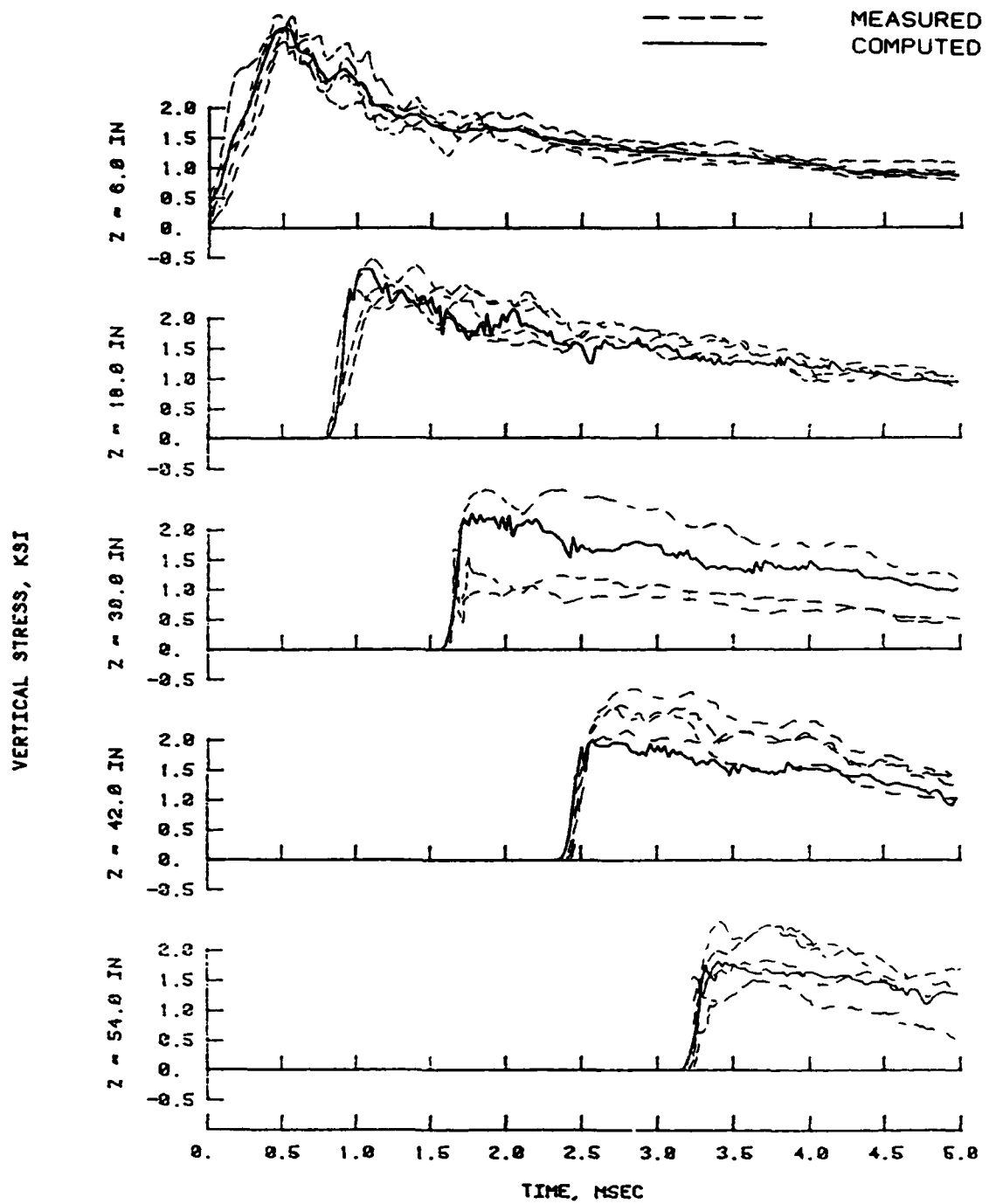
Figure 7.3.3 Predicted stress-time histories from 1D-LAYER
run using the modulus stiffening model for the
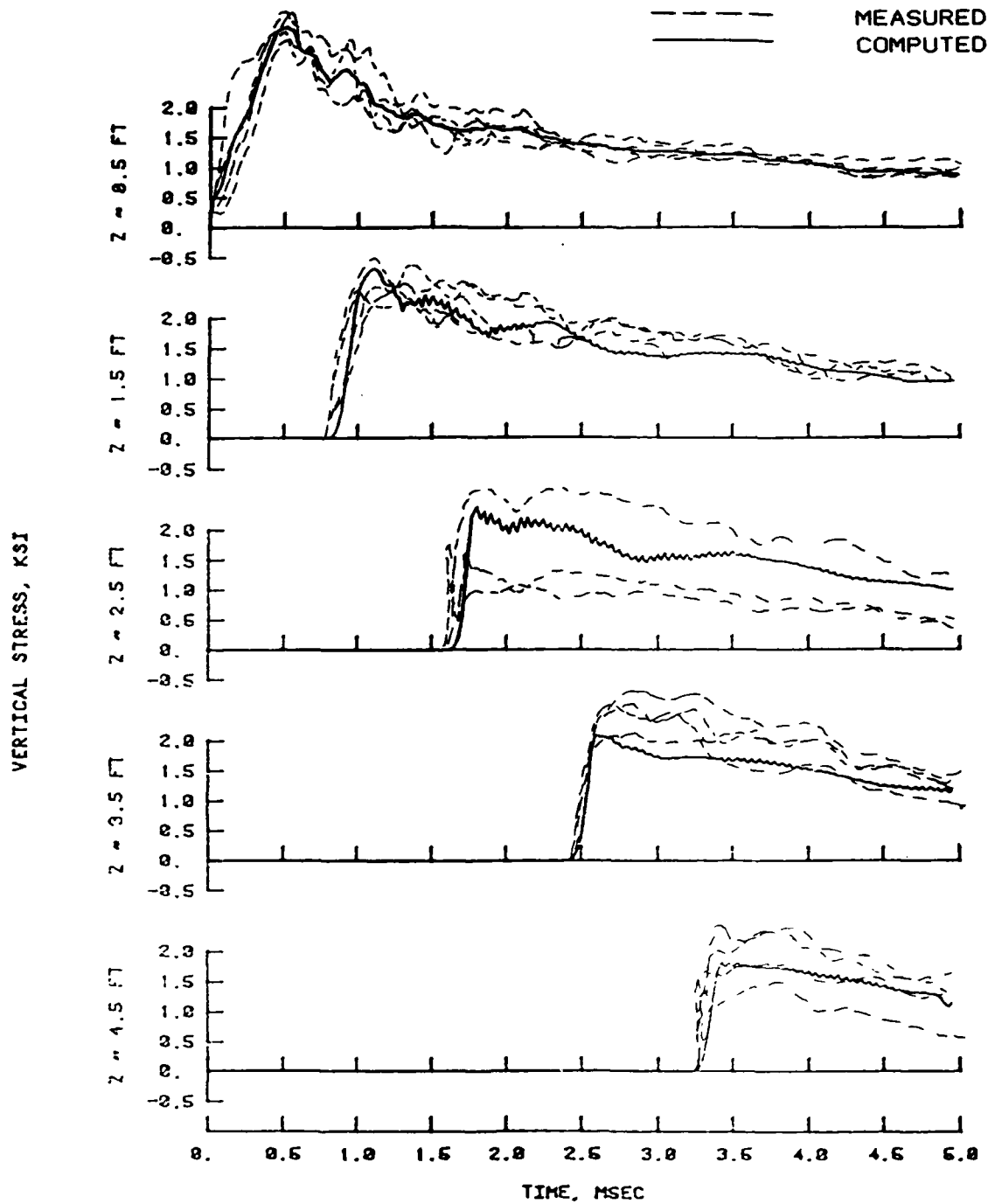Vicksburg loess backfill.

Figure 7.3.4   Predicted stress-time histories based upon 1D-LAYER
runs using a trial-and-error process for the
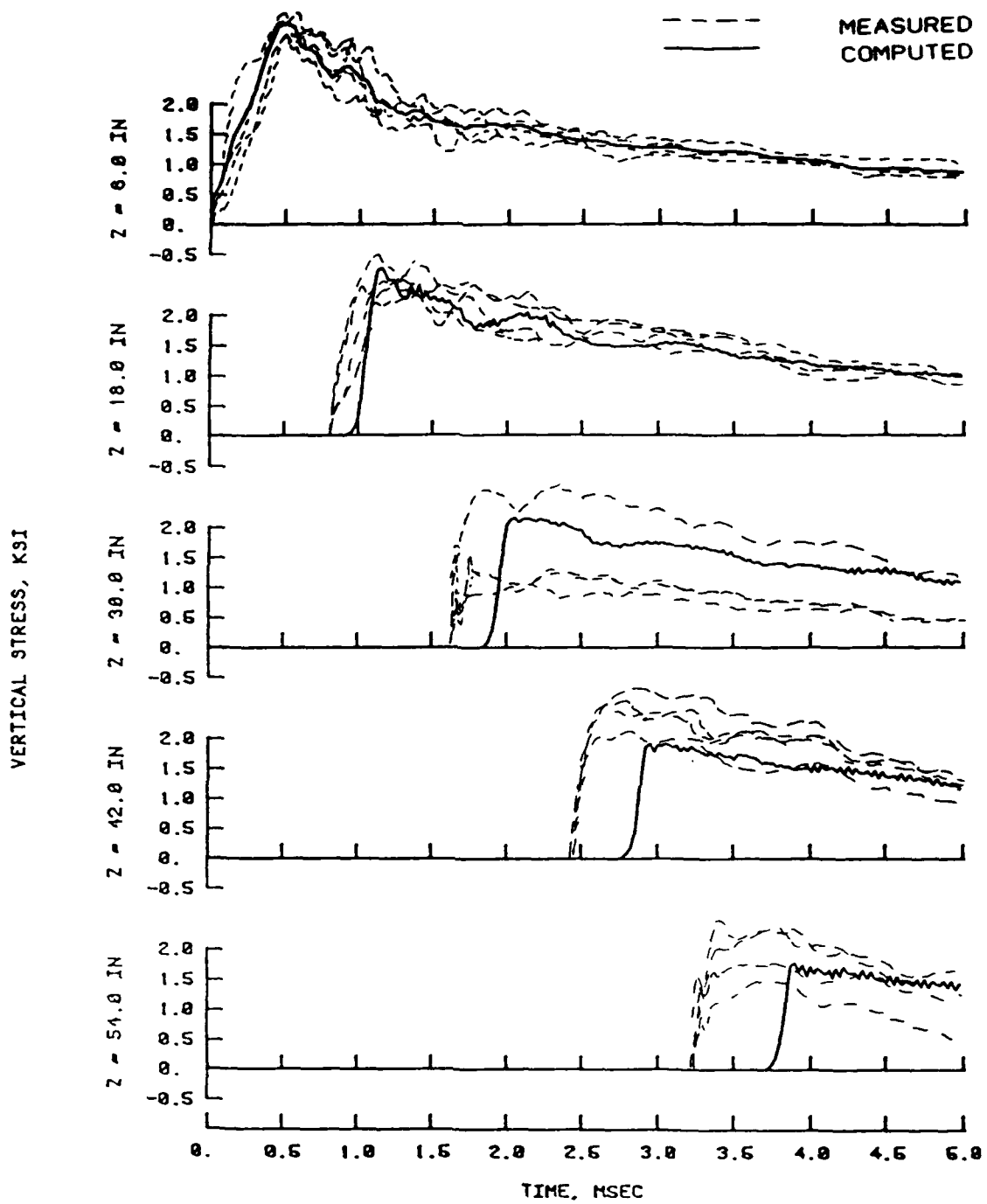Vicksburg loess backfill (from Green, 1986c).

Figure 7.3.5 Predicted stress-time histories from 1D-LAYER run using the static uniaxial strain response for the Vicksburg loess backfill.

Uniaxial Strain Results
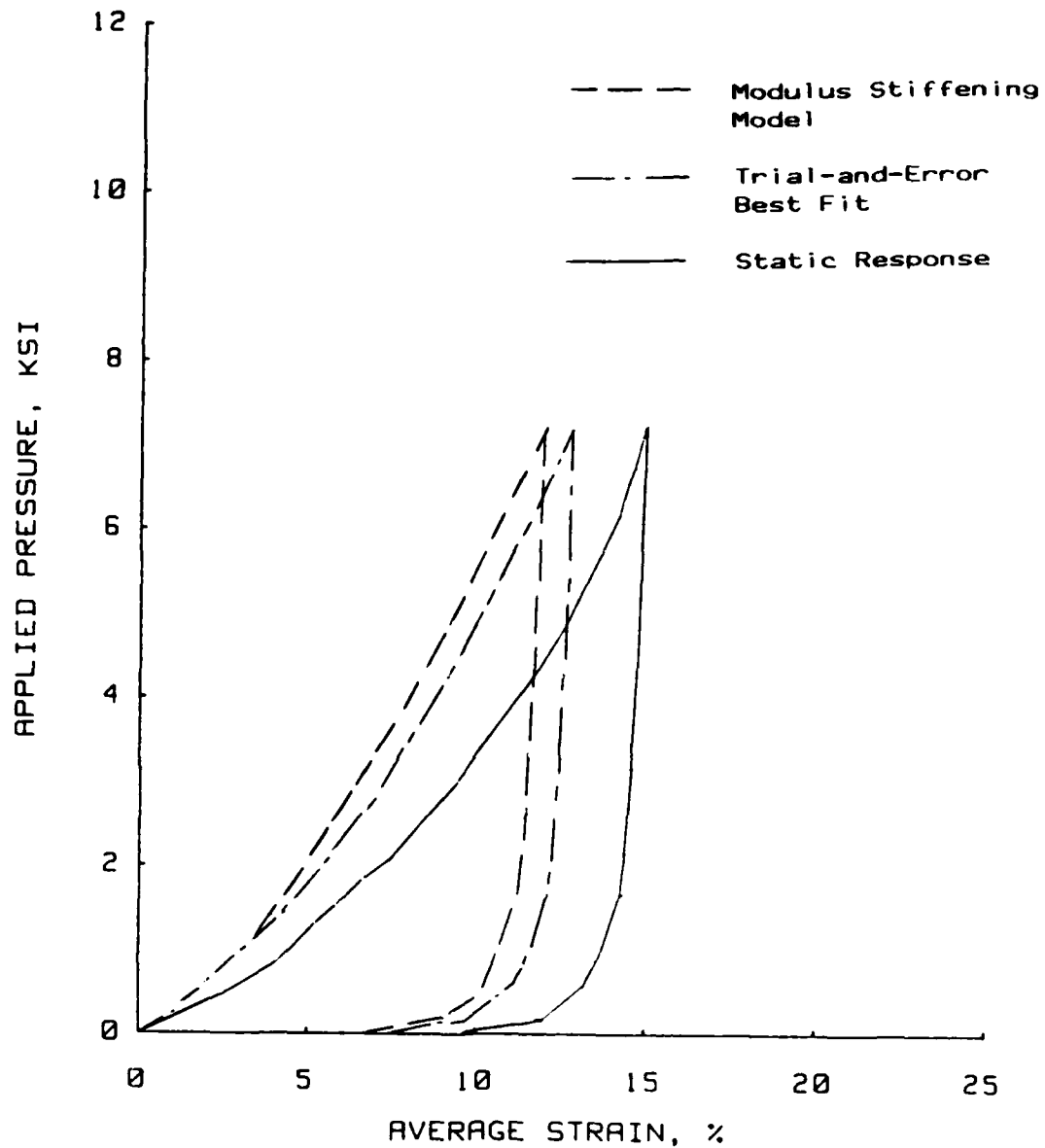Soil Type: Vicksburg Loess

Figure 7.3.6 Comparison of stress-strain curves obtained from the
modulus stiffened model, the trial-and-error best fit,
and the static uniaxial strain response for
Vicksburg loess.

REANALYSIS OF PUBLISHED SUBMILLISECOND

TEST RESULTS

8.1 Introduction

Test results have been presented showing that, as the rise time to peak of large transient pressures approaches the submillisecond range, the shape of the uniaxial strain stress-strain curve is not drastically affected. On the other hand, the uniaxial strain test results published by Jackson, et al., (1979) showed a drastic stiffening of the initial response when the rise time to peak pressure approached the submillisecond range. The submillisecond tests presented in 1979 showed stress-strain curves with initial curvature concave to the strain axis for the FH2 backfill material. Those results do not resemble the stress-strain curve deduced from measurements obtained in the field for the same material; the basic shape of the initial portion of the field-deduced stress-strain curve was concave to the stress axis. The discrepancies between the two programs should be resolved.

The device used for the results presented herein contained some major improvements over the device described by Jackson, et al., (1979). These improvements provided for more accurate and consistent measurements. The major improvements were:

172

1) A more accurate and reliable axial deformation measurement
system was incorporated into the design of the WES 0.1-msec device.
The device described by Jackson, et al., (1979) used an LVDT measuring
system (see Fig. 3.1.1). A signal conditioning system had to be built
at WES to provide the response needed to make dynamic measurements for
that device. The accuracy of the signal conditioning equipment was not
verified under actual conditions. Another problem with the axial
deformation system was the support tripod used for the LVDT. This
tripod could create enough turbulence in the fluid to prevent uniform
loading over the sample surface. An additional problem was that the
LVDTs were often destroyed by the pressure pulse. Lastly, and most
importantly, were the effects of the large footing mass resting on the
top of the soil sample. An LVDT with a large footing mass could have
prevented the axial deformation system from tracking the true surface
displacement of the sample. All of these problems were eliminated by
using the proximeter described in Chapter III.

2) A new data acquisition system was installed to provide higher
resolution plots of stress, strain, and time. Typically, this new data
acquisition system used for the results contained herein provides over
200 points when describing one cycle of a submillisecond uniaxial
strain test, whereas the uniaxial strain results presented by Jackson,
et al., (1979) were based on about 30 points or less.

The other major difference between the results published in 1979
and those contained herein is the analysis procedure used for
submillisecond data interpretation. The one-dimensional wave
propagation analyses published in 1979 were based on an assumed three-

element rheologic model. A massless LVDT footing was also assumed. Also, the pressure is measured at some point above the sample surface during the test. The effects of this offset were not modeled in the 1979 analysis.

Section 8.2 presents a reanalysis of the data published in 1979. Using the data interpretation techniques presented herein, the discrepancies between the two sets of data can be resolved.

8.2 Reanalysis of 1979 Submillisecond Test Results

In his development of the ADLUD code, Meier (1984) reanalyzed the 1979 data. His conclusions were that the LVDT footing mass of 50 gms did not track the surface displacement in the initial portion of the test due to inertia. The analysis presented herein is essentially that analysis reproduced in greater detail using an updated version of the ADLUD code.

The FH2 backfill material referred to in Figure 8.2.1 was taken from the same source as the flume sand results presented herein. Tests FH2-D6 and FH2-D11 from Fig. 8.2.1 were reanalyzed using the same procedures as discussed in Chapter V. The actual loading pulses were digitized from the original test records and used to drive the simulations. These loading pulses are shown in Fig. 8.2.2. Figure 8.2.3 shows the actual test measurements for these two tests plotted in the form of applied pressure at the pressure cell location versus average strain calculated from deflection of the LVDT footing on the sample surface.
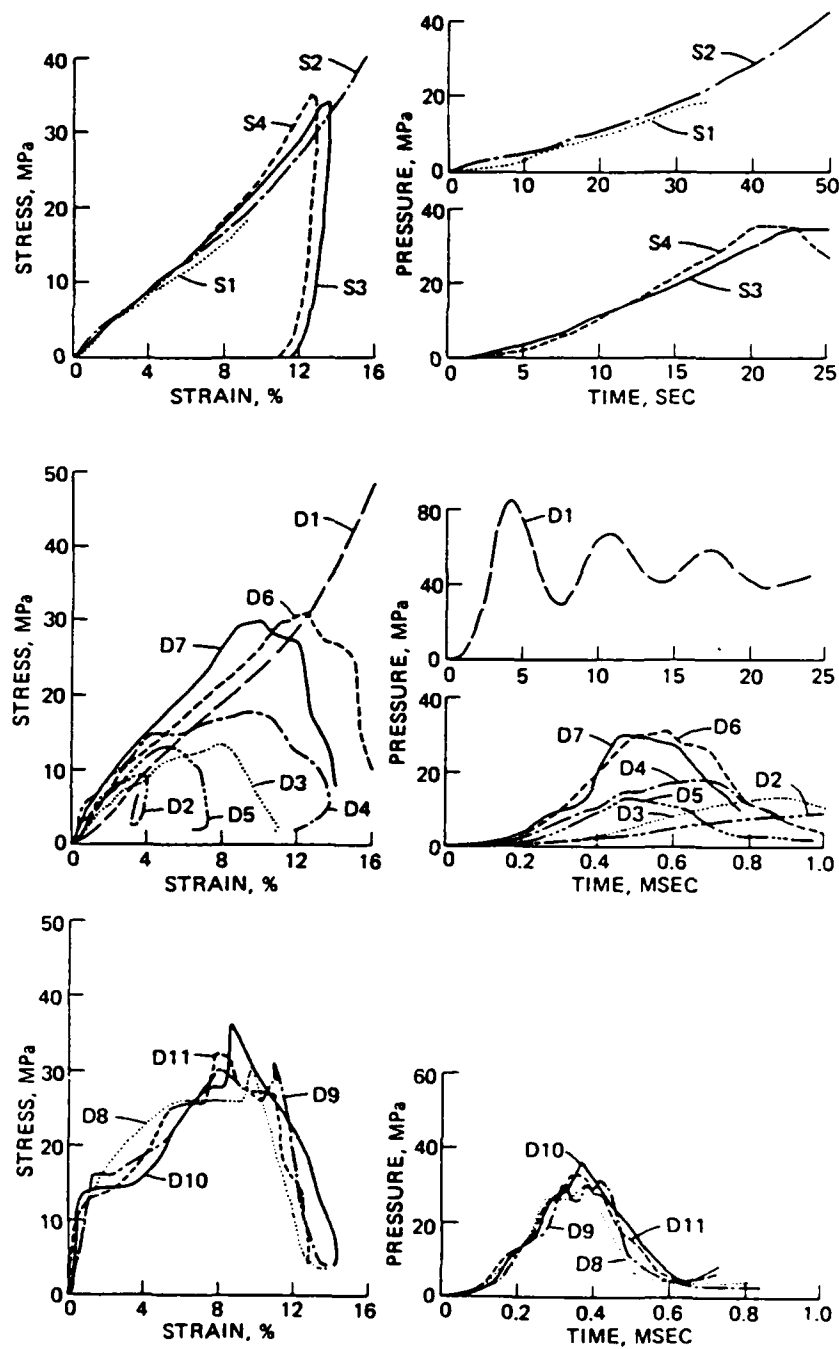
Figure 8.2.1   Uniaxial strain response of FH2 backfill material
(from Jackson, et al., 1979).

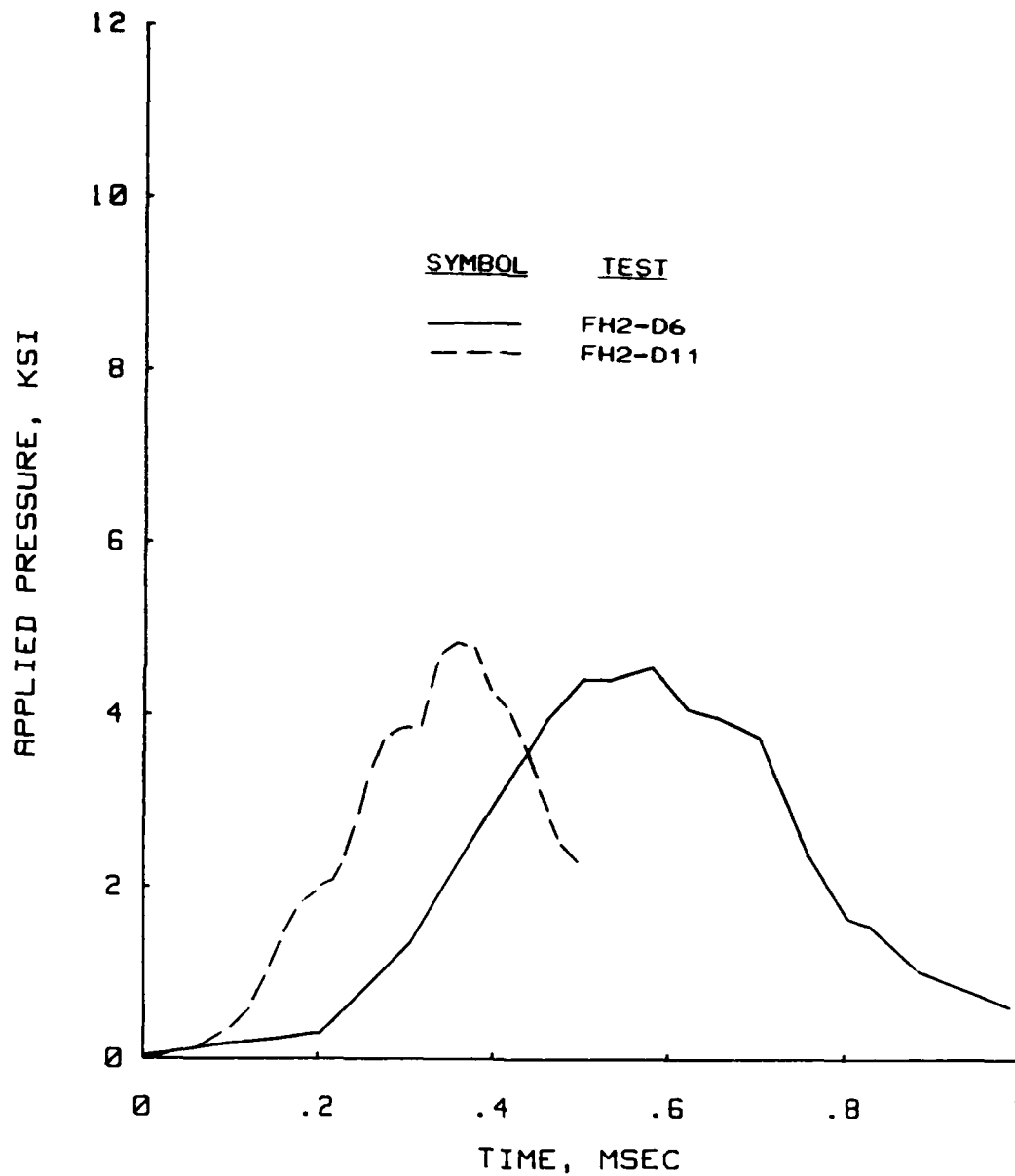## Uniaxial Strain Results
Soil Type: Flume Sand

Figure 8.2.2   Stress-time histories for tests FH2-D6 and FH2-D11.

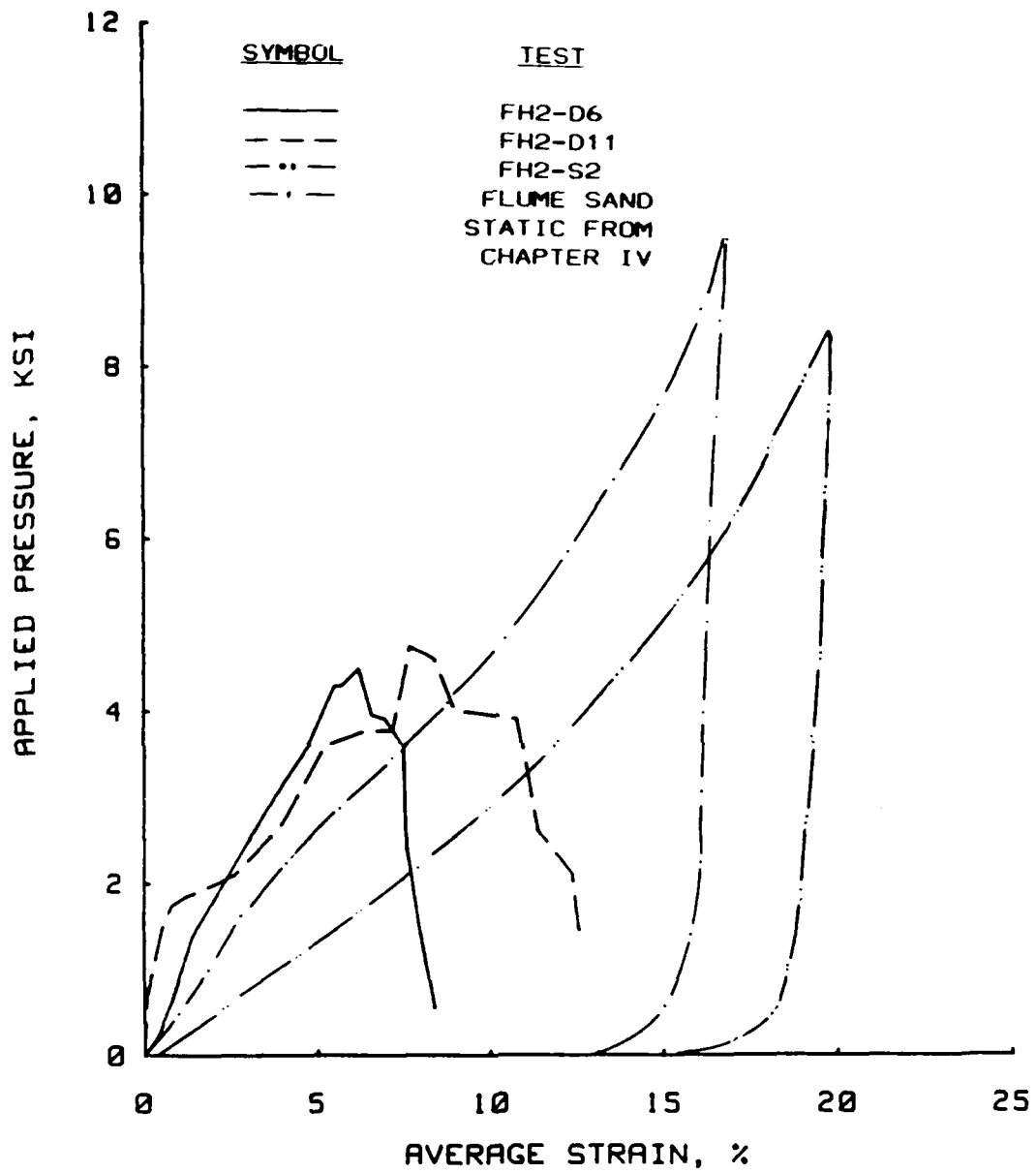## Uniaxial Strain Results
Soil Type: Flume Sand

Figure 8.2.3 Uniaxial strain results for flume sand (from Chapter IV) and FH2 backfill (from Jackson, et al., 1979).

The loading pulses shown in Fig. 8.2.2 yield some insight into why the associated stress-strain results may not be representative of the true material response. Test FH2-D6 takes about 0.2 msec to reach a value of 0.3 ksi (2.1 MPa) and an additional 0.27 msec to reach 4.0 ksi (27.6 MPa); whereas, Test FH2-D11 takes about 0.09 msec to reach 0.3 ksi (2.1 MPa) and an additional 0.23 msec to reach 4.0 ksi (27.6 MPa). Basically, the only difference between these two loading pulses is the long lead time for test FH2-D6. The loading pulses generate nearly the same loading rates after 0.3 ksi (2.1 MPa); yet, the responses measured are drastically different.

Meier (1984) reported that the LVDT footing (see Figs. 3.1.1 and 3.4.4) used to measure axial deformation weighed approximately 50 gms. For an LVDT footing to be that massive, it would have to have been constructed of stainless steel instead of an aluminum footing assembly, which weighs about 12 gms. Since some questions exist as to whether a stainless steel or aluminum LVDT footing was used, all analyses are performed for both the stainless steel and aluminum footings.

Figure 8.2.4 presents a plot of measured applied pressure versus calculated LVDT footing displacement plotted in terms of average strain for the two footings. This plot was obtained using ADLUD. The pressure time history was converted to a force time history by multiplying pressure at the sample surface by the area of the LVDT footing. This force was divided by the mass of the footing to obtain an acceleration time history for the footing. This is simply Newton's second law of motion. The acceleration time history was intergrated
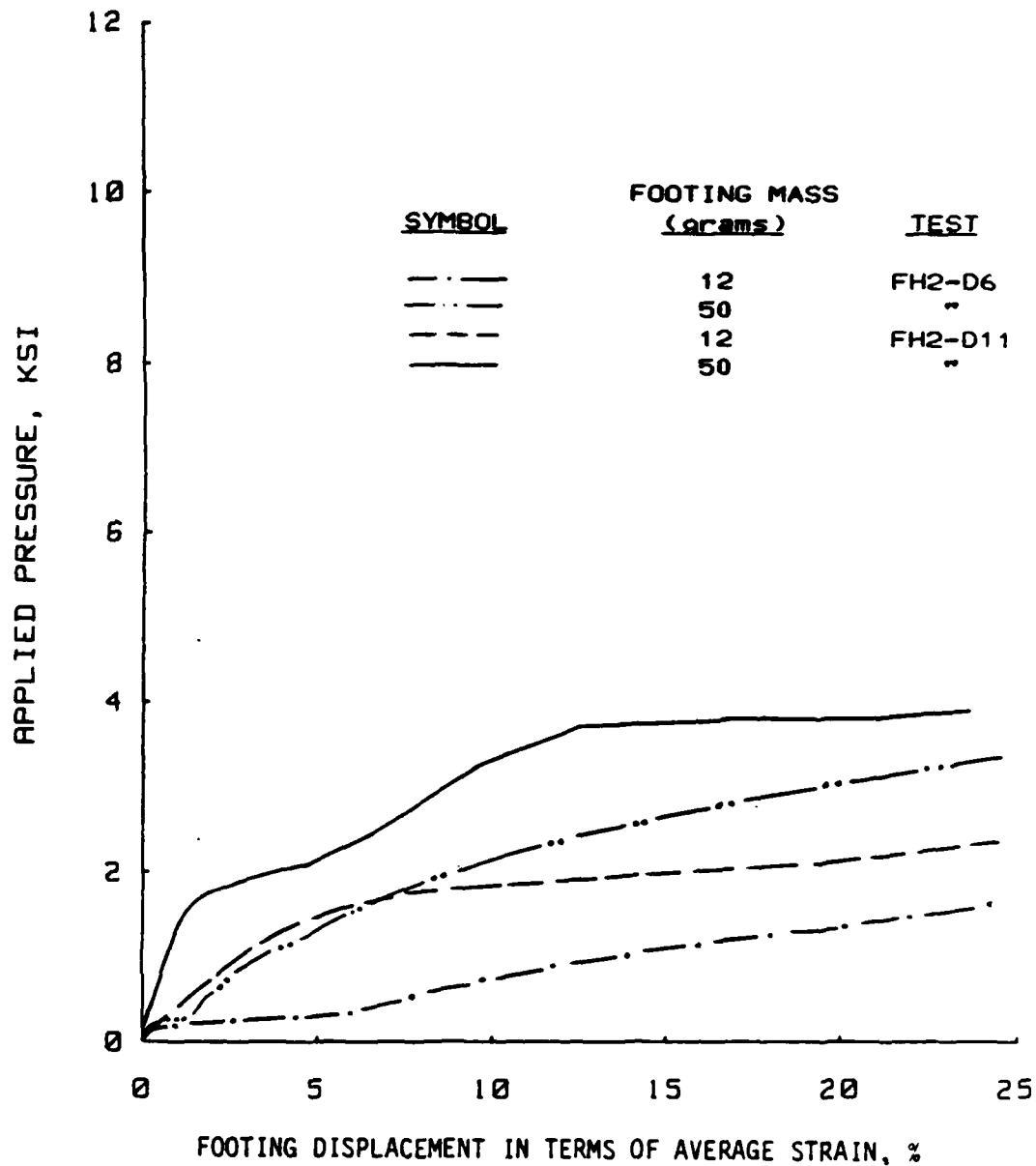
Figure 8.2.4 Plot of calculated LVDT footing displacement versus measured applied pressure for tests FH2-D6 and FH2-D11.

twice to obtain a displacement-time history. The calculated
displacement-time histories can be compared with the measured
displacements to determine whether the actual soil response is being
measured or the LVDT is lagging behind the actual surface displacement.

The FH2 backfill material was tested at a dry unit weight of
102.7 pcf (1.646 g/cc); whereas, the flume sand results contained
herein were tested at 100.5 pcf (1.611 g/cc). Also, a slight
difference in water content between the two test programs existed. The
FH2 material was tested at 3.2 %; whereas, the flume sand was tested at
5.5 %. As shown in Fig. 8.2.3, the static material response measured
in 1979 and those contained herein for flume sand are significantly
different. A comparison of the grain-size distributions shows that the
two materials are nearly identical. The flume sand static test results
from Chapter IV shown in Fig. 8.2.3 agree with those published by Green
(1986a). Both the flume sand and FH2 material static response curves
shown in Fig. 8.2.3 are used in the ADLUD reanalysis of Tests FH2-D6
and FH2-D11.

Figure 8.2.5 presents plots of applied pressure at the pressure
cell versus average strain for test FH2-D6, ADLUD predictions based
upon static test FH2-S2 with an increase in modulus of 160 %
to account for rate dependency, and the applied pressure at the
pressure cell versus average strain based on calculated LVDT footing
displacement for 12- and 50-gm footings. As shown by this plot, the
LVDT system should track the surface displacement.

Uniaxial Strain Results
Soil Type: Flume Sand

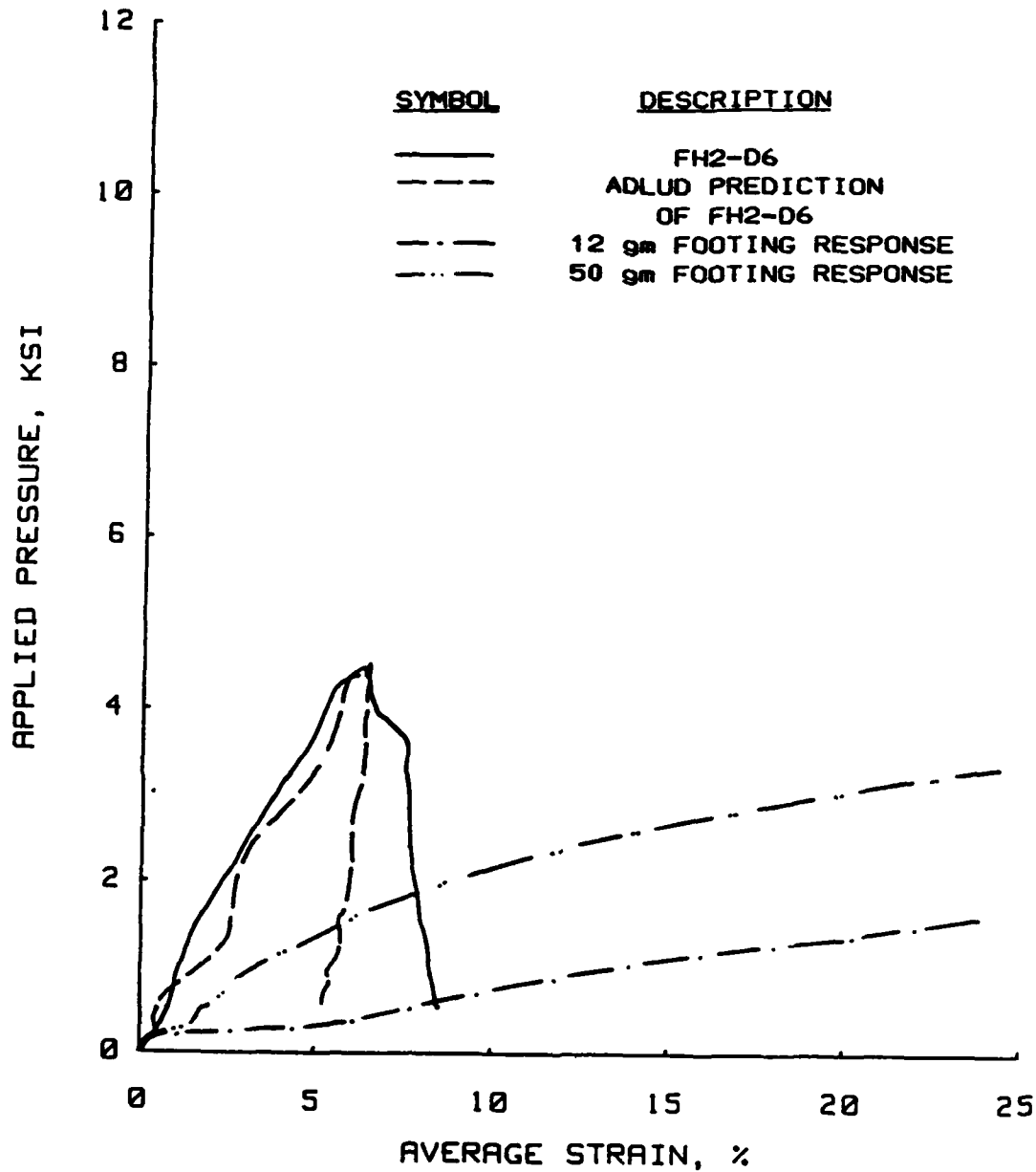| SYMBOL	DESCRIPTION
——————	FH2-D6
— — —	ADLUD PREDICTION OF FH2-D6
—·—	12 gm FOOTING RESPONSE
—··—	50 gm FOOTING RESPONSE

Figure 8.2.5 Laboratory measurement of applied pressure versus
average strain, ADLUD prediction using stiffened
FH2 static response, and two possible LVDT footing
responses for test FH2-D6.

Figure 8.2.6 presents a plot of the results for test FH2-D6 and the ADLUD predictions based upon the laboratory results and rate dependent model described in Chapter VI. The model produces about a 45 % increase in modulus of the flume sand static response. As shown in Fig. 8.2.6, the ADLUD predictions using the strain and strain rate dependent modulus model nearly reproduce the test measurements.

Figure 8.2.7 presents a plot of the actual results for test FH2-D11, ADLUD predictions using a 160 % increase in modulus of the FH2 static material response, and the applied pressure at the pressure cell versus footing response for 12- and 50-gm LVDT footings. Figure 8.2.8 presents a plot of the actual test results for test FH2-D11 and an ADLUD prediction using the strain-level and strain-rate dependent modulus model described in Chapter VI but adjusted to account for lag in the initial response due to a 50 gm LVDT footing. As shown in Figs. 8.2.7 and 8.2.8, if the LVDT footing mass was 50 gms, the footing would not track the initial displacement for test FH2-D11. At a value of about 2.0 ksi (13.8 MPa), the footing would overtake the soil and record the actual surface displacements.

It has been shown that the discrepancies between the 1979 and 1986 submillisecond results can be explained by accounting for the actual location of the pressure cell, accounting for the inertia due to the mass of the LVDT footing, using a better defined static uniaxial strain response curve, and by using the rate dependent modeling formulation developed herein rather than the lumped-parameter rheologic model. The results presented by Jackson, et al., (1979) are plotted in terms of static-to-dynamic strain ratio at 10 MPa (1.45 ksi) versus

Uniaxial Strain Results
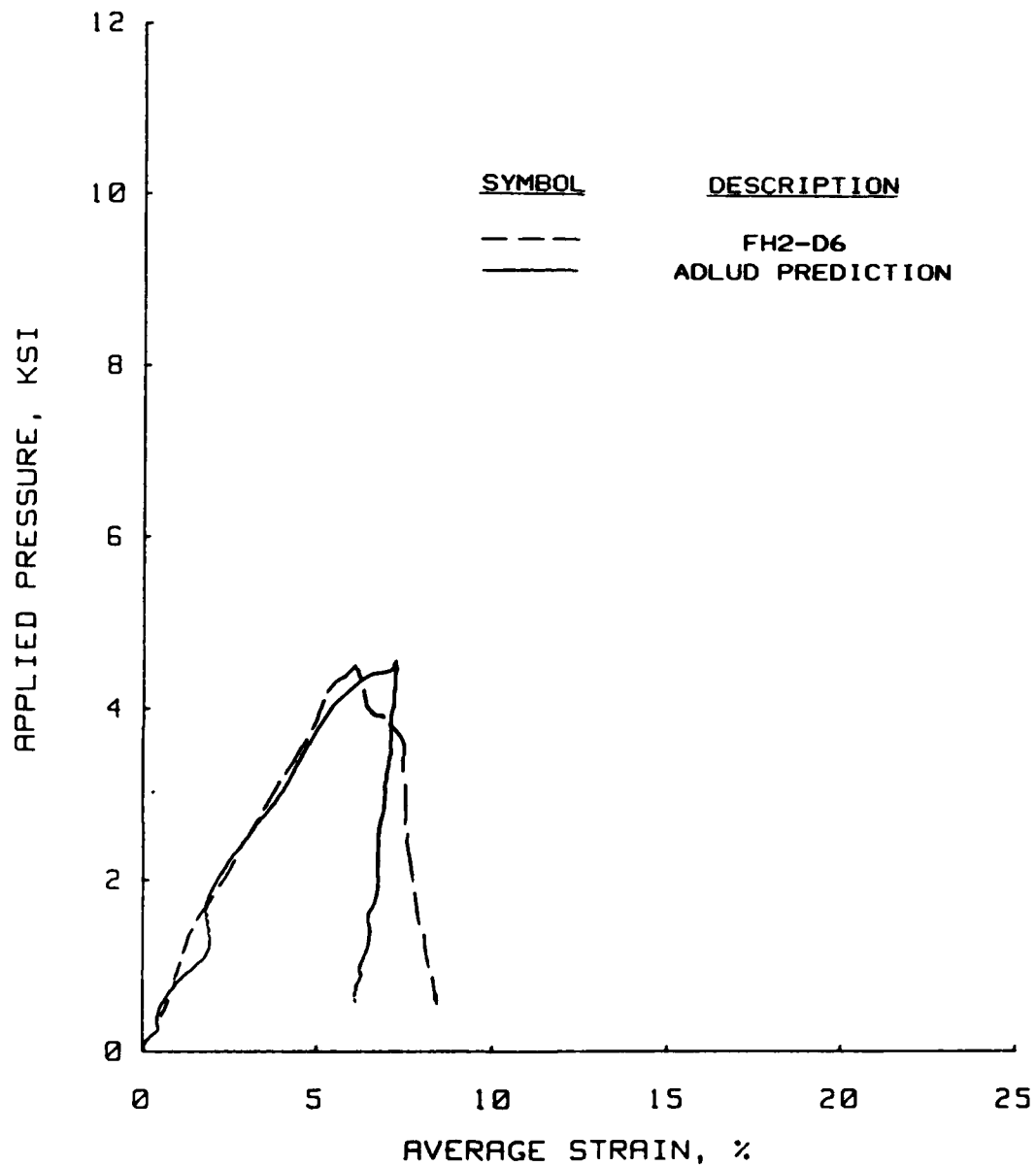## Soil Type: Flume Sand

Figure 8.2.6 Laboratory measurement of applied pressure versus average strain for test FH2-D6 and ADLUD prediction using rate-dependent model for flume sand.

Uniaxial Strain Results
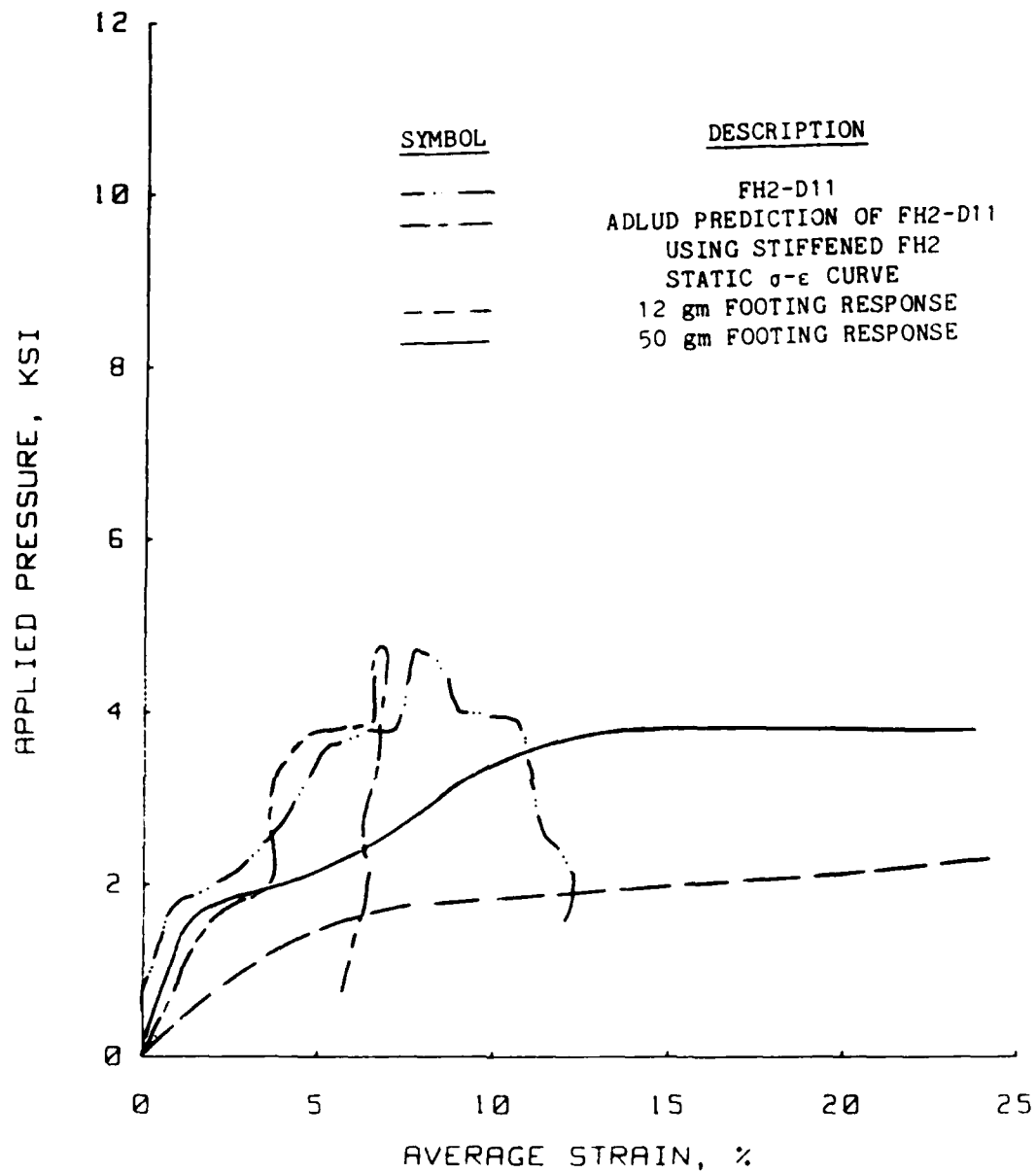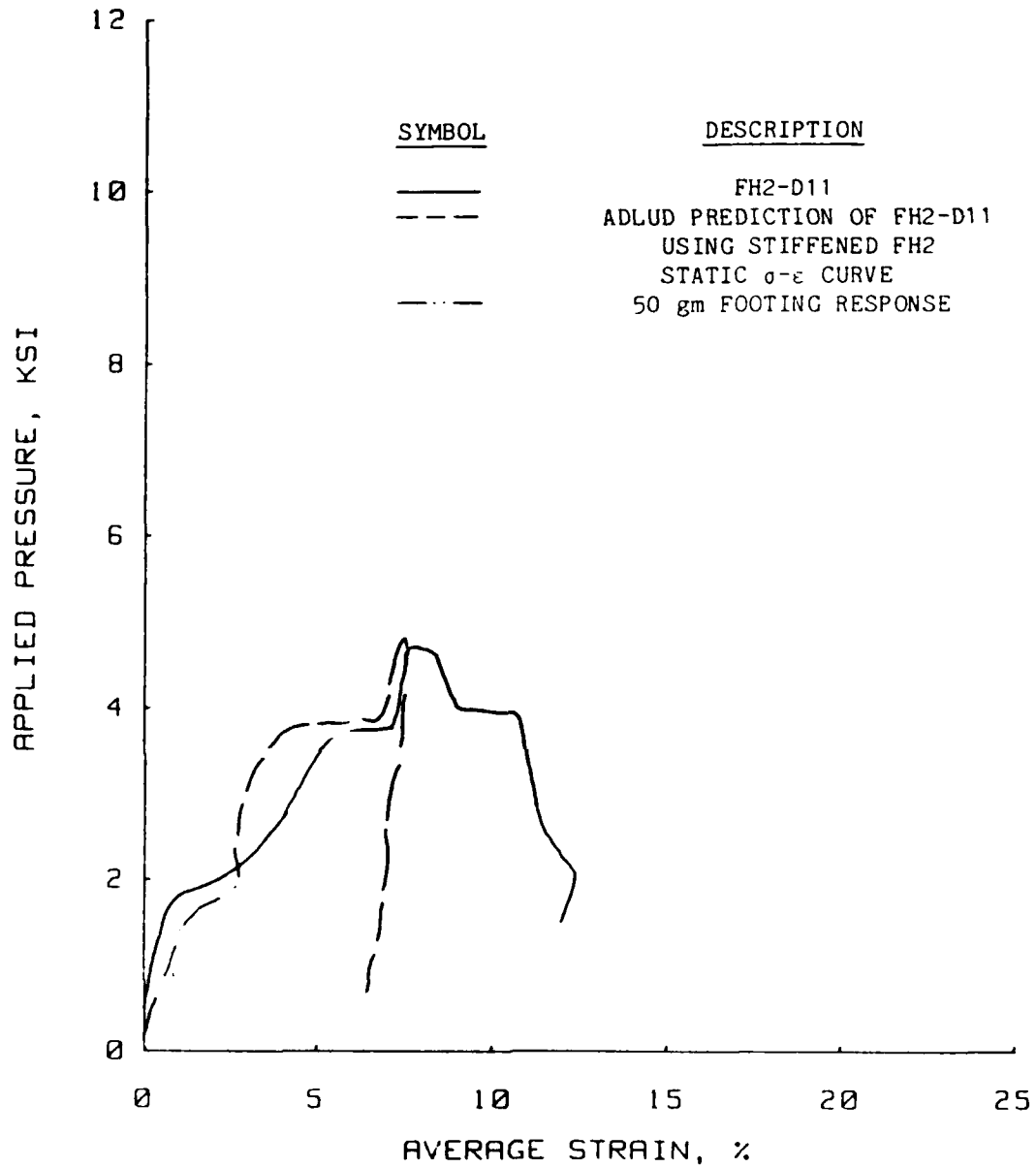## Soil Type: Flume Sand

SYMBOL	DESCRIPTION
—·——	FH2-D11
—·——	ADLUD PREDICTION OF FH2-D11
	USING STIFFENED FH2
	STATIC σ-ε CURVE
———	12 gm FOOTING RESPONSE
———	50 gm FOOTING RESPONSE

Figure 8.2.7 Laboratory measurement of applied pressure versus
average strain, ADLUD prediction using stiffened
FH2 static σ-ε curve, and two possible footing
responses for test FH2-D11.

Figure 8.2.8 Laboratory measurement of applied pressure versus
average strain for test FH2-D11 and ADLUD prediction
using rate-dependent model for flume sand coupled
with 50-gm LVDT footing response.

loading time to 10 MPa (1.45 ksi). Those results are probably still accurate for loading times to 10 MPa (1.45 ksi) greater than about 0.3 msec.

CHAPTER IX

SUMMARY, CONCLUSIONS, AND RECOMMENDATIONS

FOR FURTHER RESEARCH

9.1 Summary

The purposes of this project were to determine whether a
significant stiffening of soil uniaxial strain compressibility occurred
when the time to peak pressure approached the submillisecond range for
large transient loads, to investigate the effects of changes in soil
water content and dry density on the magnitude of this stiffening, and
to address the validity and accuracy of existing rate-dependent
constitutive models to describe this stiffening response. Initially,
samples were to be tested at two loading rates, i.e., static (minutes
to peak pressure) and dynamic (submilliseconds to peak pressure). As
the project developed, its scope was redefined to incorporate testing
at a wider variety loading rates in order to provide more data for
development of rate-dependent models. Although, some data were
obtained to investigate the effects of water content and dry density on
the magnitude of the rate effects, the majority of the laboratory
measurements were obtained from tests on samples remolded to a single
predetermined combination of water content and dry density for each
soil type.

187

An explosive-loaded laboratory uniaxial strain test device was developed at WES in 1977 to study the compressibility of soils under high-pressure loadings with submillisecond rise times. A modified, and presumably improved version, was fabricated in 1984. This second-generation device incorporated a proximeter-type of axial deformation measurement system that would hopefully overcome the deficiencies of the orginal LVDT-type measurement system. Debugging and calibrating the proximeter axial deformation measurement system and the associated electronics, developing detailed sample preparation and overall test procedures, and preparing the computer programs needed to record the test results in a digital format as well as reduce and plot the data, constituted a major portion of the project. Data obtained with this new WES 0.1-msec uniaxial strain test device was supplemented with supermillisecond and static test data obtained with a state-of-the-art production type device, which allowed assessment of soil compressibility for a wide range of loading rates. These two test devices required the use of three load application systems, two data acquisition systems, and the development of numerous data acquisition and processing programs.

Four soils (two clean sands, a clayey sand, and a silty clay) were chosen for testing because of the vast amounts of data already available concerning their mechanical behavior under both laboratory and field conditions, the wide spectrum of soil types they represented, and their importance to defense-related projects. Laboratory test values of water content and dry density were matched to actual field conditions. The silty clay material was also used to assess the

effects of water content and dry density on uniaxial strain response at two loading rates, static and submillisecond.

For each of the four soils tested, grain-crushing characteristics are assessed by comparisons of pretest and posttest grain-size analyses. The physical properties needed to describe each of these materials is also presented in the form of petrographic analyses, minimum and maximum relative density or Proctor compaction data, Atterberg limits where applicable, and specific gravity determinations.

Based on an analysis of the static and supermillisecond test results, a strain-level and strain-rate dependent incremental modulus model was developed for uniaxial strain compression. This model uses the static uniaxial strain response as a base, then adjusts the response using a series of constants developed from the laboratory results that are functions of strain level and strain rate. Under applied loadings with submillisecond rise times, however, highly nonuniform stresses and strains are generated within the uniaxial strain test specimens due to wave reflection and refraction at the bottom-rigid and top-fluid boundaries. To correctly interpret the true soil stress-strain response from these test results, computer simulations were performed with a one-dimensional plane wave propagation program or code. An existing code that had been written specifically to simulate the WES uniaxial strain test configuration was modified to incorporate the new loading-rate dependent soil model. This code was then used to numerically simulate all of the submillisecond tests. From these computer simulations, the true submillisecond uniaxial strain responses of the four soil materials were deduced.

The model was also implemented into a one-dimensional plane wave code used for calculating ground shock environments for explosive events. To validate the rate-dependent model, calculations were performed to simulate actual field test events involving two of the four soils tested in the laboratory. Following this validation, previously published submillisecond test results were reanalyzed using the rate-dependent model formulation.

9.2 Conclusions

Based upon the results of the laboratory tests and on comparisons with field test results, a **significant** stiffening of soil uniaxial strain loading moduli does **not** occur under large impulse-type loadings with times to peak pressure of less than a millisecond, as speculated by some researchers. However, results did show that a **small** increase in modulus occurs for progressively faster loading rates for the range of rates tested. Increases in moduli ranging from 45 to 125 % were determined for the four soils tested at their field values of water content and density. Some Vicksburg loess/V-series test results showed increases in moduli of greater than 125 %, but the density at which these tests were performed does not exist in the field.

The tests performed to study the effects of water content and dry density variations on the magnitude of the rate effects for the silty clay material (Vicksburg loess/V-series) indicated that, for a very dense sample (γ_d = 124.8 pcf or 2.0 g/cc), a rate effect could not be detected. However, for the same material at the same water content (14.5 %), but in a looser state (γ_d = 106.7 pcf or 1.71 g/cc), an

increase in modulus of 300 % or greater could be obtained. Hence,
variations in density can significantly affect the magnitude of the
rate effect. Increasing the water content of the silty clay material
caused a slightly softer static response. For submillisecond loadings,
a definitive conclusion concerning rate effects as a function of water
content could not be made due to scatter in the submillisecond data.
Results from both static and dynamic seem to indicate, however, that as
water content increases, compressibility increases.

Several important items concerning uniaxial strain testing were
learned while performing the work contained herein:

1) The rate at which a load is applied, even in the static range, can
be important, especially for materials that exhibit significant grain
crushing (see Fig. 4.2.3). A standard should be adopted that
designates a specific loading rate as "static". A standard loading
rate would allow for more accurate comparisons of "static" measurements
obtained from different laboratories or even from different test
devices. As a minimum, the time to peak pressure should be reported.

2) The sample preparation techniques that are used can influence
uniaxial strain response. The number of lifts and the method of
compaction (jacking the sample or compaction with a tamping rod) are
especially crucial to obtaining reproducible res.lts. Unfortunately,
the workability of the material often dictates the construction
methods. This makes development of a set of standard sample
preparation techniques difficult. If accurate and reproducible
laboratory measurements are to be obtained, the problem of variations
in sample preparation must be addressed.

3) Test results have shown that the height of the specimen can affect the uniaxial strain response due to sidewall friction (Farr, 1986). For samples with diameter-to-height ratios of 5 or greater, the amount of stress reduction is insignificant. However, uniaxial strain tests with 2-in.- (5.08-cm-) high specimens that have a diameter-to-height ratio of 2.5 or less are often performed. These tests can produce transmission ratios (load at the base of the sample divided by the load at the sample surface) of 0.7 or less.

Some means of verification of the results was needed to establish the credibility of the present work. This was accomplished by using the laboratory measurements and a rate-dependent model to numerically reproduce field events at two sites. Comparisons between the predicted and actual results were favorable. For the Vicksburg loess field event, the laboratory based uniaxial strain response predicted by the modulus stiffening model was almost identical to the material response interpreted from the field test data. For the flume sand field event, the increase in the static modulus interpreted from the field event was on the order of 25 %, while the laboratory-based model predicted an increase in modulus of about 45 %. The difference between these two values can probably be attributed to the amount of data scatter in the submillisecond test results. Sample preparation techniques that produced a stiffer response than in the field and/or sidewall friction could have contributed to this scatter. The field-determined and laboratory-based curves are qualitatively similar.

In an effort to add further credibility to the present work, the previously published submillisecond test results were reanalyzed.

Several potential sources of error associated with the 1979 test

results were identified. The true material behavior was shown to be a

progressive stiffening of the uniaxial strain response as the loading

rate increased, even into the submillisecond range.

General conclusions regarding rate effects as a function of grain

size, material type, density, water content, grain crushing, etc., are

difficult to make since it was not the goal of this project to

investigate their specific effects. However, some general conclusions

regarding loading rate effects can be made based on this work:

1) Rate effects must be considered in ground shock studies.

Laboratory and field measurements have shown that rate effects can

increase the constrained modulus by 100 % or more for most

soils even at partially saturated or dry conditions. As some point,

usually between 5 and 10 % strain, the increase in modulus is very

small and remains insignificant over the remainder of the test.

2) Creep phenomena are important to the uniaxial strain response of

soil, even for dynamic testing. As shown in Chapter IV, the soils

creeped under transient loads with short-duration hold times. Creep

effects are usually not important for ground shock studies; however, a

soil model describing all aspects of uniaxial strain behavior should

include a creep term.

3) Submillsecond laboratory test results were probably not required to

predict the behavior of the four materials tested. The results

contained herein indicate that the increase in modulus due to rate

effects tends to level off or slowly increase as the time to peak

pressure approaches the submillisecond range. The fastest loading rate

produced by the ram-type loaders (3 msec to a peak pressure of 20,000 psi, or 138 MPa) would have produced an increase in modulus similar to that interpreted from the two field events.

9.3 Recommendations For Further Research

The tools and technology now exist to deduce the uniaxial strain behavior of partially saturated soils subjected to large transient loadings in the laboratory. A wealth of data already exists that could be supplemented with a few submillisecond tests and compared with the field-determined uniaxial strain response using the techniques described herein. If needed, further research should be then directed towards refining the methods presented herein. If accurate techniques can be developed to measure the "true" uniaxial strain response in the laboratory, field events would no longer be needed to deduce the response of the soil.

In the area of laboratory measurements, further research should be directed toward developing a third-generation submillisecond test device based on the design of the WES 0.1-msec device. This test device should be designed to include:

1) The capability to test thicker specimens. The 0.5-in- (1.27-cm-) high chamber used for this research study is impractical for testing undisturbed samples and coarser materials.

2) The capability to measure load or pressure at both the top and the bottom of the test specimens. This type of configuration would serve two purposes. First, stress-time histories at the surface and base of the sample would provide more information about wave propagation within

the specimen. This would help in performing the model fits. Secondly, some insight into the amount of axial stress reduction created by sidewall friction would be obtained.

3) A better axial deformation measuring system. The proximeter system described in Chapter III is suitable for research work. However, the problems of rezeroing the electronics (which requires recalibration of the device after each test) and manually applying the calibration steps, makes the device unacceptable for production-type testing. At present an alternative measuring system cannot be recommended.

4) The capability of applying loads with either EBW caps or an externally driven ram. The WES 0.1-msec device was designed only to test into the submillisecond range using an explosive loading system. Modifications to the device allowed for static testing. However, an additional test device was required for all tests at intermediate loading rates. A device capable of being used for all of the loading rates used for this work would eliminate the problem of producing identical results between two different test devices.

In the area of data analysis, additional research should be directed toward developing a three-dimensional rate dependent constitutive model that incorporates the creep phenomena observed herein. The strain-level and strain-rate dependent incremental modulus model seems to be suitable for extension to three-dimensions. A series of submillisecond triaxial compression tests are presently being performed and analyzed by WES; these and/or other test results defining loading rate effects on shear modulus and shear strength are needed to develop a three-dimensional rate-dependent model.

APPENDIX A

DATA SMOOTHING TECHNIQUE

Most measurement systems are subject to artificial noise due to unregulated power supplies, amplifying systems, resolution of the measuring device, sampling frequency of the device, etc. To objectively compare tests and/or normalize the data, this noise should be filtered out in order to smooth the data. For a uniaxial strain test, the artificial noise can mask the true material response. Figure A.1 presents a plot of the "raw" uniaxial strain test data along with a plot for the same test after smoothing. As shown in Figure A.1, the smoothed test is easier to interpret and probably more indicative of the true values of applied pressure and average strain produced during the test.

A technique developed by Baladi and Barnes (1983) was used to filter the data. This technique is based on the concept of a marching mean square. If the measured value of the i th data point is expressed as $Y_m(X_i)$, the corresponding filtered point, $Y_f(X_i)$, can be expressed as:

$$Y_f(X_i) = \sqrt{\frac{1}{n-1} \sum_{k=i-\frac{n-1}{2}}^{k=i+\frac{n-1}{2}} Y_m^2(X_k)} \qquad (A-1)$$

Uniaxial Strain Results
Soil Type: Enewetak Beach Sand
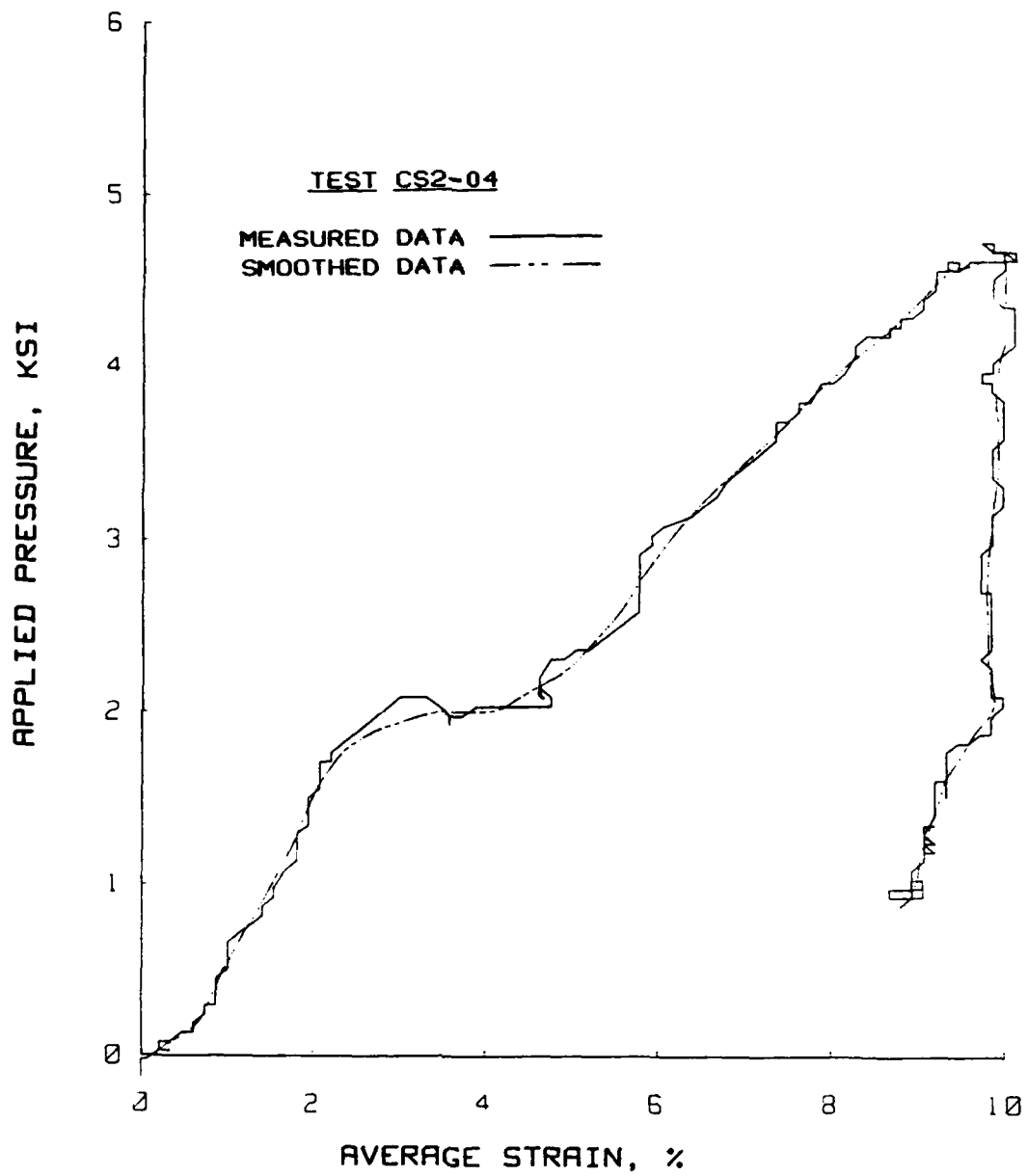
Figure A.1 Typical plot of smoothed and laboratory-measured values
of applied pressure and average strain.

Where n-1 is the window over which the marching mean square is taken. Note that $(n-1)/2$ is the number of points to the left or right of the i th point and that n must be an odd integer greater than or equal to 3. The n value can be used to control the degree of filtering. If the size of the window is increased, the degree of filtering becomes greater, producing a smoother plot of applied pressure versus average strain. This filtering technique proved to be invaluable in producing plots for data interpretation and normalization.

APPENDIX B

UNIAXIAL STRAIN TEST RESULTS

This Appendix contains the results of the 93 uniaxial strain tests performed during this work. These results are summarized in Chapter IV. The test conditions (dry density and water content) for these tests are also presented in Chapter IV. Each test is presented as plots of applied pressure verus average strain, applied pressure versus time, and average strain versus time.

Uniaxial Strain Results
Soil Type: Enewetak Beach Sand
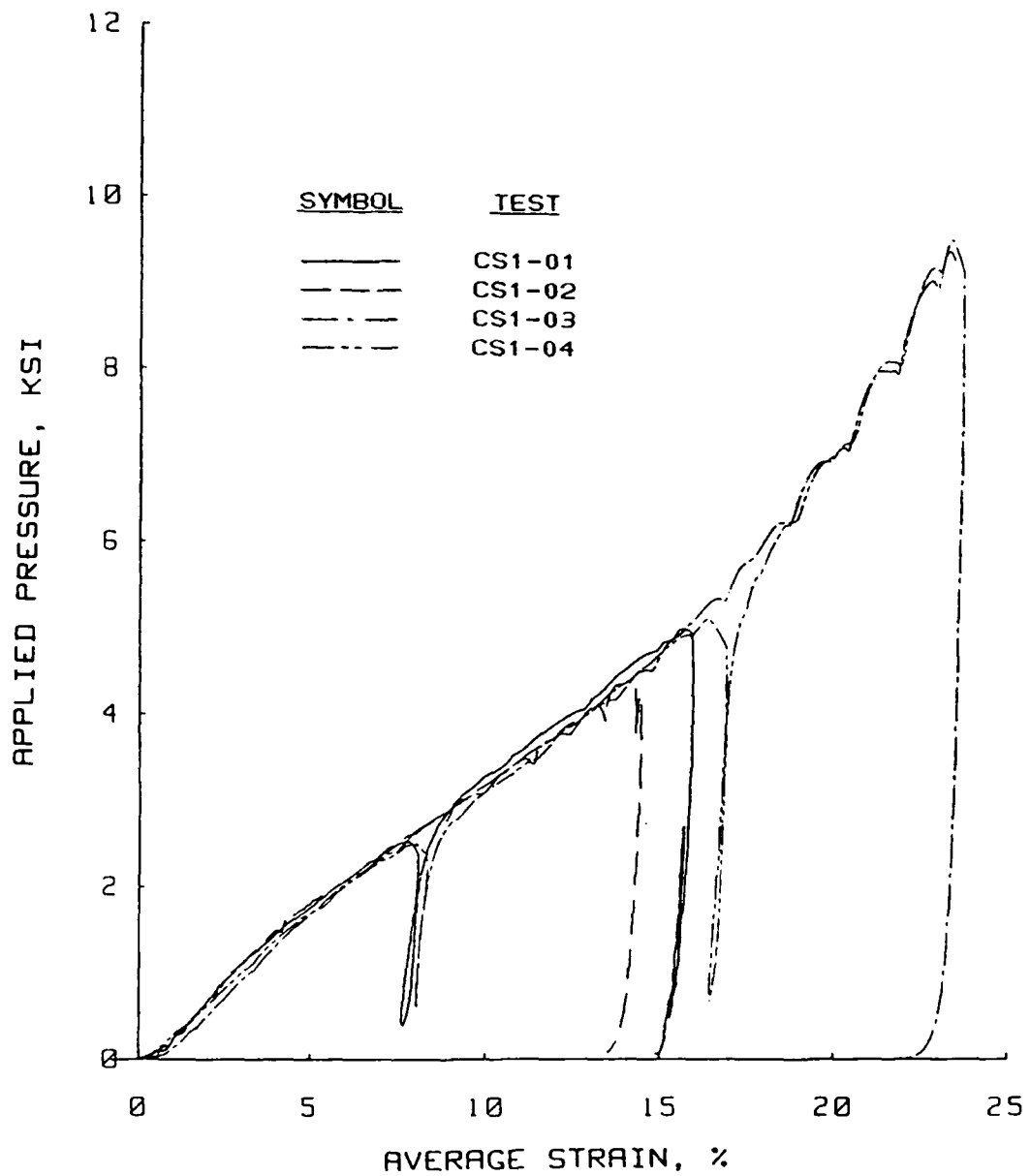
Figure B.1   Static uniaxial strain results for tests performed
in the PPUX device tests in the PPUX device on
Enewetak beach sand.

Uniaxial Strain Results
Soil Type: Enewetak Beach Sand
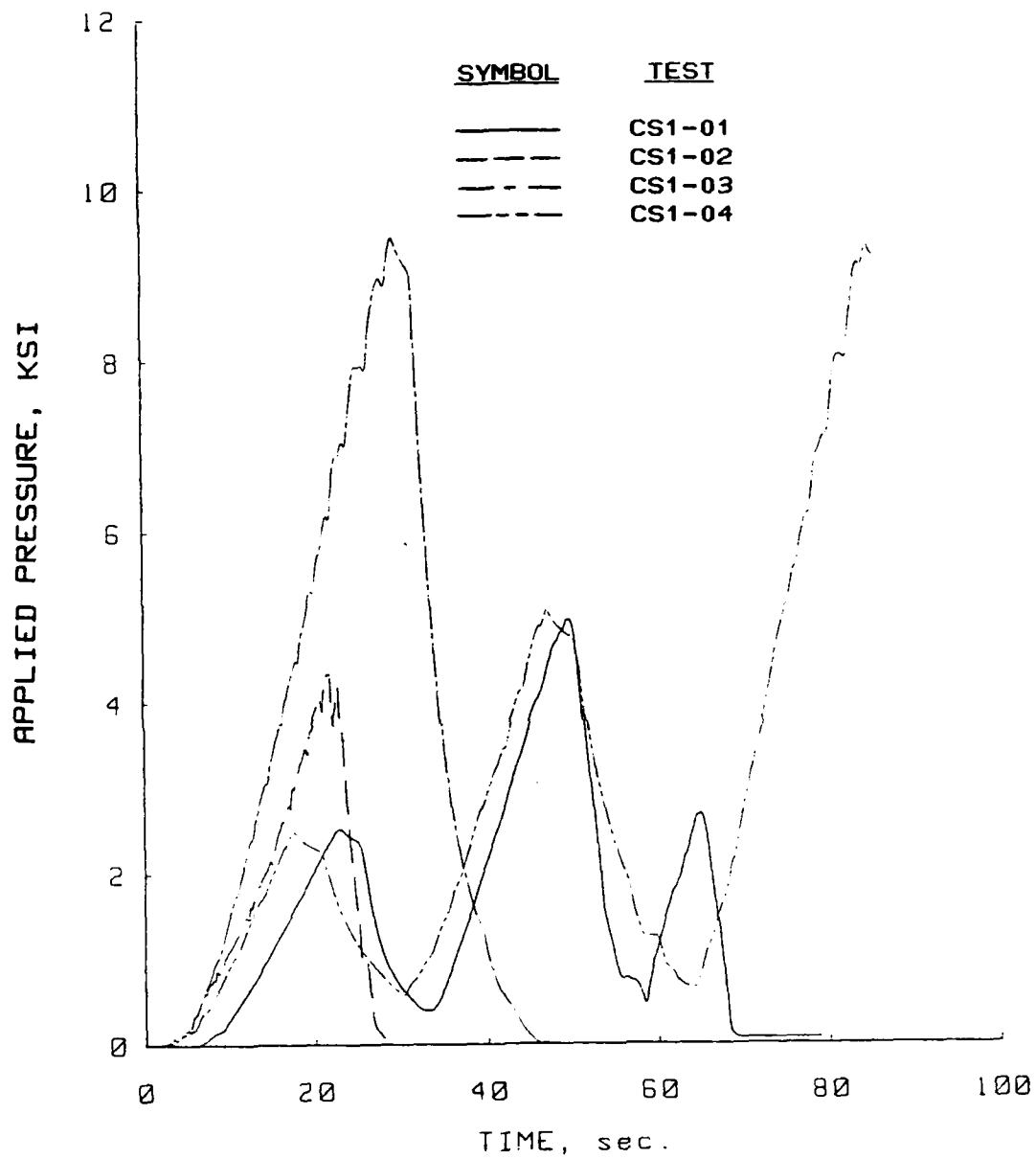
Figure B.2   Pressure versus time plots for the static uniaxial
            strain tests performed in the PPUX device on
            Enewetak beach sand.

Uniaxial Strain Results
Soil Type: Enewetak Beach Sand
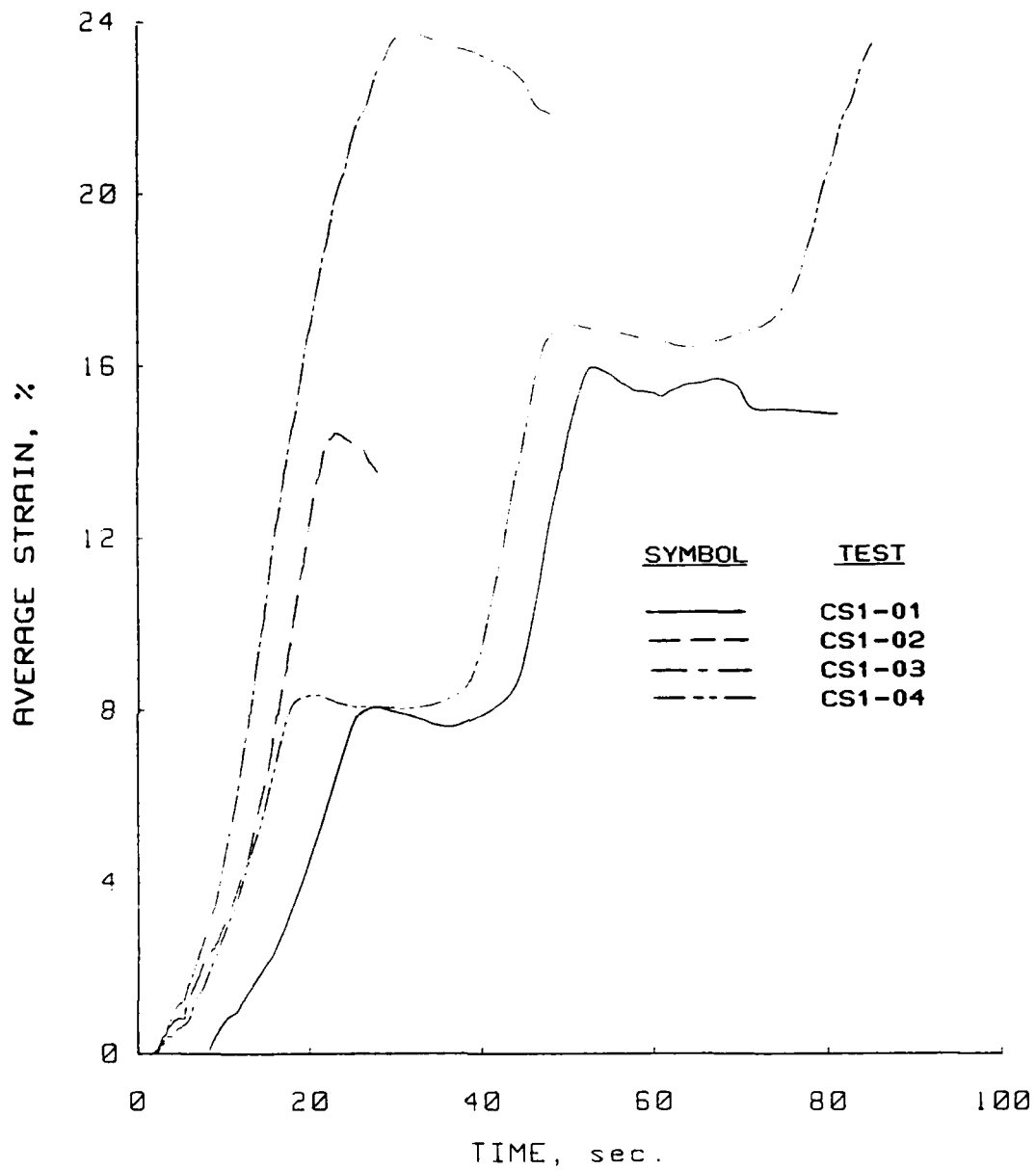
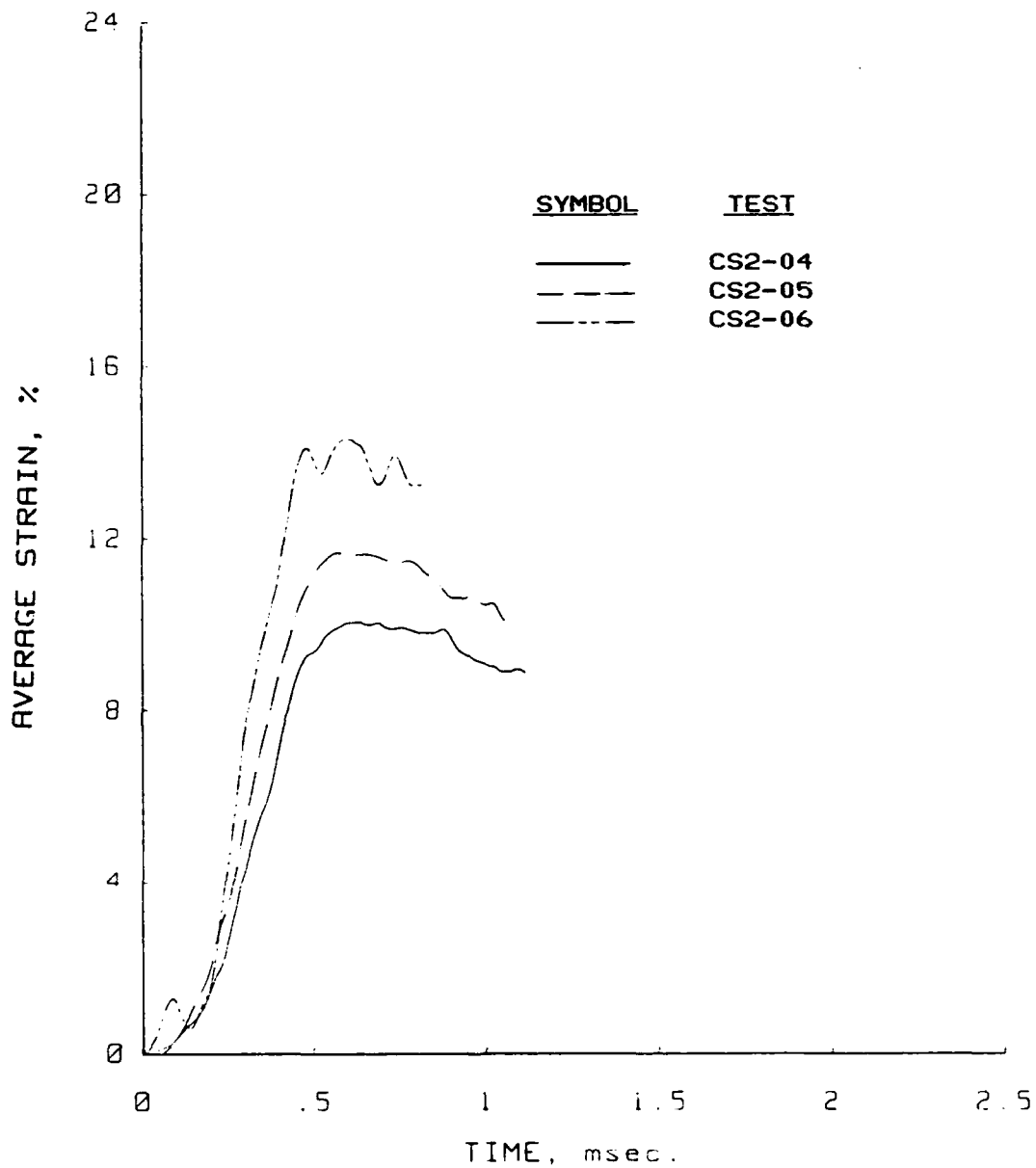Figure B.3   Strain versus time plots for the static uniaxial
strain tests performed in the PPUX device on
Enewetak beach sand.

Uniaxial Strain Results
Soil Type: Enewetak Beach Sand
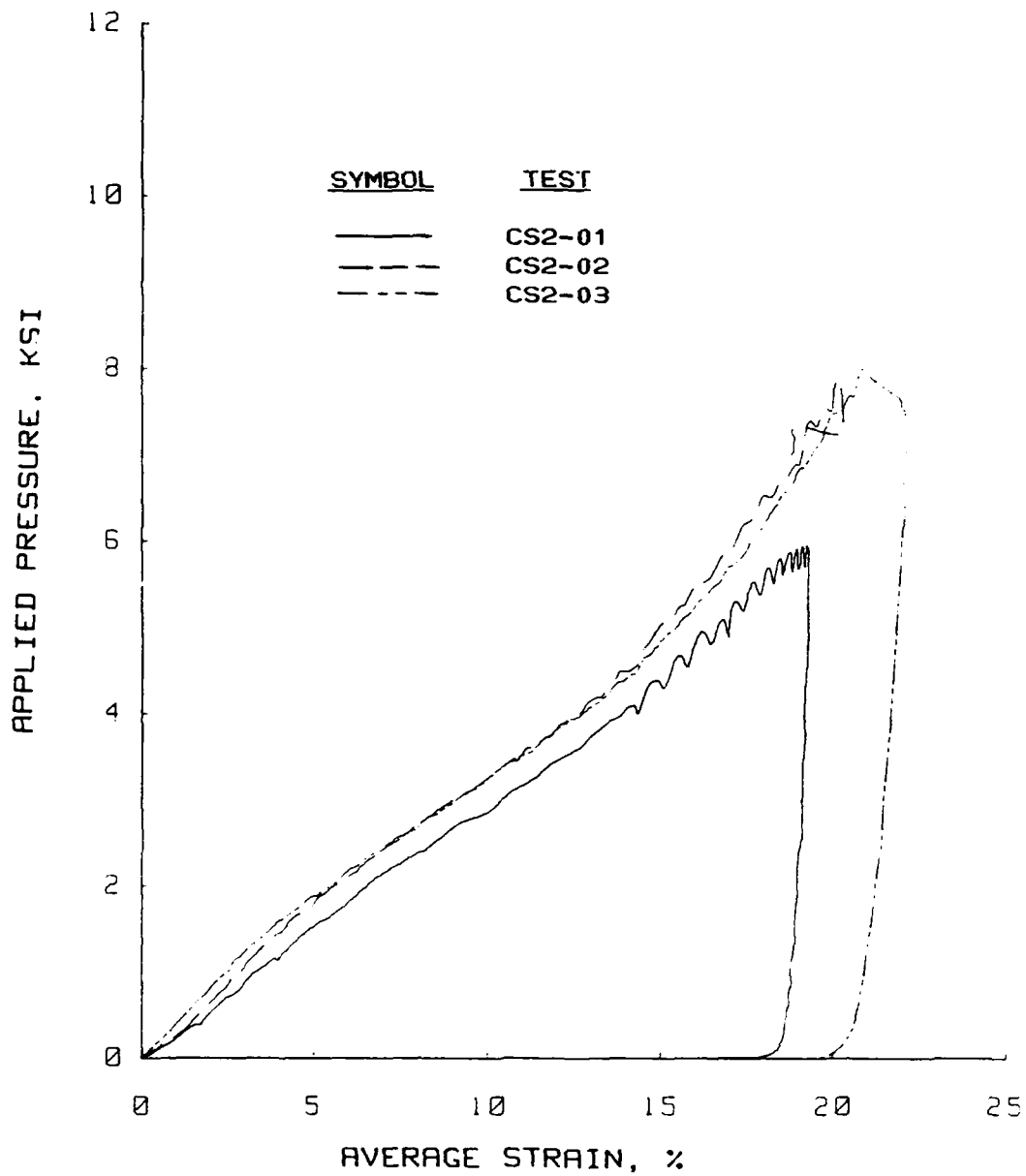
Figure B.4   Static uniaxial strain results for tests performed
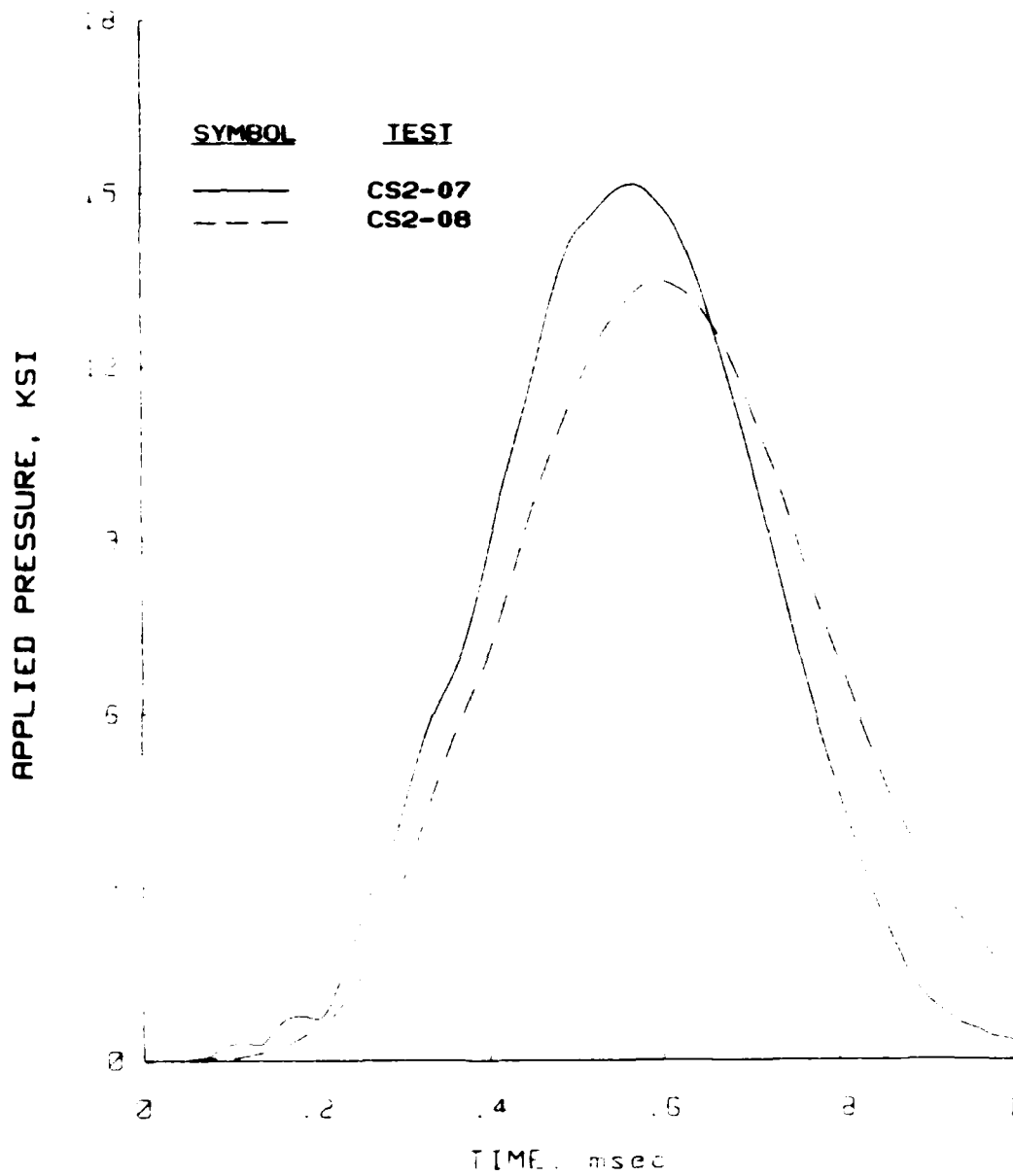in the WES 0.1-msec device on Enewetak beach sand.
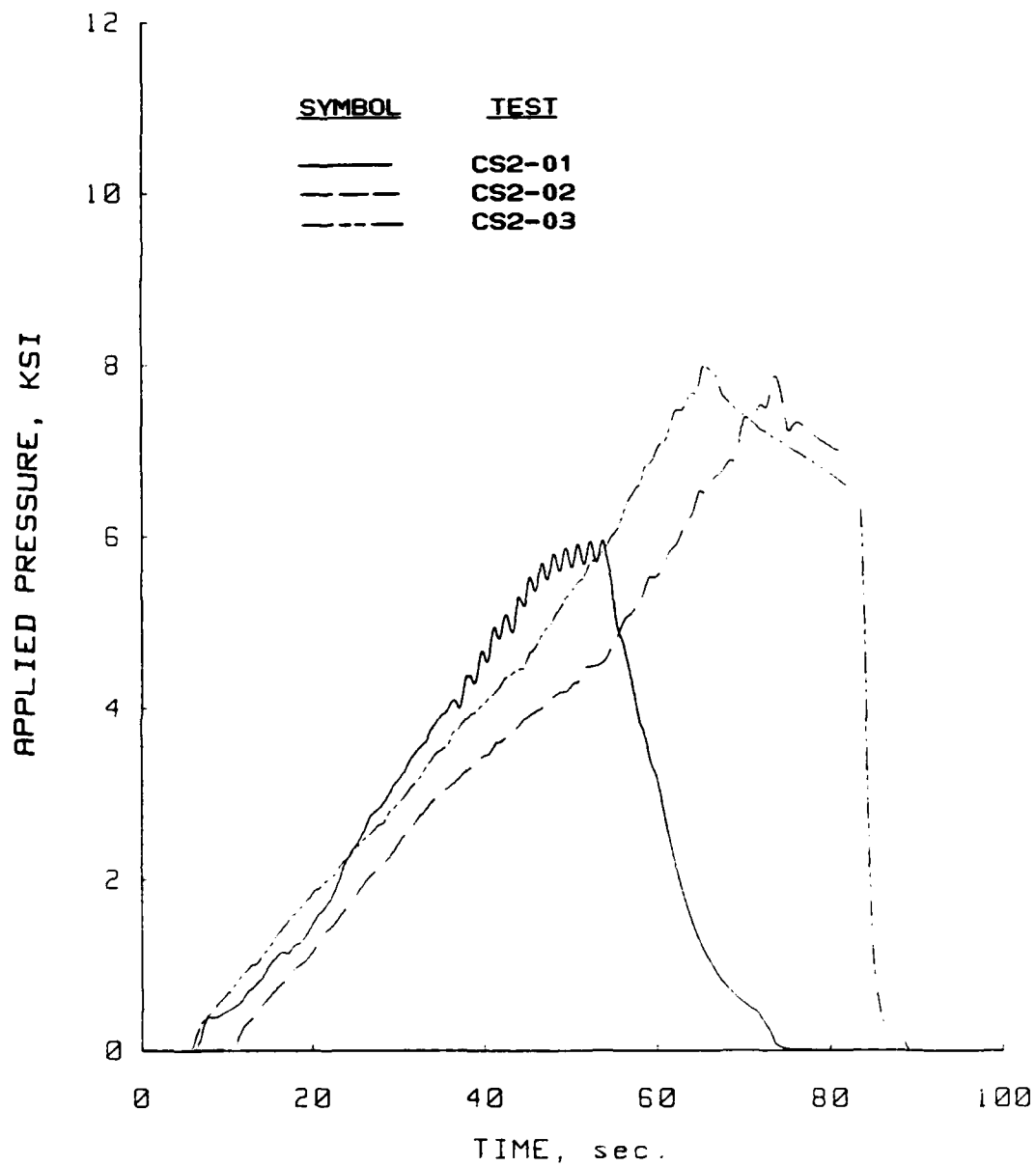
Figure B.5   Pressure versus time plots for the static uniaxial
strain tests performed in the WES 0.1-msec device on
Enewetak beach sand.
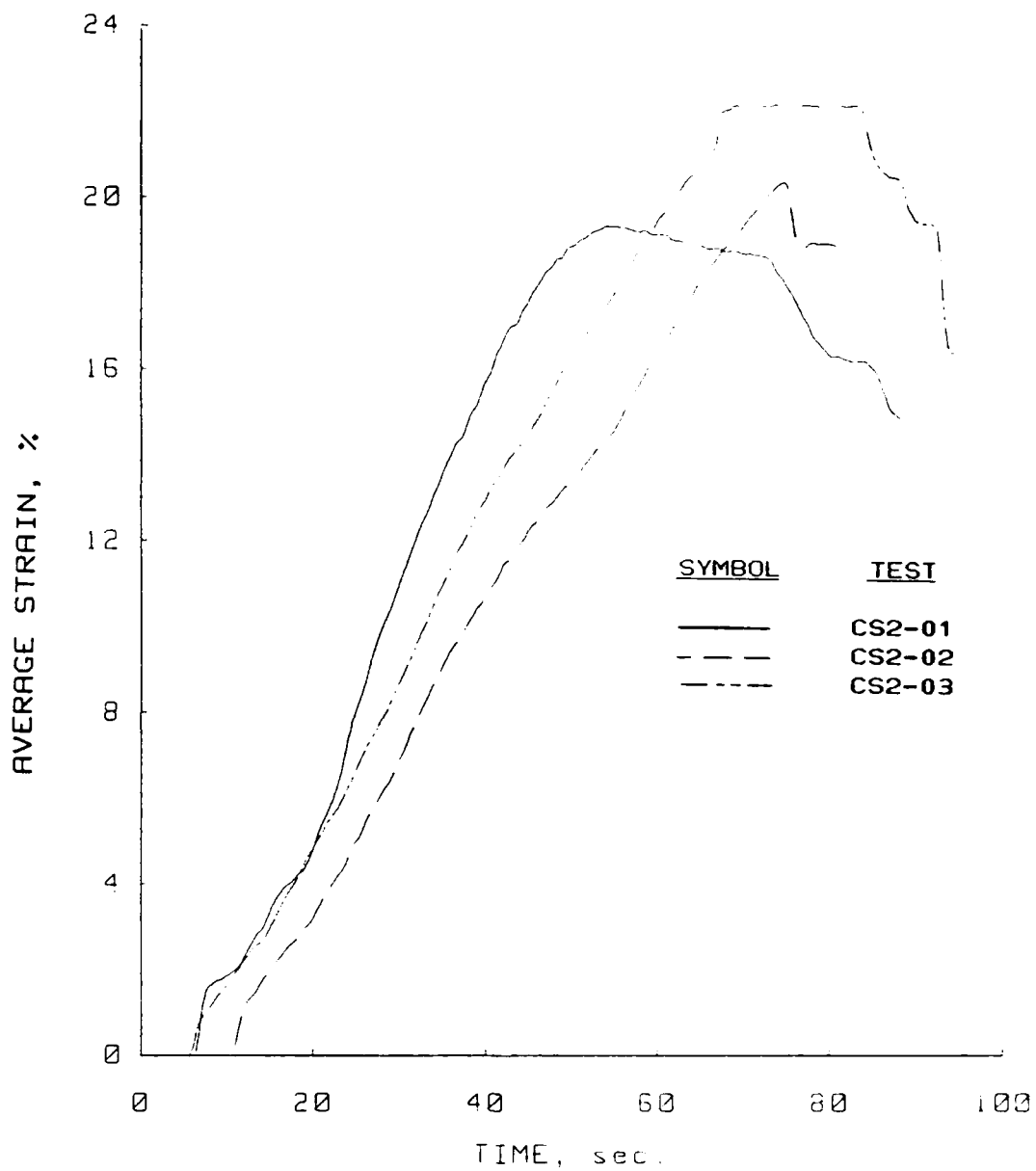
Figure B.6 Strain versus time plots for the static uniaxial
strain tests performed in the WES 0.1-msec device on
Enewetak beach sand.

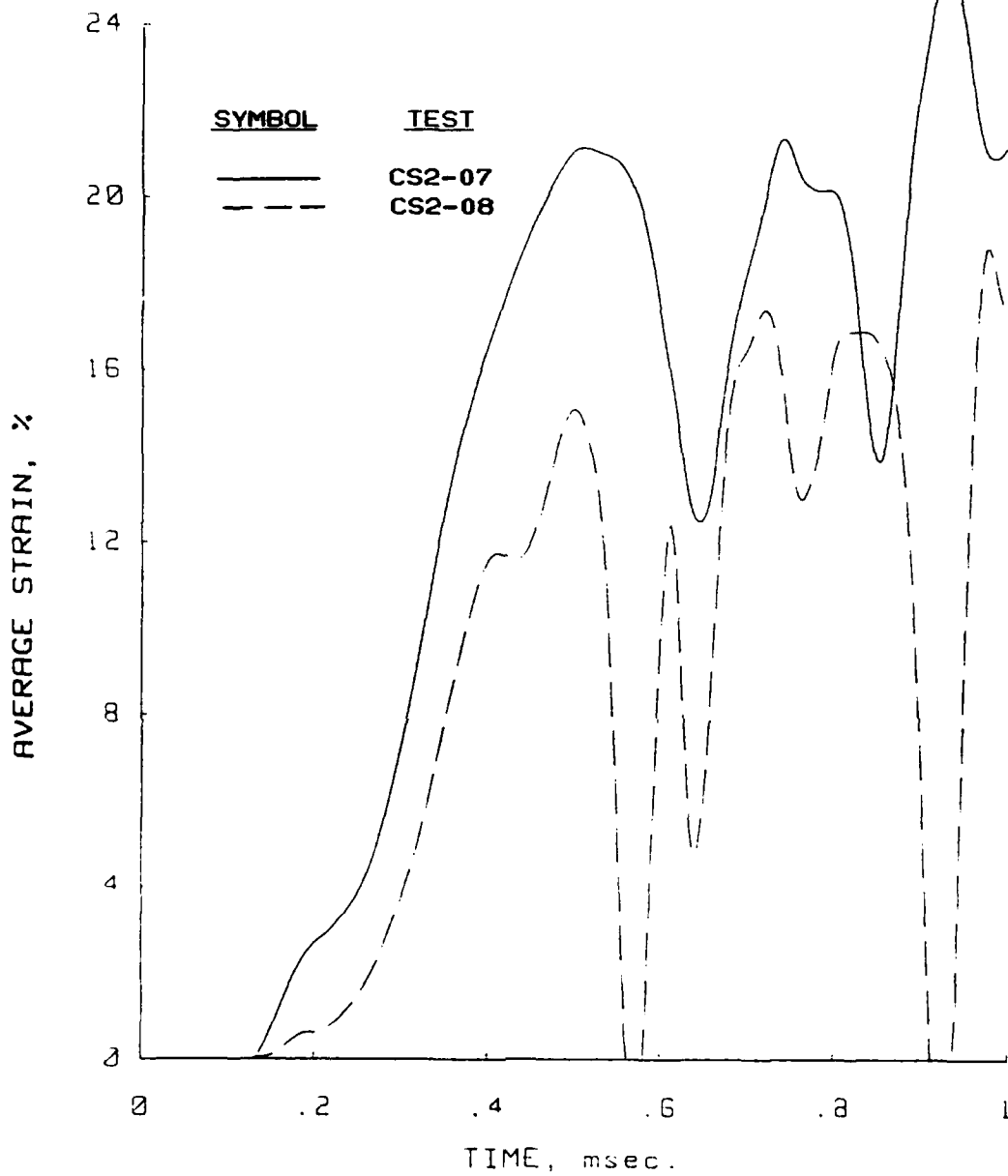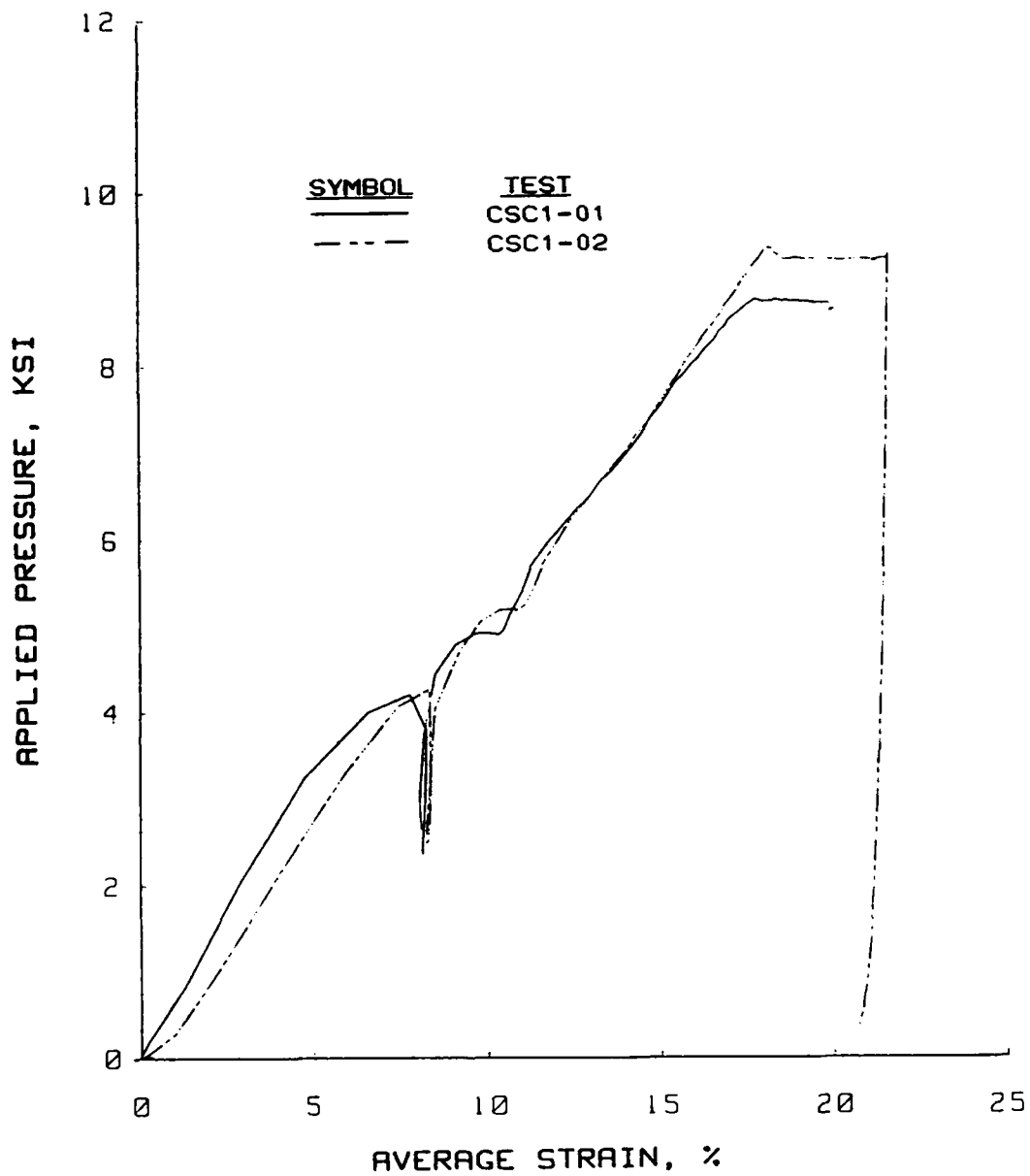## Uniaxial Strain Results
Soil Type: Enewetak Beach Sand
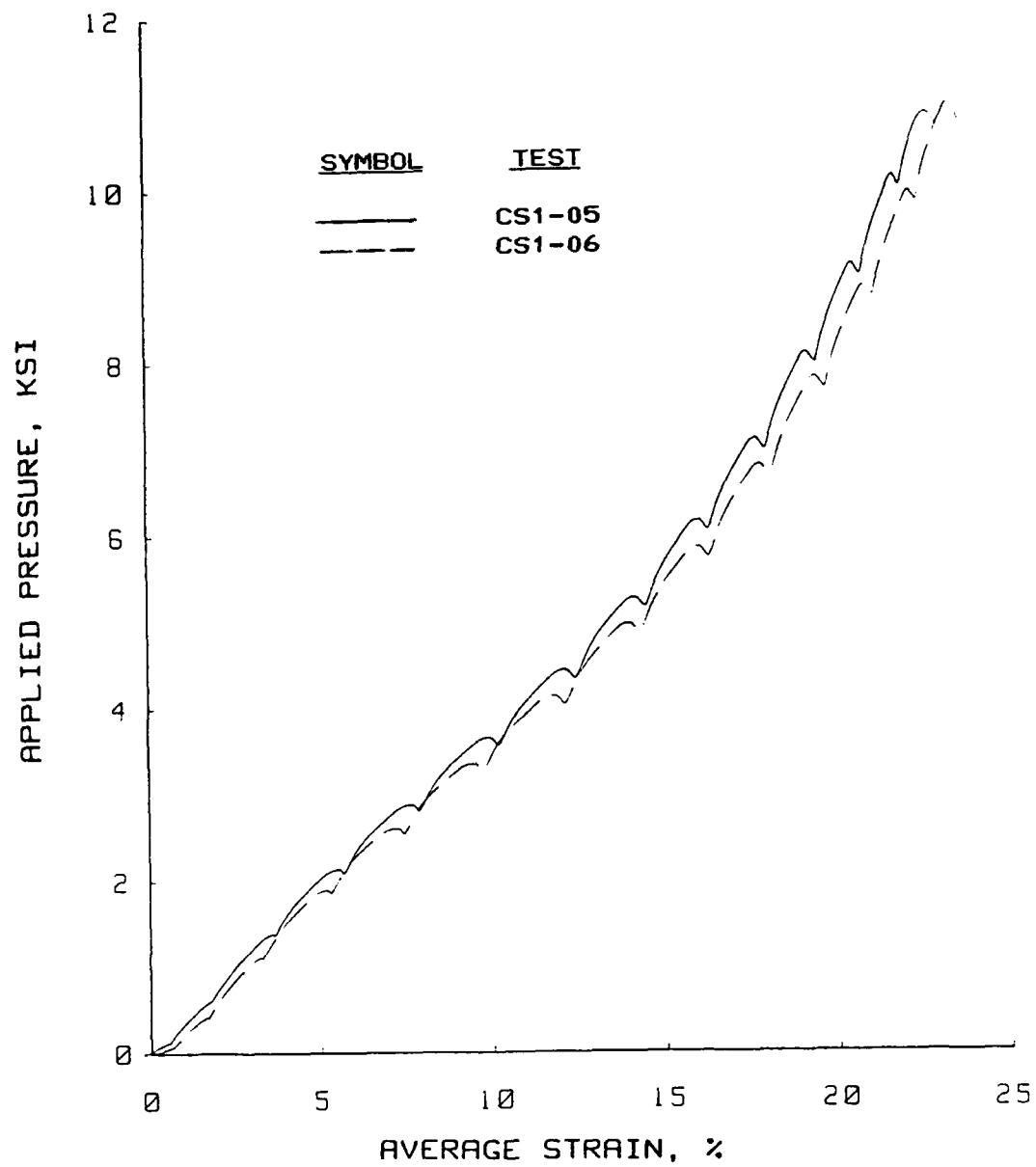
Figure B.7   Fast static uniaxial strain results for tests
performed in the PPUX device on Enewetak beach sand.
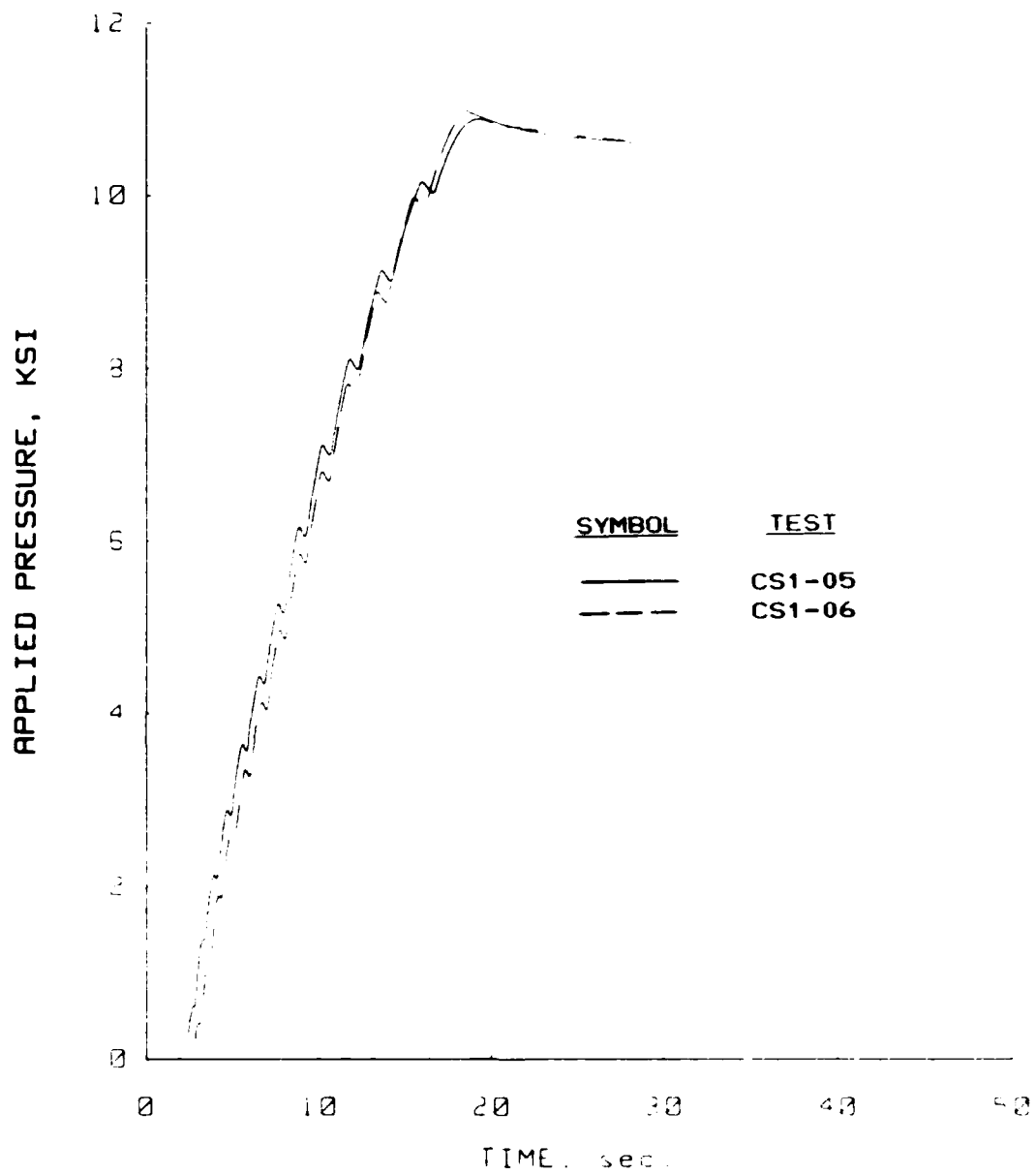
Figure B.8   Pressure versus time plots for the fast static
uniaxial strain tests performed in the PPUX device
on Enewetak beach sand.
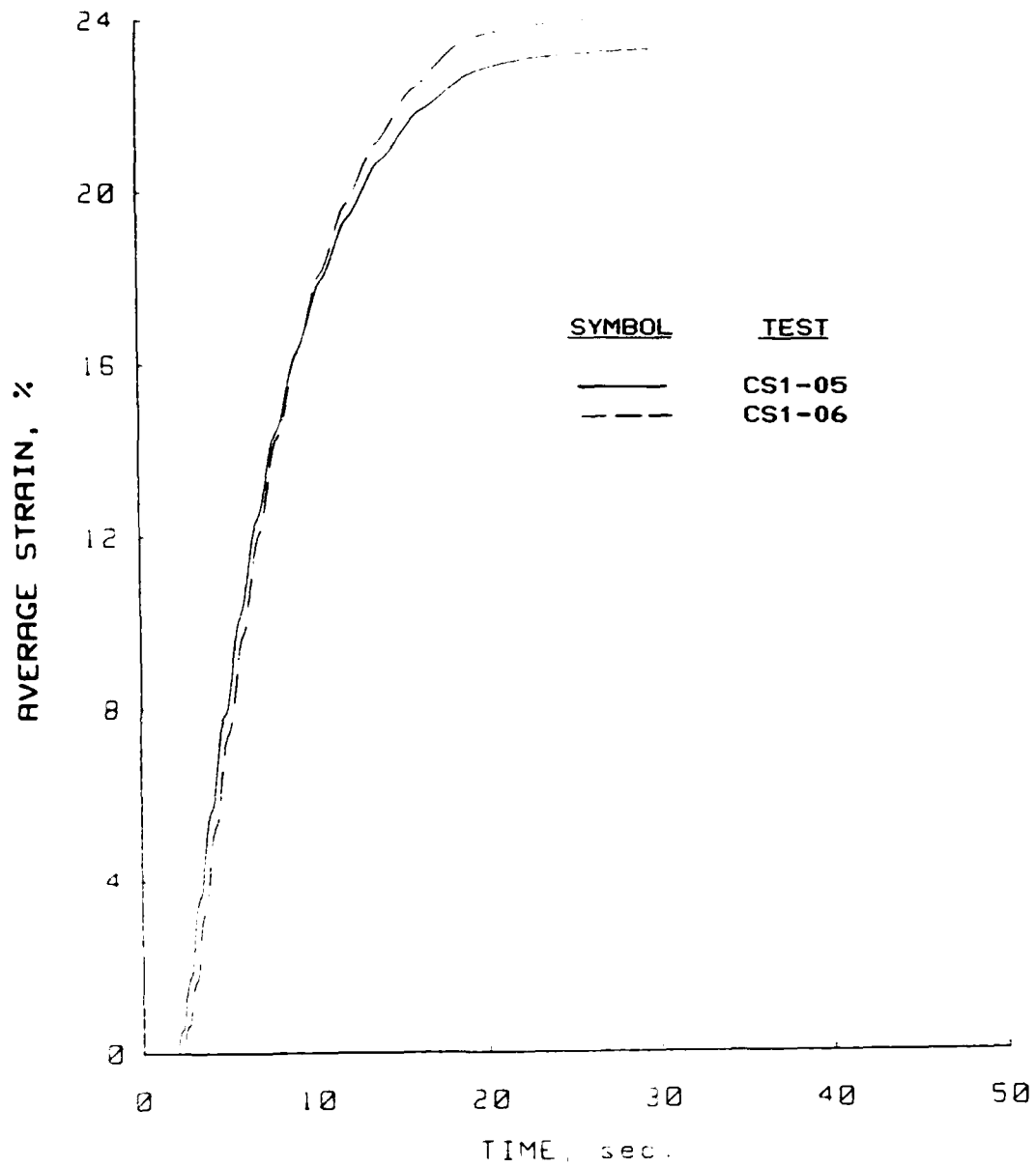
Figure B.9   Strain versus time plots for the fast static
uniaxial strain tests performed in the PPUX device
on Enewetak beach sand.

Uniaxial Strain Results
Soil Type: Enewetak Beach Sand
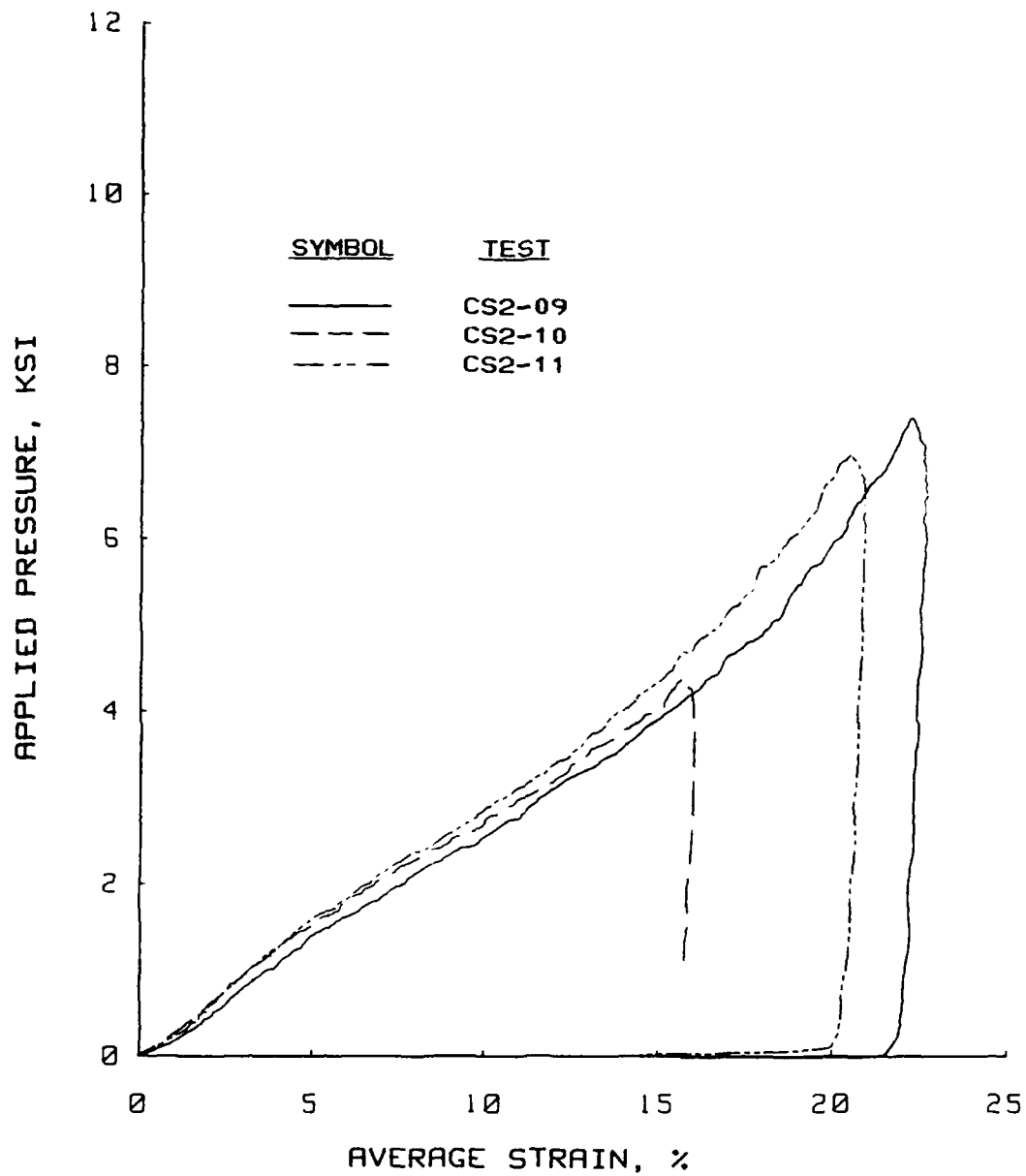
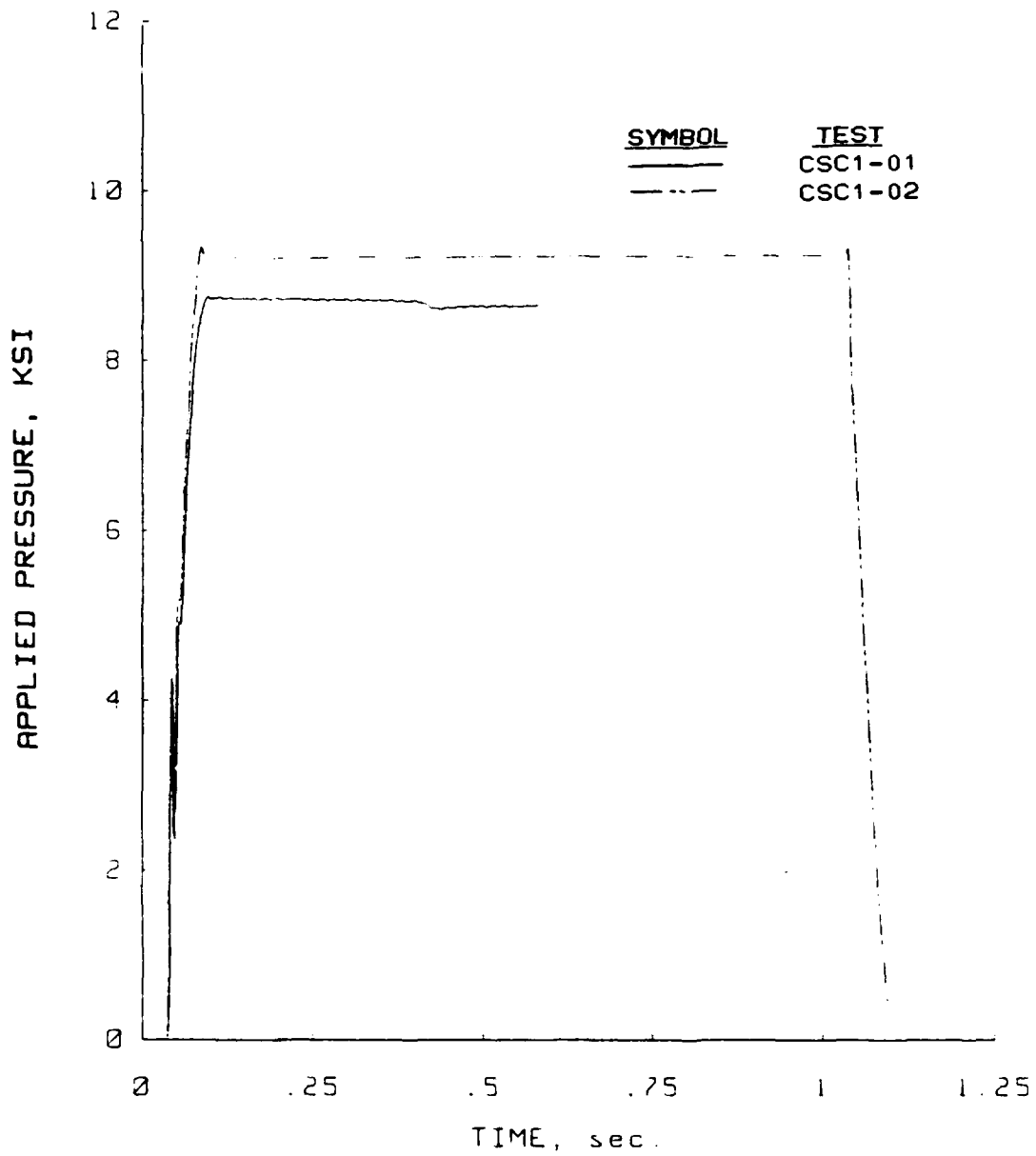Figure B.10 Slow static uniaxial strain results for tests
performed in the WES 0.1-msec device on Enewetak
beach sand.
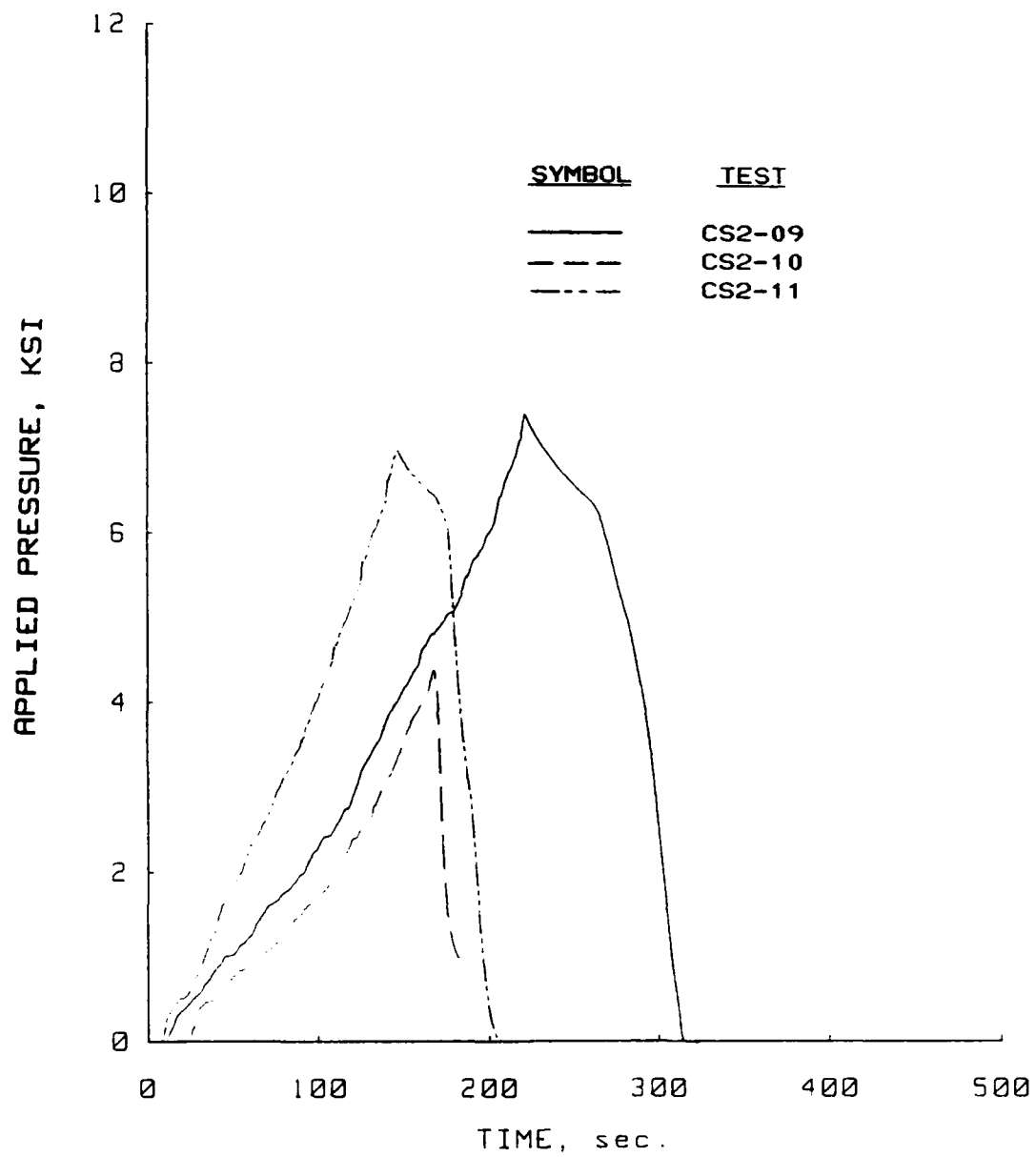
Figure B.11 Pressure versus time plots for the slow static
uniaxial strain tests performed in the WES 0.1-msec
device on Enewetak beach sand.
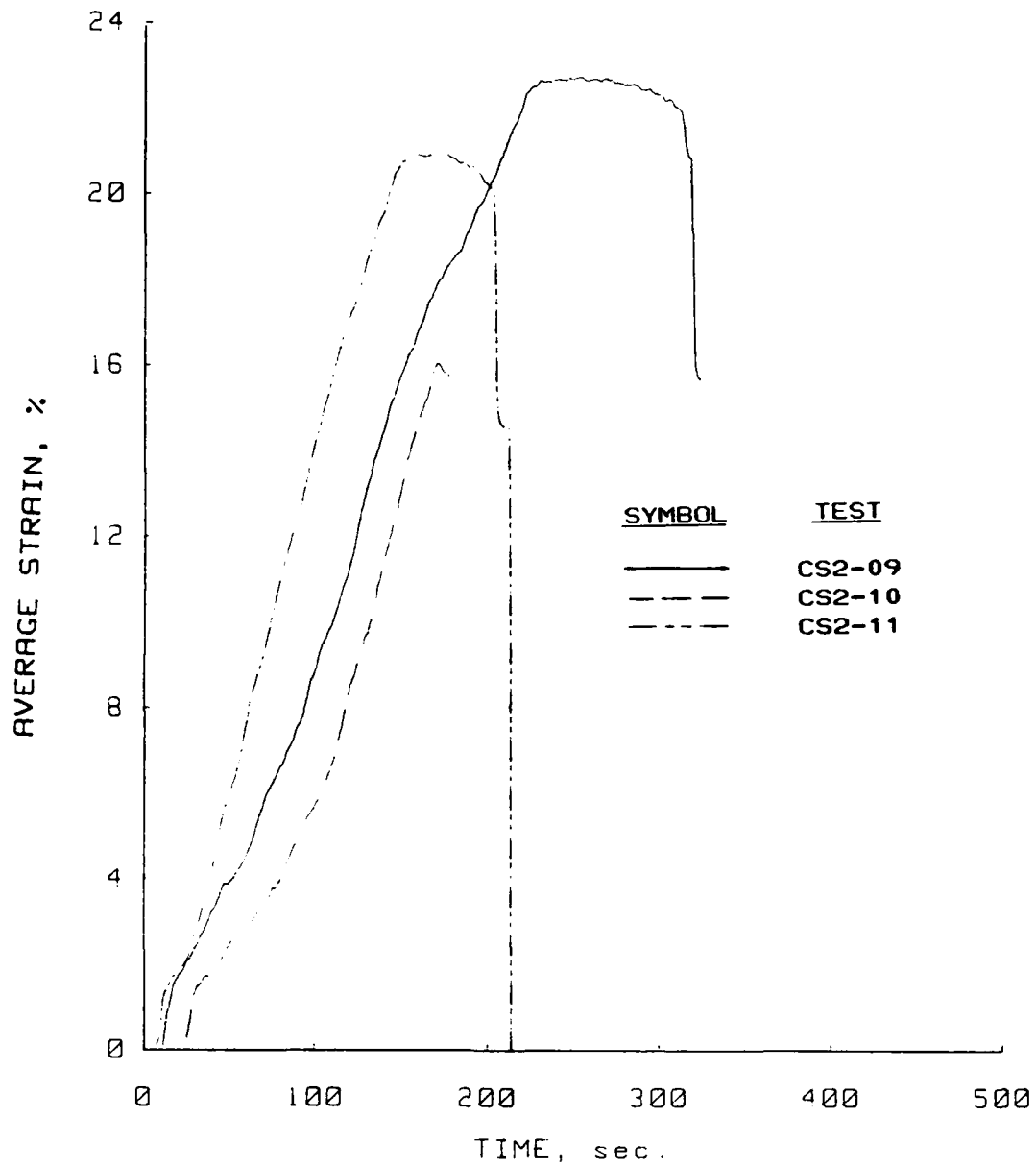
Figure B.12 Strain versus time plots for the slow static
uniaxial strain tests performed in the WES 0.1-msec
device on Enewetak beach sand.
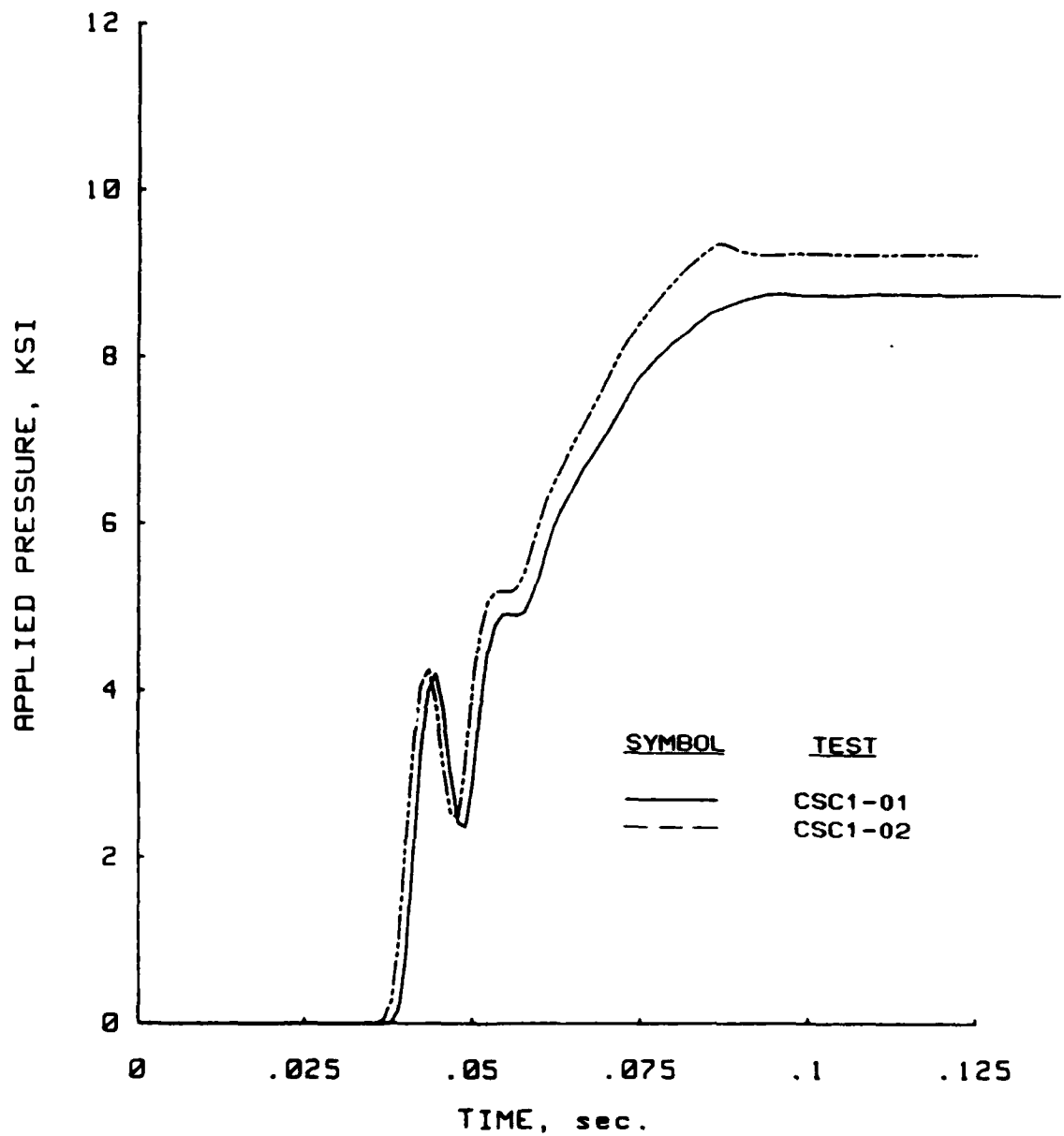
Uniaxial Strain Results
Soil Type: Enewetak Beach Sand
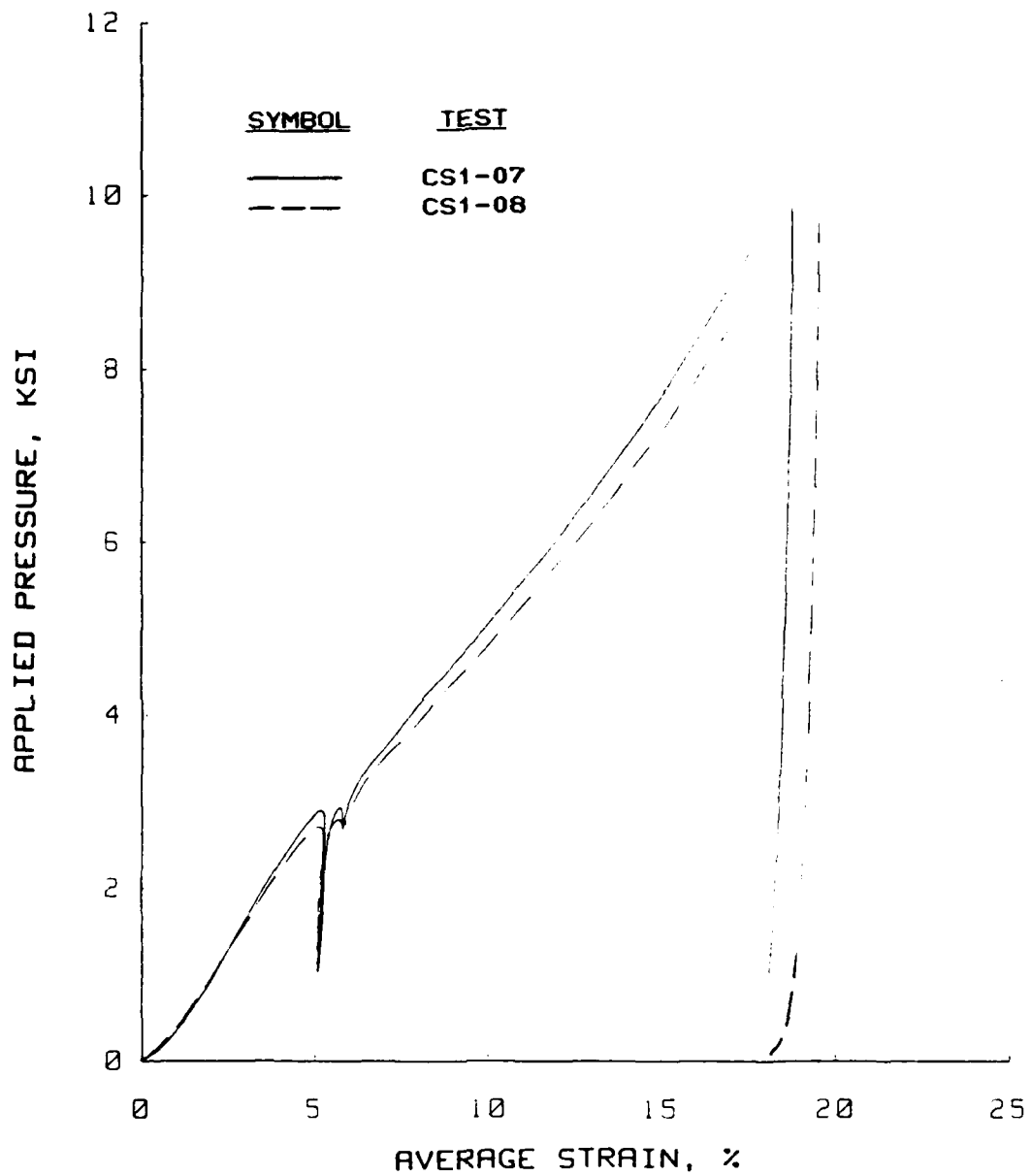
Figure B.13   Slow dynamic uniaxial strain resul:s for tests
performed in the PPUX device on Enewetak beach sand.

Uniaxial Strain Results
Soil Type: Enewetak Beach Sand
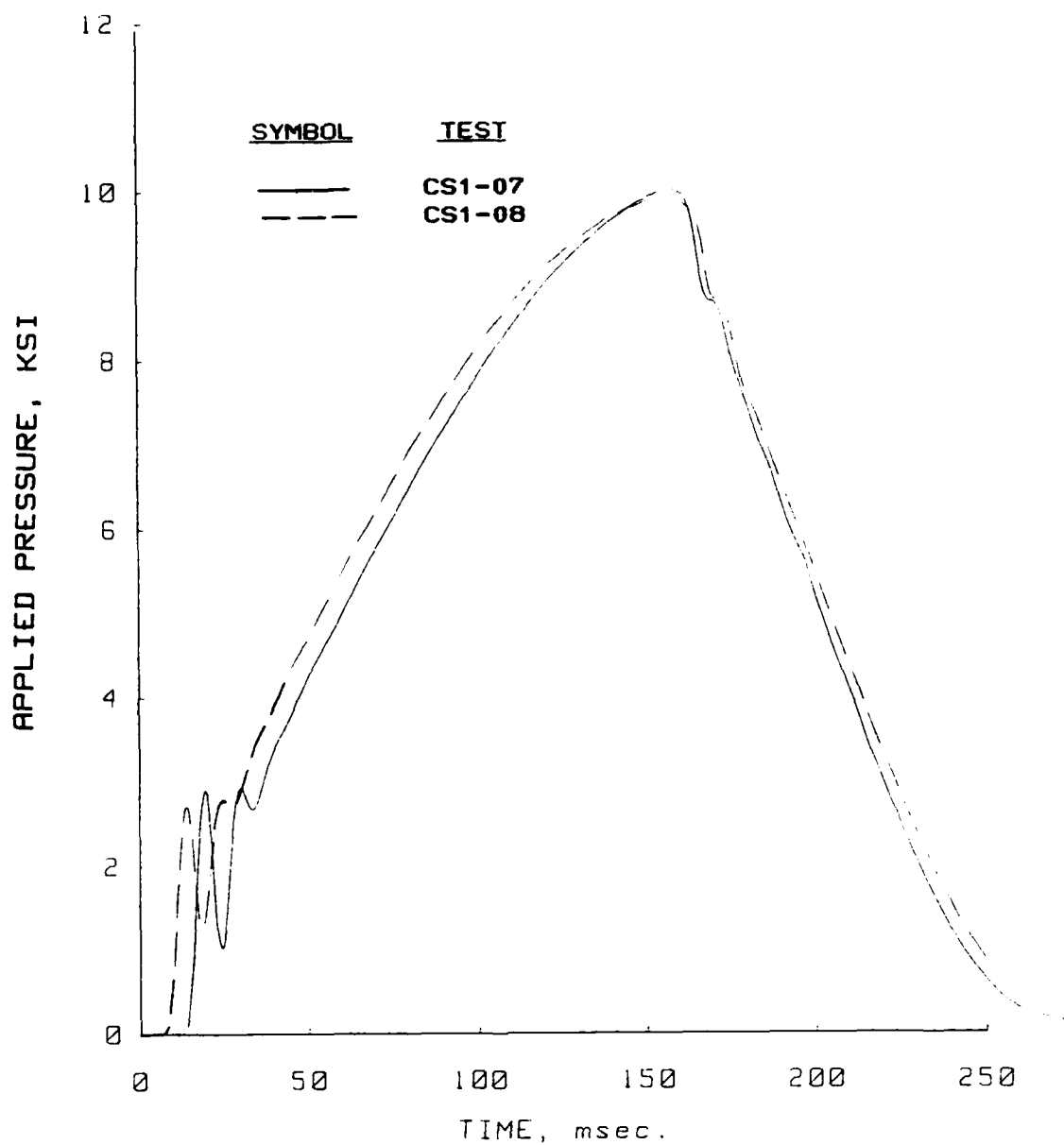
Figure B.14 Pressure versus time plots for the slow dynamic uniaxial strain tests performed in the PPUX device on Enewetak beach sand.

Uniaxial Strain Results
Soil Type: Enewetak Beach Sand
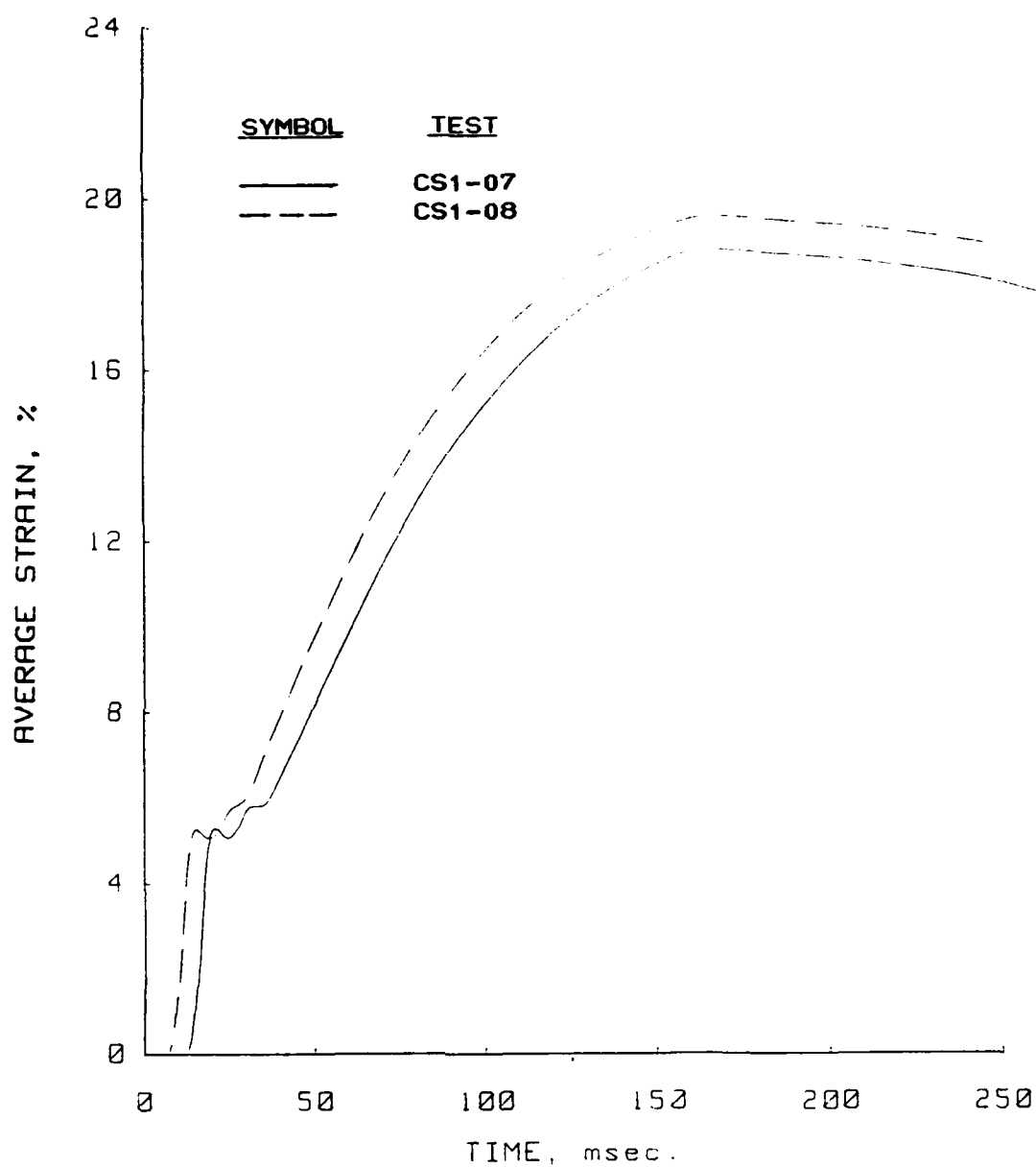
Figure B.15   Strain versus time plots for the slow dynamic
uniaxial strain tests performed in the PPUX device
on Enewetak beach sand.
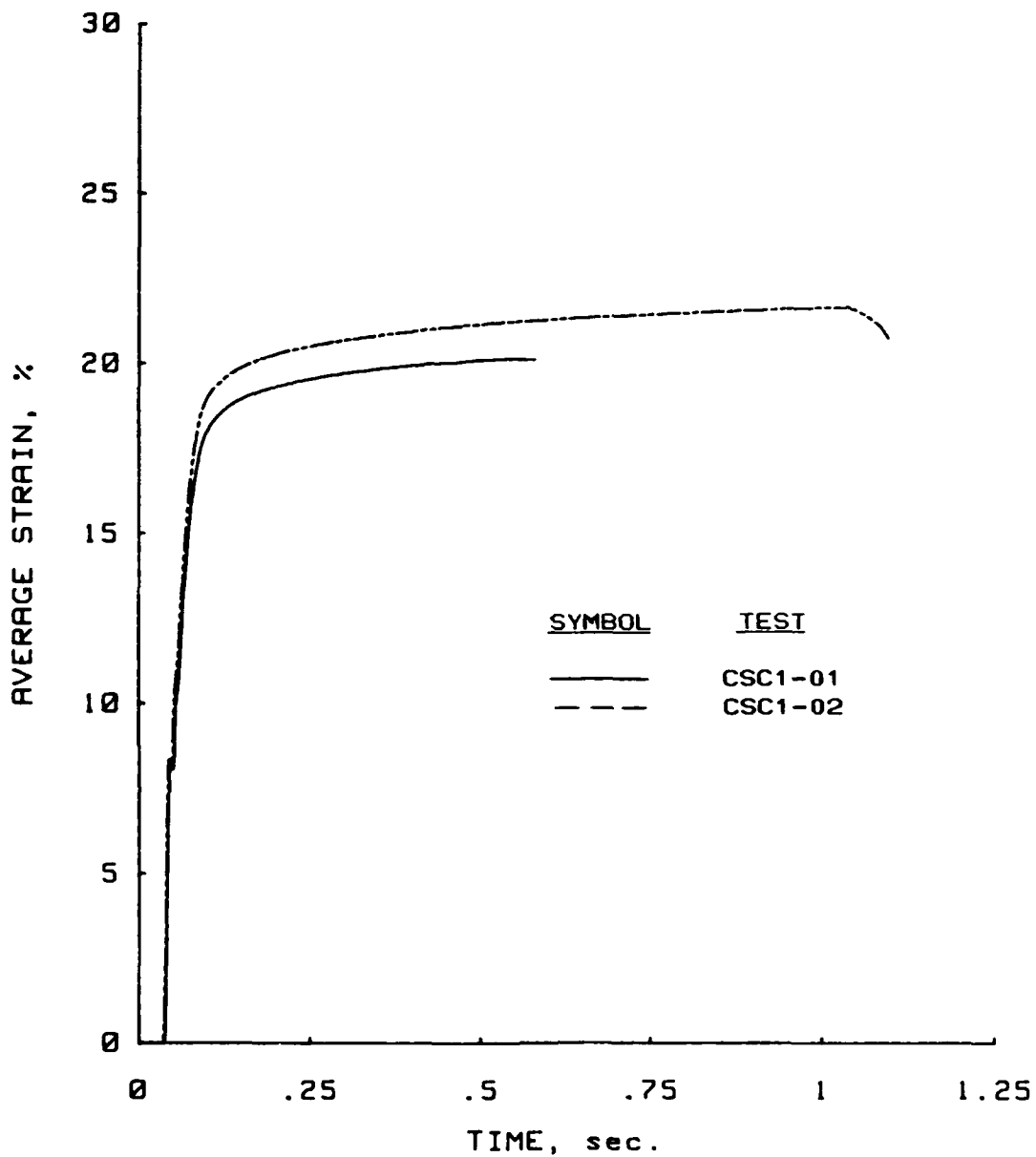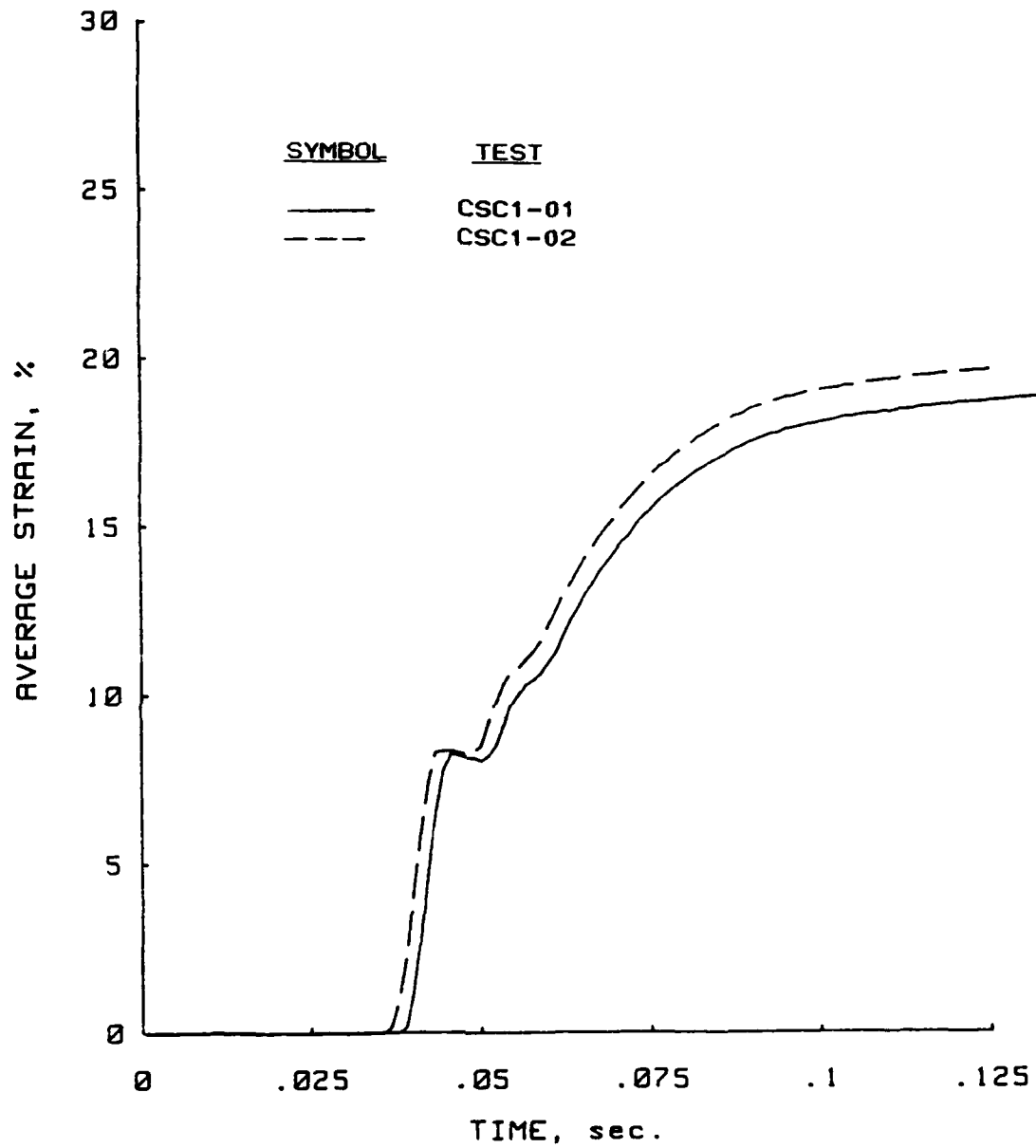
Uniaxial Strain Results
Soil Type: Enewetak Beach Sand
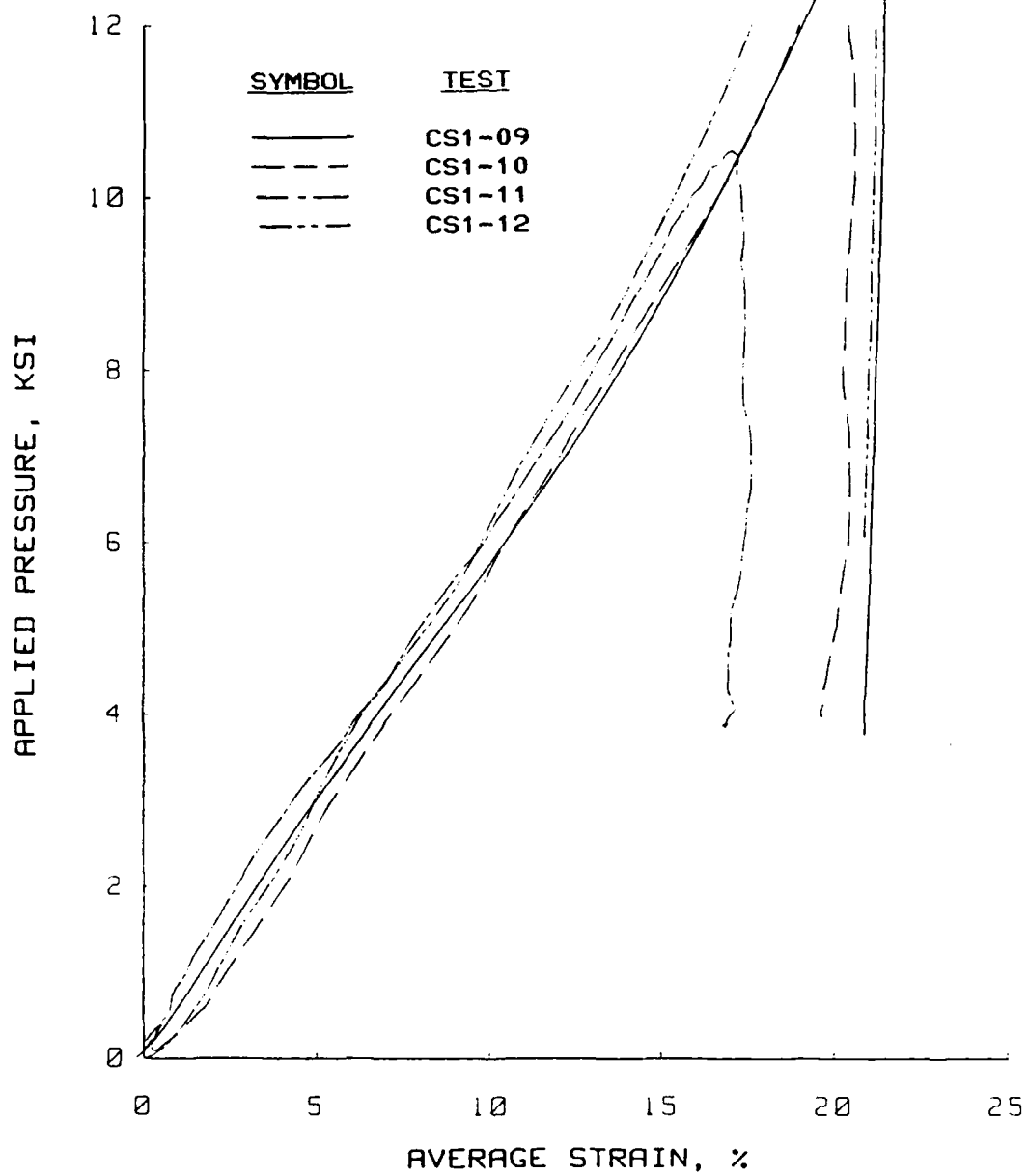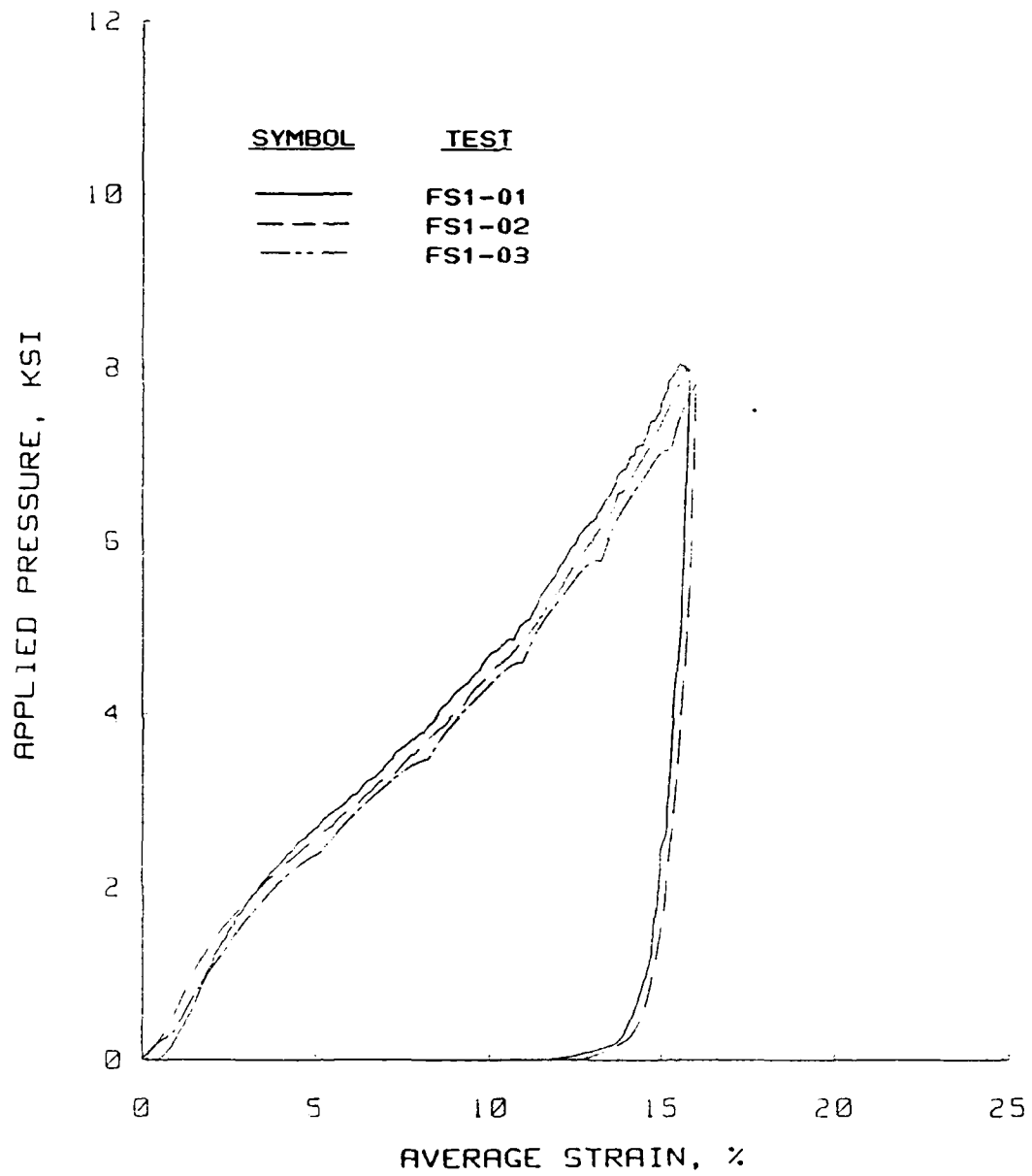

Figure B.16   Dynamic uniaxial strain results for tests performed
in the PPUX device on Enewetak beach sand.
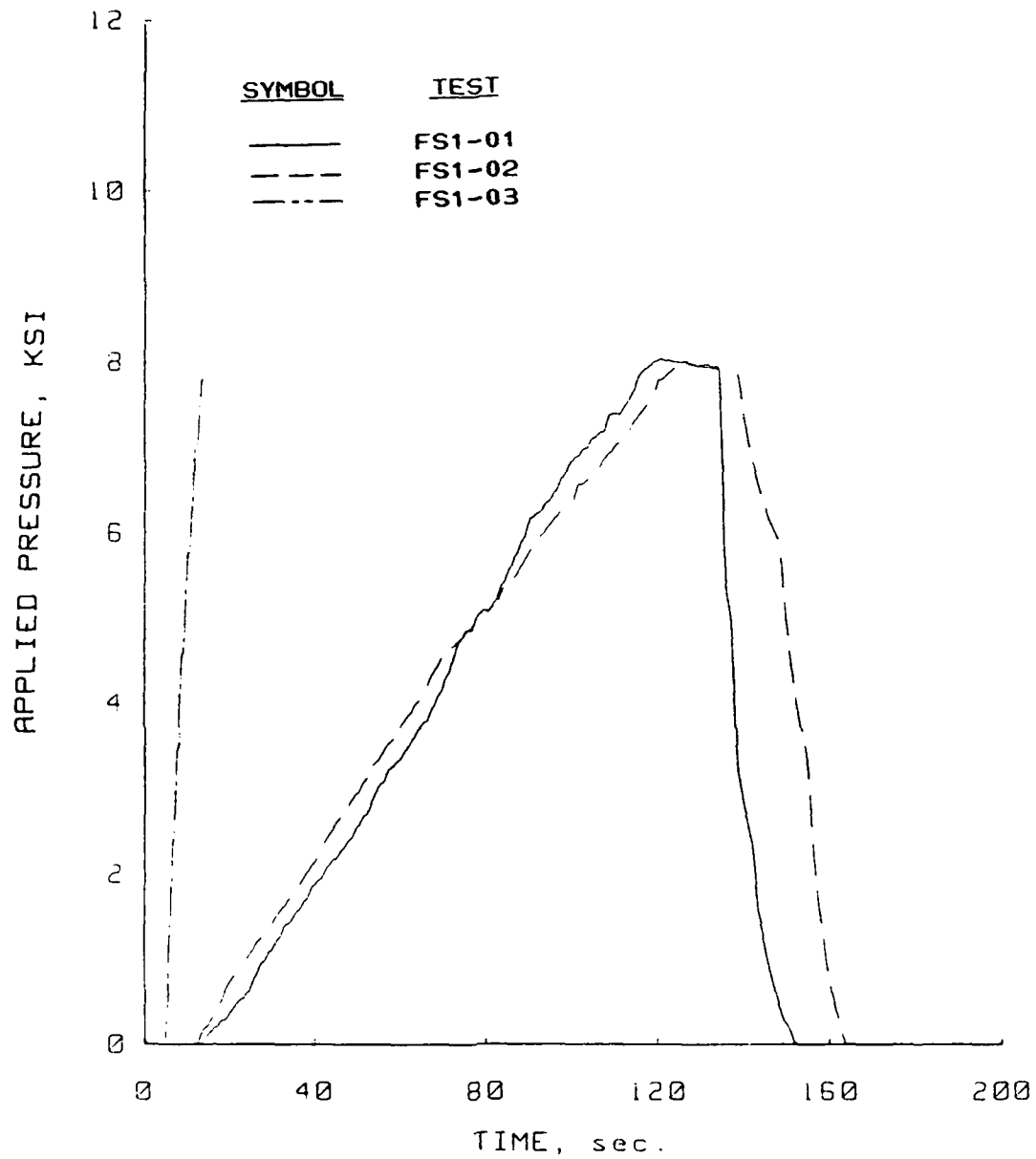
Uniaxial Strain Results
Soil Type: Enewetak Beach Sand
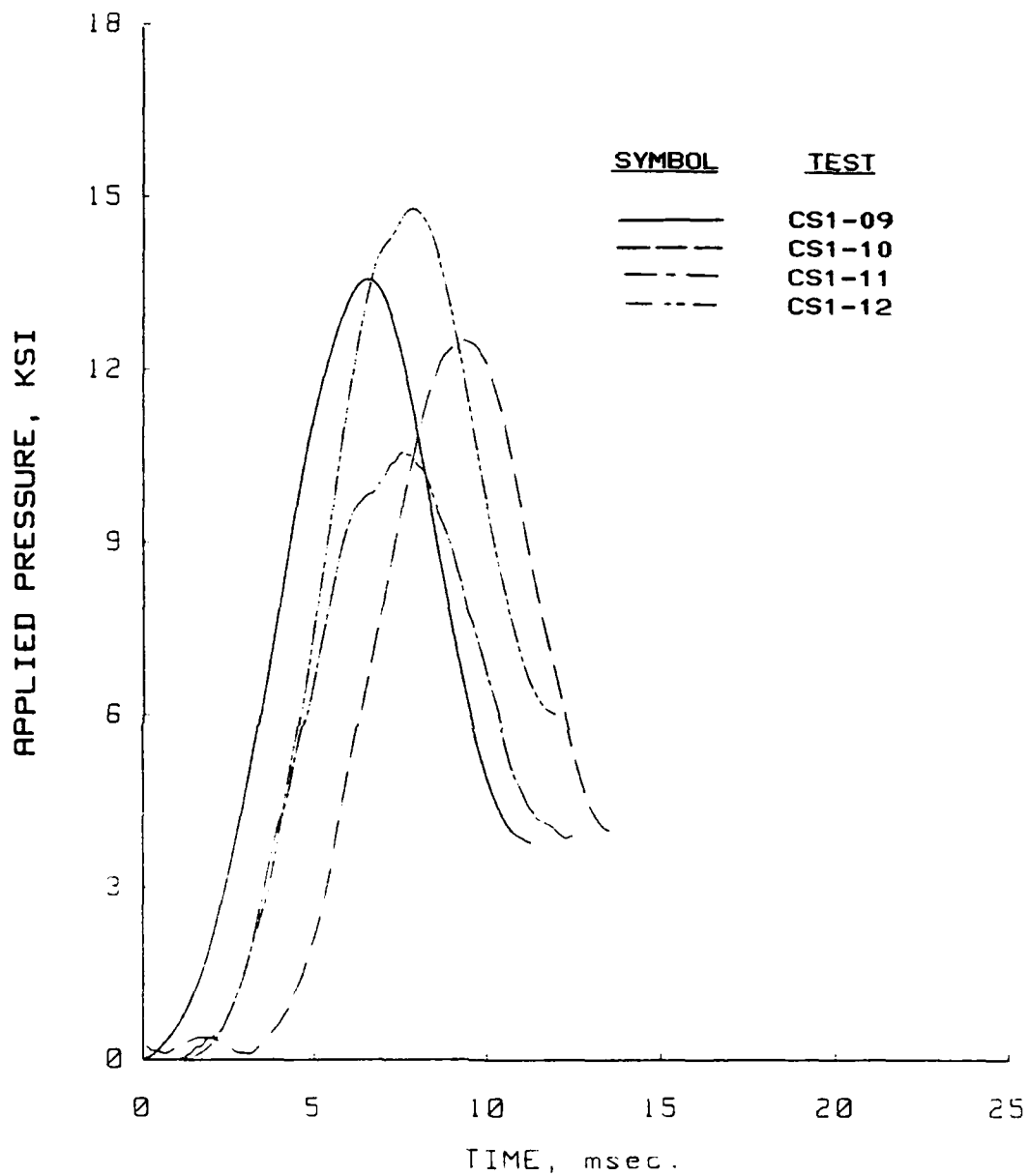
Figure B.17   Pressure versus time plots for the dynamic
uniaxial strain tests performed in the PPUX device
on Enewetak beach sand.
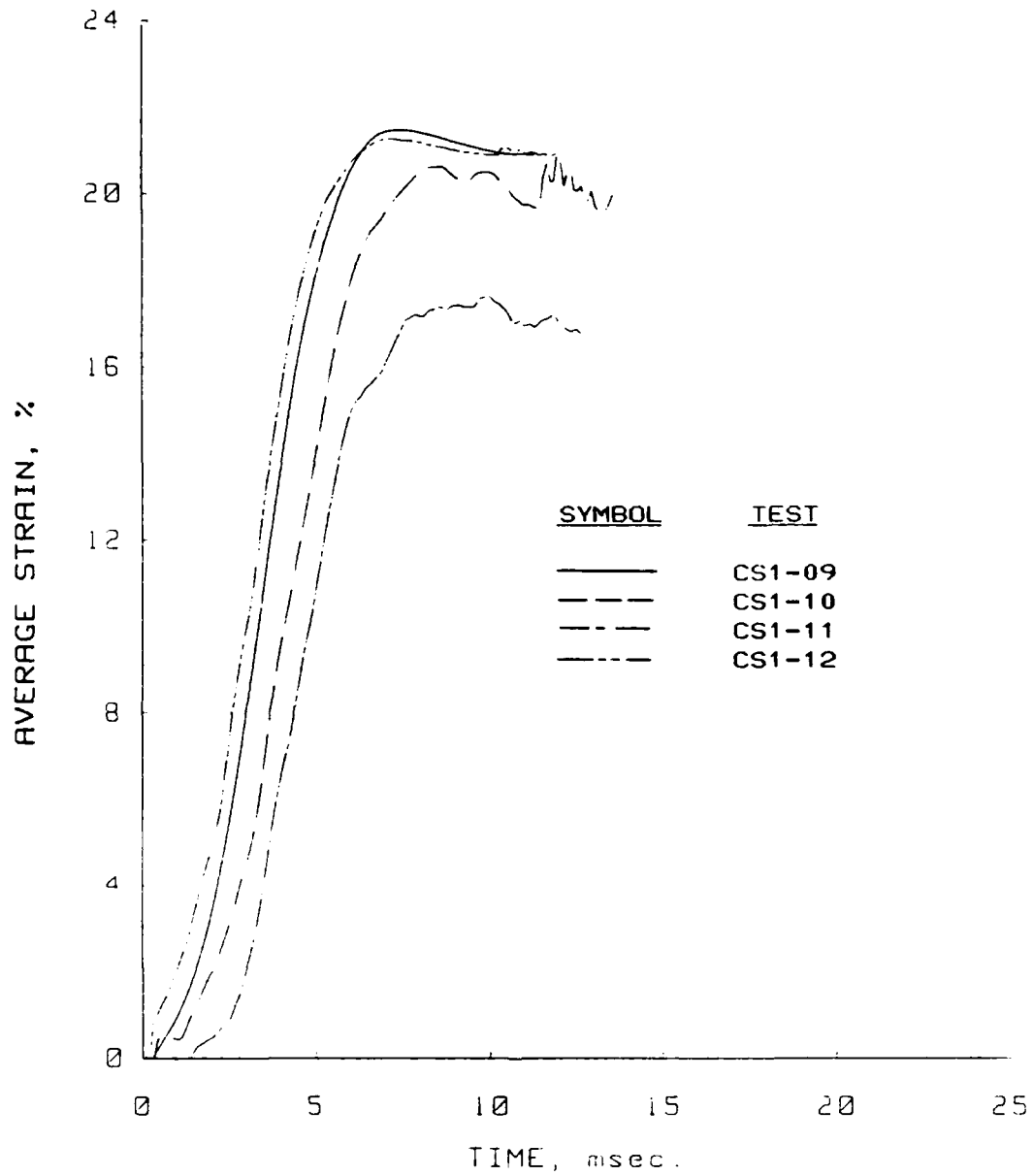
Figure B.18   Strain versus time plots for the dynamic uniaxial
strain tests performed in the PPUX device on
Enewetak beach sand.
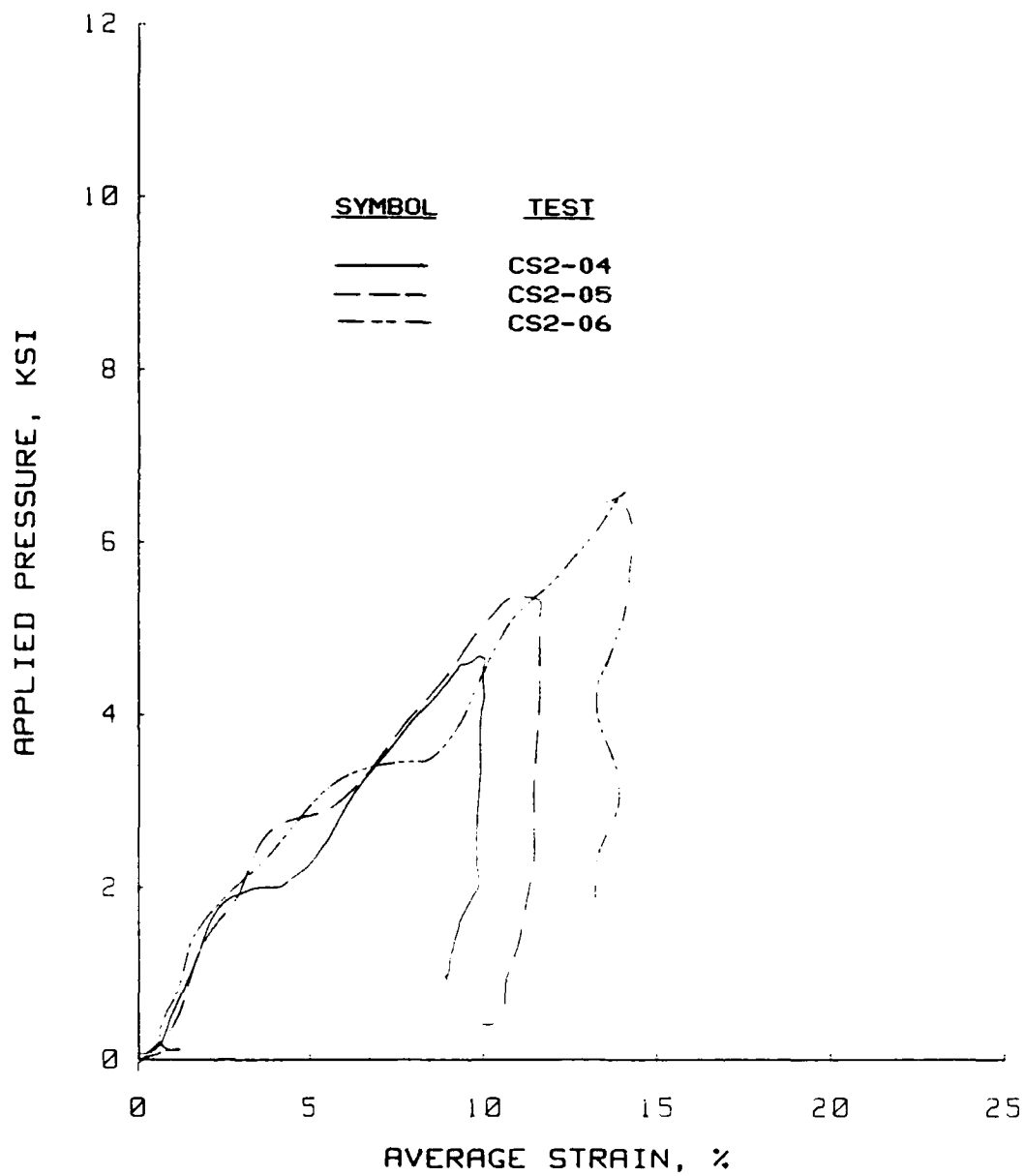
Figure B.19 Dynamic uniaxial strain results for tests CS2-04, -05, and -06 performed in the WES 0.1-msec device on Enewetak beach sand.

Uniaxial Strain Results
Soil Type: Enewetak Beach Sand
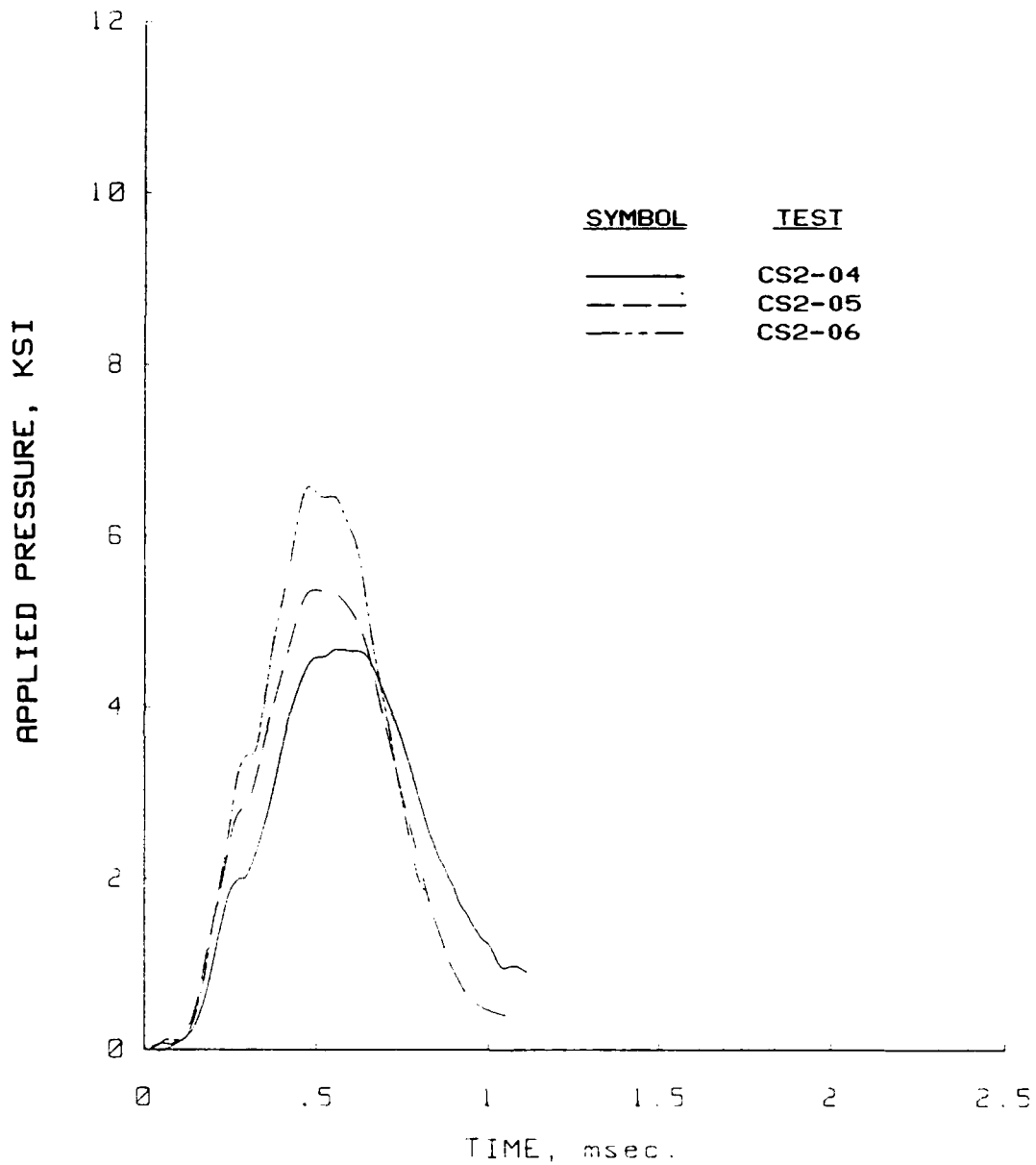
Figure B.20   Pressure versus time plots for the dynamic
              uniaxial strain tests CS2-04   -05, and -06
              performed in the WES 0.1-msec device on Enewetak
              beach sand.

Figure B.21   Strain versus time plots for the dynamic uniaxial
              strain tests CS2-04, -05, and -06 performed in the
              WES 0.1-msec device on Enewetak beach sand.

Uniaxial Strain Results
Soil Type: Enewetak Beach Sand
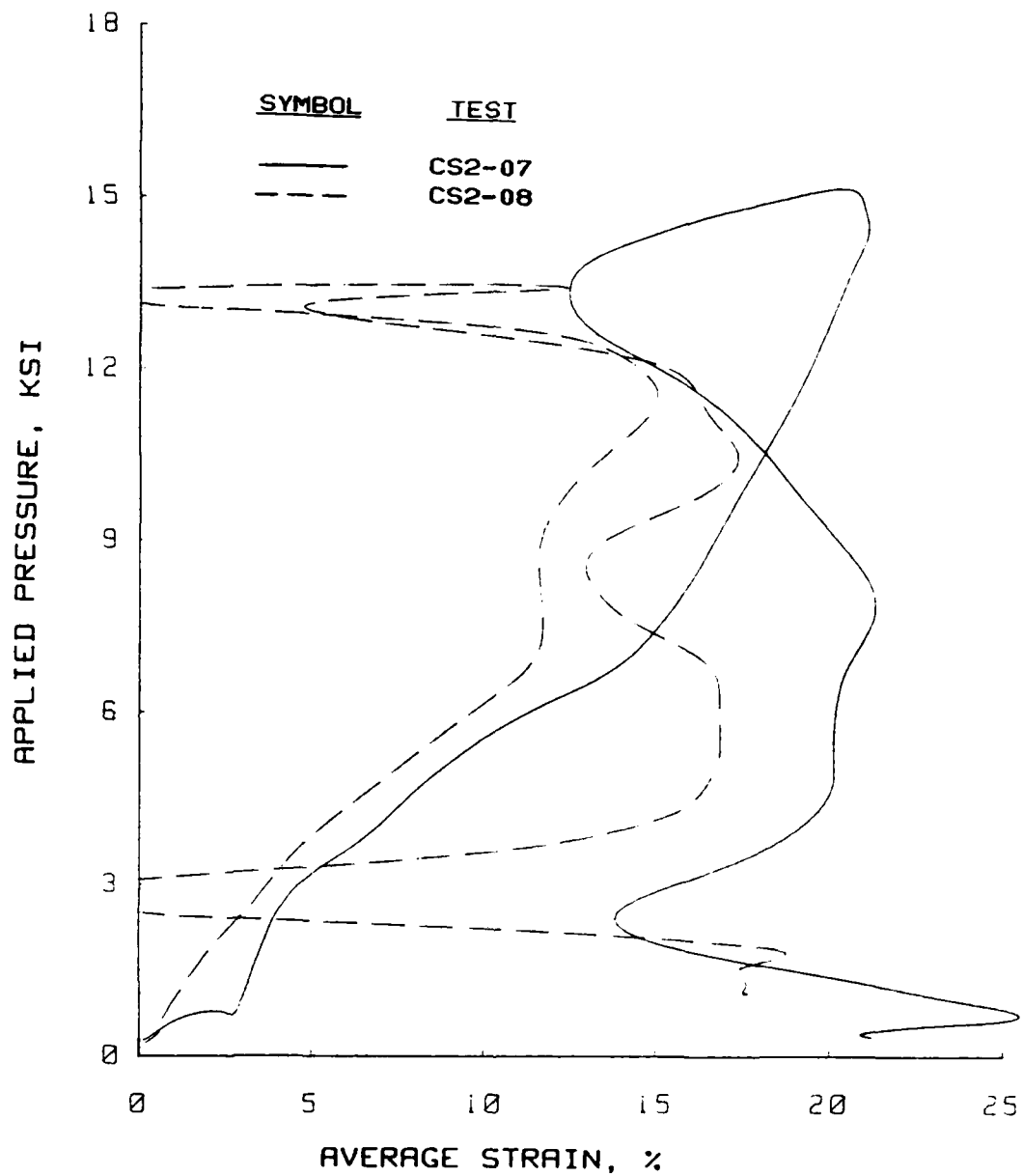
Figure B.22 Dynamic uniaxial strain results for tests CS2-07
and -08 performed in the WES 0.1-msec device on
Enewetak beach sand.

Uniaxial Strain Results
Soil Type: Enewetak Beach Sand

Figure B.23 Pressure versus time plots for the dynamic

uniaxial strain tests CS2-07 and -08 performed in

the WES 0.1-msec device on Enewetak beach sand.

Uniaxial Strain Results
Soil Type: Enewetak Beach Sand

Figure B.24 Strain versus time plots for the dynamic uniaxial
strain tests CS2-07 and -08 performed in the WES
0.1-msec device on Enewetak beach sand.

Uniaxial Strain Results
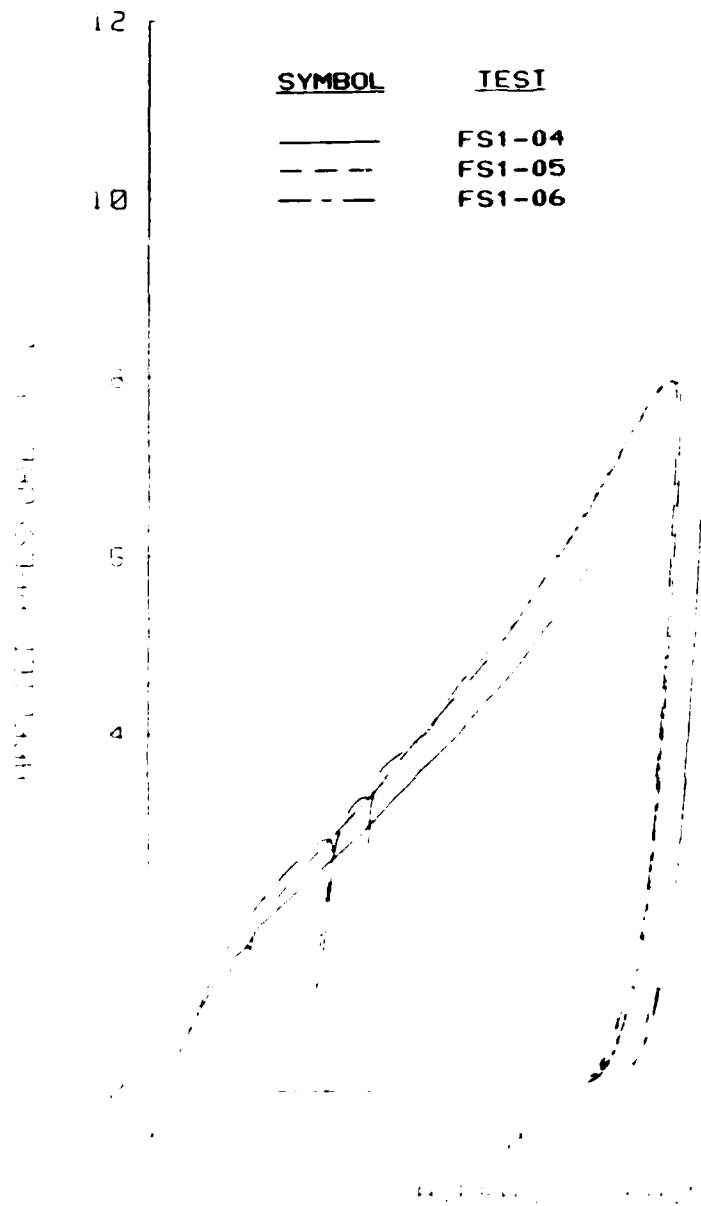Soil Type: Enewetak Beach Sand

Figure B.25 Dynamic creep uniaxial strain results for tests
performed in the PPUX device on Enewetak beach sand.

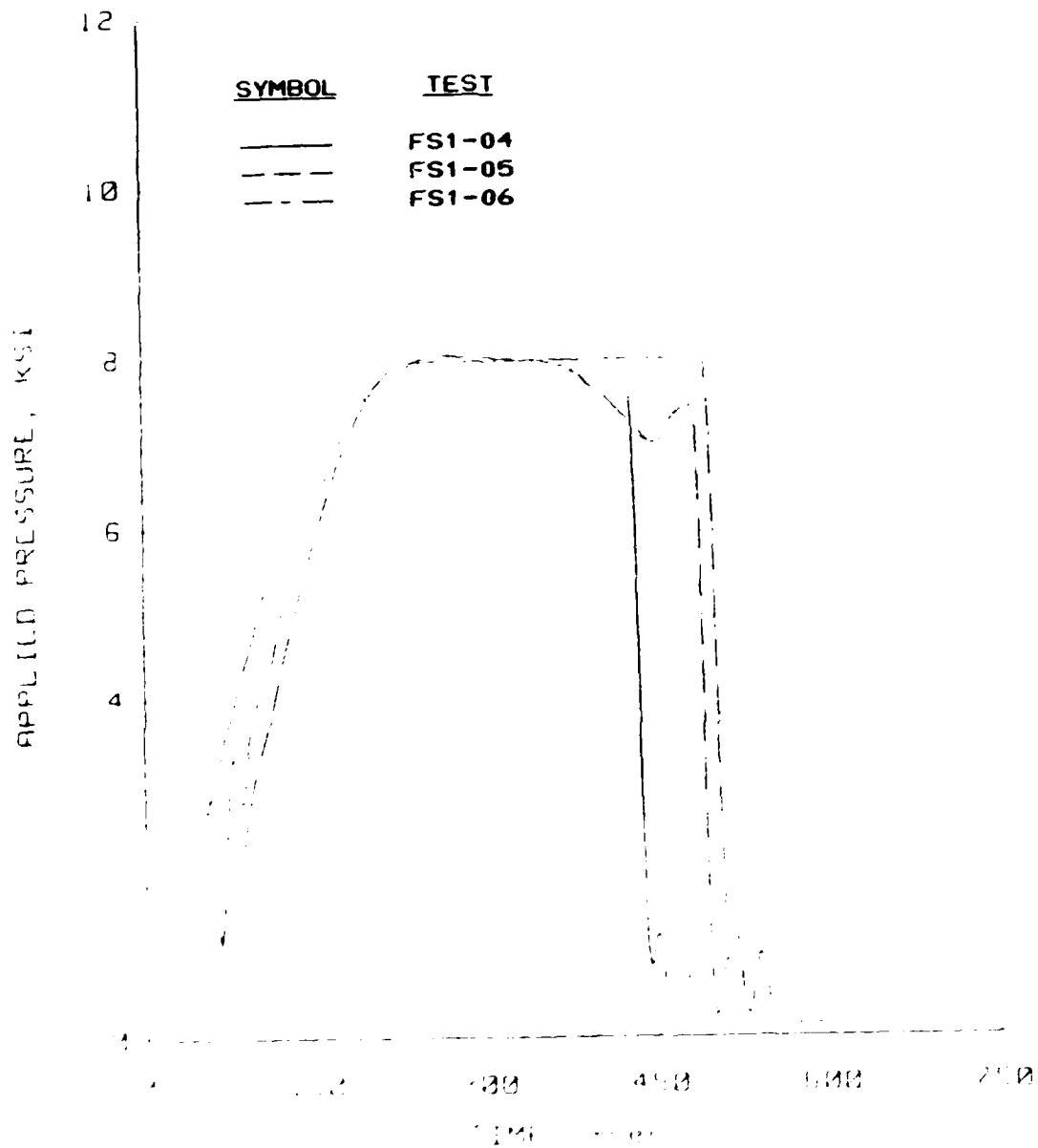Uniaxial Strain Results
Soil Type: Enewetak Beach Sand

Figure B.26   Pressure versus time plots for the dynamic creep
uniaxial strain tests performed in the PPUX device
on Enewetak beach sand.

Uniaxial Strain Results
Soil Type: Enewetak Beach Sand

Figure B.27 Pressure rise time plots for the dynamic creep
uniaxial strain tests performed in the PPUX device
on Enewetak beach sand.

Uniaxial Strain Results
Soil Type: Enewetak Beach Sand

Figure B.28   Strain versus time plots for the dynamic creep
uniaxial strain tests perfor.ied in the PPUX device
on Enewetak beach sand.

Figure B.29 Strain rise time plots for the dynamic creep
uniaxial·strain tests performed in the PPUX device
on Enewetak beach sand.

Uniaxial Strain Results
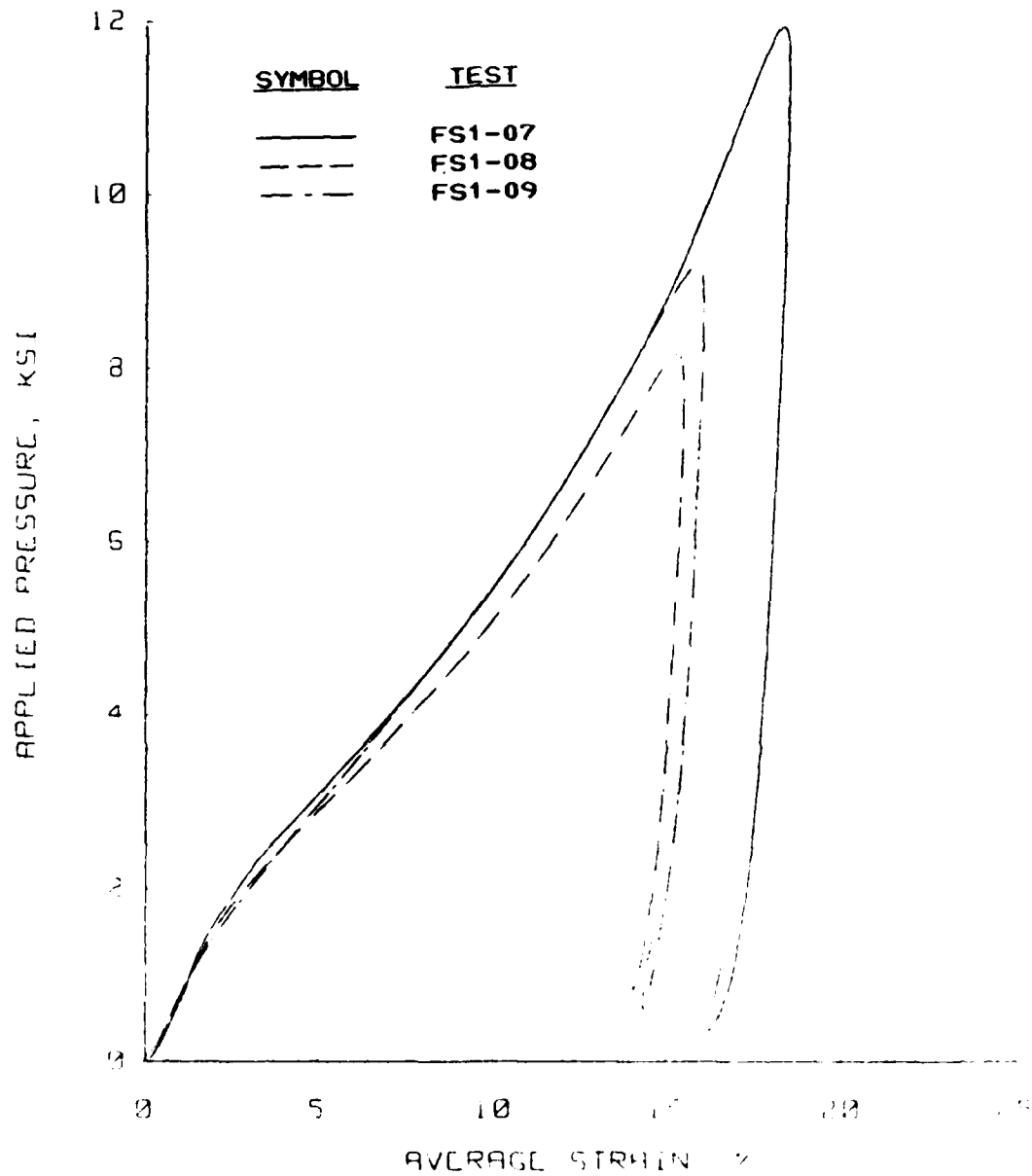Soil Type: Flume Sand

Figure B.30   Static uniaxial strain results for tests performed
in the PPUX device on flume sand.

Uniaxial Strain Results
Soil Type: Flume Sand
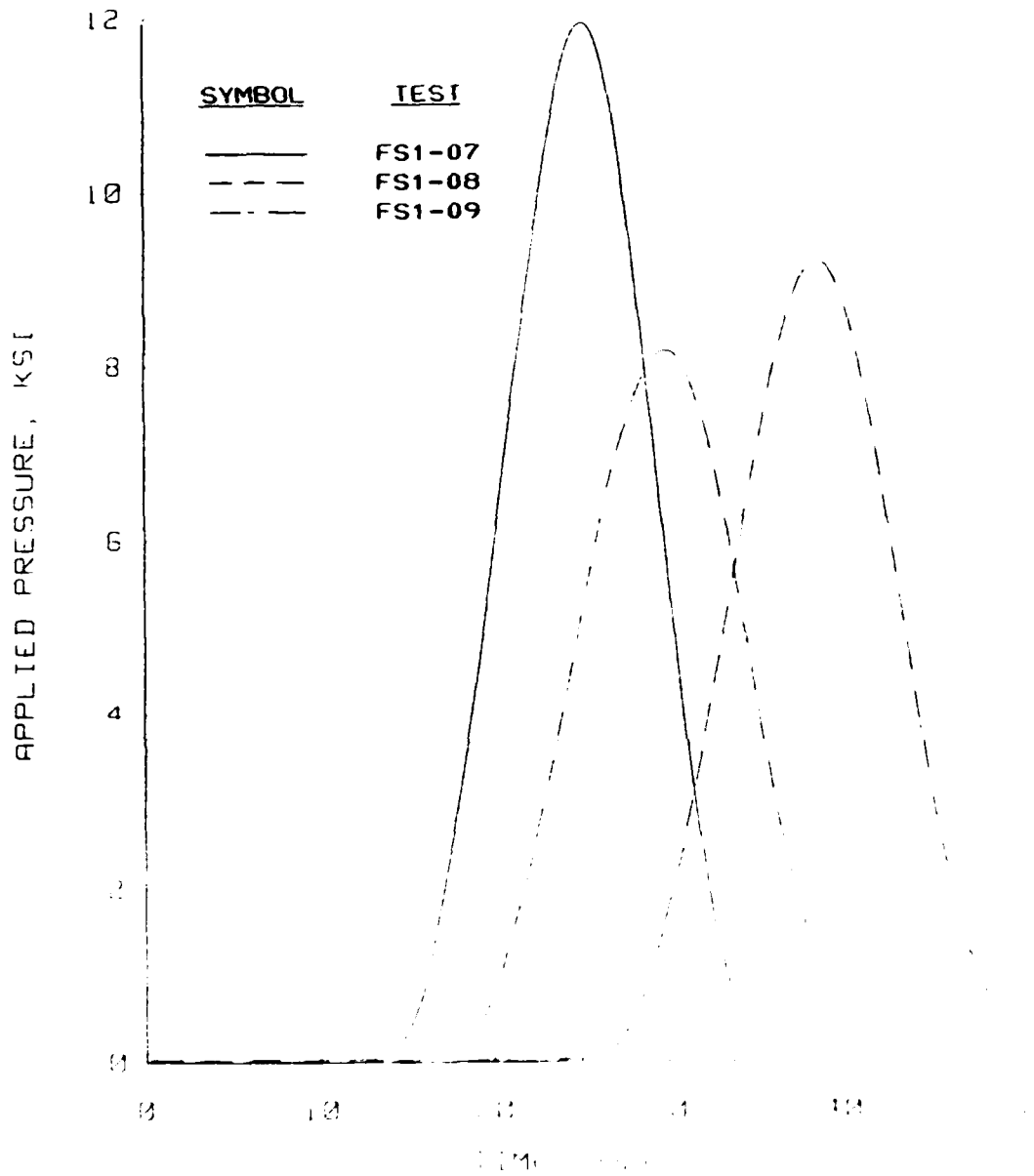

Figure B.31   Pressure versus time plots for the static uniaxial strain test; performed in the PPUX device on flume sand.

Uniaxial Strain Results
Soil Type: Flume Sand
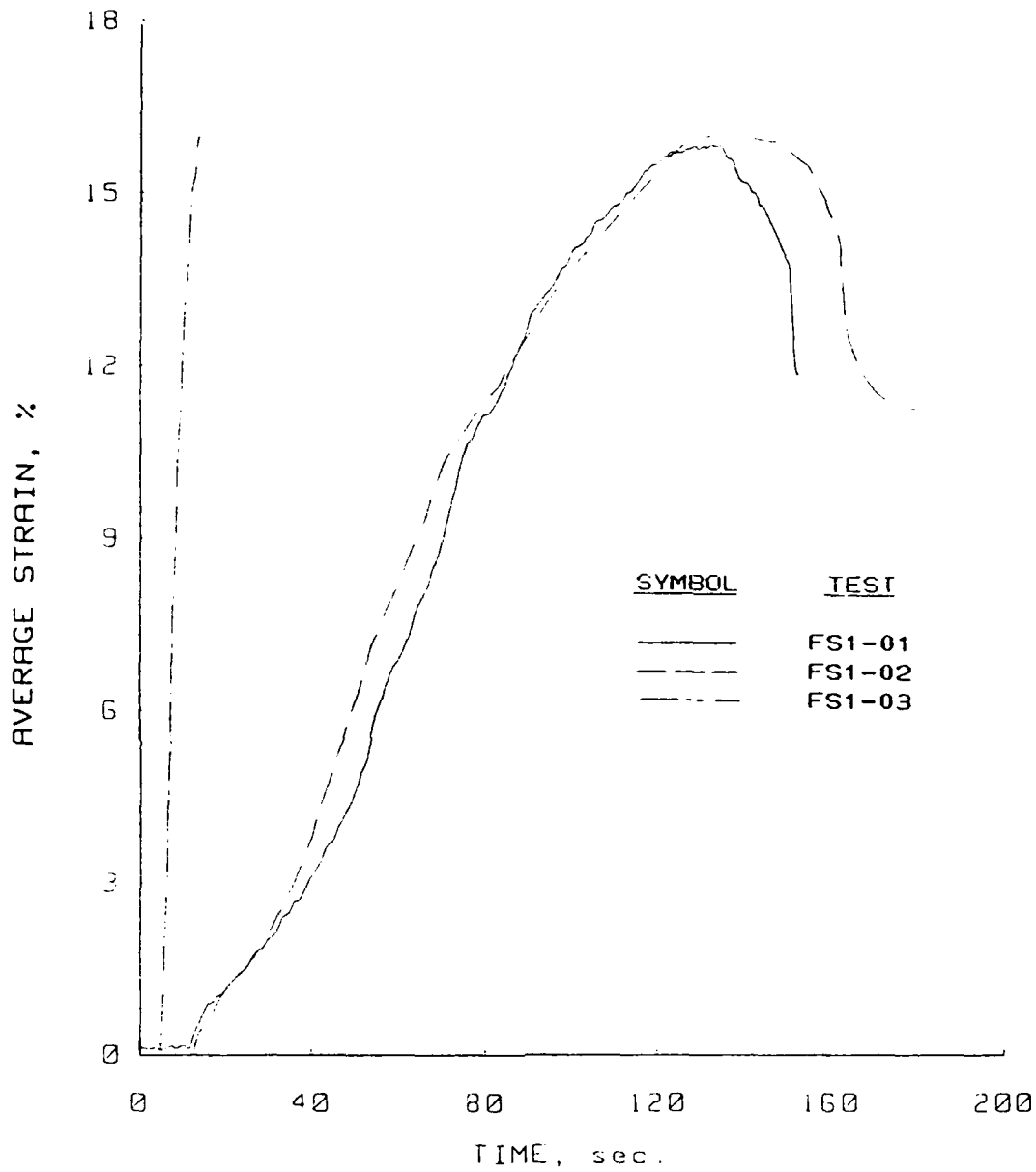
Figure B.32   Strain versus time plots for the static uniaxial strain tests performed in the PPUX device on flume sand.

Uniaxial Strain Results
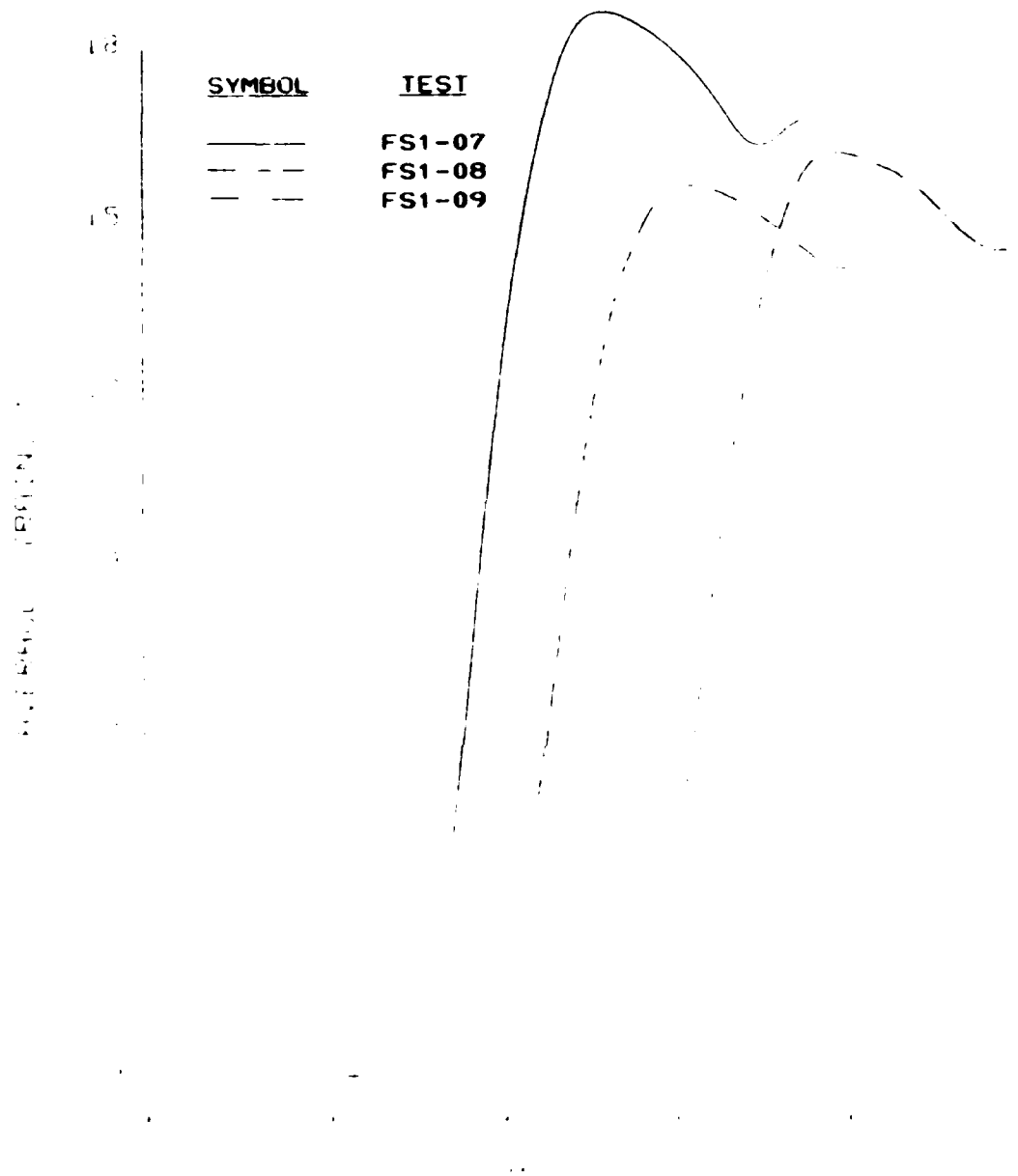### Soil Type: Flume Sand
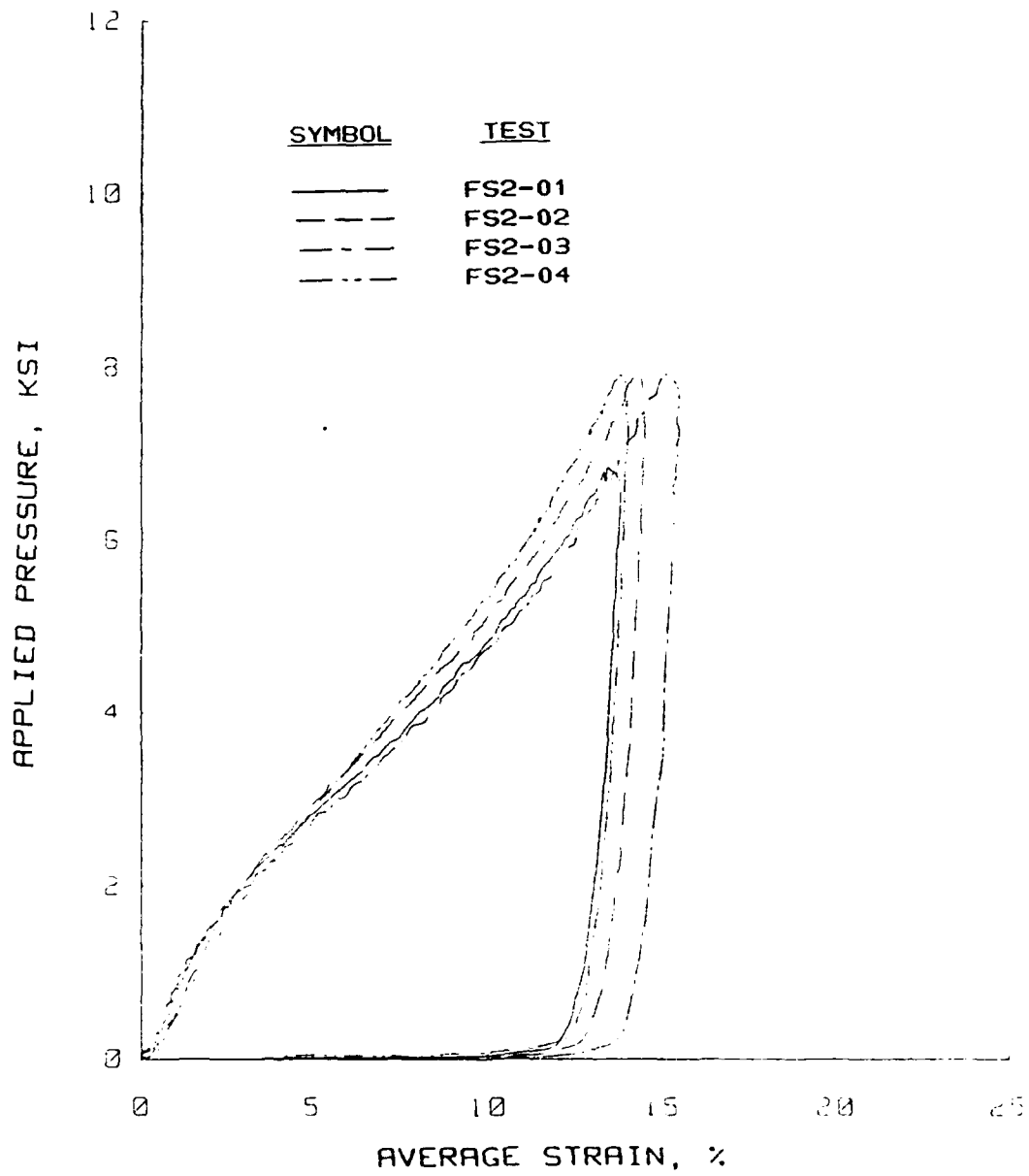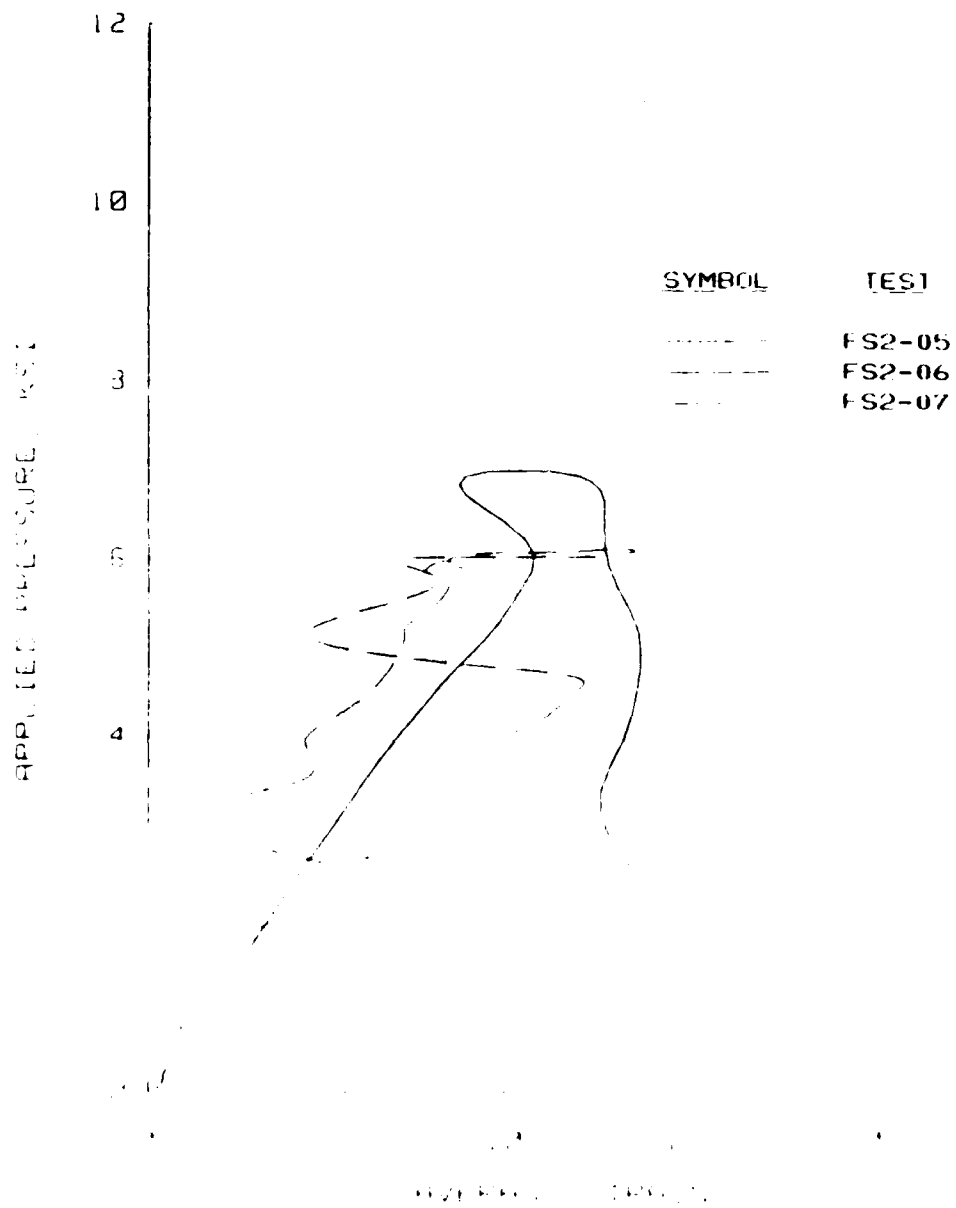

Figure B.33 Static uniaxial strain results for tests performed
in the WES 0.1-msec device on flume sand.
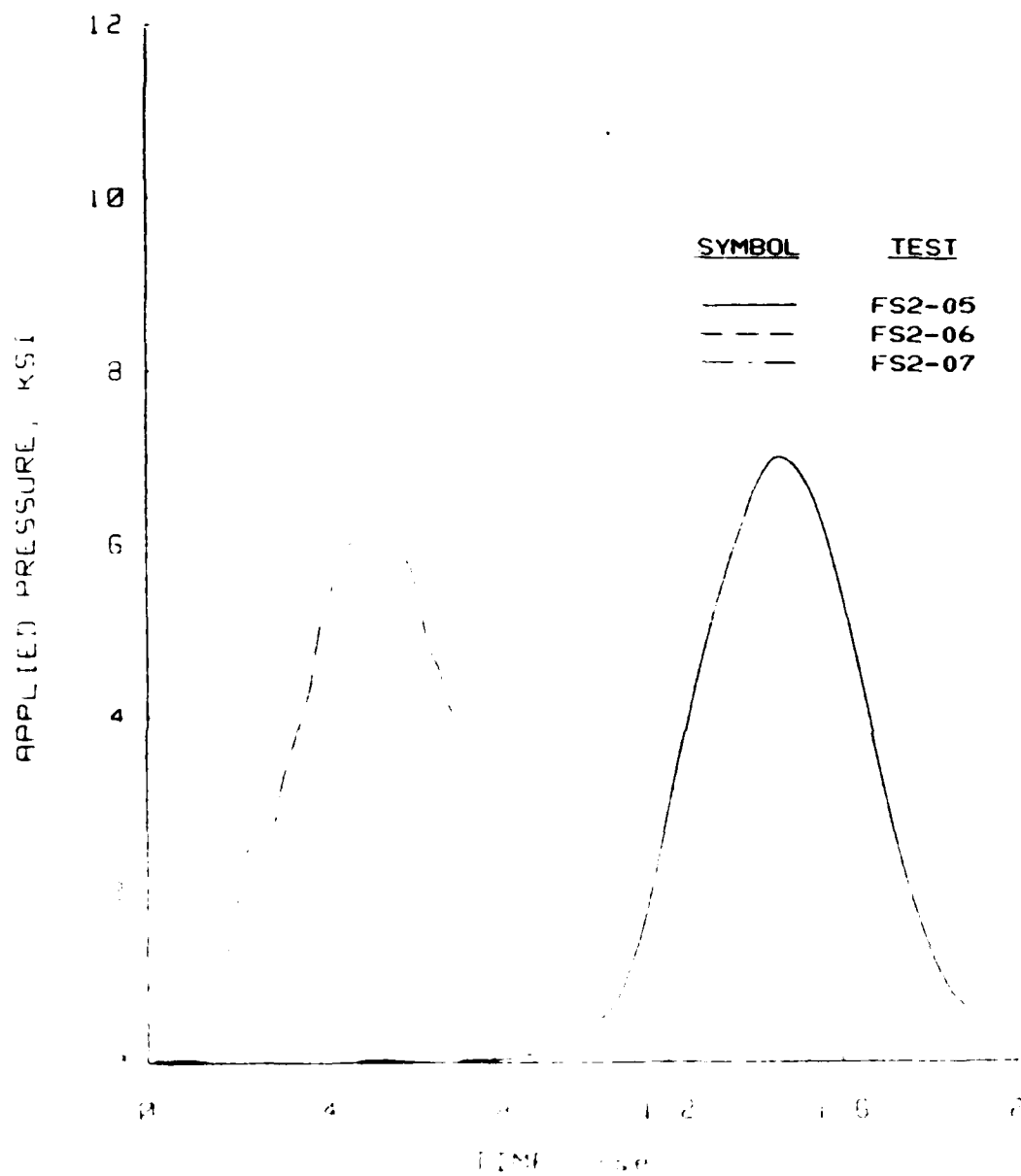
Uniaxial Strain Results
Soil Type: Flume Sand
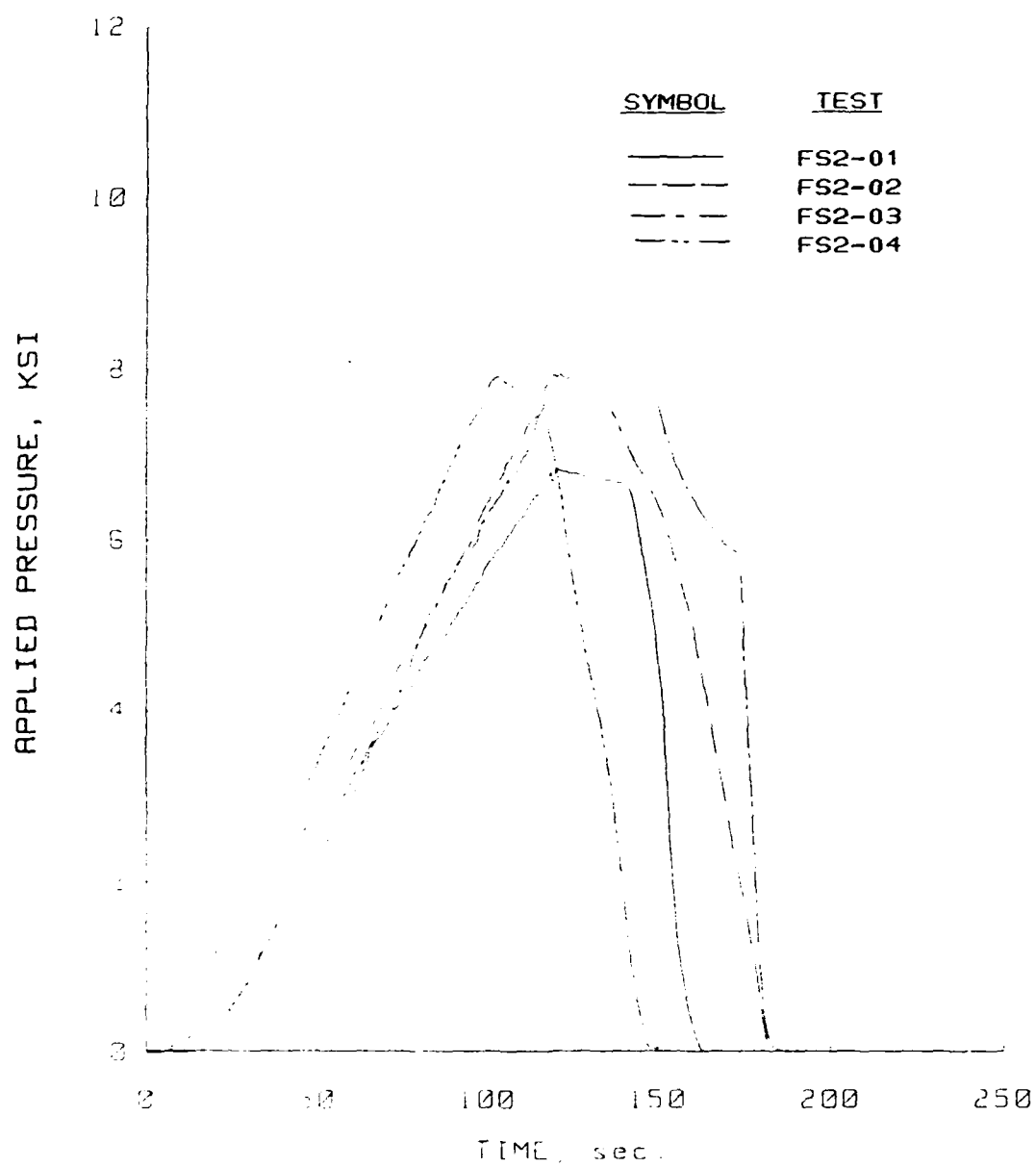
Figure B.34 Pressure versus time plots for the static uniaxial strain tests performed in the WES 0.1-msec device on flume sand.

Uniaxial Strain Results
Soil Type: Flume Sand
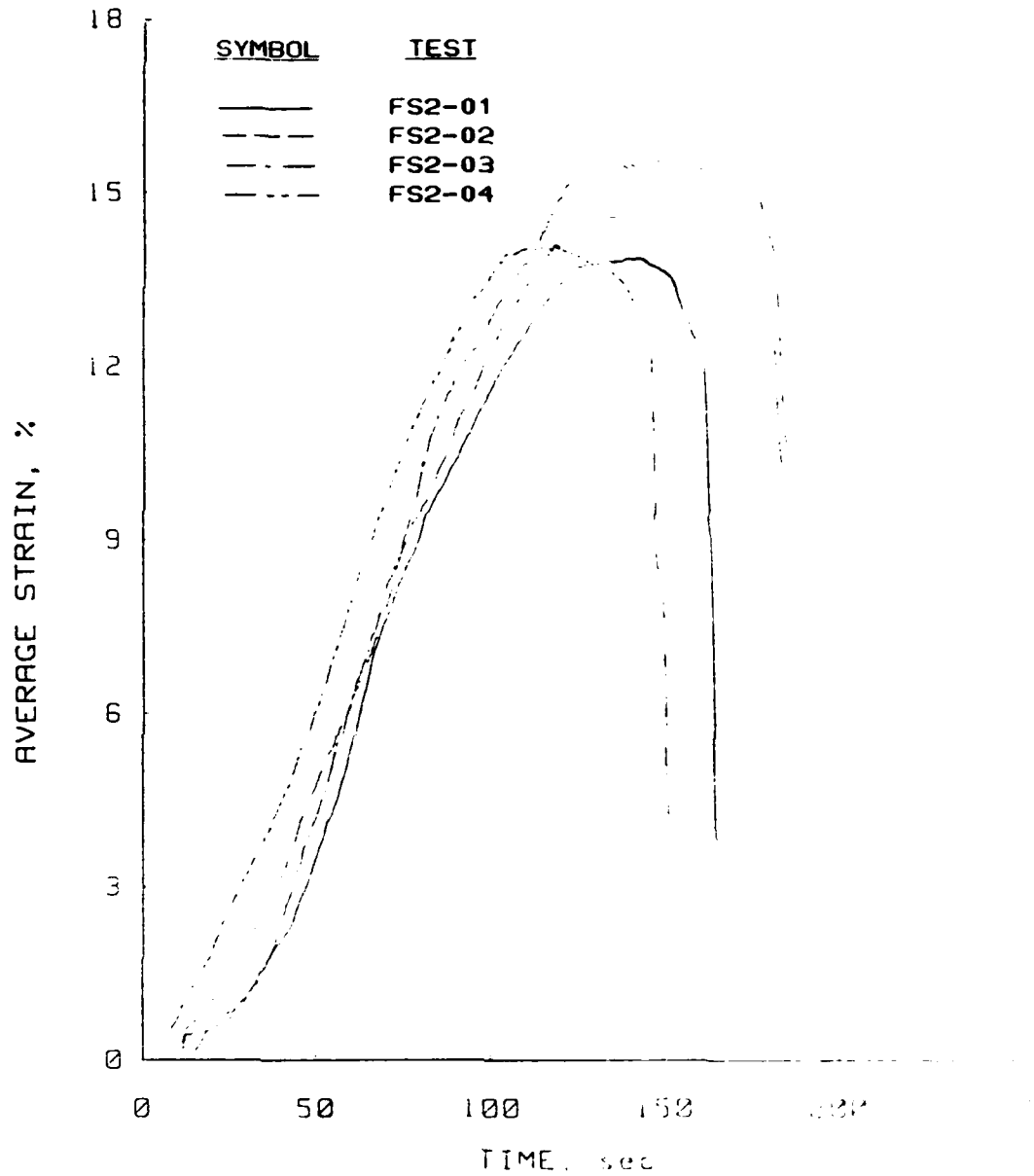
Figure B.35 Strain versus time plots for the static uniaxial strain tests performed in the WES 0.1-msec device on flume sand.
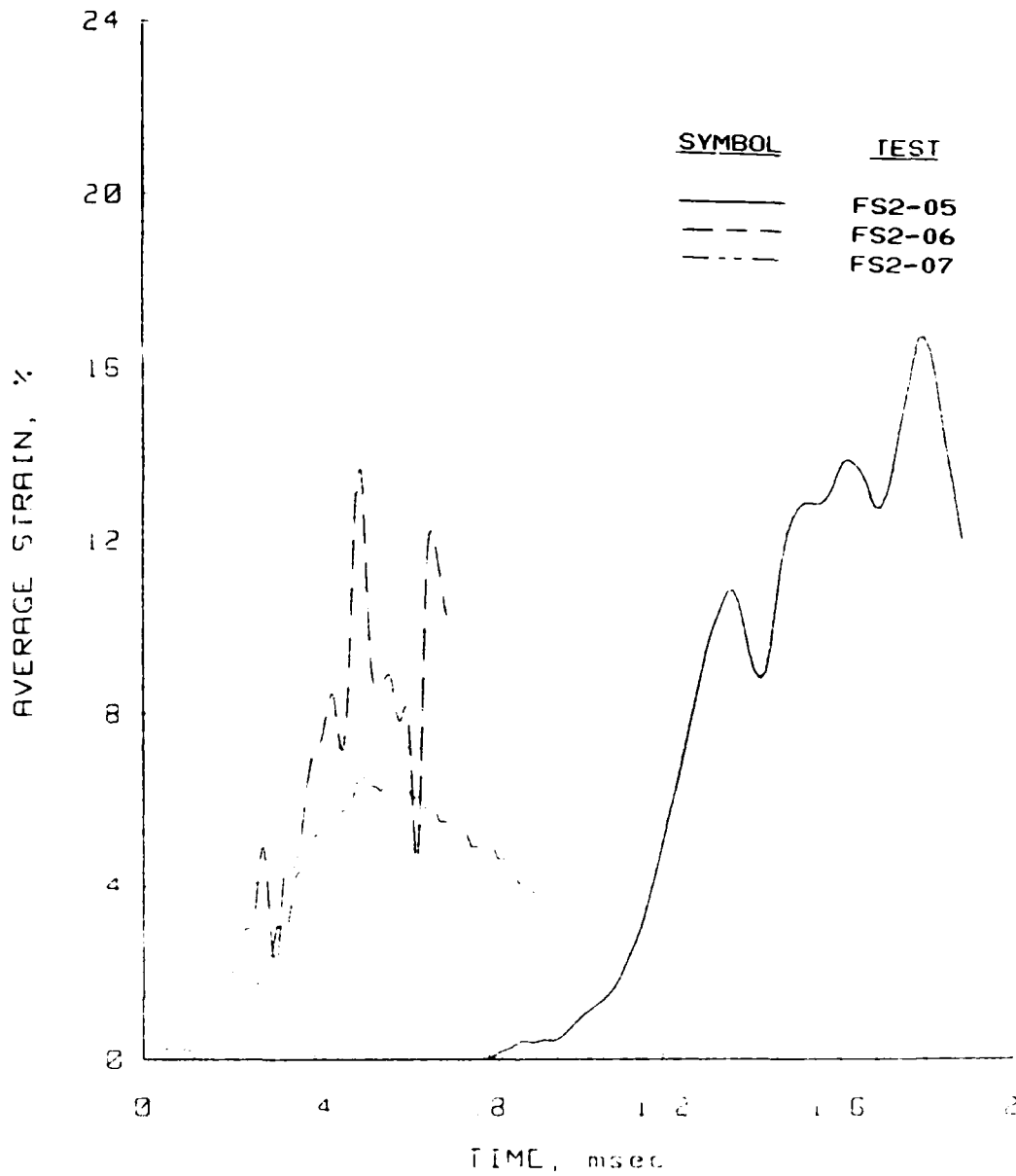
Uniaxial Strain Results
Soil Type: Flume Sand

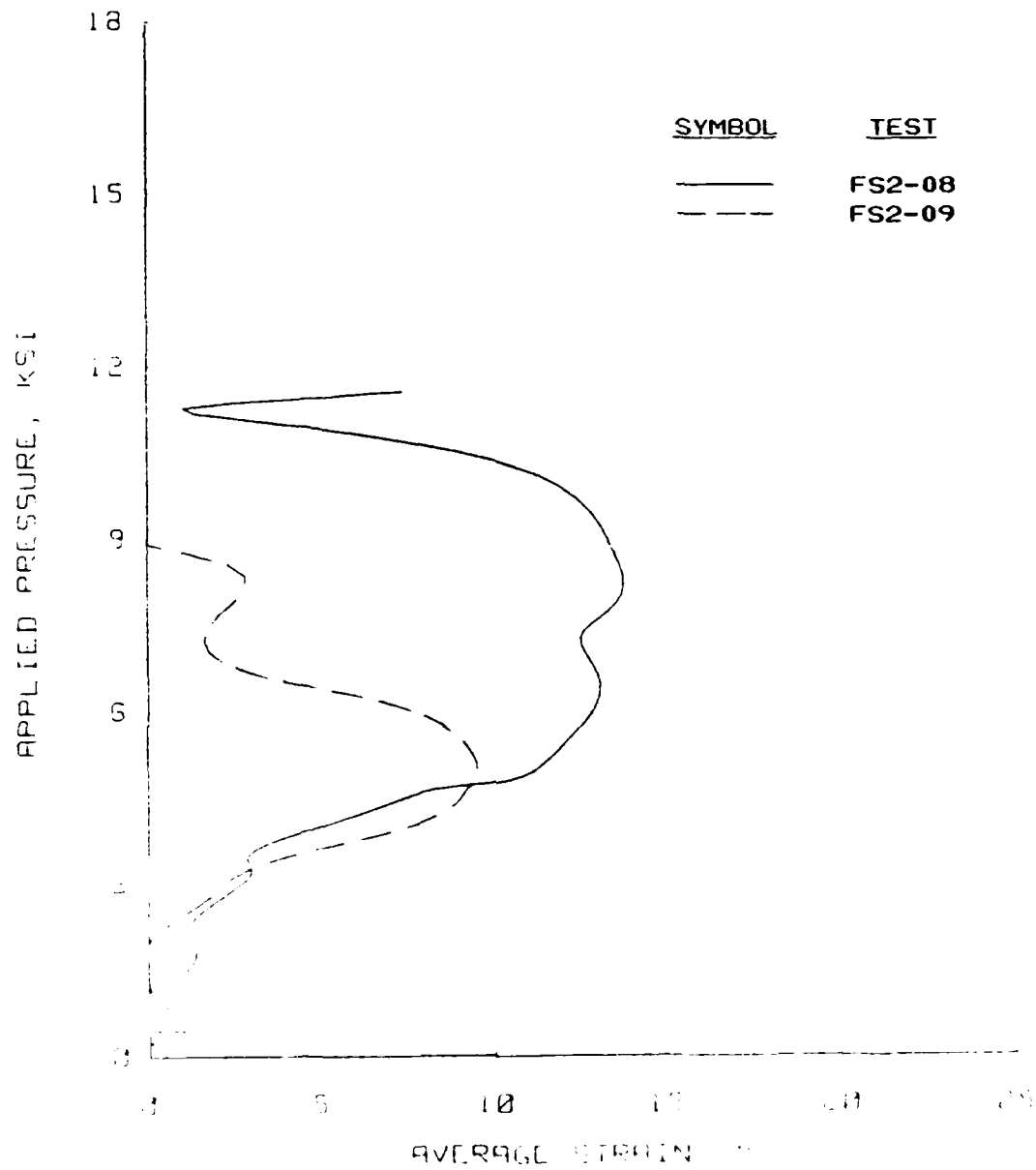| SYMBOL	TEST
———	FS1-04
— — —	FS1-05
— · —	FS1-06

Figure B.36 Slow dynamic uniaxial strain results for tests performed in the PPEX device on flume sand.

Uniaxial Strain Results
Soil Type: Flume Sand

Figure B.37 Pressure versus time plots for the slow dynamic
uniaxial strain tests performed in the PPUX device
on flume sand.

Uniaxial Strain Results
Soil Type: Flume Sand
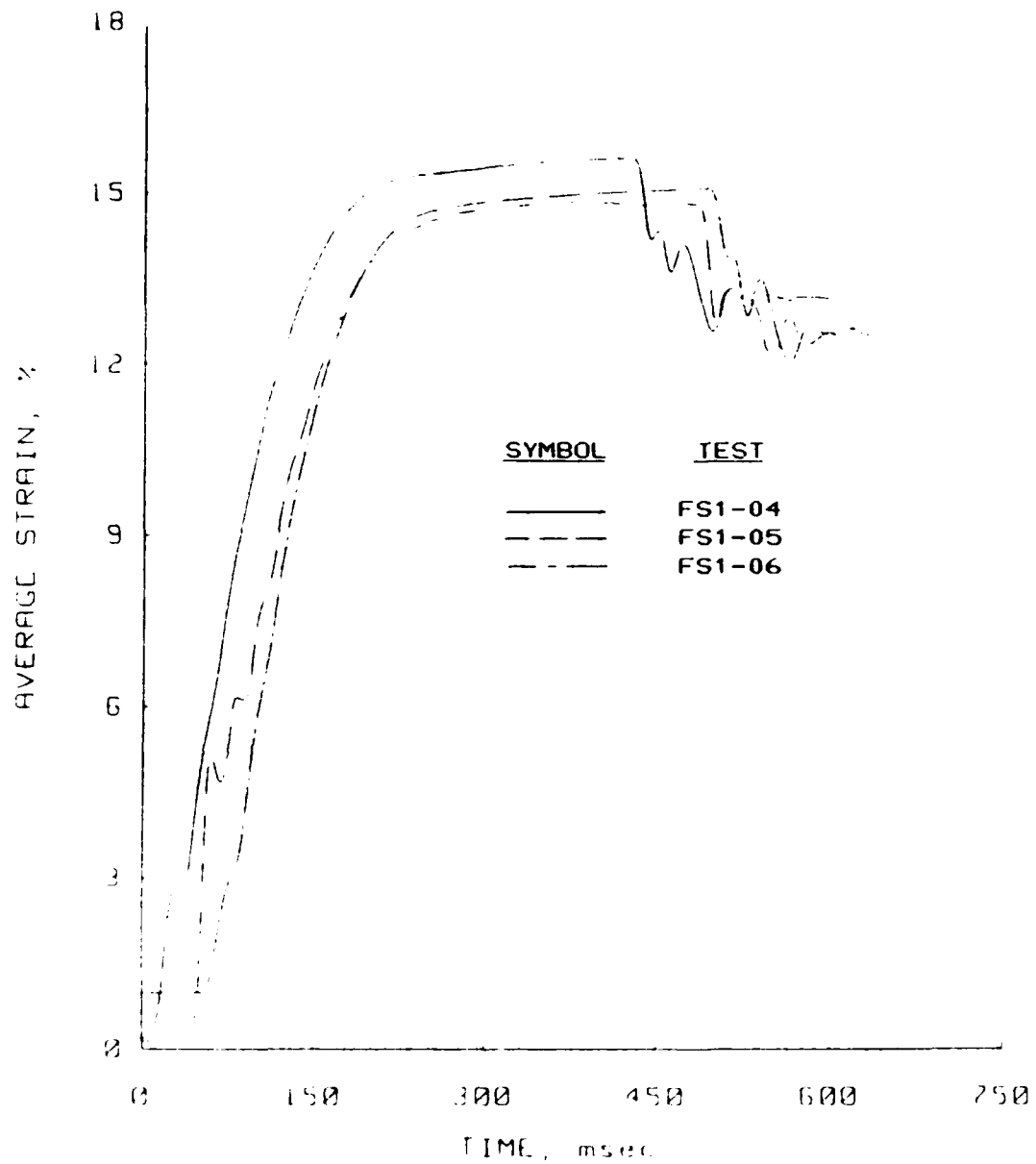
Figure B. 58   Strain versus time plots for the slow dynamic uniaxial strain tests performed in the PPUX device on flume sand.

Uniaxial Strain Results
Soil Type: Flume Sand

Figure B.39 Dynamic uniaxial strain results for tests performed in the PPUX device on flume sand.
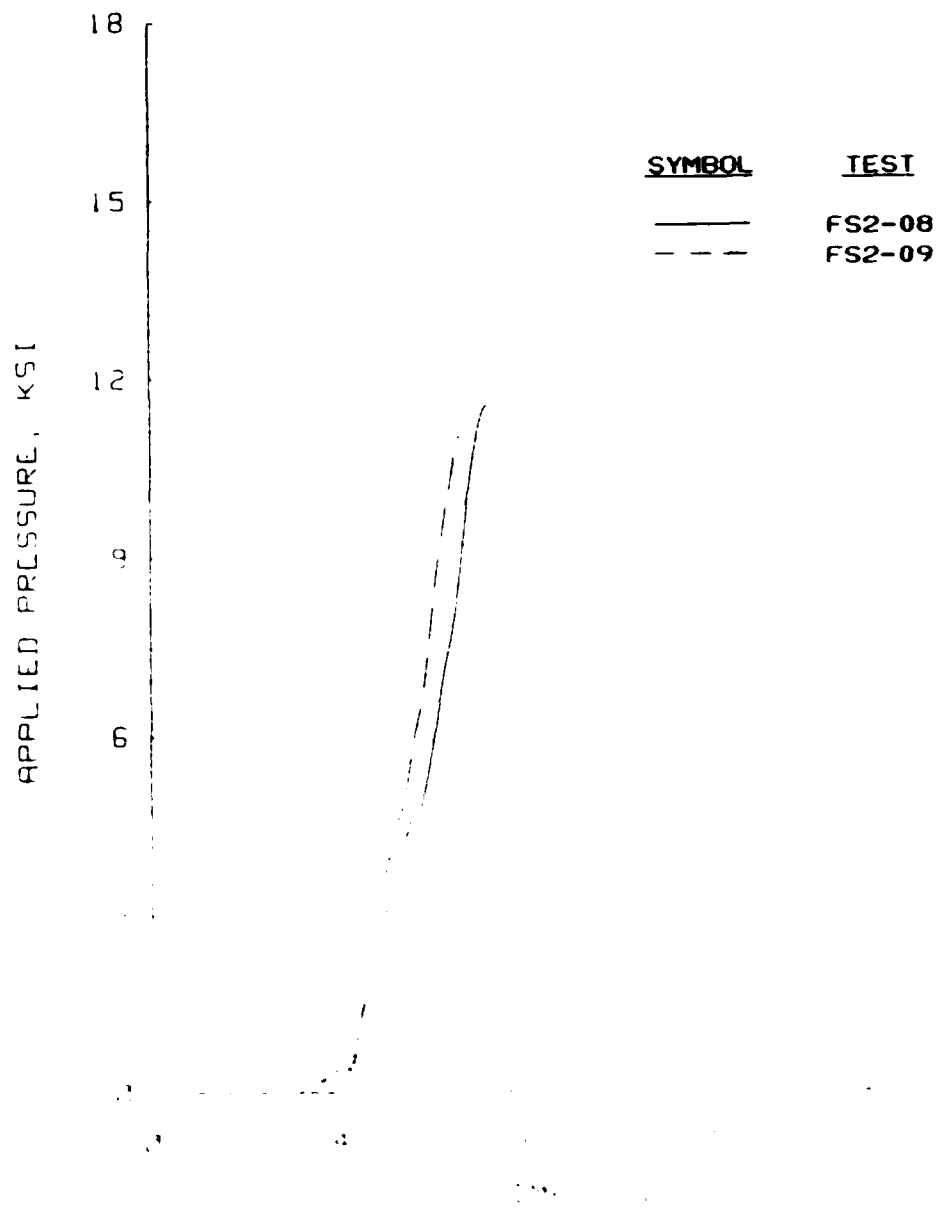
Uniaxial Strain Results
Soil Type: Flume Sand

Figure B.40   Pressure versus time plots for the dynamic
uniaxial strain tests performed in the PPUX device
on flume sand.

Uniaxial Strain Results
Soil Type: Flume Sand
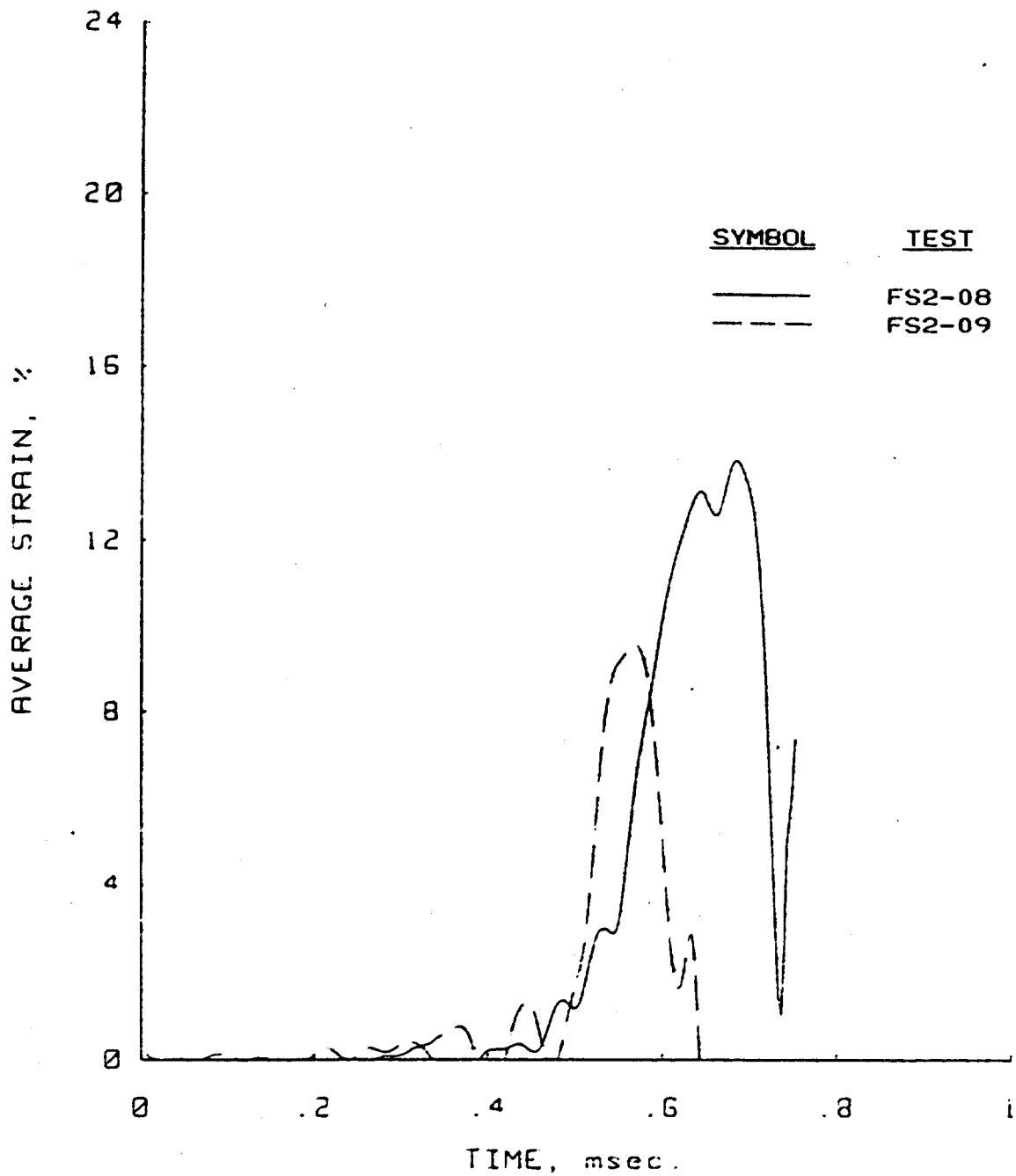

Figure B.41 Strain versus time plots for the dynamic uniaxial strain tests performed in the PPUX device on flume sand.

Uniaxial Strain Results
Soil Type: Flume Sand

Figure B.42 Dynamic uniaxial strain results for tests FS2-05, -06, and -07 performed in the WFS 0.1 msec device on flume sand.

Uniaxial Strain Results
Soil Type: Flume Sand

Figure B.43 Pressure versus time plots for dynamic uniaxial
strain tests FS2-05, -06, and -07 performed in the
WES 0.1-msec device on flume sand.

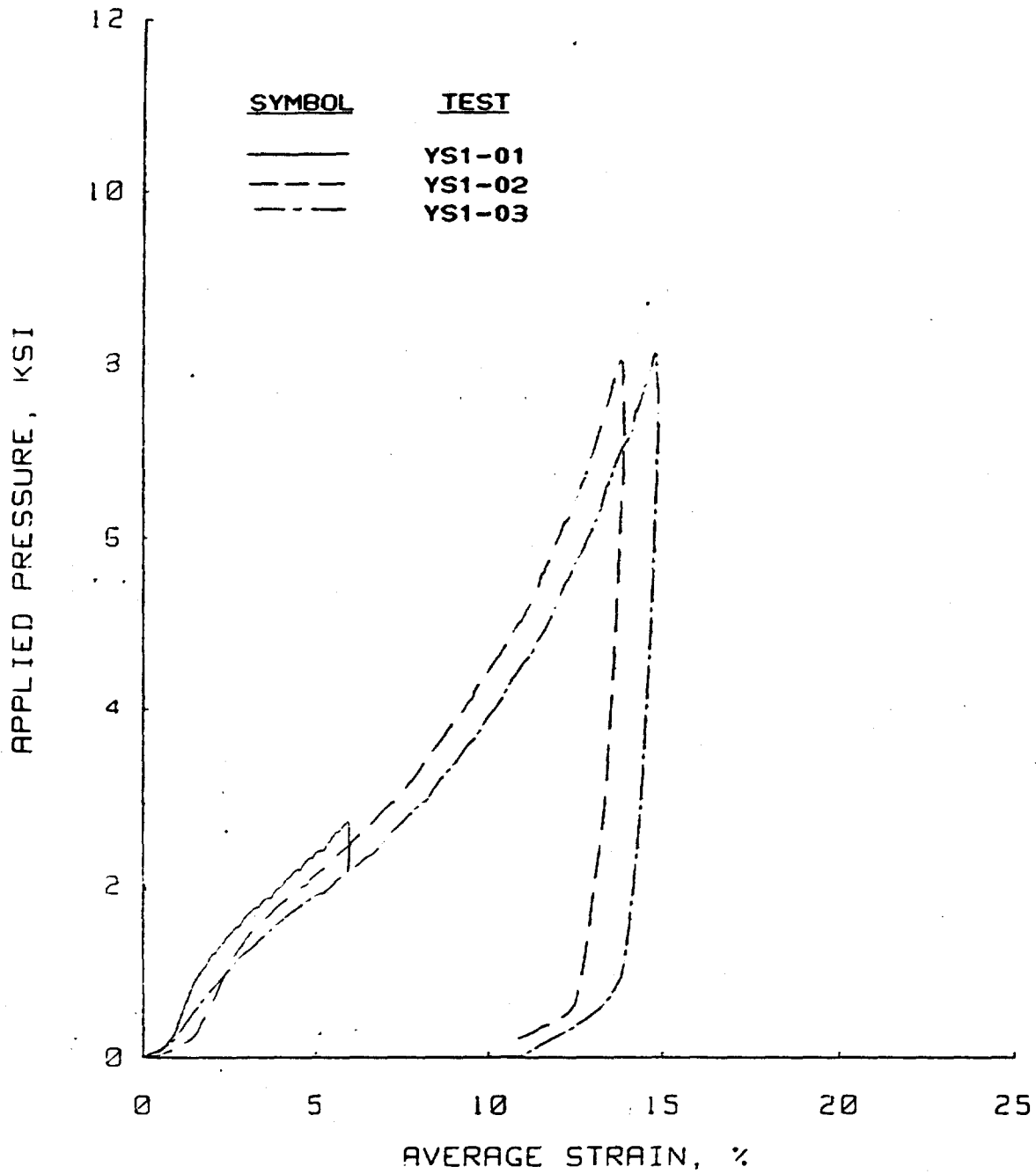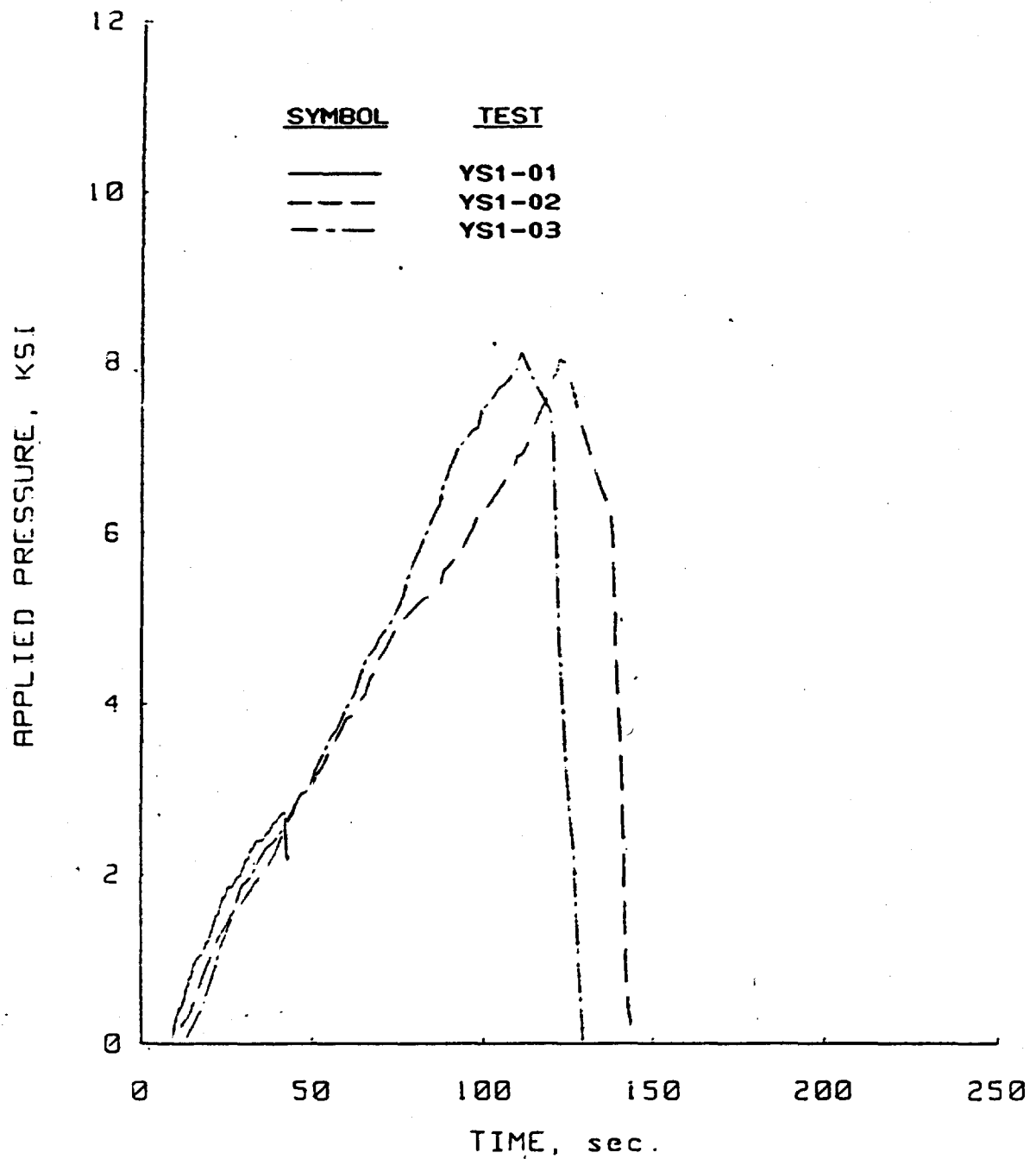# Uniaxial Strain Results
Soil Type: Flume Sand

Figure B.44 Strain versus time plots for dynamic uniaxial strain tests FS2-05, -‹6, and -07 performed in the WES 0.1-msec device on flume sand.

Figure B.45   Dynamic uniaxial strain results for tests FS2-08
and -09 performed in the WES 0.1-r sec device on
flume sand.

Uniaxial Strain Results
Soil Type: Flume Sand

Figure B.46 Pressure versus time plots for uniaxial uniaxial strain tests FS2-08 and 09 performed on the at rel msec device on flume sand

Uniaxial Strain Results
Soil Type: Flume Sand

Figure B.47   Strain versus time plots for dynamic uniaxial
strain tests FS2-08 and -09 performed in the WES
0.1-msec device on flume sand.

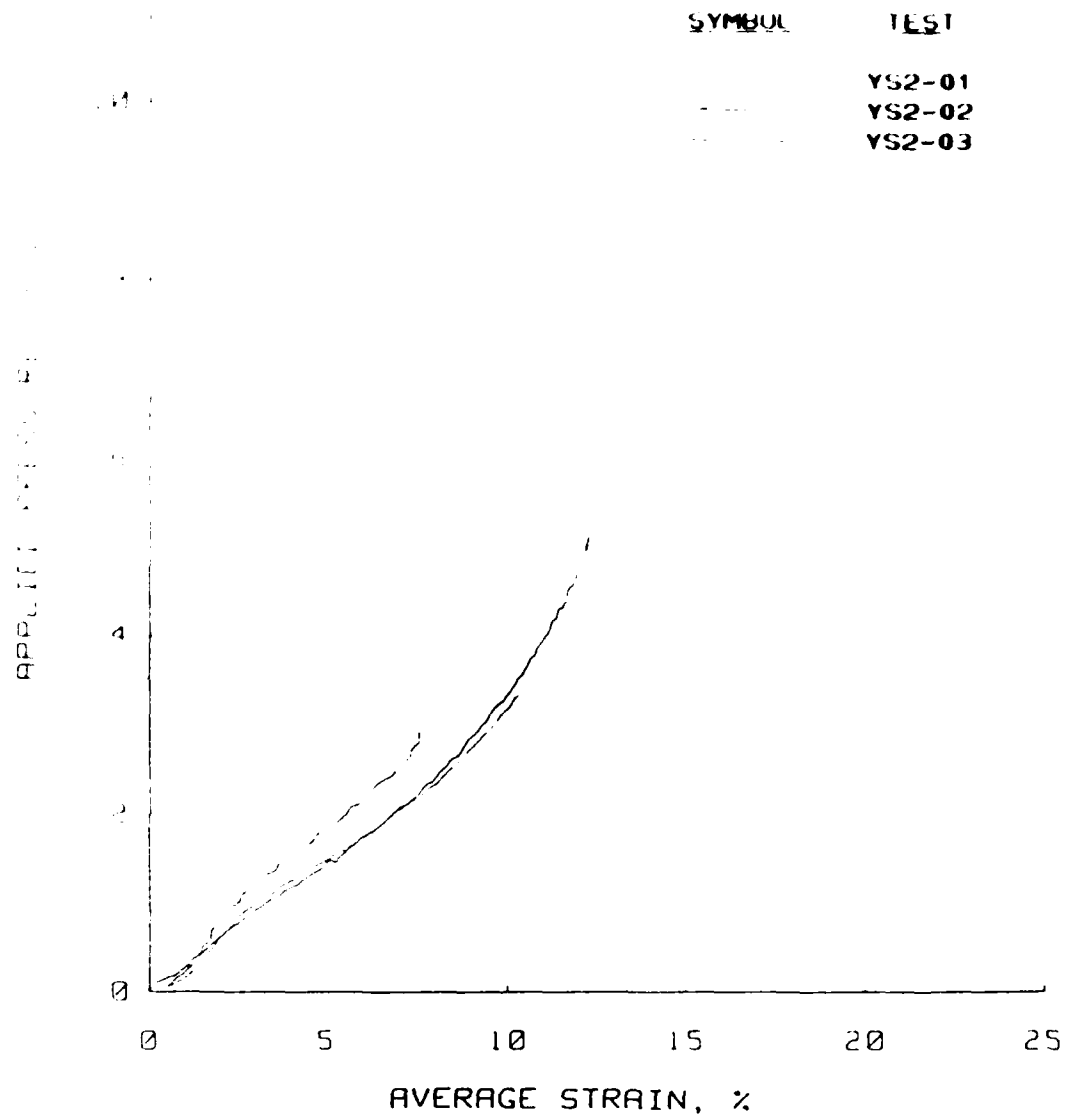# Uniaxial Strain Results
Soil Type: Yuma Clayey Sand

Figure B.48 Static uniaxial strain results for tests performed
in the PPUX device on Yuma clayey sand.
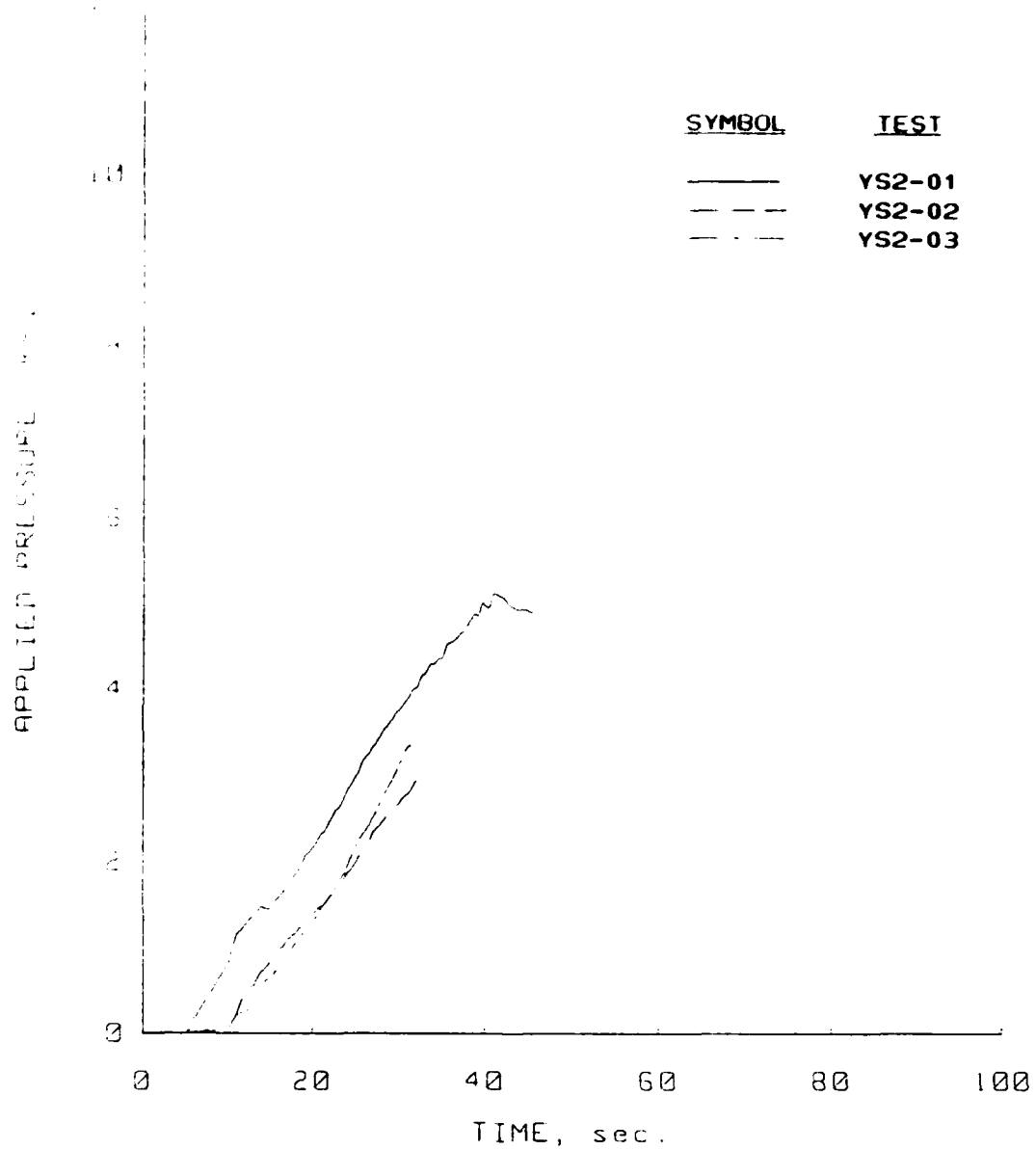
Uniaxial Strain Results
Soil Type: Yuma Clayey Sand

Figure B.49   Pressure versus time plots for the static uniaxial strain tests performed in the PPUX device on Yuma clayey sand.
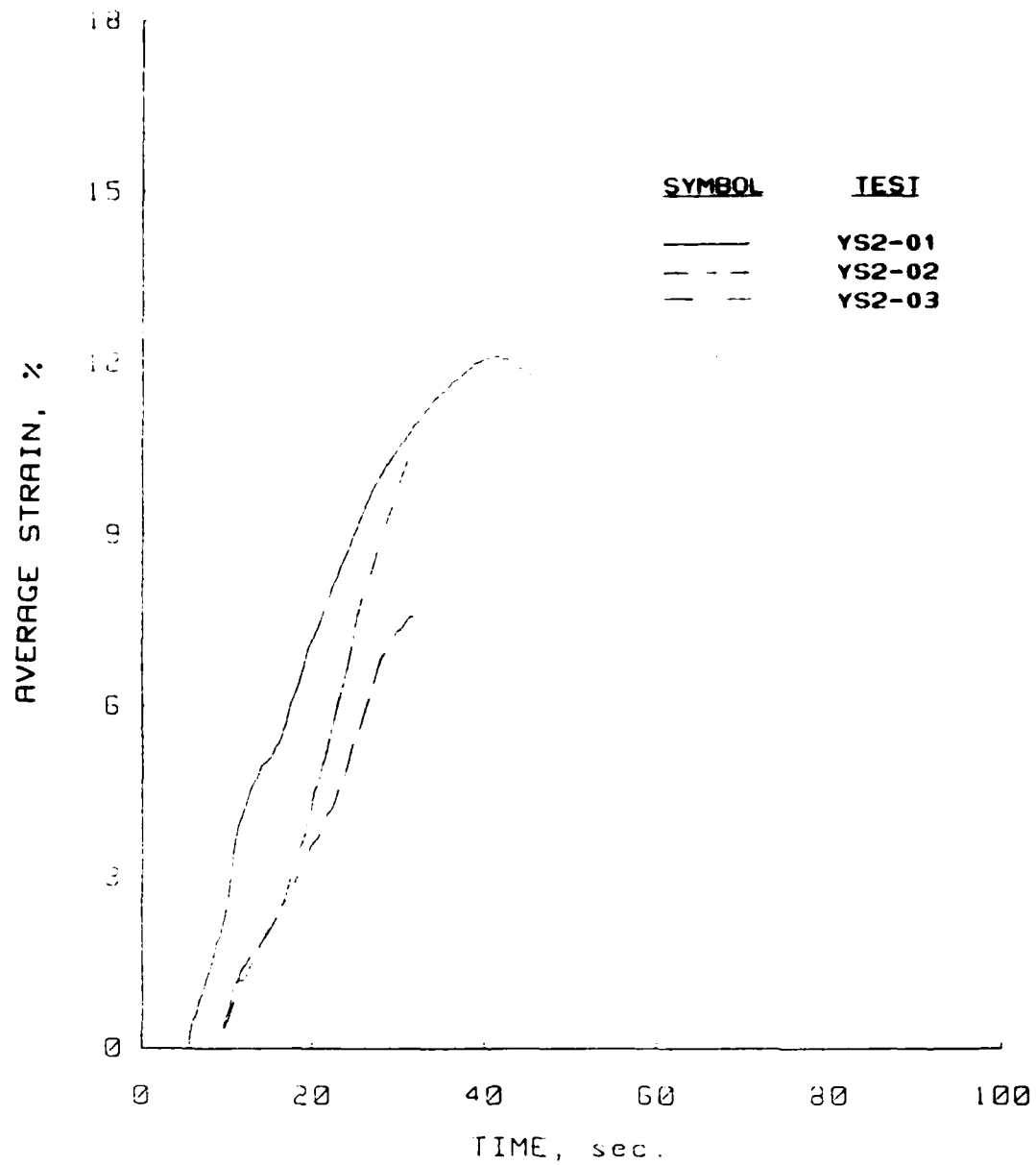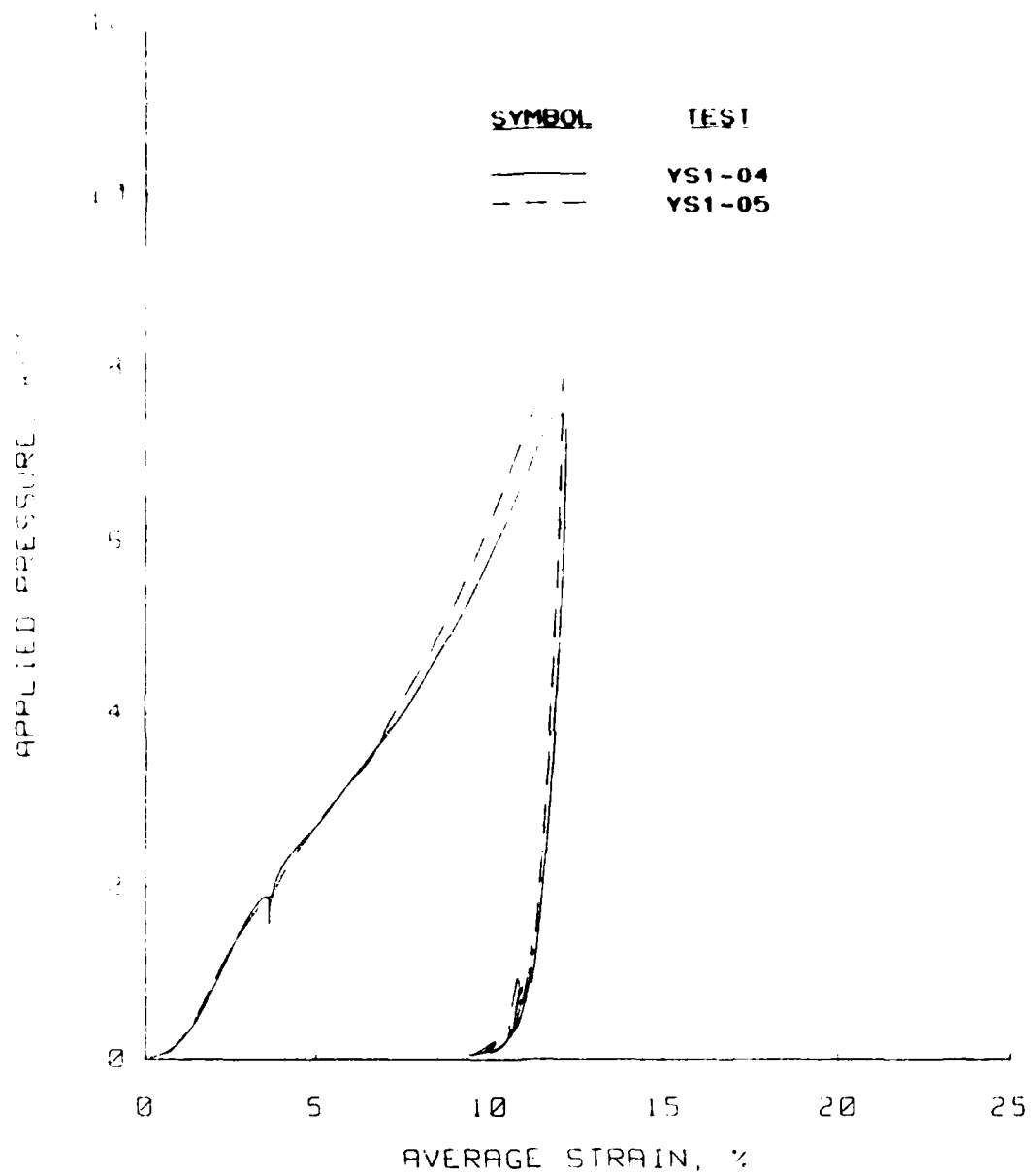
Uniaxial Strain Results
Soil Type: Yuma Clayey Sand

SYMBOL	TEST
————	YS1-01
————	YS1-02
—·——	YS1-03
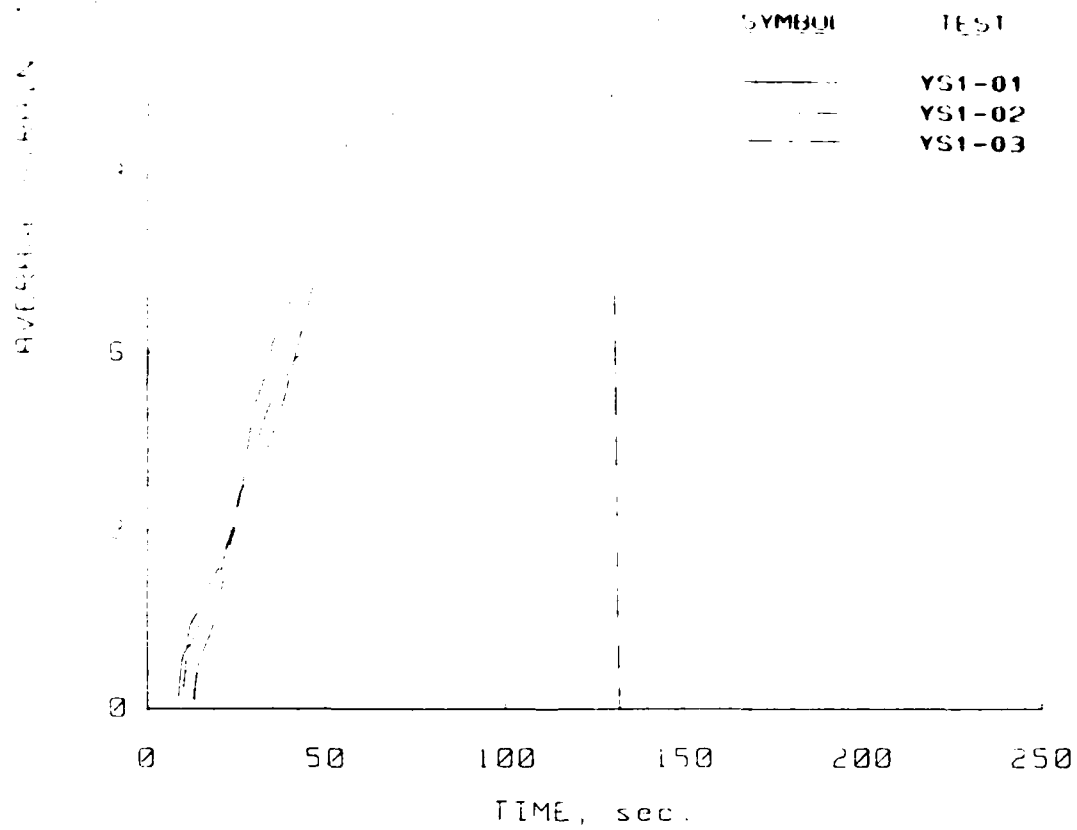
Figure B.50   Strain versus time plots for the static uniaxial strain tests performed in the PPUX device on Yuma clayey sand.

Uniaxial Strain Results
Soil Type: Yuma Clayey Sand

SYMBOL	TEST
	YS2-01
— —	YS2-02
	YS2-03

AVERAGE STRAIN, %

Figure B.51 Static uniaxial strain results for tests performed
in the WES 0.1-msec device on Yuma clayey sand.

Uniaxial Strain Results
Soil Type: Yuma Clayey Sand

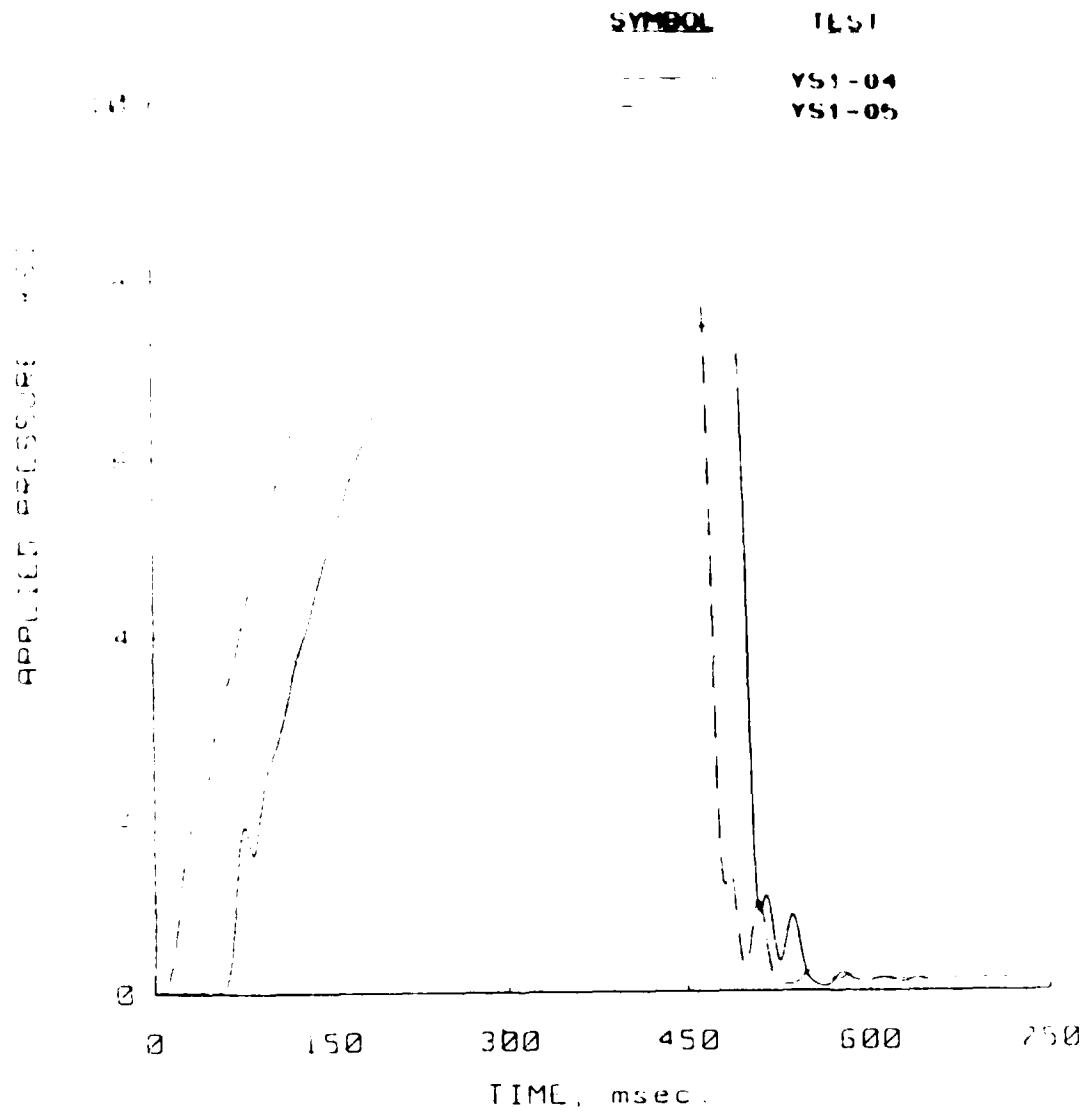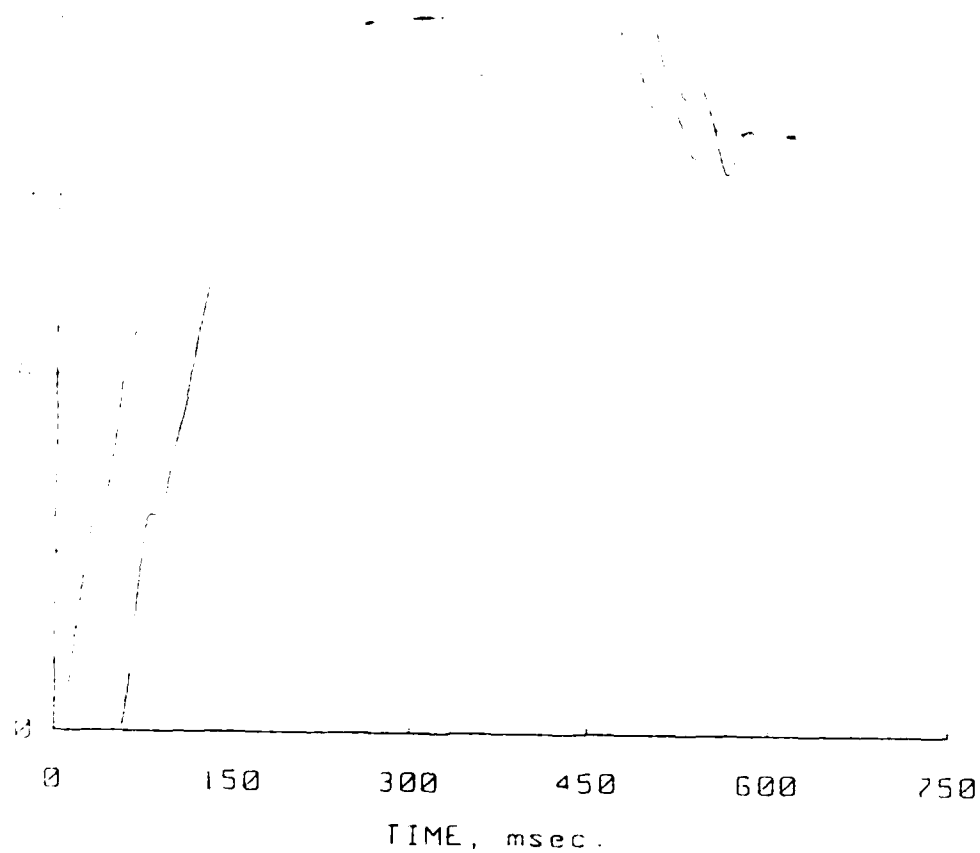| SYMBOL	TEST
————	YS2-01
— — —	YS2-02
— · —	YS2-03

Figure B.52 Pressure versus time plots for the static uniaxial strain tests performed in the WES 0.1-msec device on Yuma clayey sand.

Uniaxial Strain Results
Soil Type: Yuma Clayey Sand

Figure B.53 Strain versus time plot for the static uniaxial-
strain tests performed in the WES 0.1-msec device
on Yuma clayey sand.

Uniaxial Strain Results
Soil Type: Yuma Clayey Sand

Figure B.54   Slow dynamic uniaxial strain results for tests
performed in the PPUX device on Yuma clayey sand.

Uniaxial Strain Results
Soil Type: Yuma Clayey Sand

SYMBOL	TEST
---	YS1-04
—	YS1-05

TIME, msec.

Figure B.55   Pressure versus time plots for the slow dynamic
             uniaxial strain tests performed in the PPUX device
             on Yuma clayey sand.

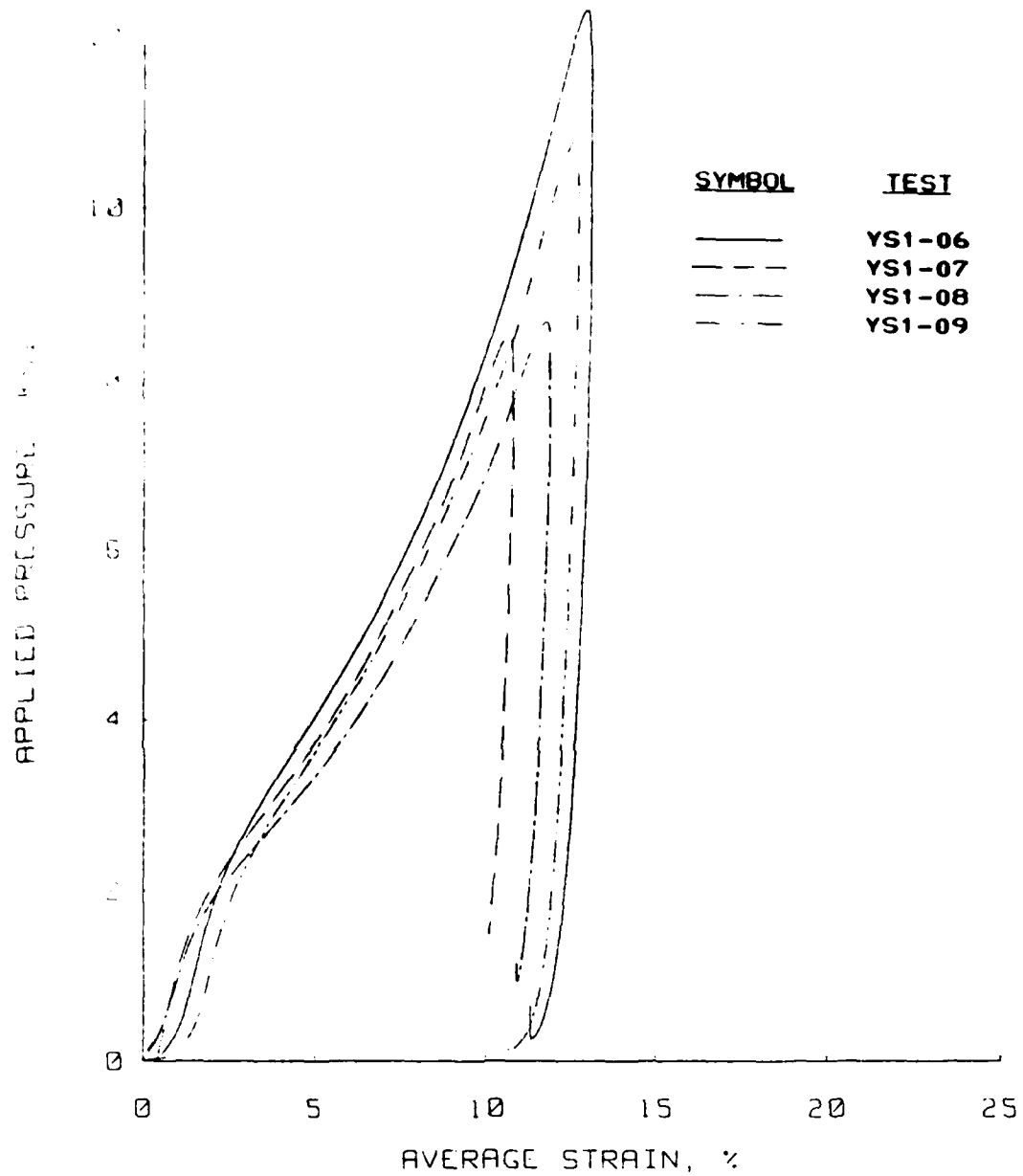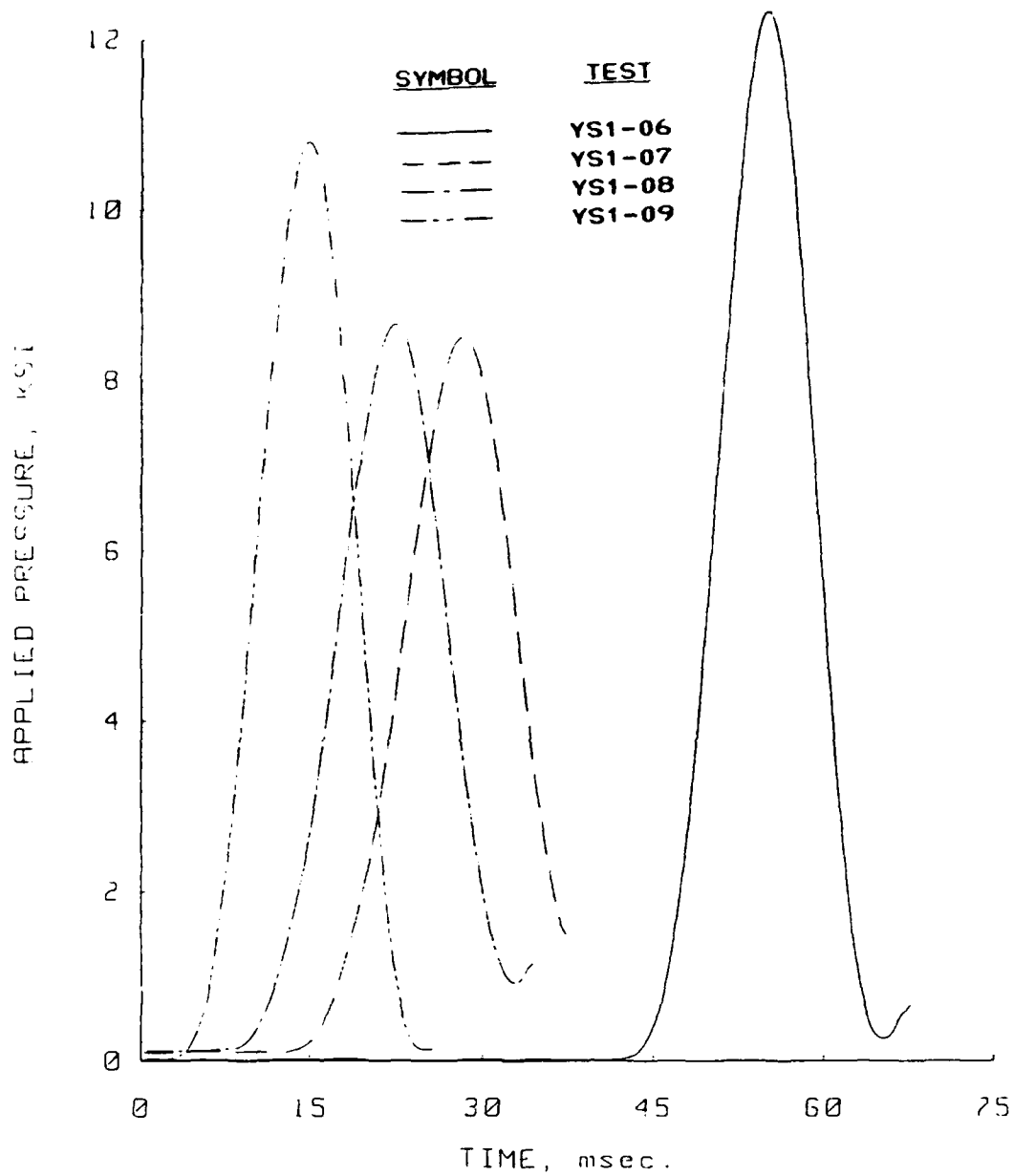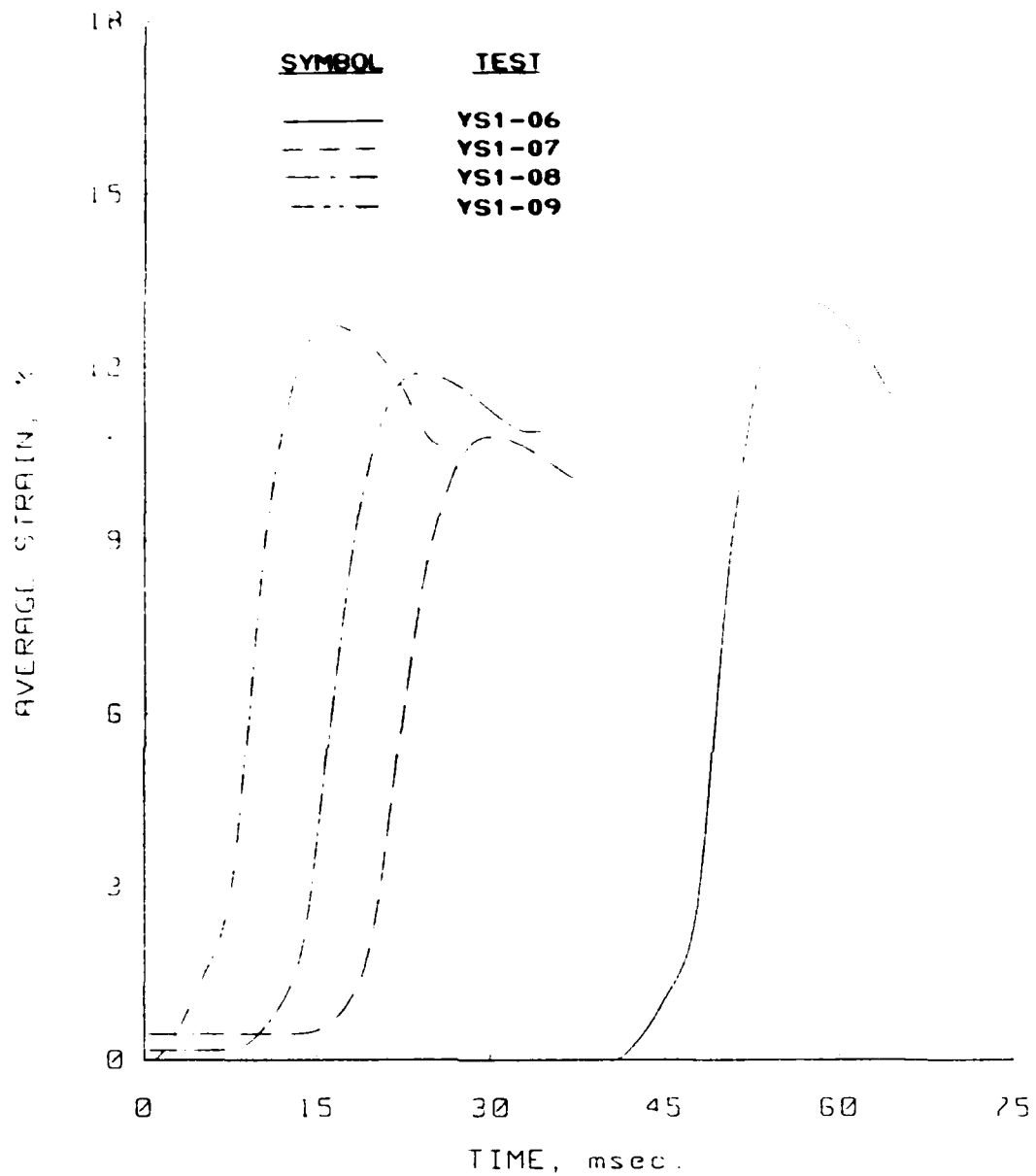Uniaxial Strain Results
Soil Type: Yuma Clayey Sand

SYMBOL	TEST
————	YS1-04
- — —	YS1-05

TIME, msec.

0   150   300   450   600   750

Figure B.56   Strain versus time plots for the slow dynamic
uniaxial strain tests performed in the PPUX device
on Yuma clayey sand.

Figure B.57   Dynamic uniaxial strain results for tests performed
in the PPUX device on Yuma clayey sand.

Uniaxial Strain Results
Soil Type: Yuma Clayey Sand

Figure B.58   Pressure versus time plots for the dynamic
uniaxial strain tests performed in the PPUX device
on Yuma clayey sand.
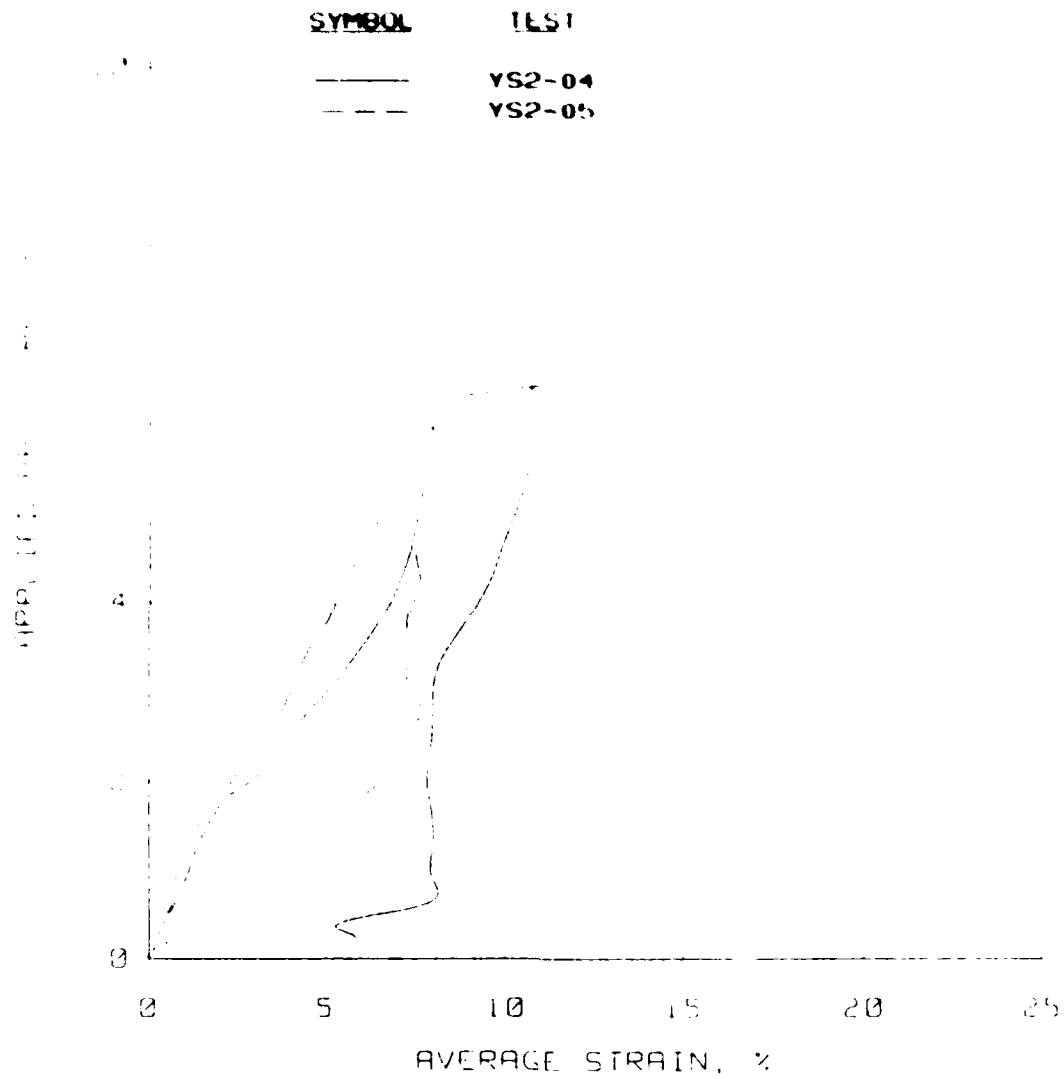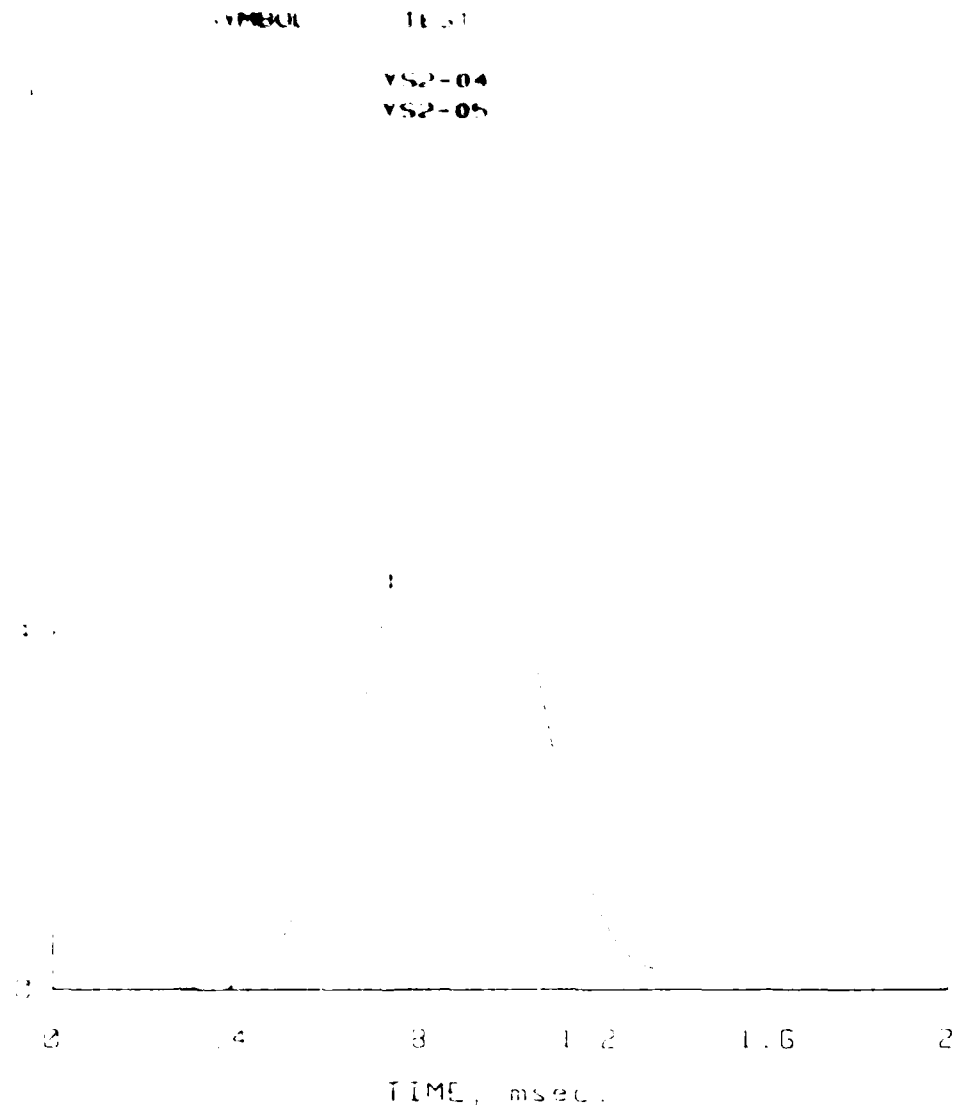
Uniaxial Strain Results
Soil Type: Yuma Clayey Sand

Figure B.59   Strain versus time plots for the dynamic uniaxial
strain tests performed in the PPUX device on Yuma
clayey sand.

Uniaxial Strain Results
Soil Type: Yuma Clayey Sand

SYMBOL	TEST
———	YS2-04
— — —	YS2-05

AVERAGE STRAIN, %

Figure B.60 Dynamic uniaxial strain results for tests YS2-04
and -05 performed in the WES 0.1-msec device on
Yuma clayey sand.

Uniaxial Strain Results
Soil Type: Yuma Clayey Sand

SYMBOL   Test

                YS2-04
                YS2-05
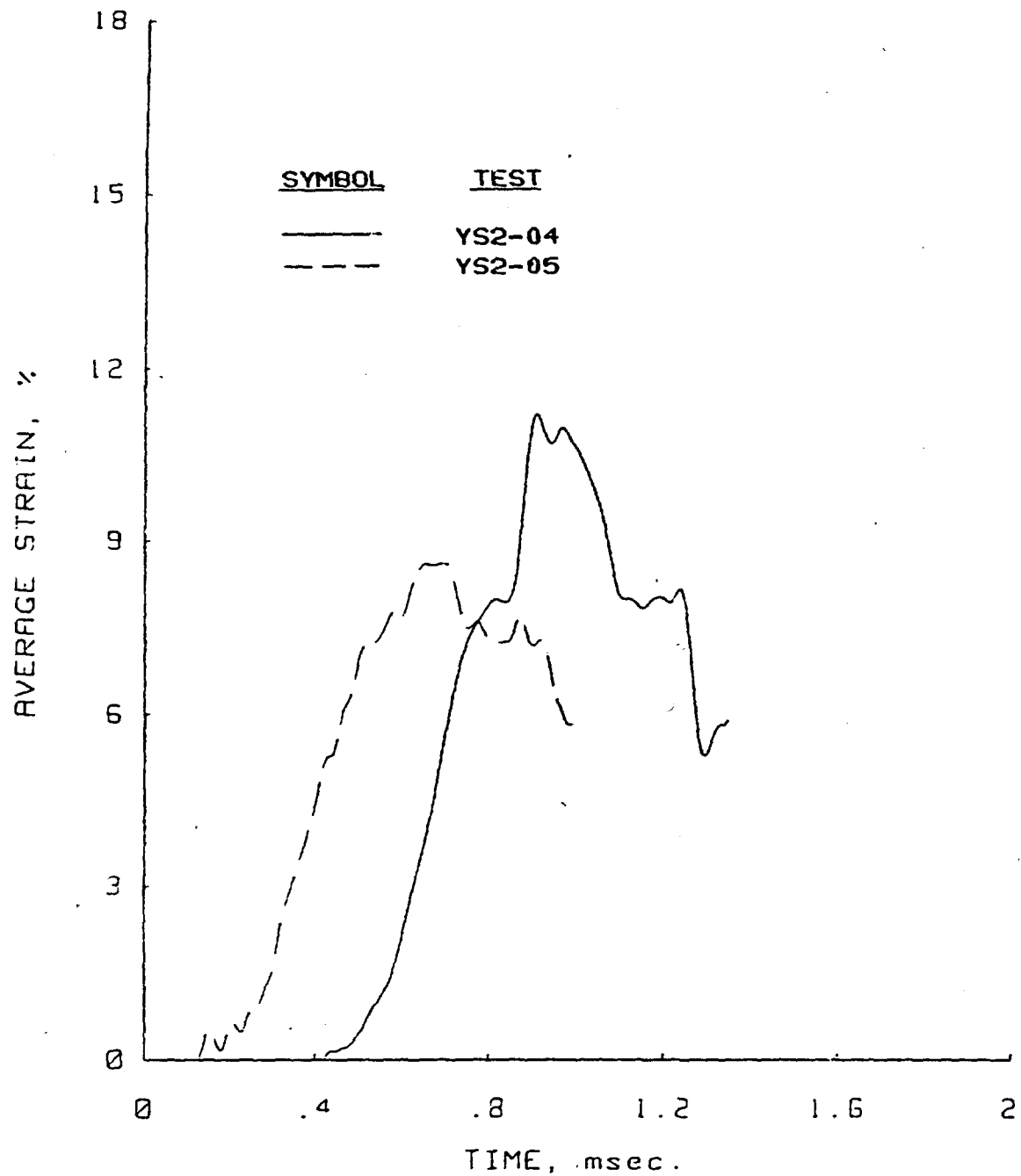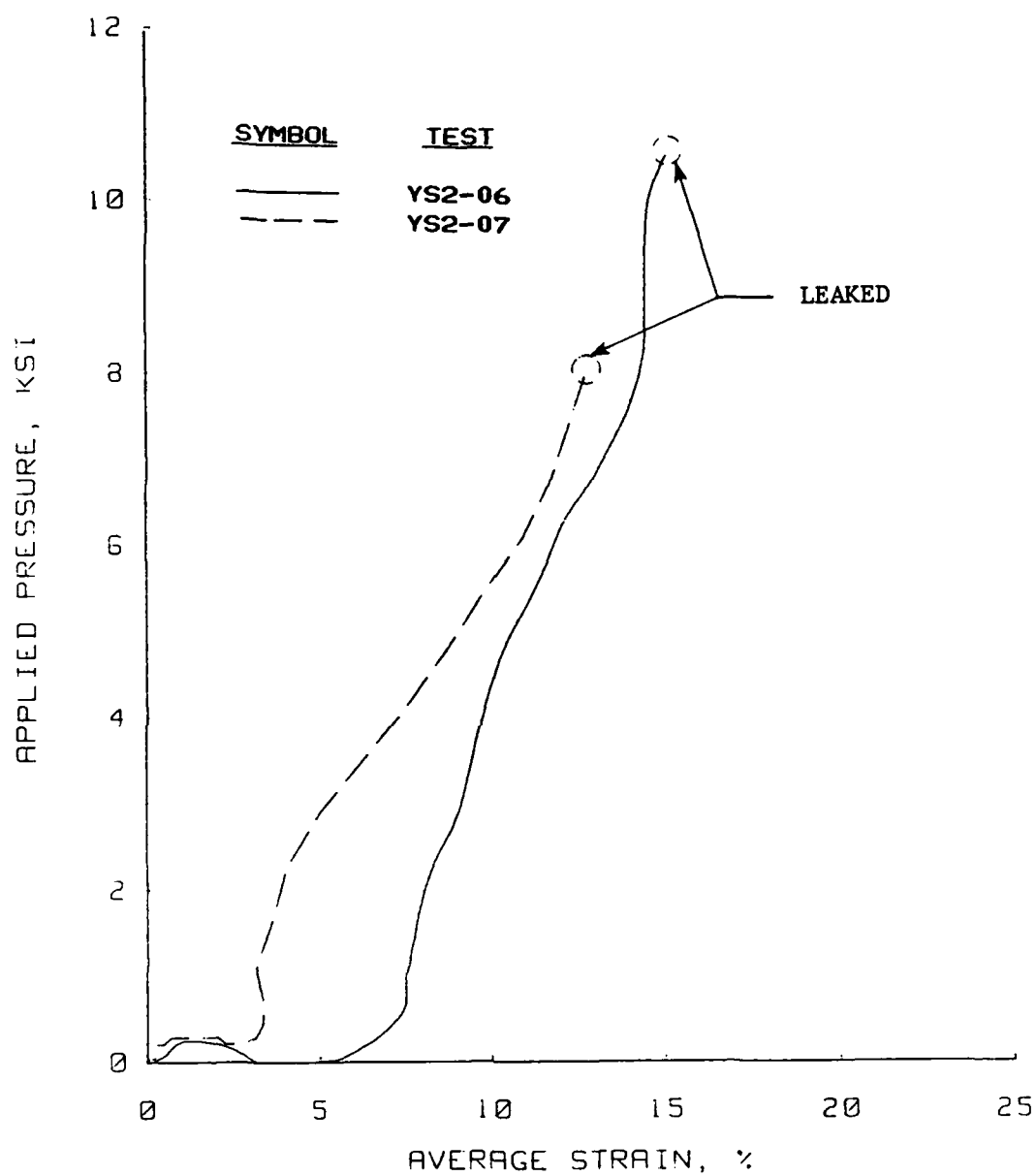
TIME, msec.

Figure B.61   Pressure versus time plots for dynamic uniaxial
              strain tests YS2-04 and -05 performed in the WES
              0.1-msec device on Yuma clayey sand.

Uniaxial Strain Results
Soil Type: Yuma Clayey Sand

Figure B.62   Strain versus time plots for dynamic uniaxial strain tests YS2-04 and -05 performed in the WES 0.1-msec device on Yuma clayey sand.

Uniaxial Strain Results
Soil Type: Yuma Clayey Sand

Figure B.63 Dynamic uniaxial strain results for tests YS2-06
and -07 performed in the WES 0.1-msec device on
Yuma clayey sand.

Uniaxial Strain Results
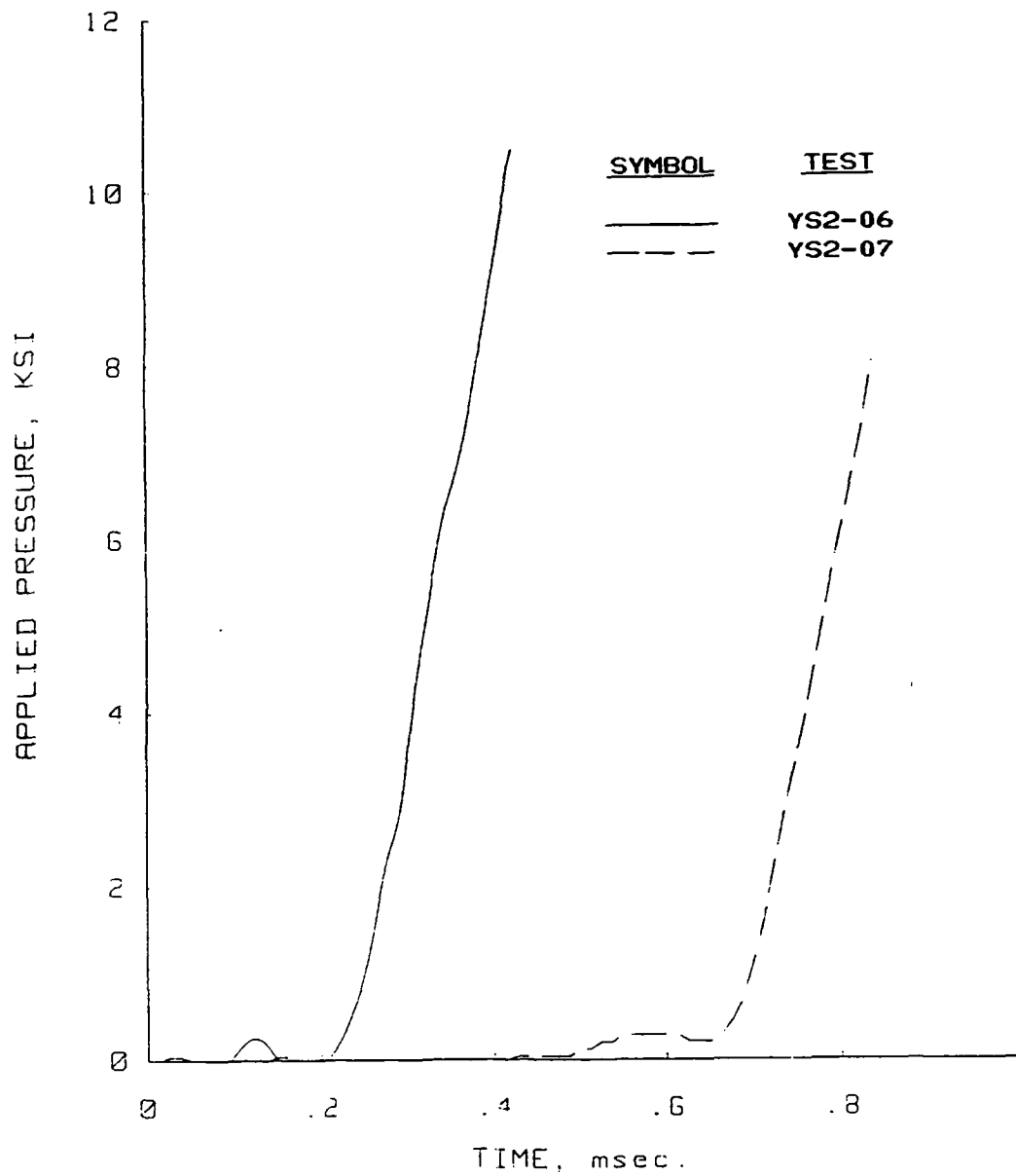## Soil Type: Yuma Clayey Sand

Figure B.64   Pressure versus time plots for dynamic uniaxial
strain tests YS2-06 and -07 performed in the WES
0.1-msec device on Yuma clayey sand.

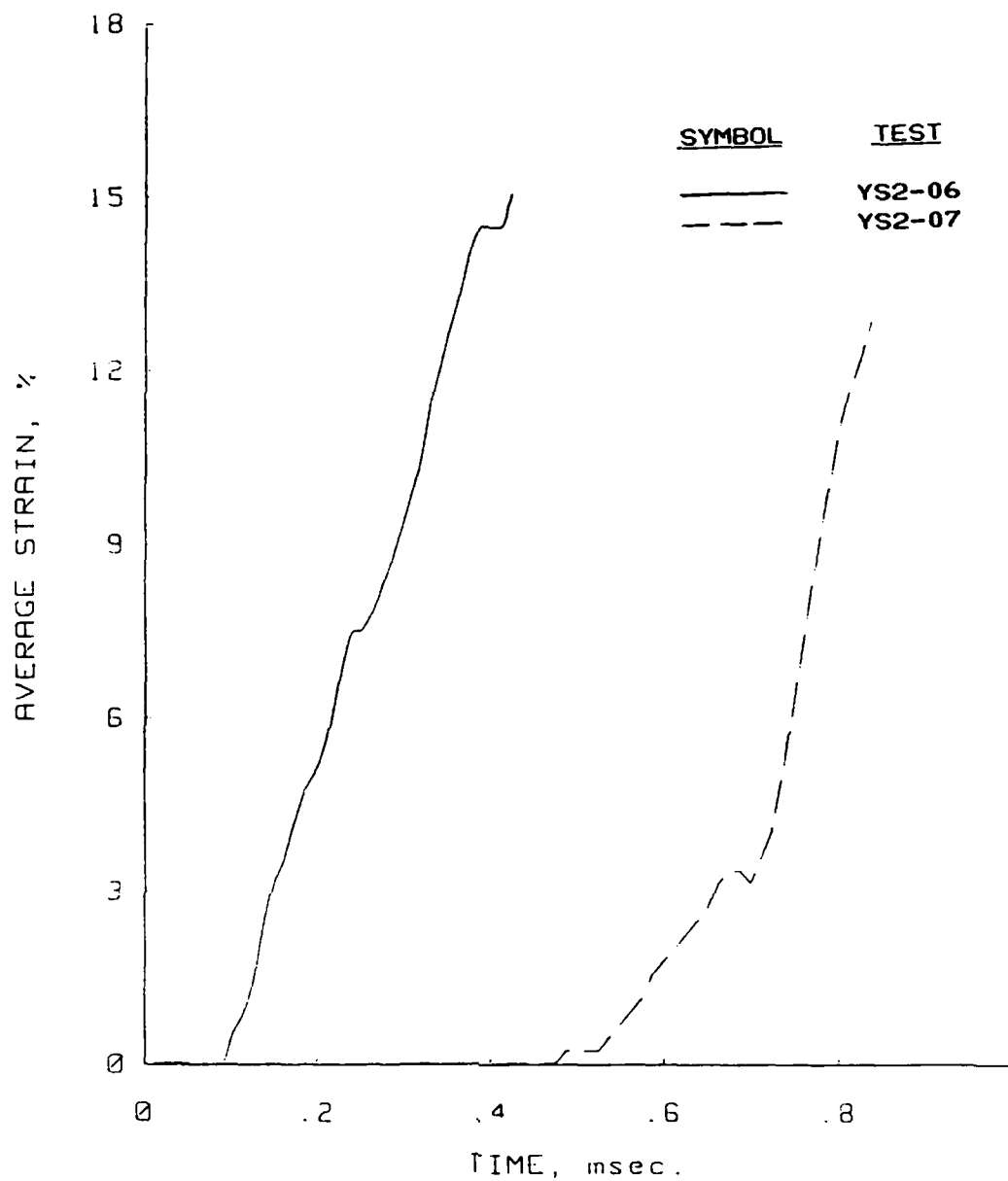## Uniaxial Strain Results
Soil Type: Yuma Clayey Sand

Figure B.65   Strain versus time plots for dynamic uniaxial

strain tests YS2-06 and -07 performed in the WES

0.1-msec device on Yuma clayey sand.

Uniaxial Strain Results
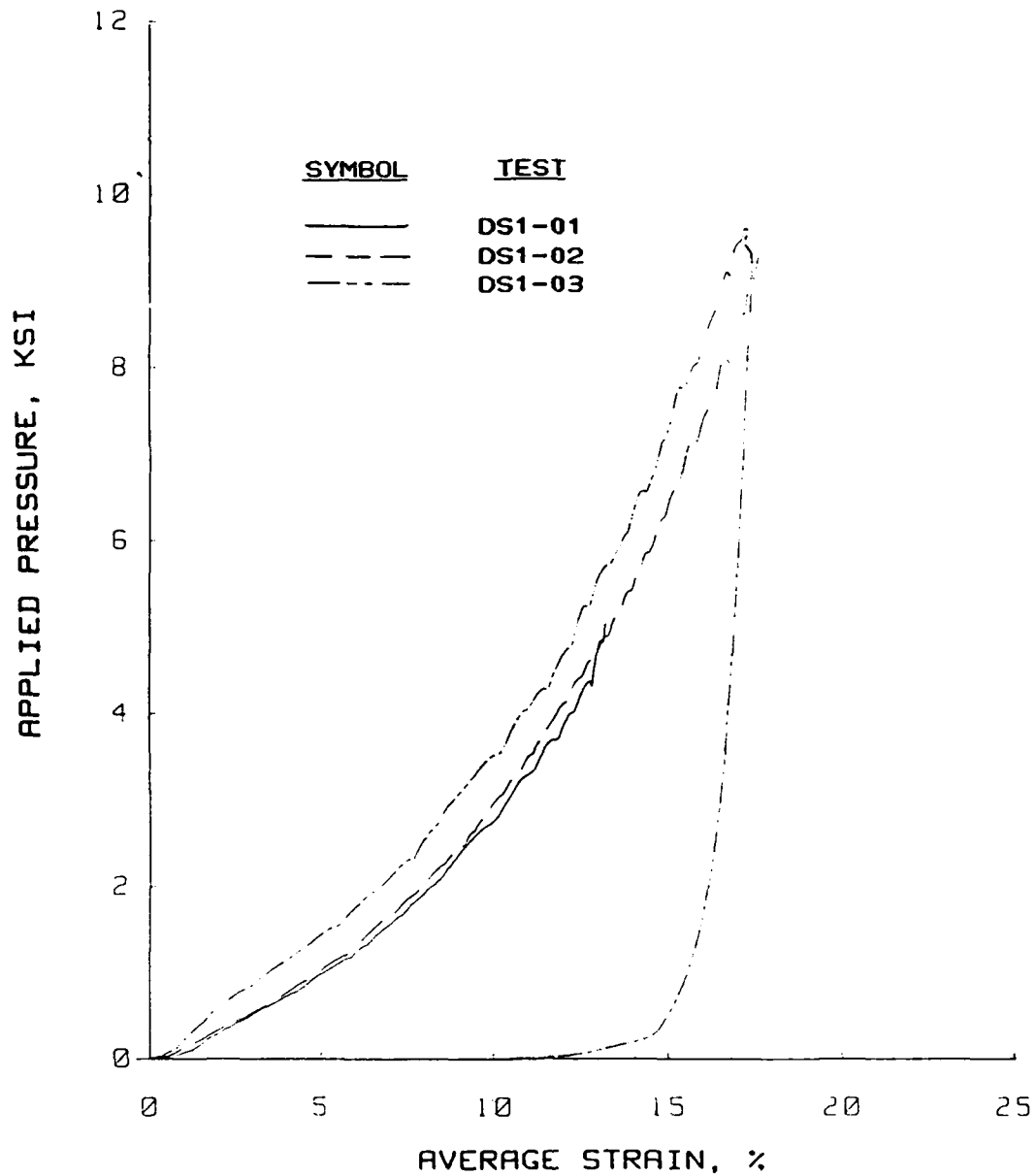## Soil Type: Vicksburg Loess

Figure B.66   Static uniaxial strain results for tests performed
in the PPUX device on Vicksburg loess, D-series.

Uniaxial Strain Results
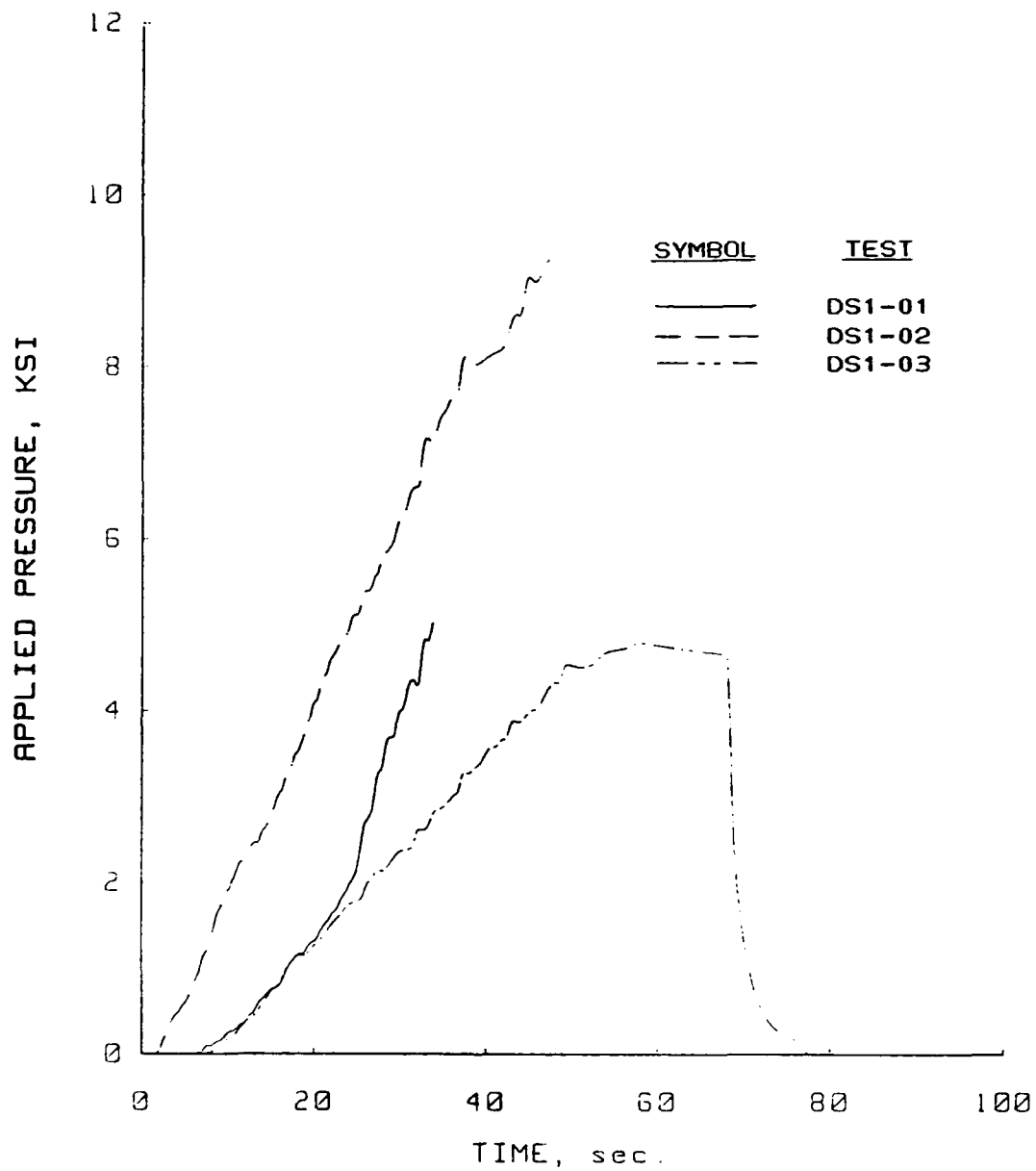## Soil Type: Vicksburg Loess

Figure B.67 Pressure versus time plots for the static uniaxial strain tests performed in the PPUX device on Vicksburg loess, D-series.

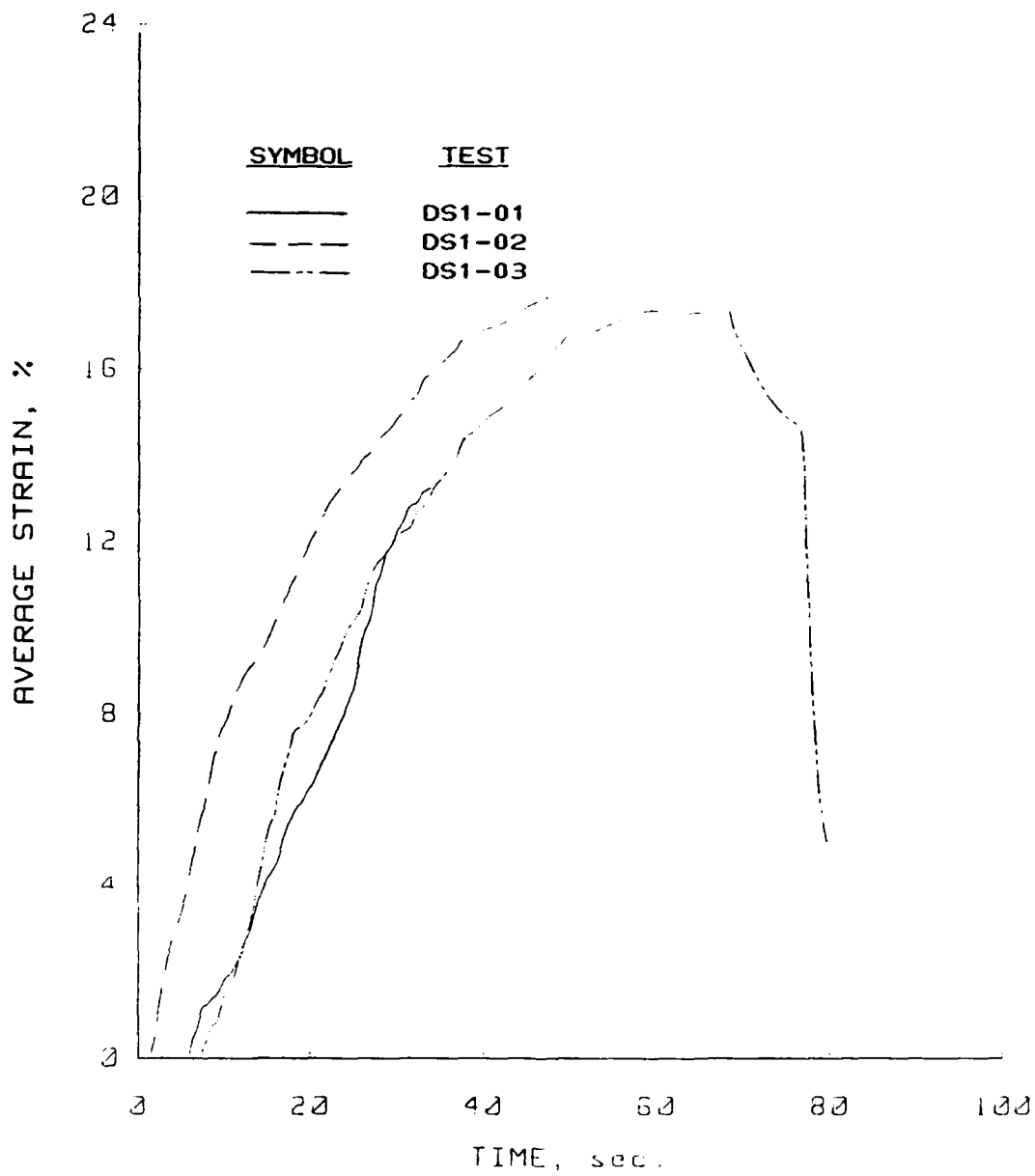## Uniaxial Strain Results
Soil Type: Vicksburg Loess

Figure B.68 Strain versus time plots for the static uniaxial
strain tests performed in the PPUX device on
Vicksburg loess, D-series.

Uniaxial Strain Results
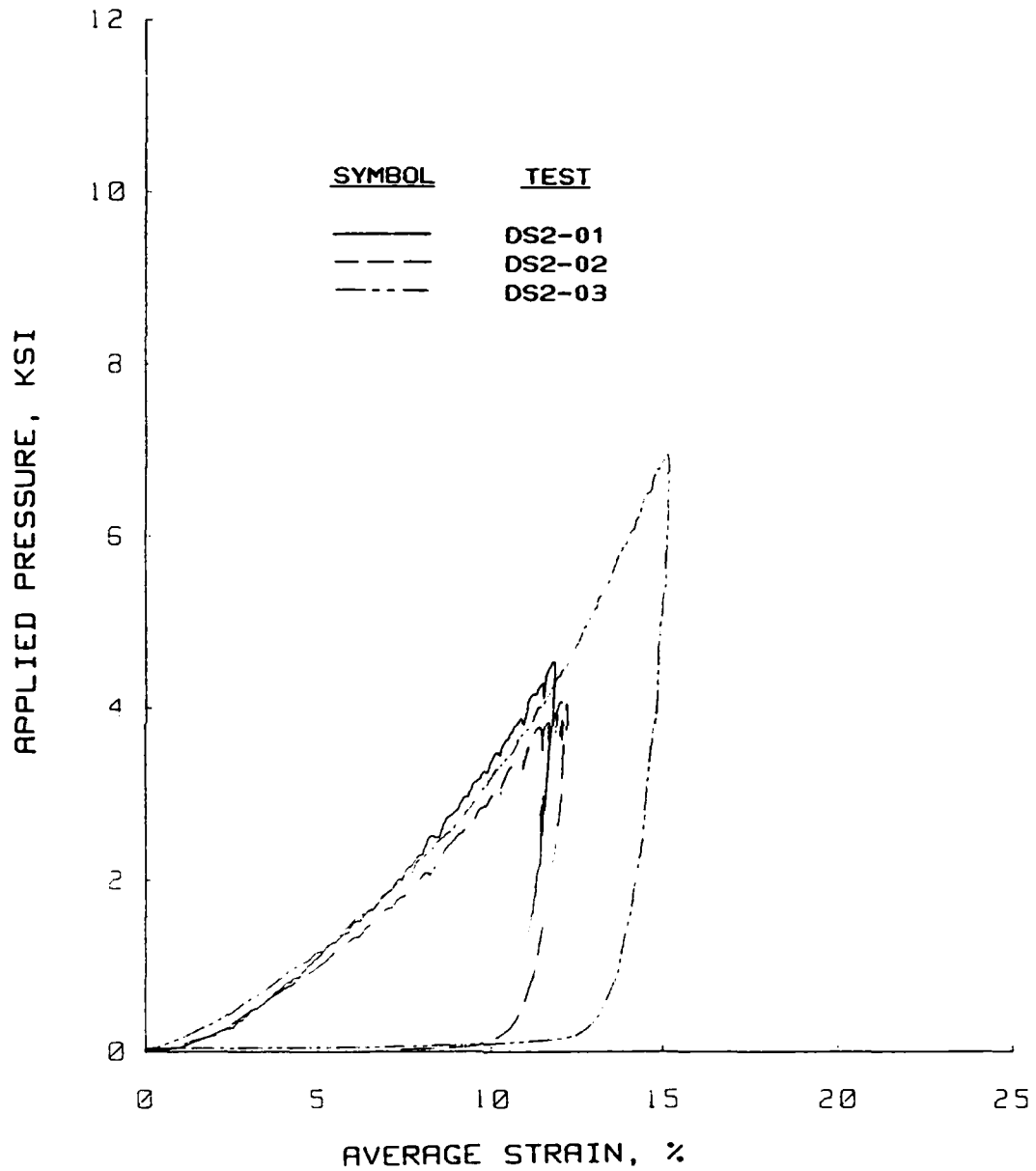## Soil Type: Vicksburg Loess

Figure B.69   Static uniaxial strain results for tests performed
in the WES 0.1-msec device device on Vicksburg
loess, D-series.

Uniaxial Strain Results
Soil Type: Vicksburg Loess

Figure B.70 Pressure versus time plots for the static uniaxial
strain tests performed in the WES 0.1-msec device
on Vicksburg loess, D-series.
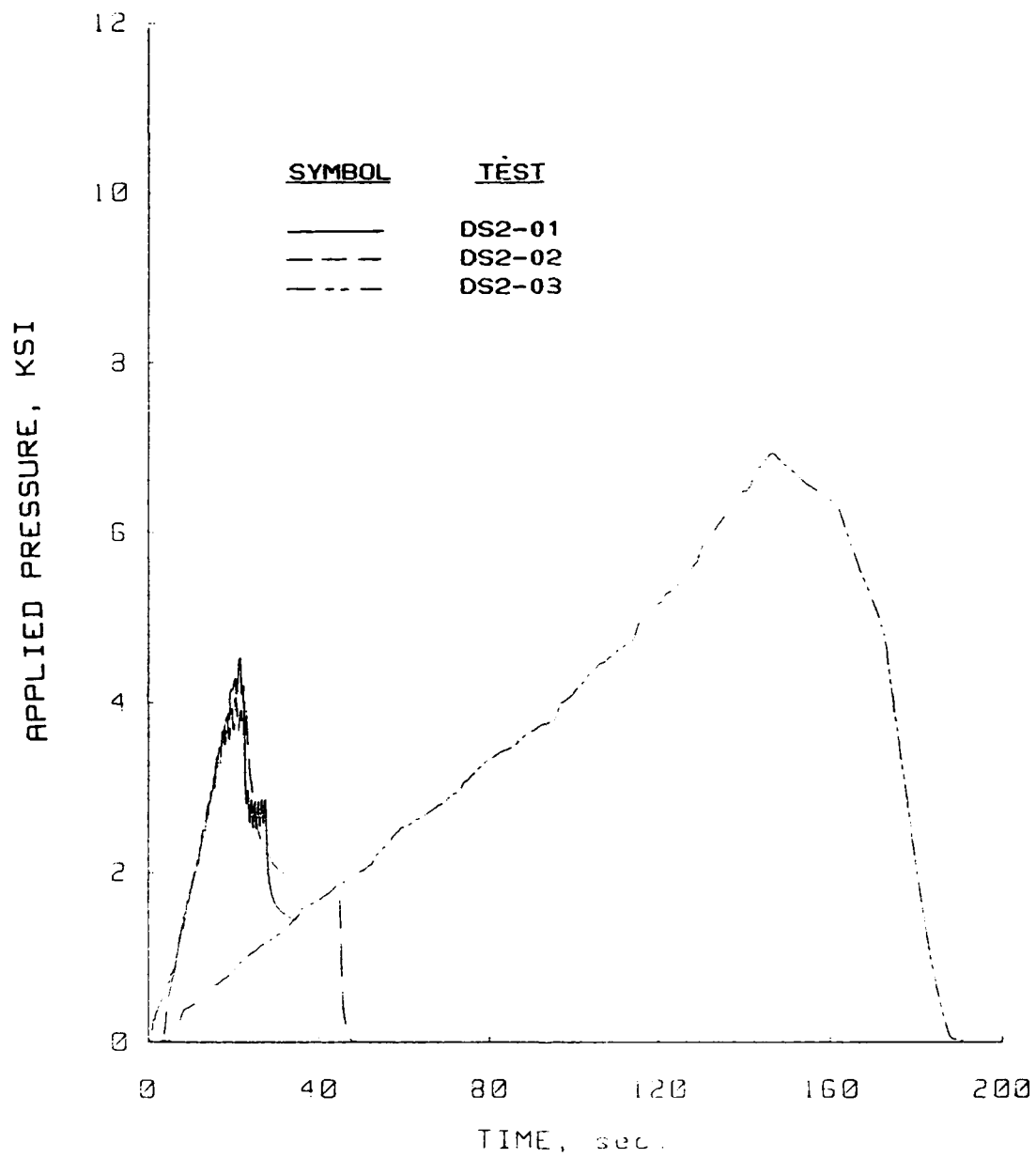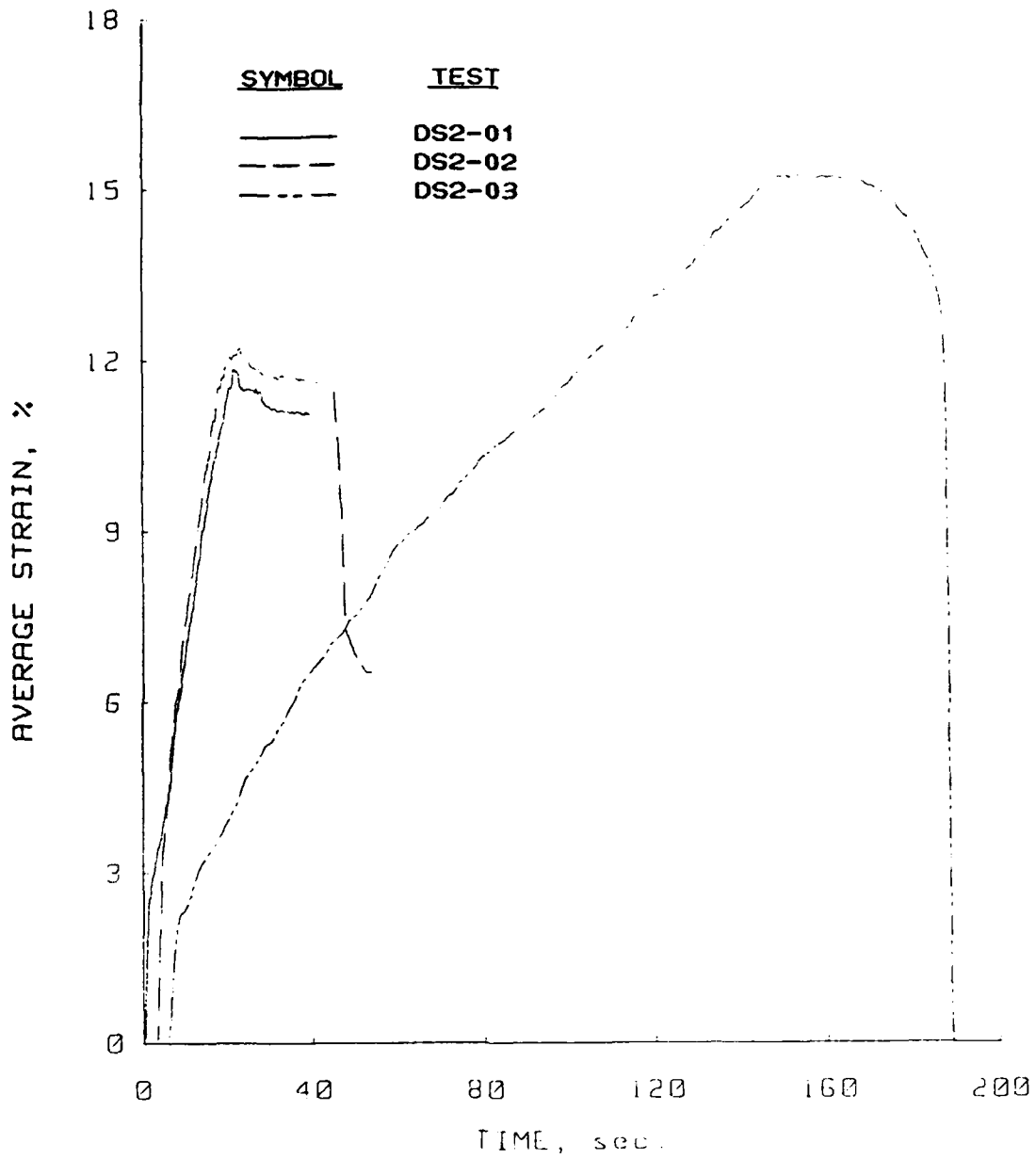
Figure B.71   Strain versus time plots for the static uniaxial
strain tests performed in the WES 0.1-msec device
on Vicksburg loess, D-series.

Uniaxial Strain Results
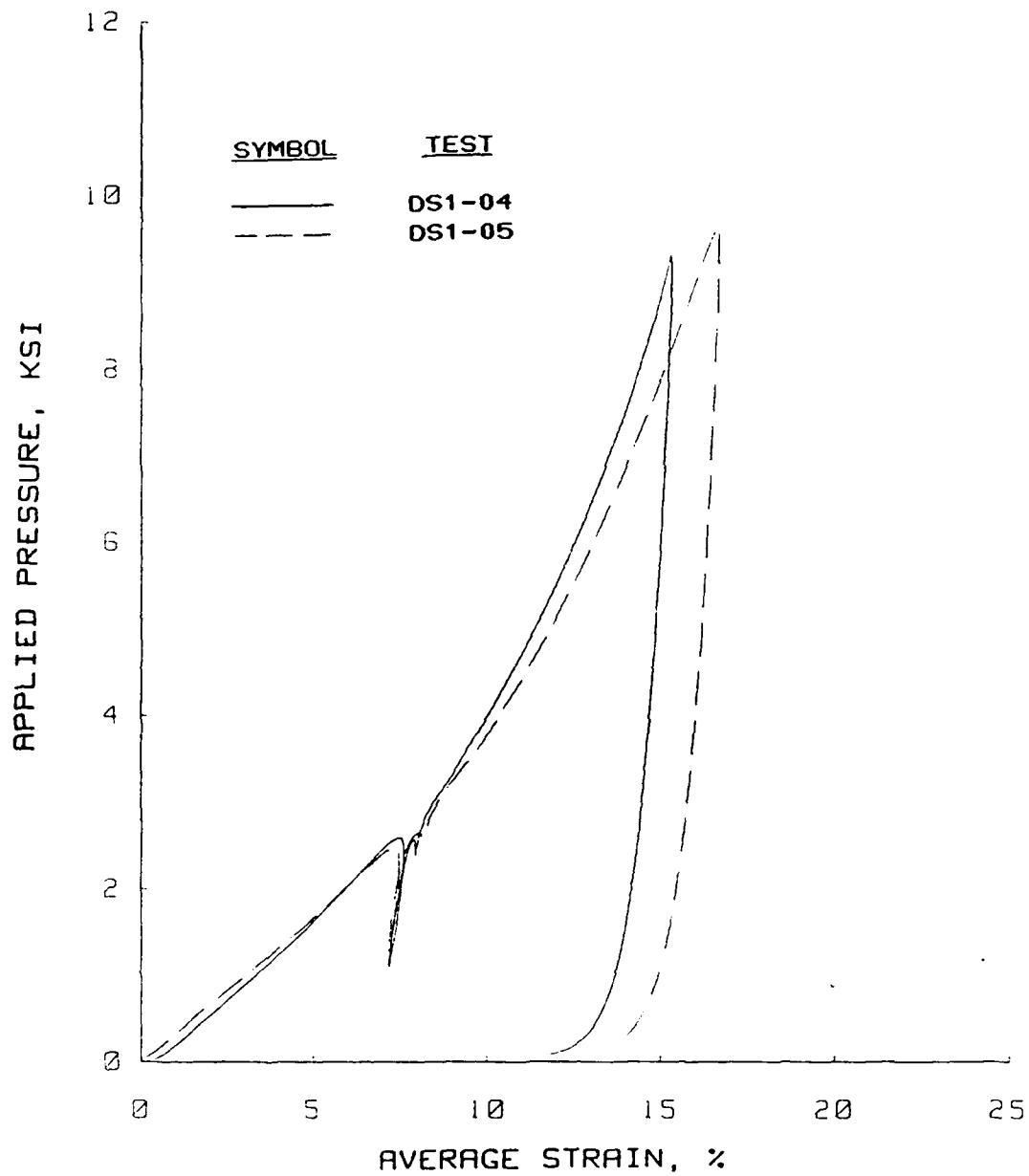## Soil Type: Vicksburg Loess

Figure B.72 Slow dynamic uniaxial strain results for tests performed in the PPUX device on Vicksburg loess, D-series.

Uniaxial Strain Results
Soil Type: Vicksburg Loess

Figure B.73   Pressure versus time plots for the slow dynamic uniaxial strain tests performed in the PPUX device on Vicksburg loess, D-series.

Uniaxial Strain Results
Soil Type: Vicksburg Loess

Figure B.74 Strain versus time plot for the slow dynamic
uniaxial-strain tests performed in the PPUX device
on Vicksburg loess, D-series.

Uniaxial Strain Results
Soil Type: Vicksburg Loess

Figure B.75 Dynamic uniaxial strain results for tests performed in the PPUX device on Vicksburg loess, D-series.

Uniaxial Strain Results
Soil Type: Vicksburg Loess

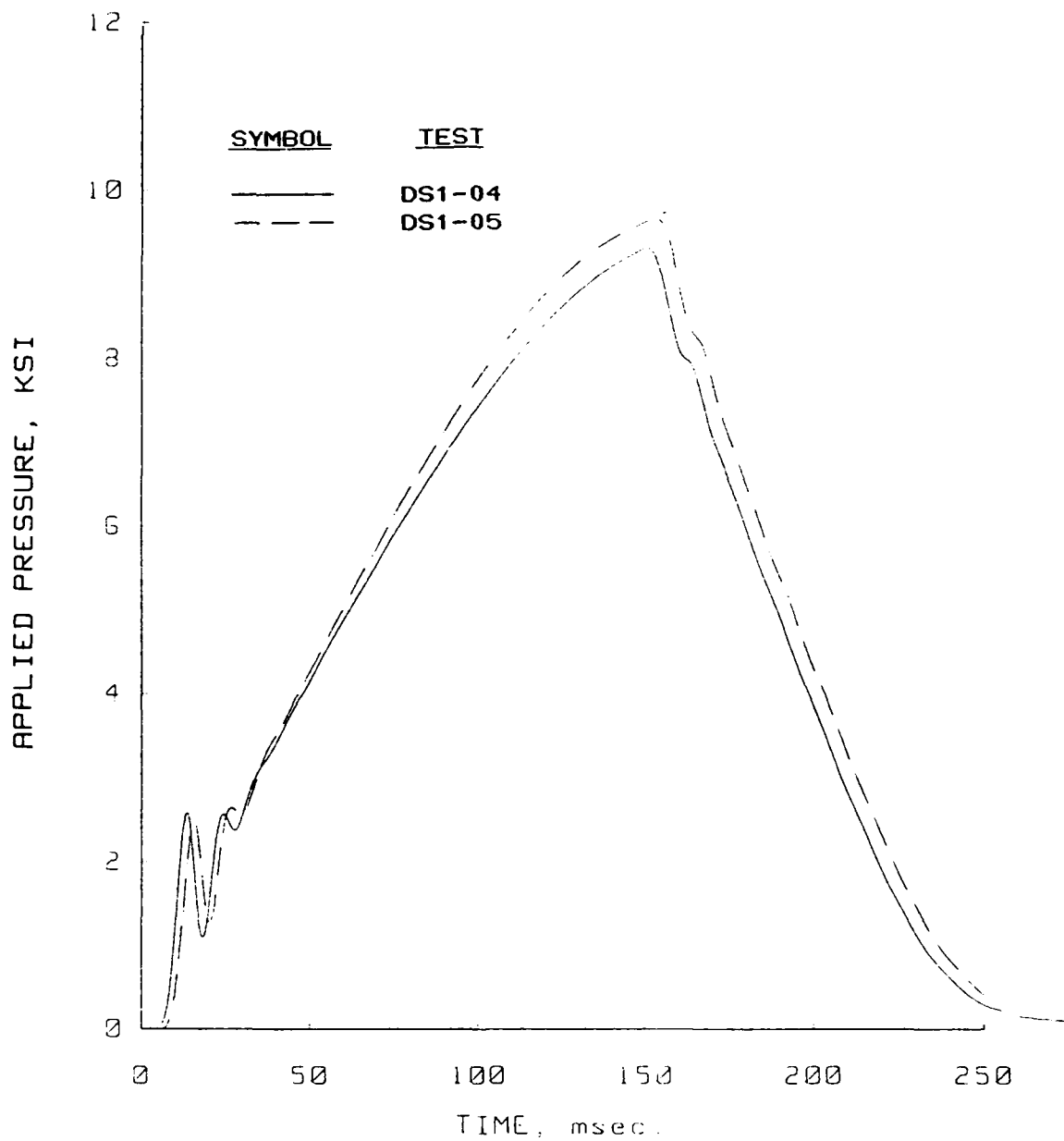
Figure B.76   Pressure versus time plots for the dynamic
uniaxial strain tests performed in the PPUX device
on Vicksburg loess, D-series.

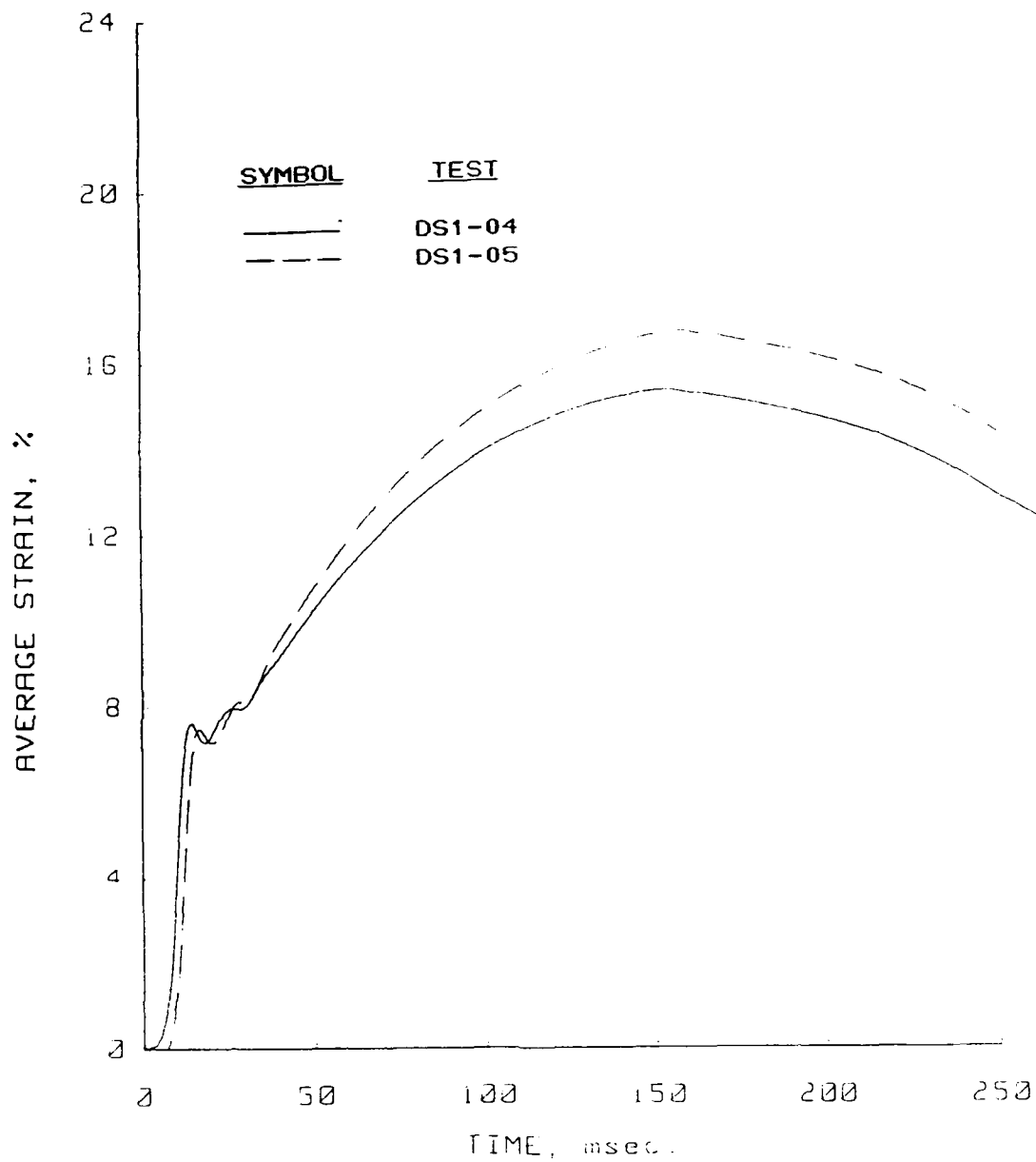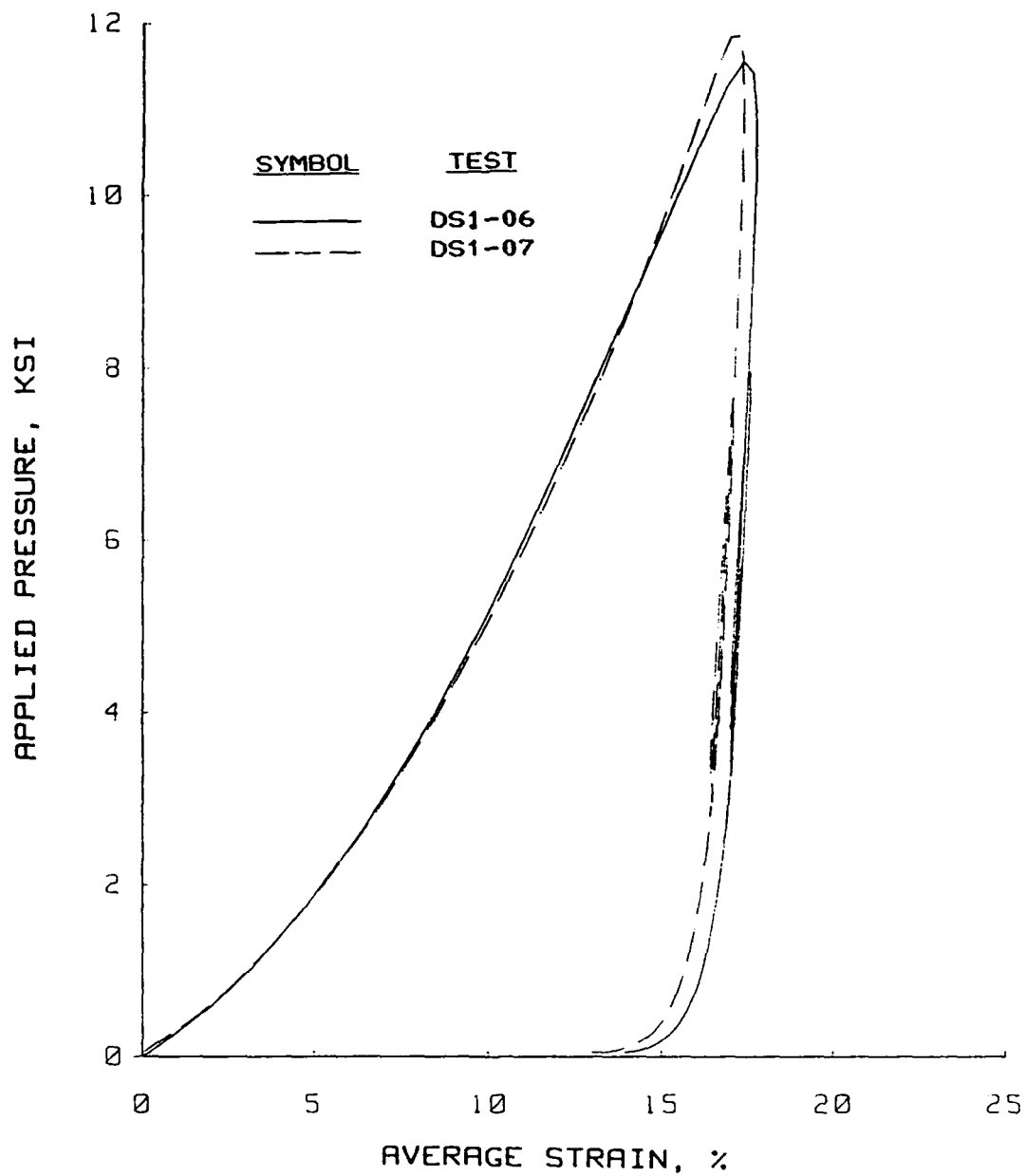# Uniaxial Strain Results
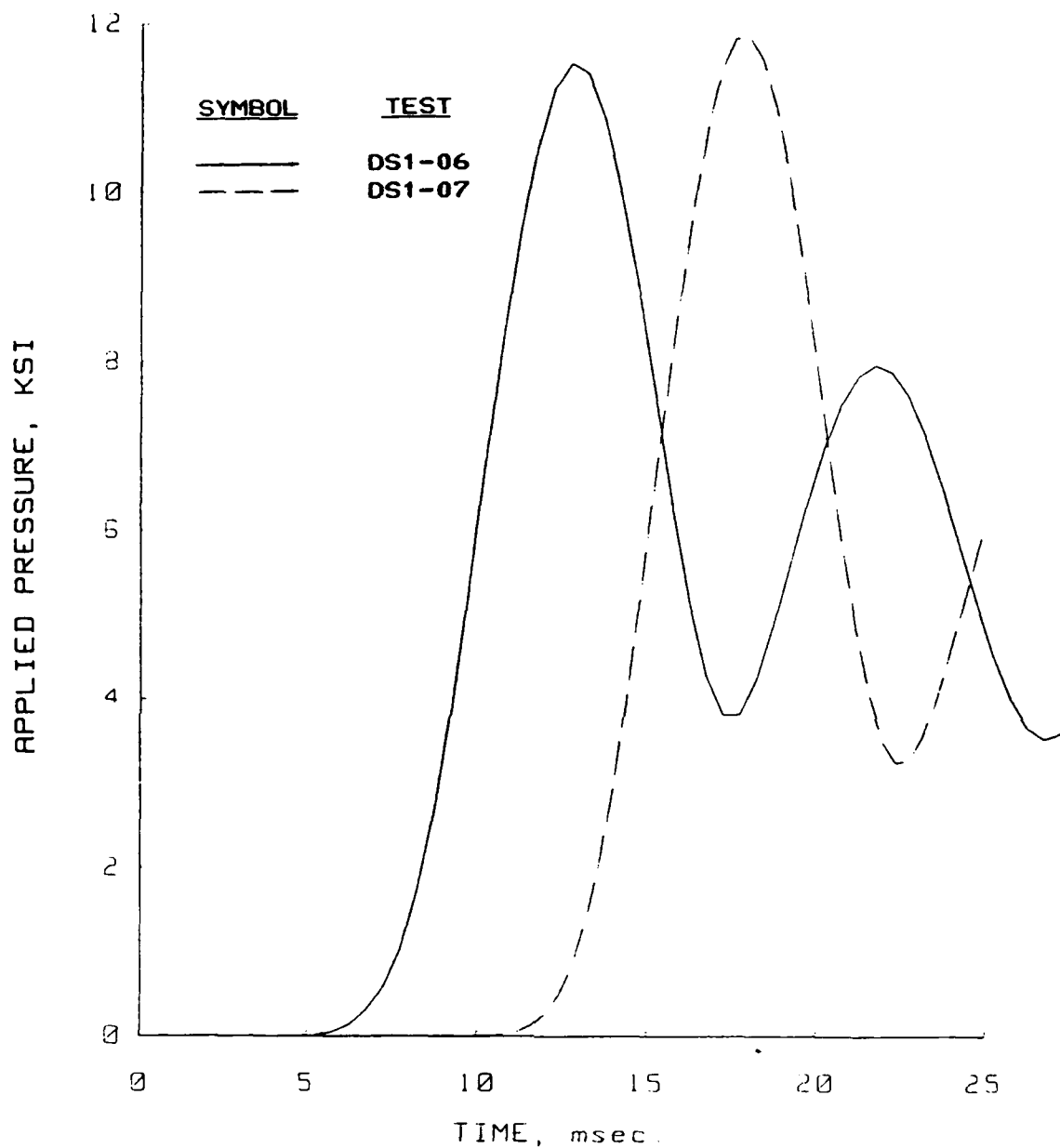## Soil Type: Vicksburg Loess
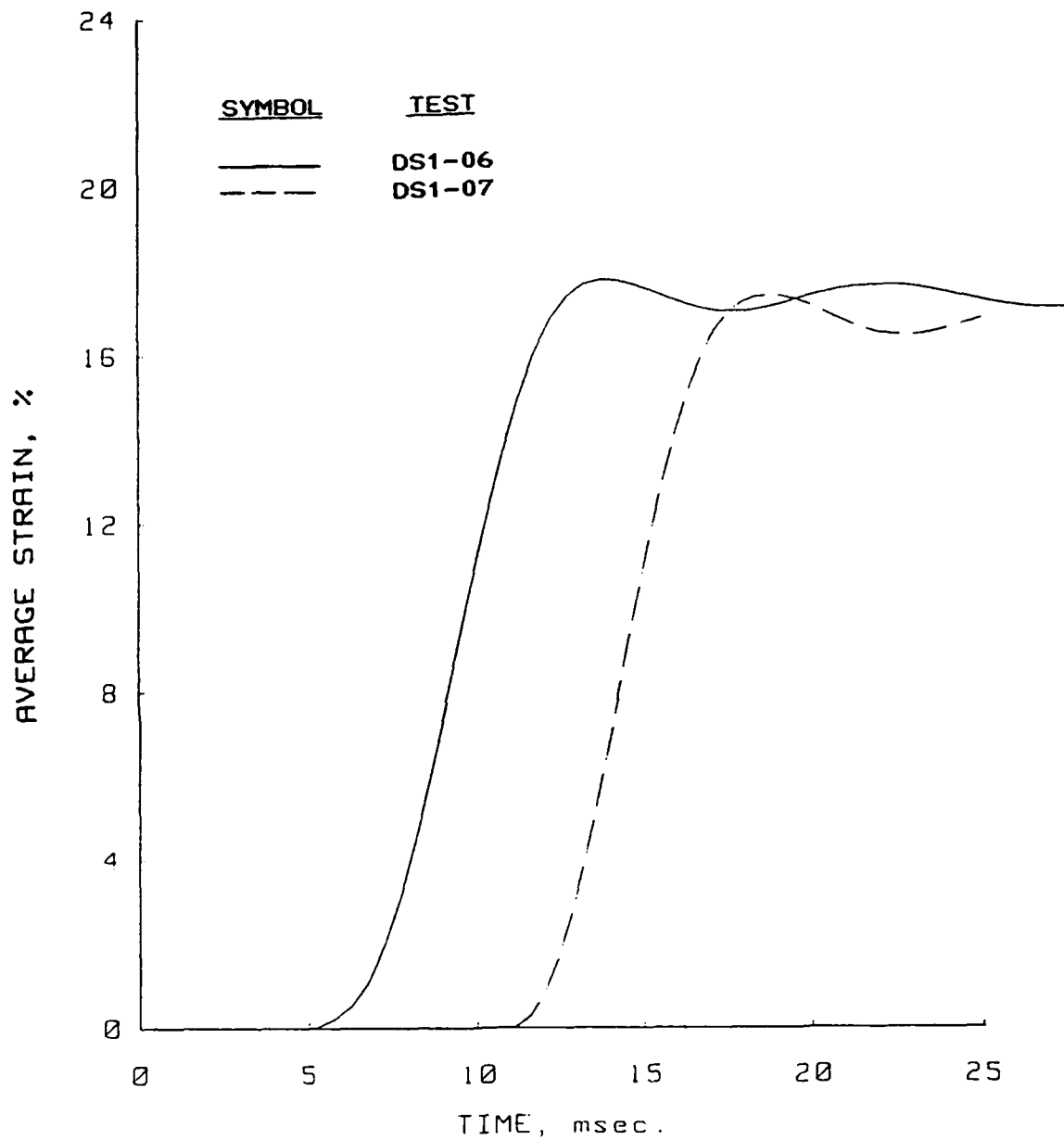
Figure B.77   Strain versus time plots for the dynamic uniaxial
strain tests performed in the PPUX device on
Vicksburg loess, D-series.

Uniaxial Strain Results
Soil Type: Vicksburg Loess

SYMBOL	TEST
————	DS2-04
— — —	DS2-05
— — —	DS2-06
— - - —	DS2-07
— . —	DS2-08

Figure B.78 Dynamic uniaxial strain results for tests DS2-04, -05, -06, -07, and -08 performed in the WES 0.1-msec device on Vicksburg loess, D-series.

Uniaxial Strain Results
Soil Type: Vicksburg Loess

Figure B.79 Pressure versus time plots for dynamic uniaxial
strain tests DS2-04, -05, -06, -07, and -08
performed in the WES 0.1-msec device on Vicksburg
loess, D-series.
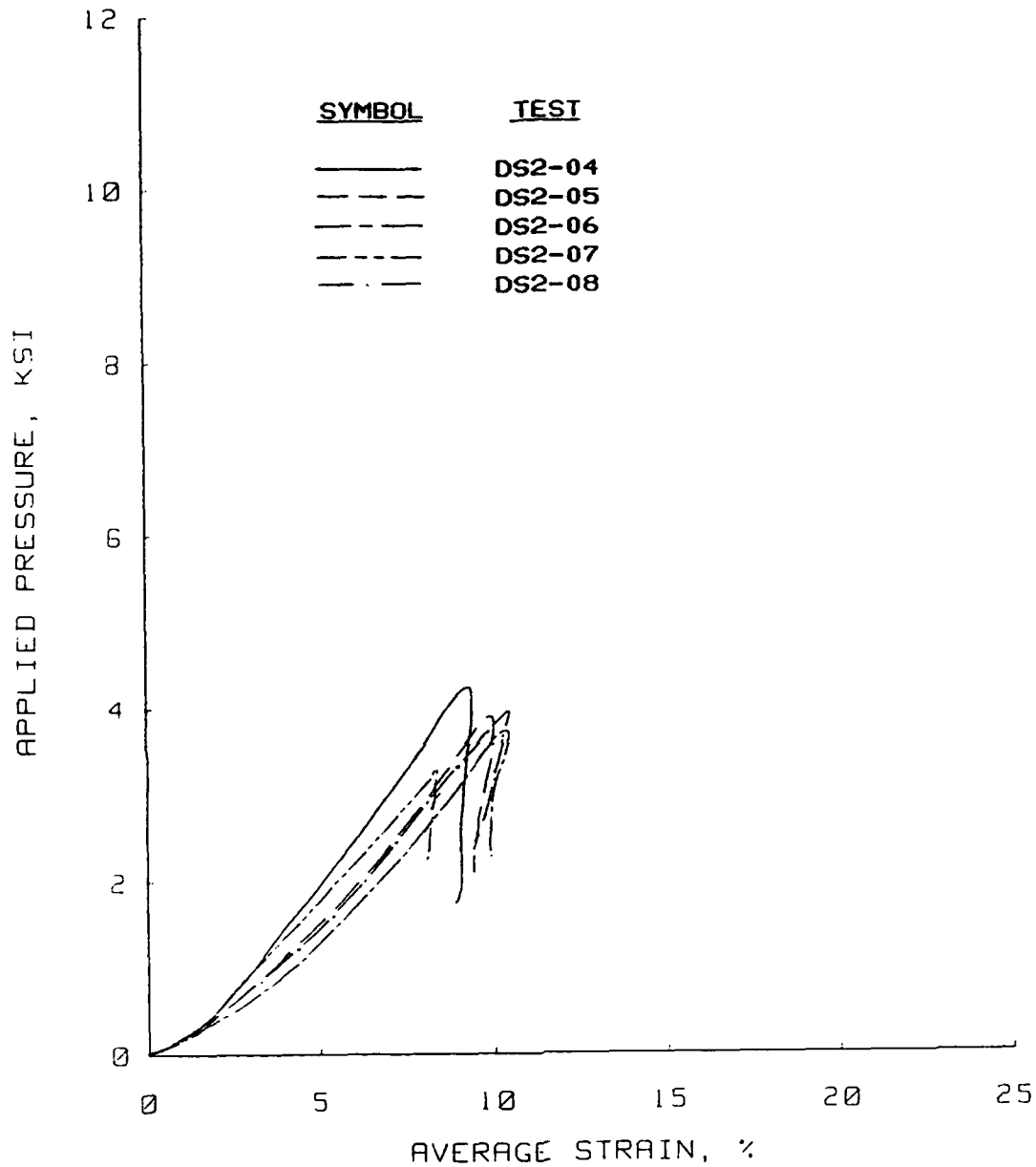
Uniaxial Strain Results
Soil Type: Vicksburg Loess

Figure B.80   Strain versus time plots for the dynamic uniaxial strain tests DS2-04, -05, -06, -07, and -08 performed in the WES 0.1-msec device on Vicksburg loess, D-series.

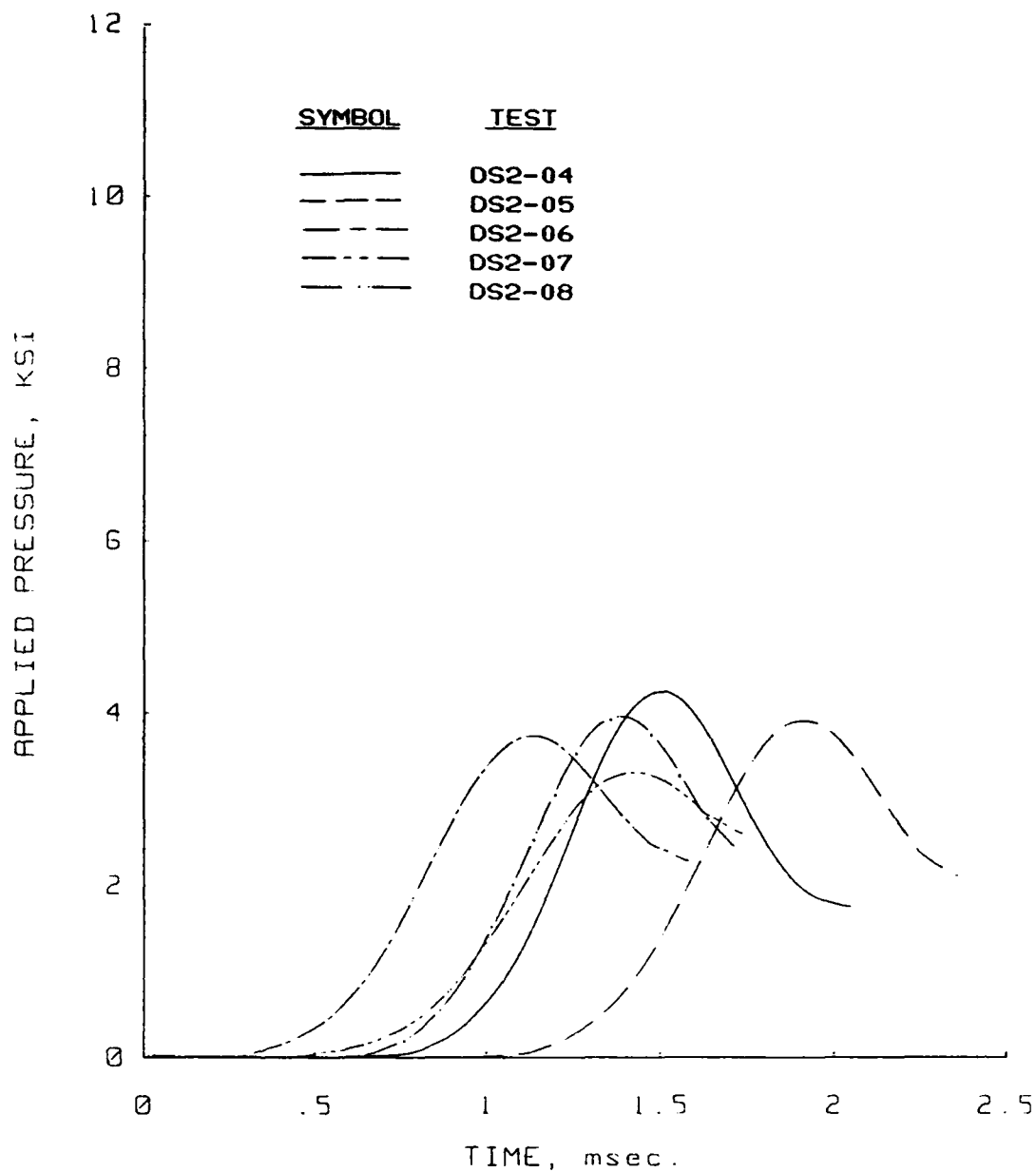# Uniaxial Strain Results
Soil Type: Vicksburg Loess

Figure B.81   Dynamic uniaxial strain results for tests DS2-09
and -10 performed in the WES 0.1-msec device on
Vicksburg loess, D-series.

Uniaxial Strain Results
Soil Type: Vicksburg Loess
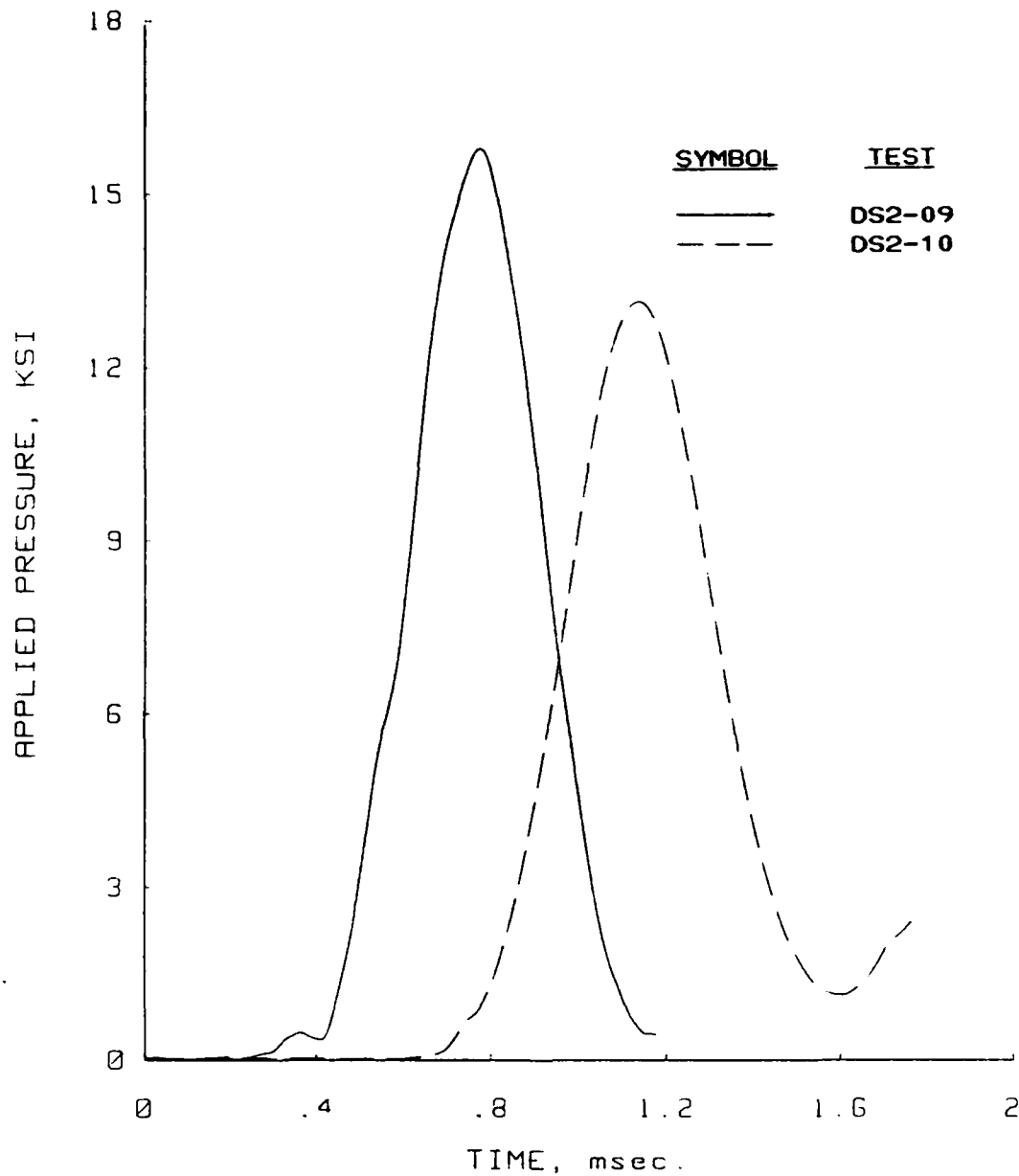
Figure B.82   Pressure versus time plots for dynamic uniaxial
strain tests DS2-09 and -10 performed in the WES
0.1-msec device for Vicksburg loess, D-series.

Figure B.83   Strain versus time plots for dynamic uniaxial
strain tests DS2-09 and -10 performed in the WES
0.1-msec device on Vicksburg loess, D-series.
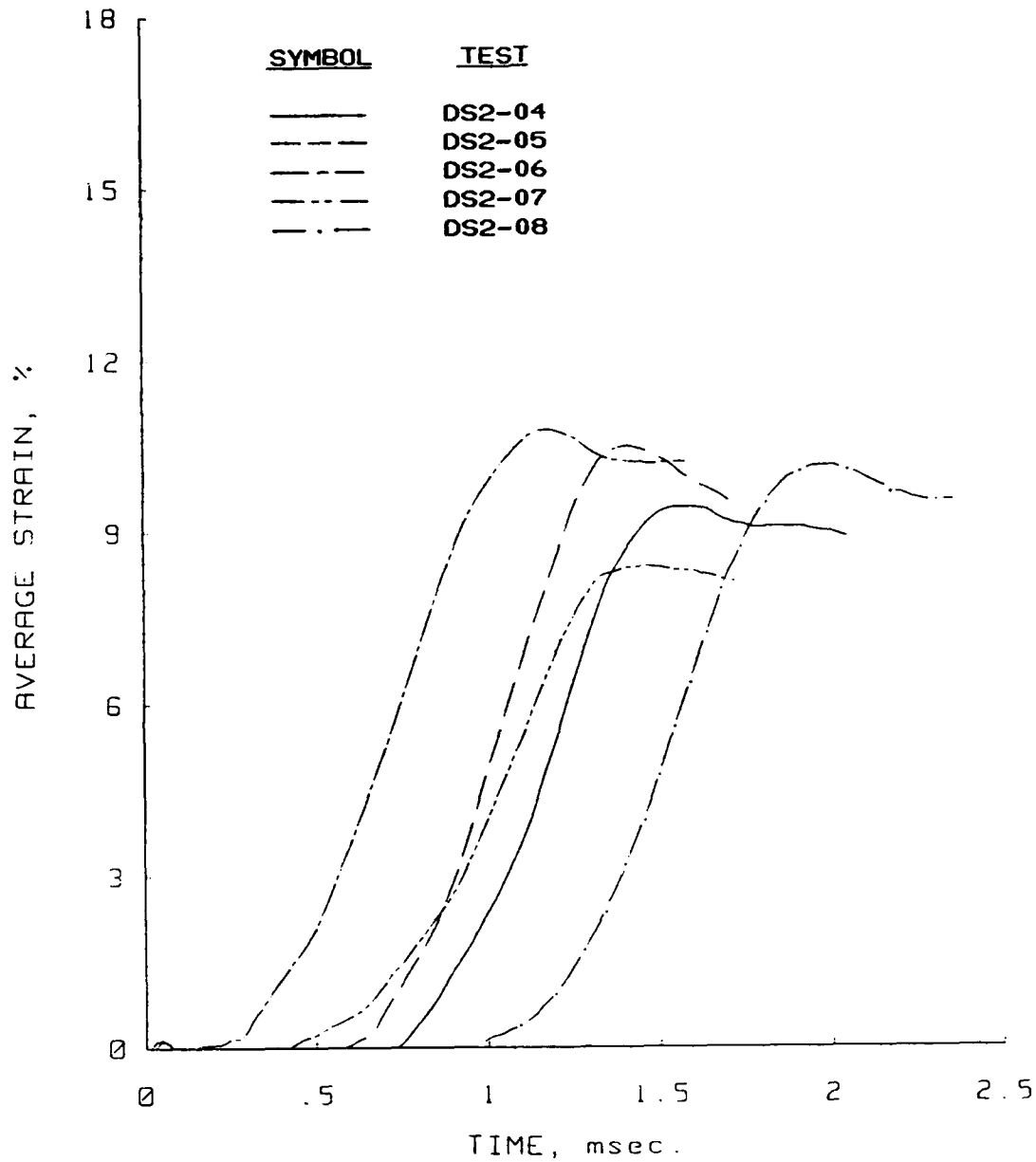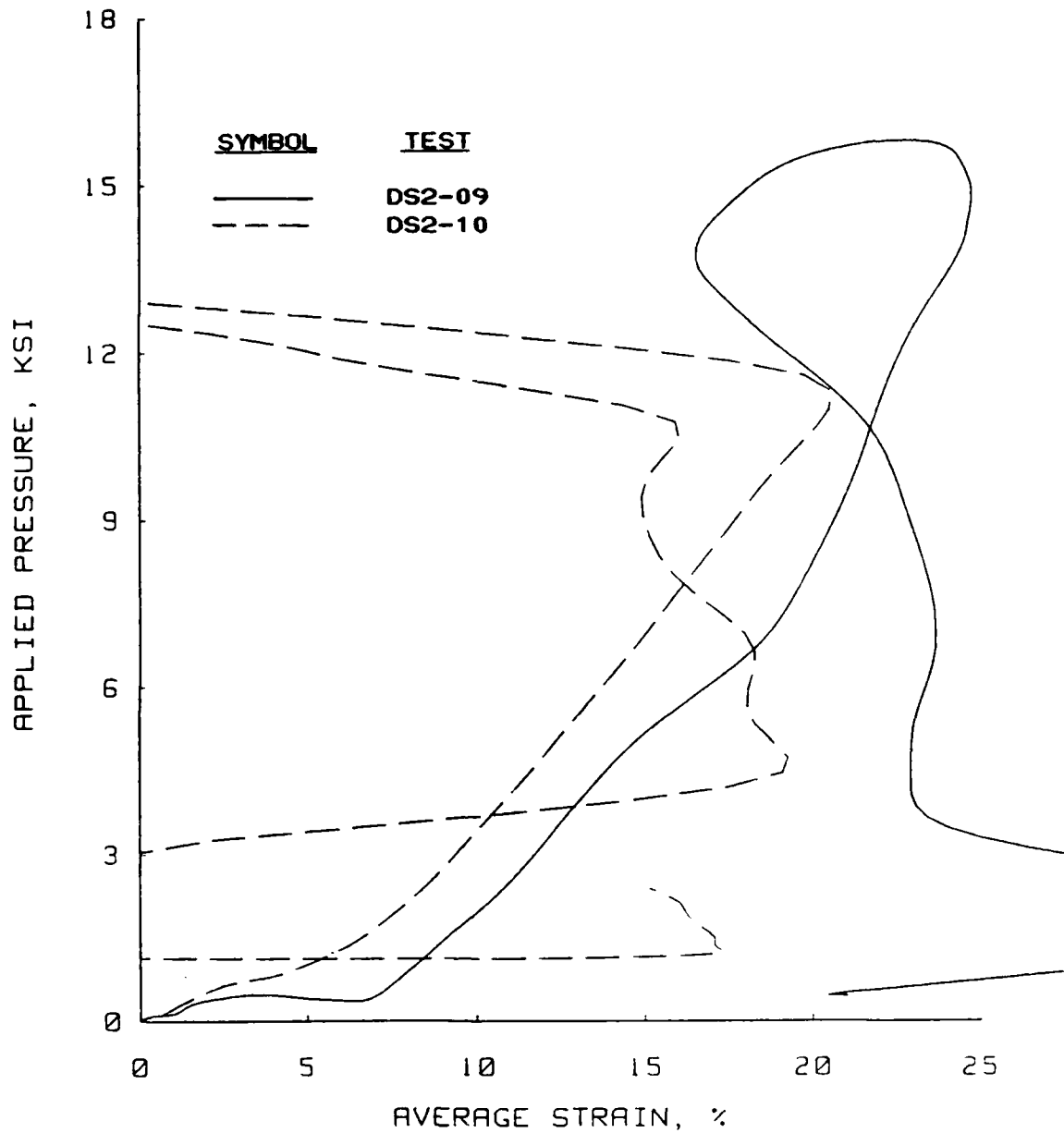
Uniaxial Strain Results
Soil Type: Vicksburg Loess

Figure B.84 Dynamic creep uniaxial strain results for tests
performed in the PPUX device on Vicksburg loess,
D-series.

Uniaxial Strain Results
Soil Type: Vicksburg Loess
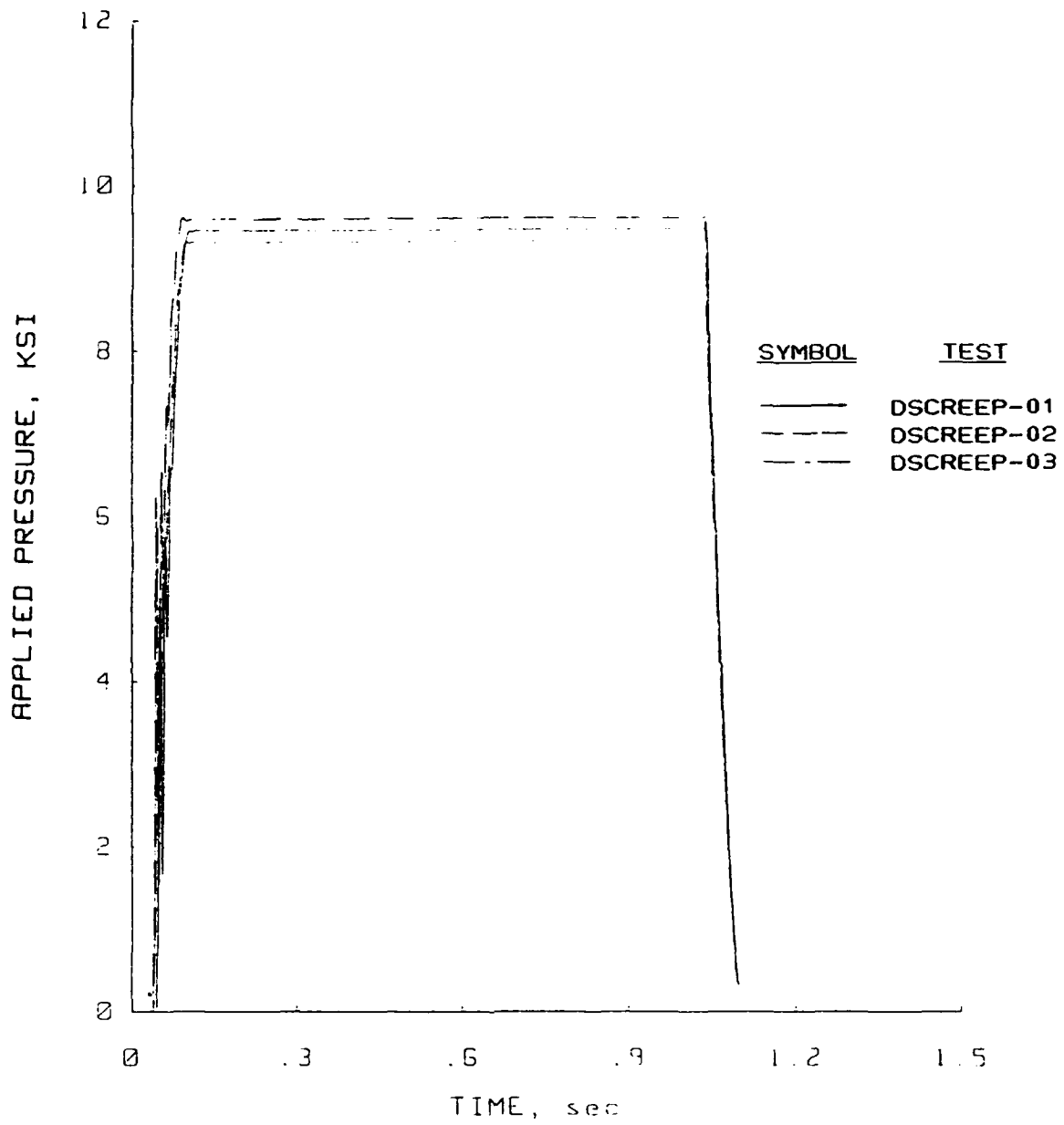
Figure B.85   Pressure versus time plots for the dynamic creep
uniaxial strain tests performed in the PPUX device
on Vicksburg loess, D-series.

Uniaxial Strain Results
Soil Type: Vicksburg Loess
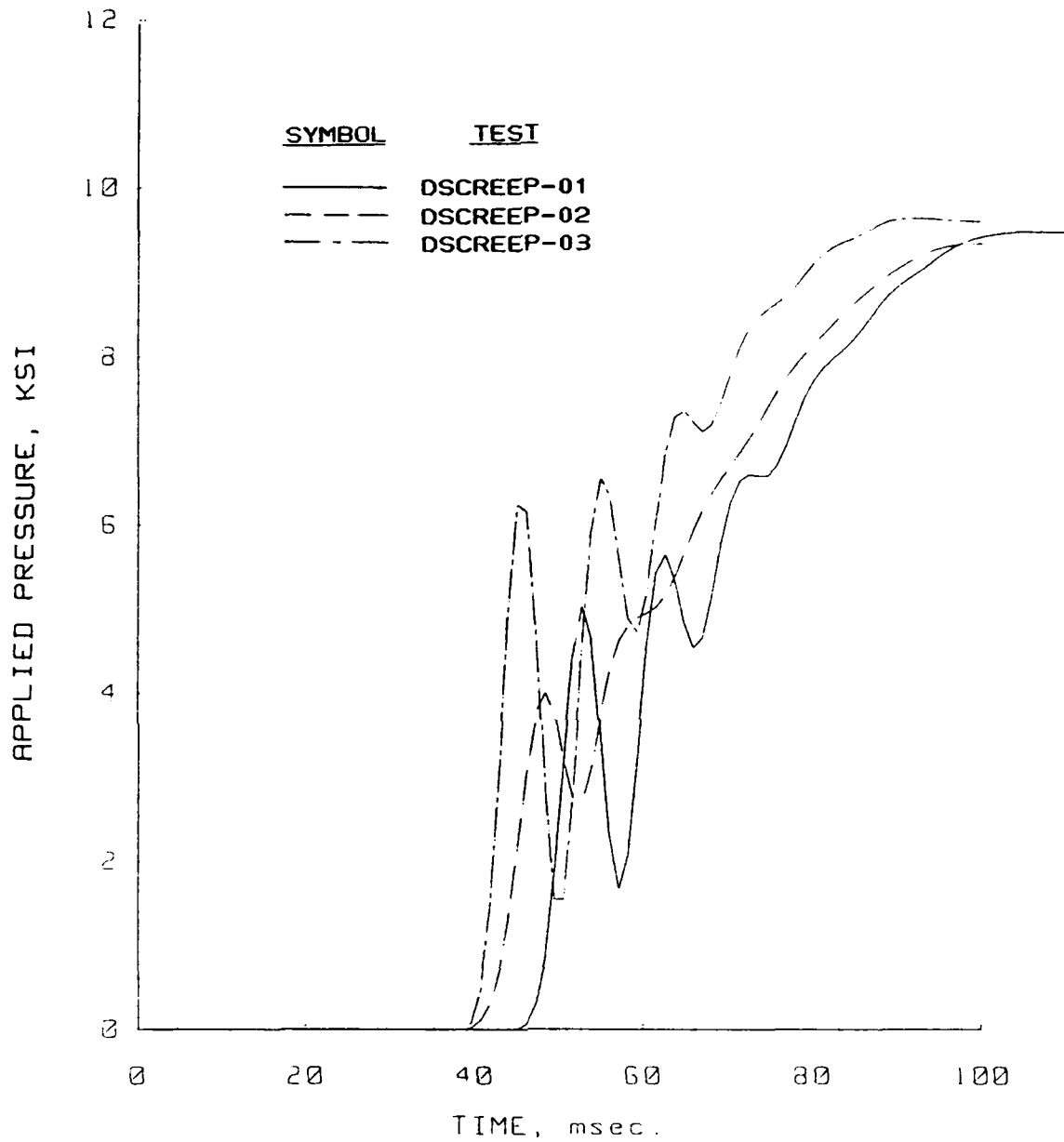
Figure B.86   Pressure rise time plots for the dynamic creep
uniaxial strain tests performed in the PPUX device
on Vicksburg loess, D-series.

Uniaxial Strain Results
Soil Type: Vicksburg Loess
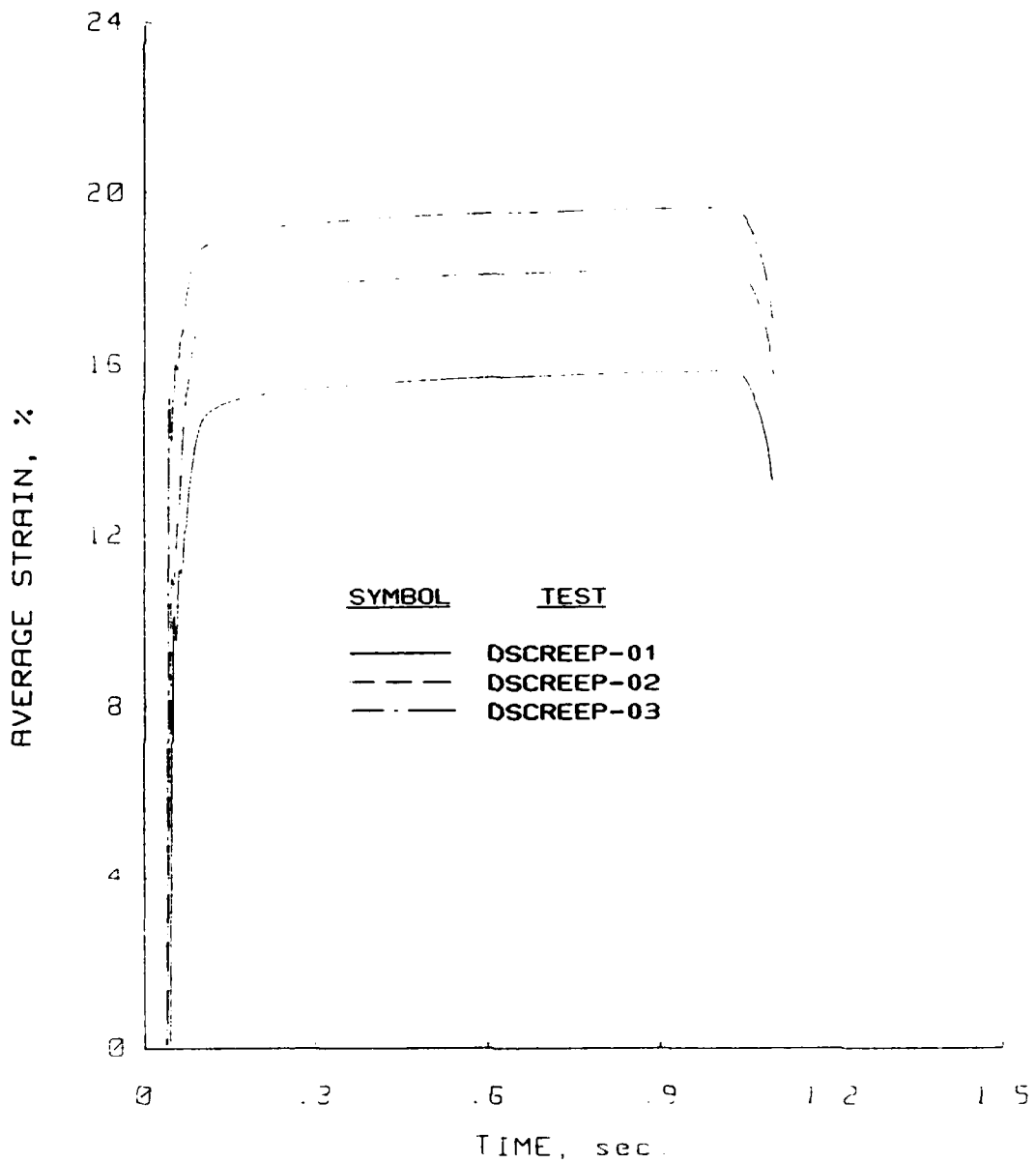
Figure B.87 Strain versus time plots for the dynamic creep
uniaxial strain tests performed in the PPUX device
on Vicksburg loess, D-series.

Uniaxial Strain Results
Soil Type: Vicksburg Loess
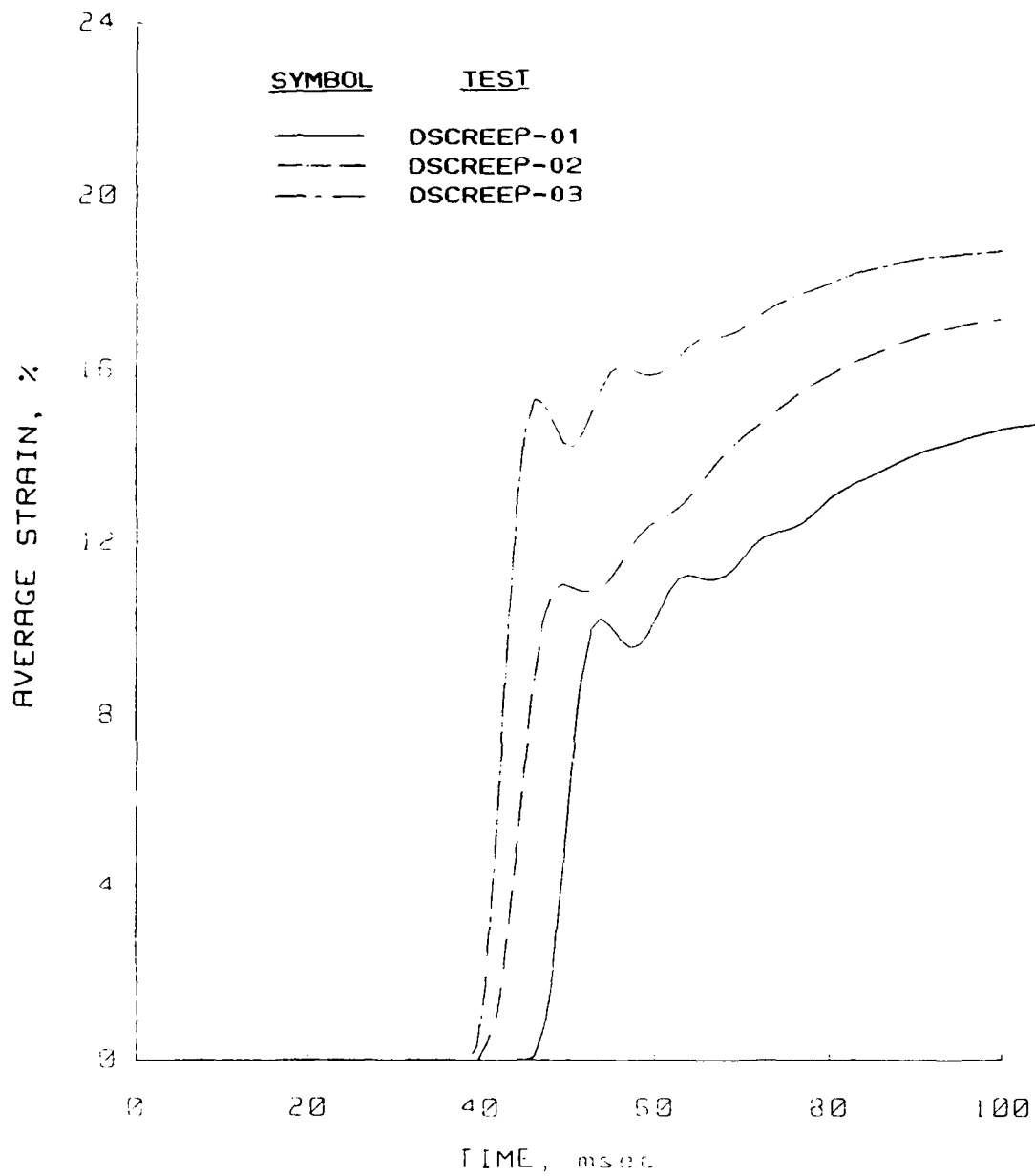
Figure B.88 Strain rise time plots for the dynamic creep
uniaxial strain tests performed in the PPUX device
on Vicksburg loess, D-series.
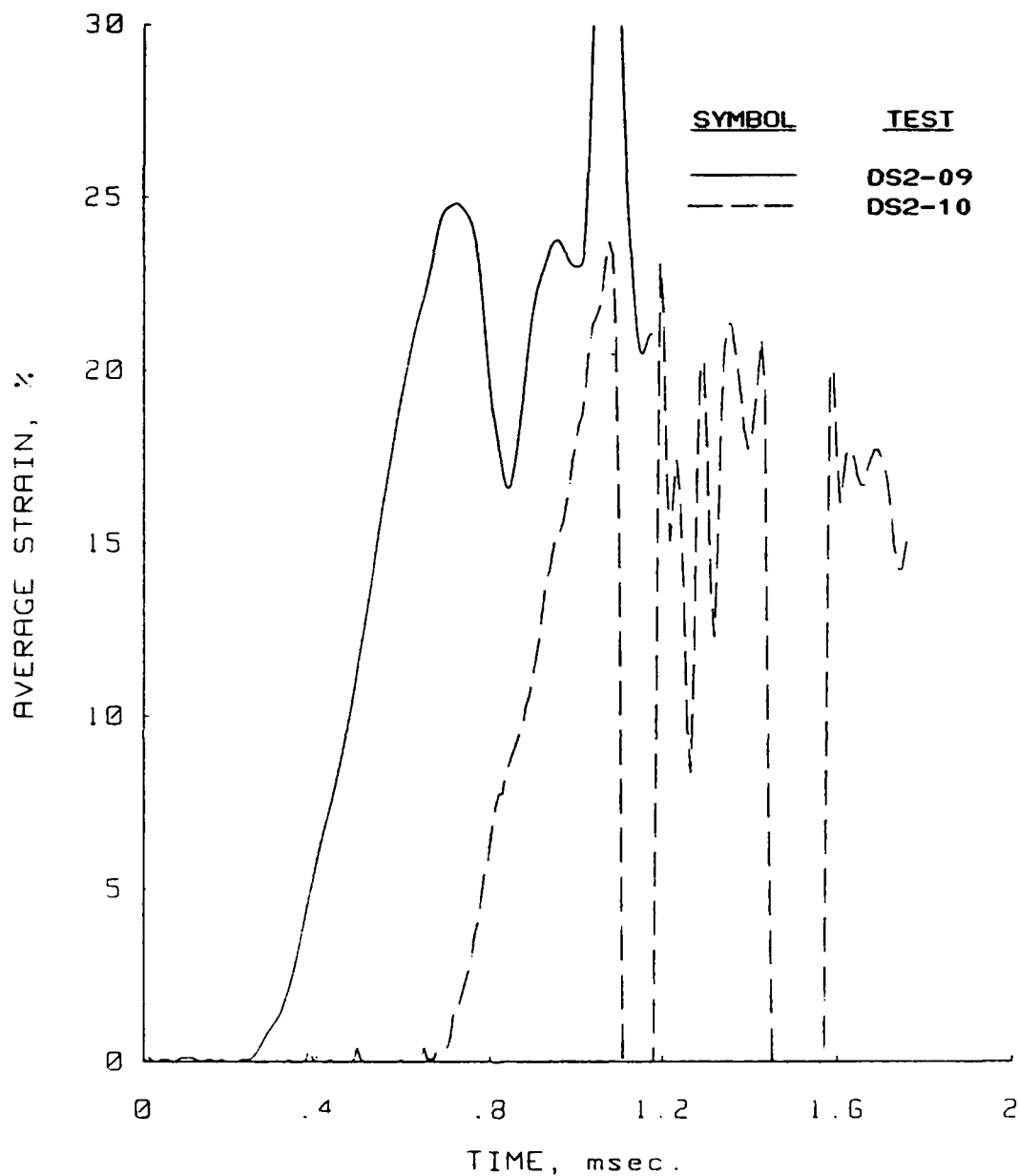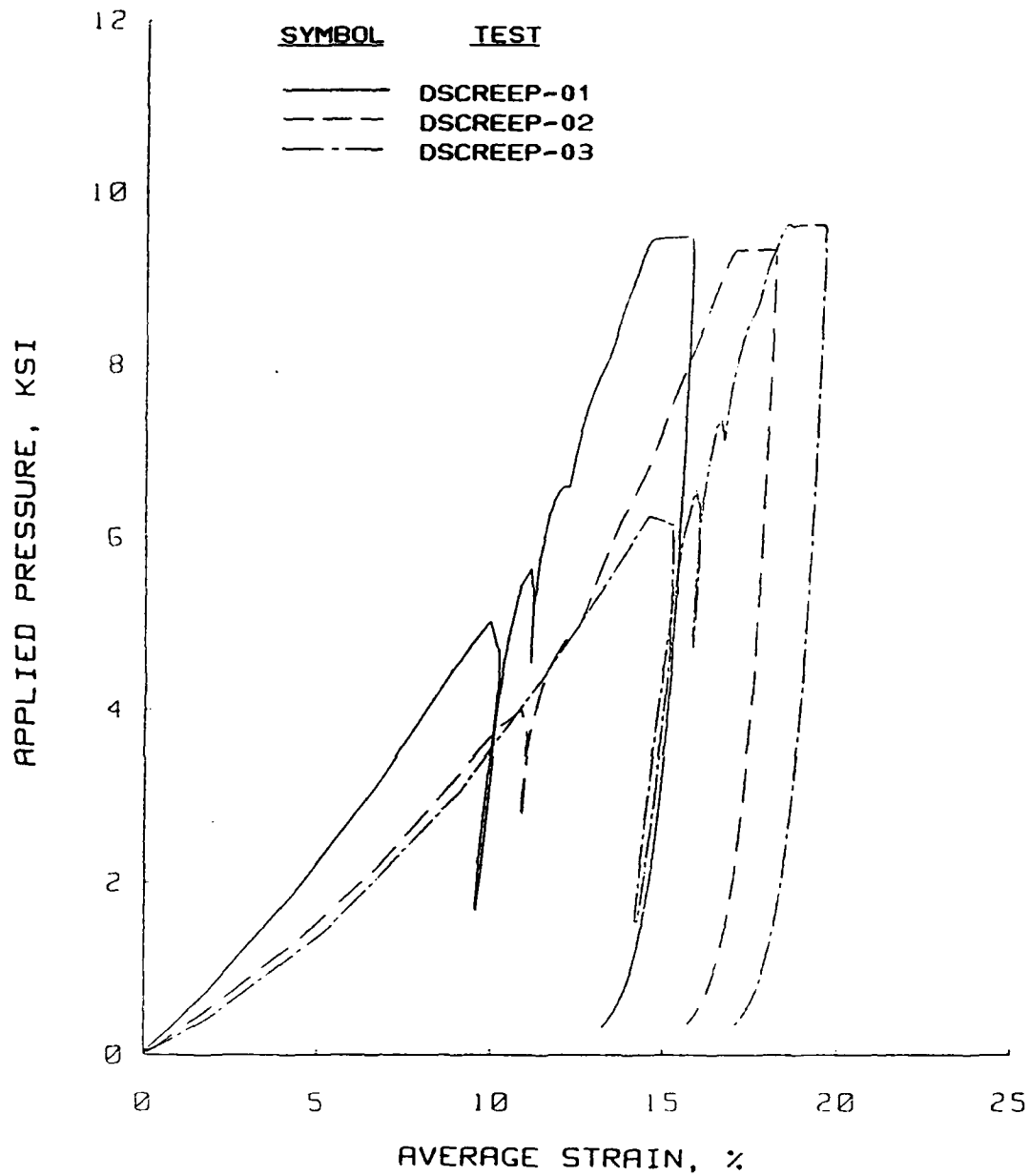
Uniaxial Strain Results
Soil Type: Vicksburg Loess

Figure B.89   Static uniaxial strain results for tests VSS-11,
             -12, -21, -22, and -23 performed in the WES 0.1-
             msec device on Vicksburg loess, V-series.

Figure B.90   Pressure versus time plots for static uniaxial-
strain tests VSS-11, -12, -21, -22, and -23
performed in the WES 0.1-msec device on Vicksburg
loess, V-series.

Uniaxial Strain Results
Soil Type: Vicksburg Loess

Figure B.91   Strain versus time plots for static uniaxial strain
tests VSS-11, -12, -21, -22, and -23 performed in
the WES 0.1-msec device on Vicksburg loess,
V-series.

Uniaxial Strain Results
Soil Type: Vicksburg Loess

SYMBOL	TEST
————	VSS-24
————	VSS-25
—·—·—	VSS-31
—··—··—	VSS-32

Figure B.92   Static uniaxial strain results for tests VSS-24, -25, -31, and -32 performed in the WES 0.1-msec device on Vicksburg loess, V-series.

Uniaxial Strain Results
Soil Type: Vicksburg Loess

SYMBOL	TEST
———	VSS-24
— — —	VSS-25
—·—·—	VSS-31
—··—··—	VSS-32

Figure B.93 Pressure versus time plots for static uniaxial
strain tests VS-24, -25, -31, and -32 performed in
the WES 0.1-msec device on Vicksburg loess,
V-series.

Uniaxial Strain Results
Soil Type: Vicksburg Loess

Figure B.94 Strain versus time plots for static uniaxial strain
tests VSS-24, -25, -31, and -32 performed in the
WES 0.1-msec device on Vicksburg loess, V-series.

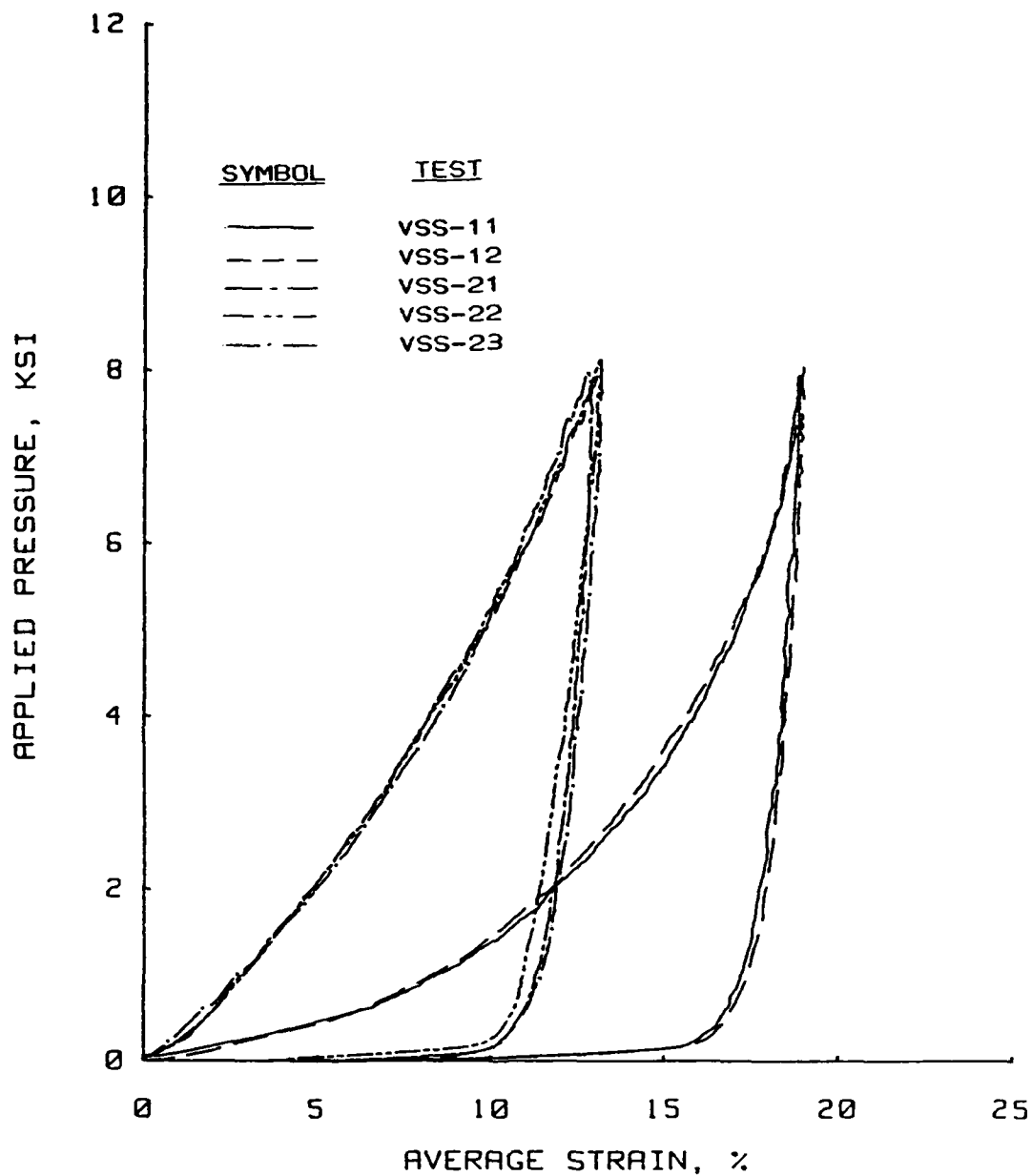# Uniaxial Strain Results
Soil Type: Vicksburg Loess

Figure B.95   Dynamic uniaxial strain results for tests VSD-11,
-12, -21, and -22 performed in the WES 0.1-msec
device on Vicksburg loess, V-series.

Uniaxial Strain Results
Soil Type: Vicksburg Loess

Figure B.96   Pressure versus time plots for dynamic uniaxial
strain tests VSD-11, -12, -21, and -22 performed in
the WES 0.1-msec device on Vicksburg loess,
V-series.

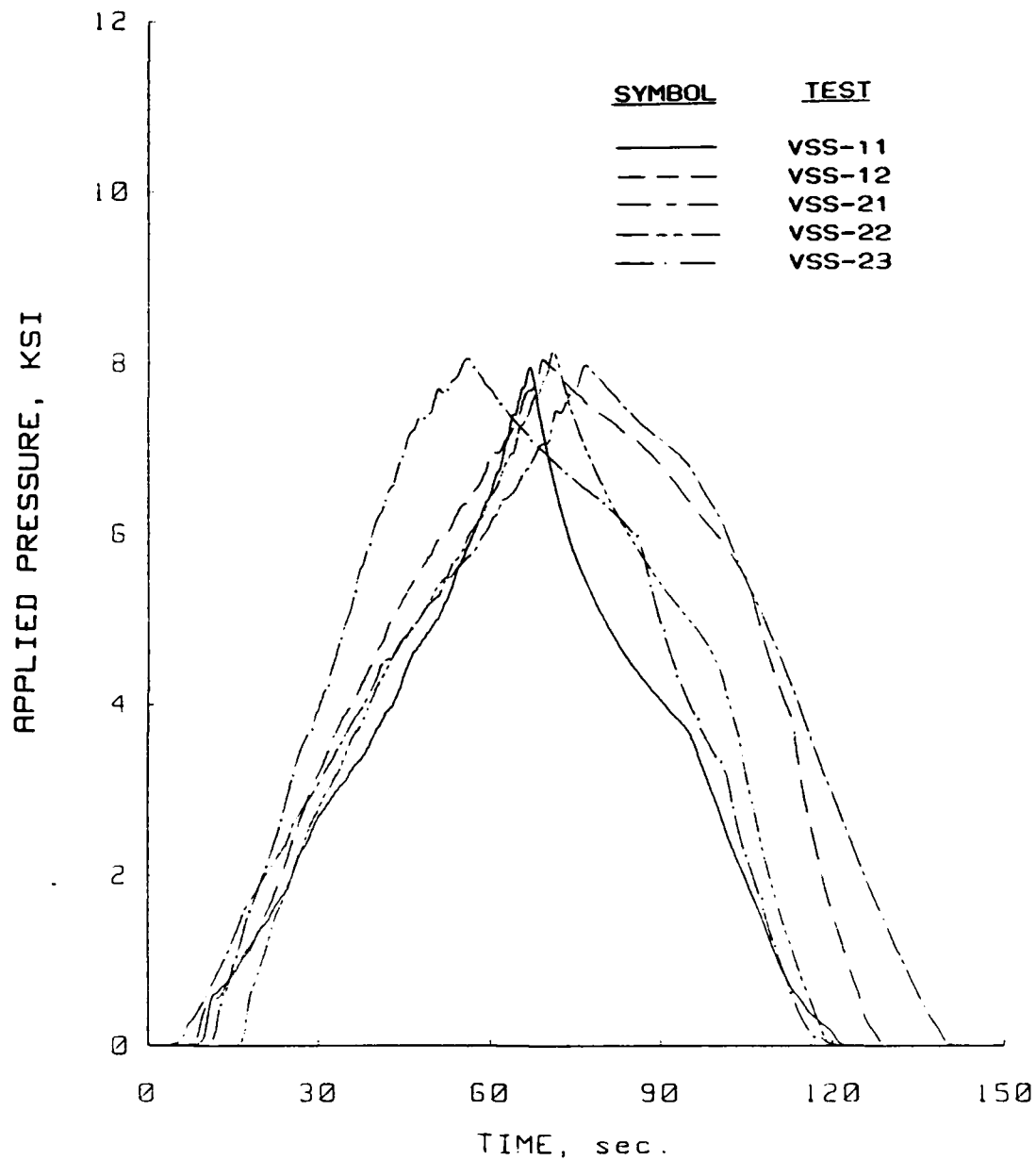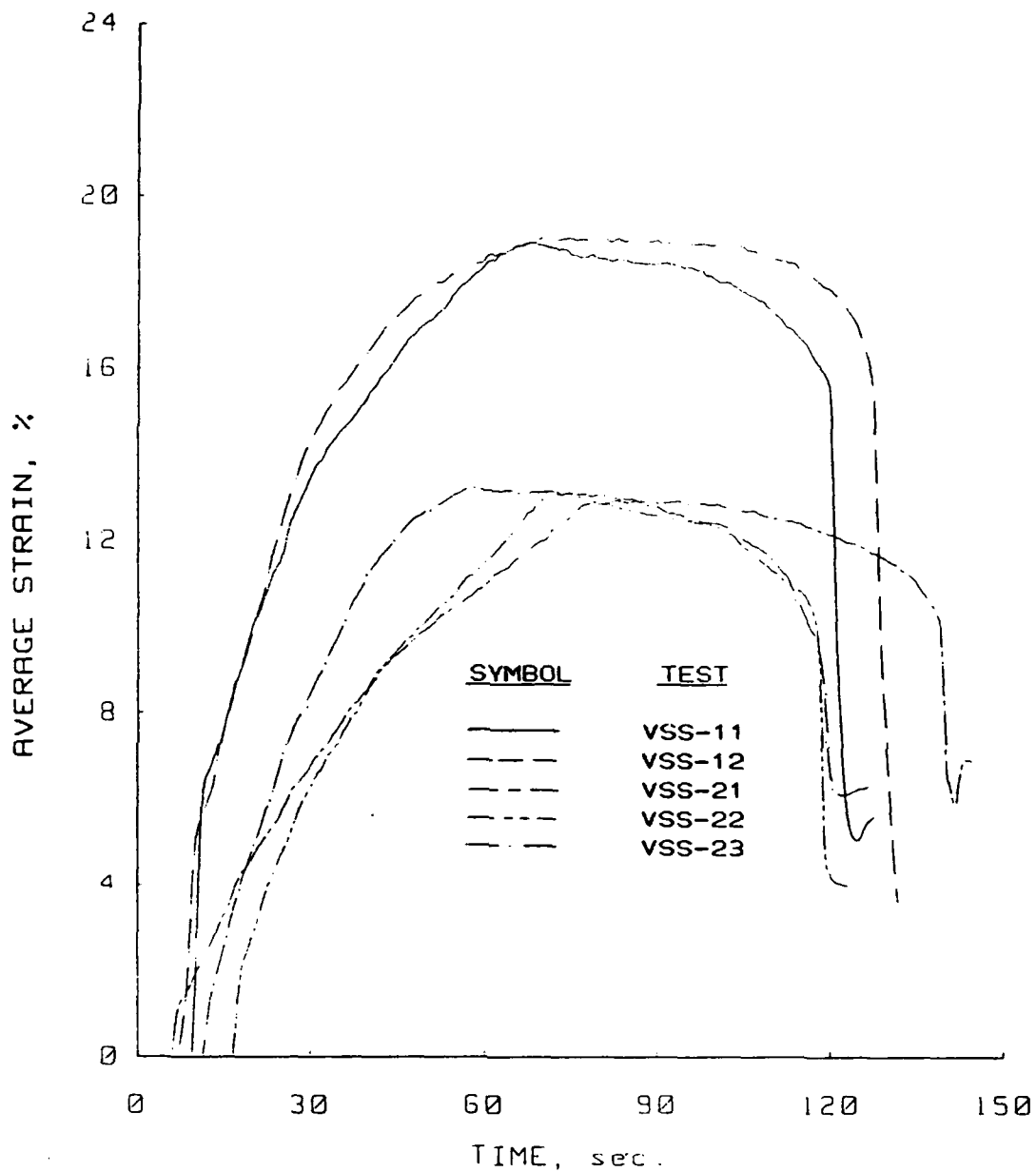## Uniaxial Strain Results
Soil Type: Vicksburg Loess

Figure B.97   Strain versus time plots for dynamic uniaxial
strain tests VSD-11, -12, -21, and -22 performed in
the WES 0.1-msec device on Vicksburg loess,
V-series.

Uniaxial Strain Results
Soil Type: Vicksburg Loess
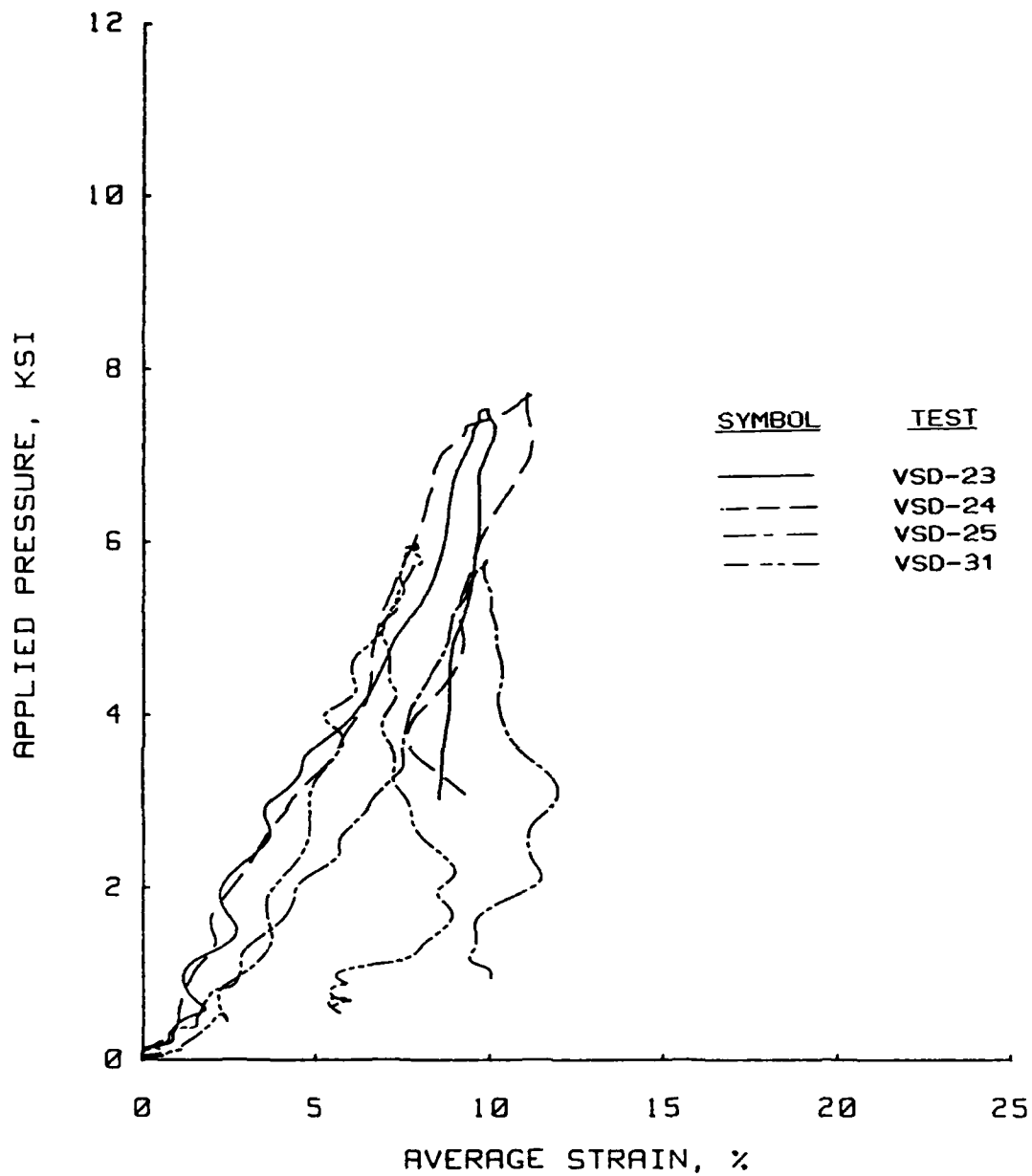
Figure B.98   Dynamic uniaxial strain results for tests VSD-23,
-24, -25, and -31 performed in the WES 0.1-msec
device on Vicksburg loess, V-series.

Uniaxial Strain Results
Soil Type: Vicksburg Loess
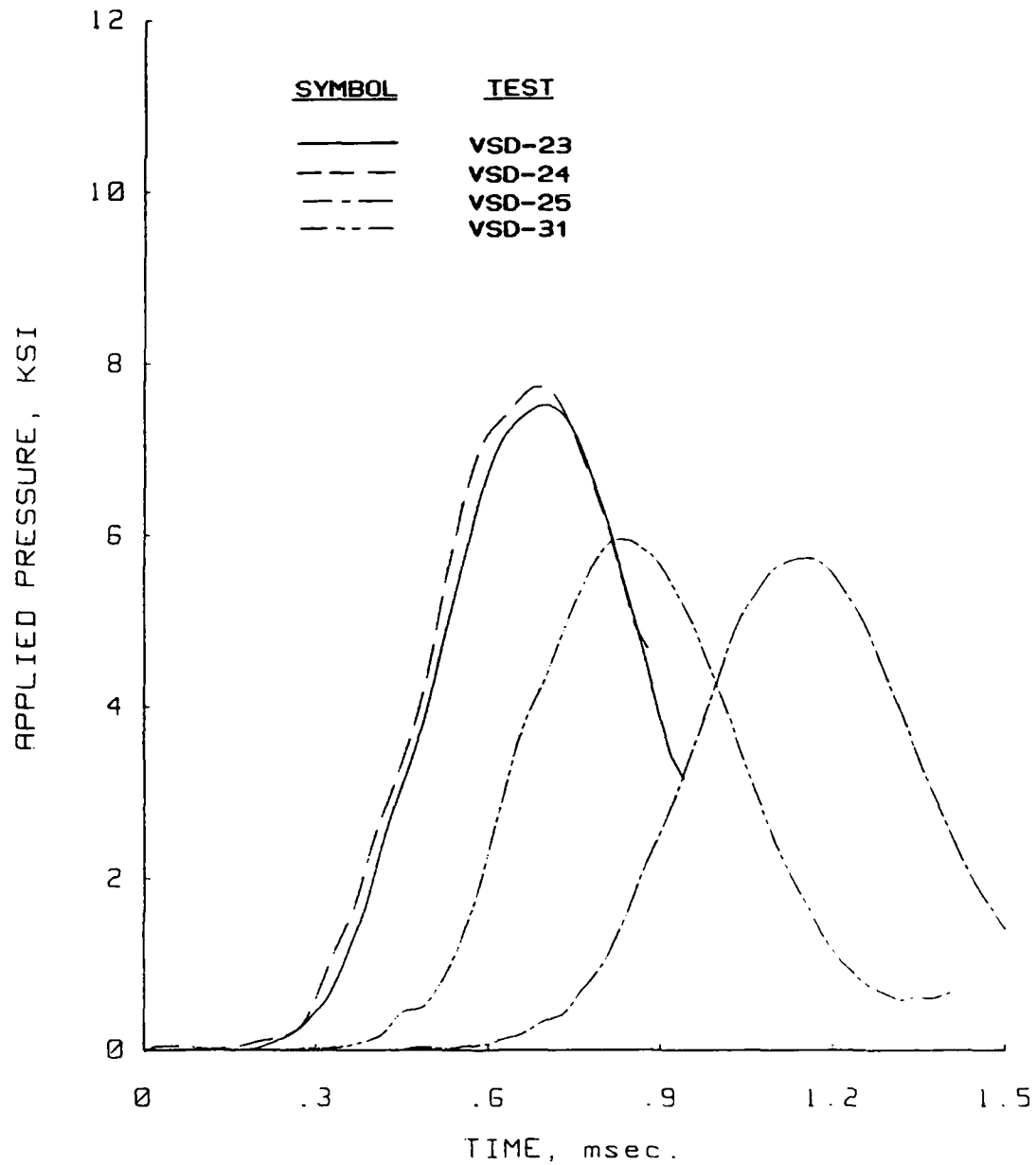
Figure B.99 Pressure versus time plots for dynamic uniaxial
strain tests VSD-23, -24, -25, and -31 performed in
the WES 0.1-msec device on Vicksburg loess,
V-series.

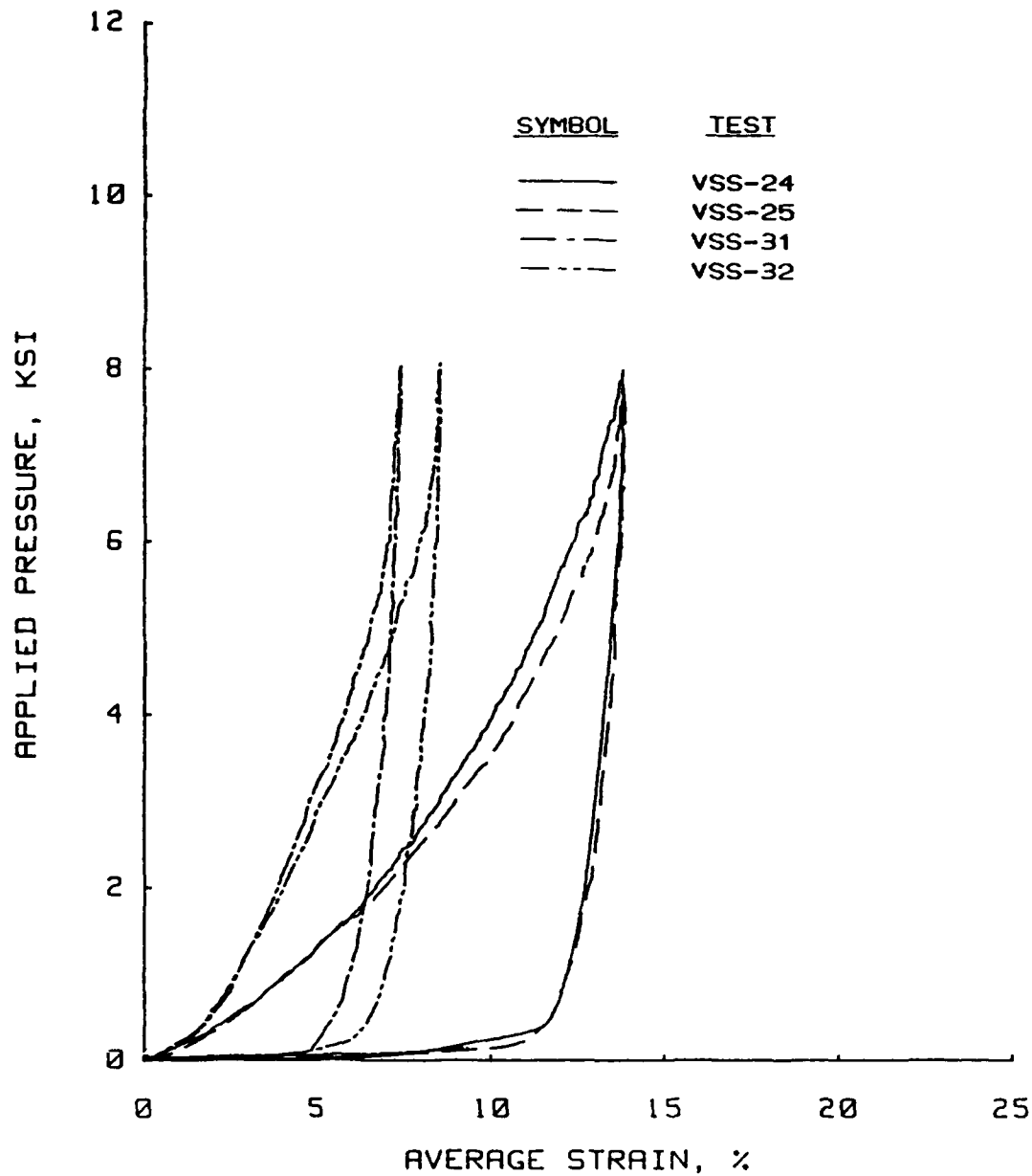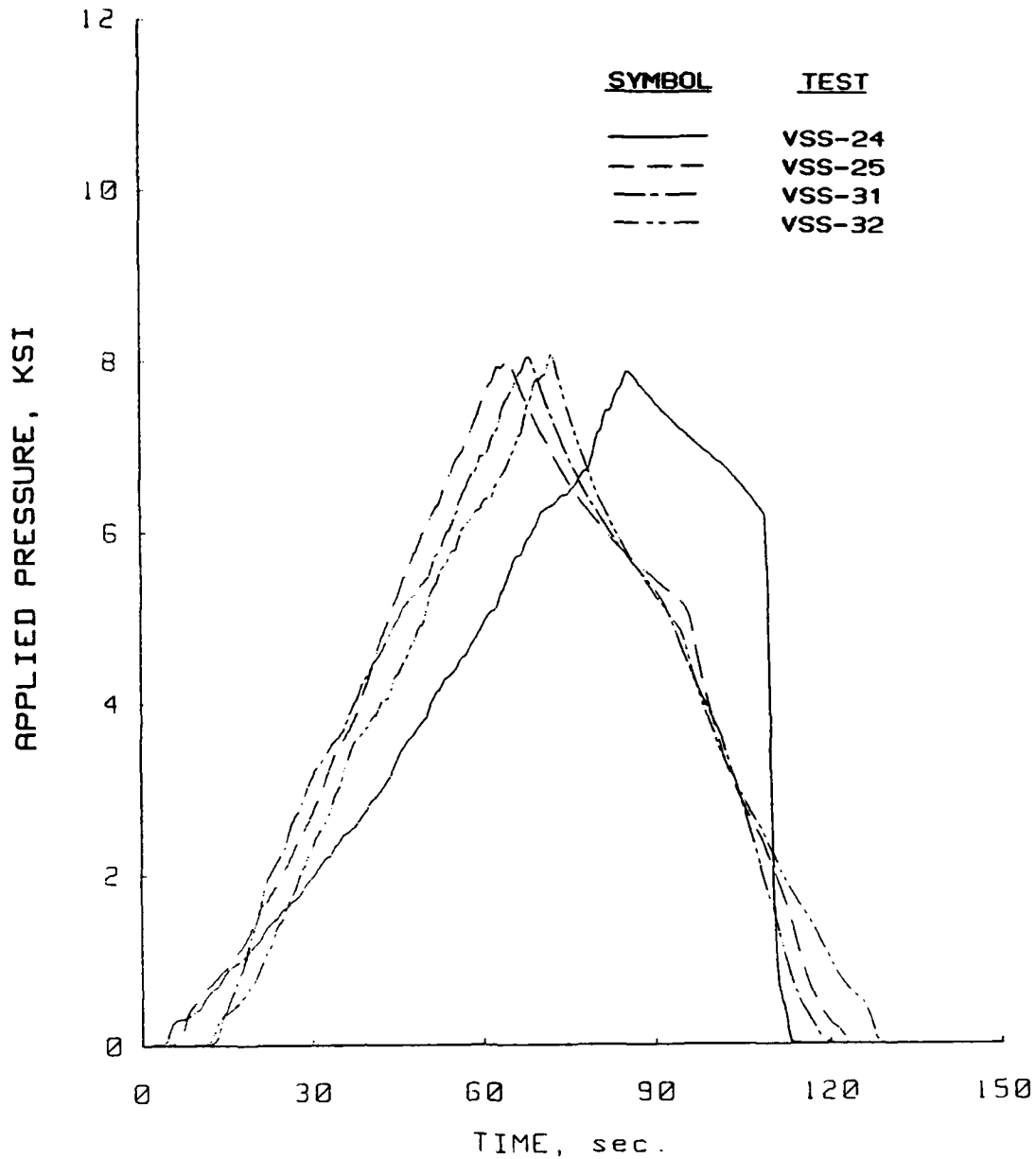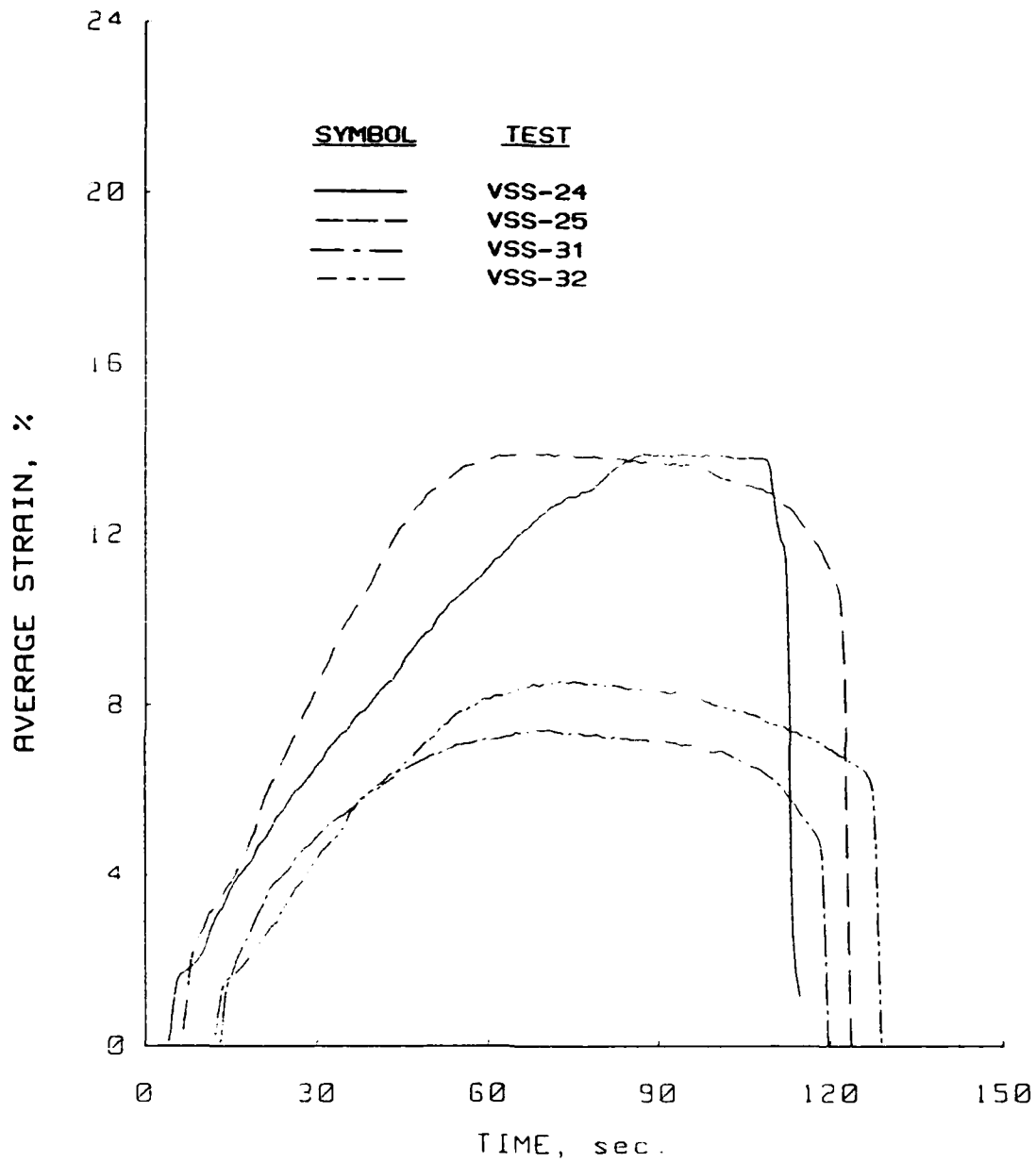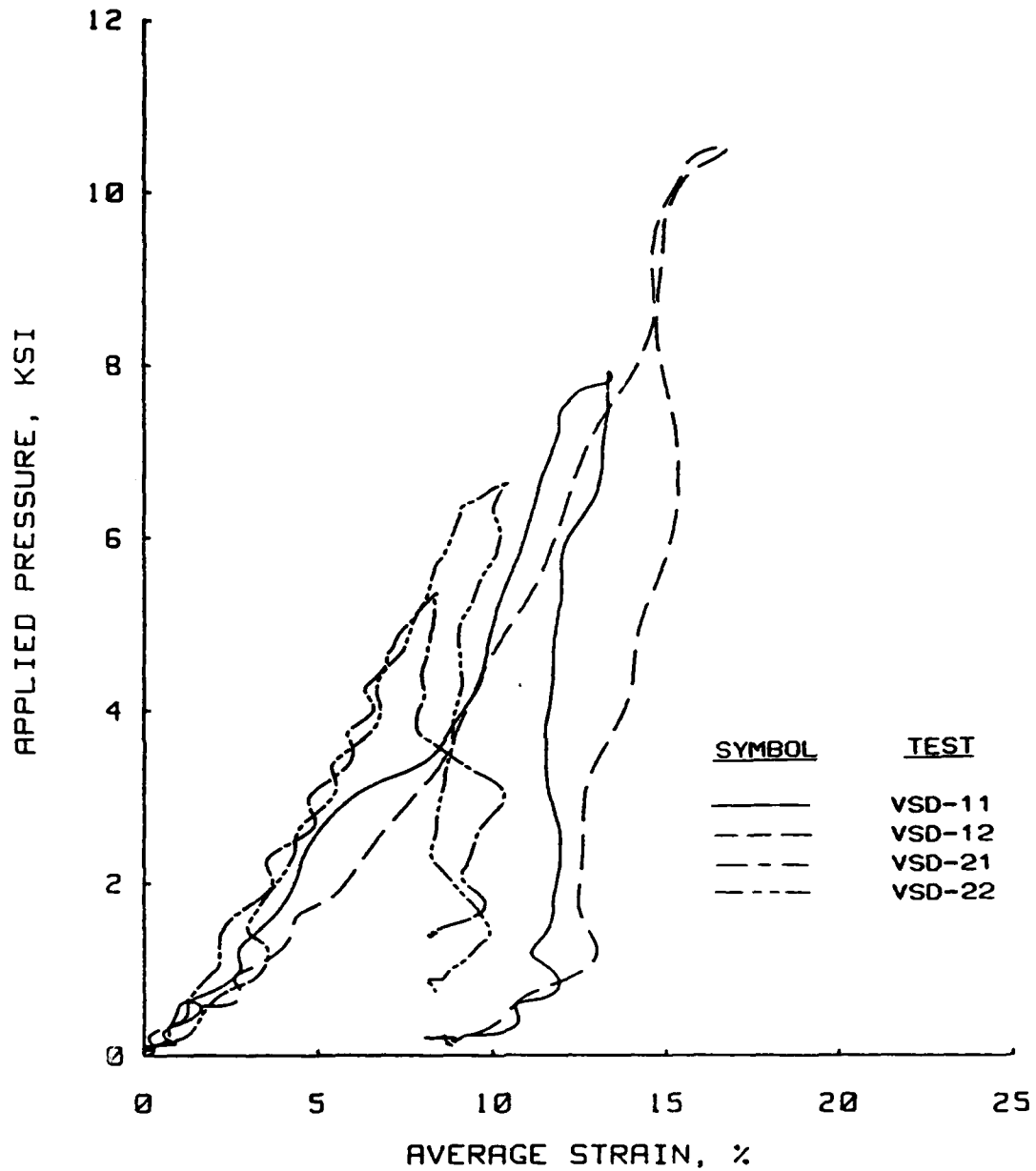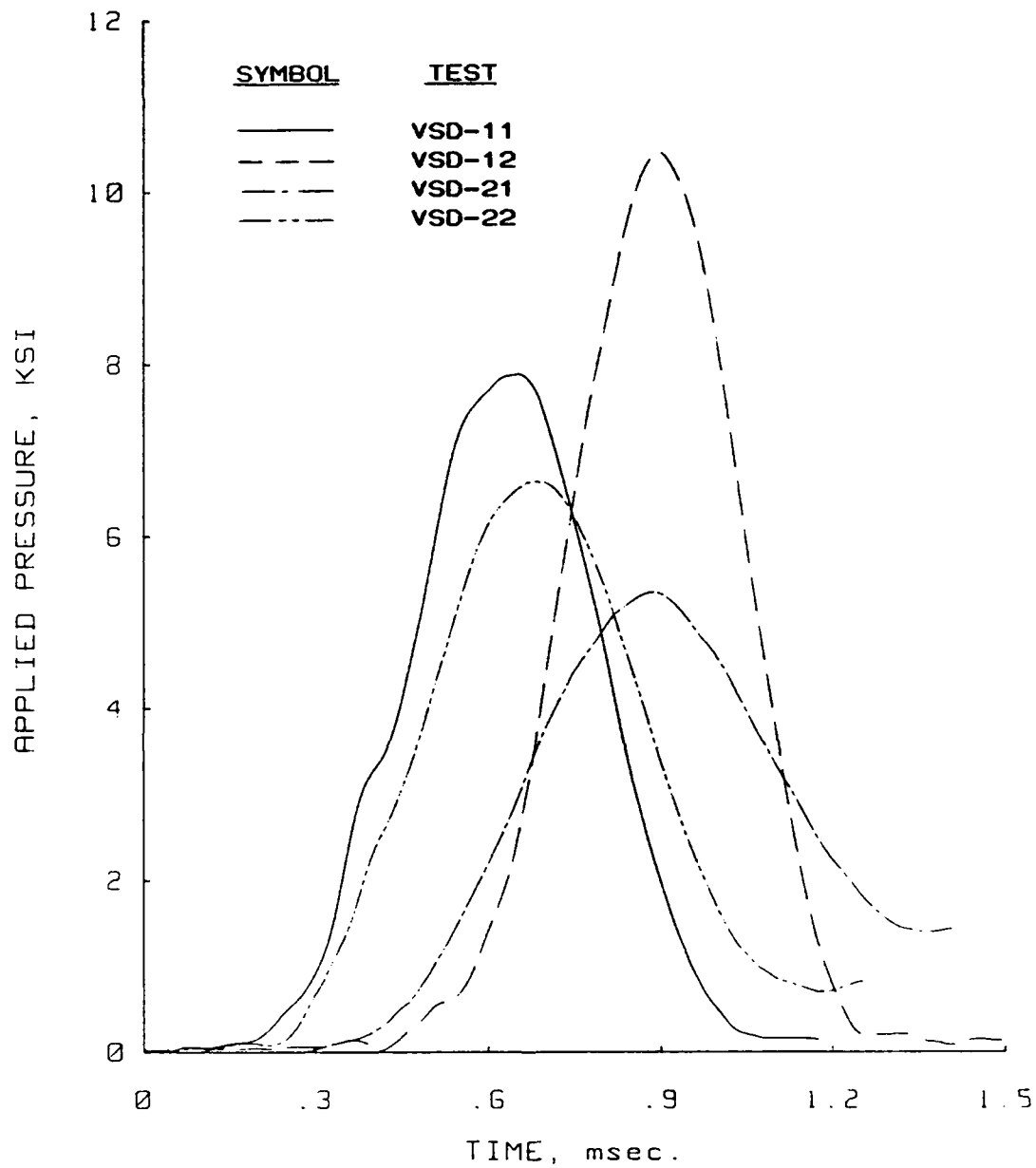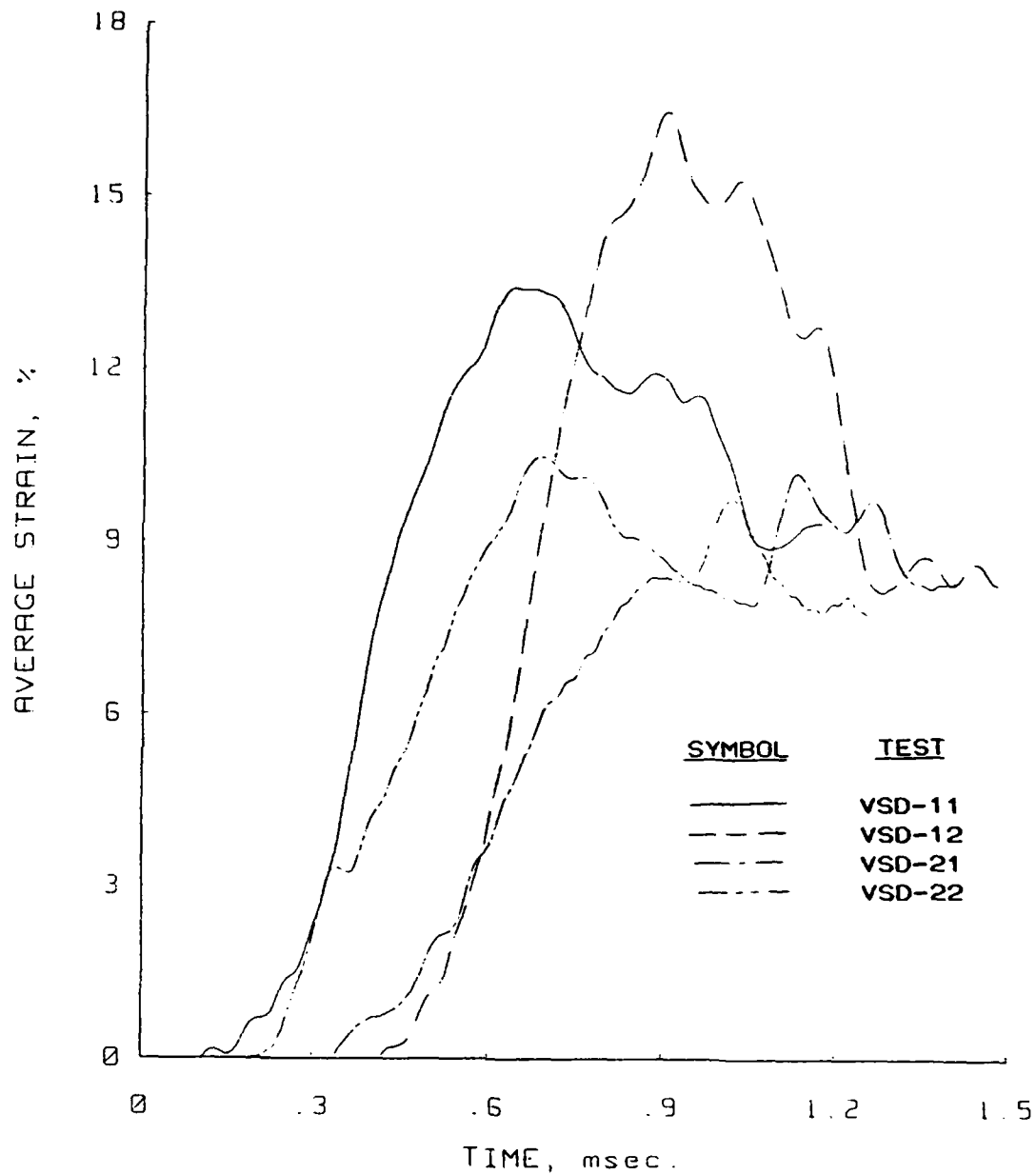# Uniaxial Strain Results
Soil Type: Vicksburg Loess
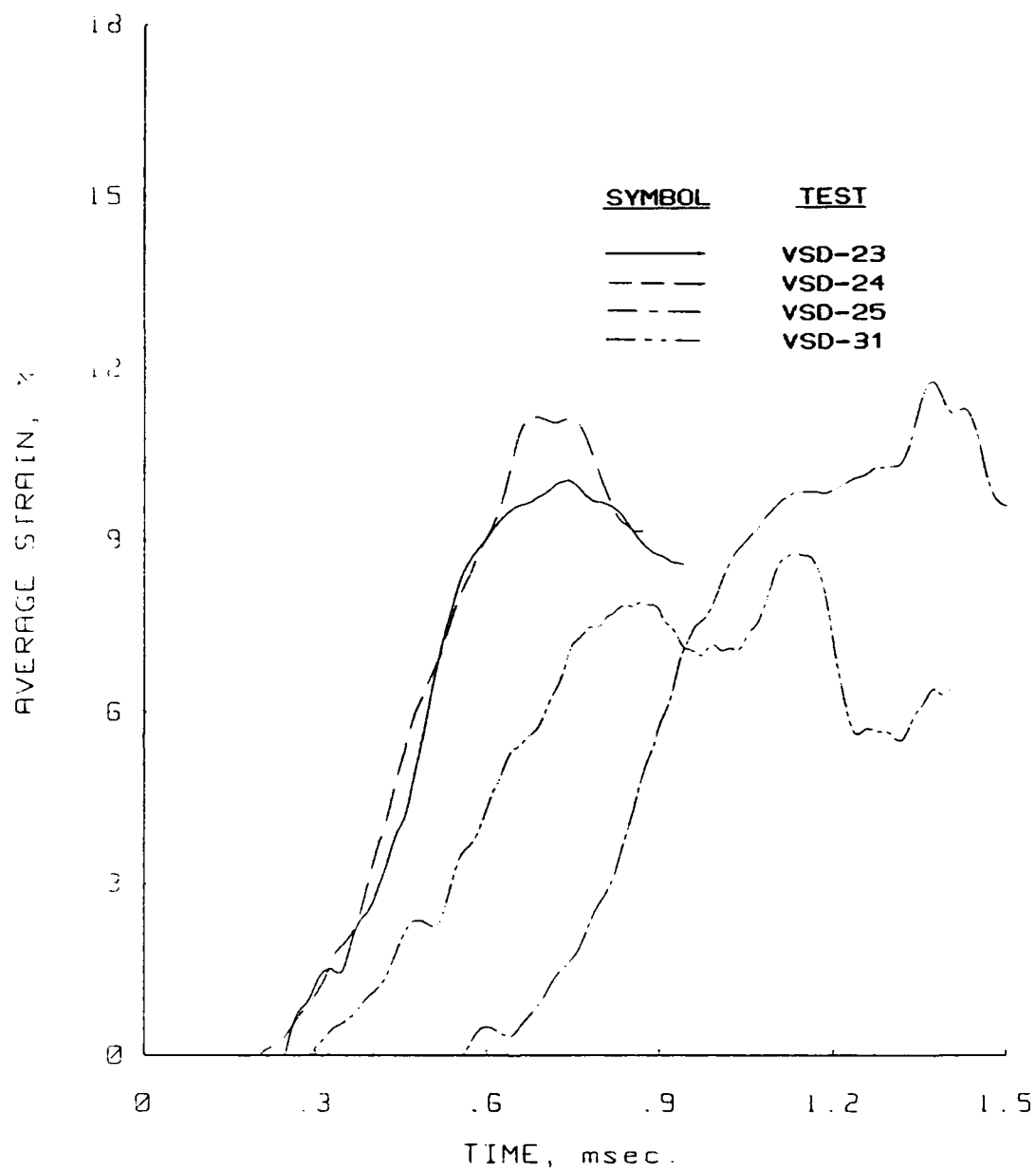
Figure B.100 Strain versus time plots for dynamic uniaxial
strain tests VSD-23, -24, -25, and -31 performed
in the WES 0.1-msec device on Vicksburg loess,
V-series.

APPENDIX C

DESCRIPTION OF ADLUD COMPUTER PROGRAM

The one-dimensional, finite-difference code ADLUD was developed by Meier (1984) to analyze the results from dynamic uniaxial strain tests. The original version of the program was updated to include a rate-dependent incremental stiffening modulus model and a more efficient numerical computation scheme.

A continuous medium can be modeled by a series of masses interconnected by springs. The springs are used to represent the constitutive properties of the material being modeled. This type of model is often referred to as a lumped-parameter model and can be readily solved using numerical methods.

The ADLUD code simulates the conditions within the WES 0.1-msec device by incorporating a fluid layer overlying a soil layer resting on a rigid boundary. The fluid layer must be modeled to account for the distance between the transducer and the top of the soil sample. This distance creates a time lag between the measured pressure and the actual pressure applied at the sample surface (see Fig. 2.2.3). The base of the soil container is accounted for by treating the bottom of the finite difference grid as a rigid (totally reflective) boundary.

The computer code ADLUD uses a fixed double computational grid consisting of mass and stress nodes as shown in Fig. C.1. All particle motions (accelerations, velocities, and displacements) occur at the mass points. Stresses and strains are defined at points midway between the mass points which are referred to as stress points.

The program ADLUD uses simple one-dimensional wave propagation theory. An element loaded in one-dimensional compression can be represented as shown in Fig. C.2. Applying Newton's second law of motion yields:

$$F = m\ a = m\ \frac{d^2u}{dt^2} \tag{C-1}$$

where: F = force
m = mass of the element
a = acceleration of the element
u = displacement in the z direction
t = time

By summing the forces shown on the element in Fig. C.2, Eq. C-1 can be rewritten as:

$$- \rho\ A\ dz\ \frac{d^2u}{dt^2} = \left[\left(\sigma + \frac{d\sigma}{dz}\ dz \right) A - \sigma\ A\ - \rho\ g\ A\ dz \right] \tag{C-2}$$

where: ρ = mass density of the element
A = cross-sectional area of the element
g = gravity constant

Equation C-2 reduces to:

$$a = \frac{d\dot{u}}{dt} = -\frac{1}{\rho} \frac{d\sigma}{dz} + g \tag{C-3}$$

where: $\dot{u}$ = velocity in the z direction
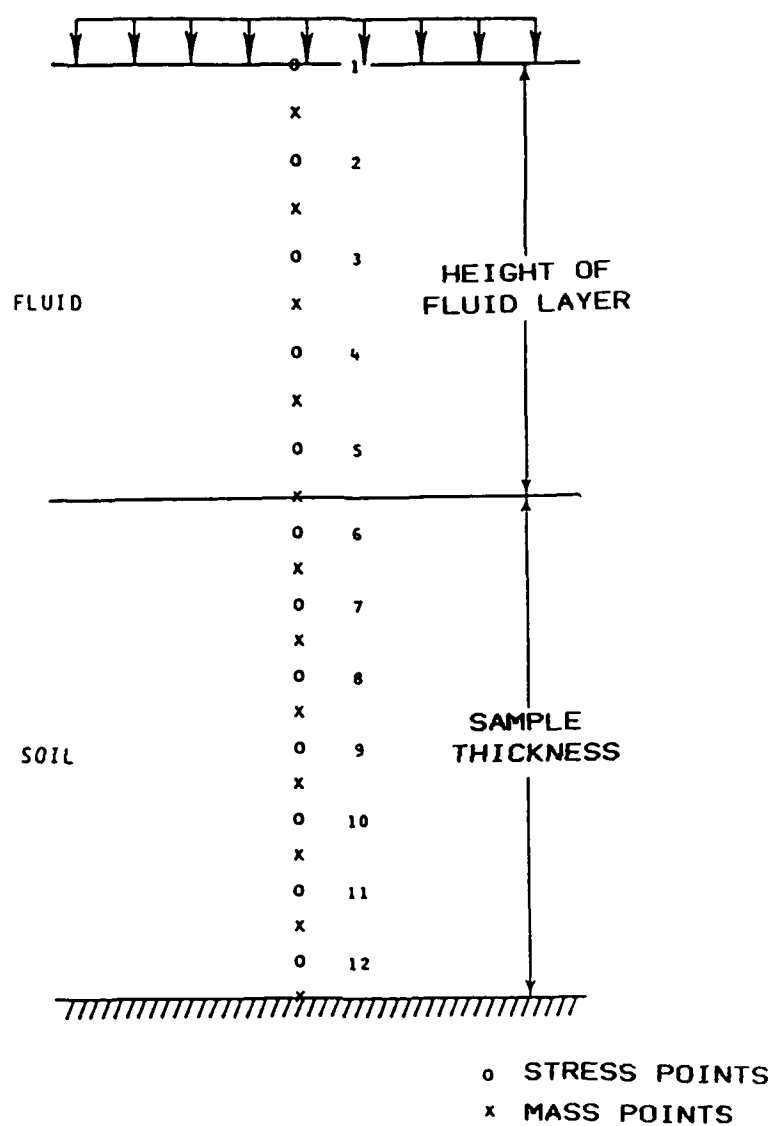
Figure C.1 Finite-difference grid for computer code ADLUD.
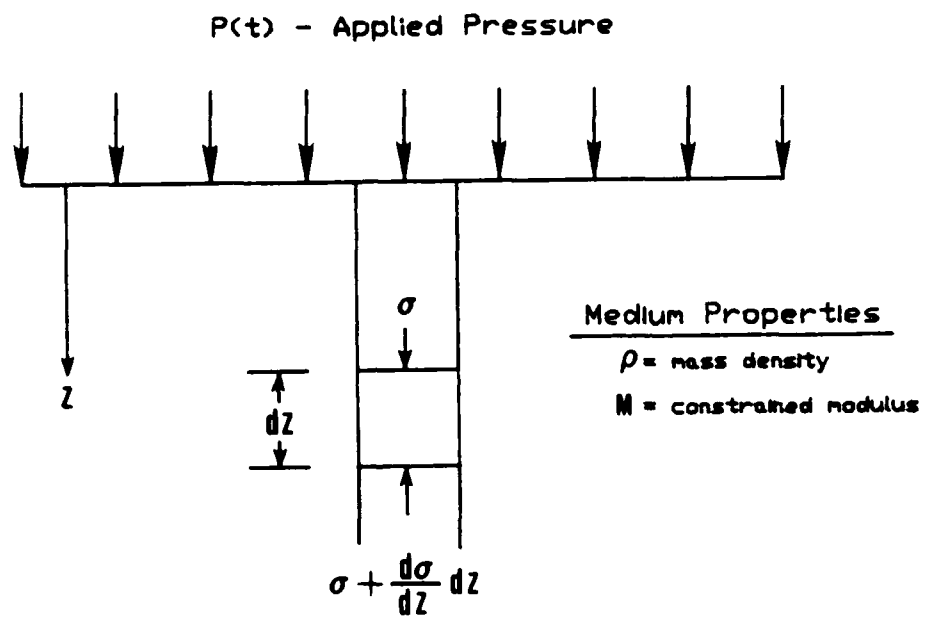
Figure C.2 One-dimensional wave propagation.

Equation C-3 can be expressed in finite-difference form as:

$$\frac{\dot{u}^{t+1} - \dot{u}^t}{\Delta t} = - \frac{1}{\rho} \frac{\Delta \sigma}{\Delta z} + g \tag{C-4}$$

or

$$\dot{u}^{t+1} = \dot{u}^t - \Delta t \left[\frac{1}{\rho} \frac{\Delta \sigma}{\Delta z} - g \right] \tag{C-5}$$

This equation can readily be adapted to computer solutions. However, a more numerically efficient equation can be derived from Eq. C-5 (Meier, 1985). The value of $\Delta \sigma$ can be expressed in terms of dead (gravity) and live (applied pressure) components, which are denoted as $\Delta \sigma^D$ and $\Delta \sigma^L$, respectively. Equation C-5 can be rewritten as:

$$\dot{u}^{t+1} = \dot{u}^t - \Delta t \left[\frac{1}{\rho} \frac{\Delta \sigma^D}{\Delta z} + \frac{1}{\rho} \frac{\Delta \sigma^L}{\Delta z} - g \right] \tag{C-6}$$

The dead load can be expressed as:

$$\sigma^D = \sum_{i=1}^{n} \gamma_i \Delta z \tag{C-7}$$

where: γ = unit weight of the material

The change in dead load between two adjacent nodes can be expressed as:

$$\sigma^D_i - \sigma^D_{i-1} = \sum_{i=1}^{n} \gamma_i \Delta z - \sum_{i=1}^{n-1} \gamma_i \Delta z \tag{C-8}$$

or

$$\sigma^D = \gamma \Delta z \tag{C-9}$$

Equation C-6 can be rewritten using the results of Eq.C-9 as:

$$\dot{u}^{t+1} = \dot{u}^t - \Delta t \left[\frac{\gamma}{\rho} + \frac{\gamma}{\rho} \frac{\Delta\sigma^L}{\Delta\sigma^D} - g \right] \qquad (C\text{-}10)$$

The mass density of any material can be expressed as:

$$\rho = \frac{\gamma}{g} \qquad (C\text{-}11)$$

Equation C-10 can be rewritten using Eq. C-11 as:

$$\dot{u}^{t+1} = \dot{u}^t - \Delta t \left[g + g \frac{\Delta\sigma^L}{\Delta\sigma^D} - g \right] \qquad (C\text{-}12)$$

or

$$\dot{u}^{t+1} = \dot{u}^t - g \Delta t \left[\frac{\Delta\sigma^L}{\Delta\sigma^D} \right] \qquad (C\text{-}13)$$

Rearranging:

$$\frac{\dot{u}^{t+1} - \dot{u}^t}{\Delta t} = - g \left[\frac{\Delta\sigma^L}{\Delta\sigma^D} \right] \qquad (C\text{-}14)$$

from which:

$$a = - \left[\frac{\Delta\sigma^L}{\Delta\sigma^D} \right] \qquad (C\text{-}15)$$

Where a is the acceleration in g's.

The orginal ADLUD code was modified to incorporate Eq. C-15 in lieu of of the conventional finite-difference form (Eq. C-5) in the solution of the governing differential equation for one-dimensional wave propagation.

The soil properties are modeled using piecewise-linear approximations in the form of digitized stress-strain results. The digitized stress-strain curve is inputted in the form of virgin loading and unloading curves. This unloading curve translates along the virgin

loading curve to model unloading and reloading from a previously applied stress. Hysteresis isn't used in the unloading-reloading response. Hysteretic behavior isn't critical for the high pressures generated during the laboratory testing program (see Fig. B.1).

A constitutive equation based on laboratory tests is used to model the fluid layer. The fluid layer was assumed to be nonlinear and elastic. A hyperbolic relationship (from Meier, 1984) was used to calculate the bulk modulus as a function of pressure:

$$K = \frac{K_i}{1-K_1} \left(1 - K_1 \exp \left(- K_2 p \right) \right) \tag{C-16}$$

where: K = bulk modulus of the fluid
K_i = initial bulk modulus
K_1, K_2 = material constants
p = fluid pressure

This equation is illustrated in Fig. C.3(a). The constants K_i and K_1 are determined as shown in Fig. C.3(b). The constant K_2 is determined by trial and error.

Incremental elasticity can be used to formulate a relationship between stress and strain using the bulk modulus:

$$d\sigma = K \, d\epsilon \tag{C-17}$$

where: ϵ = strain in the fluid layer

Intergrating Eq. C-17 yields a relationship between axial stress and strain:

$$\epsilon = \frac{1 - K_1}{3 K_2 K_i} \ln \left[\frac{\exp \left(K_2 \sigma \right) - K_1}{1 - K_1} \right] \tag{C-18}$$

This equation can be inverted to define stress as a function of strain:

$$\sigma = \frac{1}{3 K_2} \ln \left[K_1 + \left(1 - K_1 \right) \exp \left(\frac{3 K_2 K_i \epsilon}{1-K_1} \right) \right] \tag{C-19}$$
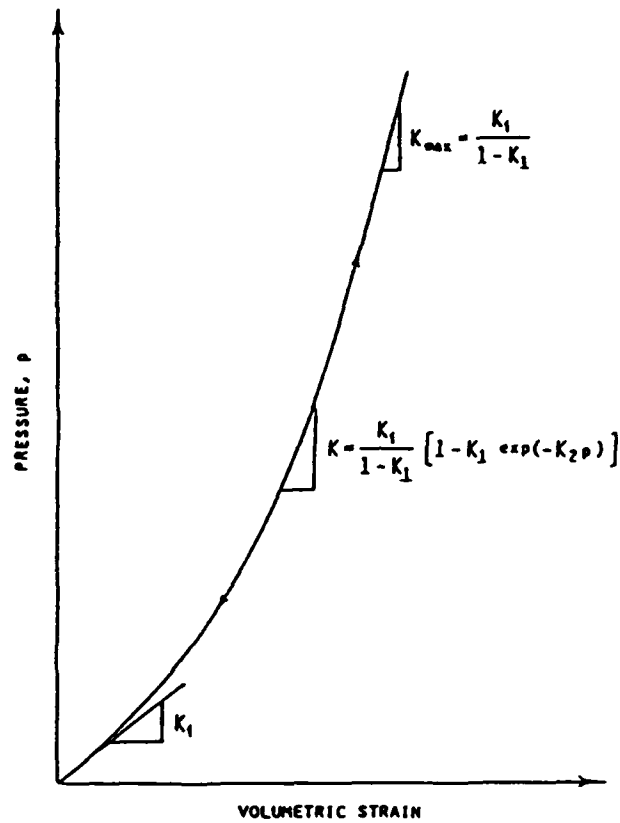
a. Constitutive model for the fluid layer.
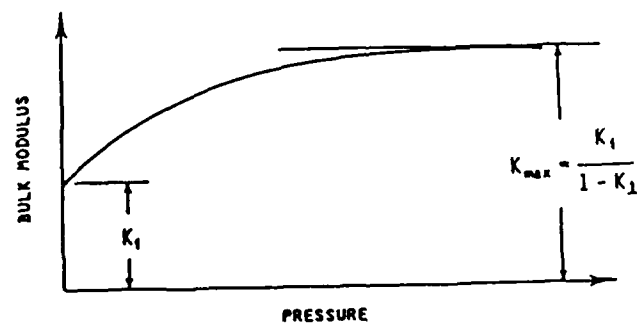
b. Limiting bulk modulus, K_{max}.

Figure C.3 Stress-strain relationships for the fluid layer
(from Meier, 1984).

The code is driven with an actual piecewise-linear representation of the stress history measured during the test. The ADLUD results are very sensitive to subtle changes in the applied pressure pulse. Therefore, the stress histories must be accurate.

Stresses are determined at stress points, as shown in Fig. C.1. Using Eq. C-15, an acceleration can be determined based upon the relative change in applied pressure between two adjacent stress points. This value of acceleration is assigned to the mass node located midway between two stress nodes (see Fig. C.1). This value of acceleration can be intergrated with respect to time to determine velocity and displacement. The displacement gradient between two adjacent mass points is equal to the strain increment, or:

$$d\varepsilon = \frac{du}{dz} \qquad (C-20)$$

This value of strain is assigned to a point midway between the mass points, which corresponds to a stress point. This value of strain is used to determine a corresponding stress based upon either the constitutive model for the fluid (Eq. C-19) or and soil layers. Loading rate effects are taken into account by the constitutive equation for the soil.

A stiffening function was placed in ADLUD to model rate effects. This equation has the form of:

$$\frac{M_D}{M_S} = S(\varepsilon, \dot{\varepsilon}) \qquad (C-21)$$

where: M_D = dynamic modulus
M_S = static modulus
$S(\varepsilon, \dot{\varepsilon})$ = strain softening, which is a function of strain level and strain rate

For a given time step, the strains are known at the stress points based upon the computational scheme presented. The strain rate can easily be determined for a given time step. From the digitized static stress-strain curve, a static modulus can be determined for the given strain increment. This modulus is stiffened depending upon the function $S(\varepsilon, \dot{\varepsilon})$. Using the dynamic modulus and the strain increment, a new stress can be computed. This process is continued throughout the grid. For the next time step, an increase in pressure is applied at the top of the grid and the process repeated.

The principal output from the code is the applied pressure at the transducer and the average strain over the depth of the sample. These results can then be compared to actual laboratory measurements to assess the accuracy of the rate dependent model. The stresses and strains can also be outputted at each node to obtain the true material response.

APPENDIX D

ADLUD SIMULATIONS OF SUBMILLISECOND TESTS

This Appendix contains the results of the ADLUD simulations versus the actual test measurements of applied pressure and average strain for the submillisecond uniaxial strain tests performed during this study. The results are summarized in Chapter V along with a discussion of the procedures used to obtain the plots. A discussion of the computer code ADLUD is presented in Appendix C.

Uniaxial Strain Results
Soil Type: Enewetak Beach Sand

Figure D.1   Laboratory measured versus ADLUD predicted values of applied pressure and average strain for Test CS2-04, Enewetak beach sand.

315

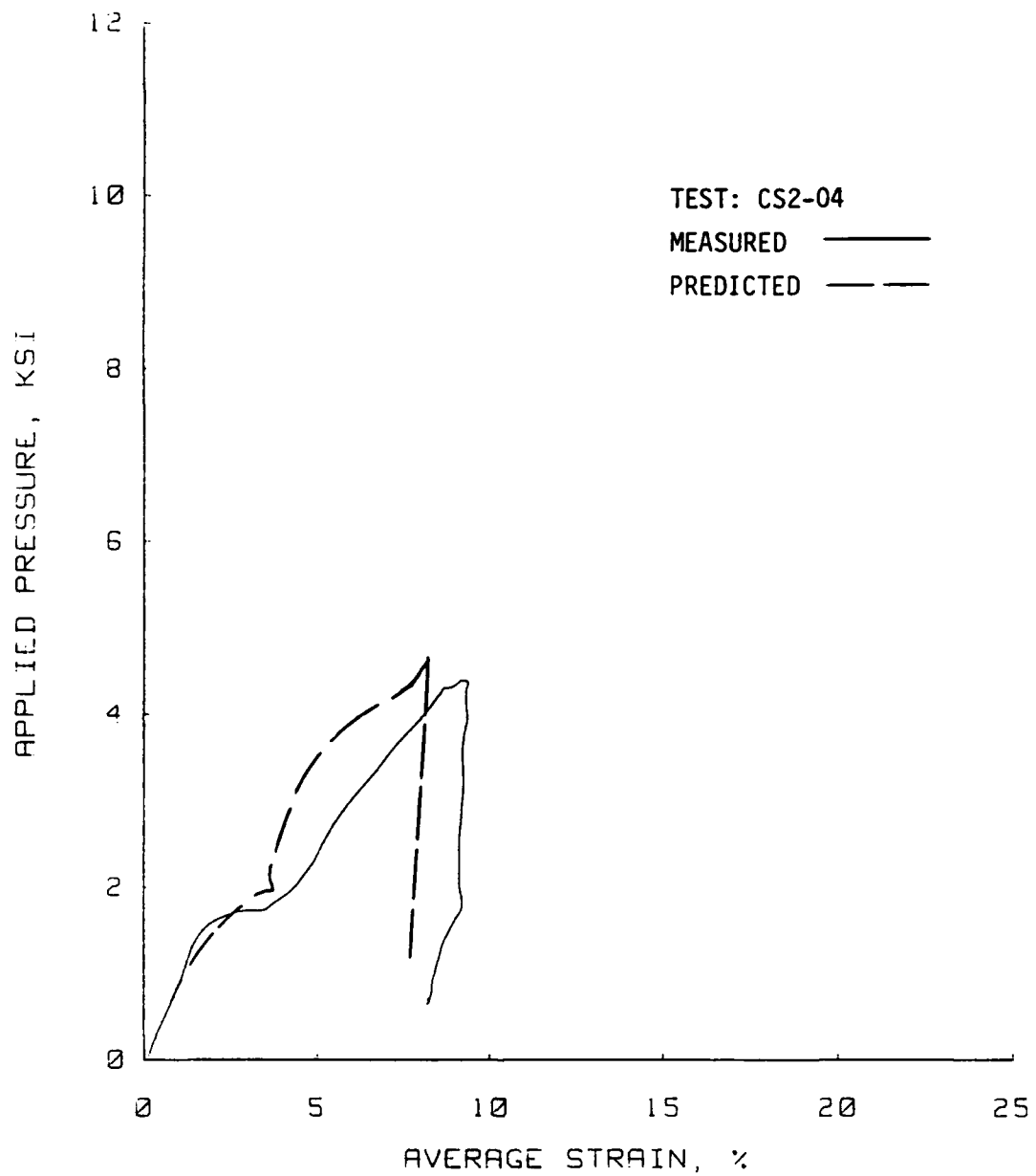Uniaxial Strain Results
Soil Type: Enewetak Beach Sand

Figure D.2 Laboratory measured versus ADLUD predicted values of
applied pressure and average strain for Test CS2-05,
Enewetak beach sand.

Uniaxial Strain Results
Soil Type: Enewetak Beach Sand

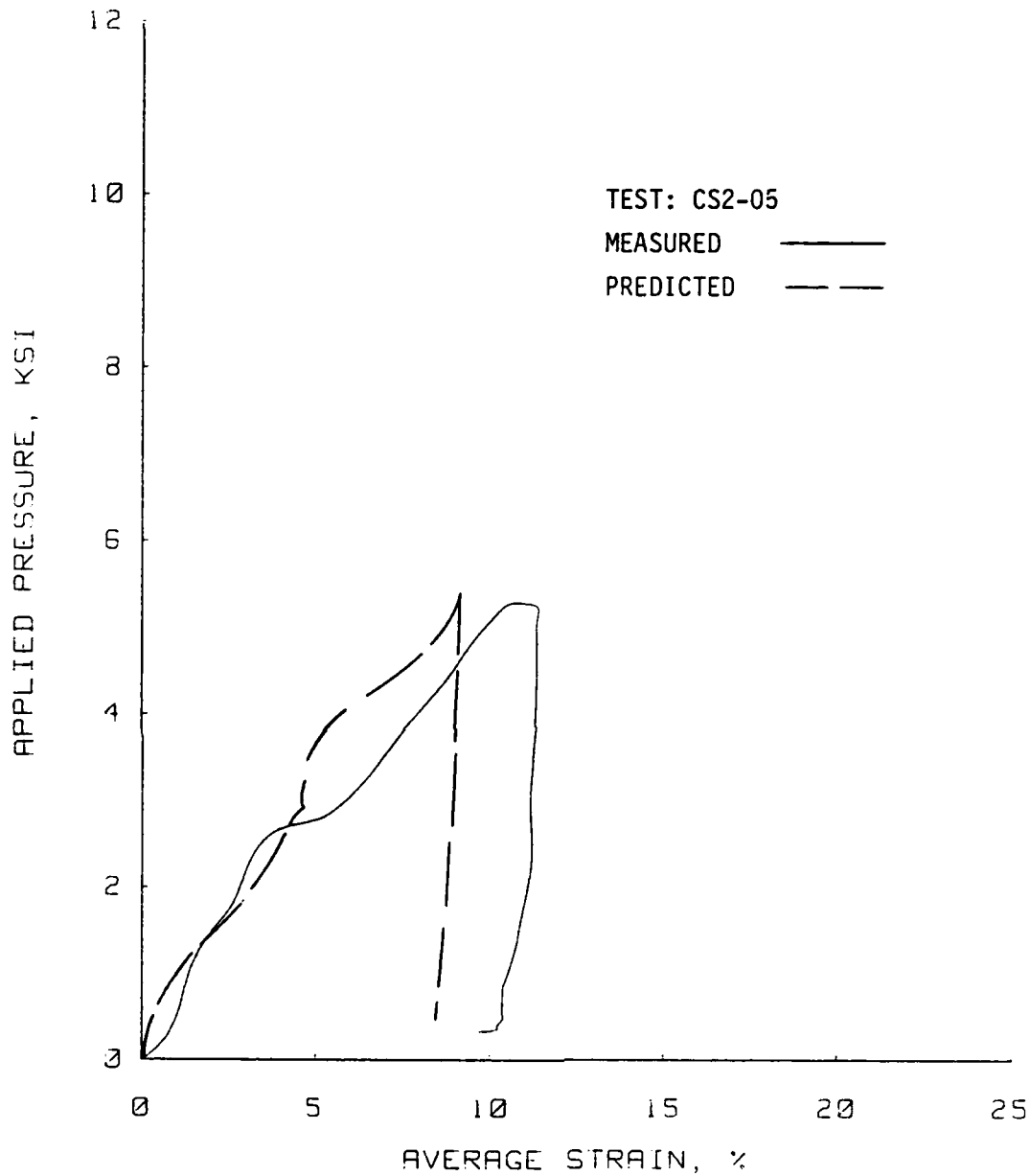Figure D.3 Laboratory measured versus ADLUD predicted values of
applied pressure and average strain for Test CS2-06,
Enewetak beach sand.

Figure D.4   Laboratory-measured and ADLUD-predicted plots of
applied pressure versus average strain for test
CS2-07, Enewetak beach sand.

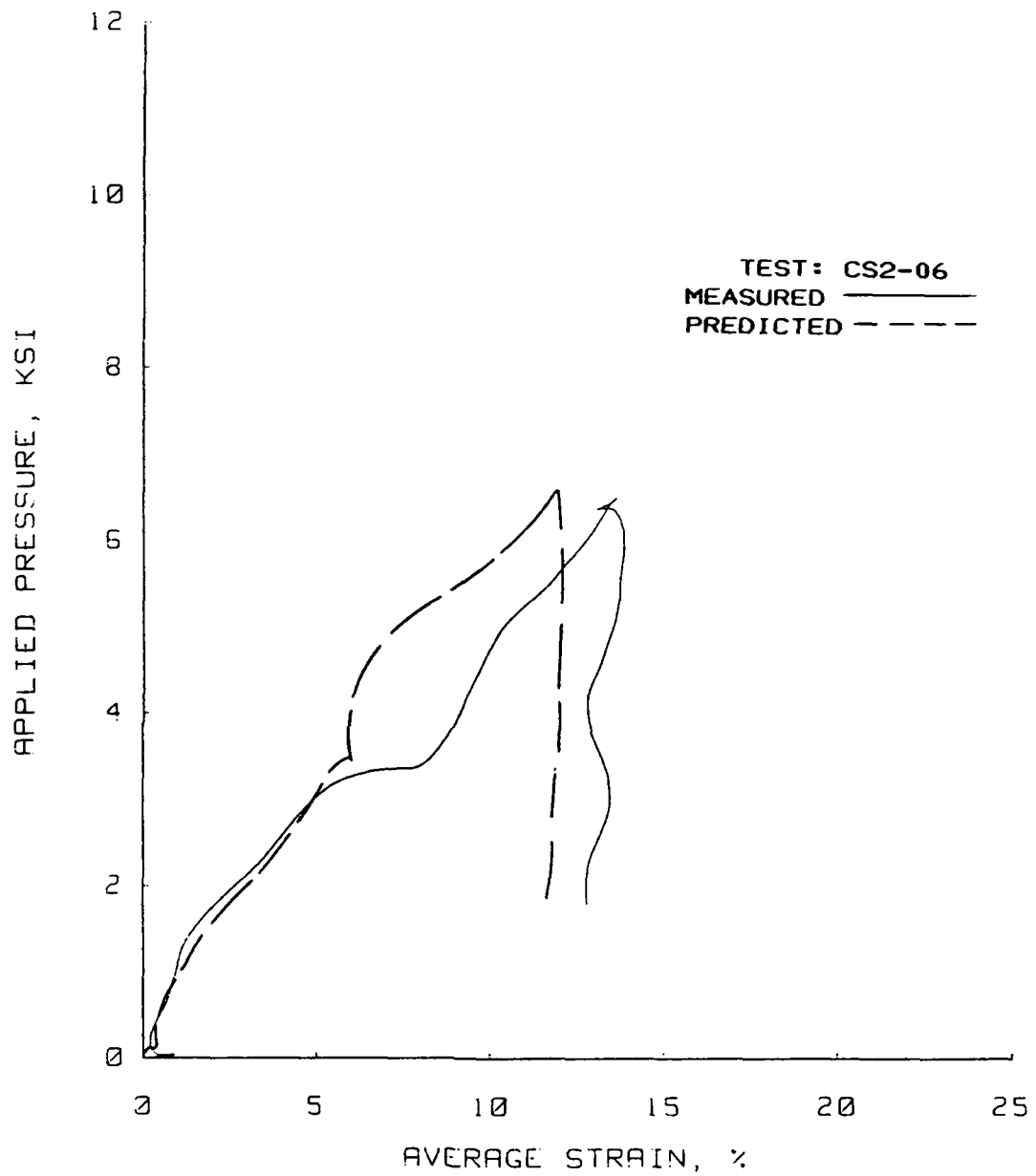## Uniaxial Strain Results
Soil Type: Enewetak Beach Sand

Figure D.5   Laboratory-measured and ADLUD-predicted plots of
applied pressure versus average strain for test
CS2-08, Enewetak beach sand.

Uniaxial Strain Results
Soil Type: Flume Sand

Figure D.6   Laboratory-measured and ADLUD-predicted plots of
applied pressure versus average strain for test
FS2-05, flume sand.

Figure D.7 Laboratory-measured and ADLUD-predicted plots of applied pressure versus average strain for test FS2-06, flume sand.

Figure D.8 Laboratory-measured and ADLUD-predicted plots of applied pressure versus average strain for test FS2-07, flume sand.
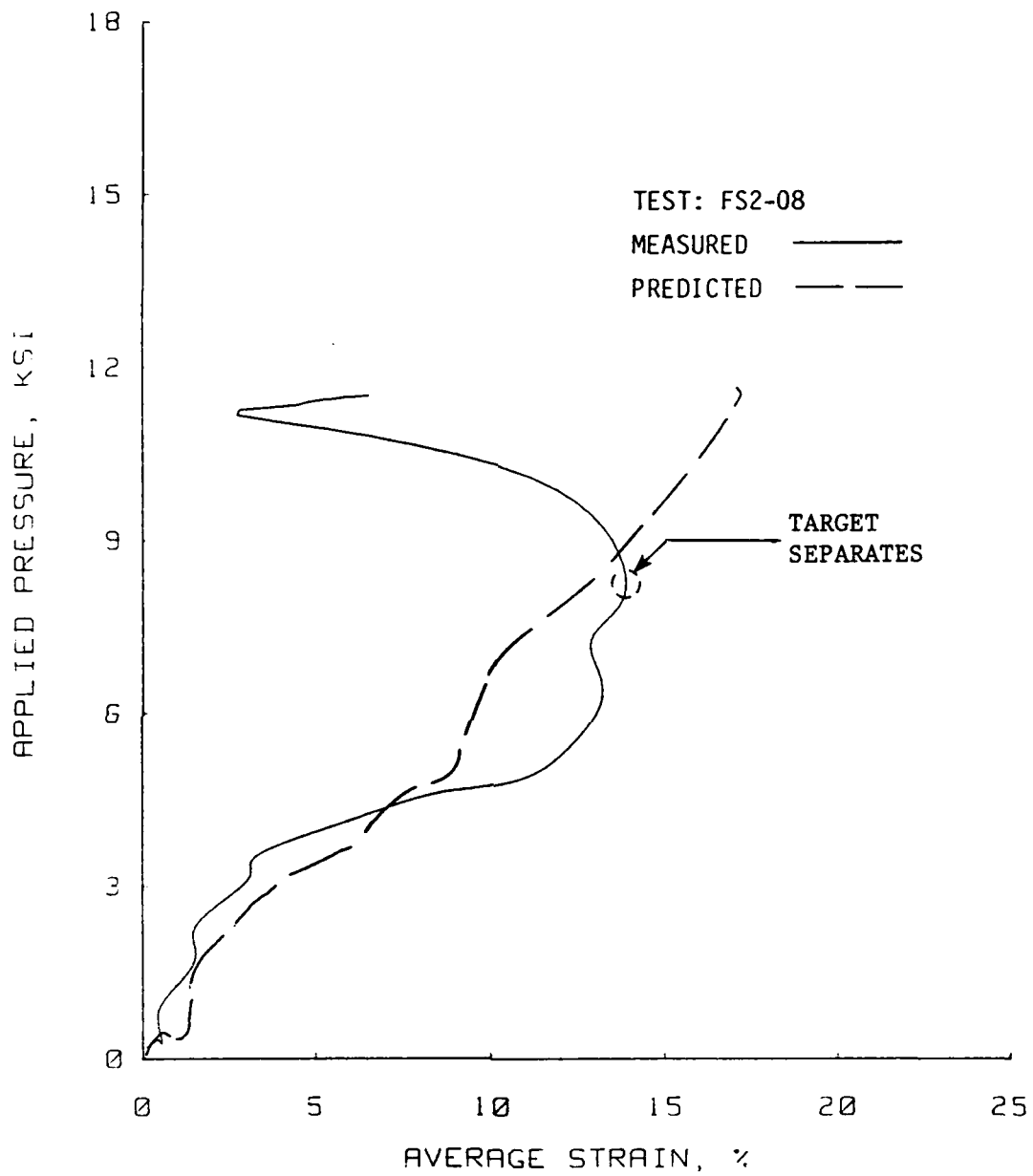
Figure D.9 Laboratory-measured and ADLUD-predicted plots of
applied pressure versus average strain for test
FS2-08, flume sand.

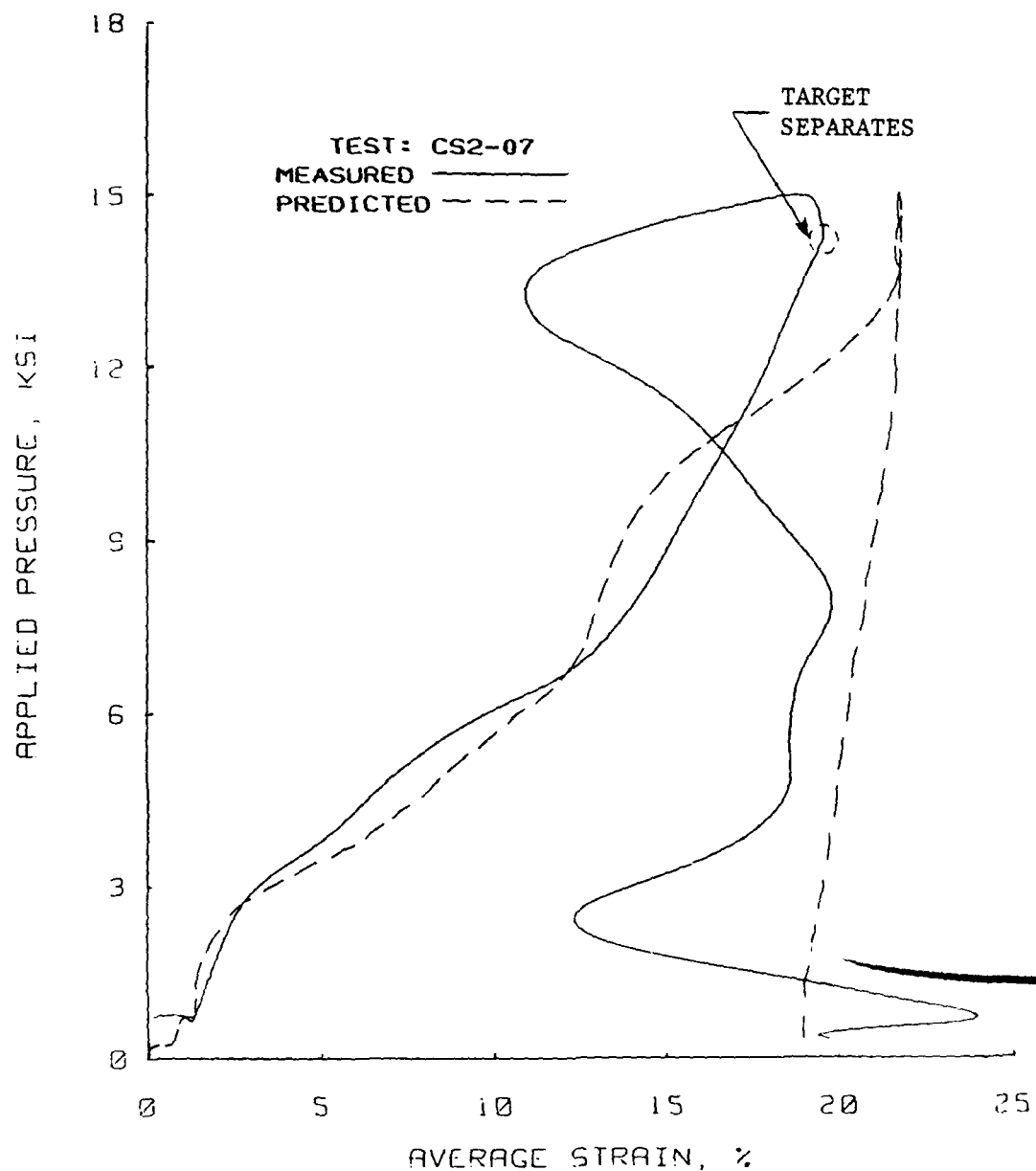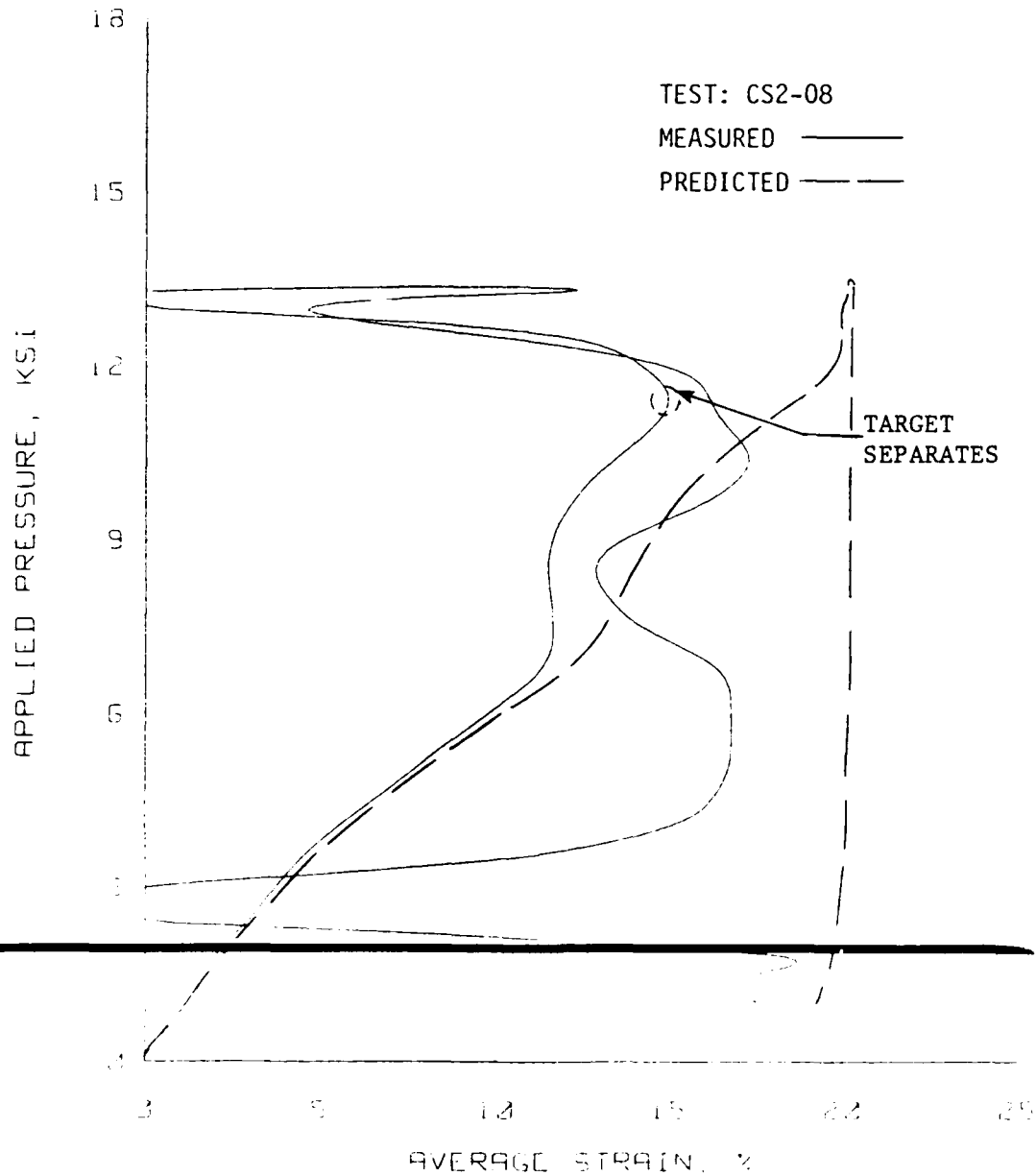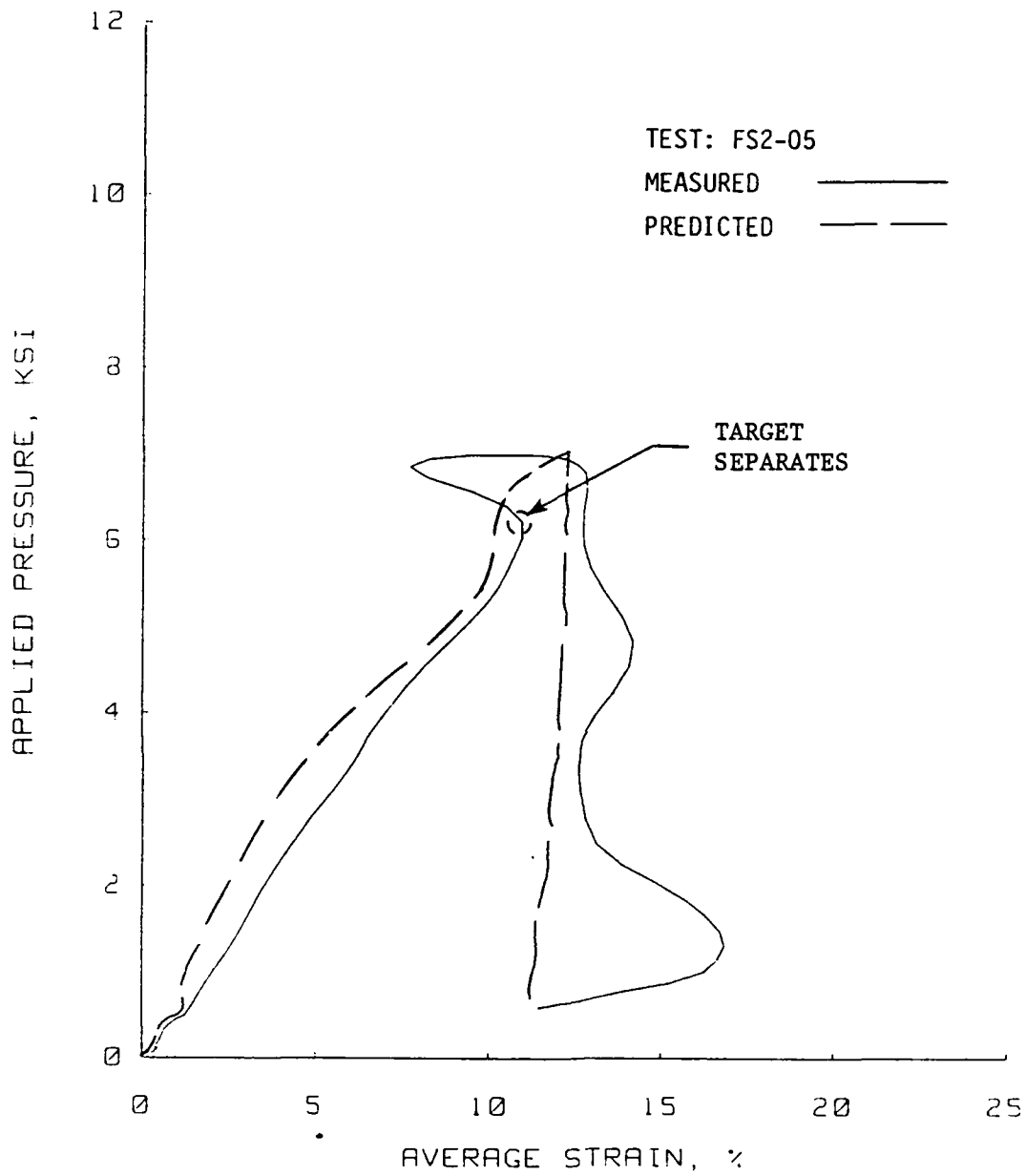Figure D.10 Laboratory-measured and ADLUD-predicted plots of applied pressure versus average strain for test FS2-09, flume sand.

Uniaxial Strain Results
Soil Type: Yuma Clayey Sand

Figure D.11   Laboratory-measured and ADLUD-predicted plots of
applied pressure versus average strain for test
YS2-04, Yuma clayey sand.

Uniaxial Strain Results
Soil Type: Yuma Clayey Sand

Figure D.12   Laboratory-measured and ADLUD-predicted plots of
applied pressure versus average strain for test
YS2-05, Yuma clayey sand.

Uniaxial Strain Results
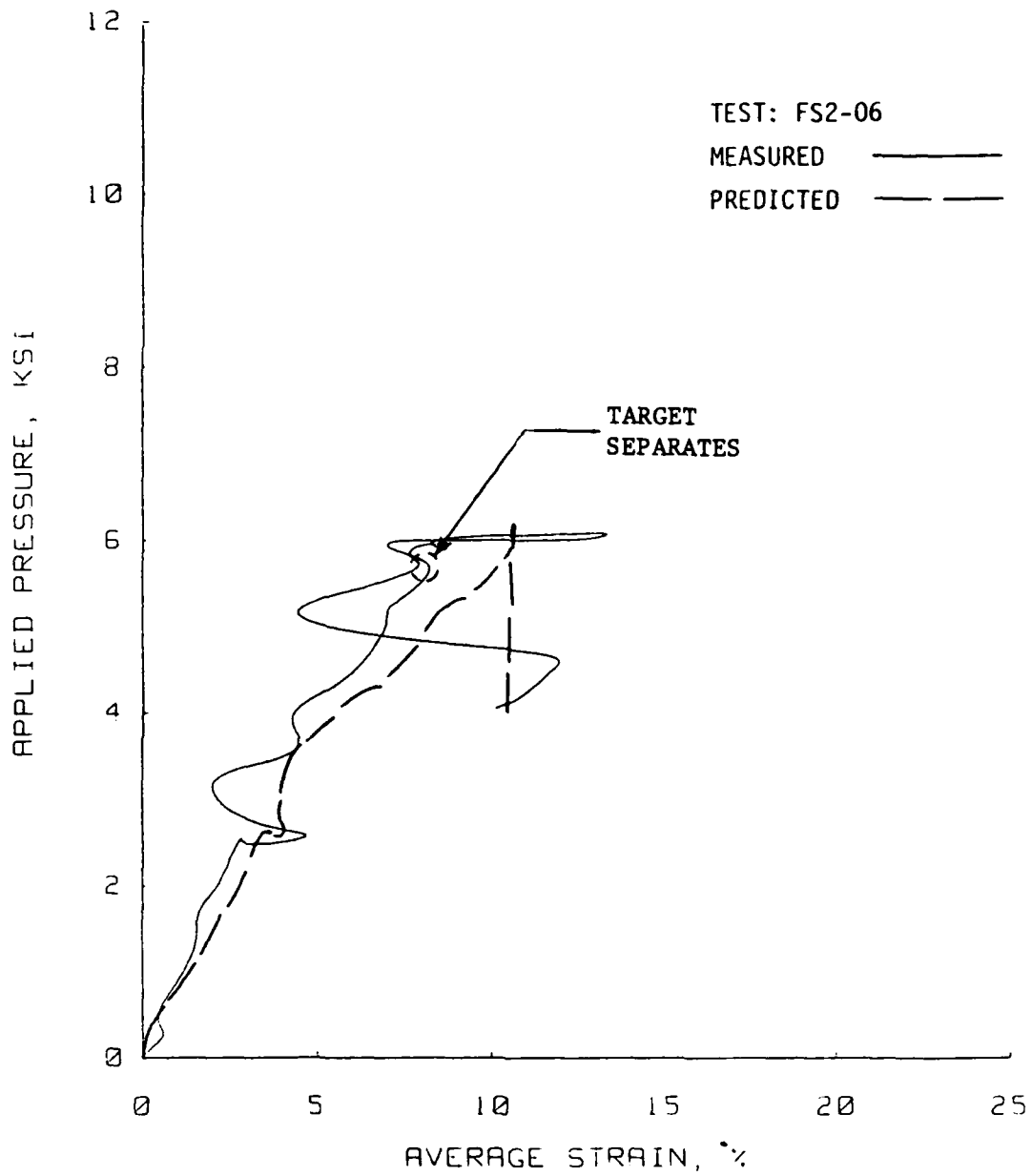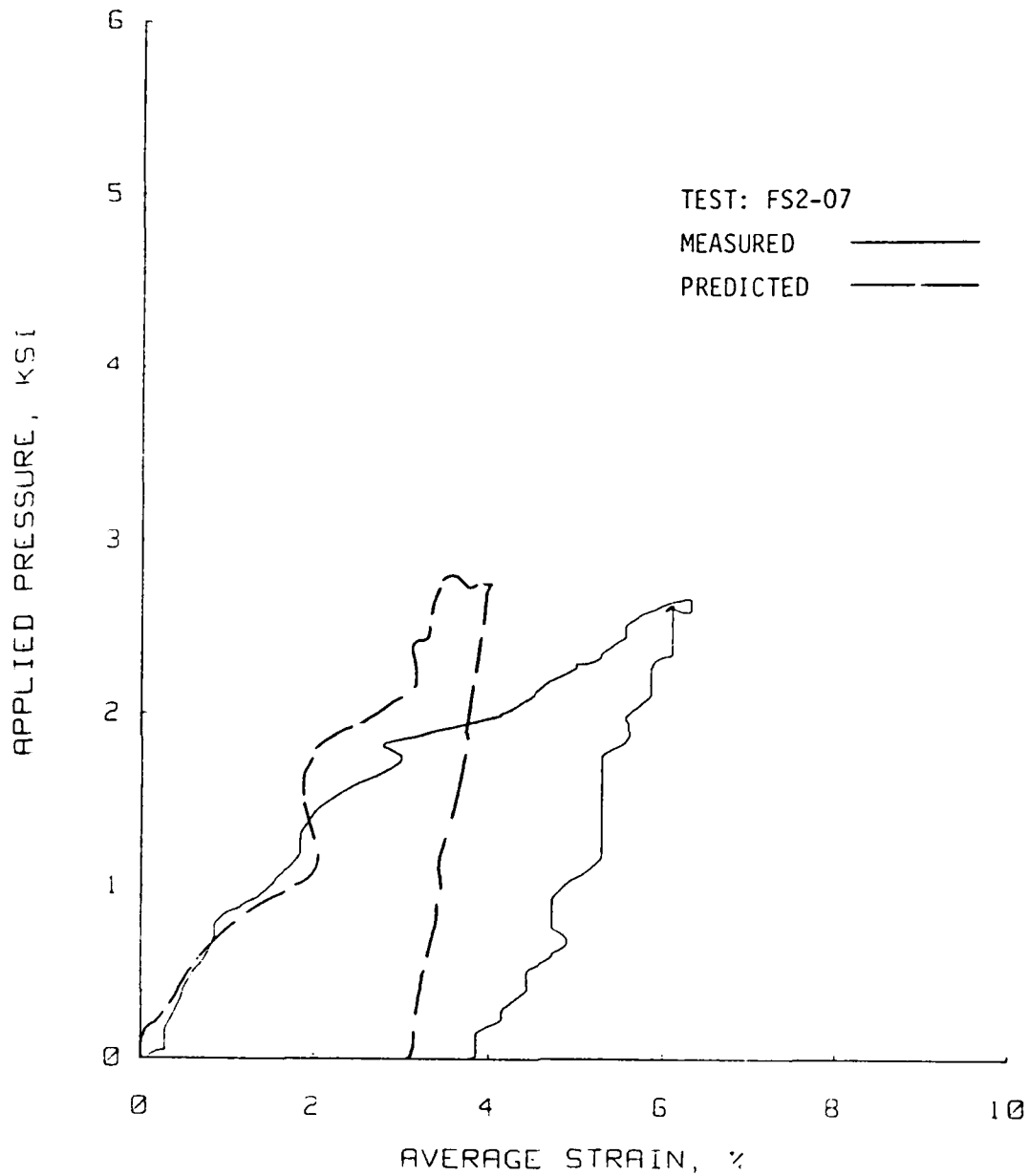## Soil Type: Yuma Clayey Sand
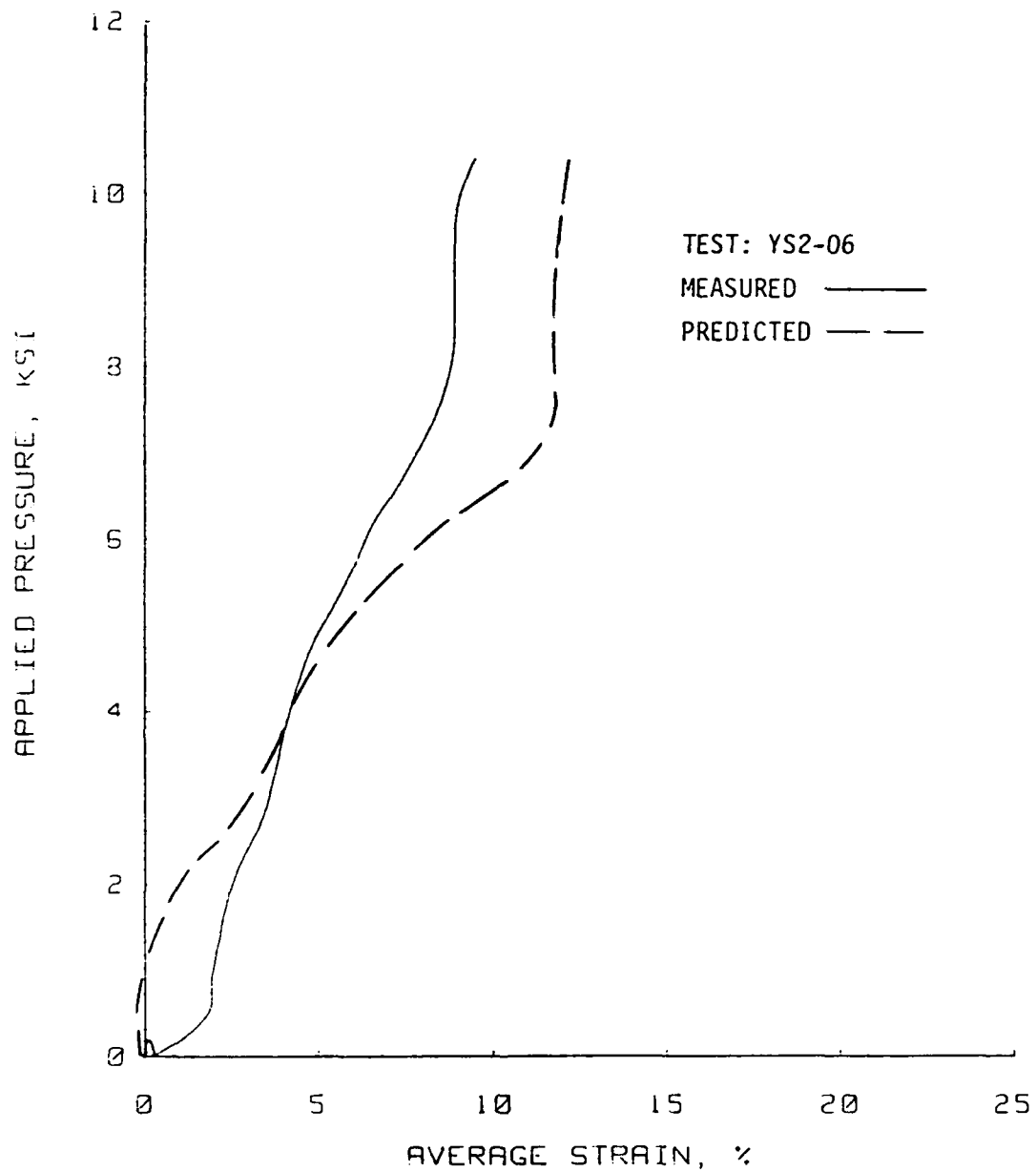
Figure D.13 Laboratory-measured and ADLUD-predicted plots of
applied pressure versus average strain for test
YS2-06, Yuma clayey sand.

Uniaxial Strain Results
Soil Type: Yuma Clayey Sand
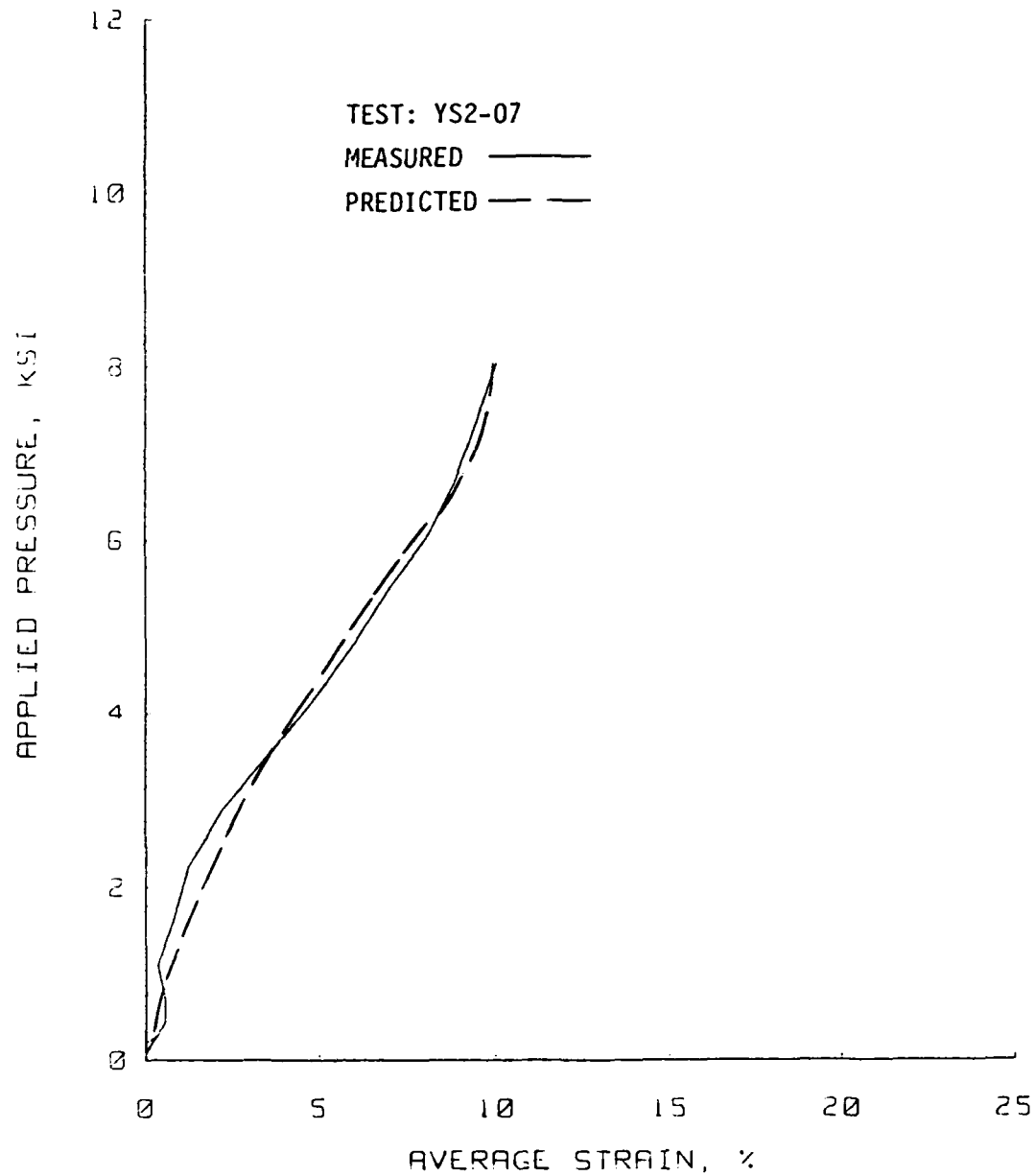
Figure D.14 Laboratory-measured and ADLUD-predicted plots of
applied pressure versus average strain for test
YS2-07, Yuma clayey sand.

Figure D.15   Laboratory-measured and ADLUD-predicted plots of
applied pressure versus average strain for test
DS2-04, Vicksburg loess D-series.

Uniaxial Strain Results
Soil Type: Vicksburg Loess

Figure D.16   Laboratory-measured and ADLUD-predicted plots of
applied pressure versus average strain for test
DS2-05, Vicksburg loess D-series.

Uniaxial Strain Results
Soil Type: Vicksburg Loess

Figure D.17   Laboratory-measured and ADLUD-predicted plots of
applied pressure versus average strain for test
DS2-06, Vicksburg loess D-series.

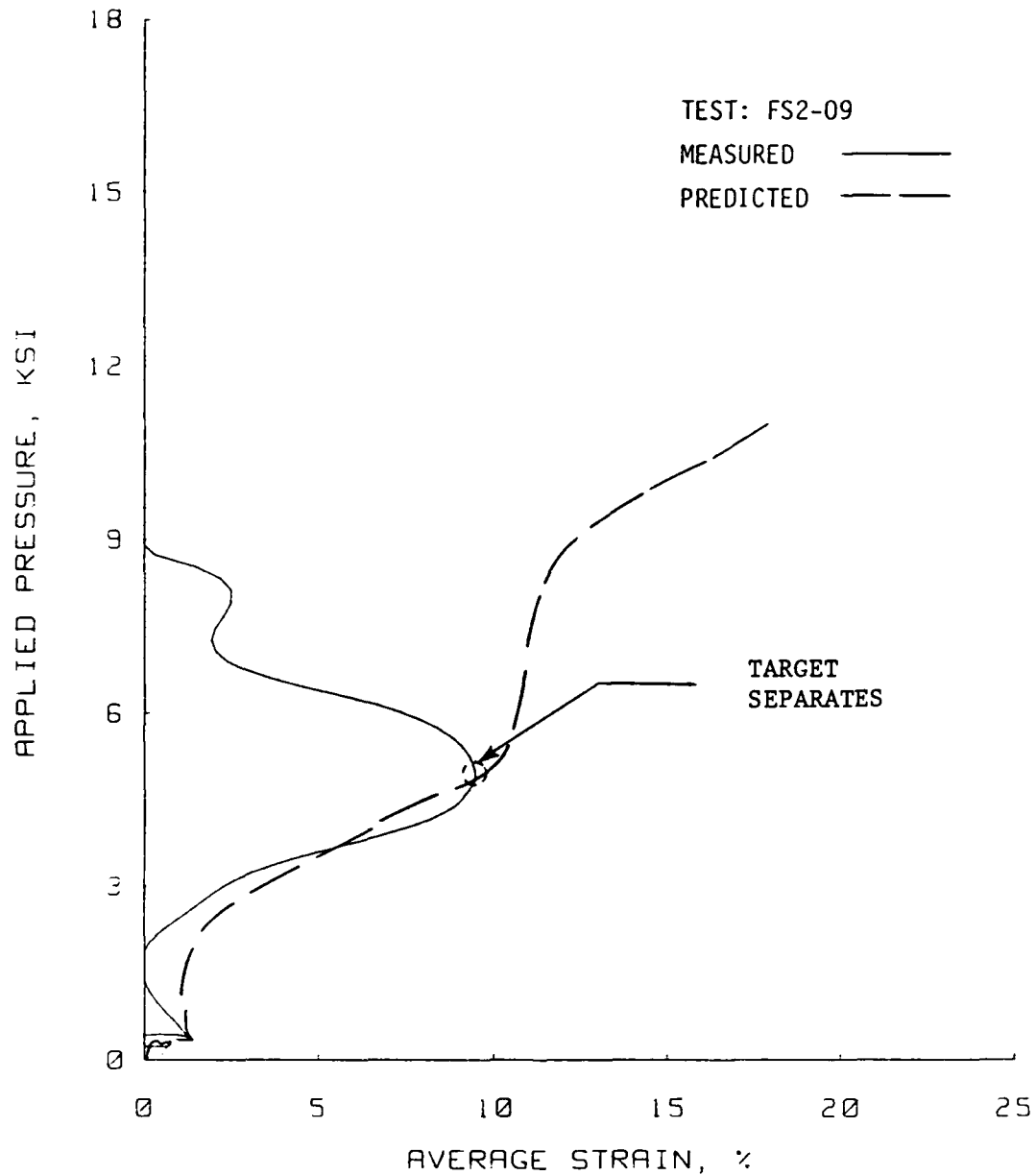Figure D.18   Laboratory-measured and ADLUD-predicted plots of
applied pressure versus average strain for test
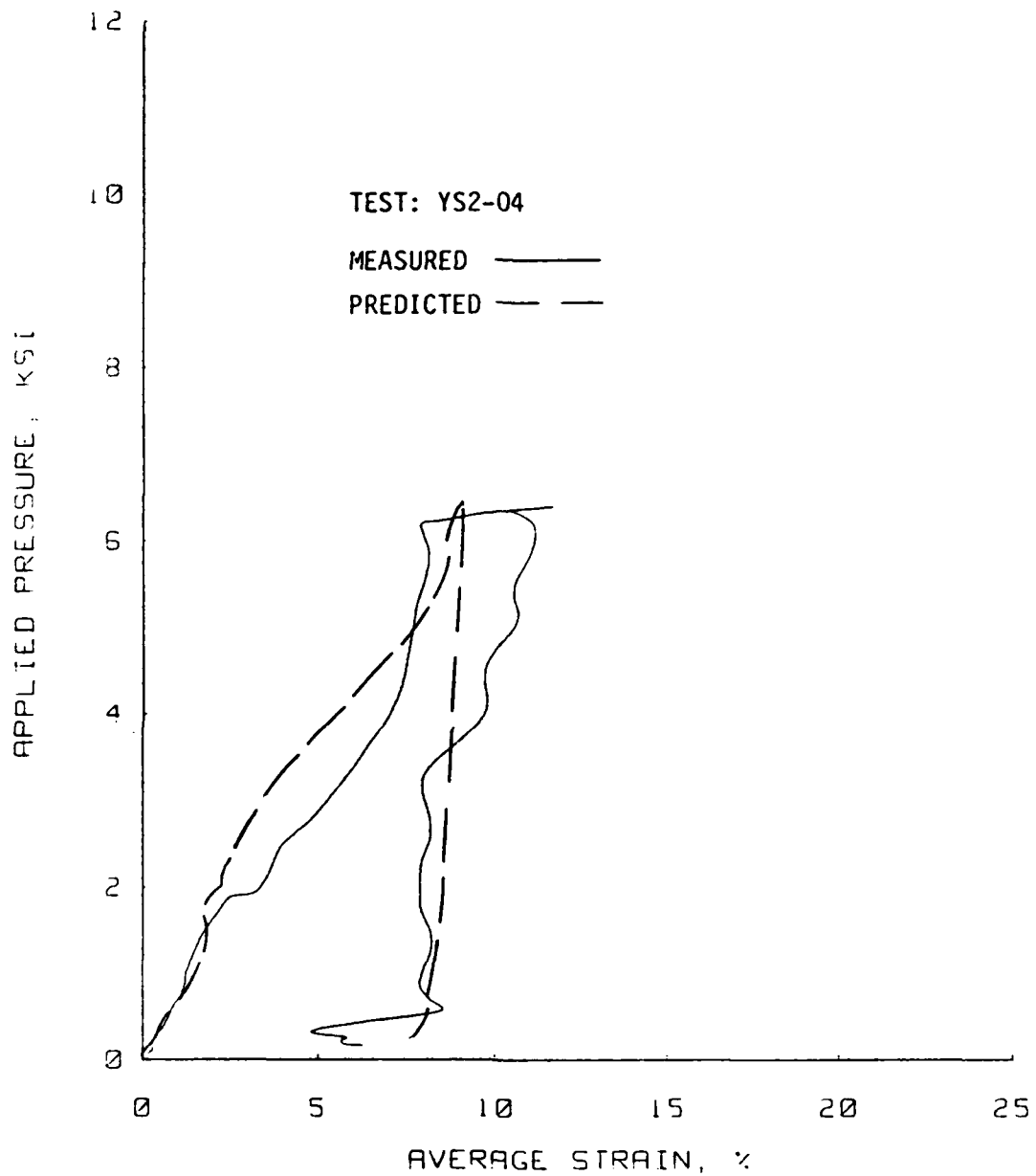DS2-07, Vicksburg loess D-series.

Uniaxial Strain Results
Soil Type: Vicksburg Loess

Figure D.19   Laboratory-measured and ADLUD-predicted plots of
applied pressure versus average strain for test
DS2-08, Vicksburg loess D-series.

Uniaxial Strain Results
Soil Type: Vicksburg Loess

Figure D.20   Laboratory-measured and ADLUD-predicted plots of
applied pressure versus average strain for test
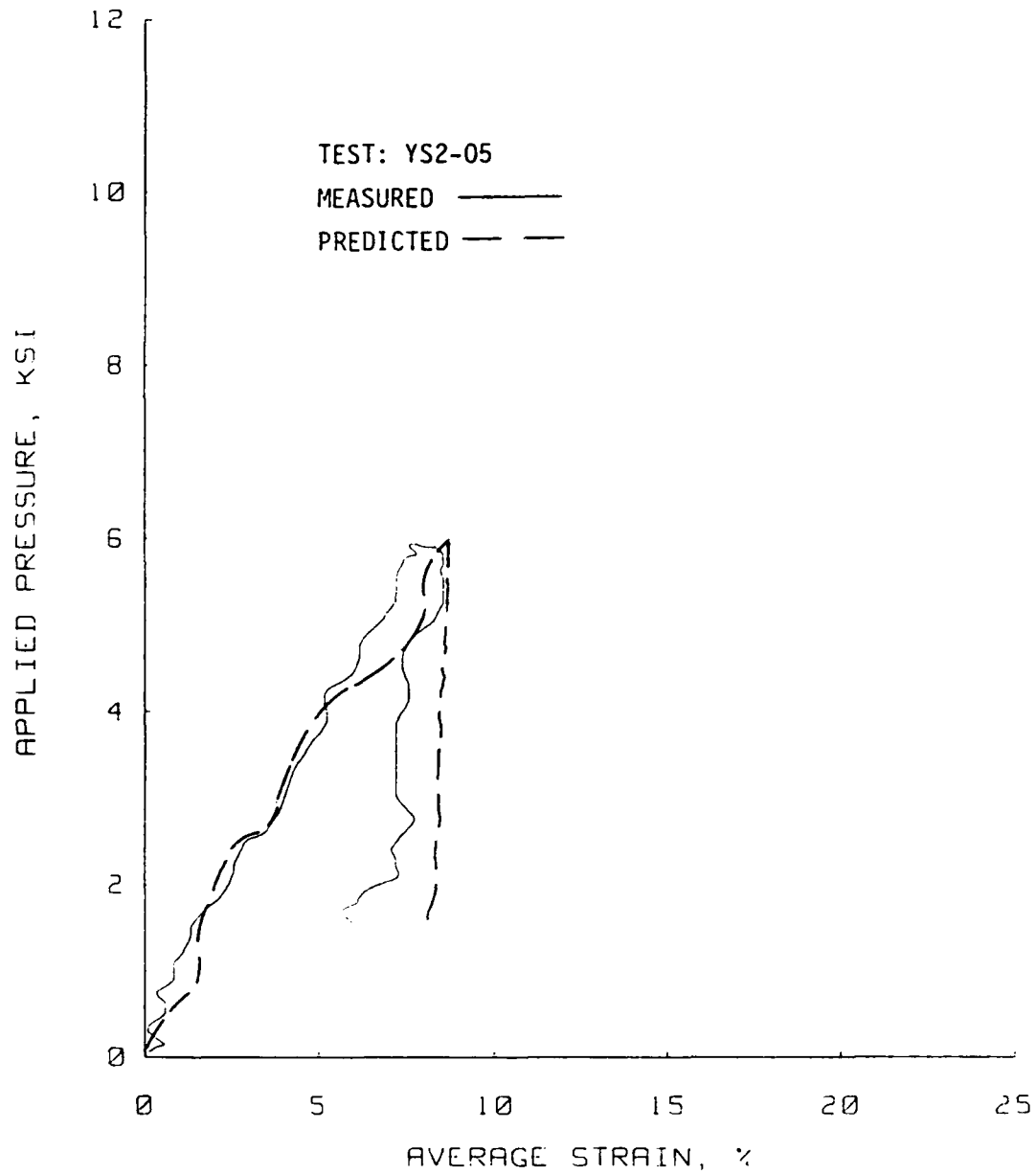DS2-09, Vicksburg loess D-series.

Figure D.21   Laboratory-measured and ADLUD-predicted plots of
applied pressure versus average strain for test
DS2-10, Vicksburg loess, D-series.

Uniaxial Strain Results
Soil Type: Vicksburg Loess

Figure D.22   Laboratory-measured and ADLUD-predicted plots of
applied pressure versus average strain for test
VSD-11, Vicksburg loess, V-series.

Figure D.23 Laboratory-measured and ADLUD-predicted plots of
applied pressure versus average strain for test
VSD-12, Vicksburg loess V-series.

Uniaxial Strain Results
Soil Type: Vicksburg Loess

Figure D.24   Laboratory-measured and ADLUD-predicted plots of
applied pressure versus average strain for test
VSD-21, Vicksburg loess V-series.

Uniaxial Strain Results
Soil Type: Vicksburg Loess

Figure D.25   Laboratory-measured and ADLUD-predicted plots of
applied pressure versus average strain for test
VSD-22, Vicksburg loess V-series.

Uniaxial Strain Results
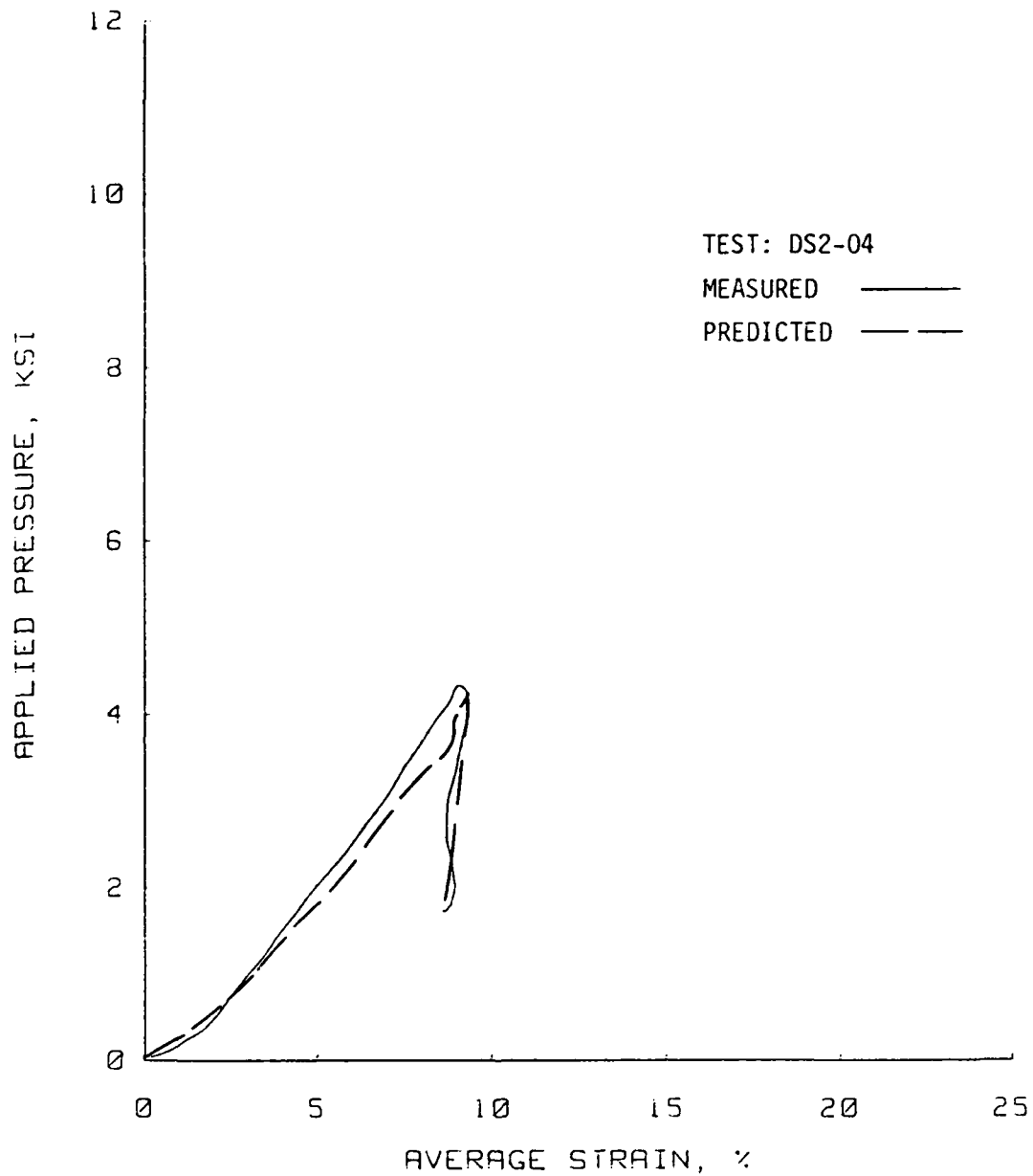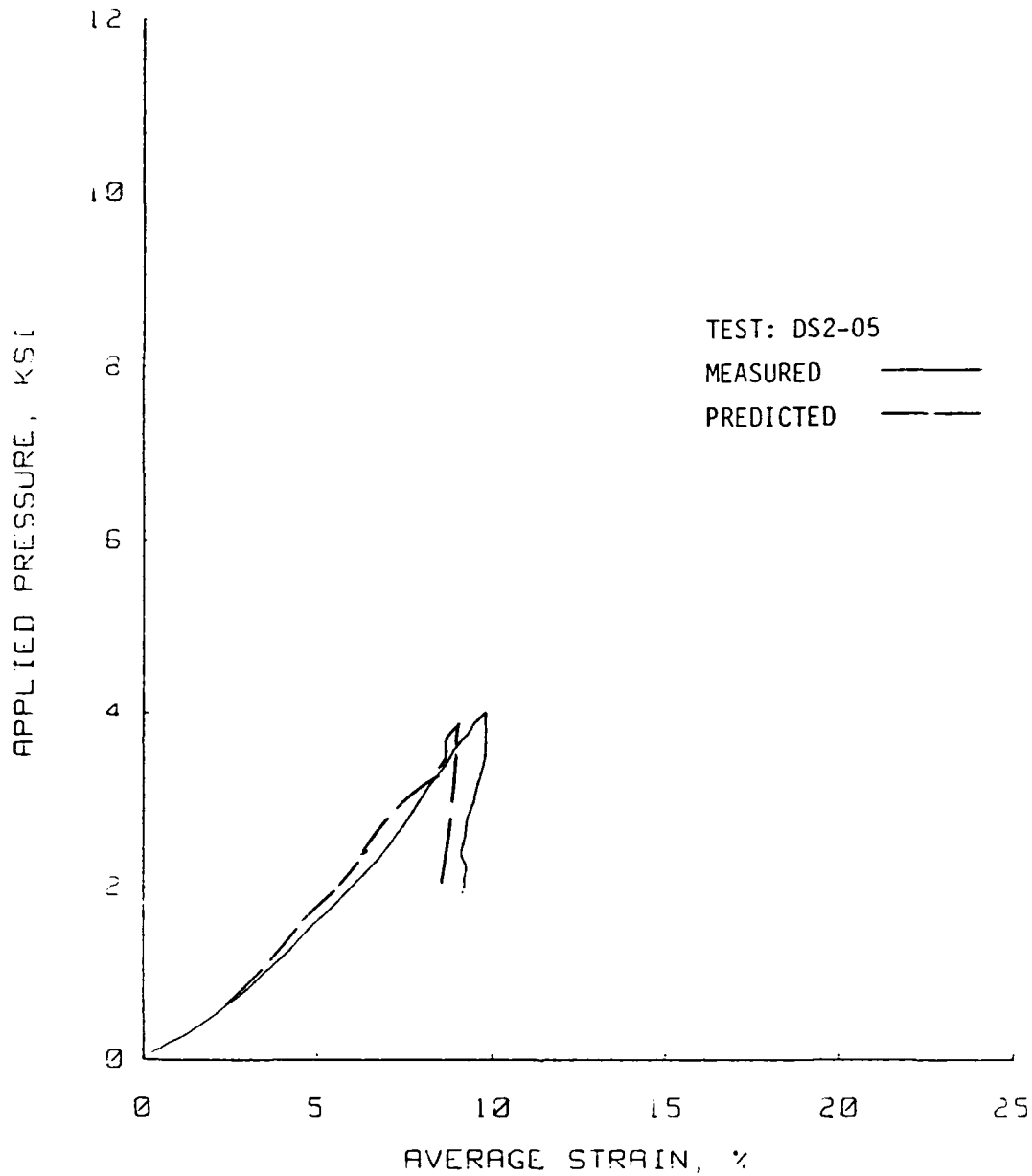**Soil Type: Vicksburg Loess**
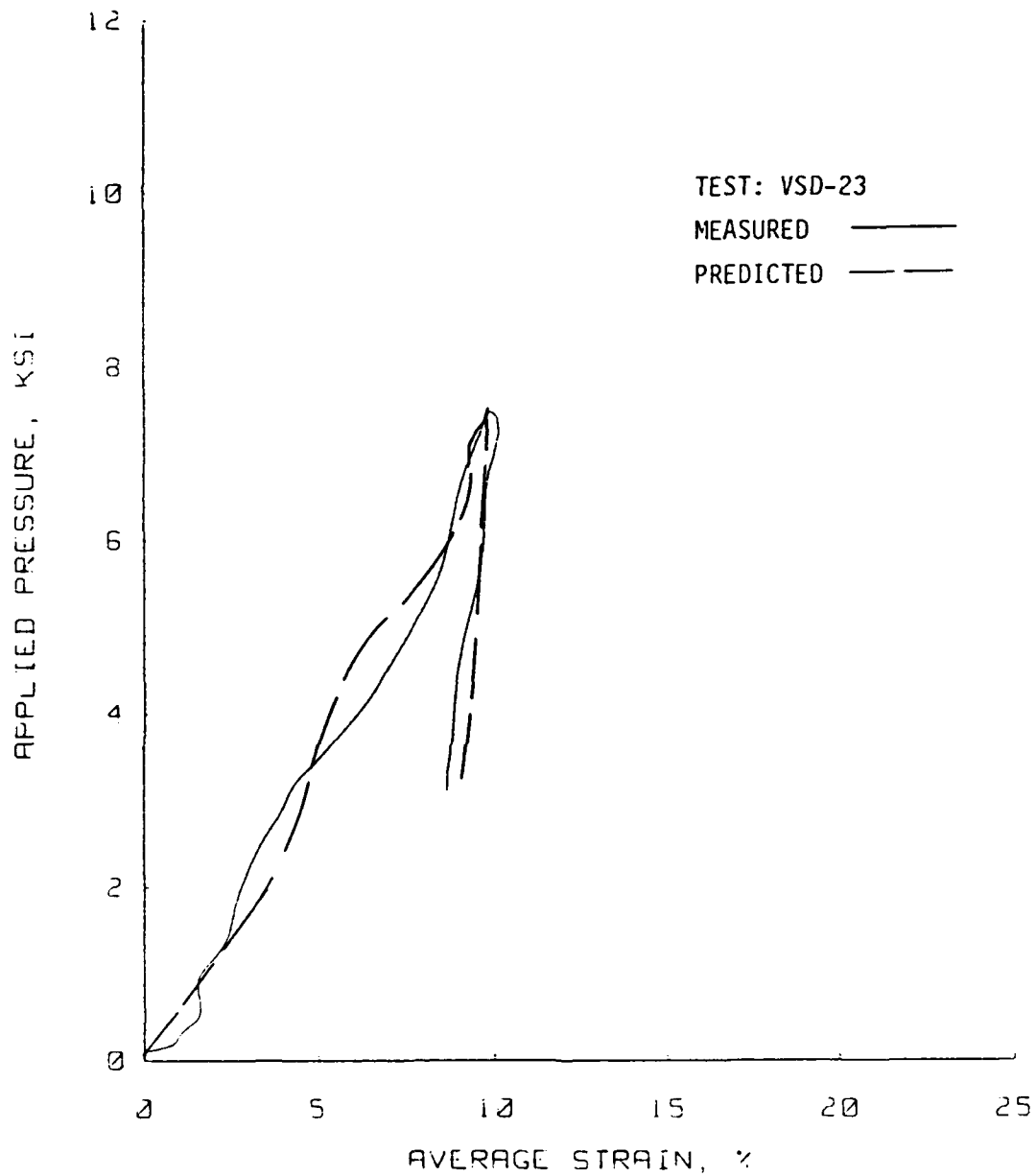
Figure D.26 Laboratory-measured and ADLUD-predicted plots of applied pressure versus average strain for test VSD-23, Vicksburg loess V-series.

Uniaxial Strain Results
Soil Type: Vicksburg Loess
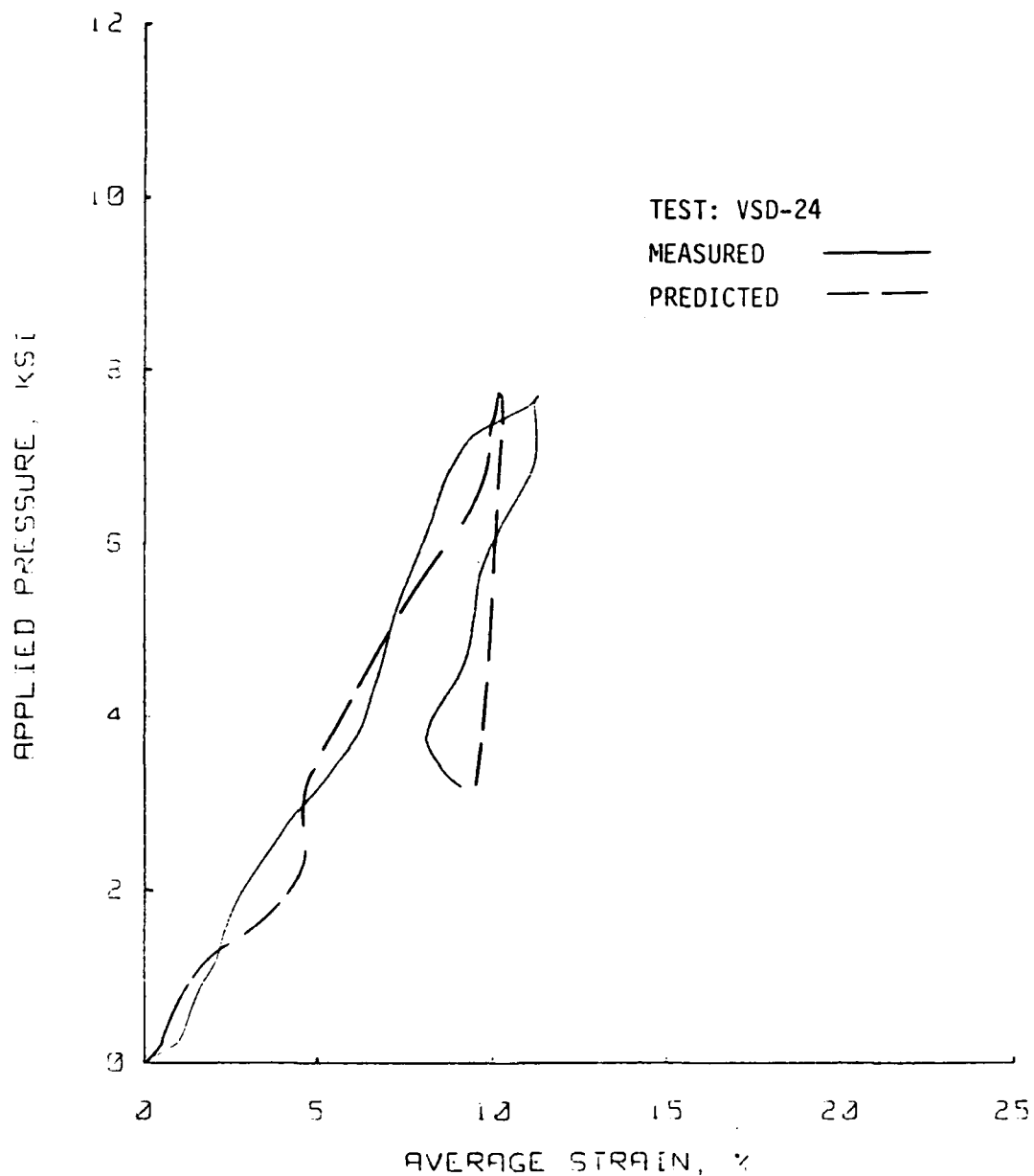
Figure D.27   Laboratory-measured and ADLUD-predicted plots of
applied pressure versus average strain for test
VSD-24, Vicksburg loess, V-series.

Uniaxial Strain Results
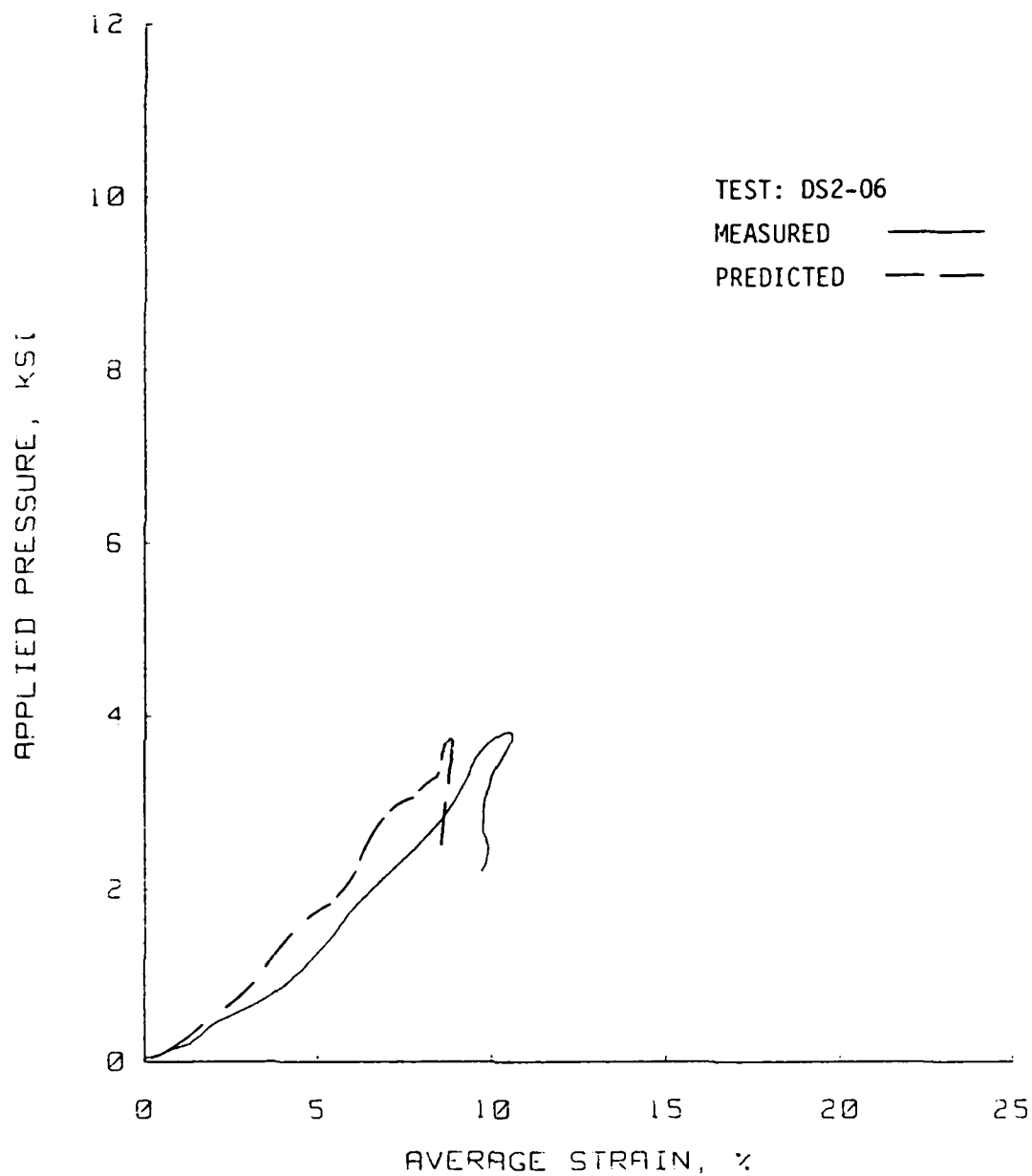## Soil Type: Vicksburg Loess
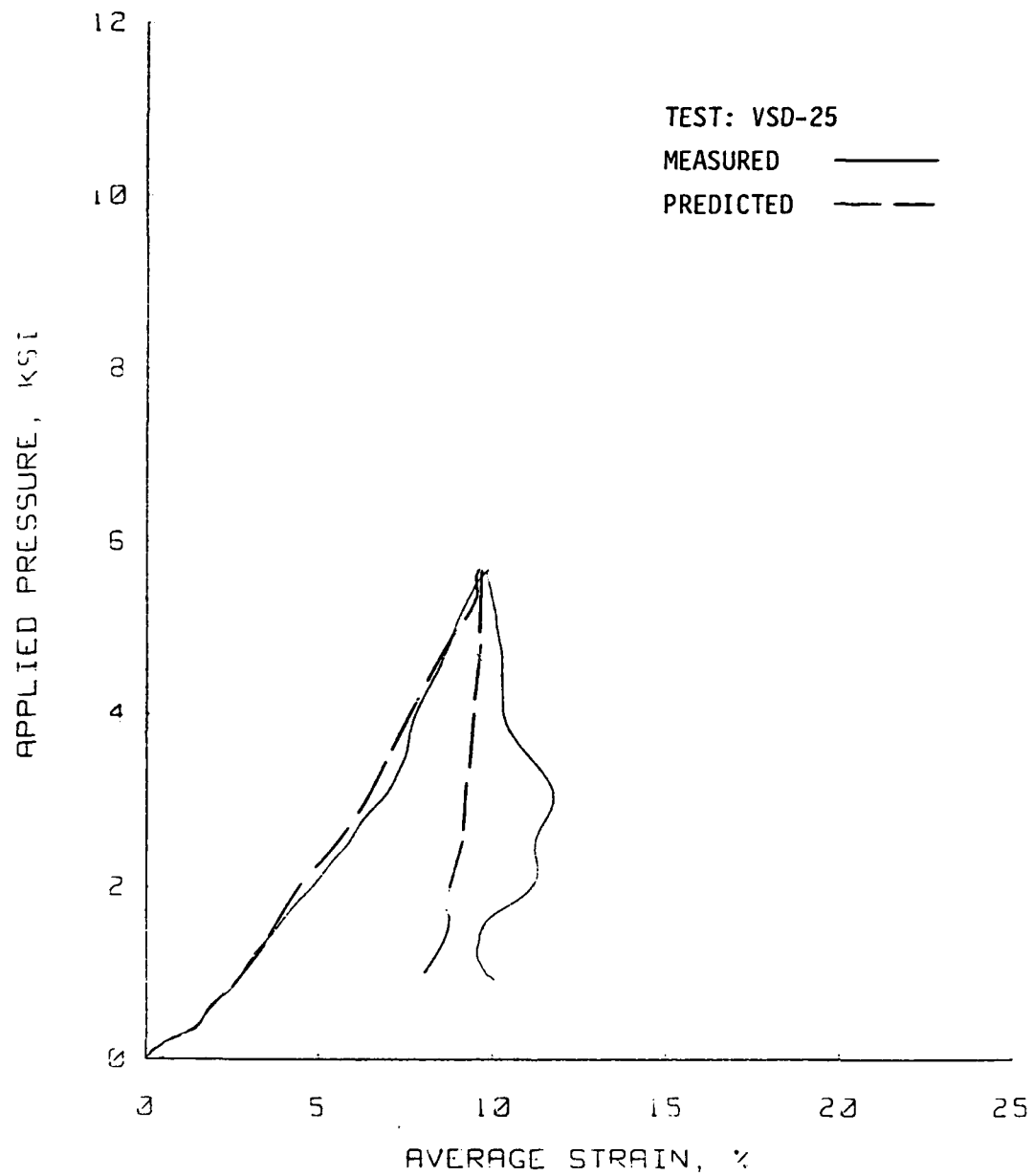
Figure D.28   Laboratory-measured and ADLUD-predicted plots of
applied pressure versus average strain for test
VSD-25, Vicksburg loess V-series.

Uniaxial Strain Results
Soil Type: Vicksburg Loess
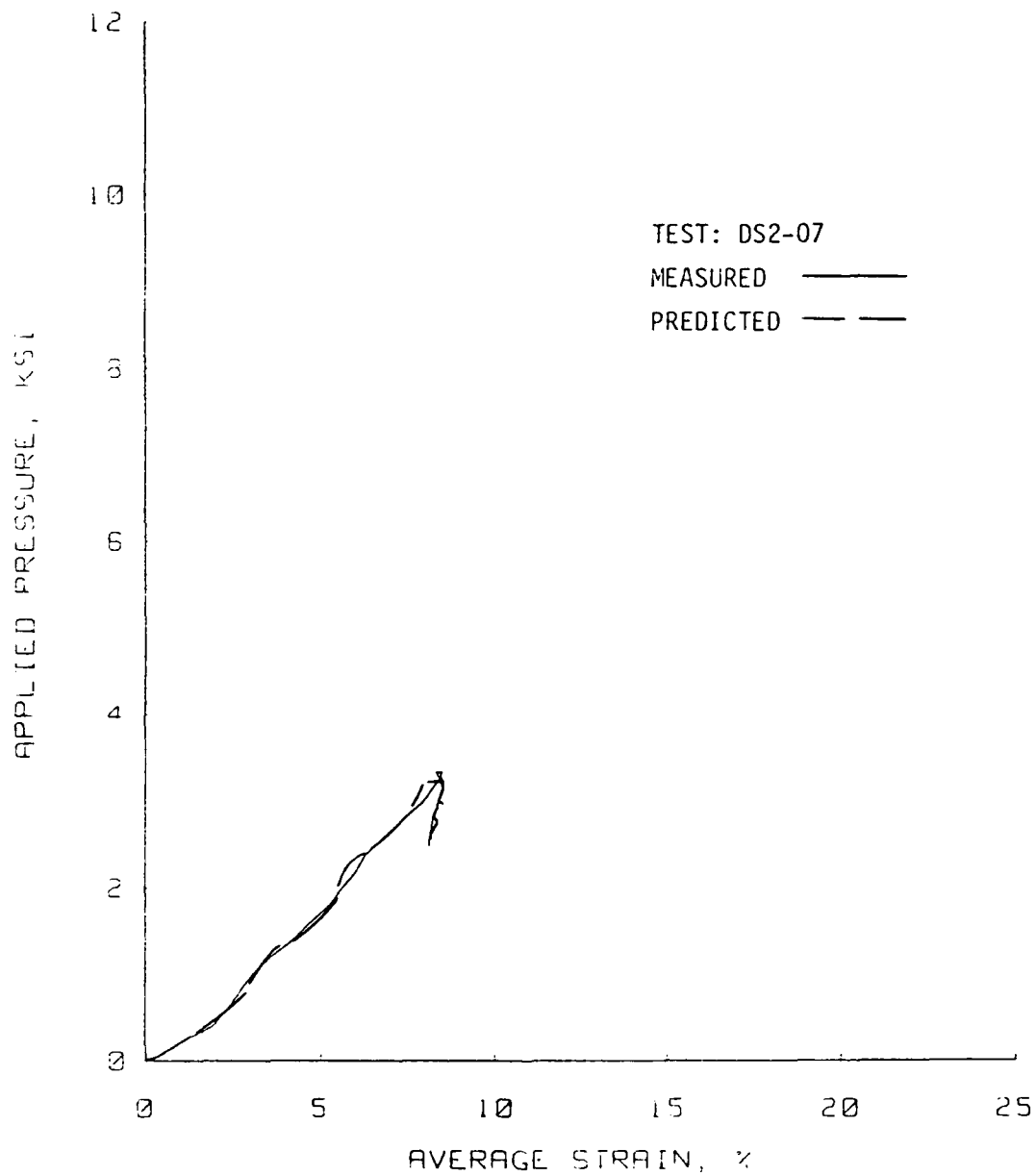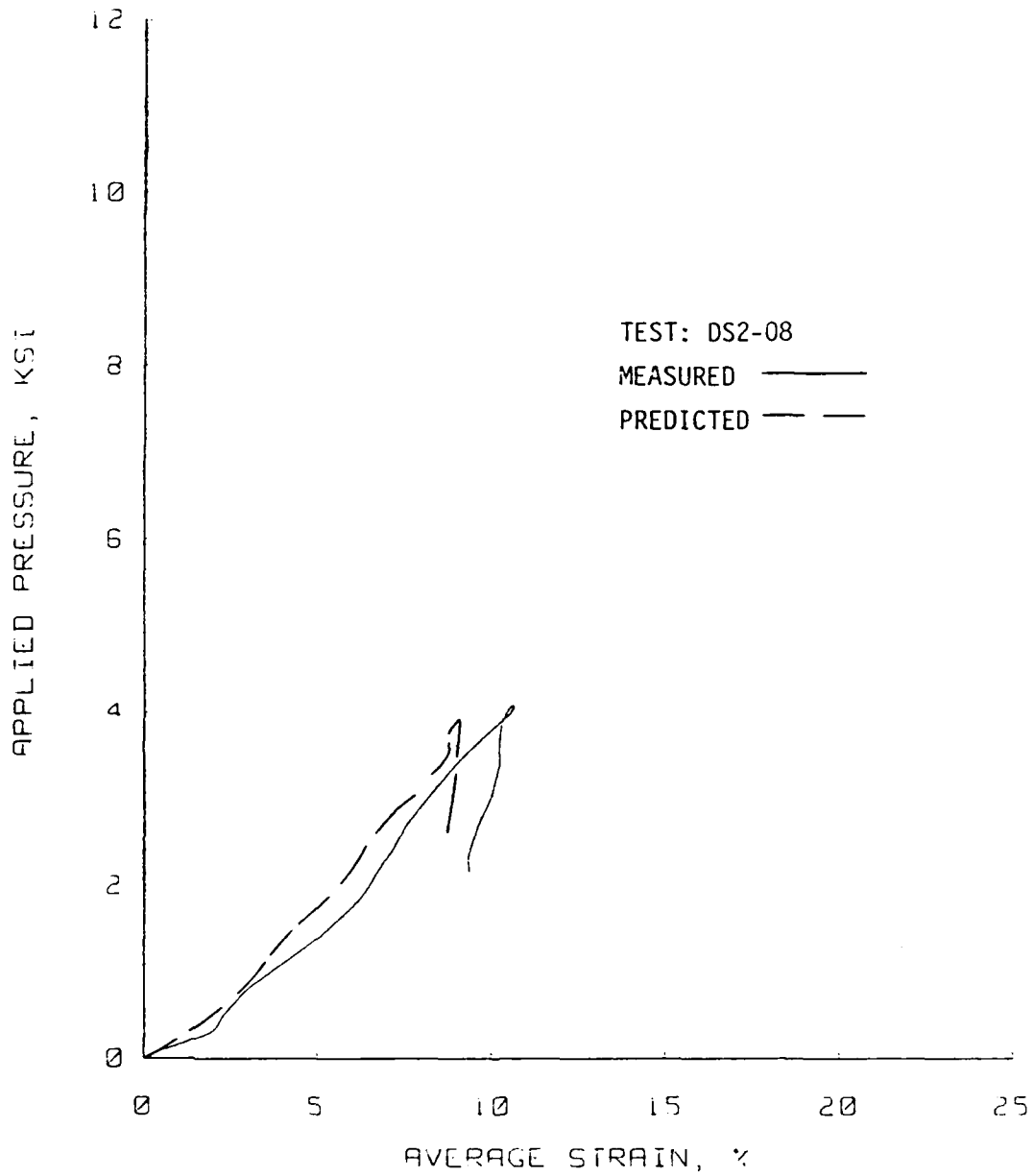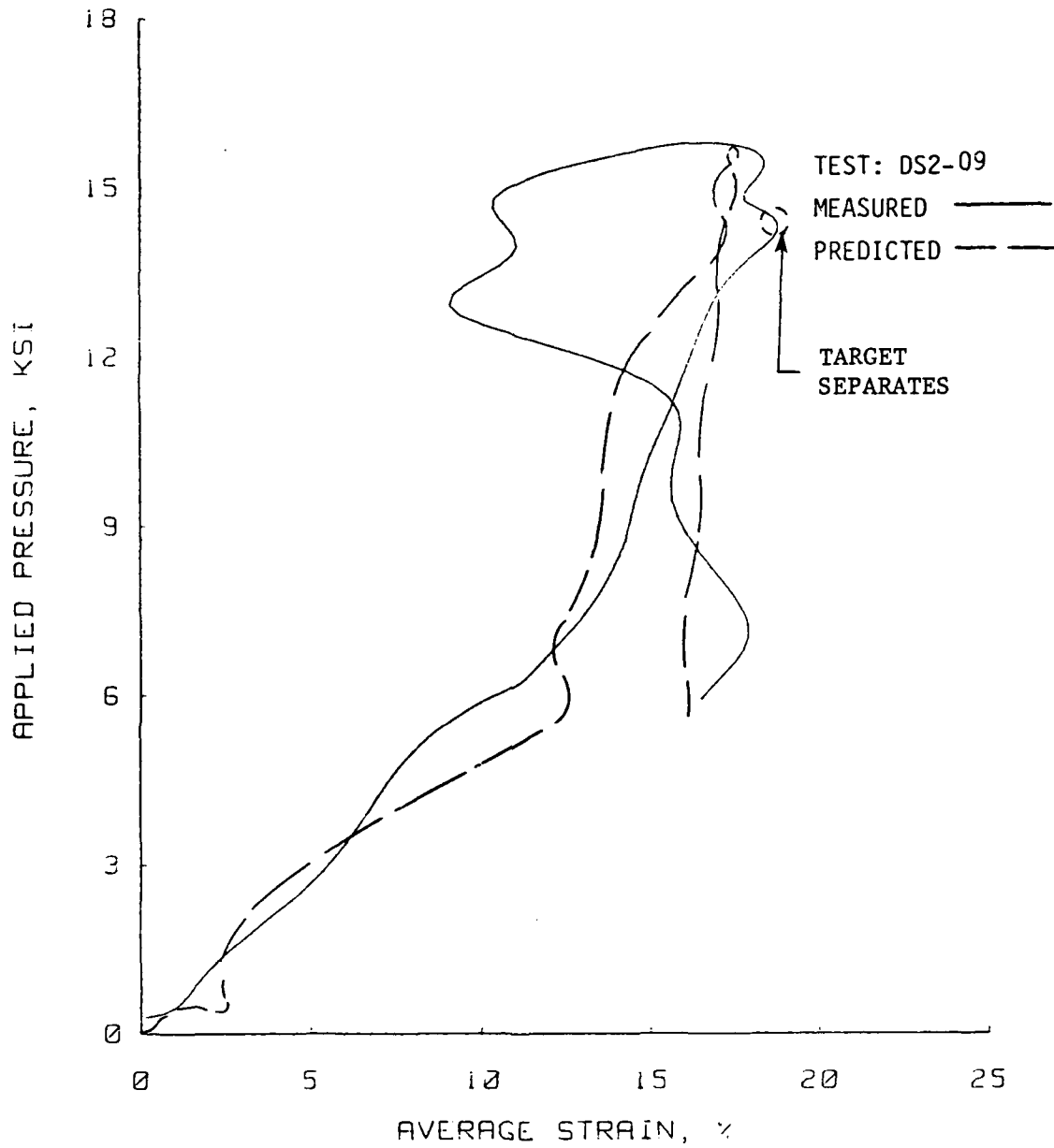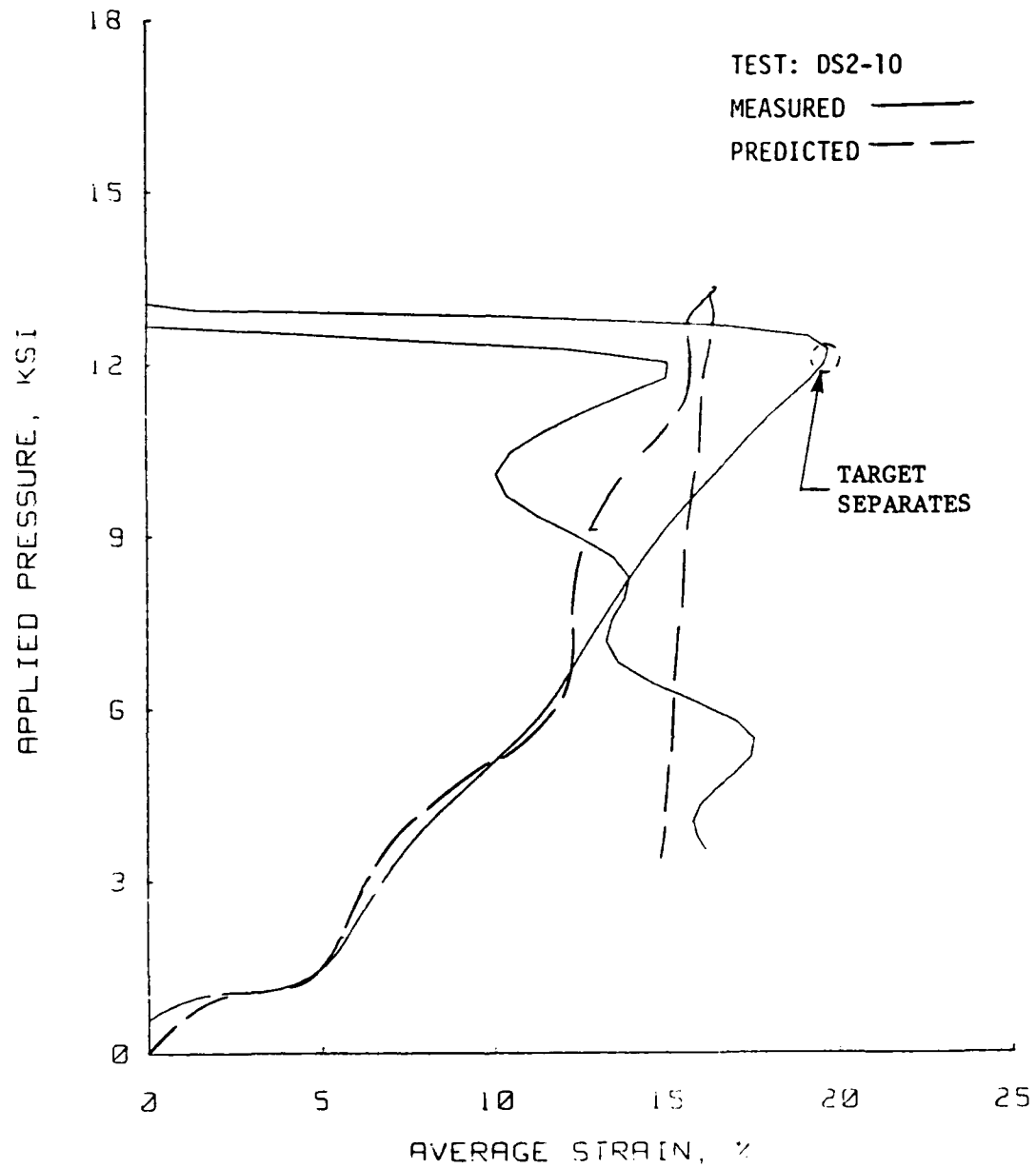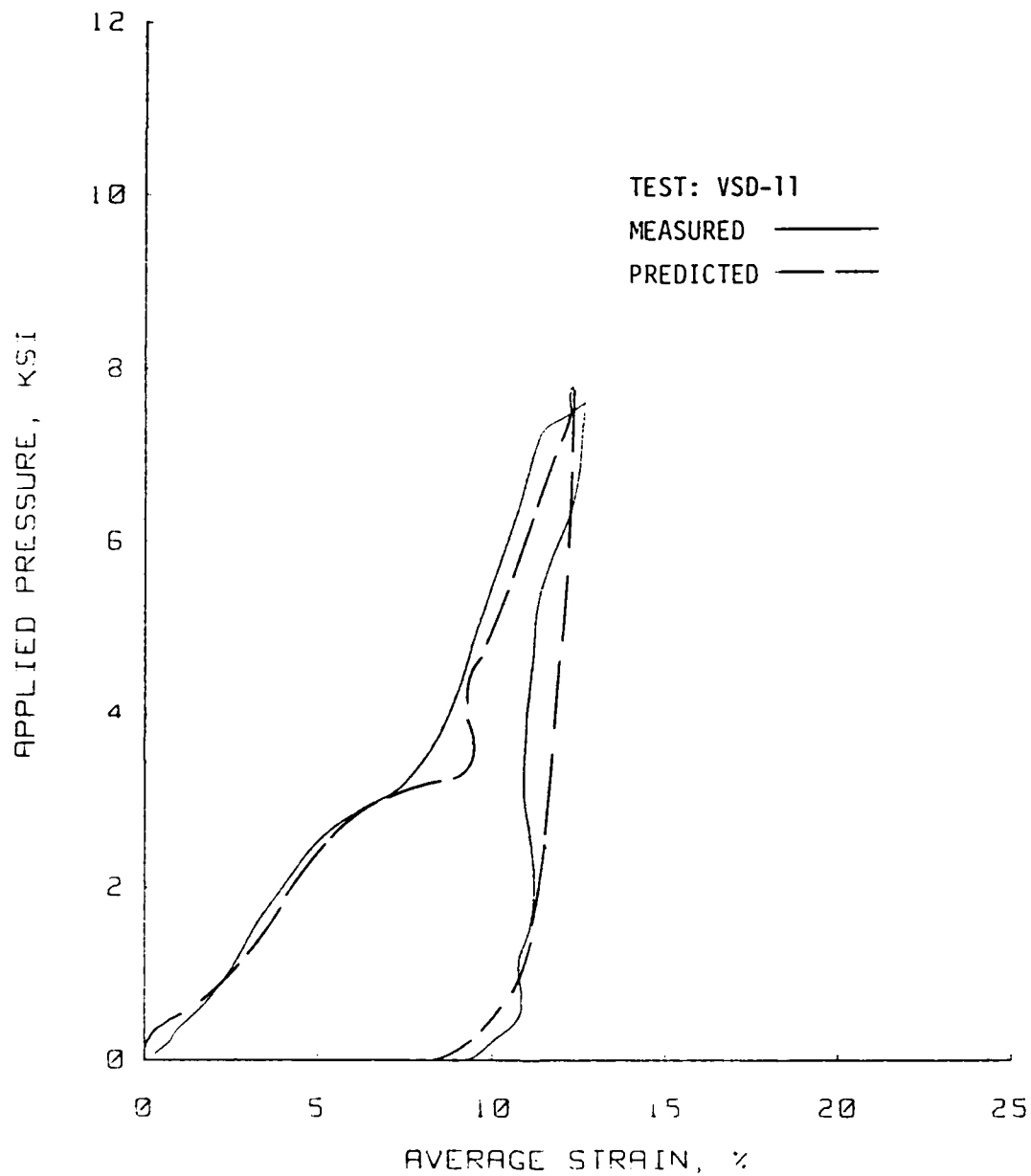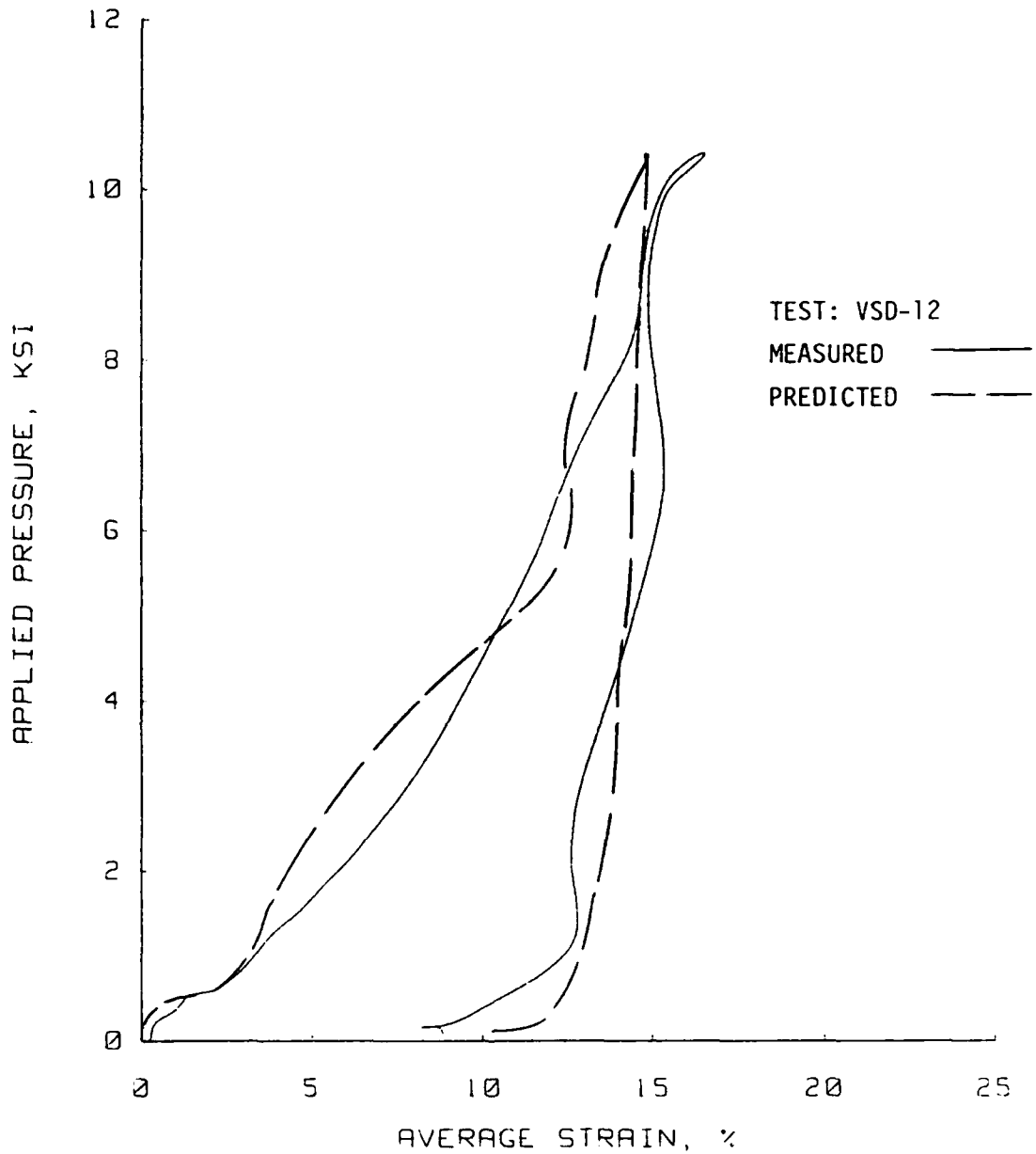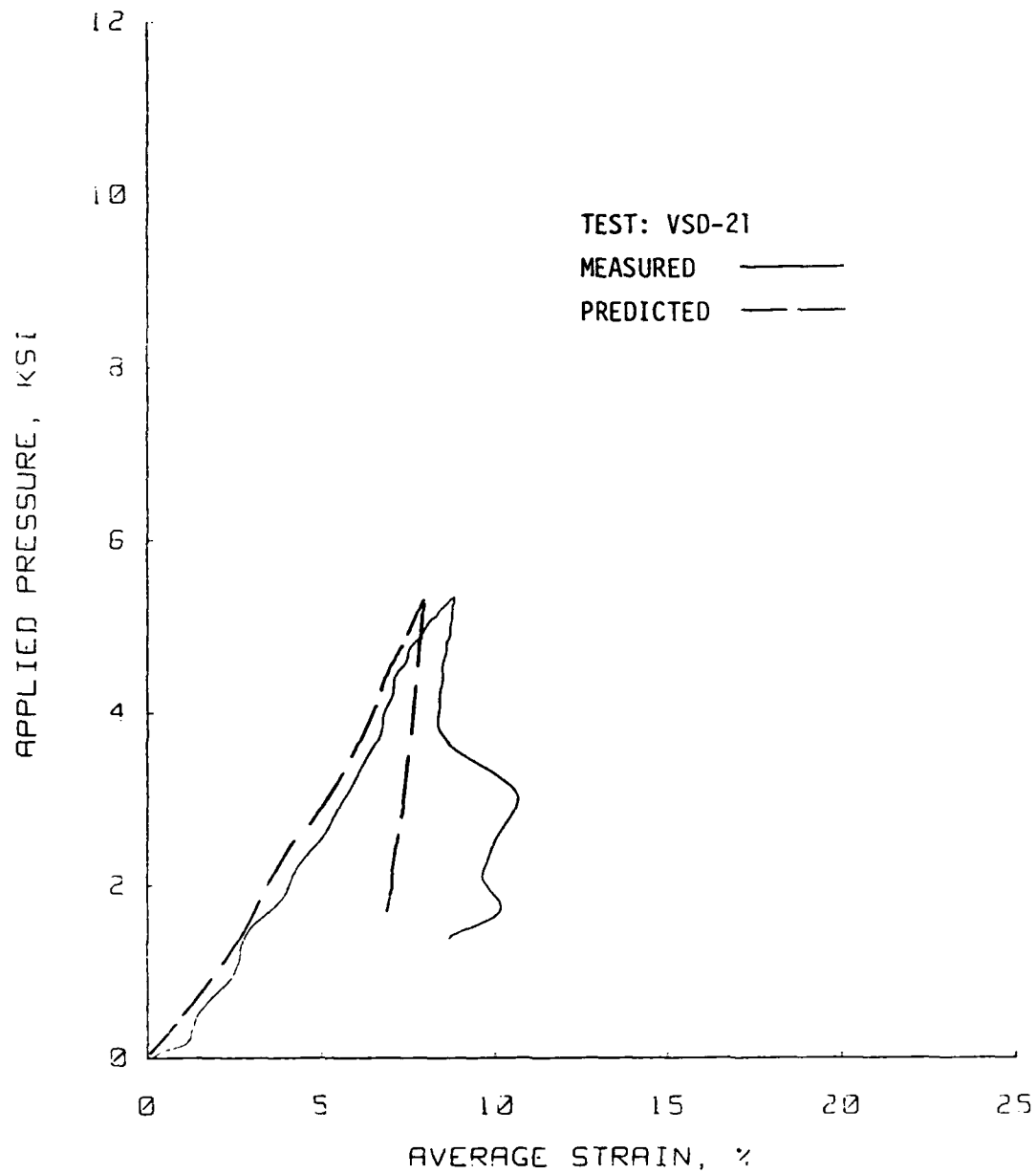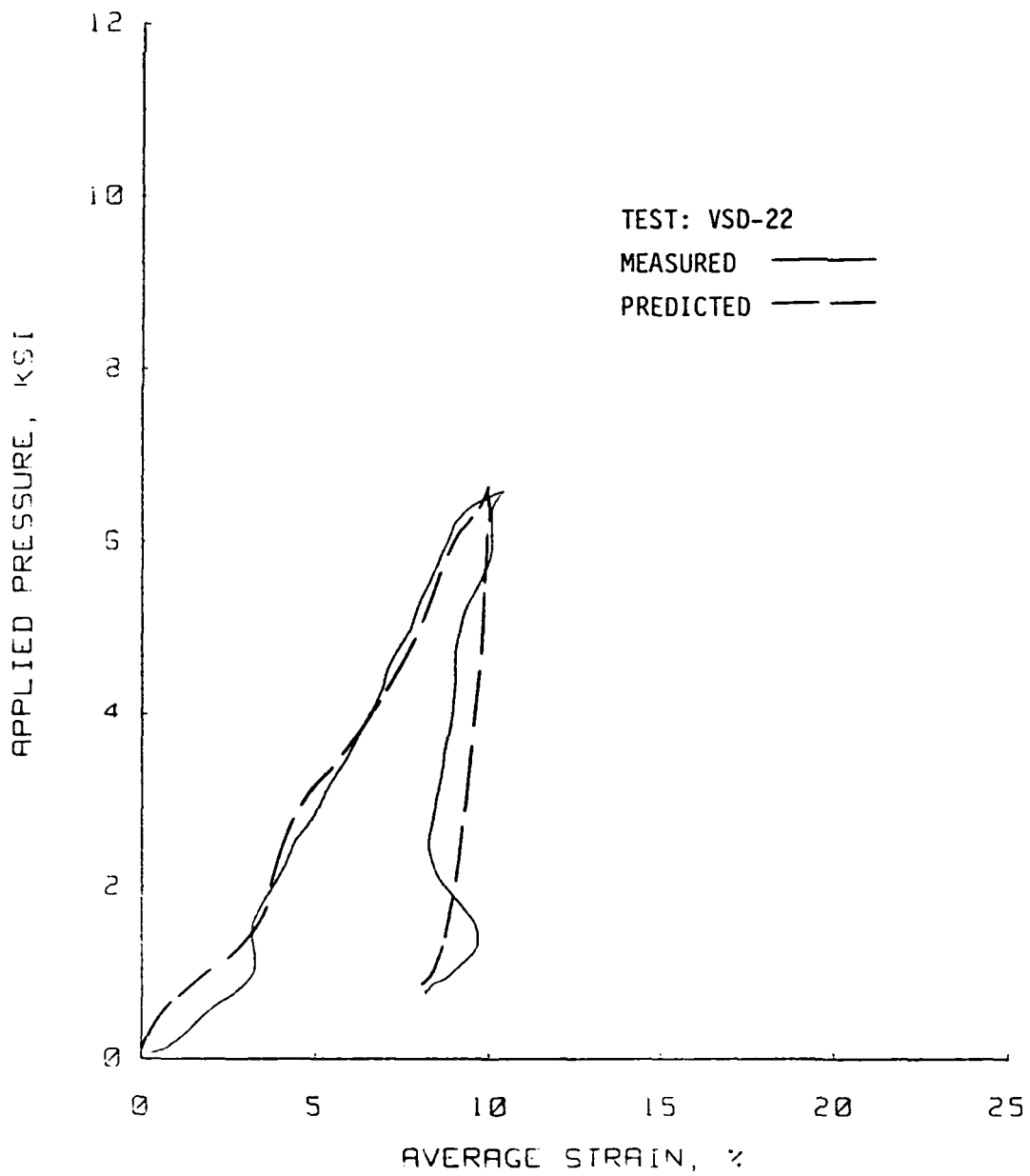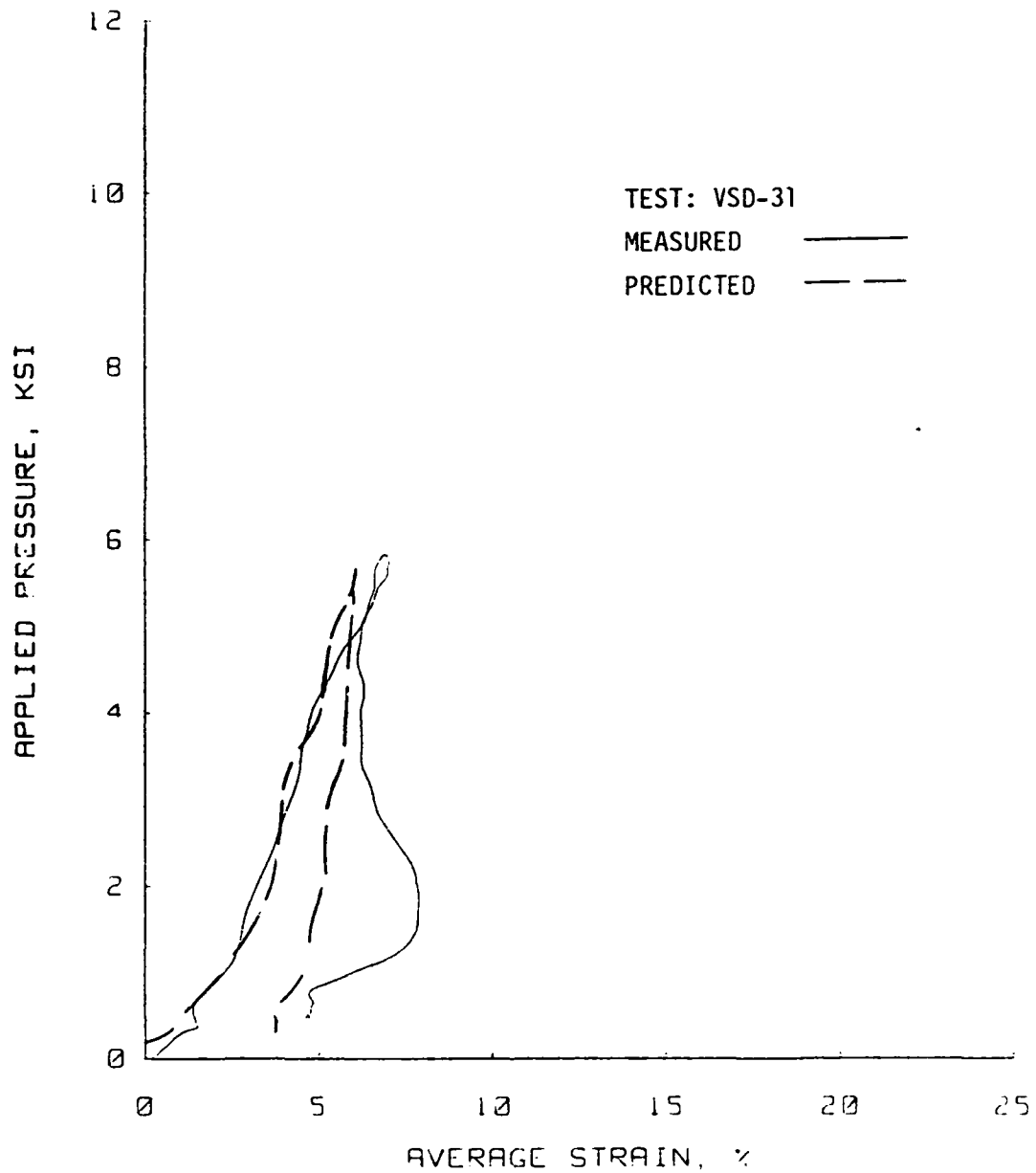

Figure D.29   Laboratory-measured and ADLUD-predicted plots of applied pressure versus average strain for test VSD-31, Vicksburg loess V-series.

REFERENCES

1. Akers, Stephen A., Reed, P. A., Ehrgott, John Q, "WES High-Pressure Uniaxial Strain and Triaxial Shear Test Equipment," Technical Report SL-86-11, U.S. Army Engineer Waterways Experiment Station, Vicksburg, Mississippi, August, 1986.

2. Akers, Stephen A., "Uniaxial Strain Response of Enewetak Beach Sand," to be published, U.S. Army Engineer Waterways Experiment Station, Vicksburg, Mississippi, 1986.

3. Baker, Warren J., "Wave-Propagation Studies in Laterally Confined Columns of Sand," Technical Report No. AFWL-TR-66-146, Air Force Weapons Laboratory, Kirtland Air Force Base, New Mexico, June, 1967.

4. Baladi, George Y., and Barnes, Donald E., "An Objective Waveform Comparison Technique," Technical Report SL-83-4, U.S. Army Engineer Waterways Experiment Station, Vicksburg, Mississippi, October, 1983.

5. Baladi, George Y., and Rohani, Behzad, "An Elastic-Viscoplastic Constitutive Model for Earth Materials," Technical Report SL-82-10, U.S. Army Engineer Waterways Experiment Station, Vicksburg, Mississippi, December, 1982.

6. Blouin, Scott E., Martin, Randolph J., III, and McIntosh, Kenneth A., "Laboratory Investigation of the Mechanical Properties of Enewetak Coral Sand," report prepared for the Air Force Office of Scientific Research by Applied Research Associates, Inc., South Royalton, Vermont, May, 1984.

7. Brode, H. L., "A Review of the Nuclear Explosion Phenomena Pertinent to Protective Construction," Report R-425-PR, United States Air Force Project Rand, Rand Corporation, May, 1964.

8. Calhoun, D. E., and Kraft, D. C., "An Investigation of the Dynamic Behavior of a Partially Saturated Silt with Applications to Shock Wave Propagation," report to Air Force Weapons Laboratory by the University of New Mexico, The Eric H. Wang Civil Engineering Research Facility, May, 1966.

9. Cargile, James D., "Geotechnical Investigation for the Cares-Dry Site: Report 2, Laboratory Test Results," Technical Report SL-86-12, U.S. Army Engineer Waterways Experiment Station, Vicksburg, Mississippi, September, 1986.

10. Crawford, Robert E., Higgins, Cornelius J., and Bultmann, Edward H., "The Air Force Manual for Design and Analysis of Hardened Structures," Report AFWL-TR-74-102, Air Force Weapons Laboratory, Kirtland Air Force Base, New Mexico, October, 1974.

11. Cunny, R. W., and Sloan, R. C., "Dynamic Loading Machine and Preliminary Small-Scale Footing Tests," Symposium on Soil Dynamics, Sixty-Fourth Annual Meeting of the American Society for Testing Materials, June, 1961.

12. Dietrich, Richard V., and Skinner, Brian J., "Rock and Rock Minerals," John Wiley & Sons, Inc., 319 pg., 1979.

13. Ehrgott, J. Q., and Sloan, R. C., "Development of a Dynamic High-Pressure Triaxial Test Device," Technical Report S-71-15, U.S. Army Engineer Waterways Experiment Station, Vicksburg, Mississippi, November, 1971.

14. Farr, John V., "Sidewall Friction in the Uniaxial Strain Device," to be published, U.S. Army Engineer Waterways Experiment Station, Vicksburg, Mississippi, 1986.

15. Felice, C. W., Brown, J. A., Gaffney, E. S., and Olsen, J. M., "An Investigation Into the Strain-Rate Behavior of Compacted Sand Using the Split-Hopkinson Pressure Bar Technique," Proceedings of Second Symposium on the Interaction of Non-Nuclear Munitions with Structures, Panama City Beach, Florida, April, 1985.

16. Gaffney, E. S., Brown, J. A., and Felice, C. W., "Soils as Sample for the Split Hopkinson Bar," Proceedings of Second Symposium on the Interaction of Non-Nuclear Munitions with Structures, Panama City Beach, Florida, April, 1985.

17. Green, Mark L., "Shear Friction Test Support Program: Report 1, Laboratory Test Results for WES Flume Sand Backfill," Technical Report SL-86-20, U.S. Army Engineer Waterways Experiment Station, Vicksburg, Mississippi, September, 1986a.

18. Green, M. L., "In Situ Backfill Property Test Program: Report 5, Laboratory Test Results for Silty Clay Backfill," Technical Report SL-86-21, U.S. Army Engineer Waterways Experiment Station, Vicksburg, Mississippi, September, 1986b.

19. Green, M. L., "DISKO-3: Posttest Calculations of Soil Stress and Particle Velocity," to be published, U.S. Army Engineer Waterways Experiment Station, Vicksburg, Mississippi, 1986c.

20. Hadala, P. F., "The Effect of Placement Method on the Response of Soil Stress Gages," Technical Report No. 3-803, U.S. Army Engineer Waterways Experiment Station, Vicksburg, Mississippi, November, 1967.

21. Howard, Amster K., "Laboratory Classification of Soils, Unified Soil Classification System," Earth Sciences Training Manual No. 4, Bureau of Reclaimation, Engineering and Research Center, Denver, Colorado, 1977.

22. Jackson, J. G., Jr., Ehrgott, J. Q., and Rohani, Behzad, "Loading Rate Effects on Compressibility of Sand," Miscellaneous Paper SL-79-24, U.S. Army Engineer Waterways Experiment Station, Vicksburg, Mississippi, November, 1979.

23. Katona, Michael G., "Evaluation of Viscoplastic Cap Model," Journal of Geotechnical Engineering Division, American Society of Civil Engineers (ASCE), Vol. 110, No. 8, August, 1984.

24. Massachusetts Institute of Technology , "The Response of Soils to Dynamic Loads, Report 3, First Interim Report on Dynamic Soil Tests," Publication 104, Report to U. S. Army Engineer Waterways Experiment Station by the Soils Engineering Division of Massachusetts Institute of Technology, Cambridge, Massachusetts, October, 1959.

25. Meier, Roger W., "An Analytical Technique for Use in Examining the Response of Soils to 0.1 MSEC Uniaxial Strain Loadings," to be published, U.S. Army Engineer Waterways Experiment Station, Vicksburg, Mississippi, 1984.

26. Meier, Roger W., "Users Guide to 1-D LAYER," to be published, U.S. Army Engineer Waterways Experiment Station, Vicksburg, Mississippi, 1985.

27. Merrit, J. L., and Newmark, N. M., "Nuclear Geoplosics, A Sourcebook of Underground Phenomena and Effects of Nuclear Explosions, Part Five - Effects on Underground Structures and Equipment, " prepared for the Defense Atomic Support Agency for publication by the Stanford Research Institute, Menlo Park, California, May, 1964.

28. Mitchell, James K., "Fundamentals of Soil Behavior," John Wiley & Sons, Inc. 422 pg., 1976.

29. Moore, Peter J., "The Response of Soils to Dynamic Loadings, Report No. 21: One Dimensional Compression and Wave Propagation in Sand," Research Report R63-43, report to U.S. Army Engineer Waterways Experiment Station by the Department of Civil Engineering, Massachusetts Institute of Technology, Cambridge, Massachusetts, October, 1963.

30. Reynolds Industries, "Operations Manual of Model FS-14 EBW Firing System," Reynolds Industries, Marina del Ray, California, 1978.

31. Sauer, F. M., Clark, G. B., and Anderson, D. C., "Nuclear Geoplosics, A Sourcebook of Underground Phenomena and Effects of Nuclear Explosions, Part Five - Effects on Underground Structures and Equipment," prepared for the Defense Atomic Support Agency for publication by the Stanford Research Institute, Menlo Park, California, May, 1964.

32. Schindler, Larry, "Design and Evaluation of a Device for Determining the One Dimensional Compression Characteristics of Soils Subjected to Impulse - Type Loads," thesis presented to the University of Illinois, Urbana, Illinois, subsequently published as Technical Report SL-68-9, U.S. Army Engineer Waterways Experiment Station, Vicksburg, Mississippi, November, 1968.

33. Schreyer, Howard L., and Bean, James E., "Third Invariant Model for Rate-Dependent Soils," Journal of the Geotechnical Engineering Division, ASCE, Vol. 111, No. 2., February, 1985.

34. Seaman, L., "One-Dimensional Stress Wave Propagation in Soils," report to Defense Atomic Support Agency, prepared and published by the Stanford Research Institute, Menlo Park, California, February, 1966.

35. Seaman, Lynn, "Evaluation of WES One-Dimensional Dynamic Soil Testing Procedures, " Miscellaneous Paper SL-83-8, prepared for the U.S. Army Engineer Waterways Experiment Station by the Stanford Research Institute, Menlo Park, California, June, 1983.

36. Seaman, L., Bycroft, G. N., and Kriebel, H. W., " Stress Wave Propagation in Soils," report for Defense Atomic Support Agency under Contract DA-49-146-XZ-018, Stanford Research Institute, Menlo Park, California, May, 1963.

37. Smith, Joseph A., and Glover, Tracy A.,"Hopkinson Bar Simulation Using DYNA2D," Proceedings of Second Symposium on the Interaction of Non-Nuclear Munitions with Structures, Panama City Beach, Florida, April, 1985.

38. United States Atomic Energy Commission, "The Effects of Nuclear Weapons," prepared by the United States Department of Defense, 730 pg., Februaury, 1964.

39. Wilson, Stanley D., and Sibley, Earl A., "Ground Displacements From Air-Blast Loading," Journal of the Soil Mechanics and Foundations Division, Proceedings of the American Society of Civil Engineers, December, 1962.

40. Windham, J. E., "Shear Friction Test 2-3: Presentation of Test Results," to be published, U. S. Army Engineer Waterways Experiment Station, Vicksburg, Mississippi, August, 1985.

41. Whitman, Robert V., "The Response of Soils to Dynamic Loading, Report No. 17: Stress-Strain-Time Behavior of Soil in One Dimensional Compression," Contract Report R63-25, U.S. Army Engineer Waterways Experiment Station, Vicksburg, Mississippi, May, 1963.

42. Whitman, R. V., "Nuclear Geoplosics, A Sourcebook of Underground Phenomena and Effects of Nuclear Explosion, Part Two - Mechanical Properties of Earth Materials, Soils Section," prepared for the Defense Atomic Support Agency for publication by the Stanford Research Institute, Menlo Park California, May, 1964.

43. Whitman, R. V., "The Response of Soils to Dynamic Loadings, Report 26: Final Report," Contract Report No. 3-26, U.S. Army Engineer Waterways Experiment Station, Vicksburg, Mississippi, May, 1970.

44. Zaccor, J. V., Mason, H. G., and Walter, D. F., "Study of the Dynamic Stress-Strain and Wave-Propagation Characteristics of Soils; Report 1, Concepts, Equipment, and Techniques for the Study of the Dynamic Behavior of Soils," Contract Report 3-91 to the U.S. Army Engineer Waterways Experiment Station, United Research Services, November, 1964.

43. Zukas, Jonas S., Nicholas, Theodore, Swift, Hallock F., Greszczuk, Longin B., and Curran, Donald R., "Impact Dynamics," John Wiley & Sons, 452 pg., 1982.

DISTRIBUTION LIST

Defense Technical Information Center
ATTN: TC
Cameron Station
Alexandria, VA 22314

Director
Defense Nuclear Agency
ATTN: SP (Dr. D. A. Linger)
SPSS (Mr. C. B. McFarland)
SPSS (CPT Michael A. Reed)
SPSS (Dr. Chester Canada)
Technical Library
Washington, DC 20305-1000

Director Defense Advanced Research
Project Agency
ATTN: Technical Library
1400 Wilson Blvd.
Arlington, VA 22209

Director Defense Intelligence Agency
ATTN: Technical Library
Washington, DC 20301

Commander
Ballistic Missile Office (AFSC)
ATTN: MGET (MAJ D. J. Peters)
MYEB (LTC D. H. Gage)
Norton Air Force Base, CA 92409-6468

Air Force Weapons Laboratory (AFSC)
ATTN: NTEDE (Mr. J. N. Thomas)
NTESG (CPT Conrad W. Felice)
Technical Library
Kirtland Air Force Base, NM 87117

Air Force Office of Scientific Research
ATTN: AFOSR/NA
Bolling Air Force Base, DC 20332

Air Force Engineering and Services Center
ATTN: Technical Library
Tyndall Air Force Base, FL 32403

Air Force Institute of Technology
Air University
ATTN: Technical Library
Wright-Patterson Air Force Base, OH 45433

Commander
U.S. Army Corps of Engineers
ATTN: DAEN-RDM (Mr. B. O. Benn)
DAEN-RDL (Ms. Sharon Vannucci)
DAEN-ECE-T (Mr. R. L. Wight)
DAEN-ASI-L
Washington, DC 20314

Director
U.S. Army Construction Engineering
Research Laboratory
ATTN: Technical Library
P. O. Box 4005
Champaign, IL 61920

Commander/Director
U.S. Army Cold Regions Research and Engineering
Laboratory
ATTN: Technical Library
P. O. Box 282
Hanover, NH 03755

Commandant
US Army Engineer School
ATTN: Technical Library
Ft. Belvoir, VA 22060

Commander
Ballistic Missile Defense Systems Command
Department of the Army
ATTN: BMDSC-HLE (R. C. Webb)
P. O. Box 2500
Huntsville, AL 35807

Commander
US Army Laboratory Command
ATTN: Technical Library
2800 Powder Mill Road
Adelphi, MD 20783-1145

Commander
US Army Nuclear and Chemical Agency
ATTN: Technical Library
7500 Backlick Road, Bldg. 2073
Springfield, VA 22150

Deputy Chief of Staff for Research,
Development and Acquisition
Department of the Army
ATTN: Technical Library
Washington, DC 20310

Naval Civil Engineering Laboratory
ATTN: Technical Library
Port Hueneme, CA 93043

Naval Facilities Engineering Command
ATTN: Technical Library
200 Stovall Street
Alexandria, VA 22332

Lawrence Livermore National Laboratory
ATTN: Ms. Barbara C. Davis (L-196)
Technical Library
P. O. Box 808
Livermore, CA 94550

Los Alamos National Laboratory
ATTN: Technical Library
P. O. Box 1663
Los Alamos, NM 87545

Sandia National Laboratories
ATTN: Technical Library
P. O. Box 5800
Albuquerque, NM 87185

Sandia National Laboratories
ATTN: Technical Library
Livermore, CA 94550

Mr. J. L. Bratton
Dr. C. J. Higgins
Applied Research Associates, Inc.
4300 San Mateo Boulevard, NE, Suite A220
Albuquerque, NM 87110

Mr. S. E. Blouin
Applied Research Associates, Inc.
South Royalton, VT 05068

Dr. J. G. Trulio
Applied Theory, Inc.
930 S. LaBrea Avenue
Los Angeles, CA 90036

Dr. S. L. Strack, Mail Stop 13-13
Boeing Aerospace Company
P. O. Box 3999
Seattle, WA 98124

Mr. K. N. Kreyenhagen
Dr. Y. Marvin Ito
Mr. S. H. Schuster
California Research & Technology, Inc.
20943 Devonshire Street
Chatsworth, CA 91311-2376

Dr. D. L. Orphal
California Research & Technology, Inc.
5117 Johnson Drive
Pleasanton, CA 94566-3343

Dr. E. J. Rinehart
California Research & Technology, Inc.
1900 Randolph Rd, SE, Suite B
Albuquerque, NM 87106

Mr. John Karagozian
Karagozian and Case Structural Engineers
1100 Fair Oaks Avenue
South Pasadena, CA 91030-3312

Mr. P. E. Pagel, Mail Stop D-6374
Martin Marietta Denver Aerospace
P. O. Box 179
Denver, CO 80201

Dr. R. D. Woods
Dr. R. D. Hryciw
Dr. F. E. Richart, Jr.
The University of Michigan
Department of Civil Engineering
2232 G. G. Brown Bldg.
Ann Arbor, MI 48109

New Mexico Engineering Research Institute
ATTN: Dr. H. L. Schreyer
       Technical Library
Box 25, University Station
University of New Mexico
Albuquerque, NM 87131

Dr. R. T. Allen
Pacifica Technology
P. O. Box 148
Del Mar, CA 92014

Dr. J. L. Chameau
Dr. R. D. Holtz
Purdue University
School of Civil Engineering
Grissom Hall
West Lafayette, IN 47907

Mr. J. G. Lewis
Mr. Don Simons
R&D Associates
P. O. Box 9695
Marina del Rey, CA 90291

Dr. John Schatz
Science Applications International Corporation
P. O. Box 2351
La Jolla, CA 92038-2351

Mr. Stephen Peyton
Dr. H. E. Read
S-Cubed
P. O. Box 1620
La Jolla, CA 92038-1620

Dr. Lynn Seaman
Dr. Mohsen Sanai
SRI International
333 Ravenswood Avenue
Menlo Park, CA 94025

Mr. S. J. Green
Mr. William Klauber
Terra Tek, Inc.
420 Wakara Way
Salt Lake City, UT 84108

Mr. Norman Lipner
Dr. M. B. Balachandra
Dr. Richard Cramond, Jr.
Dr. M. G. Katona
TRW Defense Systems Group
P. O. Box 1310
San Bernardino, CA 92402

Dr. D. J. Ness, Bldg. 134/Rm 9835
TRW Defense and Space Systems Group
One Space Park
Redondo Beach, CA 90278

Dr. Ivan S. Sandler
Dr. Ivan Nelson
Weidlinger Associates
333 Seventh Avenue
New York, NY 10001

Dr. Jeremy Isenberg
Dr. H. S. Levine
Weidlinger Associates
620 Hansen Way, Suite 100
Palo Alto, CA 94304